Examining the taphonomic challenges to the 3D digitisation of fragmented bone.

Volume I of II

Andrew David HOLLAND

Submitted for the Degree of

Doctor of Philosophy

School of Archaeological and Forensic Sciences

University of Bradford

2017

Abstract

The utilisation of 3D digitisation and visualisation has grown considerably since 2008 and is becoming an increasingly useful tool for the digital documentation and metric analysis of archaeological artefacts and skeletal remains. It provides public access to rare and fragile specimens of palaeontological and palaeopathological importance whilst reducing the physical impact on these remains.

Research in engineering and computer vision provides some insight into the impact of surface properties such as colour, specularity, reflectance and shape on the quality of the recorded 3D image, but within the archaeological and palaeontological disciplines comparable work has not yet been developed.

If archaeology and anthropology are to provide long term reliable data from archaeological and palaeontological specimens in a way that doesn't require repeated re-digitisation, we need to understand the impacts that the taphonomic histories of such samples have on our ability to 3D record them. Understanding the relationship of these taphonomic histories and the surface and optical properties will promote informed choices about the suitability of recording techniques.

This thesis considers the taphonomic processes that affect the preservation of bone over archaeological, forensic and palaeontological timescales and the effect this has on the quality of 3D digital models. The digital refit of fragmentary bone samples is considered in relation to the effect of taphonomic alterations to bone.

Conclusions regarding the key taphonomic factors and 3D digital model quality are drawn and areas of further work are identified.

Keywords: Laser Scanning, Structured Light, Photogrammetry, Weathering, Degradation, Fossil Bone, Demineralised Bone, Collagen Loss, Metrology

Supervisors

Principal supervisor: Dr. Andrew S. Wilson
Associate supervisors: Prof. Hassan Ugail
Dr Louise Leakey

Acknowledgements

I would firstly like to thank Dr. Andrew Wilson for encouraging my interest in 3D digitisation and for his supervision, support, patience and encouragement throughout the research. I would also like to thank Professor Hassan Ugail and Dr Louise Leakey who co-supervised this research and offered support and guidance on more specific aspects.

I would like to acknowledge the support provided by the Arts and Humanities Research Council who funded this research through a studentship.

For access to samples I would like to thank the MONREPOS Archaeological Research Centre and Museum for Human Behavioural Evolution in Neuwied, Germany who provided a travel stipend to visit the museum to digitise the Schöningen material. The Turkana Basin Institute Ileret field research centre for the opportunity to digitise amazing fossil material. In particular I would like to thank Professor Maeve Leakey and Professor Mikael Fortellius for detailed and engaging discussion on extinct fossil taxa. The British Museum at Franks House, London for access to the scanner to digitise some samples. The Star Carr research team for access to the Star Carr frontlet material. Thanks also to John Edwards of Edwards Analytical, Durham for exposing bone samples in the Hereaus Suntester.

Many people have supported this research in some way and deserve wholehearted thanks: my colleagues in the PhD office who have supported me, sometimes with useful and interesting advice, and sometimes with distraction and cake; my friends and family who have repeatedly shown their faith in me, supported me and kept me believing this research was possible. The Fragmented Heritage and Bradford Visualisation teams for their support. Several people have kindly provided the free use of images under creative commons, they are credited at the appropriate point in the text.

And finally I am hugely indebted to Kirsten for your love, support and encouragement. You have kept me going, never losing faith in me even at the most trying and difficult points. And also for the huge amount of more practical help as reference wrangler, excel data magician and as my editor reading and commenting on every single word of every draft. I would never have achieved this without you.

Table of Contents

Volume I of II

Volume II of II

List of Figures

List of Tables

Chapter 1. Introduction

As a material that survives at a gross level for a significant time depth in the archaeological record, long after many other forms of biological evidence have decayed, bone forms a critical function in our understanding of the past. The major physiological factors of our lives are indelibly marked onto our skeletal structure: disease, nutrition, trauma, as well as the physical activities of people in the past can be traced through their skeletal remains.

Archaeology and anthropology, and their allied forensic sub disciplines, attempt to decipher these indications of past events and lives. Whilst the physical proportions of skeletal elements provide the stature, age, sex etc., fracture patterns, blade and ballistic injuries may illuminate both the perimortem events leading to an individual's death, but also, through the study of healed injury, the medical and technological skill of the individual's past society.

In forensic cases, the determination of these attributes provide for the forensic individualisation of otherwise unidentified remains, giving back the deceased's identity and providing a foundation on which further criminal investigation can be built.

At a biomolecular level, bone encapsulates information in the form of proteins, DNA, isotopic signatures and the biomarkers of disease microbes which all speak to the relationships, travel, diet and environment of the past. Due to its chemical and physical properties bone behaves as an ion exchange medium and thus, through fossilisation, is preserved from the deep past to provide a primary source for the study of our earliest ancestors, their physical capabilities and the development of our human species.

However, the robusticity of skeletal material from the past is deceptive, once in the depositional environment, bone is fragile, brittle and easily fragmented. Surface evidence of disease and activity may be easily removed with too vigorous handling. Fossil hominid remains are rare, and often incomplete. These factors make bone a finite resource and pressure of access to skeletal material becomes a key factor in its long term curation.

Approaches to curation in cultural heritage have in general, concentrated on limiting access and handling of material to reduce, but not eliminate, the inevitable damage, but this approach also risks reducing scientific discovery, public engagement and understanding. The latter is particularly pertinent to human skeletal material as it is often limited in its museum presentation to the public, due to the considerations of ethics and moral suitability.

Recording methods have attempted to bridge this gap between demand for access and curatorial protection, with hand drawings, measurements and high quality photography all offering some limited success. More recently the adoption of 3D digital recording techniques from the engineering sciences have been explored to give high fidelity 3D facsimiles of cultural heritage material with some notable high profile examples including the Smithsonian X 3D project (Smithsonian Institute 2016).

3D digitisation of skeletal material has offered a tool for its greater preservation, increased access and public engagement, with the display of 3D images of skeletal remains being considered ethically more justifiable than that of the original material itself. A series of major projects have recently used 3D digitisation to provide access to human and faunal (both extant and extinct) remains online including several projects at the University of Bradford (e.g. From Cemetery to Clinic (www.barc.brad.ac.uk/FromCemeterytoClinic), Digitised Diseases (www.digitiseddiseases.org) and Visualising Animal Hard Tissues (www.3dbones.org/visual/)).

Furthermore, whilst the metric analysis of skeletal material had previously been limited to 2D measurements, with shape only examined through the relationship of a limited number of these 2D measurements, 3D digitisation has opened new avenues of research for the metric analysis of both archaeological artefacts and skeletal remains, taking 3D digitisation beyond just recording or imaging, and into its rightful place as an investigative tool.

Within engineering and computer vision, research is already examining the impact of surface properties such as colour, specularity, reflectance and shape on the quality of the recorded 3D image, but within archaeology, anthropology and palaeontology, comparable work has not yet been developed.

Whilst some of these engineering studies can inform research in archaeology and anthropology, engineering based 3D digitisation technologies were designed for quality assuring manufactured engineering parts, and therefore are optimised for newly machined materials with the uniform and uncorroded surfaces of such parts. Engineering materials do not, therefore, always provide suitable or comparable data to their archaeological counterparts.

Furthermore, the recording of complex biological tissues such as bone hold greater challenges than the engineering literature can currently answer and the taphonomic changes that such biological materials undergo, within the buried or surface deposition environments add further complexities.

The engineering research becomes less applicable as the 3D recording of archaeological material expands beyond simple recording and becomes an investigative tool. The recording, reconstruction and estimation of the mechanical properties of fragmentary archaeological remains provide an important example; such research requires an understanding of the taphonomic and fracture mechanics of degraded bone, and such data and understanding is not available from the engineering literature.

If archaeology and anthropology are to provide long term reliable data from archaeological and palaeontological specimens in a way that doesn't require repeated re-digitisation, we need to understand the impacts that the taphonomic histories of such samples have on our ability to 3D record them, to understand the influence of their surface and optical properties and to be able to make informed choices about the suitability of recording techniques.

If 3D digitisation in archaeology and anthropology is to go beyond simple 3D recording of images and become a reliable tool for the measurement of 3D volume, shape etc. and to use these measurements as the basis for further investigation of fracture surface matching, artefact condition monitoring, physical load and capability modelling etc. then understanding the taphonomy of archaeological materials and its interaction with 3D recording quality is an essential pre-requisite for reliable and reproducible data.

Finally, if 3D recording is to form a part of the long term archaeological archive, we need to know what the best methodology is for a given type of material and

for a given level of preservation, in order to improve interpretation and inform conclusions derived from the data in future work.

The following thesis presents research into the effects of taphonomic processes on mammalian bone, and the interaction of the changes to the surface properties of bone induced by such taphonomic processes on the quality of a range of 3D digitisation techniques.

1.1. Aim

The aim of this research is to examine the effect of taphonomic changes to mammalian bone on the outcome of 3D digital recording methods and the digital refit of fragmentary bone.

1.2. Objectives

The objectives of this research are to:

- Survey existing literature and manufacturer's documentation for differing 3D digital recording techniques and assess their potential for recording degraded mammalian bone;
- Create technique comparison standards to assess the response of 3D digitisation techniques to the colour, opacity and surface roughness properties of objects;
- Use accelerated laboratory degradation and natural field-based exposure methods to simulate taphonomic change to mammalian bone;
- Assess the impact of the taphonomically induced changes to bone on the quality of 3D digitisation techniques;
- Carry out a comparison of 3D digitisation techniques by recording the same experimentally degraded bone samples with each technique and comparing their response; and
- Examine the impact of taphonomic changes on the digital refitting of fractured experimentally degraded bone samples and compare it to similar fragmentary material from archaeological and palaeontological examples.

1.3. Fragmented Heritage project

The research in this thesis was completed as a funded doctoral award within the Fragmented Heritage project. Fragmented Heritage is an Arts and Humanities Research Council funded beacon project in the area of digital transformation and aims to introduce new technology to dramatically improve the scale and quality of the analysis of fragmentary materials from the past.

The project takes a multi scale approach to fragmentary heritage materials, from the refitting of artefacts within sites, to landscape survey to identify and reconnect diffused sites and material (Fragmented Heritage 2013).

At the object scale the project is developing the use of computer automation to digitally refit lithic tool cores from the flakes found across sites in order to elucidate social and behavioural patterns in the past. The research in this thesis explores the challenges that need to be addressed to extend the Fragmented Heritage refit system to fragmentary bone.

When carrying out field survey work humans subconsciously bias the search areas, avoiding unstable surfaces, steep terrain and using past experience to positively reinforce probable search areas. The Fragmented Heritage project is exploring new technological approaches to addressing this through a focus on 'Citizen Science' where members of the public take part in the primary data analysis. An initial field trip to the fossiliferous bearing beds at Lake Turkana, Kenya to collect high precision aerial imagery of the ground surface was supported by project partners Turkana Basin Institute and the National Museums of Kenya. The citizen science analysis is carried out online via the project's Fossil Finder website (www.FossilFinder.org) using the 'wisdom of crowds' to map the locations of fossil and artefact locations on the aerial imagery. To validate this approach the Fragmented Heritage team have carried out several field visits to ground truth the initial results and 3D digitise some of the identified material. A selection of fragmentary material from these trips is examined within this thesis.

1.4. Thesis structure

Chapter one outlines the project rationale, aims and objectives, the placement of the research within the wider Fragmented Heritage project and introduces the thesis.

Chapter two summarises the structure, gross anatomy, chemical, histological and biological makeup of bone.

Chapter three summarises the taphonomic changes that occur to bone in the depositional environment and considers the mechanics of bone fracture and fragmentation.

Chapter four summarises 3D digitisation techniques and outlines a brief history of their use within the study of both the past and of skeletal elements.

Chapter five describes the methodology behind sample selection, the exemplar case sites and the production of both experimentally degraded bone samples and baseline technique comparison standards used as targets for digitisation.

Chapter six describes the digitisation methodologies used and the post processing of the digital data.

Chapter seven presents the results of the analyses applied to the samples.

Chapter eight uses the data to discuss the challenges to the study and digitisation of fragmentary bone using 3D digitisation technologies.

Chapter nine draws out aspects of the methods and data which add to the field of 3D digitisation in heritage including novel and unexpected findings. The potential for further work is discussed.

Chapter 2. Mammalian bone

The fracture and fragmentation properties of bone are governed by their composition and microstructure and these in turn influence the physical and optical properties which dictate the quality of 3D imaging techniques (chapter four). Furthermore, the taphonomic changes that occur to bone within a variety of depositional environments (chapter three) are driven by and alter the underlying complex and varied structure of bone at a gross and histological level. Additionally, the selection of suitable animal analogues for human bone (chapter five) relies on an understanding of the differences in biochemistry, formation and histology of bone from differing species. The following chapter describes the gross anatomy, biochemical composition, structures and histology of mammalian bone.

The bones of mammalian skeletons have a fourfold function: to support the body distributing the mechanical loads and providing protection to the internal organs; to act as attachment points for the musculature and the tendons (Benjamin et al. 2006); to act as a store for minerals needed by the body or sequestered from doing harm to the body (e.g. heavy metals) (Copp & Shim 1963, Confavreux 2011); and to provide a highly vascularised area for the storage of fat (the yellow marrow) and production of white and red blood cells (the red marrow) (Bain et al. 2009, Farhi 2009).

At a basic level, bone is a bio-composite material formed from a fibrous organic matrix of long protein chains (20% by dry weight), in-filled with an insoluble inorganic material (70% by dry weight) (Mays 2010) with a fine crystalline structure, the principal components of which are calcium and phosphate in the form of hydroxyapatite or biological apatite. The remaining 10% by weight of dry human bone is water, held by the strong hydrophilic attraction of both the mineral and proteinaceous phases.

2.1. General characteristics of mammalian bone

The structure of human and other mammalian long bones is that of a tubular dense outer cortex (cortical bone) varying in thickness based upon the mechanical load and muscle attachment points, supported at each end of the bone and, where changes in loading occur, with trabecular (or cancellous) bone.

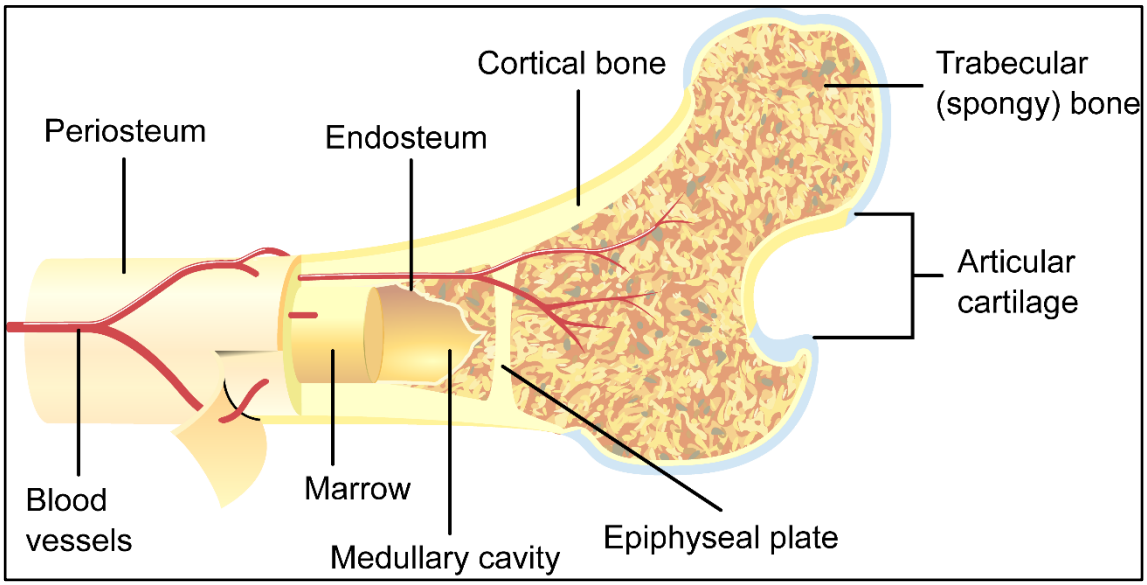

Figure 2.1: Cut away diagram showing the main structures of long bones (Image "The cross-section of a bone" by Ryan Wilson is licenced under CC BY 3.0).

The central medullary cavity (figure 2.1) within long bones is filled with "bone marrow" a mixed set of tissues which vary in function from the "yellow marrow" which primarily stores fat in the centre of long bones adjacent to areas of cortical bone, to "red marrow" which is primarily found at the distal and proximal ends of the bone surrounding the trabecular bone and which is filled with hematopoietic (blood forming) cells.

Bone is covered on the outside surfaces by the periosteum and on the internal surfaces by the endosteum.

2.1.1. Cortical bone

Cortical bone is that which makes up the outer shell (or cortex) of bones and which accounts for 80% of the weight of the skeleton in adults (Clarke 2008). Cortical bone is composed of primary or secondary lamellar bone, although the

cortex of the long bones of rapidly growing mammals such as sheep and cattle may also include plexiform bone. The cortical bone is highly organised compared to woven bone (section 2.2.1) and cortical bone can be distinguished from trabecular bone at the microscopic level based on the presence of secondary osteons and their Haversian canals which carry one or more blood vessels large enough to supply blood, oxygen etc. to the thicker cortical structures (Cowin 1999, Lubarda et al. 2012).

2.1.2. Trabecular bone

Trabecular or cancellous bone forms a spongy network of lattice-shaped spicules or trabeculae first accurately described and illustrated by Cisóstomo Martinez in the late 17th century (Gomez 2002, Valverde 2009). The network of thin trabeculae (figure 2.2) provides structural stability as well as flexibility with a greater degree of elasticity compared to cortical bone (Lubarda et al. 2012).

As with cortical bone the mature trabeculae are constituted of lamellar bone but differ from the secondary lamellar structure of the cortex in that their 200 μm diameter does not provide sufficient room for remodelling via the formation of secondary osteons whilst maintaining their integrity. Without the presence of vascular channels to supply nutrients, trabeculae can only be remodelled from their surface resulting in lamellar bone that is histologically organised in crescent shaped packets called hemiosteons (van Oers et al. 2008).

Figure 2.2: 3D models obtained from micro-CT of the distal femur of transgenic mice highlighting the trabecular structure (blue) and the cortical bone (light grey) (after Dumas et al. 2009 p. 439).

The thinness of trabeculae, and the lack of the blood vessel carrying Haversian canals, mean that trabeculae can be supplied via the canaliculi linked to the surrounding red, hematopoietic, bone marrow. Thus, trabecular bone is both highly porous and highly vascularised

(Barou et al. 2002) and accessible to groundwater and microbiota in the depositional environment. The high degree of vascularisation and high surface area to volume ratio (a healthy adult human has a trabecular surface area of c. 7 m^2 (Clarke 2008)) allows the bone mineral within trabeculae to act as a bio-accessible store of calcium and phosphorous thus facilitating hormonal regulation of calcium and phosphorous levels within the blood (DeLuca 1979); as such trabecular bone is affected to a greater extent by osteoporosis in mature adults than cortical bone (Thompson et al. 1995).

The alignment of the trabeculae show a strong correlation with the direction of mechanical loads on the bone (Pidaparti & Turner 1997, Huiskes et al. 2000) and their small size and high osteogenic potential mean that trabecular structures can alter to reflect changes in mechanical load on a bone over time.

2.1.3. Articular surfaces

The articular surfaces of synovial joints in long bones are covered by hyaline cartilage over subchondral bone. The hyaline cartilage is a layer of between 2 mm and 4 mm in thickness. Hyaline cartilage is avascular and is formed of an extracellular matrix of collagen fibres (predominantly type II and IX) with evenly dispersed chondrocytes in lacunae. The hyaline cartilage forms a smooth joint surface protecting the underlying subchondral bone from abrasion and shock compression forces. The subchondral bone is formed of two parts: a subchondral bone plate of cortical bone that overlies the subchondral vascular spaces and subchondral trabecular bone. The deepest layer of the hyaline cartilage at the junction with the subchondral bone plate are usually mineralised, showing a distinct line of mineralisation (the ‘tide mark’) (Hoemann et al. 2012), but the difference between vascularised subchondral bone plate and avascular mineralised hyaline cartilage can be distinguished in SEM imagery (Clark & Huber 1990, Milz et al. 1995).

2.1.4. Periosteum and endosteum

Bone is covered on both the external and internal surfaces by the periosteum and endosteum respectively (figures 2.1, 2.3 & 2.8), connective tissue membranes that contain osteogenic potential and which derive from the aggregation and differentiation of stem cells in the early stage of bone formation *in utero*.

The periosteum covers the whole external surface of the bone (figure 2.1) except those areas covered with cartilage (i.e. the joint surfaces), and is made up of two layers.

The outermost layer is a structural fibrous layer (figure 2.3) of collagen fibres with embedded fibroblasts and incorporating the nerve cells and larger blood vessels which penetrate through the periosteum and supply the osteocytes in the underlying bone via the Volkmann's canals (section 2.2.4).

The inner cambium layer (named for its similarity to the cambium layers of trees), is a sparse matrix of collagen which holds differentiated osteogenic progenitor cells, fibroblasts and osteoblasts, the latter of which are held in contact with the underlying cortical bone surface and are responsible for appositional bone growth around the circumference of the bone.

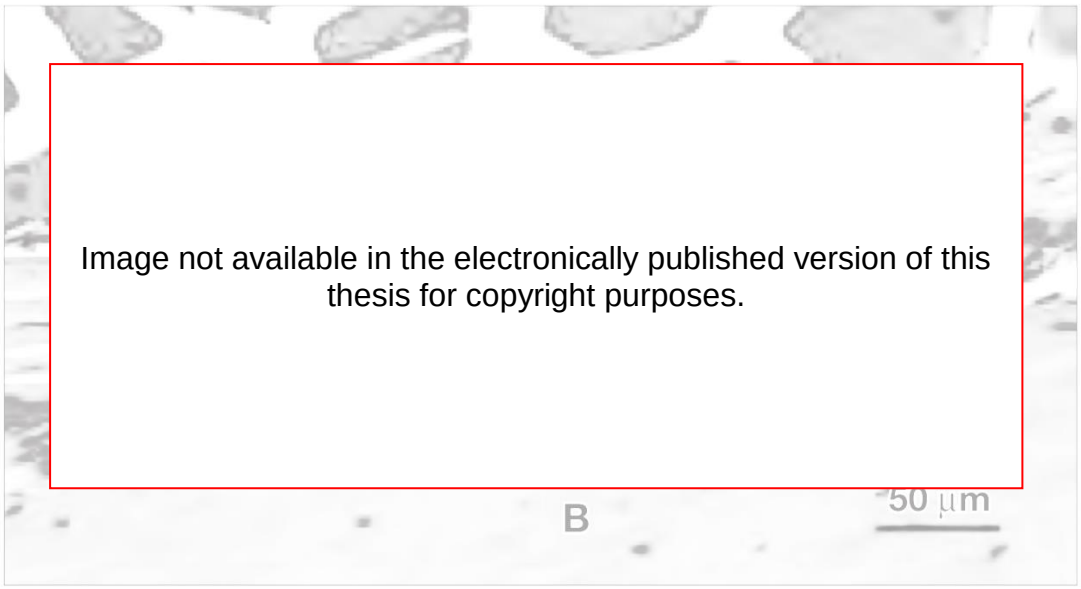

Figure 2.3: Photomicrograph of rat periosteum. B: bone; CP: cambium layer of periosteum; FP: fibrous periosteum; M: muscle. Stained with haematoxylin and eosin (Burr & Guillot 2012 p.224).

The highly osteogenic nature of the cambium is responsible for the rapid stage of primary lamellar bone formation in foetuses when the cambium is at its thickest (Dwek 2010). The cambium also anchors the periosteum to the outer lamellar layer of the cortical bone via collagenous Sharpey's fibres (Junqueira & Carneiro 2005).

The endosteum surrounds the bony trabeculae and forms the lining of the central medullary cavity of the bone as well as the Haversian canals and the internal surfaces of compact bones. Unlike the periosteum, it is formed of a single layer, with flat spindle like endosteal cells held within a loosely organised structure of connective tissue (Islam et al. 1990).

2.2. Bone Microstructure

From a histological viewpoint, all mammalian bone can be considered in two basic types: lamellar and woven bone (White & Folkens 2005) and distinguished by the level of organisation of the collagenous fibres laid down to initially form the bone. Cortical lamellar bone can be further divided into primary and secondary lamellar bone by the type of osteons present.

In addition, a composite of woven and lamellar bone, plexiform bone, is found in the bones of some rapidly growing mammals.

2.2.1. Woven bone

Woven bone is the first bone to form in response to pathology as part of the inflammatory response (e.g. sub-periosteal new bone formation and fracture calli). It is characterised by a coarse, fibrous and poorly organised structure made up of bundles of collagen fibres in a random pattern (Smith 1960) that show no directional orientation in line with the direction of load. The irregular arrangement of the collagen fibres (figure 2.4) that give it its woven appearance (and hence its name) result from the rapid production of osteoid (the organic component of bone, (section 2.4)) by the osteoblasts.

The high cell count of osteocytes at the site of deposition of woven bone allows bone formation and initial mineralisation to occur quickly, but with lower mineral density levels than lamellar bone, leading woven bone to be weaker in compression, but more flexible than lamellar bone (Buckwalter et al. 1995).

Whilst woven bone forms in two different situations (foetal initial ossification and in response to pathology), the bone is otherwise similar (Mays 2010).

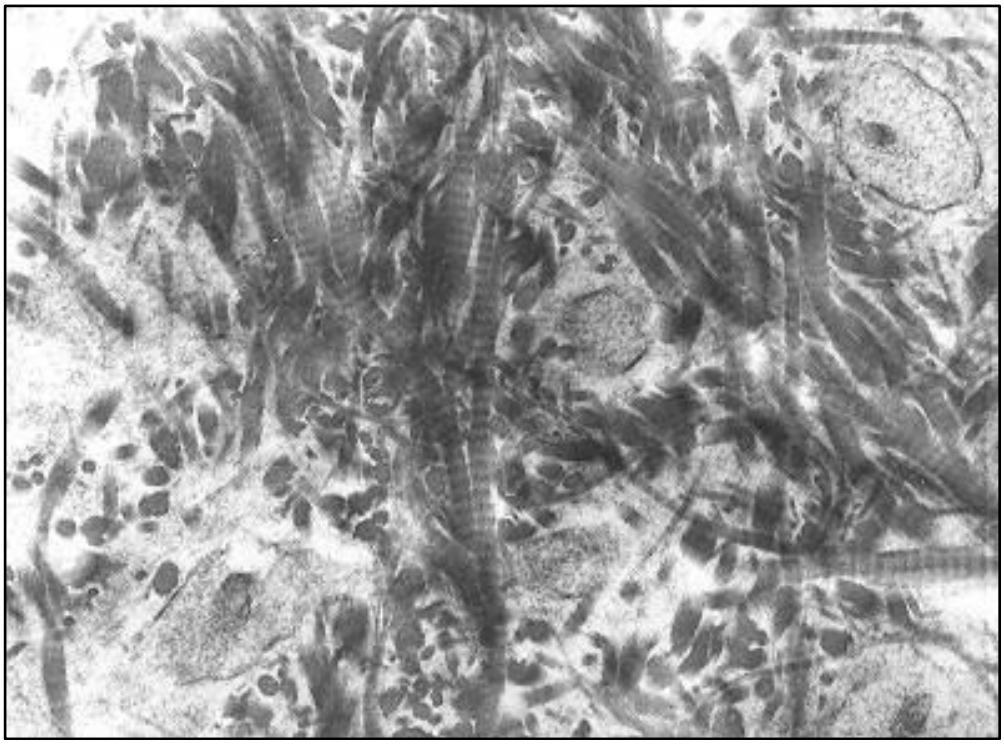

Figure 2.4: Transmission electron micrograph of disorganised collagen fibres in decalcified woven bone matrix (Image: "Woven Bone" by Robert M Hunt is licenced under CC BY 3.0).

2.2.2. Lamellar bone

The compact bone of the cortex and more porous trabecular bone are composed of mature or lamellar bone. Lamellar bone, by contrast to woven bone, exhibits parallel layered or lamellar organised structure (figure 2.5). Initially built up as layers of dense bone during appositional growth (De Ricqles et al. 1991), it is later remodelled by osteoclast and osteoblast activity in either secondary osteon (cortical bone) or hemiosteon (trabeculae) structures. This more complex lamellar structure has been shown to be phylogenetically a more recent evolution than woven bone

Figure 2.5: Mature trabecular bone exhibiting lamellae (after de la Roza & Damron 2016).

(White & Folkens 2005) and the resulting lamellar bone has a higher mineral density and greater strength under compression than woven bone (Kini & Nandeesh 2012).

The concentric lamellae sheets of lamellar bone have collagen fibrils orientated in a regular direction, and are laid down more slowly than woven bone at a rate of less than 1 µm per day (Boyde 1980). The regular direction of collagen fibrils in textbook models of lamella is normally described as having all the fibrils orientated in a single direction, but as Currey points out (Currey 2012) this is an oversimplification, arguing that fibrils are constant only within “small domains” of approximately 30 µm - 100 µm across, but that they vary in direction within the lamella. However adjacent lamellae do exhibit generally differing orientations of fibrils which provides additional strength to the bone. This characteristic has been compared to the opposing direction of grain in layers within ply board by Giraud-Guille (1988) and Francillon-Vieillot et al. (1989) and the analogy is broadly comparable.

2.2.3. Cortical primary lamellar bone

Cortical primary lamellar bone is formed by the deposition of lamellar bone around the shaft of the diaphysis leading to increase in the bone diameter and increasing cortical thickness.

Nutrients cannot diffuse rapidly enough through the calcified tissue of bone to maintain and nourish the cells beyond 250 µm of a nutrient source (blood vessel). As the circumferential lamellae of the new bone cortex is laid down at the periosteal - bone junction through appositional deposition, the vascular network within the periosteum forms vascular channels in the newly deposited lamellar bone. These channels are then infilled by the deposition of bone by osteoblasts lining the bone surface to produce concentric lamellae with blood, nerve and lymphatic vessels at its centre. These primary osteons form the characterising structure of primary lamellar bone and provide the nutrient supply for the bone cells.

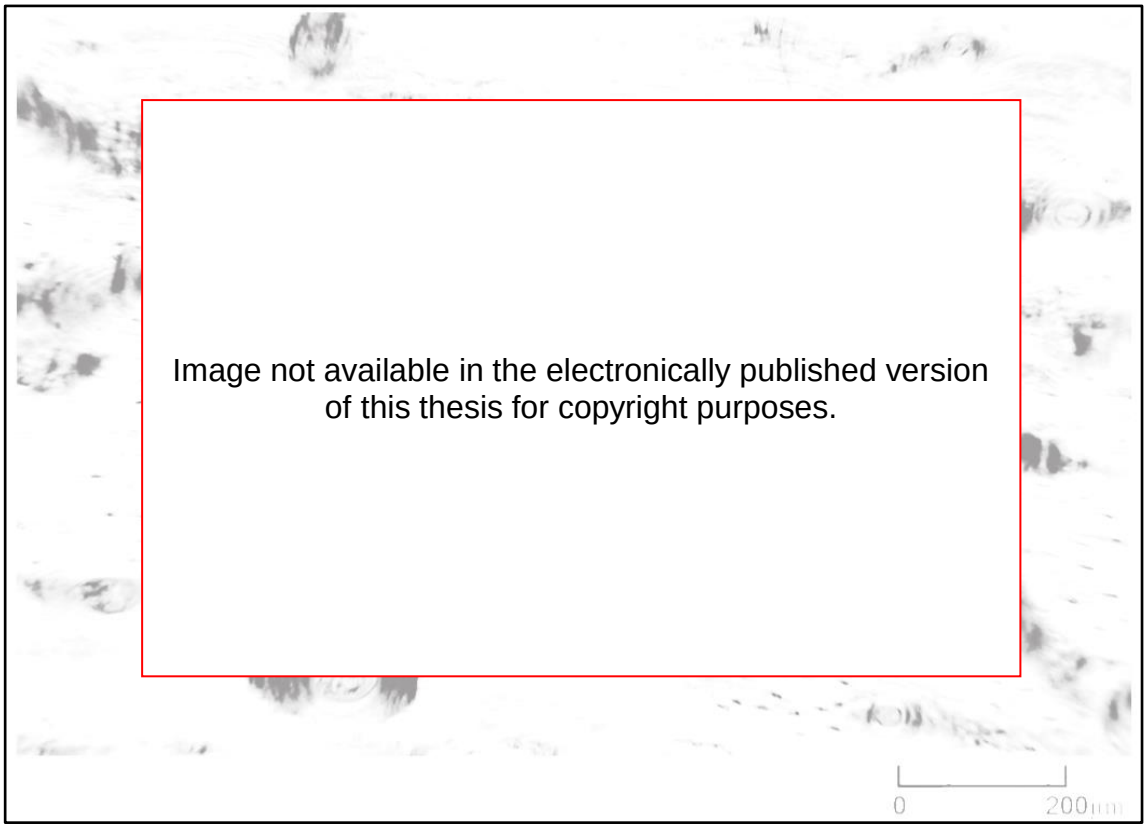

Figure 2.6: Transverse section of human femur showing primary lamellar bone structure with primary osteons (Cuijpers 2009 p. 79).

Primary osteons can be distinguished from secondary osteons (and hence secondary lamellar bone) by the level of integration of the outer lamellae of the primary osteons with the surrounding bone (lacking a cement line), their smaller size (50 µm – 100 µm in diameter) and the small number of concentric lamellae (< 10) (Burr & Akkus 2014).

2.2.4. Cortical secondary lamellar bone

Cortical secondary lamellar bone is characterised by the presence of secondary osteons which resorb and replace existing bone. Secondary osteons develop as a reaction to the biomechanical loads on bone and cut through the original primary lamellar structure. Osteon formation is driven by blood borne osteoclast cells which erode through the bone in an approximately 200 µm x 300 µm cone (Martin & Burr 1982). As the cone is eroded, osteoblast cells deposit osteoid (an organic matrix mostly made up of collagen) onto the walls of the cavity which is mineralized into lamellae in concentric rings, eventually producing a column within the original bone (figure 2.7) and entrapping osteoblasts within small cavities between the lamellae to form osteocytes (section 2.2.5).

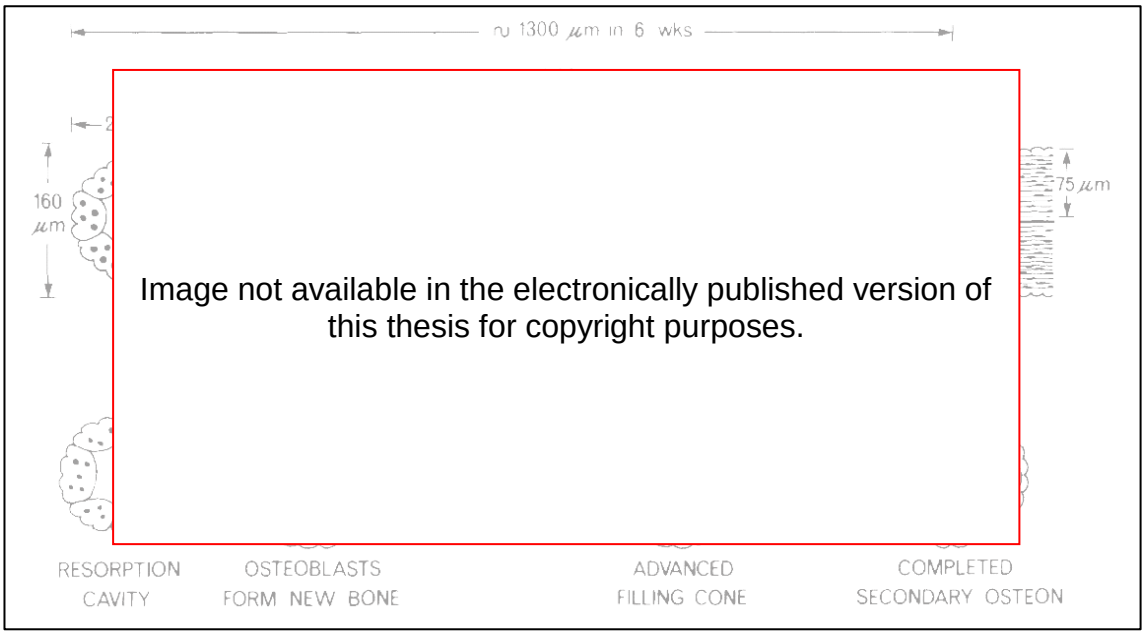

Figure 2.7: Secondary osteon formation in rabbit femoral cortical bone (rates of formation in rabbit are c.3x human remodelling rates) (after Roberts et al. 1984 p. 107).

As with primary lamellar bone, the textbook model of secondary osteons normally suggests that the direction of the collagen fibrils within each of the concentric lamellae rings alternates in direction to provide strength, but again the directionality is probably not as uniform as this simplified model suggests (Currey 2012). The remaining small channel at the centre of the new secondary osteon carries the blood and lymphatic vessels as well as a nerve supply and are collectively referred to as a Haversian canal. Running at right angles to the Haversian canals are additional cavities containing blood vessels, nerves and lymphatic vessels, referred to as Volkmann's canals (figure 2.8). Volkmann's canals are smaller in diameter than the Haversian canals and link the Haversian structures to each other and to the vascular network of the endosteum and periosteum.

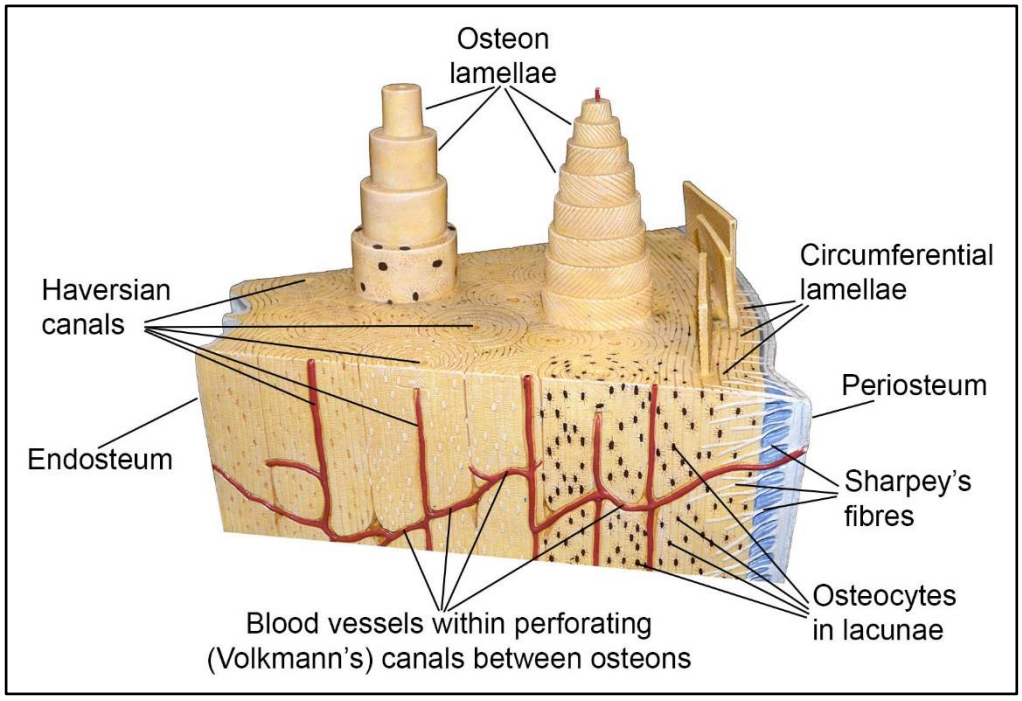

Figure 2.8: Histological structure of cortical bone showing osteons, circumferential lamellae and Volkmann's canals (source: author).

The network of Haversian canals and Volkmann's canals form the Haversian system named after Clopton Havers who first accurately described it in 1691 (Dobson 1952). It is the repeated formation of new secondary osteons (eventually over previous secondary osteons) that provide the mechanism for the continued turnover and remodelling of cortical bone (Currey 2012).

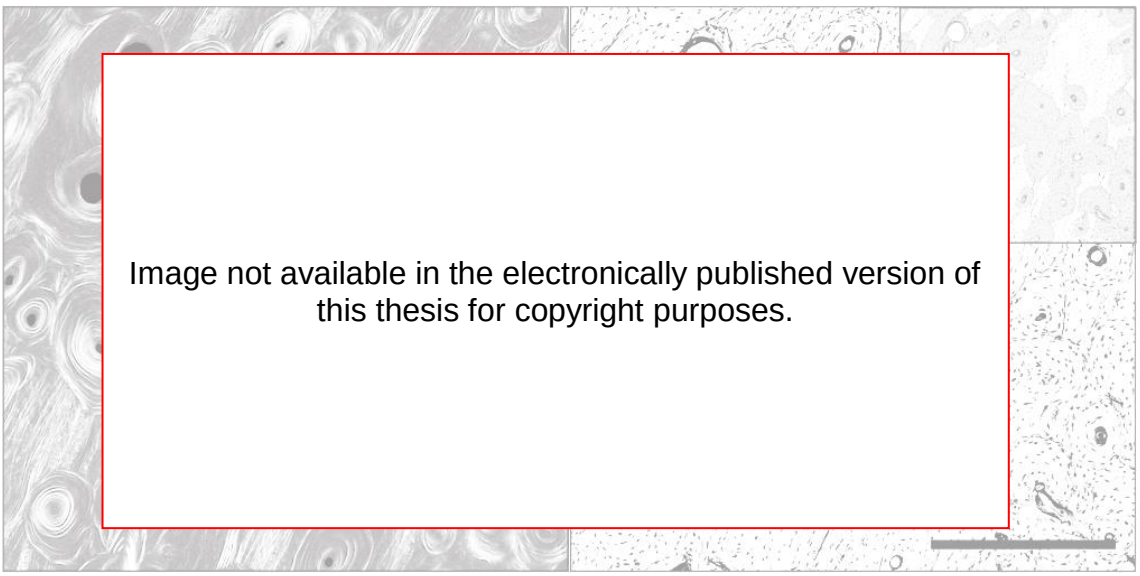

Figure 2.9: Micrograph of overlapping secondary osteons under circularly polarized light (left) with lamellae appearing as alternating bright and dark bands (white arrow), and brightfield image of the same field of view (right) with Haversian canal (HC) and cement line boundary (CL) marked. Scale bar: 0.5 mm (McFarlin et al. 2008 p. 309).

Histologically, secondary osteons are differentiated from primary osteons by the presence of a cement line between the outer concentric lamellae and the surrounding bone, by the intercutting of older osteons and the larger size (100 μm – 250 μm in diameter) and number of concentric lamellae (c.20 - 25) of secondary osteons compared with primary osteon structures (figure 2.9). Additionally, the remodelling of cortical bone by secondary osteons will leave behind areas of pre-existing bone representing either the primary or secondary lamellar bone. The presence of this interstitial bone between osteons leads to areas which (due to its older age) are more highly mineralised and more likely to promote microcracking both *in vivo* and during the degradation of the bone (Burr & Akkus 2014).

2.2.5. Osteocytes, lacunae and canaliculi

The osteoblast cells entrapped during their secretion of osteoid matrix during the formation of bone become osteocytes. These lie within small obligate ovoid lacunae (cavities) formed between lamellae. Osteocytes are supplied with nutrients and communicate via long cytoplasmic / dendritic processes within small fluid filled channels, referred to as canaliculi, which radiate out from the lacunae and are linked to the Haversian system and other osteocytes. Osteocytes are the most prolific of cells within bone and their density varies by species, with up to 93,200 osteocytes per cubic millimetre in rat cortical bone (Mullender et al. 1996).

The canaliculi provide a very high surface area for molecular exchange within the cortex of bone, as much as 133 times that of trabecular bone (1200 m^2 vs 9 m^2 for the adult human male skeleton (Noble 2008)). The pervasiveness and high surface area of the canaliculi/lacunae system allows autolytic enzymes to pervade the surrounding bone postmortem, initialising the early stages of postmortem bone degradation (chapter three) (White & Booth 2014).

2.2.6. Plexiform bone

Plexiform bone (sometimes also referred to as fibrolamellar bone) is a mix of woven bone and lamellar bone. Formation of plexiform bone begins with the intramembranous ossification of a bud of fine-fibred woven bone, formed *de novo* within the fibrous periosteum and grows out perpendicular to the outer bone surface. As the buds enlarge they merge with their neighbouring buds and form a layer of bone parallel to the outer bone surface.

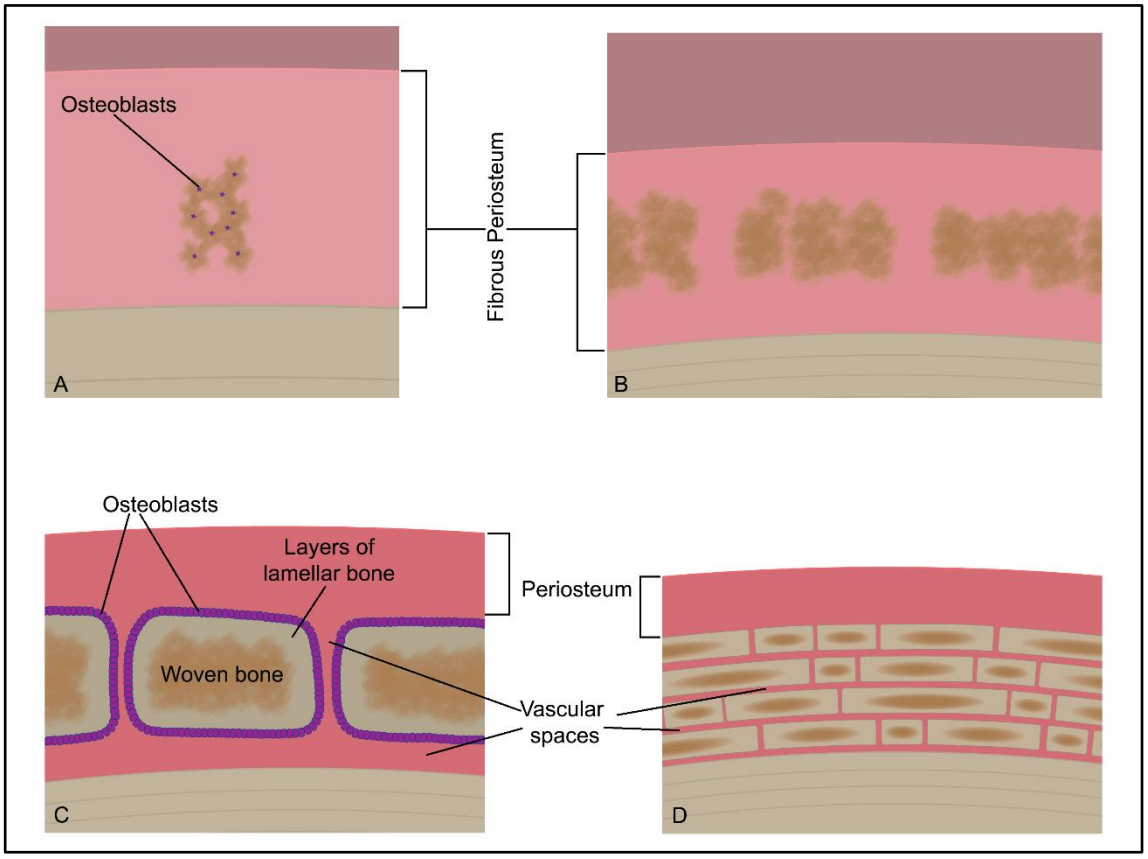

Figure 2.10: Development of plexiform bone. A: osteoblasts deposit woven bone within the fibrous periosteum growing perpendicular to bone surface; B: areas of new bone merge to form plates parallel to bone surface; C: osteoblasts deposit lamellar bone around woven bone; D: resulting "brick and mortar" form of plexiform bone (source: author).

As the buds form within the periosteum and not sub-periosteally on the surface of the bone cortex (as occurs in response to inflammation) the newly formed layer of bone is surrounded by the vascular spaces extending from the periosteum. The vascularized surface of the bud is therefore accessible on all sides allowing the appositional deposition of dense lamellar bone by osteoblasts onto the underlying woven bone encapsulating it. Thus, each subsequent layer of plexiform bone is surrounded by a vascularized area, leading to a structure

that in section is similar to brickwork (figures 2.10 & 2.11), with the bone “bricks” surrounded by an interconnecting vascular network (or plexus from which plexiform bone derives its name) and which allows for faster formation compared to the more restricted vascular supply of purely compact lamellar bone.

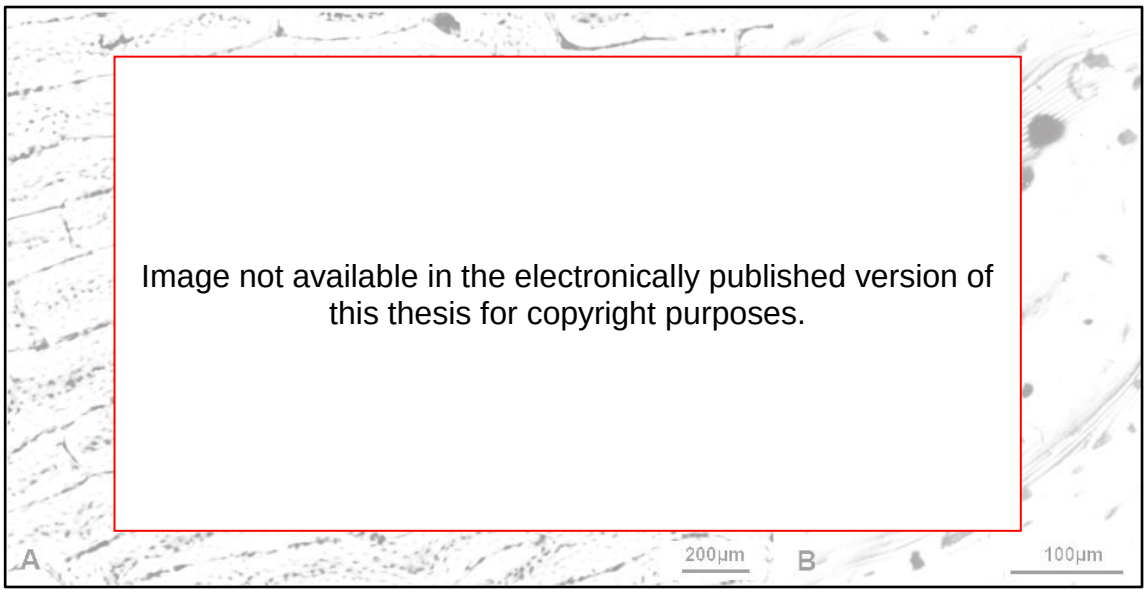

Figure 2.11: Plexiform bone’s “brick and mortar” appearance; A: reflecting light microscopy showing the general pattern of plexiform bone; B: backscatter electron microscopy showing the lamellae surrounding the woven bone in the centre of adjacent “bricks” (Burr & Akkus 2014 p. 14).

Plexiform bone’s composite nature offers the advantage that it forms quickly due to its woven bone component, but with the added structural strength of lamellar bone. It is therefore most commonly seen in animals that exhibit rapid growth, particularly large animals during their initial growth stages (Jee et al. 1970, Wang et al. 1998) but is rarely found in human bone (Hillier & Bell 2007).

2.3. Formation of bone

2.3.1. Formation of bone *in utero*

The development of bone in the foetus occurs through two differing pathways: intramembranous and endochondral, both of which involve the initial deposition of woven bone by osteoblast cells, although the source of these osteoblasts differs in each pathway.

In long bones, the bone is initially formed via both the intramembranous and endochondral pathways (Scheuer & Black 2004). The earliest type of formation (and the oldest phylogenetically (Carter et al. 1998)) is intramembranous, where an initial bone collar is formed perichondrially around the shaft by osteoblasts, differentiated from mesenchymal stem cells during the formation of the perichondrium (Dirckx et al. 2013), and which deposit osteoid directly onto the surface of the underlying hyaline cartilage anlage (Karsenty et al. 2009). The deposition of osteoid matrix and its subsequent mineralisation results in the encapsulation of osteoblasts within the matrix which then differentiate into osteocytes.

The formation of the bone collar around the hyaline cartilage anlage reduces the infusion of nutrients into the cartilage and triggers endochondral bone formation, as chondrocytes within the hyaline cartilage anlage are deprived of nutrients resulting in cell death, the formation of cavities, and mineralisation of the cartilage. These cavities are then penetrated by the blood vessels, lymphatics and nerves of a periosteal bud. The periosteal bud also delivers osteogenic cells in the form of osteoblasts which deposit bone onto the mineralised cartilage scaffold to form trabeculae (Deen 2014).

Thickening of the bone collar occurs as bone is resorbed on the endosteal surfaces and deposited as lamellar bone on the periosteal surface of the bone resulting in appositional growth. This appositional deposition of lamellar bone incorporates blood, nerve and lymphatic vessels to form primary osteons and forms the circumferential lamellae.

2.3.2. Formation of bone in response to trauma and infection

Immature bone formation occurs in response to inflammation due to either traumatic injury, infection or during the formation of some tumours (White & Folkens 2005) and the presence of immature bone in skeletalised remains is key to differentiating antemortem injuries from those occurring at death (perimortem) or as postmortem damage.

In fractures the break tears the periosteum and endosteum as well as rupturing blood vessels within the Haversian system leading to the formation of a haematoma around the fracture site (Claes et al. 2012). The inflammatory response leads to the replacement of the haematoma with granulated tissue (Galloway et al. 2014) and then, through the action of fibroblasts and chondrocytes, into a cartilage scaffold (Sarmiento & Latta 1995). In response to the injury, the periosteum is repaired and forms over the cartilage scaffold. The progenitor cells within the periosteum and endosteum are, through the action of inflammatory response derived cytokines (notably bone morphogenic proteins of the transforming growth factor beta superfamily), stimulated to differentiate into osteoblasts (Cho et al. 2002, Ai-Aql et al. 2008, Murao et al. 2013). Intramembranous appositional bone formation by these osteoblasts deposits woven bone to bridge the fracture gap and produces a hard callus around the fracture site (Dimitriou et al. 2005). Later remodelling into lamellar bone reduces the size of the callus and, where the two fractured components of the bone are in good alignment and the fracture surfaces are close together, the callus is remodelled until it may only be visible in radiographs.

The response of bone to infection is similarly driven by the inflammatory response, with vascular proliferation within the periosteum leading to thickening of the normal periosteum and thus an increased blood supply. This increased supply of nutrients stimulates increased osteoblastic activity and the intramembranous appositional deposition of osteoid on the outer surface of the bone, and thus the formation of new bone.

If the source of the injury / inflammation of the site of injury persists the formation of bone continues faster than the new bone can be remodelled into lamellar bone. This leads to either multiple layers of new bone with thin layers of lamellar bone between, or as spiculated periosteal reaction where the

Sharpey's fibres and the periosteum's vascular channels are stretched out from the underlying original lamellar surface to the periosteum, with the rapidly forming new bone forming along the lines of these structures. The resulting sunburst pattern of spiculated periosteal reaction is most often seen in rapidly developing tumours such as aggressive osteosarcomas (Brothwell 2012).

If the source of the injury or inflammation is not persistent then the reaction subsides as inflammation (and thus vascular proliferation) decreases, leaving a 1 - 2mm layer of new woven bone on the surface which later remodelling can either resorb or incorporate into the cortical bone.

2.4. Bone composition: organic fraction

The organic fraction of bone is deposited by osteoblasts in the form of osteoid during bone formation. 90% is made up of collagen (predominantly type 1), a family of fibrous structural proteins. The remaining 10% is constituted of other proteins, usually grouped together under the term ‘non-collagenous proteins,’ and lipids (Geneser 1989).

2.4.1. Collagen

Collagen proteins are found throughout the body in the connective tissues and their elasticity and tensional strength when bundled together provide the main structural properties of these connective tissues (section 3.6.2).

Collagen is a protein made up of three strands of polypeptide chains in a right handed helix. The polypeptide chains in collagen have a common repeating pattern to their amino acid sequence in the general form of:

- gly - X - Y - gly - X - Y -

in which the amino acid glycine is followed by any two of the other 16 amino acids that make up the protein. Most often X and Y are proline and hydroxyproline. This repeated pattern and the tertiary structure of the three polypeptide chains to form collagen fibrils results in the glycine residues being stacked above each other and promotes covalent bonding (cross-linking) between the polypeptide chains within the collagen fibrils and between collagen fibrils when they are stacked together to form fibres (Pollard & Heron 2008). The cross-linking within and between collagen fibrils results in strong and water insoluble elastic fibres (Francillon-Vieillot et al. 1989) (figure 2.12) which form the framework on which bone mineral in the form of platelets is deposited. The association of bone mineral platelets with collagen fibrils is substantial enough to prevent access of extracellular enzymes damaging the collagen fibrils (Lees 1989).

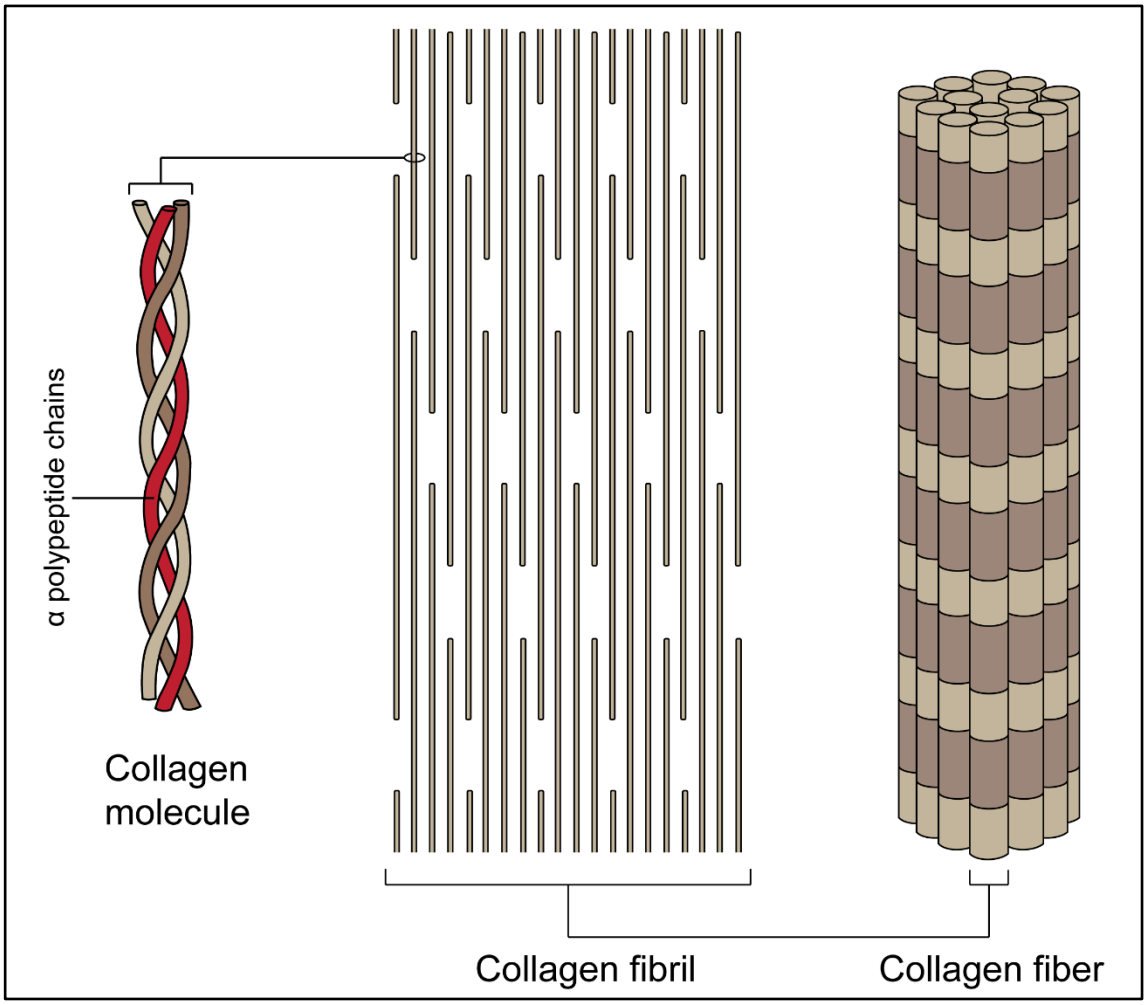

Figure 2.12: Collagen structure from the α polypeptide chains arranged in regular patterns into collagen fibrils which are joined to form collagen fibres. 67 nm banding within the collagen fibril is formed by the overlaps at the tail and head of collagen molecules (adapted from Riso et al. 2016 p. 47).

Bone collagen has been the focus of significant archaeological interest as its extraction, isolation and sample preparation is relatively simple (Hedges & Law 1989, van Klinken 1999) and it is the primary target molecule from faunal remains for both radiocarbon dating (Longin 1971) and stable isotope analysis (Fogel et al. 1997) and more recently proteomic studies such as the ZooMS research (Collins et al. 2010).

2.4.2. Non-collagenous proteins

The non-collagenous proteins include osteonectin, osteocalcin, osteopontin, bone sialoprotein, albumin and other blood serum proteins (Boskey 1989, Roach 1994, Freundorfer et al. 1995). Whilst the full extent of the functions of these non-collagenous proteins is still being investigated, they have already

been shown to have an essential role in the initiation of bone mineralisation and the regulation of mineral crystallization and crystal size (Roach 1994, Gorski 1998). The role of non-collagenous proteins in growth and development and in response to injury have made them of interest in archaeology when studying epidemiology and palaeopathology (Freundorfer et al. 1995, Wiechmann et al. 1999, Larsen 2002).

2.4.3. Bone lipid content

The lipid constituents of bone represent only about 0.1% by dry weight and can be grouped into phospholipids, free fatty acids and free and esterified cholesterols (Williams & Elliott 1990). They have long been shown to contribute to the process of calcification and ossification of bone (Irving 1958, Cruess & Clark 1965). Recent work has shown that lipids (and in particular the phospholipids) act as signalling compounds to stimulate the growth of osteoblasts and therefore have an important role in both bone development and repair (Blackburn & Mansell 2012).

2.5. Bone composition: inorganic fraction

Bone mineral is made up of calcium and phosphorous in the form of bioapatite. In general apatites have a formula of $Ca_{10}(PO_4)_6X_2$ in which X is most commonly fluorine or a hydroxyl group and are therefore referred to as fluorapatite and hydroxyapatite respectively. In artificial hydroxyapatites the structure is ionic with the ions in a hexagonal close-packed arrangement (Elliott 1973). However, in bone this ideal hexagonal close-packed arrangement is interrupted by the presence of either negatively charged hydroxyl or fluoride ions (OH^- F^-) or calcium ions (Ca^{2+}) stacked within the channels in the hexagonal close-packed structure (Williams & Elliott 1990). The resulting mineral is therefore more correctly described as a carbonate hydroxyapatite with a stoichiometry of $Ca_5(OH)\{[PO_4]_{0.5\text{-}0.9}[(CO_3)(OH)]_{0.1\text{-}0.5}\}_3$ which they suggest is closest to the mineral dahllite (Pollard & Heron 2008). Weiner and Traub used transmission electron microscopy to show that this carbonate hydroxyapatite mineral is formed into platelets of about 2-3 nm thick in lamellar bone (Weiner & Traub 1992) embedded within the bundles of collagen fibres. This corresponds with earlier research that showed particular points on the collagen fibril act as nucleation sites (Glimcher 1987) for the growth of these crystalline bone mineral plates. In immature / woven bone these platelets have also been observed, although the size of the platelets was noted as being smaller than that seen in lamellar bone, probably due to the higher levels of resorption of woven bone within the highly vascular periosteum (Su et al. 2003).

The source for the calcium and phosphate in bone mineral is derived from the extracellular fluid within the body, which is supersaturated with calcium phosphates in metastable equilibrium. The metastable equilibrium means that the extracellular fluids are in a state where the addition of further calcium or phosphate ions, the presence of a nucleation site, or a crystal of apatite, will destabilise the equilibrium and result in precipitation of the calcium phosphates and crystal growth. Research suggests that the non-collagenous proteins and lipids within the osteoid expressed by osteoblasts, are key to triggering and regulating this process (Roach 1994, Gorski 1998, Blackburn & Mansell 2012).

2.6. Chapter summary

The structure and composition of bone dictates its optical and surface properties. The ratio of organic and mineral content dictates the opacity of bone influencing the quality of 3D imaging and in combination with the structure of bone impact the patterns of fragmentation.

Chapter three discusses these taphonomic changes in a range of depositional environments in relation to the structure and composition of bone outlined in this chapter and relates this to the fracture mechanics of bone and its impact on fracture surface shape and quality.

Chapter 3. Taphonomy of bone

3.1. Taphonomy

First defined in 1940 by the Russian scientist Ivan Efremov as the “laws of burial” from the Greek words for burial, *taphos (τάφος),* and law, *nomos (νόμος)* (Efremov 1940), and initially used to describe the transition of organic material from the biosphere through the process of fossilisation and into the lithosphere; taphonomy is the study of the processes which preserve, alter or destroy organic material from the point of death onwards.

The study of what Efremov later described as “the science of burial”, was first examined by geologists and palaeontologists, who explained the formation of sediments and geological stratigraphy by reference to processes ongoing in the present. This direct link, based on the principle of uniformitarianism, between contemporary and past natural processes, forms the scientific basis for the study of taphonomy (Beary 2016). It underpins the use of observations within experimental taphonomy to reproduce and understand the changes observed in the evidential, archaeological or geological record.

Taphonomy is thus a very broad subject which speaks to disciplines as diverse in focus as forensic investigation, archaeology, palaeontology and evolutionary biology; and in timescale from the immediate present to the very earliest evidence of the development of life on the planet.

Whilst it is frequently viewed as a study only of decay, decomposition and therefore loss of information, Martin (1999) points out that the opposite is the case, the taphonomic examination of the forensic, archaeological or fossil records offers the ability to look beyond the degraded remains and examine the environment in which they were formed.

Whilst this thesis concentrates on mammalian bone taphonomy (and its implications for 3D digitisation quality), the forms of taphonomic change studied require data to be synthesized from palaeontological, zooarchaeological, palaeoanthropological, human osteological and forensic studies. This breadth of taphonomy related sub-disciplines can lead to confusion with regard to terminology use founded on variation in the focus of approach within each

taphonomic sub-discipline. Some of this confusion can be clarified through an understanding of the development of taphonomy as a discipline.

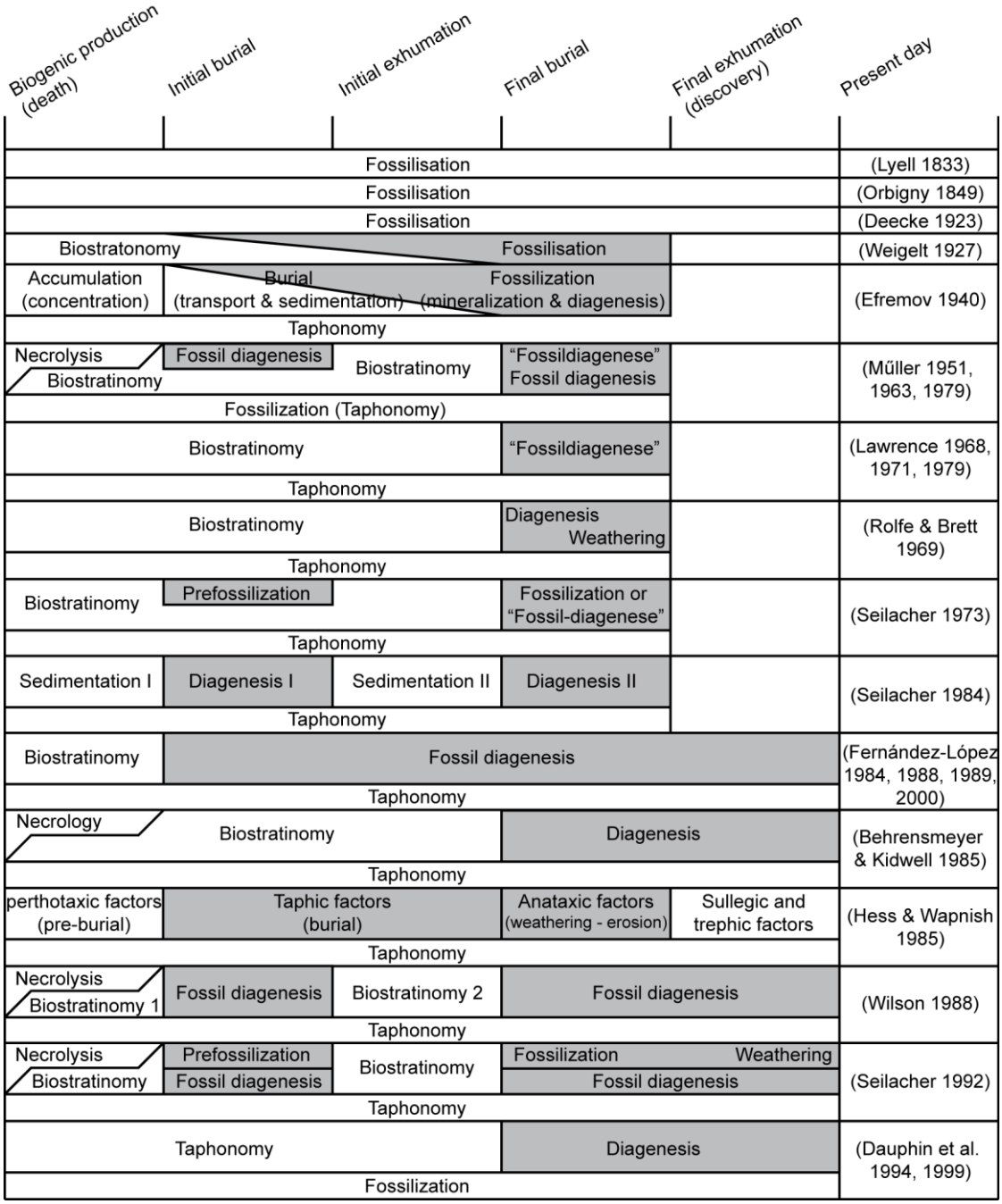

Table 3.1: History of classifications within taphonomy (after Fernández-López & Fernández-Jalvo 2002 p. 29).

Within geology and palaeontology prior to the work of Weigelt all processes following death of an organism were grouped under the single term 'fossilisation'. Following the introduction of the term biostratinomy (originally biostratonomy) by Weigelt (1927) to cover changes between death and burial, the term fossilisation was limited to the post burial alteration of organic materials. Efremov (1940) then grouped fossilisation and biostratinomy as

stages within the wider study of taphonomy and subsequent researchers, whilst varying the stages included under taphonomy, have maintained the use of the term to cover the overarching subject (table 3.1).

The focus of palaeontological research on fossilisation highlights the problem of terminology. The term ‘fossil’ is an anglicisation of the Latin *fossilis* meaning “that which is dug up” (Finks 1979), and in the strictest sense includes all organically derived material that is excavated, including archaeological remains. Whilst palaeontology utilises this definition of the term fossil (Lyman 1994), any material of organic origin that survives to sufficiently deep timescales to become the subject of palaeontological research only does so through the process of mineralisation. Thus in palaeontology the focus of taphonomy is self-selecting on the preservation (i.e. fossilisation) end of a spectrum of taphonomic alteration. However, for those overlapping disciplines that also study taphonomic change to organic material, but which do so over shorter timescales, a wider region of the spectrum of taphonomic alteration must be considered. Within these disciplines therefore, the classification under the term ‘fossil’ of all organically derived materials that are recovered from buried contexts is problematic. Therefore outside of palaeontological research the term ‘fossil’ is more widely reserved for remains of living organisms, which through natural processes, are preserved in rocks (Finks 1979). Fossilisation therefore, includes all the processes by which lead to fossils being preserved within rock in an identifiable form and these definitions will be used throughout the following thesis.

Whilst most terms in taphonomy are temporally and stage specific, the term weathering is more general and was defined by Behrensmeyer as:

> “The process by which the original microscopic organic and inorganic components of bone are separated from each other and destroyed by physical and chemical agents operating on the bone *in situ*, either on the surface or within the soil zone”
>
> (Behrensmeyer 1978a p. 153).

This definition clearly spans multiple taphonomic stages, and for buried deposits is synonymous with diagenetic alterations. Throughout this thesis we have limited the use of the term to surface weathering and included the chemical and

physical alteration of bone (i.e. subsurface weathering) under the term early diagenesis (section 3.4)

3.2. Taphonomy of bone

The degradation of bone from the point of death onwards is subject to a wide range of assaults on the organic fraction in the form of bacteria, mycota and protozoans (Piepenbrink 1986, 1989, Garland 1987, Child 1995a) from both within the remains themselves (Bell et al. 1996, White & Booth 2014, Kontopoulos, et al. 2016) as well as their depositional environment (Dent et al. 2003, Wilson et al. 2007); and on the inorganic fraction through changes in porosity, crystallinity and ion exchange (Pate et al. 1989, Weiner et al. 1993, 1995, Sponheimer & Lee-Thorp 1999, Lee–Thorp 2002).

Taphonomic change to bone begins shortly after death with the onset of autolysis in which the body's own enzymes, lacking the normal control mechanisms of homeostasis, attack and damage the tissues immediately surrounding them (Janaway 1996, Clarke et al. 1997). Whilst autolytic enzymes have limited direct effect on mineralized tissues such as bone (Schultz 2001), they are a key factor in the loss of integrity of the gut wall and thus gut microbiota are able to enter the blood and lymphatic systems and spread throughout the body (Janssen 1984) including the hard tissues like bone.

Taphonomic models of bone deterioration have in the past generally ignored the early postmortem decay of soft tissues as having little or no impact (Piepenbrink 1986). Biological attack of bone was assumed to derive from exogenous microorganisms, citing the presence of collagenase-producing bacteria within burial soils (Child et al. 1993, Child 1995a).

However, following from the earlier work of Jans (Jans 2008, Turner-Walker 2008), White and Booth have shown experimentally that the gut microbiota are strongly associated with histological damage to bone in the form of tunnelling microorganisms producing histologically identifiable non-Wedl micro-foci of destruction resulting in increased microporosity (White & Booth 2014, Kontopoulos, et al. 2016). In turn this increase in microporosity increases access of water and other agents into the bone leading to further degradation and eventually a shift in the pore size distribution to macro-porosity (Nielsen-Marsh & Hedges, 2000).

Whilst the collagen - mineral composite of bone is resistant to collagenase producing bacteria in its *in vivo* form, the decay by-products from the breakdown of the body's soft tissues include organic acids. These organic acids dissolve bone mineral (Manning 2000) which in combination with the increased porosity, provide loci for collagen degradation, liberating protons which in turn can react with bone mineral promoting further degradation and promoting the oxidation, deamination and racemisation of the collagen polypeptides (Collins et al. 1995).

The loss of collagen structure results in changes to the level to which mechanical loads to the bones are dissipated. Additionally, the increase in pore size reduces the load bearing potential of the bone (Bignon *et al.* 2003; Dellinger *et al.* 2006) and introduces points of weakness through which forces can propagate. Therefore, when mechanical loads exceed the flexibility or strength of the bone the fracture patterns exhibited are considerably different in bones of differing levels of degradation. Thus, immediately postmortem, relatively high mechanical loads are required to effect fracture of the bone and these loads are similar to those required during life. However, as degradation progresses and protein or bone mineral is lost the loads required to fracture bone are reduced, with alteration to the shape and pattern of the fracture surfaces themselves.

3.3. Surface weathering of bone

Surface (or subaerial) deposited skeletalised remains are subject to weathering damage due to the rapid changes in local environment caused by the fluctuations in weather and season. The remains form a source of food for scavenging animals (Payne 1965, Haglund et al. 1988, 1989) as well as providing ideal conditions for a succession of invertebrates (Payne et al. 1968) as well as mycota (Cooke 1963) and vegetation (Vass 2001). Assuming a skeletalisation pathway for the remains, the bone will have been subject to the effects of putrefaction and liquefaction of the soft tissues and eventually be left exposed to the climate, or have been previously buried and re-exposed as they erode out of their original deposits.

Weigelt's study (1927) into the decomposition and incorporation into the fossil record of animal remains, for the first time considered what happens to decomposing remains while on the surface, including the initial skeletalisation of bone, scavenging and damage through the physical interactions of the bone with the surface environment. Weigelt was also the first to highlight the potential value of observed natural surface degradation to forensic medicine, laying the groundwork for the development of the field of forensic taphonomy.

Early work concentrated on characterising the stages of bone weathering in more extreme environments where the rate of bone weathering was more apparent. Shipman (1977) in Western Kenya created a series of nine weathering stages linked to the microenvironment and interactions with the local sedimentary deposits making up the ground surface.

Shortly after her Behrensmeyer (1978) published a paper that described how to identify bone weathering and ascribed the macroscopic changes she observed in animal bone from Amboseli, Kenya to six progressive stages graded from 0 (no observable alteration) to 5 (disintegration). Significantly, Behrensmeyer also tied these stages to Post Mortem Interval (PMI) and subsequent work has shown the importance of osseous weathering based PMI estimates in filling the gap between entomological PMI estimates and archaeometric dating methods such as radiocarbon (Junod 2013, Junod & Pokines 2013).

Behrenmeyer's work was important to the development of bone taphonomy in that it provided a common structure to which future researchers could refer, offering comparability of results of bone weathering experiments or observations within differing environments. Subsequent studies have tested Behrensmeyer's stages applicability and recorded bone weathering rates based on a range of microclimates such as arid desert (Coe 1978, Andrews & Whybrow 2005), arctic (Sutcliffe 1990, Todisco & Monchot 2008, Janjua & Rogers 2008), temperate (Andrews & Cook 1985, Andrews & Armour-Chelu 1998, Miller 2009, Madgwick & Mulville 2012), savannah (Trueman et al. 2004) and tropical rainforest environments (Tappen 1994, Ross & Cunningham 2011).

All of these studies demonstrate that weathering rates are highly dependent on the microclimate in which skeletal material is deposited and also illustrate the difficulty of carrying out experimental studies into osseous weathering due to the very long timescales that are required to produce meaningful change in skeletal remains (Behrensmeyer & Miller 2012). The natural variation in weathering requires a large number of samples to observe patterns and to achieve comparability of results. In order do so, research has either sought to reduce the timescales necessary by studying environments where the climatic conditions are sufficiently extreme to rapidly produce taphonomic change, or has concentrated on regions with high natural predation rates of large mammals (e.g. Behrensmeyer's use of Amboseli) where large data sets can identify statistical outliers. Due to this pattern, skeletal weathering research is biased strongly towards large mammals, which while applicable to palaeontological research, pose questions of comparability to human remains when used in a forensic context.

Research specifically examining the weathering of human skeletal remains, particularly for forensic research, is reliant upon either recent forensic cases or a small number of human taphonomy research centres, the location of which are often chosen for their legal and public health requirements, rather than their forensic applicability. Forensic cases seen by forensic anthropologists and medical examiners are generally uncommon, and those with surface deposition of remains for periods long enough to induce osseous weathering are especially so. The exceptions are those limited number of locations where the combination of low population densities, open access to land and extreme climate can result

in remains going undiscovered for sufficient time to develop osseous weathering. Such conditions often occur in relation to desert or arctic environments especially where such terrain is located on a national border with a flow of illegal migrants e.g. Southern California (Hinkes 2008). Whilst these locations provide larger numbers of remains that can be studied, the difficulty in identification and lack of antemortem data make estimations of PMI uncertain and limits the conclusions and data attainable from osseous weathering research (Beary & Lyman 2012). The pattern of research into osseous weathering is therefore one of investigation of environmental extremes or characterisation of a limited number of specific environments or microclimates. The application of this data has the potential for misuse when timescales developed in a specific environment are applied in forensic PMI determinations to remains found in a similar but different environment (Lyman & Fox 1989, 1996, Junod & Pokines 2013). Additionally, the need to create a comparable experimental record for each local environment, has diverted attention away from experimental investigation of the chemical and physical mechanisms driving osseous weathering at a level below that of gross changes, although more recent research has begun to address this lack (e.g. Beary 2005).

In order to understand the impact of the changes to the bone surface and optical properties on the quality of 3D digitisation methods, it is important to understand the gross changes to bone, and where they are now known, the physical and chemical changes. The following sections will outline the current understanding of osseous weathering, starting with the general pattern of gross changes in weathered bone and then examining the alterations induced by specific conditions.

3.3.1. General patterns

Whilst surface weathering, like many taphonomic studies is only as good as its local environmental applicability, the general pattern of changes may be examined as broadly similar, if with greatly varying weathering rates. The general pattern of weathering of bone was described by Behrensmeyer from samples collected in the Amboseli Basin in Kenya and is one of organic content loss, reduction in moisture content, surface bleaching and crack propagation leading to flaking, and fragmentation of the bone (Behrensmeyer 1978).

Behrensmeyer's stages reflect the continuous loss of the composite nature of bone, slowly breaking down the lamellar cortical structure and forcing layers apart. Whilst Behrensmeyer's stages provide a process that she asserts is generally similar in differing environments, in reality the disintegration of bone along this pattern is probably more reflective of the underlying microstructure of bone, in that differing mechanisms weaken the bone and cause it to fracture, crack or delaminate along the same lines of weakness between lamellae, osteons etc. (Tappen & Peske 1970). It has been noted that in the case of heating of long bones, they follow a similar degradation pathway as in weathering (Gifford-Gonzalez 1989), but that the denaturing of the collagen fibres caused by heat in these cases is a different taphonomic pathway to that seen in surface weathering in Amboseli, Kenya (Shipman 1990) where dehydration and UV radiation are more significant factors. However, whilst different environments produce differing degradation processes at the histological level, Behrensmeyer's assertion that the stages are broadly the same has been shown to be generally true through the comparison of weathering patterns in Wales (Andrews 1990, Andrews & Armour-Chelu 1998), Africa (Tappen 1994), the United Arab Emirates (Andrews 1995), Australia (Littleton 2000) and in North America (Tappen & Peske 1970, Janjua & Rogers 2008) when the timescales are adjusted for temperature.

3.3.2. Surface cracking and delamination

Bones deposited on the surface and exposed to the environment undergo change via a number of taphonomic pathways (sections 3.3.3 to 3.3.7). Many of these lead to surface damage and disruption of the surface and structure of bone, particularly through the loss of collagen. *In vivo* collagen fibrils impart strength to the bone and a resistance to tensile stresses (Doblaré et al. 2004, Turner-Walker & Parry 1995). Once exposed on the surface, the loss of collagen makes bone brittle and repeated cycling of stresses results in fatigue microcracks to the bone and eventually to failure. Failures in surface weathered bone are observed in two main forms: cracking and delamination.

Cracking in bone are splits that penetrate perpendicular to the surface into the bone and follow the underlying osteonal structure. They occur as tensional

stresses are set up by differential levels of shrinkage and swelling in multiple layers of the bone and are usually failures parallel and between collagen fibrils.

The most extreme forms are wet-dry cracks: wide cracks in the cortex (usually of the diaphysis) that penetrate through to the medullary canal and account for the fragmentation of bone. The outer edges may be upturned. These are predominantly due to cycles of wetting and drying where swelling and contraction of the bone can be rapid and therefore set up repeated high tension loads across the full radius of the cortical bone (figure 3.2).

Delamination (exfoliation) are splits that run circumferentially around the cortical surface usually failing between the circumferential lamellae or between layers of plexiform bone. Cracks through layers allow the delaminating lamellae to flake away from the outer cortical surface of bone (figure 3.1). Surface weathering processes that directly impact the bone from the outside in (e.g. photodegradation, freeze-thaw) degrade the collagen weakening the more accessible outer layers first. Delamination is therefore layer by layer degradation due to loss of adhesion of the collagen between the circumferential lamellae etc. and thus leading to their separation and loss. Delamination results in gradual reduction in the overall circumference of bone and eventually to a loss of integrity as the cortical bone is lost. Plexiform and lamellate bone both delaminate when exposed to surface weathering, but the differences in the underlying structure (sections 2.2.2. and 2.2.6.) result in variations to the regularity of delaminating flakes between the two types of bone (Junod 2013, Junod & Pokines 2013).

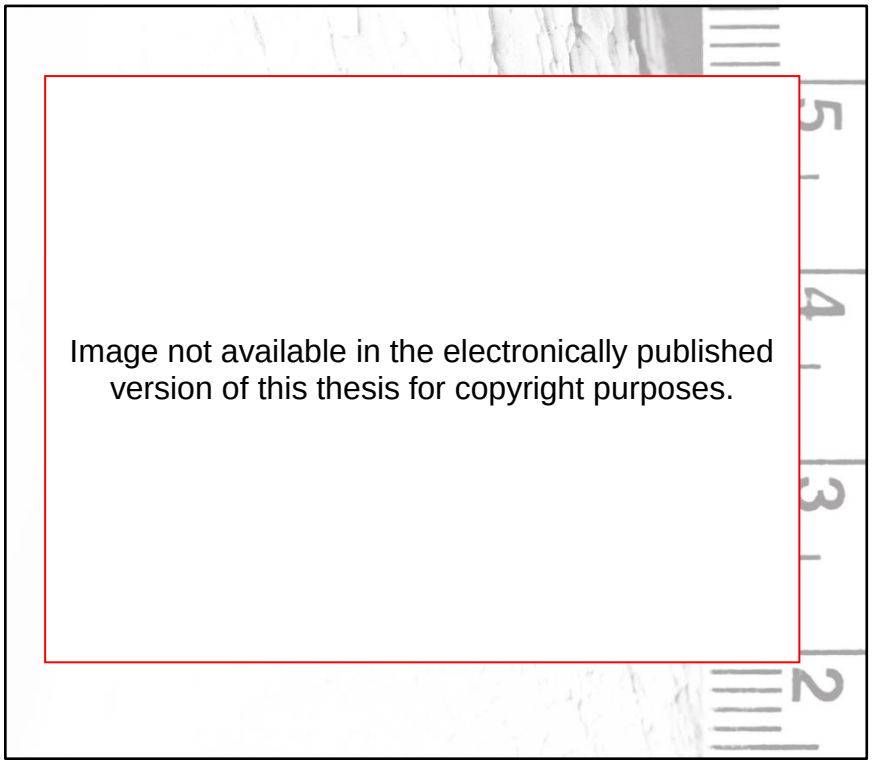

Figure 3.1: Detailed view of severe surface weathering to a non-human long bone. Delamination of the outer layers is combined with shallow cracks to produce flaking, eroding the cortical surface (Junod & Pokines 2013 p. 288).

3.3.3. Effect of fluctuation in moisture content of surface weathered bone

During the early stages of taphonomic alteration, bone is protected from moisture loss and other weathering effects by the liquefying soft tissues surrounding the bone. Once these have decomposed or been consumed by scavengers or insect activity, surface weathered bone begins to dry. Initially bone drying is limited by its high lipid content giving it a hydrophobic surface "greasy" layer, although this is rapidly removed through photodegradation, microbial action and leaching to the ground surface (Junod & Pokines 2013). Once the water repellent lipid content is lost, the moisture content of surface weathered bone is driven by wetting of bone through inundation, precipitation and the upward capillary transport of groundwaters; and by loss of moisture through evaporation in hot environments and freeze-drying in cold environments with sufficient air movement. Additionally bone is hygroscopic, meaning that it will absorb or expel moisture to maintain a state of equilibrium with the surrounding air (Museums and Galleries Scotland 2009).

Water stabilises the structural properties of the hydroxyapatite - collagen interaction and is therefore critical to the stability of bone as a whole (Rai & Sinha 2011, Wang et al. 2013). As bone dehydrates, the spacing between fibrils of collagen, and between collagen fibrils and the hydroxyapatite platelet surface is reduced resulting in shrinkage of the bone (Lees et al. 1984, Finlay & Hardie 1994, Lievers et al. 2010, Rai & Sinha 2011). Additionally, drying results in an increase in the Young's modulus of bone, and a reduction in the strain to fracture and toughness (Rho & Pharr 1999). These changes make dry bone less flexible and more susceptible to fracture at lower stress loads.

When bone is rehydrated, water is reabsorbed by the collagen fibrils and the distance between fibrils, and that between collagen fibrils and the bone mineral increases again, allowing the bone to swell.

Repeated wetting and drying subjects bone to cycles of shrinkage and swelling. However, the slow diffusion of water through bone means that the degree of shrinkage and swelling is not uniform throughout the bone, setting up tensional stresses within the bone and leading to wet-dry cracking (section 3.3.2 and figure 3.2) (Prassack 2011, Evans 2013). Whilst this taphonomic mechanism has received limited attention in surface weathered bone (Prassack 2011), the effect is known from conservation literature on waterlogged biocomposite materials such as wood, bone and ivory, where rapid drying can result in significant damage (Stone et al. 1990, Turner-Walker 2007).

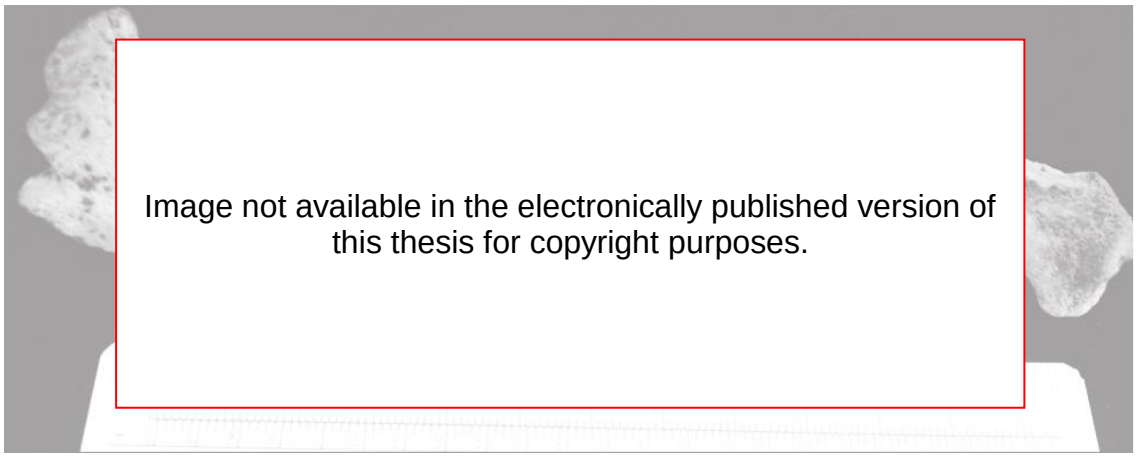

Figure 3.2: A large longitudinal crack along the length of a white tailed deer femur exposed on the surface in Massachusetts, USA for 39 weeks, consistent with wet-dry cracking (Lacroix 2013 p. 62).

The water content of surface weathered bone is an important factor in freeze-thaw damage (section 3.3.4.1) and damage due to the crystallization of salts (section 3.3.6). Additionally, photodegradation has been shown to be greater in dry bones (Golcuk et al. 2006) as water reflects incident light, reducing the amount of solar radiation to reach the bone surface and the depth to which it can penetrate (section 3.3.5).

3.3.4. Effect of temperature on surface weathered bone

Surface exposed bone is subject to considerable variation in temperature from variations in solar heating on the minute scale to diurnal temperature fluctuations and seasonal variations throughout the year. The direct effect of temperature change on bone results in thermal expansion and contraction which, over long periods produce thermal stress fatigue in the form of microcracks (Junod & Pokines 2013). However, the indirect effect of fluctuating temperature on the water contained within surface weathered bone is more marked and can lead to significant damage.

In full sun, the upper surface of bone is exposed to the photochemical effects of ultraviolet and visible solar radiation (section 3.3.5), and also heated by the radiant heat (infrared radiation) of the sun, dissipating some of that heat to the surrounding air through convection. In extremes of climate, bones may experience temperatures as low as -20°C or as high as 60°C. The thermal expansion coefficients for human bone were determined by Pal and Saha (Pal & Saha 1989) who recorded the maximum coefficient of $3.7x10^{-6}$/°C meaning that a tibia from a UK white male of average height (i.e. 177 cm (Shape Analysis 2012)) would expand from 390.000 mm to 390.043 mm in length when heated by the sun from 30°C to 60°C. Whilst changes on such a small scale do not have significant effects after a single linear expansion - contraction cycle, the accumulation of cycles results in fatigue and the accumulation of micro fractures. Given enough time, these can join and form larger cracks. Sudden large scale changes in temperature (thermal shock), although rare in natural environments can hasten this process.

The lower surfaces of bones are heated to a lesser degree and where bones are in direct contact with the soil, moisture and heat sink effects can widen the

temperature difference between upper and lower bone surfaces. This amplifies the effect of the diurnal temperature range and increases the tensional stresses and resulting fatigue cracking generated in each cycle. As a result upper surfaces tend to weather at a faster rate than those in contact with the ground surface (Behrensmeyer 1978a, Miller 2009).

In addition to thermal expansion-contraction changes to bone, higher temperatures result in more rapid rates of the background chemical hydrolysis of bone collagen and increased reproduction and growth rates for bacteria and fungi within the bone with their associated damage (section 3.3.7).

3.3.4.1. Freeze-thaw

Whilst the effects of temperature fluctuations directly on bone are limited, the effects of temperature fluctuations on water held within bone are more significant.

In hot and dry environments, free water evaporates and capillary action draws the water out from the pore spaces until the bone is dry. In all other environmental conditions, water is absorbed into the fine pore structure of bone and held there. In cortical bone the Haversian canals, Volkmann's canals and canaliculi all provide space in which water can be absorbed (Turner-Walker 2008), and these represent about 12% by volume of the bone cortex (Junod & Pokines 2013). In colder environments the water within these pore spaces can freeze and expand producing tensional stresses on the surrounding bone.

In climates that experience temperatures around freezing for periods of the year, the repeatedly changing strain loads exerted on the bone cortex through cycles of freeze-thaw have a strong effect on the rate of weathering of bone (Guadelli & Ozouf 1994, Texier et al. 1998).

The unique properties of water mean that unlike most substances, its density (and therefore its volume) does not follow a linear relationship to temperature. The density (ρ) of a substance is a function of its mass (m) and volume (v):

$$\rho = m / v$$

In most substances as temperature is reduced the kinetic energy of molecules decreases allowing molecules to be packed more closely together, giving a greater mass of molecules in a given volume and thus lower densities. This relationship is observed in water to a peak density of 1 g/cm^3 at 3.98°C. However the hydrogen bonding properties of water molecules give solidifying water a hexagonal crystal lattice that is less dense than liquid water and consequently a 9% increase in volume between liquid water at 3.98°C and ice (Eisenberg & Kauzmann 2005). Water in the pore spaces of bone that is below 3.98°C expands to exert over 200 MPa of pressure (Junod & Pokines 2013); this pressure forces apart existing small fissures within bone (e.g. those produced by photodegradation) making them larger. Periods of thawing allow water to flow further into the now enlarged fissures, exposing collagen to greater chemical hydrolysis. Subsequent freezing of the water enlarges the fissure further along the longitudinal lines of least stress resistance (figure 3.3).

Within cortical bone, the osteonal structures, circumferential lamellae and spaces between plaques of plexiform bone run longitudinally and provide lines of weakness throughout the bone. Cracks propagate between two lines of weakness and then run longitudinally. The histological structure of bone means that small fractures in bone can easily develop into larger fissures. Due to the low diffusion of nutrients through densely mineralised bone *in vivo*, all bone tissue needs to be within at least 250 µm of a nutrient source (section 2.2.3). In surface weathered bone these now empty spaces that previously provided nutrient supply are therefore at a maximum distance of 500 µm allowing short cracks to easily propagate between them.

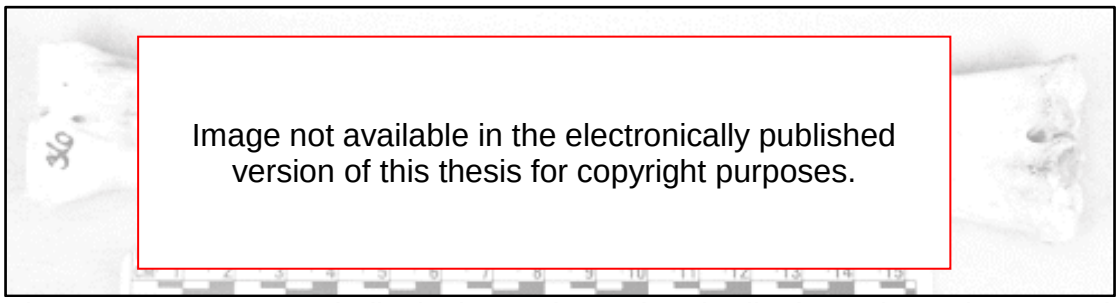

Figure 3.3: Metacarpal displaying a large longitudinal crack on its posterior surface due to freeze-thaw cycles (Pokines et al. 2016 p. 597).

Whilst the collagen of fresh bone imparts some degree of flexibility, studies into the effect of freeze-thaw cycles on the loading capacity of fresh bone have

shown that four cycles were enough to induce small but observable change and each freeze-thaw cycle added further incremental damage (Boutros et al. 2000) (figure 3.3).

As collagen is lost through other taphonomic processes and the tensional strength is reduced, the effect of freeze-thaw damage becomes more severe. Additionally, the increasing porosity of degraded bone due to recrystallization (section 3.4.5), and microbial damage (section 3.4.1), significantly increase the size of pore spaces, providing more room for water and greater levels of expansion. Porosity is therefore a dominant factor in freeze-thaw damage to surface weathered bone (Lee & Jasiuk 2014).

The insulating capacity of bone is limited and at temperatures at or just below freezing, the outer layer of bone surface will freeze (e.g. during heavy frost) whilst the inner portion of bones may not. The outer layer of surface weathered bone will therefore be subject to greater numbers of freeze-thaw cycles than the internal layers. In combination with the reduced levels of collagen at the surface due to solar radiation, the outer layers of bone experience greater degrees of damage.

As freeze-thaw cycles expand fissures within the bone cortex, deeper areas of the bone are opened up to taphonomic alteration, to the separation of the cortical layers within the bone and eventually to splintering, full delamination of the surface, fragmentation and loss of bone.

3.3.5. Solar radiation

Surface deposited bones are subject to solar radiation filtered by the atmosphere in the form of ultraviolet (100 nm - 380 nm), visible (380 nm - 750 nm) and infrared radiation (>750 nm) (figure 3.4) with a one-sun irradiance of 1,000 W_m^{-2} (ISO 1992). Infrared wavelength radiation has limited impact on the chemical structure of surface weathered bone beyond temperature changes (section 3.3.4) due to infrared heating. The shorter wavelengths of visible light and ultraviolet radiation however, are significant factors in the surface weathering of bones through photo-degradation in the form of photobleaching and denaturation & decomposition of the organic fraction.

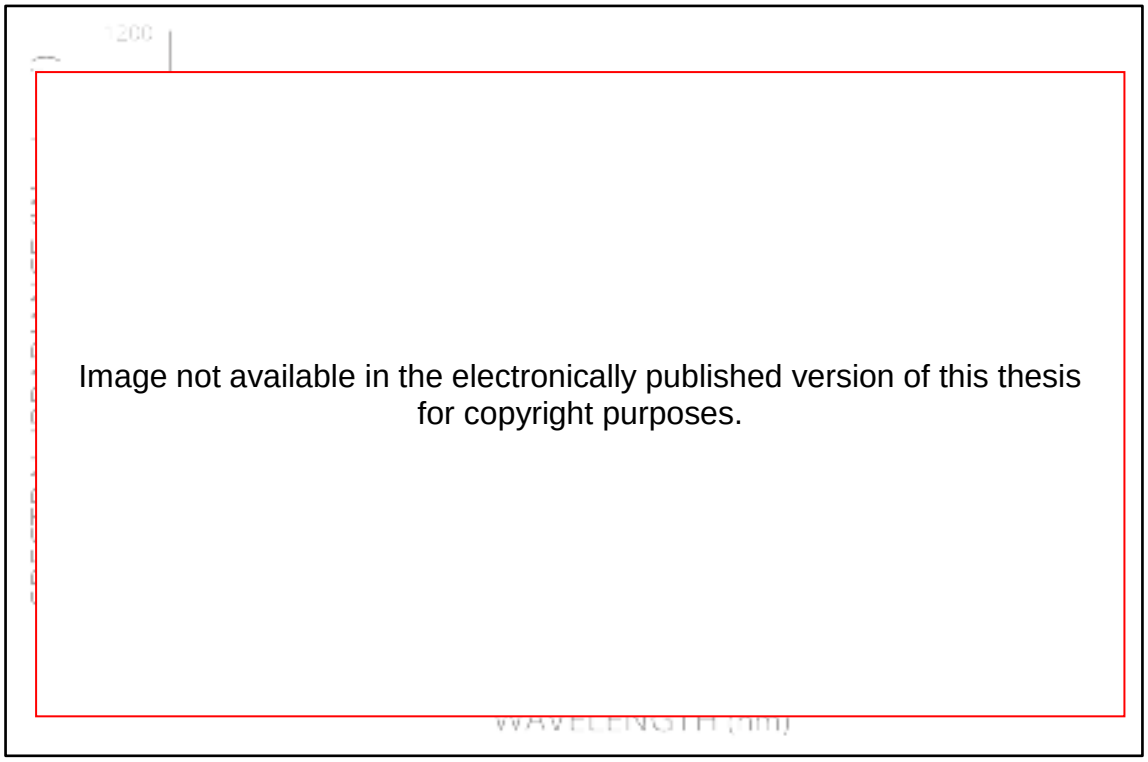

Figure 3.4: Spectrum of solar radiation without atmospheric absorption and at the Earth's surface (Rohde 2007).

UV radiation is classified in three bands, UV-C (100 nm - 280 nm), UV-B (280 nm - 320 nm) and UV-A (320 nm - 380 nm). However, the atmosphere filters much of the short wavelength high energy solar radiation before it reaches the Earth's surface through Rayleigh scattering and broad band absorption by gaseous molecules in the stratosphere and troposphere (Zerlaut 1994). All UV-C and the majority of UV-B is absorbed by both diatomic oxygen (100 nm - 200 nm) or by triatomic oxygen (i.e. ozone) and therefore the UV radiation that reaches the Earth's surface is only of wavelengths over 280 nm. UV-A is therefore the most important of these in terms of its weathering effects in natural environments (Andradi et al. 1998).

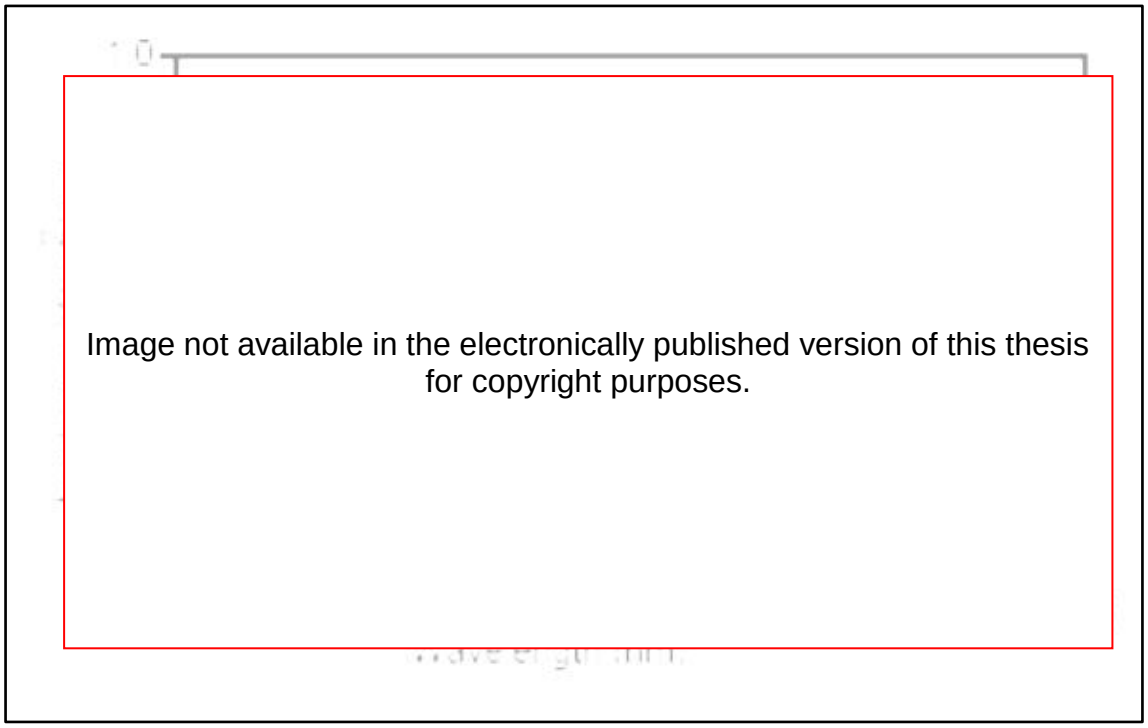

Figure 3.5: Solar UV radiation reaching the Earth's surface (Zayat et al. 2007 p. 1272).

Rayleigh scattering and molecular absorption of solar radiation is strongly wavelength dependant ($\sim\lambda^{-4}$) and therefore a higher proportion of the longer wavelength UV-A penetrates the atmosphere than shorter wavelength UV-B (figure 3.5). Following from this, the levels of solar radiation reaching the Earth's surface vary in relation to the angle of incidence of solar radiation, and therefore the solar spectrum is biased towards longer wavelengths (i.e. the red end) at dawn and sunset when solar radiation has to travel through more atmosphere. Visible light and UV-A, having longer wavelengths, are not as easily absorbed as UV-B and therefore UV-B exhibits a greater level of variation throughout each day and season. UV and visible radiation reach their peak levels at noon at midsummer when the angle of incidence of solar light is closest to perpendicular to the surface (figure 3.6).

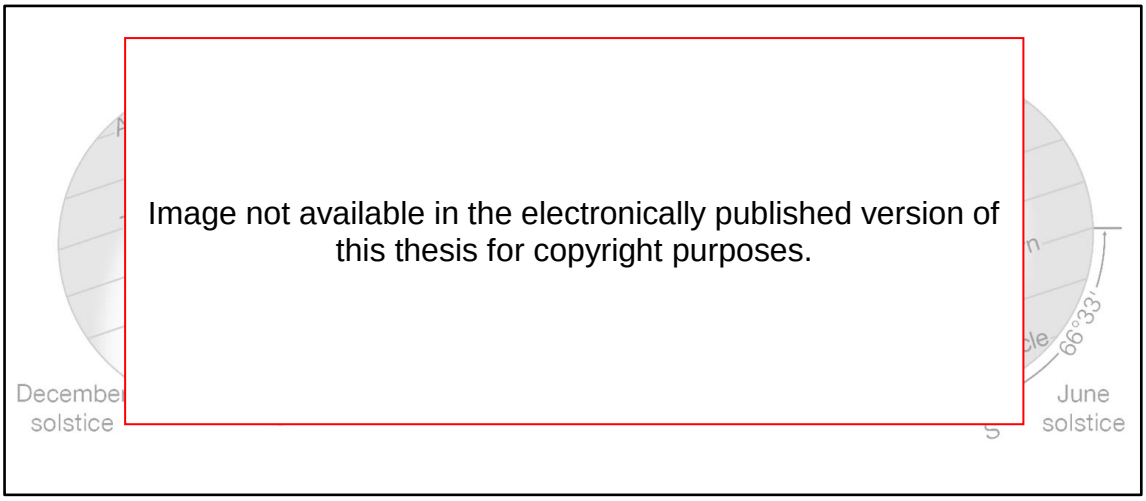

Figure 3.6: The Earth's axial tilt at the summer and winter solstices and its influence on the angle of incidence of solar radiation (Encyclopædia Britannica 2013).

Figure 3.6 also illustrates the effect of latitude on levels of solar radiation. Higher latitudes have greater seasonal variation in the angle of incidence of solar radiation. Increased angle of incidence therefore also increases the in atmosphere distance that radiation has to travel, and therefore have greater absorption of shorter wavelengths. UV-B levels are thus significantly higher at the equator. Andrews and Armour-Chelu's (1998) study of sheep (*Ovis aries*) remains in Wales showed much lower levels of surface weathering than those of Behrensmeyer's (1978) original study. Whilst the weathering that was observed was still comparable to the Behrensmeyer's early weathering stages, the rate of weathering was much slower reflecting the decreased UV-B levels in Wales compared to Africa.

The published work on surface weathering of bone addresses the measurement and characterisation of the physical changes due to exposure to solar radiation, but does not explain the mechanism of photodegradation. The specific mechanism of photodegradation of skeletal tissues has received very little attention, with the notable exception of the research of Beary (2005). However, the interaction of solar radiation with other synthetic and natural polymer based materials is of economic importance and has received considerable research within materials science. Furthermore, therapeutic and diagnostic use of UV and visible light on biological tissues *in vivo* has been explored (for a review see (Jacques 2013)) and at a general level the mechanisms of visible light and UV interaction with biopolymers are understood and can be applied to the biomineralized collagen polymer of bone.

3.3.5.1. Photobleaching

At a gross level the first alterations to surface deposited bone are the colour changes. The colour of bone is an off-white cream tinted by the colour of material within the vascular network within the bone. *In vivo* when bone is irrigated with blood, bone is pinkish cream in appearance with the articular surfaces appearing white due to the thick coating of hyaline cartilage. Following death and the cessation of the circulation, the blood trapped in the vascular network and the marrow becomes fixed as blood coagulates, darkening slightly in colour.

By the point of exposure of the bone to solar radiation, anaerobic microbes have already invaded the vascular spaces in bone and products of hemolysis darken to a reddish brown, further darkening the tint of the bone. The products of soft tissue decomposition and liquefaction add a reddish grey tint to the outside of the bone (Huculak & Rogers 2009). At initial exposure, the presence of bone lipid and the high protein content gives bones a greasy texture and increases the translucency.

Following exposure, visible light and UV radiation cause photolytic and photo-oxidative degradation of organic molecules through molecular chain scission (Lennox et al. 1971, Andrady et al. 1998) breaking down molecular components into shorter molecular chains (section 3.3.5.2) and promoting either their consumption by microbes or their dissolution into the moisture held within bone under capillary pressure.

Figure 3.7: Cattle mandibles exposed on the surface for several years at a desert cattle ranch in Northern California (courtesy of Gai Swango (TheVintaquarian)).

Whilst collagen is photodegraded at the same time as the partially degraded products of hemolysis, the bone mineral structure surrounding collagen fibrils holds the collagen polypeptide chains shortened through photodegradation in place. This protection is not available to the hemolysis products and photodegradation therefore leads to loss of the reddish-brown staining from the vascular network of the outer layers of bone cortex, lightening the surface of the bone to a yellowish white colour (Huculak & Rogers 2009).

During continued exposure, photodegradation continues to decrease the collagen content with a reduction in the yellow colour associated with the organic fraction of bone. In addition, the loss of bone lipid and bone collagen increase the opacity of the bone and thus increase the reflectivity index of surface weathered bone, eventually leaving brilliant white bone (Beary 2005, Dupras & Schultz 2013, Byers 2015).

3.3.5.2. Photolytic and photooxidative alteration to bone

The energy ($\mathcal{E}$) of electromagnetic radiation is inversely proportional to its wavelength (λ) according to the formula:

$$\mathcal{E} = hc / \lambda$$

(h = Planck's constant; c = speed of light in a vacuum) and radiation of shorter wavelengths therefore has higher energy and causes greater damage. Radiation in the ultraviolet and near-ultraviolet visible spectrum have wavelengths of sufficient energy to overcome the binding energy of electrons and strip them from organic molecules to form radicals. The propagation of radicals through organic molecules such as proteins results in photodegradation. The two forms of photodegradation (photolytic and photooxidative) both occur in surface weathered bone, although the photooxidative pathway is more prevalent in natural systems due to the presence of oxygen and the greater energy requirement for direct chain scission in photolytic degradation (Hawkins & Davies 2001).

In proteins the amino acids glycine and alanine, and the aromatic side chain residues of phenylalanine, tyrosine, and tryptophan, are most susceptible to excitation of their electrons by high wavelength radiation. Excitation has been shown to trigger electron ejection (ionization) from these to form free radicals or at lower levels of irradiation, elevation of electrons to higher energy states (Bent & Hayon 1975, Creed 1984a, 1984b). In both situations, as electrons relax to fill lower energy state orbitals and return to ground state, they release energy in the form of fluorescence which can be measured by spectrophotometry. Ultraviolet absorption and fluorescence can therefore be useful when determining the response of proteins to solar radiation.

For high energy irradiation, and where there are no local oxygen molecules available, high energy radiation excites electrons to energies where electrons can be ejected and become free electrons in solution leading to photolytic degradation. The free electron generated reacts at a carbonyl group in the polypeptide backbone to form α-carbon-centred radicals (Hawkins & Davies 2001). The propagation of these radicals results in polypeptide chain scission and the formation of new crosslinks and therefore disruption and shortening of

the polypeptide (Zayat et al. 2007). Where oxygen is available, proteins undergo photooxidative degradation through the propagation of free radicals within the molecule.

Photooxidative degradation is initiated through the electron ejection at an R-H bond leading to the formation of a radical and a H^+ ion. The protein chain radical then propagates through electron transfer reactions with locally available oxygen to form oxy or peroxy radicals. Radicals continue to be formed and disrupt the polypeptide chain through addition, elimination, dimerisation, fragmentation and rearrangement reactions (Hawkins & Davies 2001). Termination of the effect of radical propagation occurs only when two radicals react with each other to form stable products.

In proteins with cys-cys disulphide cross links in their structure (e.g. α-keratin) the propagation of radicals formed from excitation of adjacent aromatic side chains is limited by proximity to the disulphide link. The electron generated by excitation of the aromatic side chain is captured at the disulphide link and results in its cleavage to form free thiol radicals. These react with other free thiols and form a new stable disulphide cross link and terminate radical propagation (Neves-Petersen et al. 2012). In proteins such as collagen, which lack disulphide cross links (cross linkage being formed by adjacent lysine groups), radical propagation is not limited in this way and consequently such proteins are more susceptible to damage from solar radiation.

In addition to radical formation and its consequential damage, the liberation of a proton (H^+) during the initiation step results in either chemical hydrolysis of the collagen polypeptide chain, or of the hydroxyl and phosphate sites in the adjacent hydroxyapatite, adding a further degree of chemical degradation in surface weathered bones.

In collagen, radical propagation results in removal of the -OH group from phenylalanine and conversion to tyrosine, which is in turn more susceptible to UVB radiation and further radicalisation cycles, decarboxylation and therefore main chain scission and hydrogen abstraction (particularly within glycine), resulting in further scission of the -N-H group and main chain cleavage (Rabotyagova et al. 2008). In addition to these specific pathways, more general oxidation of the polypeptide fragments continues as degradation progresses

with the gradual loss of the tertiary structure. Denaturation of the collagen results in dissolution and loss of the protein leaving only the hydroxyapatite bone mineral.

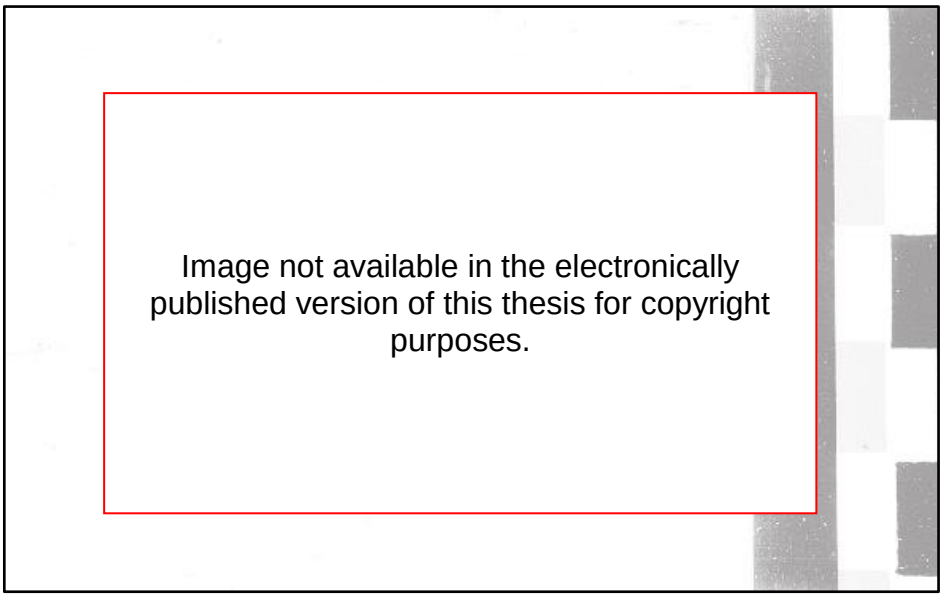

Figure 3.8: Fine scale flakes resulting in crazing of the outermost surface of bone exposed in a periglacial climate (Texier et al. 1998b p. 466).

The loss of the collagen protein that helps bind bone mineral, in combination to thermal and moisture driven expansion and contractions, results in delamination of the circumferential lamellae or plexiform bone layers, cracking between osteonal structures and flaking of irregular bone fragments. Inner layers of bone are partly protected by the bone that overlies them, although the overlying layers do not completely block all solar radiation. Solar radiation diffuses within bone through scattering (Matousek et al. 2005) but diffuse radiation can still penetrate to >300 µm within bone (Golcuk et al. 2006). The outer layers therefore exhibit the greatest levels of collagen loss due to solar irradiation with the outermost layer of bone breaking into microscopic flakes of bone. The size of flakes can vary giving an appearance from crazing for early stage solar weathering to a powdery / chalky appearance for highly weathered bone surfaces (figure 3.8).

3.3.6. Salt crystal damage

Bones deposited on or embedded in the surface of alkaline soils, and those on estuarine and intertidal areas, absorb water with high levels of mineral solutes. On alkaline lake shorelines, surface deposited bones are inundated by seasonal

water level changes and in climates with high temperatures and low humidity, increased evaporation from the upper surface of the bone can draw mineral ion rich water into the bone through capillary action. Drying of the bones increases the concentrations of minerals within the pore waters and leads to crystal growth within the internal pore spaces of bones.

As with the formation of water crystals in freeze-thaw conditions (section 3.3.4.1), the growth of large crystal lattices increases internal pressures within the pore spaces. The internal pressure cracks bone along the lines of weakness provided by the histological structures of bone and opens up fissures for further mineral salt crystal growth. The resulting damage is broadly comparable to that due to freeze-thaw conditions, although the effects are more prevalent within the outer layers of the bone cortex and promote the delamination of the surface layers.

The uptake of cation rich groundwater in these conditions also weakens bone through substitution reactions with phosphorous and calcium within bone mineral (section 3.4.4.2). Dissolution of bone mineral, transport and recrystallization further alters the structure and porosity of bone and promotes collagen damage through chemical hydrolysis and microbial degradation (Hedges & Millard 1995, Hedges et al. 1995, Nielsen-Marsh et al. 2000). Some mineral salts can inhibit microbial action and therefore limit the resultant level of collagen damage (Janaway 1996).

Hot and dry climates promote rapid evapotranspiration of groundwaters through bone. These climates also form alkaline soils (section 3.4.4.2) that are characterised by high levels of soluble mineral ions within their groundwaters.

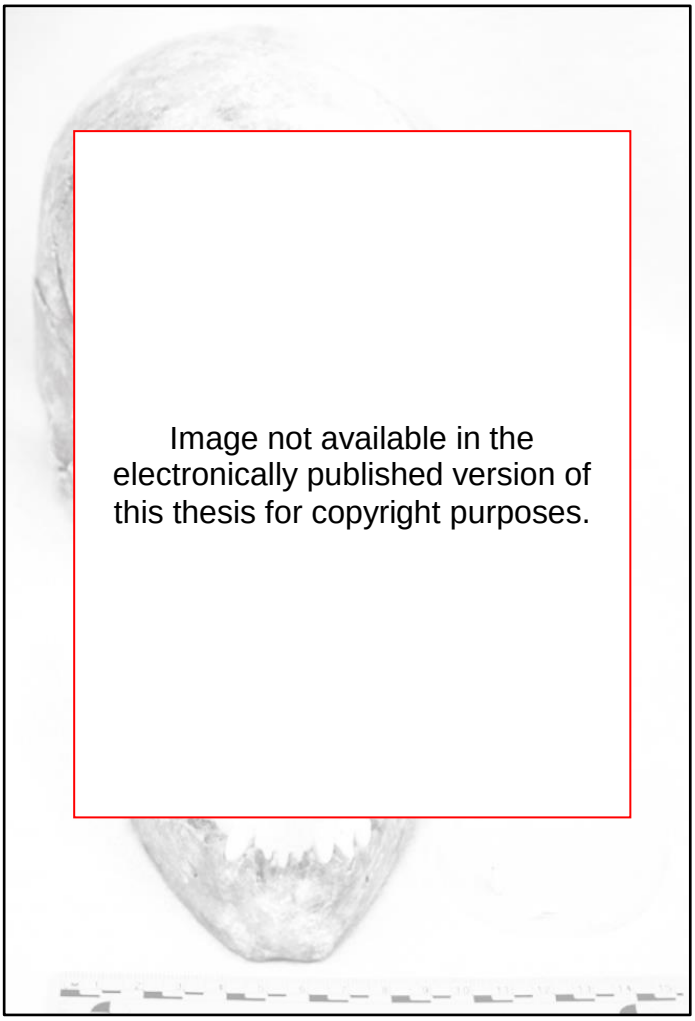

Figure 3.9: Juvenile skull showing differential staining on the skull's right side which was embedded in the soil surface and the left side which exhibits a bleached appearance due to surface weathering (Pokines 2016 p. 66).

In addition, uptake of soil groundwaters and the deposition of mineral salts within bone results in staining of the bone. Where bone is bleached through solar radiation staining clearly marks the level of embedding in the soil surface and in forensic investigations can be a useful marker of earlier disturbance of remains (figure 3.9).

3.3.7. Biological processes affecting the surface condition of bone

Whilst surface deposition of bones exposes them to the multitudinous assaults of the environment and climate discussed in the previous sections, it also makes them available to plants and animals. Even when soft tissues that would provide food for insect larvae are not present, the bones themselves attract a range of scavengers who gnaw, chew or scour the bone in distinctive patterns.

Beyond the faunal taphonomy, if the conditions allow bone surfaces are rapidly colonised by fungi and algae. Whilst both require moisture to grow, algae also require plentiful light and are therefore usually confined to the upper surfaces of bones remaining only within the most outer lamellae of cortical bone. As they photosynthesise sunlight to grow, they absorb some of the energy that would otherwise penetrate the bone and cause photodegradation (section 3.3.5) reducing its impact whilst also discolouring the bone surface green.

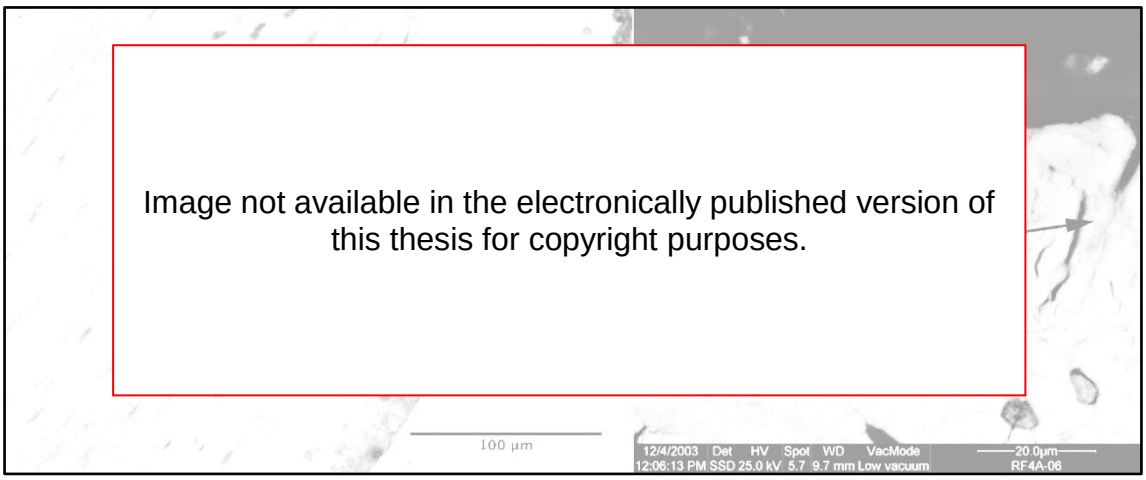

Figure 3.10: Micrographs of bone sections showing Wedl tunnelling. Left: Section with well preserved microstructure and the beginning of Wedl type 1 tunnelling at the outer edge of the bone penetrating through the microstructure (arrows) (Jans 2008 p. 402)*. Right: scanning electron micrograph of a bone section showing Wedl type 2 tunnelling (arrows) found in modern bone.* (Fernández-Jalvo et al. 2010 p. 70)*.*

Fungi, which do not require light, but do require oxygen, can penetrate deep into the bone dissolving bone mineral with excreted acids. Fungal damage to bone occurs in two forms: Wedl type 1 and type 2 tunnels (Hackett 1981) first described by Wedl in 1864. Type 1 tunnels are 10 µm to 15 µm diameter and usually extend from the surface of the bone penetrating into the cortical bone with random branching tunnels that do not respect the histological structures (figure 3.10). Type 2 Wedl tunnels are smaller (5 µm), round in cross section and extend from the Haversian system into the surrounding cortex producing tunnels that resemble canaliculi (Trueman & Martill 2002).

Wedl type 1 tunnels can result in cortical exfoliation as thin layers of bone are undermined and spall off the surface eventually leading to exposure of the cancellous bone. Fungal damage to bone, as with that caused by bacteria, accelerates other taphonomic factors in both surface deposited and buried remains.

3.4. Early diagenesis

Diagenesis is the taphonomic stage from burial onwards, sometimes referred to in archaeological literature as burial taphonomy. Whilst to some palaeontologists the stages of diagenesis and fossilisation are synonymous, fossilisation is more appropriately applied to the diagenetic processes that preserve a record of organic material as rock, i.e. lithification. The early processes of diagenesis are not distinct from those of fossilisation either, indeed many of them make essential changes to buried materials that can, in the correct geochemical conditions, facilitate fossilisation. However, in the majority of burial environments the geochemical conditions are not conducive to the formation of lithified organic materials in the form of fossils, and organic materials are completely degraded within the burial environment by the early diagenetic changes. Diagenetic change leading to fossilisation is therefore only one potential outcome for buried organic material at the far end of the probability curve, hence the need to differentiate it from the diagenetic changes that occur earlier in the diagenetic pathways of organic remains.

Early diagenesis is therefore defined here as the changes to organic materials that occur after burial and prior to their fossilisation. Early diagenesis includes taphonomic alterations that are most relevant to forensic and archaeological assemblages, encompassing the changes driven by biotic (biological) factors within the burial environment, from etching of plant roots to the effect of microflora; and the abiotic factors such as physical deformation due to overlying sediment, soil staining etc.

3.4.1. Microbial alteration to bone

The early diagenesis of most buried skeletal material is strongly influenced by the soft tissue decomposition of the body in the immediate post burial period, as ordinarily intentional inhumation includes a complete body rather than defleshed remains (Buckberry 2000).

For fleshed remains that are buried shortly after death, microbiota are responsible for the earliest bone taphonomy, beginning with the cessation of cellular life in the body via both autolysis and the invasion of gut microflora

(White & Booth 2014) although anthropogenic factors may alter this response (Booth & Madgwick 2016, Booth et al. 2015, Booth 2016, Smith et al. 2016). The invasion of the gut microflora, in association with the lowering of the pH of the extracellular environment through loss of regulation of calcium ions and the presence of putrescent bio acids, leads to initial loss of bone mineral and exposure of the collagen fibrils. The microflora liberated from the gut and transported to the bone (and other tissues) via the lymphatic and blood vessels (White & Booth 2014), access cortical bone via the physiological spaces such as the Haversian system, canaliculi and lacunae. The collagenous lining of the lacunae (section 2.2.5) provide an initial nutrient source (De La Cruz 2001) and the breakdown of collagen liberates additional protons and secondary metabolites which in turn result in further demineralisation. Collagen is not susceptible to the general proteases produced by less specific bacteria, however, collagenase producing bacteria are present in the gut microflora of most mammalian species and with soil microbiota (Child et al. 1993, Child 1995a). The collagenases cleave the polypeptide chains at sites of specific amino acid residue sequences (e.g. gly-pro-hyp) resulting in short peptide chains that provide a source of energy for microorganisms or are further broken down by other more general proteases (Child 1995a, 1995b). The resultant loss of collagen is seen histologically as tunnelling or micro-foci of destruction (Hackett 1981, Garland 1987, 1989) and leads to a total destruction of the histological structure of the bone (Bell 1990).

These assaults occur over a period of decades or centuries following deposition (Hedges & Millard 1995, Collins et al. 2002a, Hedges 2002) resulting more often in the total destruction of the bone than in its preservation through fossilisation (Nielsen-Marsh & Hedges 2000, Pike et al. 2001, Trueman & Martill 2002). Indeed a number of authors have noted that fossilised bone shows only minor changes due to microbial assault (Hedges 2002, Trueman & Martill 2002, Chinsamy-Turan 2005) suggesting that the limited microbial damage in the early depositional environment is a significant determining factor in the long term preservation and fossilisation of bone. Of particular importance in this is the dissociation of the skeletal remains from the anaerobic gut microflora (e.g. in dismemberment through predation etc.) which limits the damage that such endogenous microbes can effect (Bell et al. 1996, Farlow & Argast 2006, White & Booth 2014).

Such dissociation through predation or dismemberment will normally result in a period of surface weathering prior to the incorporation of the skeletalised bones into the burial environment. The effects of surface weathering (section 3.3), can result in gross disruption to the structure of skeletal elements leading to cracking etc. which in turn open the bone's structures to the soil microbiota promoting further degradation of the bone through dissolution of bone mineral.

3.4.2. Porosity changes to bone

A key factor in the taphonomic survival of archaeological bone in the burial environment and in fossilisation is the degree of porosity. The Haversian system and the canaliculi make bone naturally porous, however microbial degradation (section 3.4.1), chemical hydrolysis of the collagen (section 3.4.3) and chemical dissolution of bone mineral (section 3.4.4.1) all add to the level of porosity and are associated with particular ranges of pore diameter (Smith et al. 2007).

Porosity changes to bone have been categorised through mercury intrusion porosimetry and scanning electron microscopy as:

- Microporosity (s): pore diameters below the scale of the collagen fibril (<0.1µm) associated with the chemical hydrolysis of collagen;
- Mesoporosity (m): pore diameters 0.1 µm to 1.0 µm associated with microbial degradation of collagen (i.e. microscopic focal destructions (MFD) and tunnelling); and
- Macroporosity (l): pore diameters above 1 µm associated with mineral dissolution and recrystallization in bone.

(Turner-Walker et al. 2002, Nielsen-Marsh & Hedges, 1999, Hedges et al. 1995).

The ratios of these types of porosity are a useful indicator of the preservation and diagenetic history of bone (Jans et al. 2004, Jans 2013). High levels of mesoporosity and macroporosity show a high degree of correspondence with poor scores on the Oxford Histological Index (a measure of histological preservation) (Smith 2002). Pre-fossil bone on the other hand, demonstrate low

levels of mesoporosity and macroporosity but high levels of microporosity illustrating that good preservation of bone is a key factor in bone fossilisation.

Whilst degradation of archaeological bone in the burial environment leads to a gradual increase in porosity, during the later stages of diagenesis and fossilisation porosity decreases as the pores are infilled by calcite and other minerals. Indeed the mineral in-filling of pores is seen as a key factor for the fossilisation of bone (Collins et al. 2002b, Grupe 2007).

3.4.3. Chemical hydrolysis of collagen

Collagen is insoluble in normal circumstances and only broken down in short time scales through extremes of pH or by microbial action utilising collagenases (Child 1995a, Chung et al. 2004). Over longer timescales however, slow hydrolysis of the peptide bonds can denature the collagen producing shorter length peptide chains in random coil conformations (Collins 1995). These gelatines are water soluble and can be easily leached from the bone or consumed by microbial activity. This loss of the collagen results in reduced mechanical strength (loss of viscoelasticity) (section 3.6.3) (Turner-Walker & Parry 1995, Currey 2006) and an increase in the porosity of the bone producing pore diameters of less than 0.1 µm (Nielsen-Marsh & Hedges 1999, Mays 2010). Chemical hydrolysis is very slow acting and is dependent on multiple factors including the pH, the availability of water and temperature (Nielsen-Marsh et al. 2007).

3.4.4. Soil pH

Sediments and soils are constituted of three inorganic phases in dynamic interaction. The solid phase represents c.50% by volume and is made up of particles of weathered geological parent material with particle size distributions from 2 mm for sand and fine gravels down to <2 µm for clays (British Standards Institution 2015) as well as solid decomposing organic material. The soil groundwater solution (the liquid phase) of water, dissolved gases, and mineral derived ion species is held through surface tension to the outside of these mineral particles and partially fills the gaps between them (figure 3.11). A mix of

gasses fills any remaining space between the mineral particles forming the gaseous phase.

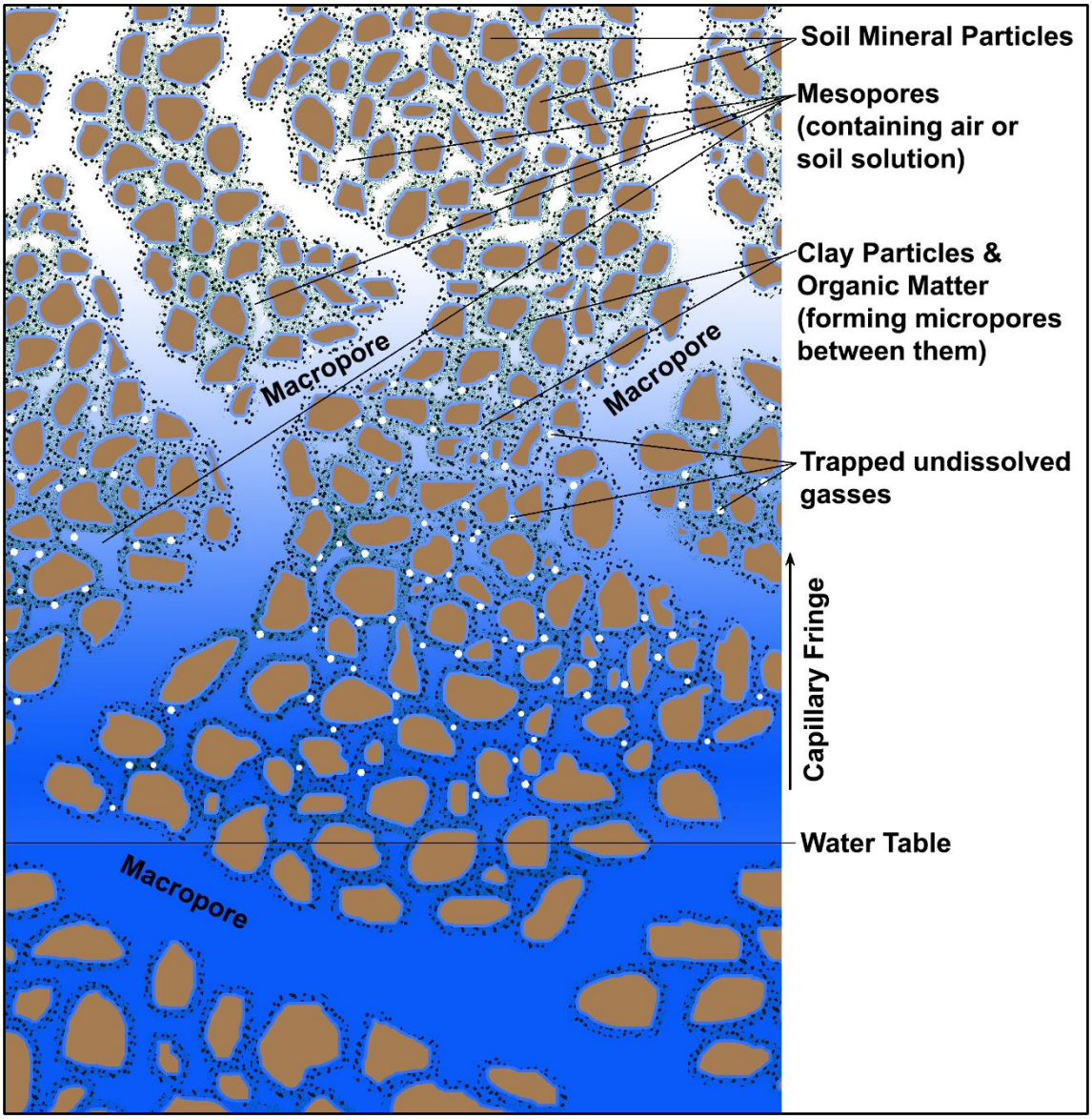

Figure 3.11: The microscopic structure of soils (source: author).

The relative volumes of the liquid and gaseous phases determines the soil moisture content and can vary both spatially and temporally due to the level of precipitation, flooding, groundwater flows, how free draining the soil is and the topology of the location. The biotic diagenetic processes occur primarily within the liquid phase of the groundwater and on the liquid - solid phase boundary, as well as within the structures afforded by buried material (Lindsay 1979). The biotic processes are reliant on, and in some cases inhibited by, the properties of the groundwater solution. Abiotic diagenetic processes altering buried materials occur within the groundwater solutions of soils and sediments. The

characteristics of the soil groundwater play a vital role in the preservation or destruction of buried archaeological remains (Caple 1996, Holden et al. 2006).

Soil groundwater solutions are a complex interaction defined not only by the general environment of the groundwater (i.e. pH, temperature, water content, redox potential etc.) but also the mineralogy, decomposing organic matter and the composition of the soil atmosphere. In addition these factors interact with each other and slight alterations to one (e.g. by disturbance of the soil to measure one factor) will likely alter the interactions of them all, making precise measurements from soils difficult and inaccurate at the molecular level (Hedges & Millard 1995). The complexity of groundwater geochemistry is addressed in other disciplines through the use of computer modelling, although the level of uncertainty extrapolated from measured data used as inputs to such reactive transition models remains problematic (van Turnhout et al. 2016). Additionally, the capacity of computer processing cycles limit the scale resolution that such models can achieve. Therefore, reactive transport models are best suited to larger scale generalised geochemical groundwater modelling and ill-suited to the complexities of diagenesis at an individual skeletal element level.

Geochemical modelling has had limited use in archaeological science, with the exceptions of the exploratory work in this field by Wilson (2004) and more recently in the consideration of preservation in situ of archaeological deposits (Historic England, 2016). Some approaches to modelling the hydrology of the bone-groundwater system have been made, but these were limited to examining the soil water movement (and related availability / dissolution of ion species) (Hedges & Millard 1995) Archaeology and conservation have instead relied on a qualitative understanding of soil groundwater interactions with buried archaeological materials with quantitative study of diagenetic change being limited to glass and metal objects.

In the simplest models for soil groundwaters the pH is controlled by the $CaCO_3$ - H_2O - CO_2 equilibria:

$$CaCO_3 \rightleftharpoons Ca^{2+} + CO_3^{2-}$$

$$CO_3^{2-} + H^+ \rightleftharpoons HCO_3^-$$

$$HCO_3^- + H^+ \rightleftharpoons H_2CO_3$$

$$H_2CO_3 \rightleftharpoons H_2O + CO_2$$

(Pollard & Heron 2008)

However, the presence of phosphate, sulphate and other ion species will impact the groundwater chemistry, and the form in which these species are present has a strong effect on the stability and solubility of other elements within the mineral and groundwater, further complicating definition of soil groundwater properties.

The following two sections therefore describe the interaction of groundwater geochemistry with buried bone tissues only in terms of general soil properties, the first in reference to low pH values (acidic soils) and the second in reference to high pH values (alkaline soils).

3.4.4.1. Acidic burial weathering of bone

Acidic soils occur widely and their formation is driven by three main factors: soil moisture and the rate of water flow through the soil (hydraulic conduction), parent geology, and the level of decomposing organic material. As pH is a measure of hydrogen ion activity, soil moisture, which through its auto-ionisation equilibrium is the main source of H^+ ions, underlies each of these and the global pattern of soil moisture (figure 3.12) is therefore strongly correlated with that of soil pH (figure 3.13).

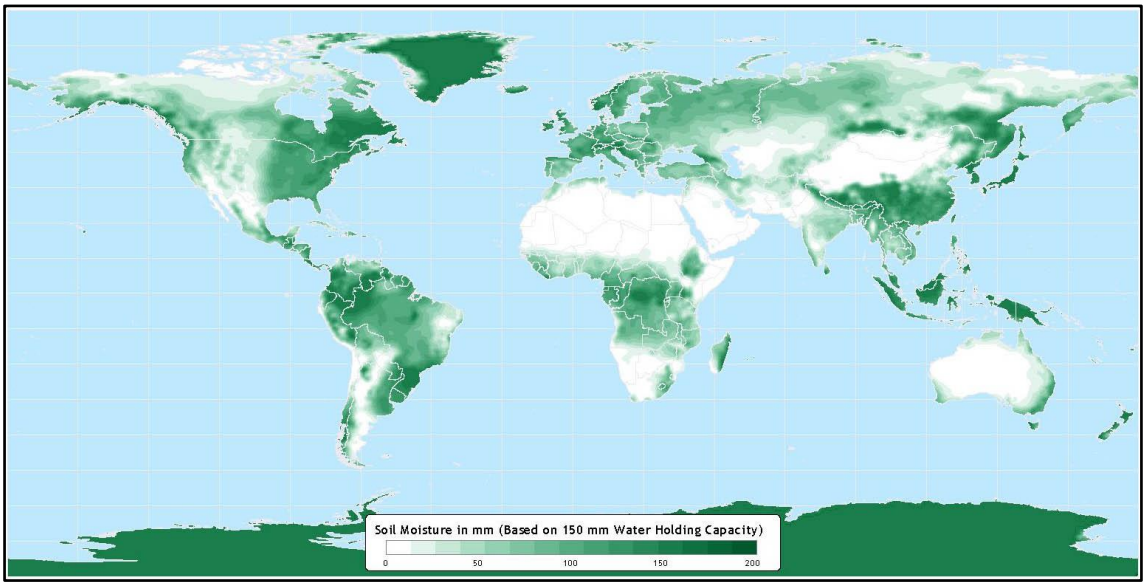

Figure 3.12: Global soil moisture content (Center for Sustainability and the Global Environment 2016 based on data from Willmott & Matsuura 2001).

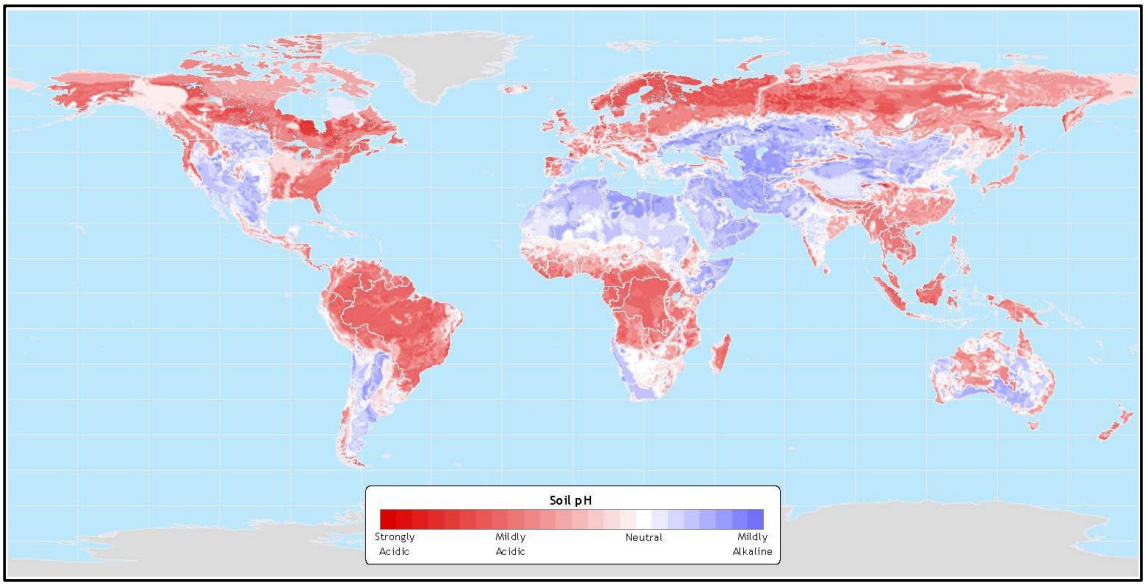

Figure 3.13: Global topsoil pH (Center for Sustainability and the Global Environment 2016).

In sands and other free draining soils (high hydraulic conduction) the alkaline cations (Ca^{2+}, Mg^{2+}, K^{+}, NH_4^{+}, Na^{+}) are replaced on the negatively charged soil colloids (fine clay particles suspended within the larger particle size sand) by higher lyotropic level cations (Al^{3+} and H^{+}), and transported away in the soil groundwater. This leaching of alkaline cations results in a drop in the cation exchange capacity and an increase in acidity. In wet soils with lower hydraulic conduction rates and which incorporate large amounts of organic matter (e.g. leaf litter), the degradation of the organic material liberates humic, oxalic and tannic acids. The lower hydraulic conduction rates mean these are not leached

away in soil groundwater transport and contribute to overall soil acidity (Kibblewhite et al. 2015).

The type of parent material from which soils are derived is significant in soils pH. Where the parent geology includes large amounts of free quartz (e.g. granites), the derived soil mineral particles in the soil weather through hydration of the quartz (SiO_2) to silicic acid:

$$SiO_2 + 2H_2O \rightarrow H_4SiO_4$$

and the addition of silicic acid to the soil groundwater increases the acidity of the soil. Additionally, the parent geologies which contain significant amounts of quartz (i.e. igneous rocks) are also those with low levels of calcium and magnesium, the weathering of which would otherwise neutralise the silicic acid (Depetris et al. 2014) (section 3.4.4.2).

Soils derived from sulfide rich parent materials such as shale, if exposed to wet oxidizing conditions, can exhibit very low pH values as the sulphide minerals (most commonly pyrite (FeS_2)) are hydrated and then oxidized to form sulphuric acid. Such soils are highly responsive to changes in the aeration and water content as anoxic reducing environments will drive the equilibrium in the reverse reaction (Akcil & Koldas 2006).

In terms of diagenetic change, acid soils are the least conducive burial conditions for preservation of skeletal elements (figure 3.14). Highly acidic soils induce rapid dissolution of the bone mineral and exposure of the organic components of bone to further destruction and can lead to complete destruction of the bone (Crow 2008, Turner-Walker 2008). The effect of acidic soils on skeletal assemblages is not uniform however. Soil pH biases skeletal population models and incident rates of some palaeopathological analysis due to the susceptibility of less dense infant or pathological bone to dissolution within acidic burial conditions (Gordon & Buikstra 1981, Pokines & De La Paz 2016).

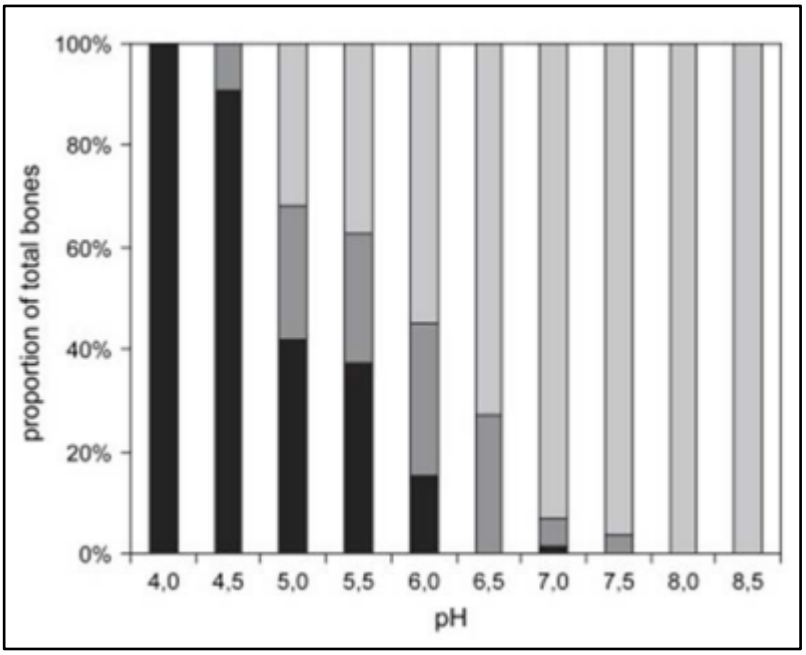

Figure 3.14: The impact of soil pH on the survival of bone. (Black, bones absent; medium grey shading, bones with >33% porosity; light grey shading, bones with <33% porosity (after Nielsen-Marsh et al. 2007).

The solubility of calcium phosphate in the form of the biomineral hydroxyapatite is sensitive to pH, figure 3.15 illustrates the change in calcium phosphate solubility with decreasing pH.

Figure 3.15: Influence of pH on solubility of bone calcium phosphate from bovine bone (Eeckhout 1990 p. 530).

At pH levels closer to neutral, calcium phosphate solubility is low, whilst below pH 5.3, the solubility of calcium phosphate increases rapidly. In burial environments, the low solubility of calcium phosphate in mildly acidic soil

groundwater conditions (above pH 5.3) will still lead to some dissolution of bone mineral, but the rate of loss is low. However, in soils with pH below 5.3 bone mineral dissolution is significantly more rapid (Eeckhout 1990) and bone is susceptible to the substitution within the apatite crystal lattice of Ca^{2+}, PO_4^{2-} or CO_3^{2-} by exogenous ions (Turner-Walker 2008). Where low soil pH is linked to high hydraulic conductivity (e.g. free draining soils and high precipitation), the higher groundwater flow rates leach away dissolved ions (Ca^{2+}, PO_4^{2-} or CO_3^{2-}) and create a solubility gradient between the groundwater within the porous structure of bone (bone pore water) and the surrounding soil. This solubility gradient results in calcium and phosphorus dissolved out of the bone mineral being transported away from the bone and the recharge of H^+ ions within the bone pore water allowing further dissolution. The greater the rate of hydraulic conduction the steeper the solubility gradient leading to very rapid loss of bone mineral in these acidic soils.

On silts and clay soils, the pore size between soil mineral particles is smaller and this impedes hydraulic conductivity (Salarashayeri & Siosemarde 2012). Such soils in areas of high precipitation result in waterlogged soils (e.g. heavy clays) and acidity is derived from the decomposition of organic matter (e.g. peat) or from the weathering of the parent material. In these burial environments the dissolution of calcium phosphate from bone mineral saturates the local bone pore water, slowing the rate of further dissolution as calcium phosphate can only be transported out of the bone's porous structures through diffusion (Hedges & Millard 1995, Kibblewhite et al. 2015).

In the presence of an abundance of protons (H^+ ions), such as in acidic conditions below pH 5.3 or as a result of collagen degradation (section 3.4.3), the protons can react at the hydroxyl and phosphate sites of the bone mineral platelets. The products of these reactions include calcium phosphate, tricalcium phosphate and most significantly brushite (calcium hydrogen phosphate) (Newesely 1989, Zylberberg & Laurin 2011). Where the hydraulic conduction level is high these minerals can be leached out of bone into the groundwater, however in conditions where the solubility gradient between bone and the surrounding groundwater is more even, the solubility of these minerals leads to their recrystallization within the bone and damage to the bone structure (section 3.4.5). In acidic soils the leaching of Ca^{2+} leads to its substitution with other

metal ions (e.g. Fe^{2+}) present in the groundwater solution, leading to the formation of mineral salts with crystal structures that are larger than hydroxyapatite (e.g. vivianite). The volumetric expansion resulting from the substitution of hydroxyapatite for large crystal minerals produces internal tensile stress within the bones pore spaces and promotes cracking. The variation in colour between hydroxyapatite and minerals such as vivianite, produces darkening of bone from acidic burial environments (Piepenbrink 1989).

In aerated acidic burial environments which promote microbiological attack of the collagen, the dissolution and disruption of the bone mineral exposes the collagen to aerobic bacterial degradation. In these burial conditions bone preservation is very poor as the combination of acidic dissolution of bone mineral and biotic consumption of the bone protein result in complete destruction of the bone. However, in burial environments that are both anoxic and acidic, particularly very low pH soils where microbial action is inhibited, bone collagen is preserved despite the bone mineral being partially or completely lost to dissolution into the soil groundwater (Turner-Walker & Peacock 2008). In these cases the collagen, whilst it is still hydrated, retains the shape and surface topography of the original bone. However, structural rigidity is lost and the bone can be easily bent and distorted (Milner et al. 2011, High et al. 2015, High et al. 2016) in this demineralised state. Once removed from the burial environment wet demineralised bone is susceptible to rapid biotic degradation unless kept in an conditions that inhibit microbial attack (i.e. cold storage between 0 - 5°C). Demineralised bone from these acidic soils retain the histological details of the original bone. The presence of undegraded collagen fibrils can be seen in the histological structure, particularly the osteon / Haversian systems, within recovered bones such as those recovered from the site of Star Carr (Giraud-Guille 1988).

In acidic soils that experience repeated wetting and drying, the low diffusion of bone pore water set up a hydraulic potential as the surrounding soil moisture decreases. This hydraulic potential pulls water from the internal pore spaces of bones transporting dissolved calcium phosphate with it. When soil moisture levels rise again, the hydraulic potential is reversed and water is pumped back into the bone, recharging the pore water with H^+ ions promoting further dissolution of bone mineral (Hedges & Millard 1995, Turner-Walker 2008).

Bone tissue that is demineralised in the laboratory as a sample preparation step in isotopic analysis (e.g. Deniro & Epstein 1981, Richards & Hedges 1999) is translucent yellow-cream in appearance, whilst archaeologically demineralised bone is generally very dark in colour due to staining from the burial environment, particularly from metal ions that are mobile within acidic soils and the formation of minerals such as vivianite within the bone structure.

3.4.4.2. Alkaline burial weathering of bone

Alkaline soils occur less frequently than acidic soils and their formation is as a result of high concentrations of ions of calcium, magnesium, sulfates, bicarbonate, sodium and nitrates within the soil (Day & Ludeke 1993). The concentrations of these ions is a function of the linked factors of soil moisture (figures 3.12 and 3.13), parent material and geology. Additionally, in the saturation of soils by sea and lake waters rich in salts can also form alkaline soils.

Soil moisture is a function of the rate of hydraulic conduction, influenced by soil pore size and the levels of precipitation and evapotranspiration (i.e. climate). In temperate regions where there is regular rainfall to maintain soil moisture levels, the soil pore size is the main factor determining the rates of hydraulic conduction. In clays and fine silts where the soil pore size is small enough to significantly impede groundwater flows, the level of leaching of ion species from either the soil mineral particles, or from buried material such as bone is limited resulting in more neutral pH. Where these conditions pertain, the formation of higher pH soils is strongly correlated to the soil geology (figures 3.16 and 3.17).

In areas of chalk or limestone geologies rock is rich in calcium carbonate, magnesium etc. and the weathering of these rocks results in an abundance of the alkaline cations (Ca^{2+}, Mg^{2+}, K^{+}, NH_4^{+}, Na^{+}) bonded to negatively charged soil colloids. In temperate regions where hydraulic conduction is low mildly alkaline soils can form. Figures 3.16 and 3.17 compare soil carbonate content with soil pH showing a strong correlation in the UK between areas of limestone and chalk geology and alkaline soils (e.g. South Downs, Yorkshire Wolds).

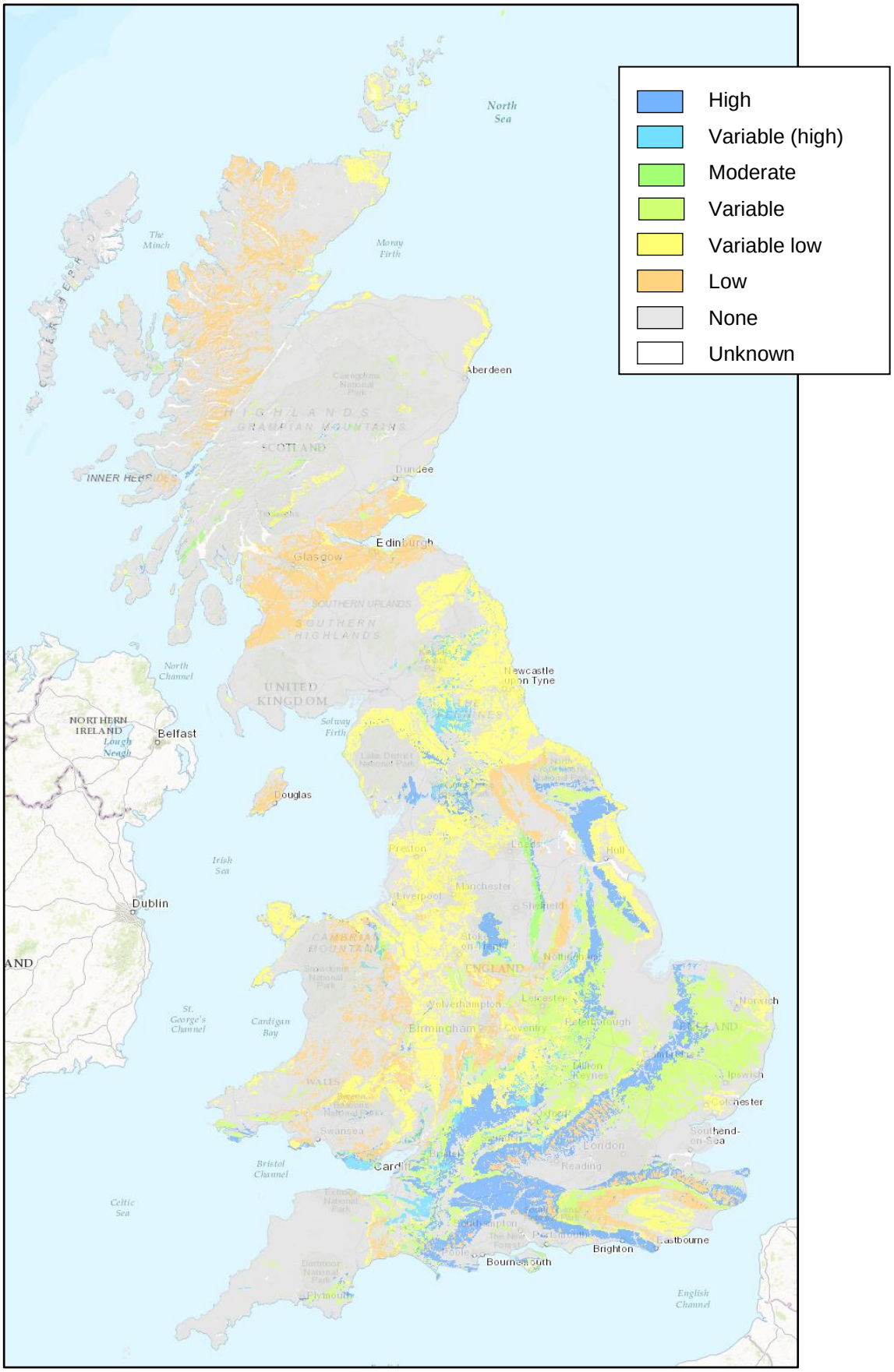

Figure 3.16: Map of carbonate content of parent materials for soils within the UK (UKSO 2016a).

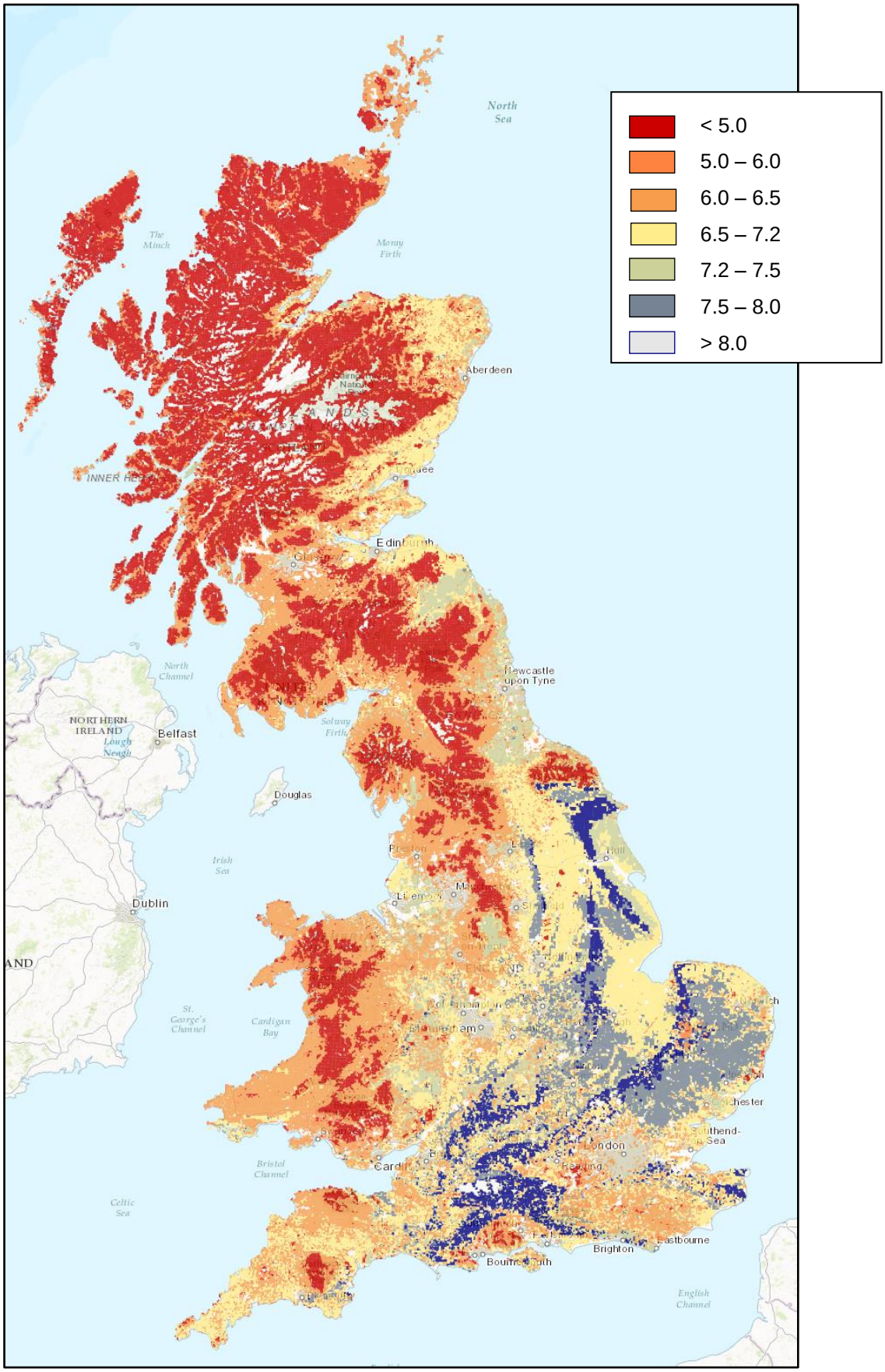

Figure 3.17: Map of topsoil pH within the UK (UKSO 2016b).

In regions with low humidity and low precipitation, soil groundwater is removed from the soil through evapotranspiration driven by either high temperatures, or the freeze-drying effect of air movement in very low ambient temperatures. The reduced soil moisture limits hydraulic conduction within soils, and capillary action draws groundwater upwards from deeper levels. The movement of groundwater from deeper stratigraphic levels enriches soils nearer the surface with mineral ions from the parent geology and produces highly alkaline soils that can inhibit microbial action and limit vegetation growth.

Within neutral to mildly alkaline burial environments, hydroxyapatite remains relatively insoluble (figure 3.15), and collagen is stable against chemical hydrolysis within pH ranges of 3 to 7.5 (Turner-Walker 2008) affording good initial preservation of both the bone mineral and the associated protein.

Over longer timescales slow chemical hydrolysis of the collagen occurs leading to chemical deterioration and denaturing of collagen (Collins et al. 2002a) but whilst this results in cutting of the fibrils into shorter peptide units, the surrounding bone mineral holds these in position and restricts diffusion.

In more strongly alkaline burial environments with high moisture contents the low redox potential promotes the chemical hydrolysis of the collagen polypeptide leading to changes in the organization of the molecule (Miles et al. 2000). In addition collagen is susceptible at very high pH values, to swelling of the triple polypeptide chain fibrils, reducing the effectiveness of the hydrophobic areas of the molecule and allowing cleavage of the polypeptide chain through hydrolysis of the peptide bond with resultant interruption to the associated bone mineral (Rudakova & Zaikov 1987, Riley & Collins 1994, Collins et al. 1995). The hydrolysis of collagen produces random coil gelatine which is more hydrophilic and swells as it absorbs water. This swelling is most severe and occurs fastest where water is most readily available via diffusion adjacent to the Haversian canal and canaliculi, producing a gradient of effect with distance from access to the bone pore water. The differential levels of swelling in adjacent lamellae produce internal tension stress within the secondary osteons leading to the formation of microcracks radiating out through the outer circumferential lamellae of the secondary osteons and increasing access to the osteon structure by water and precipitate minerals, further disrupting the structure of the bone (figure 3.18).

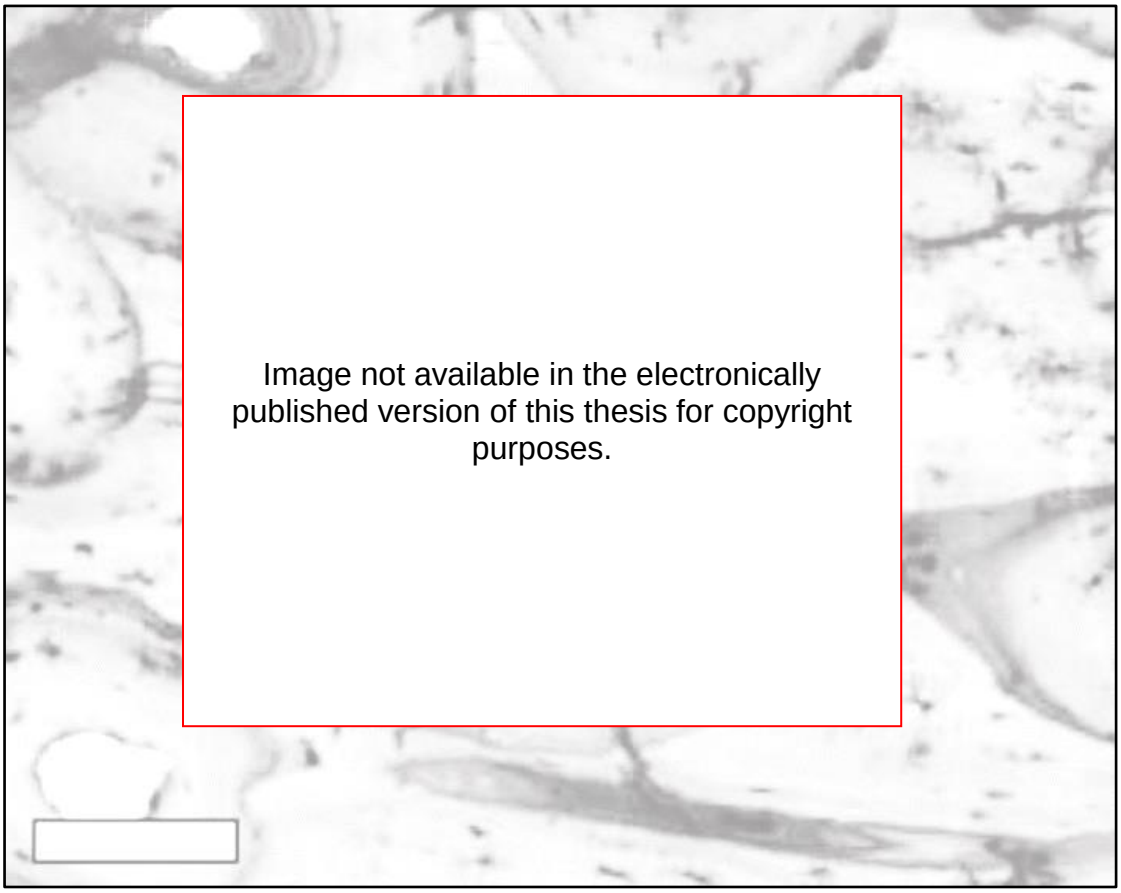

Figure 3.18: Micrograph showing radial microcracks through the cement line of a secondary osteon associated with hydration swelling of collagen and gelatine, from a long bone of Camarasaurus, CMNH 36021 (Scale bar: 100 µm) (Pfretzschner 2004 p. 608).

In regions that experience seasonal variations in climate, the cycling of very dry and wet seasons results in considerable fluctuation in the groundwater mineral concentrations. During dry periods evapotranspiration of moisture from the soil is increased and as water is lost from groundwater, dissolved minerals are concentrated, and pH rises. In very dry environments, the concentrations can reach the solubility capacity threshold for the groundwater and recrystallization of minerals occurs. The growth of large mineral crystals within the pore spaces leads to an increase in internal pressure within the bone and results in damage to the structure and mineral in-filling of cracks and pores (section 3.5). During wet periods the increased levels of soil moisture reduce the concentrations of mineral ions within the groundwater and bone pore water and allow re-dissolution, thus providing access within the damaged bone to further degradation. Cycles of wet and dry conditions therefore produce repeated crystallization and dissolution and result in poor preservation of bone and other biomineralized remains.

Degraded bone from alkaline burial environments is generally light coloured, cream or even white. The metal ions that are absorbed into bone and stain it within acidic environments are immobilised in alkaline burial conditions in carbonate or oxyhydroxide forms which are insoluble and cannot therefore be absorbed into bone (Turner-Walker 2008).

3.4.5. Recrystallization

The dissolution and recrystallization of hydroxyapatite is controlled *in vivo* by the bone cells. Calcium and phosphorous are derived from the supersaturated extracellular fluid which creates an environment where hydroxyapatite is in stable equilibrium. By contrast in most burial environments the groundwater is not saturated in calcium or phosphate ions and bone mineral can therefore be liable to dissolution and recrystallization, precipitating into more poorly crystalline forms.

Binding of collagen and bone mineral initially prevents access of enzymatic collagenases. Microscopic pores are all below 8 nm and the microbial collagenases are large molecules that can't penetrate into the small pores (Nielsen-Marsh et al. 2000, Pike et al. 2001)

The loss of the collagenous structure binding with the bone mineral reduces the energy of dissolution and makes the bone mineral more susceptible to dissolution. The resulting increase in porosity around the sites of collagen deterioration is then filled by the deposit of secondary mineral crystals which in some cases may also fill the physiological pores leading to a loss of the Haversian system, lacunae and their associated canaliculi (Collins et al. 2002b, Grupe 2007). The rate of collagen deterioration is dependent on both time and temperature (Collins et al. 1995) as well as being influenced by the rate of mineral loss due to environmental pH as discussed above.

Whilst these minerals are soluble and can be liberated into the bone/soil solution, brushite can re-crystallize within the crystal matrix of the bone mineral and between laminae (section 3.4.4.1). The crystals of brushite are much larger than those of bone mineral and this leads to an increase in pressure within the bone microstructure producing cracking, and disruption of the laminae in the osteons. The solubility of brushite makes degraded bone susceptible to slight

changes in water content, as fluctuations can drive repeated dissolution-recrystallization cycles adding a physicochemical process to the destruction of bone (De La Cruz 2001, Pike et al. 2001, Hedges 2002). Additionally the solubility of brushite has been shown to increase with the availability of Mg^{2+} and SO_4^{2-} and as brushite recrystallizes, the presence of these ions alters the size and form of brushite crystals from rhombic tabular to thickened prismatic crystals leading to greater levels of damage (Kuz'mina et al. 2014).

3.5. Fossilisation

The process of fossilisation is, in general a process of ion exchange, recrystallization and mineral pore-filling of bone. The successful preservation of bone through fossilisation is highly reliant on the environmental factors in the burial environment (Paine 1937) primarily groundwater chemistry and pH, although high temperatures clearly increase reaction rates and therefore affect the timescales involved (Hedges 2002).

To become fossilised, skeletal elements must survive the early diagenetic changes with limited damage to the overall histological structure of the bone and the bone mineral (section 3.4). Microbial damage (section 3.4.1) and mineral dissolution (section 3.4.4.1) both lead to significantly increased mesoporosity and macroporosity which open the internal structure up to the external environment and therefore prevent the long term survival of bone (Smith 2002, Jans et al. 2004, Jans 2013). Consequently the taphonomy of the immediate postmortem period may be the most important in terms of bone fossilisation; fossilisation is most common in reducing and high pH conditions (Piepenbrink 1989) which promote bone mineral preservation and low microbial activity (section 3.4.4.2). The combination of anoxic (reducing) and high pH conditions accounts for the fossilisation of bones being associated with aquatic environments such as lake or marine silt sediments (sections 5.4.1 and 5.4.2) although fossilisation does occur in some terrestrial environments (Martin 1999). The presence of collagen and its influence on the redox potential dominates the chemical milieu of the bone within the early diagenetic stage. For fossilisation to occur, with its slower pH dependant substitution reactions, it requires the loss of most of the collagen component through slow chemical hydrolysis (Trueman & Martill 2002). The product of chemical hydrolysis of the collagen is gelatine which absorbs water and swells adding internal pressure to bone structure resulting in microcracks across the cement line boundaries of the secondary osteons (figure 3.18) before the gelatine is leached out of the bone (Pfretzschner 2000, 2006). The opening of these cracks towards the end of the early diagenesis stage bridges the cement line of secondary osteons allowing further hydrolysis of collagen and exchange of ions across the bone volume considerably accelerating the fossilisation process.

Hassan et al. showed early on that bone in the burial environment underwent shifts in the proportions of phosphate and carbonate ions (Hassan et al. 1977) and whilst the position of phosphate and carbonate in the *in vivo* biological apatite structures is now well understood following the work of researchers such as Rey et al. (Rey et al. 1991, Fleet & Liu 2009) the changes in fossilisation are harder to characterise beyond general descriptions of the exchange reactions at the chemical scale and physical changes at the microscopic scale.

In general collagen is slowly replaced by minerals, particularly through recrystallisation and substitution reactions which exchange the Ca^{2+} from hydroxyapatite for the metal ions Mn^{2+}, Sr^{2+}, Fe^{2+}, U^{4+}, Zn^{2+} and Ba^{2+}. At the same time OH^- and PO_4^{3-} is substituted with Cl^-, F^- and CO_3^{2-} transforming the hydroxyapatite mineral into a high carbonate fluorapatite (Pfretzschner 2004).

The replacement of the collagen with larger recrystallizations of the hydroxyapatite alter the mineral phase to a more diagenetically stable form, decreasing access to the crystal surfaces for reactants and slowing changes to the bone (Pfretzschner 2004). Whilst the larger crystal sizes do result in some damage to the bone the gross histological structure is retained.

The end of the early diagenetic stage for pre-fossilised bone is marked by the loss of all organic content and the infilling of the small canaliculi with minerals such as pyrite. In the late diagenetic stage conditions in the bone shift to buffering by the presence of phosphates derived from the apatite in the bone to preserve the high pH and low redox conditions. Metal ions precipitate out as hydroxides lowering the pH and driving apatite dissolution and etching of the bone mineral. The liberated phosphate buffers the solution back to the high pH resulting in decreased solubility for the newly formed minerals, which precipitate out at the site of the mineral etching and thereby leading to gradual replacement of bone mineral with other mineral crystals (Michel et al. 1995, Lee–Thorp 2002).

Minerals at this stage only form in cavities which are still accessible to the groundwater solutions (Haversian systems and cracks etc). Therefore increased cracking in the early diagenesis or in surface weathering increase the access for mineral precipitation and ensure replacement of bone mineral across the whole of the bone volume. Later oxidation of the minerals can alter them further

into more durable forms e.g. the conversion of pyrite to hematite (Pfretzschner 2004).

In this way fossilisation follows a process of bone mineral replacement and a very slow increase in crystallinity (Bish & Chipera 1988, Chipera & Bish 1991, Lee-Thorp & van der Merwe 1991, Reiche et al. 2002) occurring over timescales of millennia (Sillen 1989).

3.6. Fracture of bone

The fracture surfaces of fragmentary bone reflect the underlying complex structure of bone, and their appearance therefore varies in relation to the orientation and type of fracture they have been subject to. In addition to this the level of taphonomic change further alters the fracture mechanics of bone. Therefore, when studying the challenges posed by the digital refitting of fragmentary bone, an understanding of long bone fracture mechanics and fracture patterns produced is useful.

Whilst fractures to long bones occur in both the diaphysis (mainly cortical bone) and the epiphyses (mainly trabecular bone), the research in this thesis is concerned with the digital refit of fragmentary bones. This process relies on the matching of two solid surfaces of similar morphology and therefore is currently concentrated on cortical bone where the cortical thickness is sufficient to provide a digitisable surface. The digitisation of fracture surfaces through trabecular bone is often problematic and provides too small a surface to give a statistically significant match (section 6.10). As such we concentrate in this section on the fracture mechanics of cortical bone reserving the study of trabecular fractures in the epiphyses for future research.

3.6.1. Types of fracture

The huge variety in shape of skeletal elements in nature, in conjunction with the varied circumstances and direction in which a bone might be subject to a force greater than its ultimate strength threshold value mean that fractures to bone vary almost infinitely in their appearance (Mays 2010). However, for convenience the spectrum of possible fractures may be categorised into a few generalised types of fracture.

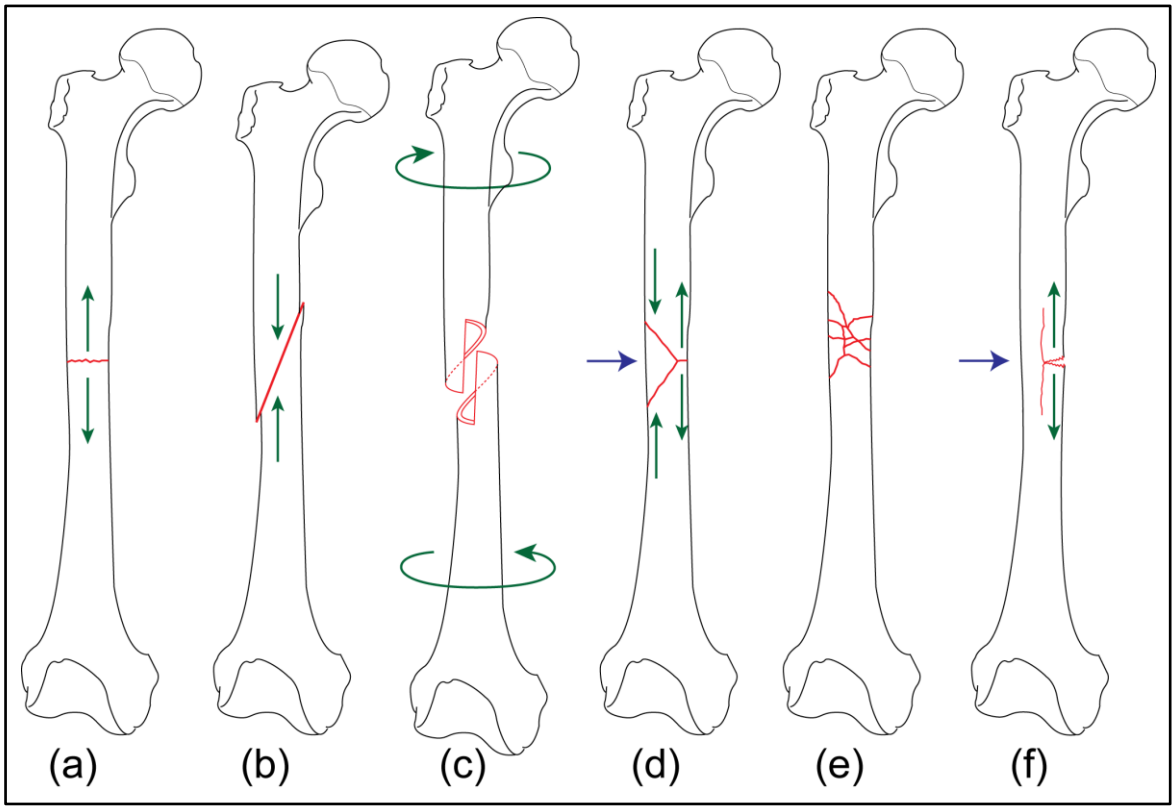

Figure 3.19: Common types of fracture (a) transverse fracture; (b) oblique fracture; (c) spiral fracture; (d) butterfly fracture; (e) comminuted fracture; (f) greenstick fracture. Green arrows show the forces acting on the bone, blue arrows show bending moment directions (source: author).

In all of these common types of fracture the mechanics involved are the result of one or more of the three strain modes:

- Compression
- Tension
- Shear

These can be applied axially (i.e. in line with the long bone's axis), transversely (i.e. to the side of the bone), or radially (i.e. the application of a twisting force around the bone's long axis).

3.6.2. Fracture mechanics

When a load is applied to a linear elastic solid, the stress (pressure) placed on that material causes it to deform, the degree to which it deforms locally (per unit area) is strain and there is a direct proportional relationship between stress and strain (Young's modulus of elasticity). Elastic materials can absorb stress (pressure) through deformation and following removal of the stress relax back to their original shape. Each material has a natural limit to the level of elastic deformation that it can undergo (the yield strength) and above the point at which it yields to the deformation pressure (the post-yield area) materials undergo plastic deformation where the deformation remains permanent upon the removal of the stress. If the stress is continued beyond the yield strength then the material continues in plastic deformation until eventually the material reaches its ultimate strength threshold and fails.

This relationship between stress and strain can be shown graphically in a load-deformation curve for materials such as that for a cortical bone specimen loaded under tension in figure 3.20.

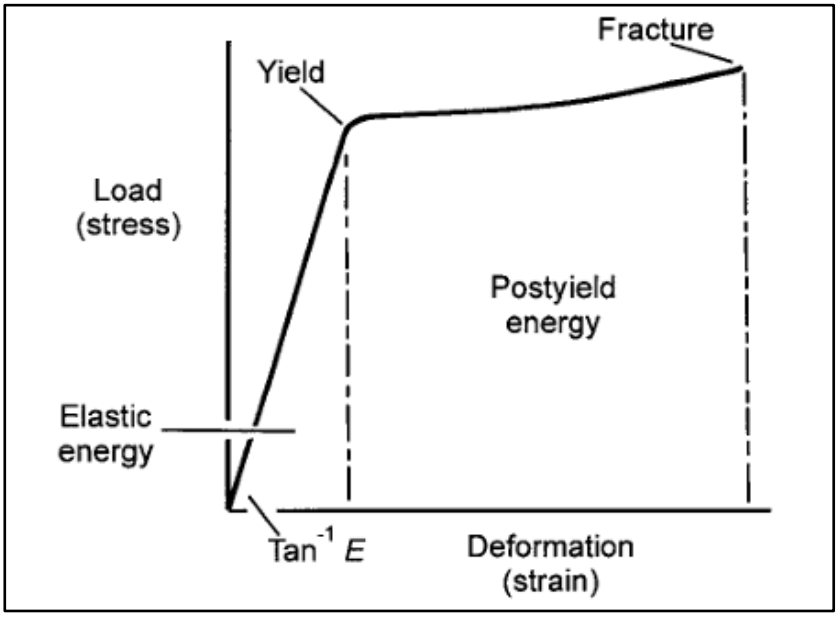

Figure 3.20: A load-deformation curve on a bone specimen loaded in tension at a strain rate of 0.01 s^{-1} (Currey 2006 p. 34)*.*

In addition, the speed at which a force is loaded has an effect as materials do not dissipate force instantly but take time to do so. The stress-strain curve is

therefore much steeper when external loads are applied faster (figure 3.21) as the material can not dissipate as much energy by mechanically bending and therefore reaches the ultimate strength threshold earlier (Hansen et al. 2008, Ural et al. 2011).

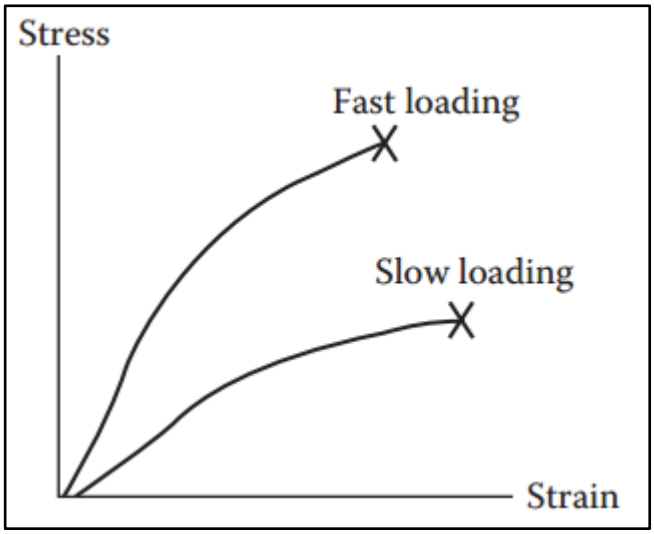

Figure 3.21: Effect of speed of loading on bone (Özkaya et al. 2012 p. 208).

Whilst most materials have the same level of compressive, tensile and shear stress thresholds irrespective of loading direction, this is not the case for composite materials such as bone where the fibrils are directional and impart different strength capabilities when loaded in different directions (anisotropy).

3.6.2.1. Anisotropy of bone

The physical anisotropy (as distinct from its optical anisotropy) of the cortex of long bones derives from a combination of the composite nature of bone and its histological structures. Bone responds to changes in stress through remodelling via secondary osteons (section 2.2.4) and through this the Haversian structure of bone, with its concentric laminae, aligns the collagen fibrils with their surrounding extra fibrilar mineral particles along the line of the physical load on the bone. The mineral fraction of bone resists deformation and thus has good compressive strength, whilst the collagen fibrils provide long overlapping structures to impart elasticity and strength under tension. As can be seen in table 3.2 though, these properties are not even and bone is strongest when loaded under compressive stress and has poor tensile and shear stress properties (Kress et al. 1995, Curry 2006). The directionality of the collagen

fibrils mean that measurements of these material properties provide values that are significantly higher when the bone is loaded along its axial direction than when loaded transversely (Reilly et al. 1974, Reilly & Burstein 1975, Liu et al. 2000), reflecting their load bearing nature (Bouxsein 2013).

Both within the body during life and in the depositional environment after, bones are loaded beyond their ultimate strain resulting in fractures and the physical anisotropy of bone means that the mode of failure of these fractures differs with the applied loading.

These differing modes of failure at the histological level should impart very different characteristics to the resultant fracture surfaces in fresh bone. The interaction of these damaged surfaces with the light from a digitisation instrument should therefore vary according to their mode of failure.

			Bovine					
	Human Haversian		*Haversian*			*Fibrolamellar (plexiform)*		
	Longitudinal	*Circumferential*	*Longitudinal*	*Circumferential*	*Radial*	*Longitudinal*	*Circumferential*	*Radial*
Tension								
Strength	133 (15.6) [21]	53 (10.7) [20]	150 (11) [10]	54 (5.8) [4]	39 (4.7) [6]	167 (8.8) [6]	55 (9) [31]	30 (3.2) [6]
Yield Stress	114 (7.1) [21]	141 (12) [10]	-	-	156 (7.9) [6]	-	-	-
Ultimate strain	0.031 (0.006) [21]	0.007 (0.0014) [20]	0.02 (0.005) [10]	0.007 (0.004) [4]	0.007 (0.002) [6]	0.033 (0.0049) [6]	0.007 (0.0013) [31]	0.002 (0.001) [6]
Compression								
Strength	205 (17.3) [20]	131 (20.7) [8]	272 (3.3) [3]	171 (25) [8]	190 (18.0) [5]	-	-	-
Ultimate strain	0.019 (0.003) [20]	0.05 (0.011) [8]	0.016 (0.0015) [3]	0.042 (0.01) [8]	0.072 (0.014) [5]	-	-	-
Shear								
Strength	67 (3.5) [12]		70 (9) [7]			64 (7) [12]		

Table 3.2: Mean, standard deviation (in parentheses) and number of specimens [in square brackets] of the strength properties (in MPa) of human and bovine bone (after Currey 2006, page 59).

Furthermore, dry bone (i.e. bone that has lost a portion of its organic fraction) has a considerably reduced elasticity resulting in very different fracture modes (Symes et al. 2013). Therefore the taphonomic changes to the mineral or organic fractions of bones within the depositional environment mean that fracture surfaces produced from identical loading events on bones at different points along their taphonomic pathways should also differ.

The following sections will briefly describe the failure modes of bone fractures under different loading regimes and the changing character of their fracture surfaces at differing points along their taphonomic pathways.

3.6.2.2. Axial compression

Under compression along the axial direction of the fibrils, bone has its highest strength properties, but the shear properties remain poor. Therefore as the shape of the bone distributes very high compressive stress loads, shear stresses are generated which exceed the shear strength of the bone and therefore fail along a slip plane. The slip plane propagates within concentric lamellae of the osteons as a result of failure of the fibrils (figure 3.22) and the extra fibrillar mineral at an oblique angle (c.30°) (Schwiedrzik et al. 2014).

Stress concentrations around openings in the bone structure (i.e. canaliculi and Volkmann's canals) and pre-existing microcracks caused by non-elastic deformation offer weaker areas of bone, and where these are most closely oriented with the line of maximum shear stress, they allow the localised shear plane fractures to join. The cement line of the secondary osteons provides a variation in material that blunts the development of the fracture at lower shear stress values, but under high loads, the shear stresses allow the fracture to cross the cement line and the fracture slip plane jumps from osteon to osteon until the fracture fails across the full thickness of the bone resulting in the oblique (figure 3.19(b)) and cross-hatched fracture planes seen in compressive fractures in cortical bone (Schwiedrzik et al. 2014).

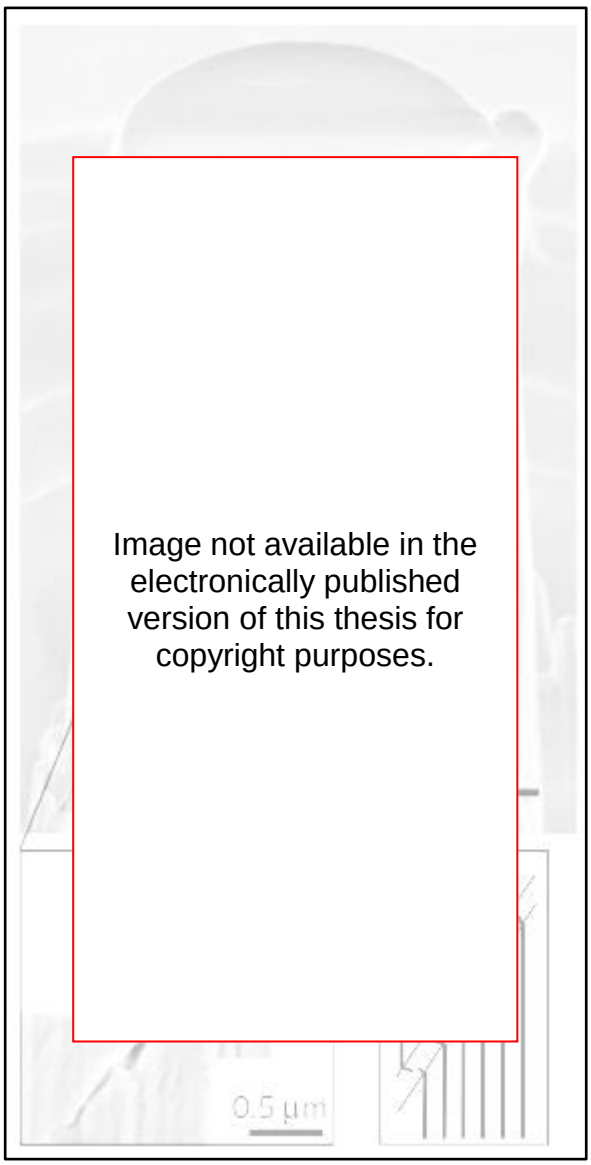

Figure 3.22: Scanning electron micrograph showing a micropillar of bone loaded in compression in line with the fibril orientation that failed through shearing (top) as well as a magnified image of the failure slip plane (bottom left) and a schematic drawing depicting the distinct failure mechanism through the fibrils (bottom right) (Schwiedrzik et al. 2014 p. 745).

In vivo at compressive stress values within the post-yield area, but before the ultimate strain and failure (figure 3.20), non-elastic deformation occurs allowing bone to dissipate unusually high one-time loads through the formation of microcracks between macrostructural elements. The formation of microcracks preserves the overall integrity (and functionality) of the skeletal element and the production of microcracks may offer a mechanism for the initiation of secondary osteon remodelling (Currey 2006). However, until secondary osteon remodelling can repair such microcracks, their formation through non-elastic deformation

provides pathways of reduced strength for future fractures to propagate reducing the bones capability to sustain high loading.

3.6.2.3. Axial tension

For loads applied under tension in line with the longitudinal axis, bone fractures via the debonding of the cement lines around secondary osteons and the osteons are pulled from the surrounding interstitial lamellar bone matrix (Frankel 1980, Moyle & Bowden 1984, Pechníková et al. 2011, Bruce Martin et al. 2015). The nature of the weakness at the cement line is still under debate: Burr et al. (1988) suggest that the cement line is poorly mineralised and therefore weaker than the surrounding secondary osteonal structure, whilst more recently Skedros et al. (2005) have shown that the cement lines are highly mineralised and very low in collagen. Examination of the immunohistochemical responses of the cement lines show that they exhibit high incidence of non-collagenous proteins such as osteopontin which is known to impact bone fracture toughness (Derkx et al. 1998, Nanci 1999, Thurner et al. 2010). Whilst the underlying mechanism of cement line weakness is yet to be fully elucidated the resulting fracture pattern is the same. The fracture planes follow the line of maximal tensile stress generated perpendicular to the axis of the applied load, through the weak points of the cement lines and failure consequently results in long bones in a transverse fracture (figure 3.19(a)) with roughened surfaces.

3.6.2.4. Transverse loading

For bone loaded transversely, the ultimate strength threshold for both tensile and compressive stress is close to the yield strength making bone relatively brittle in this orientation. Additionally because the orientation of the collagen bundles and the Haversian structures are perpendicular to the load in this orientation, they offer a pathway of weakened structure along which cracks can propagate, resulting in longitudinal fractures or “split-line cracks” (section 3.3.2) with fracture surfaces at right angles to the cortical surface (Johnson 1985).

At the micro scale, as with axial loading, compressive stress leads to shear fractures. However in transverse compression the fibrils are orientated perpendicular to the force and they contribute less to the structural strength of

bone in this orientation. The slip plane therefore propagates at a more obtuse angle (Schwiedrzik et al. 2014) through the lamellae (figure 3.23).

In crush injuries when bone is loaded transversely under compression from opposing directions, or when it is loaded at high speed and cannot deform fast enough to dissipate the load, a combination of tensile failures along the longitudinal axis and shear fractures at an angle to that axis result in comminuted fractures (figure 3.19 (e)) as the cylindrical cross section is compromised.

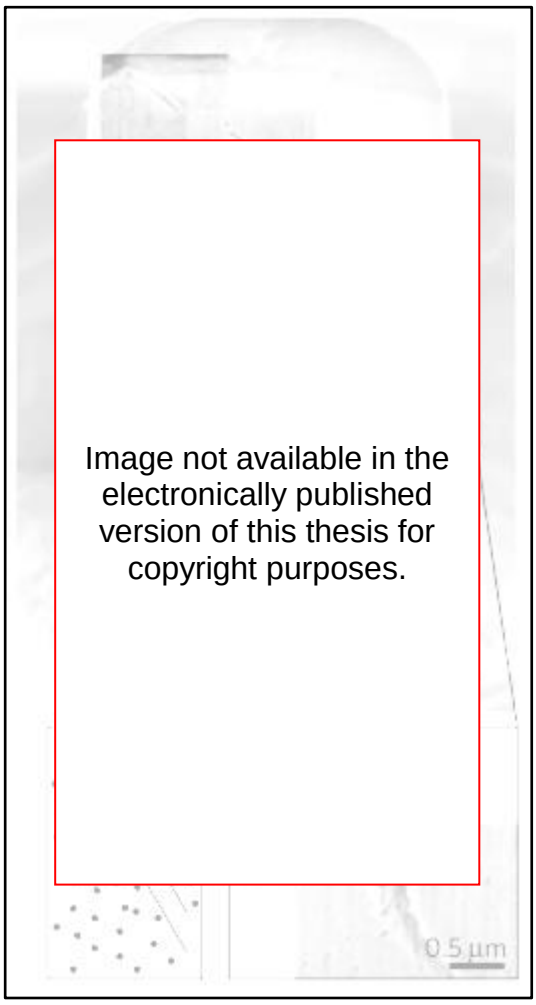

Figure 3.23: Scanning electron micrograph showing a micropillar of bone loaded in compression in line transversely to the fibril orientation that failed through shearing (top) as well as a magnified image of the failure slip plane (bottom right) and a schematic drawing depicting the distinct failure mechanism between the intact fibrils (bottom left) (Schwiedrzik et al. 2014 p. 745).

3.6.2.5. Combined axial compression and tension

Fractures to bone occur most often as a result of bending loads that exert both axial compression and tension stresses to the bone (Liu et al. 2000, Mays 2010). When a bending load is applied to a beam like material (e.g. a long bone), deformation (bending) of the material away from the load produces axial compressive stress adjacent to the point the load is applied as the material on the inner curve is compressed. At the same time the bending produces an axial tensile stress at a point opposite to the application of the load as the material is stretched around the outer curve.

If the load exceeds the ultimate strain of the material then the resulting fracture exhibits characteristics of both tensile and compressive failure. In bone this results in butterfly fractures (figure 3.19 (d)) with a transverse fracture developing under tension from the surface of the bone opposite to the applied bending load; and two oblique fractures developing under compression above and below the point of the applied bending load.

In immature bone with lower levels of mineralisation, bending forces also result in combined axial compression and tension, but whilst the tensile stress still exceeds the strength of the collagen fibrils resulting in a transverse fracture, the lower mineral content of immature bone affords greater plastic deformation preventing the concave side from fracturing (Schmuck et al. 2010, Berteau et al. 2015). The resultant partial fracture is referred to as a greenstick fracture (figure 3.19 (f)).

3.6.3. Perimortem and antemortem vs postmortem fractures

Whilst fractures to bone can occur both before and around death, they can also be the result of postmortem damage both during surface deposition and weathering and within the burial environment. These fractures can be distinguished from each other based on the presence of healing, colour (Nawrocki 2009) and the features of the fracture surface (Symes et al. 2013).

In general, perimortem and antemortem fractures occur where the organic fraction and moisture content within the bone is still relatively intact. Once the moisture content and the organic fraction has been reduced, fractures are

characterised as postmortem damage. An analogy to fresh versus seasoned wood has led bone with a high organic content remaining to be referred to as “green” or “wet” bone and bone where the organic fraction only partially remains in part to be referred to as “dry” bone.

The combination of moisture and organic content in green bone is critical, as the water hydrates the collagen and allows it to deform and retain its viscoelastic properties. Without the moisture content the organic content is more brittle and its ultimate strength threshold is closer to its yield strength (figure 3.24). This is a function of its viscoelasticity; which is a measure of the how the elastic properties of a material can act over time, and is key to dissipating loads fast enough to allow deformation. As bone loses its moisture content, the collagen fibrils dehydrate and become slower to dissipate force (reduced viscoelasticity) (Ntim et al. 2005), and high speed loading events can overtake the bone’s ability to deform resulting in fracture (Symes et al. 2013). The loss of moisture from the collagen fibrils is also responsible for a decreasing tensile strain (i.e. how much the material can deform under tensile stress prior to failure) and this further reduces the bones tensile strength (Reilly et al. 1974, Currey 2006). The loss of moisture from bone and its associated change in physical properties can occur as early as five hours postmortem (Kanz & Grossschmidt 2006), however in most cases the surrounding soft tissues retain the moisture within the bone until considerably further into decomposition and burial environments with high moisture contents can extend this further (Maples 1998, Loe 2011). It has also been shown that bone can regain some of its wet bone characteristics in damp environments (Wieberg & Wescott 2008).

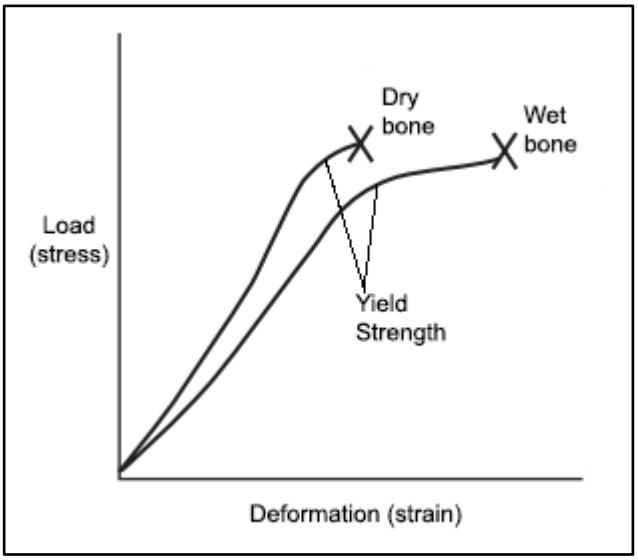

Figure 3.24: Stress-strain curve comparing the response of wet vs dry bone (adapted from Özkaya et al. 2012 p. 210).

Whilst dry bone fails under tension, compression and shear, the lack of elastic properties mean that the ultimate strength threshold is below that of the yield strength and it fails in all three almost simultaneously, resulting in much more simplistic fracture patterns, and a higher tendency to shatter but a lower tendency to distort (i.e. post-yield plastic deformation). These differences impact the surface shape and form of fracture surfaces in wet and dry bone and have important implications for the digital refitting of fragmentary bone.

3.6.3.1. Wet bone fractures

The ability of wet bone to deform and absorb higher speed loading via its viscoelastic properties results in fracture surfaces that are the product of higher energy events (Ntim et al. 2005). As a result, the fracture plane tends to be smoother with sporadic sharp projections where the fracture plane jumps to another point of weakness, and the angle between the fracture surface and the cortical surface tends to be acute or obtuse compared to the right angles of dry bone (Villa & Mahieu 1991). With regard to the axis of the bone, wet bone exhibits a curved or “V” shaped profile (Villa & Mahieu 1991, Wedel & Galloway 2013) following the extent of maximum deformation around the bones circumference, in contrast to the straighter edges of lower tensile strength failures in dry bone. The deforming bone creates localised areas of tension resulting in smooth radiation fractures away from the main fracture.

Importantly for refit research, the greater viscoelasticity of wet bone pushes the ultimate strength threshold beyond the yield strength and affords a larger post-yield energy area to the stress-strain curve (figure 3.24) (Ntim et al. 2005). In this area the deformation of the bone under load is plastic and does not relax back once the load is removed (or importantly once fracture occurs). In wet bone plastic deformation may pose a challenge to the statistical matching of bone fracture surfaces and therefore the successful digital refitting of fragmentary bone.

Axial tension fractures in wet bone (and in dry bone) where the osteon structures fail at the cement line and are pulled out from the surrounding interstitial lamellar bone matrix (Pechníková et al. 2011), produce a stepped and roughened surface as the material ruptures suddenly. The resulting surface appears roughened and mottled under low magnification SEM (Symes et al. 2013).

Where fracture planes meet the circumferential lamellae at the margins of wet bone, the lower mineral content (and higher proportion of collagen) of the lamellae and the viscoelastic properties of wet bone combine to result in differential fracturing at the margins of bone. The lower mineral content of the circumferential lamellae reduces stiffness in comparison to lamellae in the secondary osteons of Haversian bone whilst also increasing the tensile strength and ability to deform (tensile strain). Therefore, when the fracture plane propagates through the lamellae it does not fracture cleanly but preferentially follows points of weakness (Volkmann's canals, canaliculi etc). Where the fracture plane passes along the axis of the bone (parallel to the collagen fibres) the fracture margin is straight, but where it runs at an angle or perpendicular to the axis it becomes irregular, splintering, peeling and with lifting of the margins (Moraitis et al. 2009). Small chips of bone can become detached resulting in “spalling” (Knüsel & Outram 2006), or where the fracture is incomplete fragments may stay attached (or “hinged”) (Loe 2011).

Bones that have been broken through multiple forces such as those broken under bending (section 3.6.2.5) have fracture surfaces that alter in character at the point where one type of strain mode failure gives way to another and this can be seen in archaeological remains (Moraitis et al. 2009).

3.6.3.2. Dry fractures

Dry bone fractures are usually light in colour compared to the surrounding cortical surface which have been discoloured through soft tissue liquefaction and soil staining. The lack of collagen to provide longitudinal strength under tension in dry bone results in straighter fracture outlines with regard to the bone's axis and smaller and more regular fragments (Loe 2011).

In tensile fractures perpendicular to the axis of the bone, the fracture surfaces of dry bone are similar in appearance to those of wet bone. When the fracture plane reaches the circumferential lamellae (which do not contain secondary osteons) the lamellae fail differentially depending on the remaining organic content. In dry bone the loss of the collagen fibrils reduces the tensile strength of the bone and the fracture is closer to the line of the main fracture plane producing a jagged edge.

In tensile fractures in line with the axis of the bone, the fracture exposes the laminar face within the bone and the fracture surface is usually smooth in dry bone (Shipman 1981) with right angles between the fracture surface and the cortical surface (Villa & Mahieu 1991).

The lack of collagen fibrils mean compression fractures in dry bone fail under shear and have more obtuse angles than those from wet bone (section 3.6.3.1).

The lack of viscoelastic properties in dry bone make it brittle in all strain modes and the lower ultimate strength threshold below that of the yield strength (figure 3.24) mean that the bone fractures before it plastically deforms. As such dry bone fragments are likely to be provide better statistical surface matches in digital refit.

3.7. Chapter summary

The reliability of interpretations of the skeletal remains is dependent on a clear understanding of the taphonomic processes that have resulted in their survival. It follows therefore, that the development of new interpretive tools must also be informed by a clear understanding of the taphonomic changes that affect the material.

The effect of taphonomic changes on bone and their influence on the digitisation of fragmentary skeletal material are discussed in relation to the development of the methods used in chapters five and six and the results of this research in chapter seven.

Chapter 4. Digitisation

This chapter describes digital encoding of 3D data, its associated terminology and digitisation quality measures. The three main techniques of object surface digitisation (laser scanning, structured light and photogrammetry) are discussed and the digital refitting of fragmentary material is outlined.

4.1. How 3D space is digitally encoded

In three dimensional computer graphics, 3D models exist in a virtual 3D rectangular Cartesian coordinate space. Each point, P, in a model is defined by a set of three numerical coordinates describing signed distances on three mutually perpendicular planes, measured in the same unit of length from a consistent origin. The numerical values for the coordinates are always quoted in the same order and thus every point in 3D space can be described with reference to its ordered triple (x, y, z) coordinates from the origin, O, which has the coordinates (0,0,0) (figure 4.1). In most digital 3D formats the unit of length used is initially undefined allowing the same software programs to work with cloud point data of varying scales. The unit of measure must therefore be defined by the 3D digitisation instrument or within the 3D program.

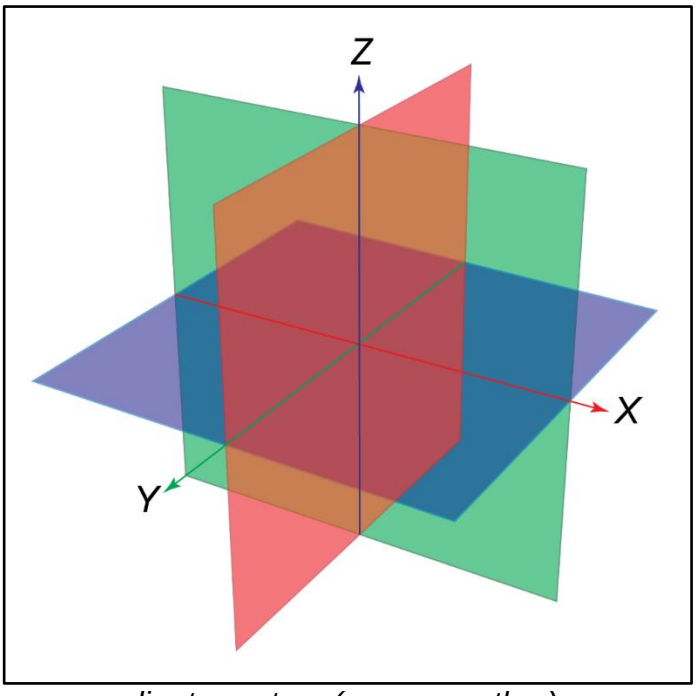

Figure 4.1:The x,y,z coordinate system (source: author).

4.1.1. Point clouds and meshes

The three dimensional points derived from 3D digitisation techniques (section 4.3) result in a large number of recorded points with respect to the instrument origin in the form of a 'point cloud'. To create a 3D object, a polygonal mesh surface is derived from the point cloud, producing vertices (points), edges (a line between two vertices) and faces (a surface between 3 or more vertices).

Deriving a polygonal mesh from point cloud data requires two steps, firstly the correct identification of the surface described by a cloud of unconnected points, and secondly, solving the best fit of 2D polygons to that surface. This process of meshing can be achieved in a number of ways although the two most common are the use of triangulated irregular networks (figure 4.2) and through the interpolation of the point cloud via a regular grid (Stylianidis et al. 2016) (figure 4.3).

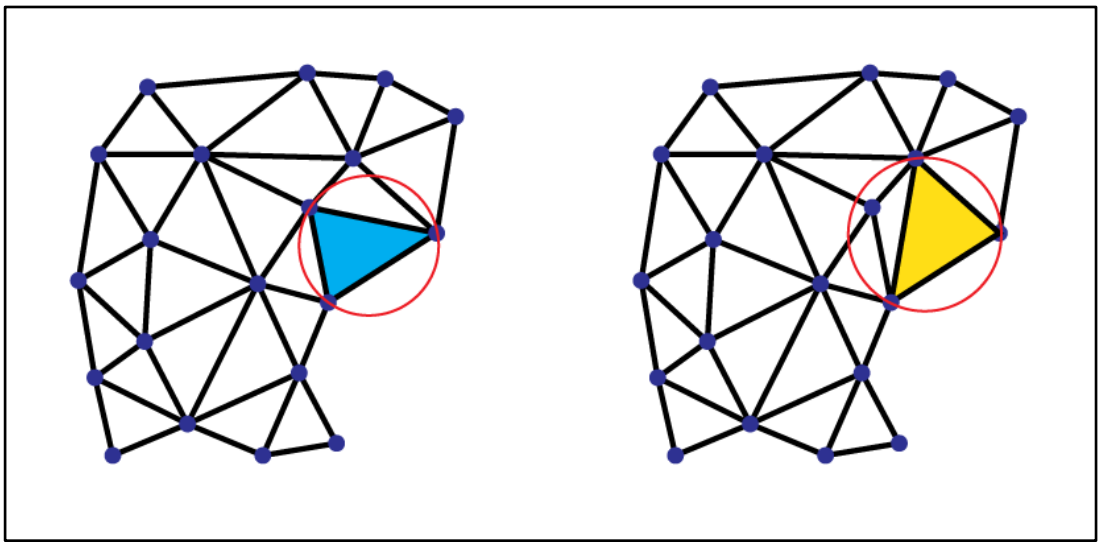

Figure 4.2: Delaunay triangulation used to determine conformation of mesh faces in triangular irregular networks by fitting a circle to the vertices of the triangle. Left: no other vertices occur within the area of the circle resulting in correct Delaunay triangulation. Right: Incorrect triangulation results in the occurrence of other vertices within the area of the circle (source: author).

In triangulated irregular network meshing, groups of three neighbouring points are joined together forming a surface of non-overlapping triangles. Whilst multiple triangle conformations are possible from the same arrangement of points, conformation with very narrow triangles and those that distort the mesh are avoided through the application of Delaunay triangulation (figure 4.2) (De Loera et al. 2010, Sonka et al. 2015).

Regular grid meshing utilises a planar equidistant grid as a base parameterisation. By applying the grid onto the point cloud surface the random points within the point cloud can then be fitted to the nearest node on the grid. The deformation of the gridded points above or below the imposed grid is determined based on a weighted mean of the nearest random points. The resultant mesh has a regular grid pattern of points when viewed perpendicular to the surface, and the height of the vertices varies to provide the shape. The size of the grid used is usually determined by the user as the “Interpolation Step” in the meshing software.

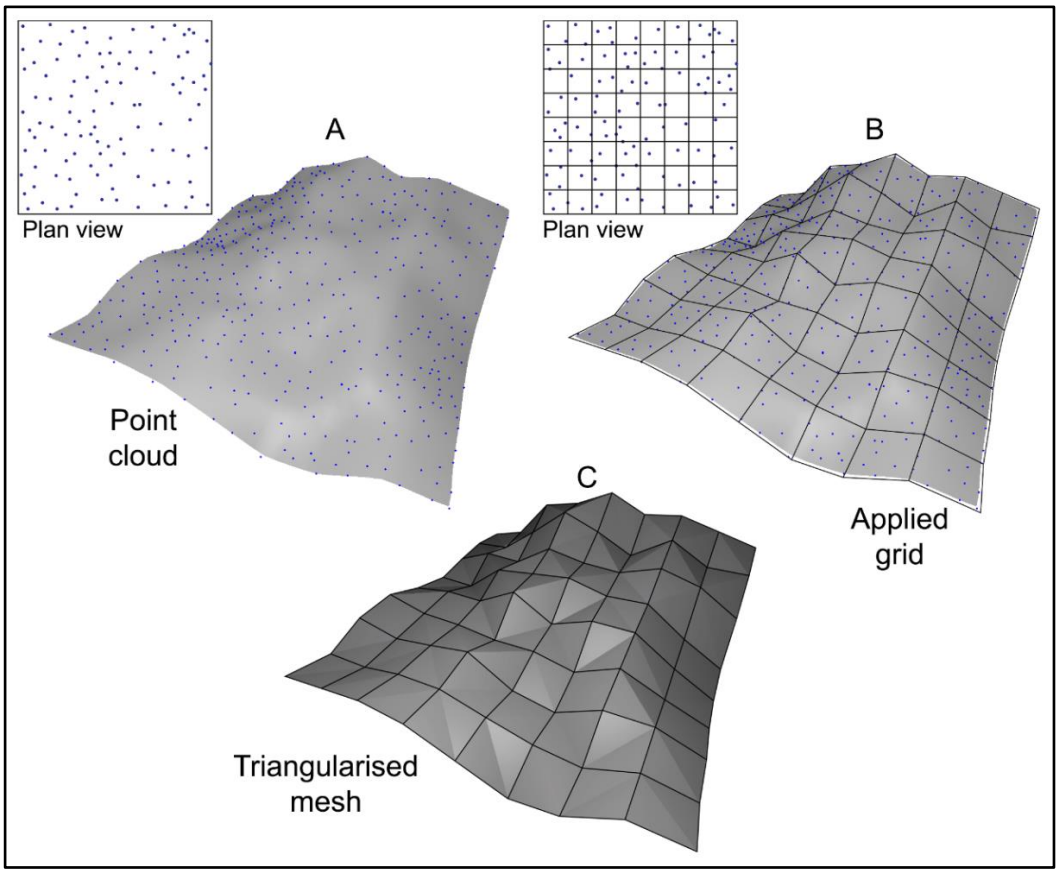

Figure 4.3: Grid based interpolation of irregular points. A: irregular points of the point cloud; B: a regular grid is fitted to the point cloud; C: positions of points are averaged at the nearest grid node (source: author).

The creation of a surface polygonal model from a point cloud involves the embedding of 2D shapes within three dimensional space and a computer polygonal model is therefore a 2 ½ dimensional representation of the 3D input data (point cloud) and not a true 3D surface (Böhm & Pateraki 2006).

4.1.2. Surface normals

The 2D shapes that form the faces of polygonal meshes are one sided and have no thickness. To designate which side of the face has reflective and colour properties each surface has a vector perpendicular to the face designated as the surface normal. The surface normals can be used to calculate the effect of lighting and shaders (algorithms that calculate the level of shadow) and as the surface normal is an expression of the underlying surface shape, normals have also been used to compare and align models in some applications (Viola & Wells 1997, Smith & Hancock 2006).

4.1.3. UV unwrapping and texture mapping

There are two approaches to the recording of colour within 3D objects, recording of basic colour values on a per vertex or per face basis, and the recording of high detail colour through the association of each face with a region of a high detail texture image.

Per vertex and per face colouring produces small file sizes and for simple objects with a uniform single colour surface it can be very effective. However, for objects with surfaces that vary in their colour, reflectivity and other optical properties, it is less useful as the output model does not accurately reflect the appearance of the original object.

The application of a texture file to an object allows each triangle or quad that makes up the surface mesh to be associated with a discrete region of a larger image file which can be derived from high resolution photography of the original object. This approach provides high fidelity surface appearance in 3D objects and is particularly valuable for cultural heritage objects as small variations in the surface that are otherwise too small to be accurately digitised in the mesh are retained in the texture image.

Image files are 2D and in order to associate each triangle or quad from the 3D object polygon mesh to a 2D image, the polygon mesh must first be flattened out, a process known as UV unwrapping, referring to u and v texture image coordinates. As already described (section 4.1.1) 3D objects are defined by x,y,z coordinates. In 2D images the pixels are arranged in a Cartesian grid with x and

y coordinates. In order to avoid confusion between 3D and 2D x and y coordinates, texture image coordinates are referred to as u and v.

The process of UV unwrapping for anything other than primitive shapes (cubes, cylinders, balls, tori etc.) is complex resulting in the breaking up of the polygon mesh into discrete areas that have a degree of flatness so as to avoid significant distortion. The process can best be understood if the reader imagines trying to make a cylinder out a piece of light card (Nitsch 2008), where the 3D shape is broken into two circles (the ends of the cylinder) and a flat section that represents the sides of the cylinder (figure 4.4).

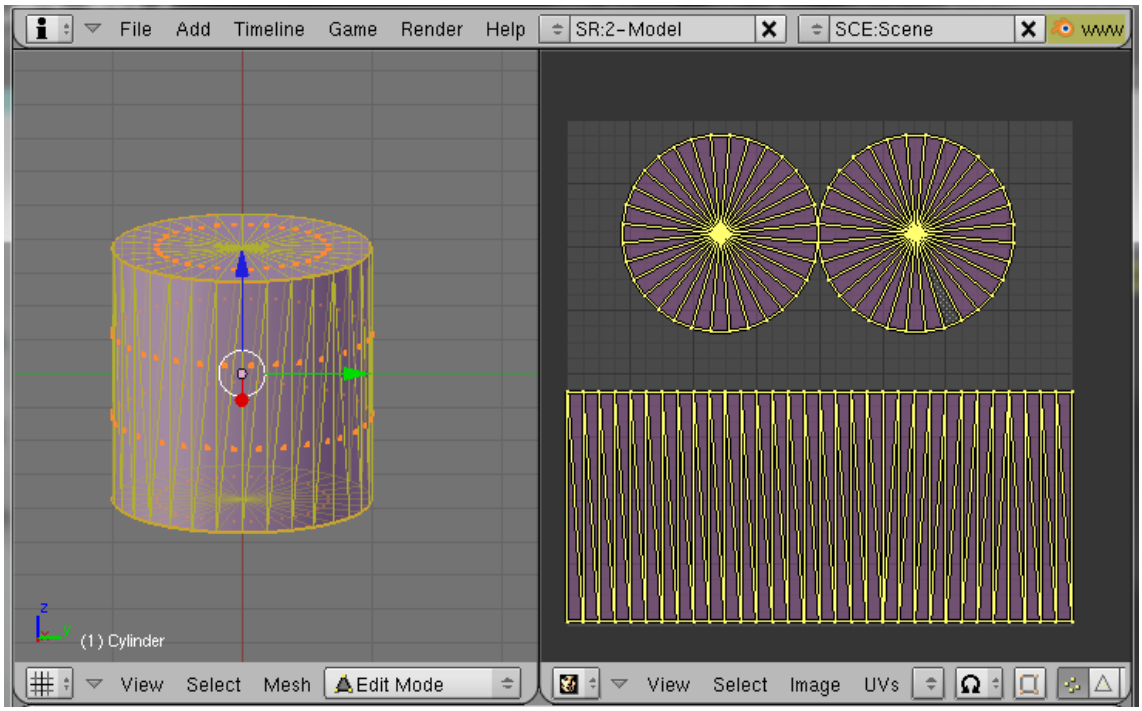

Figure 4.4: UV unwrapping a 3D cylinder into flat shapes (source: author).

The algorithms used to automatically achieve good quality UV unwrapping in 3D polygons is a non-trivial computing problem and continues to be the focus of research in applied mathematics (Igarashi & Cosgrove 2001, Ghyme et al. 2008, Schäfer et al. 2012).

Once the object has been unwrapped, the flat sections can be associated with an area of the texture image (UV mapping) wherein the *x,y,z* coordinates for each flattened section of the object polygonal mesh is mapped to the *u,v* coordinates of the 2D texture image file (figure 4.5).

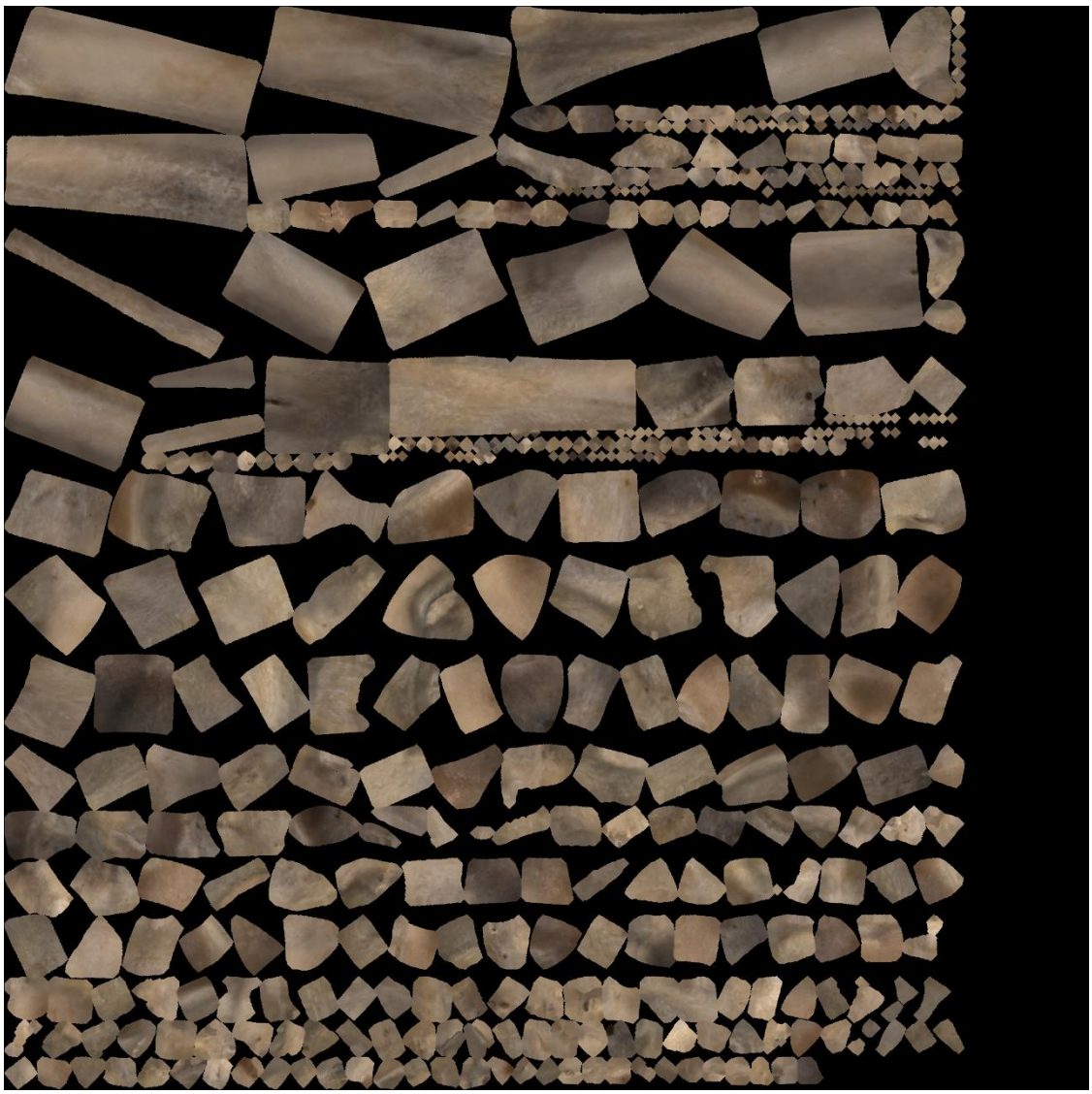

Figure 4.5: A texture file for one of the experimental bone samples showing the textures for large numbers of discrete unwrapped polygon sections (source: author).

Where 3D scanning instruments incorporate colour cameras, the colour texture information can be captured during the digitisation process. Laser based scanners, with their fixed wavelength laser, cannot and require an additional camera attachment or are reliant on separate photography and post-processing for texturing. For those scanning instruments that incorporate colour cameras, separate texture photography may also be used as it is considered to produce superior photo-realistic end results.

4.2. Digitisation quality

That the utility of the resultant point cloud from 3D digitisation is highly reliant on the point quality (i.e. the digitisation process quality) has long been recognised within engineering and quality control testing (Contri et al. 2002, Lartigue et al. 2002), but within cultural heritage this has not been explored to a significant level. The idea that “the camera cannot lie” often means that visualisations are given greater authority than they warrant. Furthermore, there is an assumption both in the lay audience and those within cultural heritage practice that 3D digitisations capture an accurate complete model of whatever the scanning instrument is pointed at. Indeed, it is rare for visualisations to be presented with more than a single interpretation, to be accompanied by error information or a discussion of methodological approaches with an eye to critical evaluation of the quality of the resultant image (Wittur 2013). It is important to state therefore that 3D digitisations are not direct measures of reality. As with any recording device, digitisation instruments record to stated levels of precision and accuracy and are subject to a wide variety of factors that influence the quality of their results.

Before considering the impact of taphonomic changes on the quality of 3D digitisations of bone, an understanding of the basics of digitisation quality itself are required.

Name	Manufacturer	Form factor	Light source	Point accuracy (+/- µm)	Volumetric accuracy (mm)	Maximum resolution (mm)	Data rate (point/sec)	Texture capture	Working distance (mm)	Reference
FARO Edge ScanArm ES	FARO (Lake Mary, FL)	Fixed Arm & Laser	Red Laser	35	+/-0.34	0.054	45,120	No	80 – 165	(FARO Technologies 2013a)
FARO Edge ScanArm HD	FARO (Lake Mary, FL)	Fixed Arm & Laser	Blue Laser	25	+/-0.34	0.04	560,000	No	115 - 230	(FARO Technologies 2013b)
FARO Quantum Scan Arm & V3 Laser	FARO (Lake Mary, FL)	Fixed Arm & Laser	Red Laser	35	+/-0.027	0.054	19,200	No	95 - 180	(FARO Technologies 2009)
FastScan Cobra C1	Polhemus (Colchester, VT)	Hand Held	Red Laser	750	(not stated)	0.5mm	51,200	No	80 - 220	(Polhemus 2011)
HandySCAN 300	Creaform (Lévis, Québec)	Hand Held	Red Laser	40	0.020 + 0.100mm/m	0.1	205,000	No	300 - 550	(Creaform 3D 2016a)
HandySCAN 700	Creaform (Lévis, Québec)	Hand Held	Red Laser	30	0.020 + 0.060mm/m	0.05	480,000	No	300 - 550	(Creaform 3D 2016a)
MetraScan 210	Creaform (Lévis, Québec)	Hand Held	Red Laser	85	0.085	0.1	36,000	No	300 - 500	Creaform 3D 2015)
MetraScan 70	Creaform (Lévis, Québec)	Hand Held	Red Laser	85	0.085	0.05	36,000	No	300 - 500	(Creaform 3D 2015)
NextEngine 2020i	NextEngine Inc (Santa Monica, CA)	Desktop	Red Laser	100	(not stated)	0.1	50,000	Yes	280 - 430	(NextEngine Inc. 2010)
ROMER Absolute Arm 73 & HP-L-20.8 Laser	Hexagon Metrology (Cobham, Surrey)	Fixed Arm & Laser	Red Laser	75	+/-0.061	0.013	150,000	No	140 - 220	(Hexagon Metrology 2014)
ROMER Absolute Arm 73 & RS3 Laser	Hexagon Metrology (Cobham, Surrey)	Fixed Arm & Laser	Red Laser	79	+/-0.061	0.014	460,000	No	100 - 200	(Hexagon Metrology 2015)

Table 4.1: Comparison of the specifications of 3D object laser scanning instruments (source: author).

Name	Manufacturer	Form factor	Light source	Point accuracy (+/- µm)	Volumetric accuracy (mm)	Maximum resolution (mm)	Data rate (point/sec)	Texture capture	Working distance (mm)	Reference
Artec Eva	Artec 3D (Luxembourg)	Hand Held	White flash bulb	100	0.03% @ 100cm	0.5	2,000,000	Yes	400 - 1000	(Artec 3D 2016
Artec Eva Lite	Artec 3D (Luxembourg)	Hand Held	White flash bulb	100	0.03% @ 100cm	0.5	2,000,000	No	400 - 1000	(Artec 3D 2016)
Artec Space Spider	Artec 3D (Luxembourg)	Hand Held	Blue LED	50	0.03% @ 100cm	0.1	1,000,000	Yes	170 - 350	(Artec 3D 2016)
Artec Spider	Artec 3D (Luxembourg)	Hand Held	Blue LED	50	0.03% @ 100cm	0.1	1,000,000	Yes	170 - 350	(Artec 3D 2016)
BV Scanner @ 200mm FoV	Bradford Visualisation	Fixed Tripod	White Light	45	(not stated)	0.075	2,950,000	Yes	370 - 470	(Source: author)
BV Scanner @ 600mm FoV	Bradford Visualisation	Fixed Tripod	White Light	105	(not stated)	0.25	2,950,000	Yes	1040 - 1340	(Source: author)
David SLS-2	David 3D Group (Koblenz)	Fixed Tripod	White Light	60	(not stated)	0.06	(not stated)	Yes	(not stated)	(David 3D, 2015)
Geomagic Capture	3D Systems (Rock Hill, SC)	Fixed Tripod	Blue LED	60	(not stated)	0.11	985,000	No	300 - 480	(3D Systems 2015)
Geomagic Capture Mini	3D Systems (Rock Hill, SC)	Fixed Tripod	Blue LED	34	(not stated)	0.08	985,000	No	157 - 227	(3D Systems 2015)
Go!Scan 3D 20	Creaform (Lévis, Québec)	Hand Held	White LED	100	0.3mm/m	0.1	550,000	Yes	380 - 480	(Creaform 3D 2016b)
Go!Scan 3D 50	Creaform (Lévis, Québec)	Hand Held	White LED	100	0.3mm/m	0.05	550,000	Yes	400 - 650	(Creaform 3D 2016b)
HDI 109	LMI Technologies (Delta, British Columbia)	Fixed Tripod	Blue LED	34	(not stated)	0.08	985,000	No	157 - 227	(LMI Technologies 2016)

Name	Manufacturer	Form factor	Light source	Point accuracy (+/- µm)	Volumetric accuracy (mm)	Maximum resolution (mm)	Data rate (point/sec)	Texture capture	Working distance	Reference
HDI 120	LMI Technologies (Delta, British Columbia)	Fixed Tripod	Blue LED	60	(not stated)	0.11	985,000	No	300 - 480	(LMI Technologies 2016)
HDI Advance R3x @ 200mm FoV	LMI Technologies (Delta, British Columbia)	Fixed Tripod	White Light	45	(not stated)	0.075	2,950,000	Yes	370 - 470	(LMI Technologies 2016)
HDI Advance R3x @ 600mm FoV	LMI Technologies (Delta, British Columbia)	Fixed Tripod	White Light	105	(not stated)	0.25	2,950,000	Yes	1040 - 1340	(LMI Technologies 2016)
HDI Advance R4x @ 212mm FoV	LMI Technologies (Delta, British Columbia)	Fixed Tripod	White Light	36	(not stated)	0.071	2,840,000	Yes	385 - 491	(LMI Technologies 2016)
HDI Advance R4x @ 676mm FoV	LMI Technologies (Delta, British Columbia)	Fixed Tripod	White Light	84	(not stated)	0.228	2,840,000	Yes	1110 – 1448	(LMI Technologies 2016)
MechScan3D @ 110mm FoV	MechInnovations (Leamington Spa)	Fixed Tripod	White Light	10	(not stated)	0.045	284,000	Yes	927 - 972	(MechInnovations 2013)
MechScan3D @ 30mm FoV	MechInnovations (Leamington Spa)	Fixed Tripod	White Light	1	(not stated)	0.01	284,000	Yes	340 - 362	(MechInnovations 2013)
PicoScan	RSI 3D Systems (Frankfurt)	Fixed Mini Tripod	White Light	100	(not stated)	0.16	(not stated)	Yes	150 - 800	(RSI 3D Systems 2013)

Table 4.2: Comparison of the specifications of structured light scanning instruments (source: author).

4.2.1. Accuracy, precision, resolution and sensitivity

The terms accuracy and precision are often used interchangeably, but they are not one and the same thing and the distinction between them is particularly important in 3D digitisation.

In an often used analogy, precision and accuracy are presented with regards to a competition shooting target with the centre bull being the ideal “true value” being recorded (figure 4.6). Accuracy is a measure of how close the shots hitting the target (i.e. the recorded values from an instrument) are to the true value (the bull), the closer they are, the more accurate the value.

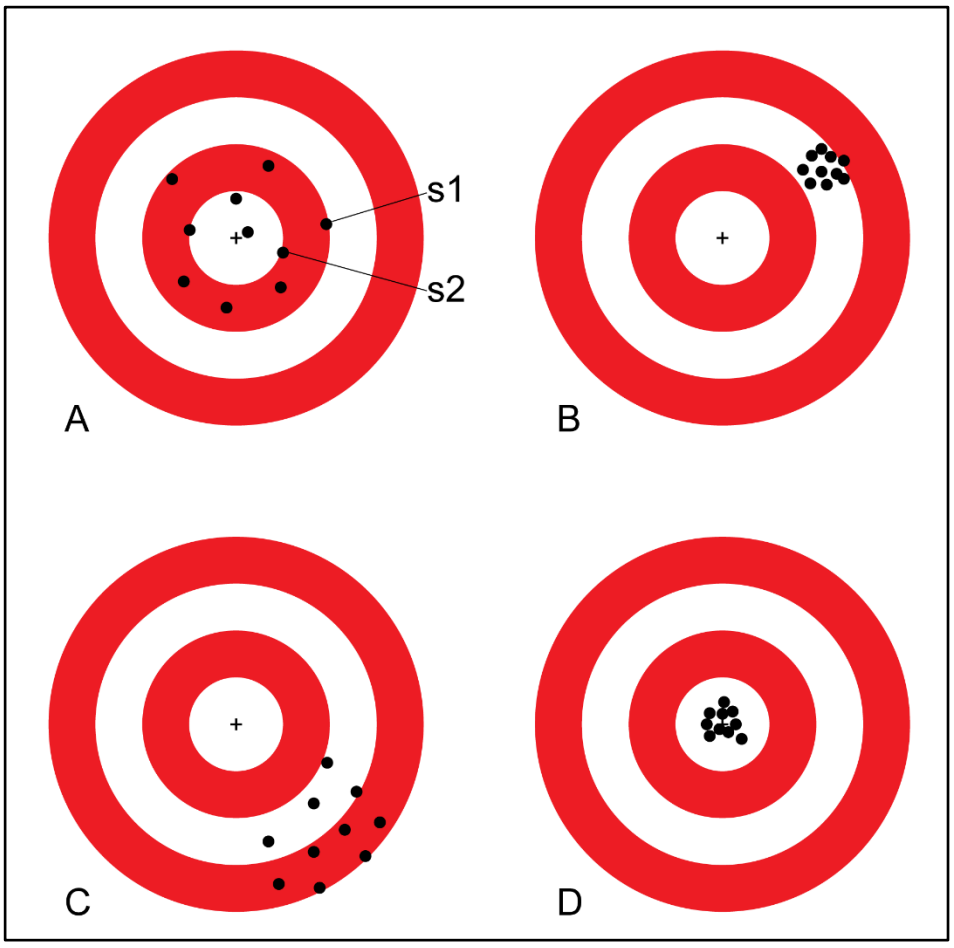

Figure 4.6: Simple model of accuracy and precision based on competition target shooting. A. Accurate but imprecise; B. Inaccurate but precise; C. Inaccurate and imprecise; D. Accurate and precise (source: author).

Precision is a measure of spread of shots across the target, i.e. the variance. Precision therefore represents a measure of the consistency of recorded values derived from an instrument (JCGM 2008).

From figure 4.6 it should be clear that recorded values can be both accurate and very imprecise (A in figure 4.6) or very precise and highly inaccurate (B in figure 4.6). Furthermore, if the target rings are removed and the recorded values are plotted (fired at) a blank target, it may be easy to determine precision based on the variance of the values, but accuracy to the now unknown true value is difficult to measure or even to recognise.

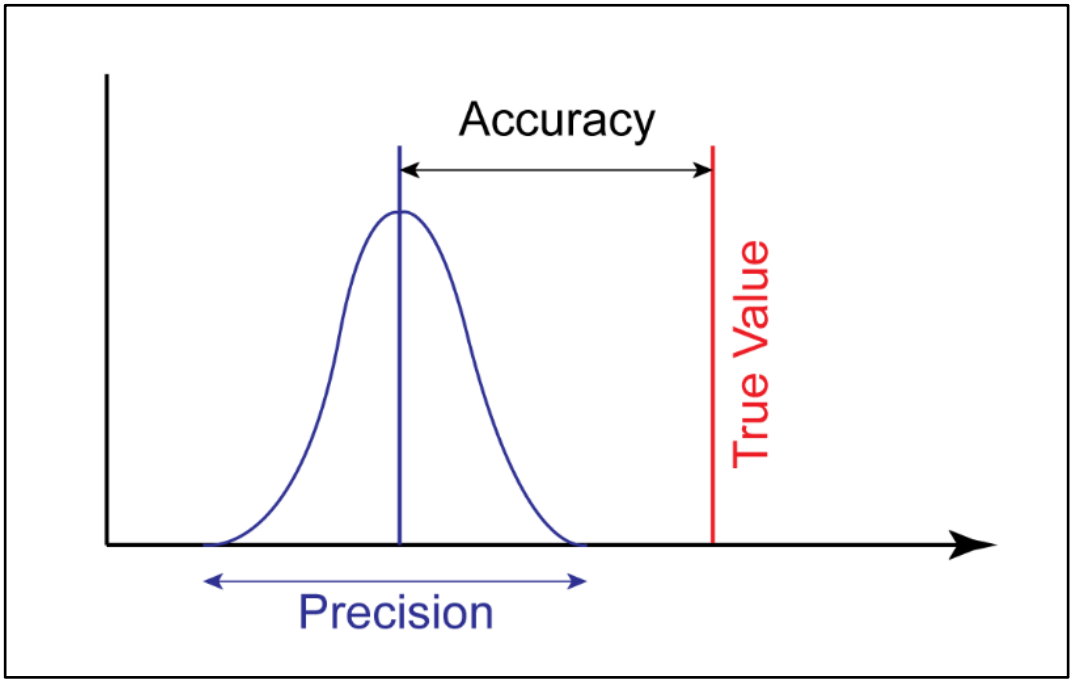

Figure 4.7: For a group of multiple recorded values, the normal distribution of recorded values around a mean describes the precision, and the distance of the mean from the true value describes the accuracy (source: author).

To measure accuracy requires the user (shooter) to know where the true value is, or where that is not possible, to know how their instrument (firearm) generally performs in relation to a known value. To achieve this the instrument must be calibrated against a known standard and, just as with competition shooting, to recalibrate when conditions change.

Additionally, when describing accuracy and precision above, the exact distances of the shots to the bullseye were measured, but the rules of competition shooting only award the same value to all shots that hit the same target ring. Thus in figure 4.6, the shot labelled “s1” records the same value as that labelled “s2”. This is a function of the resolution of the recorded values. In figure 4.8 we can see that if the number of rings are increased, it is possible to distinguish smaller differences in accuracy between shots that previously would

have been given the same score. Resolution is therefore, the smallest change that will result in a difference in the recorded value.

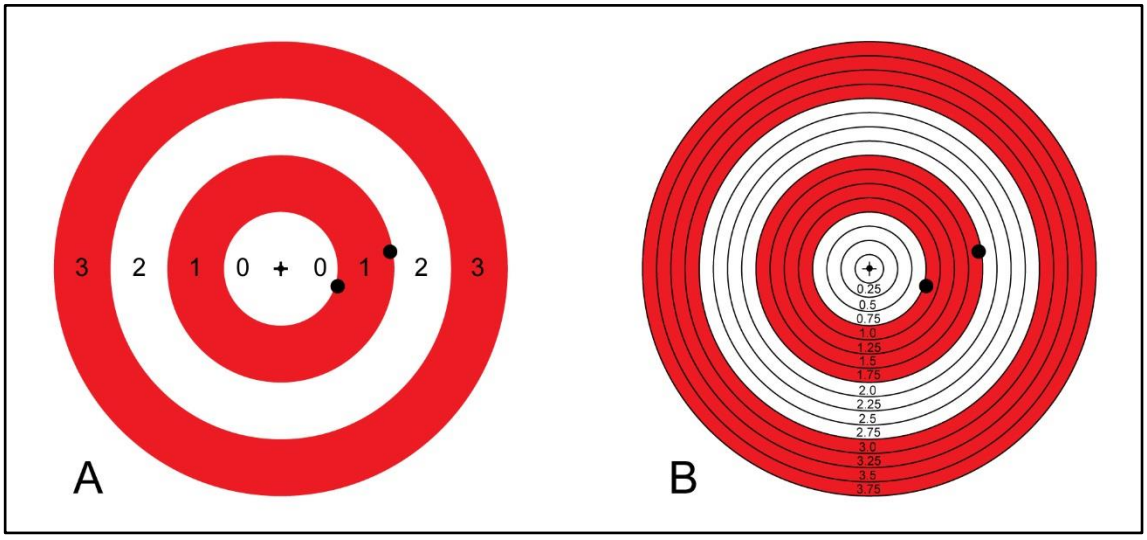

Figure 4.8: An increased number of target rings makes smaller differences in accuracy resolvable. A. Both points are measured at the same value of 1; B. The same points are measured at values of 1.0 and 1.75 (source: author).

In the analogy so far the holes made in the target are the same as all the shots were made with the same size projectiles (bullets). If, however, instead of firing 0.22cal competition bullets at the target the shooter used an elephant gun, the size of the holes would be much bigger (figure 4.9). In this scenario, the recorded value could be anywhere within the large hole in the target, probably covering multiple value target rings. If two consecutive shots hit exactly the same point (high precision) the low sensitivity of the instrument means that the recorded value for the shots might be resolved as one ring (value) for the first shot, and a different ring (value) for the second.

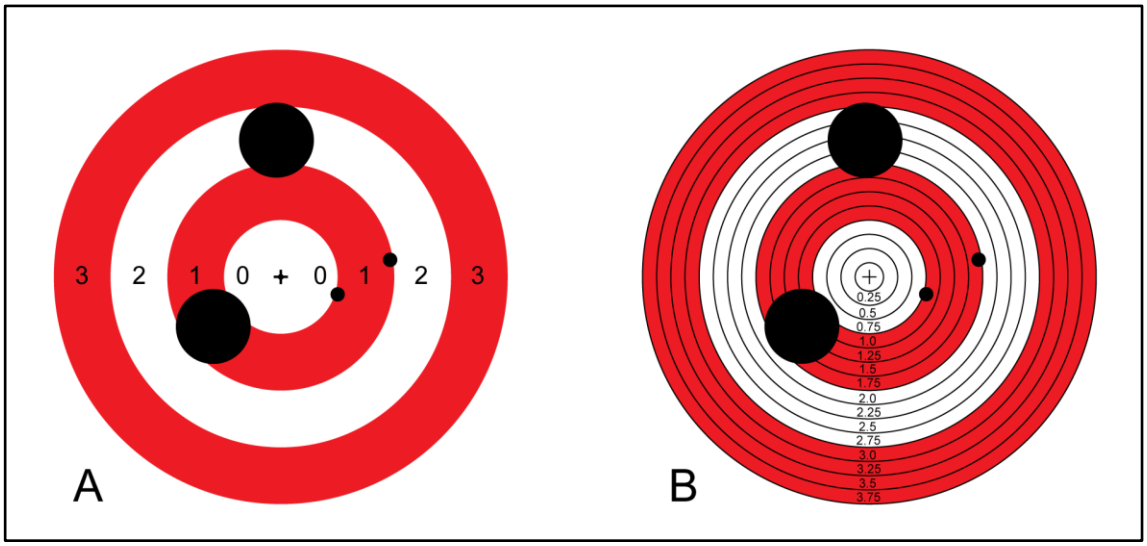

Figure 4.9: Differences in instrument sensitivity result in difficult to resolve values. A. At lower resolution the values from the lower sensitivity instrument are recorded as 1 and 2. B. At higher resolution the values cannot be reliably determined (source: author).

Another term for sensitivity is responsiveness, in that sensitivity is a measure of how responsive an instrument is to a change that is being measured. Sensitivity therefore has a direct relationship to resolution in that using low sensitivity instruments with high resolution thresholds results in higher levels of variation in recorded values, and using highly sensitive instruments with low resolution thresholds limits the potential of the instrument to that of the chosen resolution.

Having introduced these principles, the following sections will discuss how they are applied to 3D digitisation data.

4.2.2. Accuracy and precision in 3D digitisation

With 3D digitisation instruments, accuracy is usually described as point accuracy and volumetric accuracy. The point accuracy is the distance of any given recorded point within the resultant point cloud to the true value in the real world that resulted in that recorded point.

In addition, for instruments that can move their position during recording (i.e. laser scanners on articulated arms and handheld structured light scanners) an additional measure of volumetric accuracy is often quoted. This is a measure of how accurately they orientate themselves in their 3D coordinate space and is

expressed relative to the amount of movement, either as a percentage or in millimetres per metre (see tables 4.1 and 4.2).

The point accuracy and precision of an instrument should be determined by taking multiple recorded values of a known value. The mean distance from each recorded value to the true value in each of the x, y and z directions is calculated and the root mean square of these is then used to provide a single point accuracy figure. However, the quoting of accuracy and precision figures is not consistently applied by manufacturers in the technical specifications (tables 4.1 and 4.2). Importantly, the precision of 3D instruments is rarely stated in manufacturer's specifications and as has already been discussed in section 4.2.1, neither measure is very valuable on its own.

In section 4.2.1 accuracy and precision were presented in terms of a 2D target board, however, as the data is three dimensional, each circle must be turned into a sphere of volume.

The *x,y,z* coordinates for a point within the point cloud from a scan does not provide the true value for the point on the recorded surface, but rather the point's coordinates are within a spherical volume of uncertainty centred on the real world value. The radius of this sphere is determined by the point accuracy and the precision of the instrument value determines the variation in position for the other points in the point cloud. As no instrument has absolute accuracy or precision, some points for a digitised planar surface will be above the plane of the surface (local +*z*) and some below (local -*z*). All points will vary in the local *x* and *y* directions of the surface. Therefore, when the point cloud of a scanned planar surface is meshed, the resulting mesh will not be perfectly planar, but will have a random surface variation. The depth of these variations will be a measure of the accuracy and precision of the instrument and the distance between points forming points above or below the planar surface will be determined by the resolution (point density) of the instrument.

To compare scans and test refit algorithms, the same planar surface can be digitised twice providing two surfaces that in theory should be identical and thus provide a perfect match. However, the precision of the instrument will mean that the repeat scan will have a different point cloud to the first. When the two

surfaces are meshed and then compared they will not produce a perfectly refitting surface, but one in which the two surfaces have an average distance between points that is a function of the precision and accuracy.

The accuracy and precision of 3D instruments is therefore of critical importance in assessing change and for use in refit analysis; factors that influence 3D accuracy and precision may have a significant impact on the quality of digital refit.

4.2.3. Interaction of surface properties and reflected light

All 3D digitisation instruments rely on the signal light (be it white, blue or laser) being reflected back to the sensor part of the instrument. The reflective properties (the albedo) of the surface being scanned therefore have a strong influence on the quality of the data. The main factors influencing the albedo of a surface are the surface topology (surface roughness), the colour and the opacity. Additionally, the orientation and distance of the surface being scanned relative to the instrument and the type of light the instrument uses as a signal are also factors.

4.2.3.1. Surface roughness and speckle

When light rays hit a perfectly smooth surface they are reflected relative to their angle of incidence through specular reflection. The angle of incidence is measured as the difference at the point of intersection between the angle of the light ray and the normal vector of the surface (figure 4.10). The law of reflection states that the angle of reflection is equal to the angle of incidence when measured in respect to the surface normal.

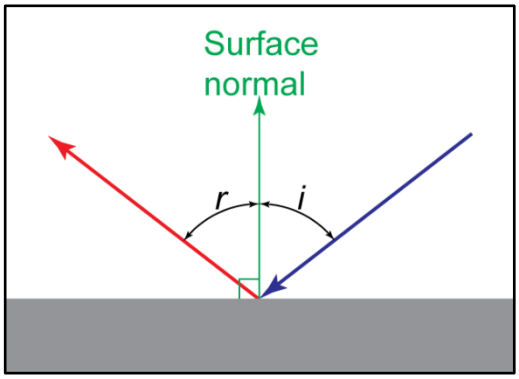

Figure 4.10: The angle of incidence (i) and angle of reflection (r) of light rays relative to the surface normal of a perfect flat surface (source: author).

Light rays from an instrument that are exactly perpendicular to the surface (i.e. have an angle of incidence of 0°) are reflected directly back along the light ray's path and returned to the instrument's sensor. For other angles of incidence, the light rays are reflected away from the instrument via specular reflection. For a curved specular surface the amount of light being returned to the instrument is reduced by specular scattering (figure 4.11).

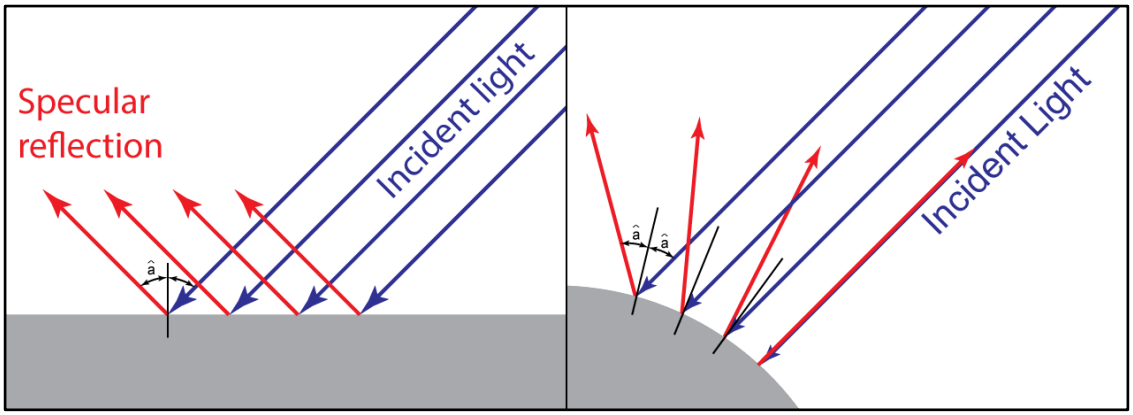

Figure 4.11: Specular reflection of incident light on a surface. Left: reflection of light on a perfect flat surface; Right: scattering of light rays by reflection on a curved surface (source: author).

However, at the scale of the interaction of light with a surface, most materials are not flat but have a degree of roughness. Rough surfaces scatter light through non-specular reflections (diffusion) as the angle between the surface and the incident light is constantly varied due to surface angle (figure 4.12) although for most materials there will still be a component of specular reflection. The degree of specular reflection has been shown to influence 3D digitisation

quality, with smoother and more specular surfaces providing poorer returns (Rak & Woźniak 2012).

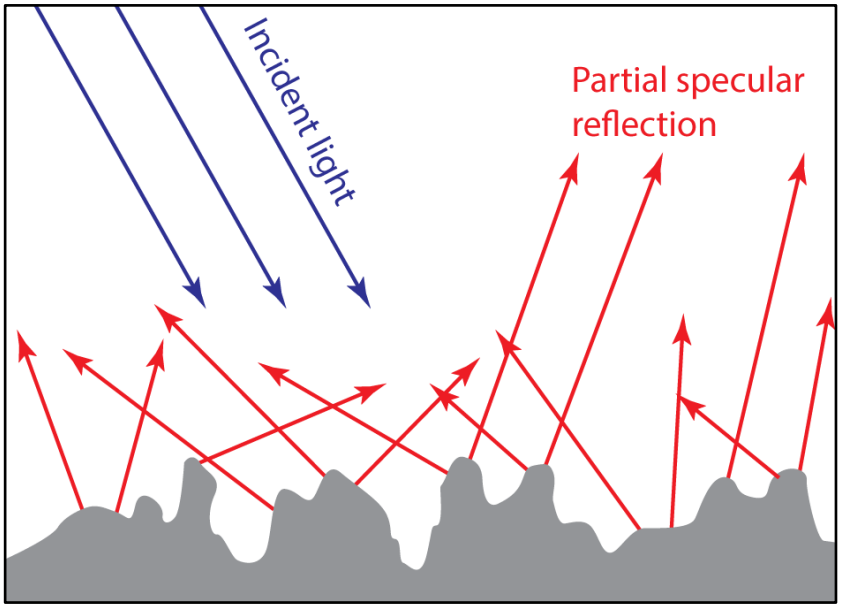

Figure 4.12: Non-specular reflection from a rough surface (adapted from Gåsvik 2002 p. 194).

The interaction of surface roughness and light is a factor of the size of the surface variations and the wavelength of the light. This relationship is known as the Rayleigh roughness criterion which states that a surface may be considered to be “rough” and therefore induce diffusion of the light if the root mean square of the heights of the surface variation is greater than an eighth of the light wavelength divided by the cosine of the angle of incidence (Rees 1990).

For specific wavelength light (e.g. in laser scanners), rough surfaces scatter the light allowing rays that are spatially and temporally coherent to interfere with each other resulting in an interference pattern of light and dark spots returned to the instrument sensor (figure 4.13). This pattern, referred to as speckle, has been shown to follow a Gaussian distribution and is a source of Gaussian noise in single wavelength digitisation instruments (Feng et al. 2001, Gåsvik 2002, Marom et al. 2003). Digitisation software used with laser scanners can apply software noise filters or increase the exposure to mitigate some of the impacts of speckle. In instruments that do not use a single wavelength light source the variation in wavelengths of light rays reduces the chance of spatial and temporal coherence of reflected rays and thus the prevalence of speckle within the returned light pattern is reduced.

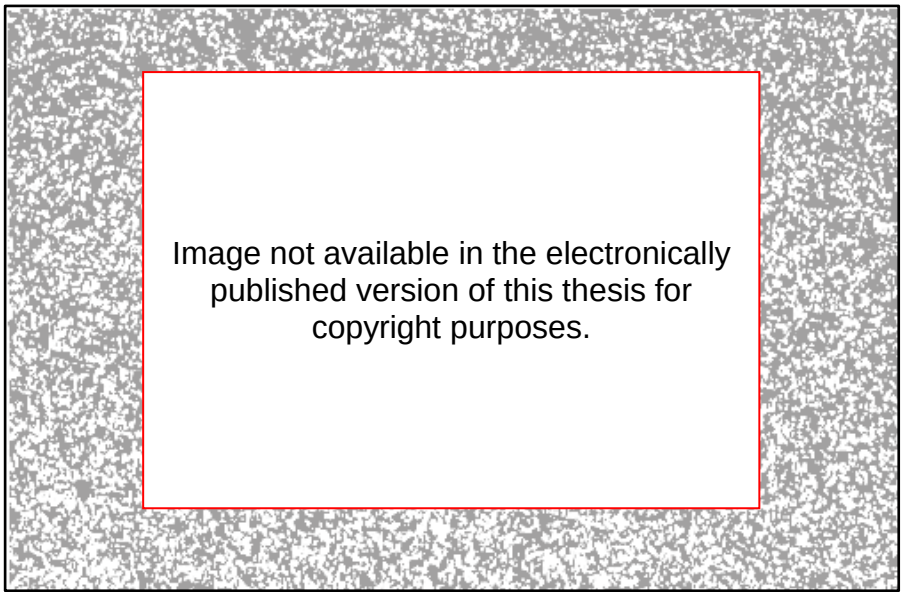

Figure 4.13: A typical laser speckle pattern (Briers 2001 p. R37).

4.2.3.2. Incident angle in 3D instruments

The incident angle of the 3D instrument light signal to the surface of the object being scanned, has been shown to be an important factor in the accuracy of measurements in 3D digitisation (Feng et al. 2001, Kaasalainen et al. 2005, Kukko et al. 2008, Vukašinović et al. 2010, 2012) and the effect is exaggerated by instrument to target distance (Soudarissanane et al. 2007, Vukašinović et al. 2010). The source of these errors has been shown to relate to the reflection properties of the target surface (Lichti & Harvey 2002, Kaasalainen et al. 2005, Kukko et al. 2008), where increased non-specular reflection, and thus increased scattering, results in what is termed angle-noise and therefore positional inaccuracies.

Several studies have demonstrated marked increases in noise and error for incidence angles of > 75° and this figure marks a good starting point for filter settings within the software for 3D instruments (Soudarissanane et al. 2007). Experience gained whilst researching this thesis indicates that the quality of calibration of structured light instruments is consistently poor if the incidence angle between the camera and the calibration target is high.

4.2.3.3. Colour

Objects appear to be different colours because they absorb some wavelengths and reflect others. In white light a blue coloured object absorbs all the wavelengths other than the blue wavelengths, which are reflected back to the observer. In 3D digitisation where it is the light reflected back to the digital sensor (camera) that is measured to create the 3D point cloud, the response of a coloured object to the nature of the instrument's light source has a large impact on 3D digitisation outcome. Darker coloured objects reflect less light back to the observer / sensor and the point accuracy will be more strongly influenced by errors (noise) (Coşarcă et al. 2009).

In photography this can be compensated for by increasing the exposure length or opening the aperture of the camera lens, and in digital photography by changing the sensitivity of the camera's digital sensor.

In 3D digitisation instruments, exposure is also adjustable and in laser scanners increased exposure time can help reduce the impact of speckle (section 4.2.3.1). Aperture changes vary the depth of field and focus spot size and therefore alter the calibration of the instrument and thus are generally avoided. As an alternative, the brightness of the light from the scanner can be increased for darker objects to ensure that a greater amount of light is reflected back to the sensor although this also increases highlights (spots of high reflectance white light).

In single wavelength instruments (e.g. laser scanners) increasing the intensity of the light produces a marked increase in speckle noise. Additionally, the response of colour surfaces to fixed wavelength instruments is not uniform across the spectrum. When using a red wavelength laser, surface colours that have a large amount of red component in them respond more (and therefore appear brighter) than those with less red and more blue. Thus red laser light does not record blue surfaces well and blue lasers do not record red surfaces well.

Red lasers are particularly poor for the digitisation of surfaces of any colour which exhibit highly specular reflection (e.g. high gloss shiny materials such as metals). In engineering, blue lasers have been developed for measuring these

materials, blue wavelengths of laser light have a lower intensity and are less susceptible to distortion and speckle on highly specular reflective surfaces. Blue light scanners are also gaining use in the measurement of organic materials where the lower intensity of blue light doesn't penetrate into the semi-opaque materials and therefore avoids the sub-surface scattering effects associated with lower opacity (section 4.2.3.4).

In cultural heritage most object surfaces do not have uniform colour or reflectivity and the choice of 3D digitisation system must take this into account. Where materials have strong contrasts between dark and light colours, or in single wavelength systems the level of one colour component in the surface colouration, the instrument's exposure and brightness settings may not be able to cover the full range of the brightness responses leaving some areas poorly covered (figure 4.14). Additionally, where only a small amount of light is returned, the averaging and filtering of response by an instrument to compensate for noise can result in poor dimensional accuracy.

Figure 4.14: The variable digitisation result for a horn spoon with high contrast light and dark portions. Left: photograph; Right: 3D laser scan result (digitised by the author for the Visualising Animal Hard Tissues project).Scale = 4 cm (source: author).

4.2.3.4. Opacity and sub surface scattering of light

Objects that are fully opaque reflect light at their surfaces. However, materials that are not fully opaque will allow some light to penetrate through the surface and then scatter below the surface. Where the intensity of the light is high enough or the material is more transparent, sub-surface reflected and scattered light can penetrate back out of the material and be returned to the instrument sensor (figure 4.15) (Coşarcă et al. 2009). When this occurs the instrument cannot distinguish between the first good return from the surface and reflections from deeper into the material. The resulting point cloud has considerable variation in the depth of the signal in line with the instrument's camera axis, resulting in poor meshing and a high degree of dimensional inaccuracy.

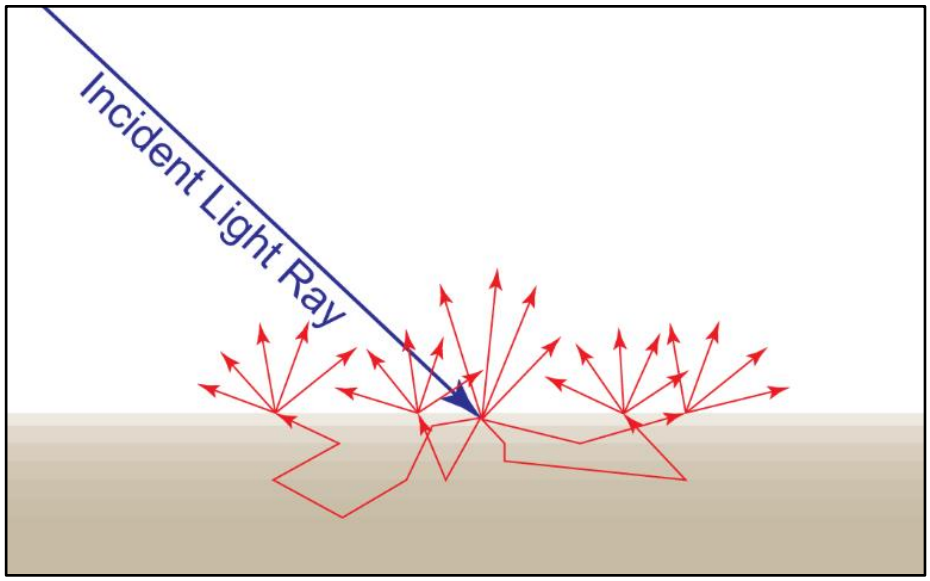

Figure 4.15: Sub surface scattering of light in a material (source: author).

Light paths within the material can be reflected laterally through the material. This results in wider appearing laser lines and blurring of the edges of fringe patterns in structured light scanning, further degrading the quality of the resultant point clouds. This has the effect of dispersing the recorded points from their true values (and the subsequent adjustment applied by calibration) and reduces both precision and accuracy of the instrument.

Biological materials and those with large crystal structures have interfaces between structures and crystals which act as internal reflective surfaces. The regular pattern of these can mimic the surface shape and lead to sub-surface scattering and reflections at multiple depths being recorded which are similar in

shape to the outer surface. When software alignment is applied to scan passes with such errors, the similarity in shape offers multiple solutions to the alignment and poor 3D reconstruction. This effect is particularly noticeable in teeth where the fine microstructure and semi-opaque but highly specular enamel, make them particularly challenging targets for 3D digitisation (Slizewski et al. 2010).

The same effect is seen in materials that have a translucent coating, with some reflection of light at the outer surface of the coating and further returns occurring at the coating - material surface (figure 4.16). The use of shorter wavelength blue light scanners and matting powders can be effective in combatting translucency derived errors and noise, although the latter may not always be appropriate on fragile or wet specimens.

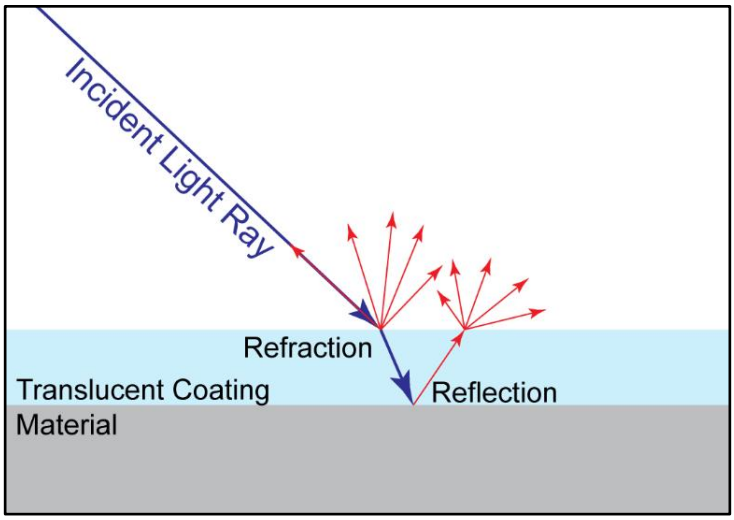

Figure 4.16: Sub-surface scattering of light in the translucent coating of a material (after Coşarcă et al. 2009 p. 120).

4.2.4. Humidity and temperature

The humidity and temperature of the scanning environment, the scanned object and the scanner itself have an impact on the quality of the resulting data. Whilst this effect is more significant in engineering environments, it has also been shown to be important in terrestrial laser scanning measurements (Dury et al. 2015) where the scanner to target object distance is long. Within object scale scanners used indoors in more controlled environments, changes in humidity can be controlled more easily and are less of a factor than changes in temperature. Most scanners operate through the use of bright lights, lasers, electronics and high end computers. These all produce heat as a by-product of

their operation and therefore transfer that heat to both the other components within the scanner and the scanning environment. The impact on quality derives from thermal expansion of both the target object and the scanner itself. Changes in the scanner can alter the base length between the digitisation camera and the light transmitter in triangulation based devices invalidating the calibration and requiring re-calibration. Changes in dimensions within the object being scanned will produce different measurements for the same region of the object scanned in multiple scan passes, resulting in poor alignment of the point clouds from each scan pass and a greater degree of error in the resultant surface mesh (Durán-Domínguez et al. 2014).

Most scanners now incorporate a temperature sensor within the instrument that warns of temperature changes over a pre-set threshold, prompting recalibration and minimising the level of error. Additionally, the construction of large scan tables can act as a heat sink to slow the changes in dimensions of the scanner and the object, never-the-less temperature change is still a potential source of scan error that operators need to account for in experimental design.

4.3. Surface Digitisation

Since the 1990s anthropology, archaeology and palaeontology have witnessed a growth in the use of 3D digitisation, analysis and visualisation, initially in the form of computed tomography, building on instrument developments in medical research, but more recently through surface scanning using instruments developed in materials engineering (Friess 2012). The growth of these research areas is founded on the increasing processing capabilities and lower cost of computing in concert with the development of 3D software tools (Wittur 2013). The high initial cost of equipment meant that outside engineering the first uses of 3D surface scanning for research were in medicine and living patients, notably in plastic surgery of the face (Moss et al. 1987, Vannier et al. 1991, Bhatia et al. 1994, Aung et al. 1995). Facial and cranial research in medicine has established crossover into palaeoanthropology and osteology and the potential of surface scanning was quickly recognised in these fields (Aiello et al. 1998, Kappelman 1998, Wood et al. 1998). At the same time the techniques of analogue 3D photogrammetry, with their foundation in aerial survey, was also adopting the increased power of computing to speed up photogrammetric reconstructions. The lower cost of photographic equipment led to the early adoption of photogrammetric 3D analysis within palaeoanthropological and archaeological research (Savara et al. 1986, White & Suwa 1987, Hartman 1989, Guanchang & Guanchang 1990).

3D digitisation of cultural heritage objects is now pursued through two approaches: the absorption of radiation signals to digitise the internal volume of an object (volume scanning) in CT (Lynnerup 2010) and Micro CT (Tuniz & Zanini 2014), and the reflection of radiation in surface scanning techniques. Whilst the impact of taphonomic change on the quality of volume scanning is a topic of future interest (chapter nine) it is otherwise outside the scope of this thesis which concentrates on surface scanning.

Contactless surface scanners generate point clouds which represent the surface geometry of the object being digitised through the recording of the response of light (in various forms) being projected onto it. The source of the light is integral to the scanning instrument in active scanners such as structured light and laser scanners, or from the environment around the object in the case of passive systems such as photogrammetric techniques (Friess 2012). The response to the light can be interpreted by the software of the scanner through the application of triangulation to locate the point on the surface of the object being observed in 3D space (figure 4.17).

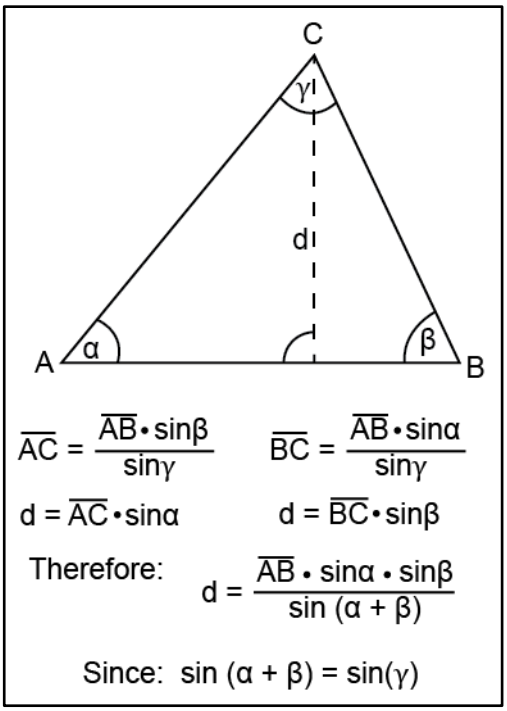

Figure 4.17: Sine law of trigonometry used in triangulation in 3D scanners (source: author).

Surface scanners therefore offer a fast and non-destructive method of recording the surface shape for fragile degraded material in cultural heritage, with 3D digital documentation methods now considered important conservation tools.

Three methods of surface digitisation are included within this research, laser scanning, structured light scanning and photogrammetry. Each of these techniques is outlined in the following sections.

4.3.1. Laser scanning

3D laser scanning incorporates a variety of laser-based recording and metric survey techniques at a range of scales. In the recording of heritage assets these range from the use of digital documentation of large landscapes using airborne LiDAR (Light Detection and Ranging) to create digital elevation models; terrestrial laser scanning (TLS) to record landscapes, buildings, excavations and larger objects; down to a variety of object laser scanning systems for the recording of objects from the medium to micro scales that are the focus of this research.

Whilst terrestrial and object laser scanners are both covered under the umbrella term of laser scanners, they have significant differences in the underlying methodology used to capture 3D positional data. The research in this thesis is focussed on object scanners used to digitise bone.

4.3.1.1. Basic principles

Unlike terrestrial scanners which utilise either phase or time-of-flight range methods, object laser scanners determine shape and distance of the objects through optical triangulation.

The method relies on points of laser light along a line reflected by the surface of an object and recorded by an optical sensor (usually a fixed wavelength camera). The fixed distance and angle between the laser emitter (*A*) and the optical sensor (*B*) creates the base of a triangle (*AB*) and each point of laser light reflecting off the surface of the object forms the third vertex of the triangle (*C*); the distance to each point on the laser line can be determined through trigonometry (figure 4.18).

To calculate the object distance, the angle between the object and the optical sensor must be known. Whilst the optical sensor is at a fixed angle it is made up of a network of millions of light sensitive pixels. Laser light rays reflected off object surfaces at different distances are focused through a lens to activate different pixels on the sensor. By calibrating the instrument in advance, the variation in pixel activation can be correlated with distance (right of figure 4.18).

The distance of a point determined by the line laser can then be added to the position and direction of the laser probe determined from the coordinate measuring machine (CMM) robotic arm creating high accuracy recording of the scanning subject (Taylor et al. 2005).

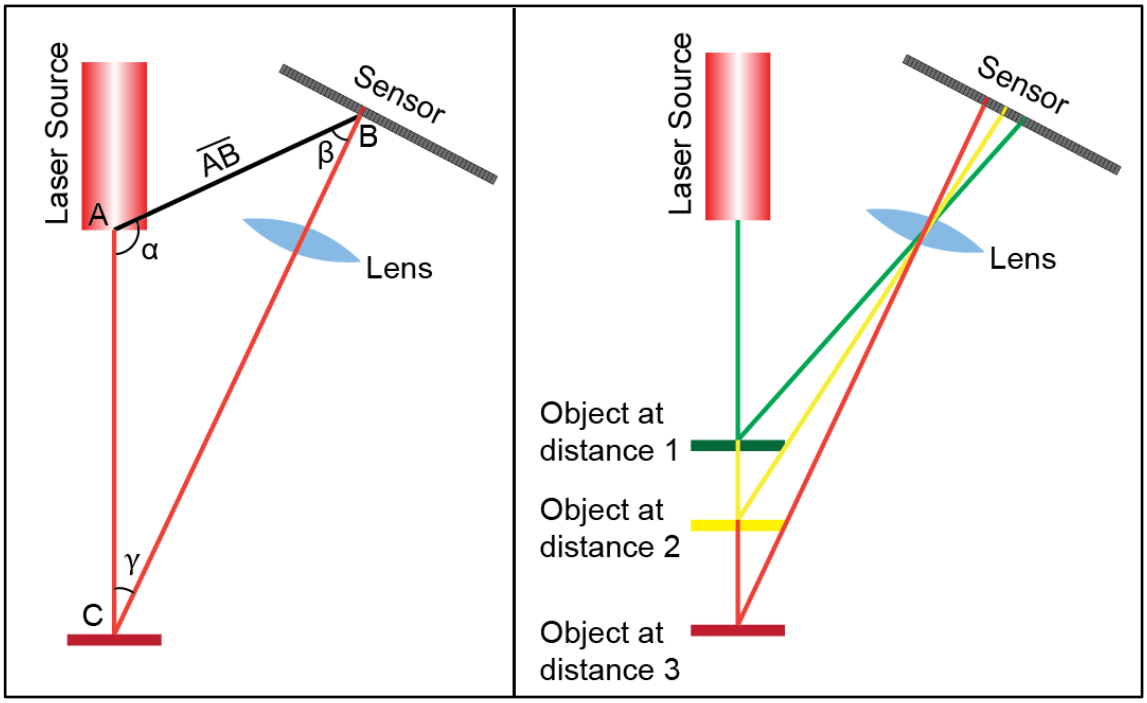

Figure 4.18: Principles of laser scanning. Left: Determination of object distance in laser scanners based on triangulation; Right: Sensor pixel activation relates to object distance (after Weber et al. 2011 p. 99).

The FARO Quantum Arm and V3 Laser Line Probe (FARO, Lake Mary, FL, USA) used for the research within this thesis, projects a line consisting of 640 points of laser light which it alters at 30 frames per second allowing the scanner to capture 19,200 points per second. In addition to the distance determination through trigonometry, the shape of the laser line's distortion when shone on an object is a function of the object's shape and allows additional refinement of the resultant 3D point cloud. The linear pattern of these laser points therefore behaves in a similar manner to that of the pattern projected in structured light scanning (section 4.3.2). The accuracy and precision of triangulation based 3D laser scanners is a function of object distance, with uncertainty of laser spot position increasing in ratio with the square of the object distance (Grussenmeyer et al. 2016). As a consequence, most object scanners have short standoff distances requiring greater operator skill, and incorporate software based filters to limit 3D point acquisition to within the recommended working distances of the laser probe (see table 4.1) to improve the quality of the data. CMM mounted laser scanners over short ranges therefore have measured accuracies of a few tens of microns (Weber & Bookstein 2011) and are less susceptible to environmental conditions. The shorter working distances limit the field of view of the laser and to capture the full surface of an object multiple

overlapping scans are needed. Each scan must be aligned to those that overlap it, introducing the potential for alignment errors.

4.3.1.2. Handheld vs CMM arm laser scanners

Laser scanners for object digitisation occur in two forms (see table 4.1), portable hand held scanners such as the Polhemus system and laser scan devices paired to a coordinate measuring arm such as the FARO arm scanners.

Handheld scanners combine a line laser and camera with a motion tracking function that allows them to position themselves in 3D space (Allard et al. 2005). The portability and lower cost of handheld scanners is attractive as a research tool in the field, although this portability and freedom of movement is offset by their lower accuracy and precision which is limited by the capabilities of motion tracking to fix their position (Grussenmeyer et al. 2016). They also suffer from motion blur in the imagery which can introduce noise to the point cloud and resultant mesh. Handheld scanners offer a valuable bridge between the landscape scale of terrestrial laser scanners and object-based scanners and in cultural heritage are useful for recording specific object detail within larger surveys (e.g. architectural details within terrestrial laser scan of a built heritage survey).

Within engineering, the need to quality test manufactured components and to reverse engineer information from used parts has led to the increasing use of coordinate measuring machines (Weckenmann et al. 2004, Bešić et al. 2011). These use a robotic arm with high resolution position encoders in each rotating joint, allowing the position of a contact probe at the end of the arm to be recorded in 3D space (Luebke 2014). Contact digitisers mounted on coordinate measuring machines provide high precision and accuracy point data (van Gestel et al. 2009) but are not suited to the digitisation of whole surfaces. Additionally, the use of contact probes with fragile materials in cultural heritage has conservation implications.

The need for digitisation of surfaces in engineering led initially to the use of handheld scanners, although their uptake was limited by the lower positional quality of the data derived when compared with contact digitisers (Feng et al.

2001) resulting in a perception that only loose tolerance items should therefore be laser scanned. However research into laser scanners showed that the accuracy of laser scan results could approach those of contact digitisers if the laser was mounted on a device that recorded the X,Y,Z coordinates of the laser head itself (Fan & K-C 1997, Chua et al. 1998, Bešić et al. 2011). Such systems included Coordinate Measuring Machines (CMM) (Santolaria et al. 2009), Computer Numerical Controlled (CNC) machines, robotic or mechanical arms (many of which are also CMMs) (Vukašinović et al. 2010) already in use in engineering; the co-mounting of the laser with such devices reduced recorded errors to tens of microns in ideal circumstances (van Gestel et al. 2009).

4.3.1.3. Calibration

Calibration methods for optical measuring devices (e.g. laser and structured light scanners) rely on the optical measurement of known values with an instrument and the calculation of offset values to mitigate consistent directional inaccuracies. However, in 3D digitisation the position of the calibration target in 3D space is not known and therefore must first be determined. In coordinate measuring machine mounted laser systems, calibration of the laser is preceded by calibration of the contact probe attached to the end of the arm. The now calibrated probe can then be used to measure the position of a laser calibration target with a high degree of accuracy. The mounting of laser scanners on coordinate measuring machines therefore results in improved calibration (and therefore increased accuracies) over other systems.

4.3.1.4. Use in cultural heritage

Compared to widespread use of terrestrial laser scanning, coordinate mounted laser scanning systems took longer to be adopted within cultural heritage. However, their use is now increasing, particularly for the recording of skeletal material where digitisation and online dissemination can provide access to rare or fragile specimens. Object laser scanners are being used to create online faunal or fossil reference collections, improving the identification and analysis of animal remains in archaeology and palaeontology (Hennessy & Stringer 2002,

Dawson & Levy 2005, Strait & Smith 2006, Strait et al. 2007, Smith & Strait 2008, Wolniewicz 2009, Larson et al. 2009, African Fossils 2016).

The high precision and accuracy makes 3D laser scanning a valuable tool in archaeological artefact conservation and research, supporting the reconstruction preservation and study of opaque material artefacts from Roman statuary (Manferdini et al. 2016), Cretan ceramics (Durán-Domínguez et al. 2014), to paintings (Taylor et al. 2005) and as a method to digitally preserve the diverse culturally specific maritime craft of Wales and Ireland (Tanner 2013).

Laser scanning has seen a greater uptake in anthropology and palaeontology, through virtual anthropology. Whilst the earliest three dimensional image capture and analysis methods concentrated on contact probes and medical computed tomography, the rapid advance in computer performance has meant surface scans of hominid skeletal remains are now accessible to researchers and the quality of laser scans makes these models viable research subjects. The diversity of research utilising laser scanning is broad including research in hominid cranial volumes (Sholts et al. 2010), inner ear function (Stoessel et al. 2016), cranial morphology (Bromage et al. 2008, Toneva et al. 2016), cold adaptation and facial shape (Friess et al. 2002), foot morphology (Bennett et al. 2009, Jungers et al. 2009, Harcourt-Smith et al. 2015, Fernández et al. 2016), footprints (Bennett et al. 2013), joint surfaces and the evolutionary biomechanics of hominid species (Harcourt-Smith et al. 2008, Hammond et al. 2013, Plavcan et al. 2014). Many of these analyses have cross-over into forensic anthropology and medical skeletal anatomy and pathology (Weber et al. 2011). For a more detailed discussion of the field of virtual anthropology see Weber and Bookstein (2011).

Prior to this research the author was involved in a series of high profile projects supported by funding from JISC, University of Bradford and HEIF to laser scan pathological human skeletal remains (figure 4.19) (Digitised Diseases 2014, Biological Anthropology Research Centre 2014) and by an AHRC funded project entitled Visualising Animal Hard Tissues to explore the digitisation of other animal hard tissues such as ivory (Bradford Visualisation 2014). These projects highlight the rapid expansion of access to digital resources which are

being used to engage and educate the public, students and researchers whilst also protecting the fragile collections from handling damage.

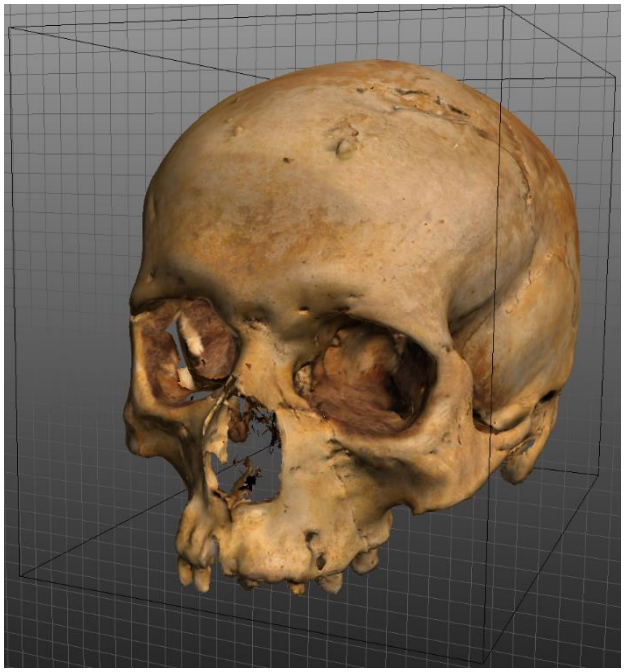

Figure 4.19: Screenshot of textured 3D digitisation for specimen B1226 laser scanned by the author as part of the JISC funded Digitised Diseases project (Digitised Diseases 2014).

4.3.2. Structured light scanning

Structured light scanners use the deformation of a series of binary structured fringe images (figure 4.20) projected onto an object (Inokuchi et al. 1984, Pribanić et al. 2010, Salvi et al. 2010) to identify its shape and position in 3D space through the use of machine vision cameras (Inokuchi et al. 1984, Salvi et al. 2004).

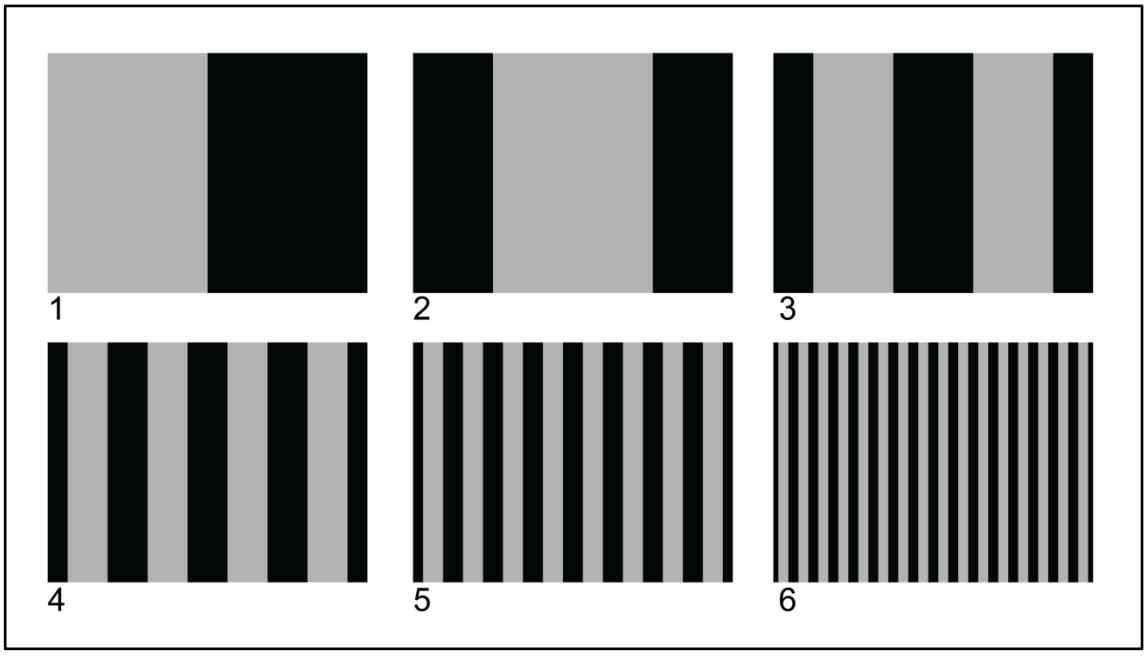

Figure 4.20: A typical sequence of binary structured fringe pattern images used in structured light scanning (source: author).

4.3.2.1. Basic principles

As with object laser scanners (section 4.3.1), a fixed distance between the emitted source of the structured light patterns (A) and the camera sensors (B) is used to provide data, which through optical triangulation (figure 4.17) provides for the calculation of the distance from the sensor to each point identified by the pattern of light (C) (figure 4.21).

Phase-shifting the structured fringe patterns over the object's surface uses the full spatial resolution of pixels on the camera sensors resulting in higher quality scans. As phase-shifting of the pattern uses multiple camera images in rapid succession and averaging of point information between patterns, structured light systems have a reduced susceptibility to specular reflections (Zhang 2010) and greater adaptability to ambient light conditions but longer acquisition times (Bathow et al. 2010, Ekstrand et al. 2013).

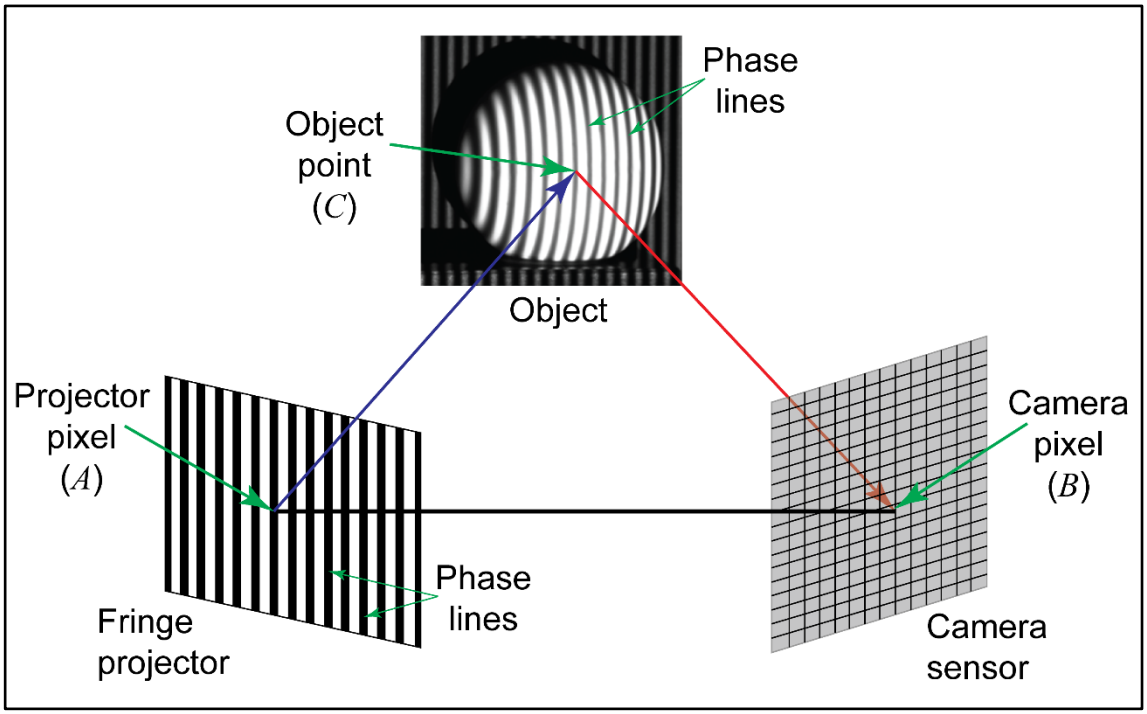

Figure 4.21: A typical setup of a single camera digital fringe projection structured light system (adapted from Zhang 2010 p. 149).

Structured light scans are produced from a fixed viewpoint and unlike laser scanning, where the scan head is moved around the object on an articulated arm, the object must be rotated to allow for multiple view angles to be recorded to produce a full 3D model. Rotation of the object between scans of different angle views introduces potential for errors. Each scan, as with laser scanning, must then be aligned with those that overlap it, also introducing the possibility of alignment errors. Scan to scan alignment is usually achieved through the use of an iterative closest point algorithm (Rusinkiewicz & Levoy 2001, Bouaziz et al. 2013). As structured light scans capture the whole scene, additional scans follow a pattern of diminishing returns (Friess 2012). Small scale imprecision in each scan leads to a level of accumulated error that requires exponentially increasing processing time to resolve alignments of new scans. One approach to mitigate this is the addition of multiple cameras which through calibration can provide greater point accuracy (Zhang & Yau 2008).

4.3.2.2. Calibration

All cameras introduce distortion to the image sensor through inaccuracies in the lens glass, aperture ring alignment, and geometric distortions such as barrel or

pincushion distortion (Remondino & Fraser 2006). These result in the pixel position for any given point being translated ($\Delta x,\Delta y$) from the expected value. In structured light instruments the camera or cameras are focused at the same focal depth as the projector focus point and the aperture and focus is then locked. Because distortion is a function of lens settings, once these settings are fixed the distortion can be measured and corrected for by applying the reverse translation ($-\Delta x,-\Delta y$) to achieve more accurate depth calculations.

With laser scanning, the target for calibration can be directly measured physically, whilst structured light systems must rely on known dimension calibration boards (figure 4.22).

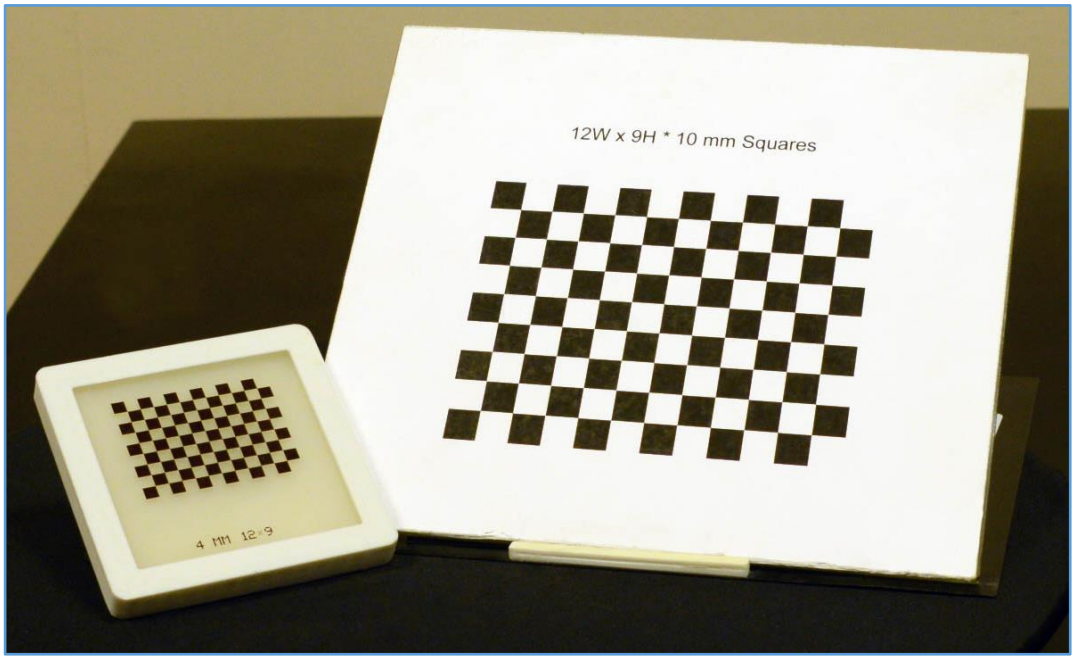

Figure 4.22: Two different scale structured light calibration boards (source: author).

As structured light systems are optimised to detect variations between black and white patterns in normal operation, calibration boards are based on a grid of alternating light and dark squares forming a machine vision readable point at each corner. By comparing the measured values of the points at each corner within a size regular grid with the expected values, the positional inaccuracy can be determined for each camera lens (Han et al. 2013). The incorporation of a digital projection system as the light emitter of structured light systems offers the opportunity to re-project the calibration corner points onto the calibration board affording an assessment of the 're-projection error' as a quality check.

The size of the calibration grid must be matched to the resolution of the camera and projector components in the instrument. Small scale structured light scanners therefore require the production of much smaller calibration boards. Small inaccuracies in the surface flatness of calibration boards, which may not be significant at larger scales, can produce large errors in relation to the scale of the scan volume. Additionally, the tolerance of line widths in printing the grid pattern for smaller scale scanners becomes critical and this is a limiting factor when reducing the field of view size of structured light systems (Stone 2015).

4.3.2.3. Use in cultural heritage

Structured light scanning saw slower initial uptake as compared with laser scanning in archaeology and heritage, although some initial work has been carried out using the technique in museums to record ceramics and pieces of art (Breuckmann 2008, Karasik & Smilansky 2008), as well as the creation of online reference collections of faunal remains (Niven et al. 2009).

The technique is most developed in the recording and analysis of highly specular surfaces particularly metal and flint where laser scanning would be more problematic (Grosman et al. 2008, 2011, Bretzke & Conard 2012). The ENTRANS project, a pan European project examining the highly dynamic cultural and social identities in Iron Age Europe, has benefited from experience at Bradford, with use of structured light scanning to digitise, research and present Iron Age art and material culture. Many of these artefacts are metallic and would be difficult to accurately digitise with other techniques (Büster et al. 2016).

In a wider archaeological context, handheld structured light scanners have been used as a substitute to terrestrial laser scanning to record archaeological remains in-situ, demonstrating its portability as well as offering faster recording of close range targets than TLS (McPherron et al. 2009). Additionally, the greater tolerances to ambient light variations and specular reflection from wet surfaces offer some potential for handheld structured light scanning's increased use on archaeological sites (Beaubien 2008, Gernat et al. 2008, McPherron et al. 2009).

Anthropometric scanning has seen a rapid increase in the use of structured light systems. White and blue light scanners offer safer options with regard to eye safety compared to laser scanners and are increasingly taking over from laser scanners for facial scanning. The ability to integrate multiple cameras into structured light systems has the potential to limit movement errors within scans of living patients (Fink et al. 2014), whilst the use of both structured light and laser scanners for research on skeletal tissues is now established (Friess 2012).

4.3.3. Photogrammetry

Photogrammetry is the determination of metric information from multiple photographic images utilising the same physical properties of light and optics that allow the 3D perception of the world in human binocular vision.

Stereo photography has a long history dating to the early development of photographic image production. The potential to use the multiple photographic images to provide metric information of the photographic subject was quickly recognised and individual experimentation with photogrammetric techniques throughout the latter half of the 19th century culminated during the First World War in the use of photogrammetry to rapidly produce military maps from overlapping stereophotographs taken from Royal Flying Corp and German reconnaissance aircraft (Collier, 2002). These early forms of stereoscopic 3D imagery utilised two cameras at a fixed distance and angle to each other and metric information was derived by hand measurement and calculation.

The introduction of digital cameras and the use of computers to calculate 3D geometries from images means that only one camera is now needed. By moving the camera around an object, the spatial relationship of the image positions can be determined by the comparison of the appearance of the same features visible in the overlapping regions of each of the multiple images. Because the difference in the image is due to movement of the camera, photogrammetric 3D modelling sometimes termed structure from motion, although that term is more correctly reserved for techniques based on video images (Pollefeys et al. 2007).

4.3.3.1. Underlying principles of photogrammetry

In the same way that human binocular vision provides slightly different images to the brain, the parallax within the two images produces a stereoscopic view which provides 3D depth.

Using two or more photographs of the same subject from different positions, photogrammetry can reconstruct three dimensional information (Linder 2006) using the collinearity principle. The collinearity principle relies on the central

perspective projection within optics to determine the relationship between the 2D image coordinate system and the 3D object coordinate system.

In a photographic image (figure 4.23) a point in the real world (A) is projected through the lens onto a planar light sensitive surface (i.e. the camera sensor) to produce a point on the image (a) as a 2D positional record (x_a, y_a) of the 3D point in the real world (X_A,Y_A,Z_A). The ray of light that connected the real world point (A) to the recorded point on the sensor (a) passes through the focal point of the image (perspective centre (X_0, Y_0, Z_0)) which is at a known distance from the sensor plane (the focal length (f)). The image on the sensor is therefore upside down to the real world (Albertz & Wiggenhagen 2009, Schindler 2015).

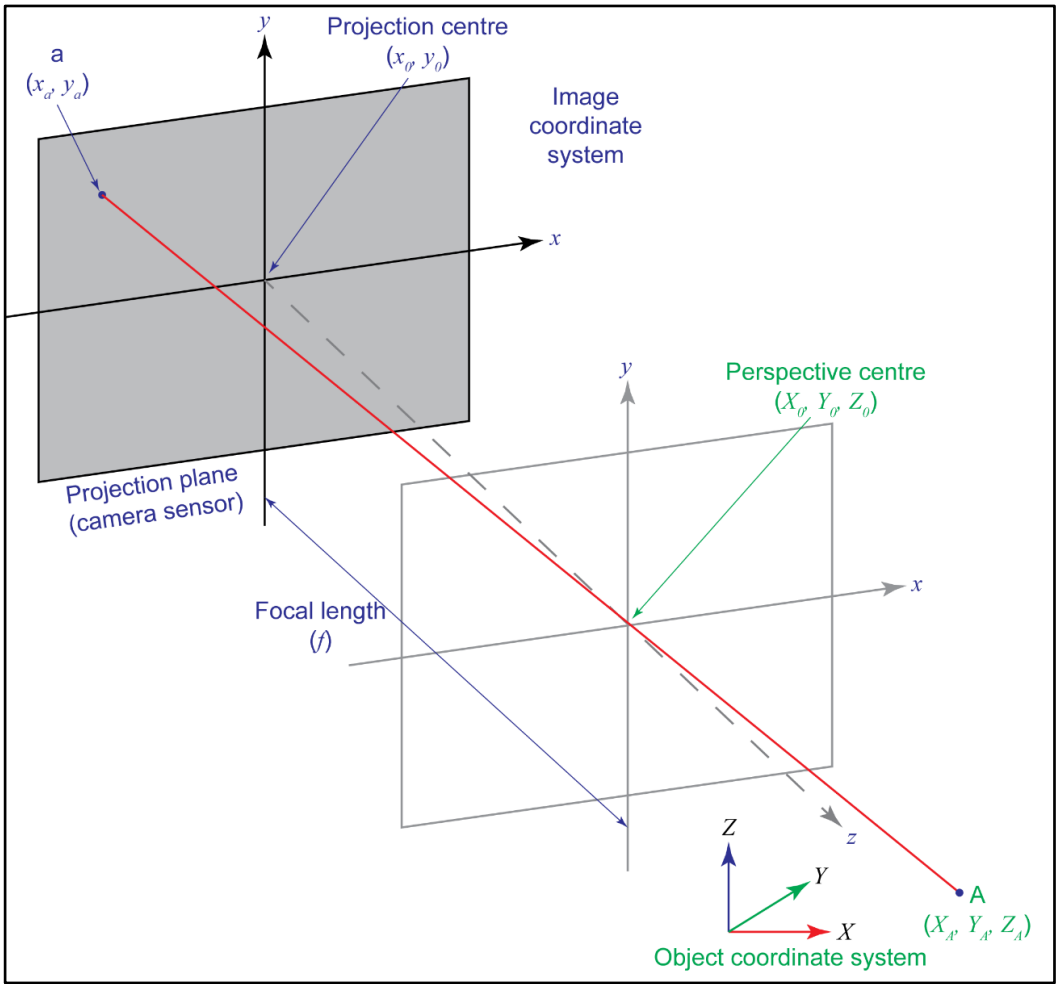

*Figure 4.23: Central perspective projection of a real world point (A) to produce a 2D point (a) on the image sensor. Blue: variables in the image coordinate system. Green: variables in the object coordinate system (*after Stylianidis et al. 2016 p. 265)*.*

There is therefore a fixed ratio (λ) between the relationship of the coordinates of the recorded point on the sensor to the perspective centre (X_0, Y_0, Z_0) and the

relationship of the perspective centre to the real world point (A) coordinates such that:

$$x_a - X_0 = - \lambda (X_A - X_0)$$

$$y_a - Y_0 = - \lambda (Y_A - Y_0)$$

$$f = \lambda (Z_A - Z_0) \qquad \text{(Expression 1)}$$

Expression 1 can be simplified by solving for λ to produce:

$$x_a - X_0 = - f \frac{X_A - X_0}{Z_A - Z_0}$$

$$y_a - Y_0 = - f \frac{Y_A - Y_0}{Z_A - Z_0} \qquad \text{(Expression 2)}$$

The coordinates for the point A in the object coordinate system can be considered to have been undergone a transformation from the object coordinates system to the camera coordinate system. This transformation can be mathematically described as a translation from the origin of the object coordinate system at the perspective centre (X_0, Y_0, Z_0) to the origin of the camera coordinate centre at the projection centre (x_0, y_0), followed by a rotation to bring the axis of the two coordinate systems into alignment (Schindler 2015).

The transformation, expressed as a matrix (r) therefore transforms the relationship between the X_A,Y_A,Z_A coordinates to the perspective centre into:

$$x_A - x_a = r_{11} (X - X_0) + r_{21} (Y - Y_0) + r_{31} (Z - Z_0)$$

$$y_A - y_a = r_{12} (X - X_0) + r_{22} (Y - Y_0) + r_{32} (Z - Z_0)$$

$$z_A - z_a = r_{13} (X - X_0) + r_{23} (Y - Y_0) + r_{33} (Z - Z_0)$$

(Expression 3)

Expressions 2 and 3 can be combined by substitution to derive the pair of collinearity equations:

$$x = -f \frac{r_{11}(X - X_0) + r_{21}(Y - Y_0) + r_{31}(Z - Z_0)}{r_{13}(X - X_0) + r_{23}(Y - Y_0) + r_{33}(Z - Z_0)} + x_0$$

$$y = -f \frac{r_{12}(X - X_0) + r_{22}(Y - Y_0) + r_{32}(Z - Z_0)}{r_{13}(X - X_0) + r_{23}(Y - Y_0) + r_{33}(Z - Z_0)} + y_0$$

(Remondino 2014, Schindler 2015).

Digital images use an x,y system to encode the pixel positions on the sensor, however, the standard system for all digital images is to place the origin at the top left corner of the image. The x_a,y_a coordinates therefore need to be converted from the image coordinate system to the sensor coordinate system via a simple affine transform operation.

In images of the same object, taken from differing viewpoints, common points are identified on the surface of the object, referred to as tie points. For each set of tie points in paired images, collinearity rays are produced via the above collinearity equations (figure 4.24 top). The arrangement of tie points in numerous images allows multiple images to be compared and their collinearity equations are grouped into a system of equations. The system is then resolved through the application of an iterative least squares method allowing the positions of points on the object to correlated in 3D space (figure 4.24 bottom).

Once features on multiple images have been identified and correlated, further calculation must be carried out to determine 3D shape from the variation between the identified features. The most common current methods of achieving this are Semi-Global Matching, Sum of Absolute or Squared Differences, Normalised Cross Correlation, Census Transformations and Rank Transformations. For a more detailed comparison and review of these see Ahmadabadian et al. (2013) and Dall'Astra and Roncella (2014).

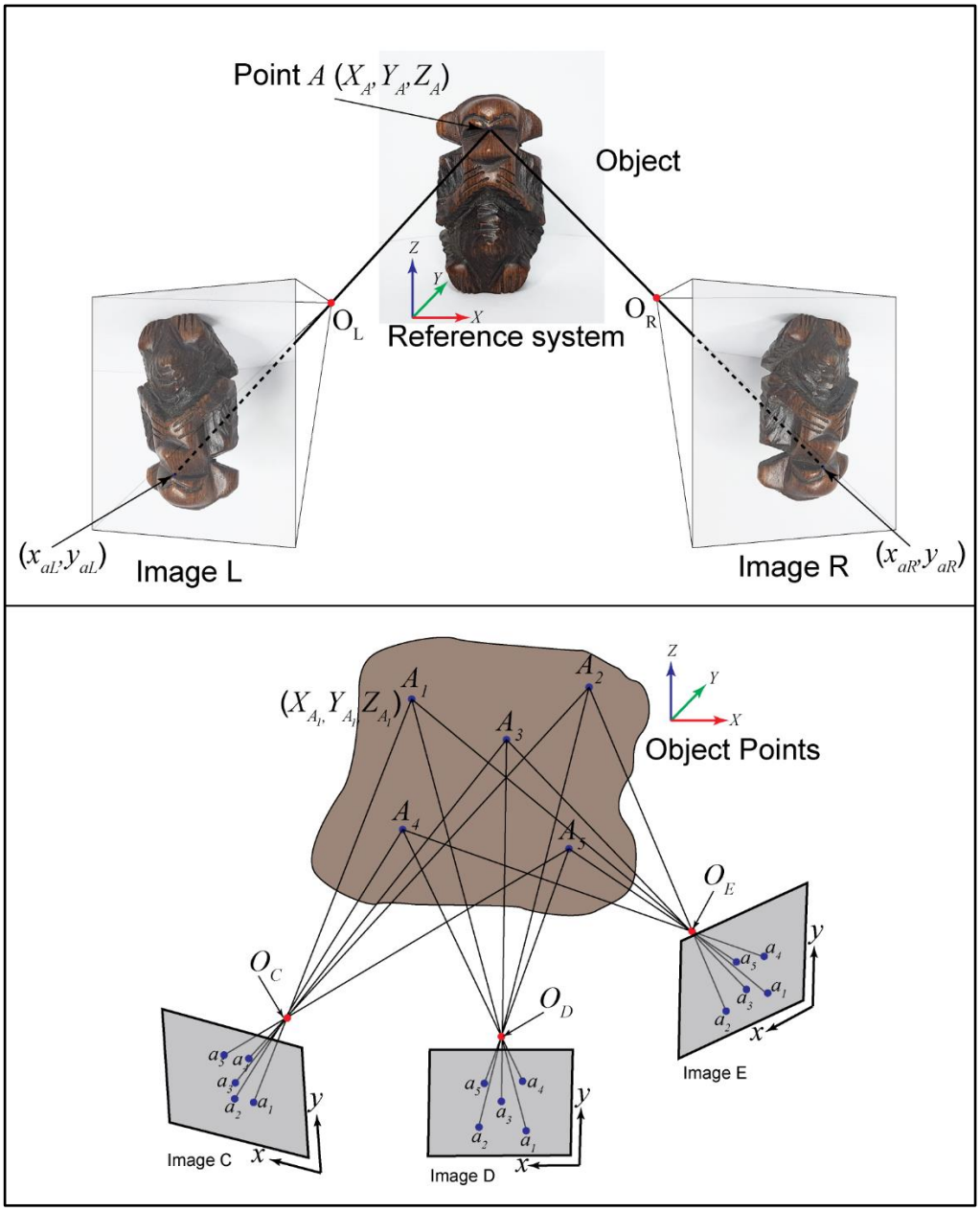

Figure 4.24: Combining collinearity from multiple images. Top: calculating the collinearity rays for the same point (A) in two different images. Bottom: A 3D object surface can be reconstructed using multiple collinearity rays between corresponding image points (adapted from Remondino 2014 p. 64).

4.3.3.2. Feature identification

The use of the collinearity principle within photogrammetry relies on the identification of points within digital imagery that are common to multiple photos to provide tie points.

From the 1980's onwards researchers proposed methods of automatic feature detection within computer vision starting with algorithms that matched similar patches of pixels in an image (Lucas & Kanade 1981), algorithms that identified

“corner like” features (Moravec 1983) and then algorithms that identified vectors of transformation between images such as eigenvectors (Förstner 1986, Harris & Stephens 1988). These early methods were applied to photogrammetric 3D reconstruction but often relied on the perspective and scale between images to be similar and therefore the distance between camera positions to be short, in turn requiring large numbers of images and therefore higher computing loads to produce a 3D reconstruction (Snavely et al. 2007). More recently methods have been developed to allow for wide baseline matching of images taken from dissociated viewpoints with multiple types of camera, lens and resolution (Lowe 2004, Mikolajczyk & Schmid 2004, Mikolajczyk et al. 2005, Brown & Lowe 2006). Whilst the identification of features from images in machine vision is now a complex multidisciplinary subject with applications far wider than photogrammetry (Nixon & Aguado 2012), in general features detection algorithms in digital images of objects rely at least initially on the variation in pixel colour within small pixel domains (figure 4.25) before being further processed and refined.

As can be seen in figure 4.25 the identification of a tie point through feature analysis has a degree of uncertainty at the pixel level in that a single apparent point within the full scale image is depicted by multiple pixels when zoomed in. Moving the camera viewpoint produces varying pixel patterns as the shape of the feature is foreshortened as the incident angle increases. Direct pattern matching of the pixels is therefore not viable and an algorithm for weighting the use of one of the dark pixels within a feature is used. A number of solutions to the collinearity equations for a feature may therefore exist based on each of the dark pixels’ positions leading to uncertainty of the reconstructed 3D position.

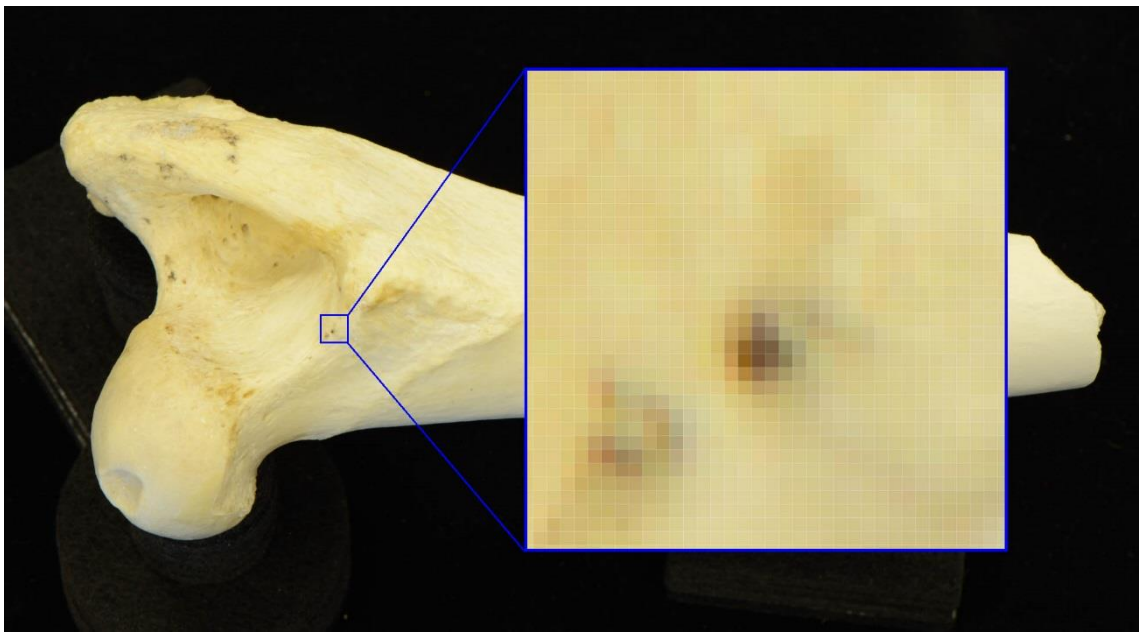

Figure 4.25: Identification of a feature within a digital image of sample A0011_F01 used as a tie point within photogrammetry (source: author).

Overcoming this uncertainty relies on the relative ratios between multiple points providing the iterative least squares operation with greater number of variables to calculate. Therefore, the larger the number of tie points within an image the smaller the variance in the position of the reconstructed 3D point (i.e. better precision) (Koutsoudis et al. 2014). Feature density within digital images is therefore an important quality factor for photogrammetric reconstructions.

In poorly focused images or where the depth of field is narrow, features become blurred over a larger area of pixels, increasing the level of uncertainty of position for the tie point until the feature becomes unusable for 3D reconstruction. Additionally, as feature identification is dependent on contrast and colour variation within the image, objects with smooth uniformly coloured surfaces where there are few natural faults, structures or variation in colouring, feature density is low and 3D reconstruction can be imprecise or fail completely (Wenzel et al. 2012, Koutsoudis et al. 2013). Whilst the use of external reference targets can offer additional tie points to improve the alignment of the camera images, without sufficient features on the object itself 3D reconstruction of the object remains poor.

Sharp variation between the general object colouring and features is best exhibited in well focused images and good feature distribution across images is

reliant on appropriate depth of field (lens aperture setting). As colour variation can be subtle within some objects, over lighting or over exposure can wash out the colour resulting in the obscuring of features.

Good photogrammetric reconstruction is therefore a function of high quality photography by an experienced and skilled photographer. In objects with subtle colour variation such as bone and other natural materials, good photographic technique is essential.

4.3.3.3. Lighting

The colour and surface response of an object to lighting impacts the quality of 3D reconstruction. Spot lighting results in hard specular reflections on the surface of the object highlighting projecting features and hard edges in the object topography. Highlights show up in the resultant digital imagery as white spots which provide very strong colour and contrast variation to the general object colouring making them easily identified as features in photogrammetric software. Equally shadows cast by highly directional lighting offer dark areas within surface variation features which are also identified as features. However, because the highlight or shadow is not a physical feature on the surface of the object, but a lighting effect, the position is not fixed. When the camera viewpoint is moved (or if the lighting is changes), different angled rays from the specular reflection are aligned with the camera lens and the highlight appears to move within the image whilst the shadows remain fixed relative to the lighting.

As the least squares method utilises the relative positions of all the tie points in multiple images to resolve the 3D position of the reconstructed points, the introduction of highlight based tie points whose movement between images does not correlate with true tie points (i.e. those derived from physical features on the object) and shadows which move with the lighting significantly degrades the quality of the reconstruction.

Good photographic lighting is therefore a key factor in the quality of photogrammetric reconstruction. In small scale photogrammetry, carried out in a photographic laboratory, highlights and shadows can be avoided using flat highly diffused lighting. In addition, this allows the object to be moved on a

turntable to ensure consistent overlap between images and the shutter and exposure times can be optimised for good depth of field through the use of tripod and trigger releases. Turning the object on a turntable in front of the fixed position camera (or moving the camera around an object) produce convergent images where the angle of the plane of the sensor varies. This arrangement minimises perspective distortions and therefore leads to improved precision in the calculation of depth (*Z* direction) (Linder 2006).

4.3.3.4. Use in cultural heritage and anthropology

Photogrammetry was initially used on digitised versions of film prints, and as recently as 2004 researchers were still promoting the use of film stereo photogrammetry as the standard method for the recording of large heritage objects in museum collections (Böhler & Marbs 2004). However, the availability of high resolution digital cameras, as well as calibrated lens corrections for those digital camera-lens pairings, means that the better quality results can now be achieved, eliminating accumulated errors from film printing, storage and digitisation. Additionally, the increase in use of digital photography and the recognition of its potential for 3D reconstruction has led to an increasing choice of software packages produced to allow both the public and researchers to create 3D models based on photogrammetric techniques. These include 123D Catch (Autodesk, San Rafael, CA, USA), PhotoScan (Agisoft, St. Petersburg, Russia), Photomodeler (EoS Systems Inc, Vancouver, Canada), Apero (IGN, Paris, France), Bundler (University of Washington, USA), Insight3D (Lucas Mach), RealityCapture (Capturing Reality S.R.O, Bratislava, Slovakia) and Photosynth (Microsoft, Redmond, WA, USA). Some of these packages have taken advantage of the development of cloud computing facilities to reduce the computer processing overhead of photogrammetric 3D reconstruction through distributed computer processing, although in some cases this requires a voluntary diminution of the copyright and property rights to the images by the user.

Large scale objects and sites have been examined extensively with photogrammetry and it is a key technique in the rapid creation of digital terrain models for archaeology. The lower cost of the equipment (camera, tripod and

computer) and software compared to other survey methods such as terrestrial laser scanning, has led to its use becoming standardised within the UK for building and site surveys (English Heritage 2011).

The photogrammetric 3D modelling of smaller objects is more challenging requiring experienced and skilled photographic recording to overcome focus, noise and precision problems, however close range photogrammetry is now offering a cheap technique for the dissemination of 3D models online (Porter et al. 2016, Smithsonian Institute 2016).

Close range photogrammetry of archaeological objects has had more limited use to date, with the lower pixel density of older digital SLR cameras limiting the camera position determination as well as the level of detail of the resultant models. The adoption of digital cameras overtook film in 2001 (Dawson et al. 2006 p. 47) and by 2006 digital to film camera sales were 20:1 (ePHOTOzine 2007) leading to increased experimentation with digital data and engendering an increase in the development of photogrammetric techniques, reflectance transformation imagery etc.

Within anthropology, early application of photogrammetry was carried out to create 3D reconstructions of anatomy for the digital analysis and identification of physical landmarks (Falk et al. 1986, Hildebolt & Vannier 1988, Spencer & Spencer 1995, Fadda et al. 1997, Stevens 1997). With the advent of high pixel digital cameras photogrammetric techniques have been routinely adopted in the analysis of odontological studies of archaeological, forensic and ancient humans (Martinón-Torres et al. 2006, Evans et al. 2010, e.g. Macaluso 2010). Within forensic anthropology photogrammetry is being used to develop anthropometric analysis of skeletal elements, collecting both traditional linear measurements as well as previously difficult to determine measurements such as volume e.g. sex assessment in the pelvis (Benazzi et al. 2008, 2009, Macaluso 2011a), hyoid (Kim et al. 2006) and glenoid fossa (Macaluso 2011b).

4.4. Refit analysis

Fragmentary remains are common in archaeology and being able to reconstruct the fragmentation of an artefact can be a powerful tool to study spatial, behavioural and technological relationships between stratigraphic layers, areas of a site and between sites themselves.

Lithic refit analysis has a long history stretching back into the late 19th Century (Cahen 1987) and it is now used to answer questions about social structure (Floss & Terberger 1990), settlement patterns (Stackelbeck 2000, 2010), resource utilisation (Proffitt & de la Torre 2014) and site formation processes (Sisk & Shea 2008) as well as local and regional variations in lithic technologies (Ashton 2007, Chiotti et al. 2013).

The distribution of stone fragments across a site is the physical manifestation of a sequence of intentional actions by an individual at a specific point in the past (Rees 2000). The robusticity of lithic flakes preserves this record of past human behaviour allowing the refit of lithic reduction sequences to be used as a research strategy that is invaluable to our understanding of prehistory (Cahen 1987).

The refitting of artefact materials other than lithic tools has received considerably less research. The initial use of manual refitting of bone was aimed at improving minimum number of skeletal elements (MNE) of animal remains, which is an important measure of abundance in the analysis of faunal assemblages and the human behaviours that are associated with their formation (Blasco et al. 2010, Marean & Spencer 1991, Marean et al. 2001). More recently fragmentary bone has been used within several archaeological studies to relate stratigraphic units both vertically and horizontally (Morin et al. 2005, Vallverdú et al. 2005, Rosell et al. 2012), as well as to address research questions about use of human remains as a food resource (Andrews & Fernández-Jalvo 2003) and non-lithic tool production technologies (Tremayne 2010). Within forensic research refit methods have been used to examine trauma and reconstruct skeletal elements (particularly in gunshot and blunt force trauma to the head) (Stephens & Heglar 1989, Yin et al. 2011) and are now being applied to bone fragmented during burning (Grévin et al. 1998).

Whilst the benefits of refit analysis are clear, the technique is still underutilised in many research projects based on the inherent challenges in its use (Laughlin & Kelly 2010). Primary amongst these is the huge investment in time required to manually compare all fragments against each other in search of refitting fracture surfaces. Additionally, the experience and archaeological knowledge of those carrying out the manual refit, the type of lithic technology represented, material and assemblage size all impact refit success rates, and therefore the time required (Laughlin & Kelly 2010, Cziesla 1990, Goring-Morris et al. 1998, Sisk & Shea 2008). In a review of lithic refit use, the average success rates for lithic refitting from a selection of 30 studies was only 20% (Laughlin & Kelly 2010) and the study with the highest success rate (over 70%) was only achieved by dedicating 6000 hours to manual refit (Hietala 1983).

To address these problems several papers have suggested a need for a method of automation within lithic refit analysis (Laughlin & Kelly 2010, Borderie et al. 2004, Cooper & Laughlin 2006) and two studies so far have attempted to apply the power of computing to refit of lithic material with some limited success (Cooper & Qiu 2006, Riel-Salvatore et al. 2002). Cooper and Qiu's approach was to use a multivariate analysis based on GIS and some basic flake attributes (cortex, dorsal scar count, size etc.) and use computerised matching algorithms to group flakes according to a suitability score ahead of targeted manual refitting (Cooper & Qiu 2006). The approach taken by Riel-Salvatore et al. is so far the only study to try to automate the fracture surface matching of lithics using 3D digitised material and computer shape analysis. Their research outlined in a brief two page paper in Antiquity noted that whilst they could achieve reconstruction of a small test assemblage of laser scanned lithics, the computer refitting was slow and "very user dependant" (Riel-Salvatore et al. 2002) suggesting that in 2002 the computation capabilities were not yet sufficient to make automatic refit viable.

The process steps developed by Riel-Salvatore et al. follows a similar pattern to that being pursued by current Fragmented Heritage research (see section 1.3). This thesis examines the challenges that must now be addressed with an aim of extending the applicability of the Fragmented Heritage digital refit of lithics to other materials including fragmentary bone.

4.5. Digital refit process

The process steps in the Fragmented Heritage digital refit system are:

- Digitisation;
- Pre-processing and decimation;
- Segmentation and fracture surface characterisation;
- Orientation and fine alignment; and
- Comparison and assessment of refit distance.

Whilst automatic refit aims to provide a faster approach compared to manual methods, additional operations need to be added to the digital workflow and the extra time added must be compensated for by the improved speed of automated comparison between lithics. Digitisation encodes the model's surface mathematically and computers outperform humans in the calculation of complex mathematical operations by many several orders of magnitude and with greater reliability.

A number of these process steps are already standardised processes in 3D digitisation and visualisation, however, some pose significant challenges to overcome in their computational mathematics. As such, the process is rapidly changing as approaches are assessed and refined or rejected. Additionally, the application of these processes to bone will require further refinement of the automatic refit system informed by the results of this thesis. Each of the sections below gives a brief overview of the processes involved for lithic material to inform discussion of the results (chapter eight) and the application of the system to bone.

4.5.1. Digitisation, pre-processing and decimation

Digitisation adds a slower additional step to the digital workflow over manual refit. Lithic materials can have highly specular surfaces and in some fabrics (e.g. obsidian) the surface has a degree of translucency. In order to overcome the challenges that the surface properties of lithic fabrics pose to digitisation

(section 4.2.3) and to minimise digitisation times, a structured light approach is utilised to digitise the fracture surfaces. Once digitised, the models are meshed and exported to .stl or .obj format. This thesis assesses whether structured light is the most appropriate technique for bone, and what variations need to be made to the digitisation and meshing settings to maximise refit reliability and surface matching quality.

Following digitisation, noise and errors inherent in all scanning must be removed from the model by removing isolated triangles not part of the surface mesh.

Structured light and laser scanning both produce very high point density models and have large file sizes. To reduce the computer processing overhead, the size of the model is reduced through standard decimation processes. The degree of decimation is a balance between increased processing speed and a decrease in refit quality. The optimum threshold for lithics is being considered within the Fragmented Heritage project. The threshold for bone from differing taphonomic pathways will be informed by the research in this thesis.

4.5.2. Segmentation and fracture surface characterisation

Humans characterise items within vision as they see them, providing understanding and relating the physical world to the visual images processed in the brain. This inherent ability in biological vision is a major challenge in machine vision and in the refit system this is expressed in both the segmentation and orientation steps. Computers can't automatically distinguish the fracture surfaces in lithics or bone from non-fracture surfaces. Therefore, in order to compare fracture surfaces between models, fracture surfaces need to be identified and isolated from the rest of the model. Additionally, models can exhibit multiple fracture surfaces and to avoid false negatives these need to be treated separately in the matching process.

To identify a fracture surface, the computer needs to be able to delineate the boundary of that surface through the application of a boundary condition (segmentation). Lithics and bone have sharp lines marking the edge of fracture surfaces and these form potential boundary points. However, lithics and bone

fracture surfaces also exhibit lines and patterns within the fracture plane and distinguishing between in-plane features and boundary features is a non-trivial computing problem. Several approaches have been explored including ridge identification and area growth algorithms and the results of this research will be published shortly (Sparrow et al. *in prep*).

4.5.3. Orientation and fine alignment

Once the models have been segmented into individual fracture surfaces, their surface shape can be compared to all others within the system to provide refit matches. However, at the point of digitisation, the orientation of a lithic flake with respect to the core is not known and so the orientation is quasi-random (digitisation practice biases the orientation of flakes with regard to the longest axis). The point clouds and their calculated meshes retain this orientation (de Marsico et al. 2013) and therefore fracture surface orientations are not uniform. To overcome this the segmented surfaces need to be re-orientated, but to do so for every comparison within the system is a large computational challenge. The automatic refit system is researching methods of initial comparison and orientation to overcome this in lithics. In bone, the bone has a known form and orientation, although this may not be clear in smaller fragments.

Once orientated two surfaces are statistically compared through an iterative least squares fine alignment.

4.5.4. Comparison and assessment of refit distance

Once a pair of fracture surfaces are aligned, the variance in distance between them is calculated as an absolute distance and root square mean difference figure allowing an assessment of the quality of a refit. For materials that do not undergo deformation or taphonomic change of their fracture surfaces, this figure should be very low for refitting surfaces and offer a high degree of certainty to the refit match. However, bone's deformation during fracture varies dependant on the taphonomic pathway. Therefore, this thesis will contribute expected values for root mean square differences and absolute difference values for bone

of known taphonomic histories to inform the assessment of match probability when the automatic refit system is applied to fragmentary bone.

4.6. Chapter Summary

The principles underlying the digitisation techniques being employed in this study, along with the factors that influence digitisation quality, error and interference are all key to the research in this thesis.

Many of these factors are present in bone and it is important therefore to establish how bone's physical and chemical structure affect digitisation; and how the taphonomic changes to the physical and chemical structures of bone might further affect its digitisation. These will be key to understanding the challenges that are posed by taphonomic alteration of bone to the quality of digital refit.

These factors are discussed in relation to the development of the methodology in chapters five and six and the discussion of the results of this research in chapter eight.

Chapter 5. Methodology 1: Samples

The following chapter discusses the selection of experimental bone samples, the selection of archaeological and anthropological samples, and the design and development of digitisation technique comparison standards. The chapter also outlines the preparation, cleaning and monitoring of these samples as they were used within the digitisation methodologies that are the outlined in chapter six.

5.1. Samples

The samples used within the research project fall into three groups:

- Experimental taphonomy samples (5.2 & 5.3);
- Archaeological / palaeontological remains (5.4); and
- Technique comparison standards (5.5).

5.1.1. Sample numbering

All samples were assigned a unique master record number (MRN) in the form of a four figure serial number preceded by a letter identifier (e.g. “A0001”). The letter identifier allowed samples from different parts of the research to be easily distinguished and sorted in electronic files with “A” designating the experimental taphonomy samples (section 5.3), “K” the samples from the fieldwork in Kenya (section 5.4.1) and “S” the technique comparison standards (section 5.5).

Where samples were fragmented, either experimentally or, in Kenya where the samples were found to be multiple refitting fragments, a suffix was added to the end of the sample number, separated by an underscore, in the form of a “F” followed by a two figure serialised number. Thus each fragment could be uniquely identified.

Each of the samples was digitised with multiple 3D imaging methods and to ensure that the digital records remained easily identifiable an additional suffix

was added in the form of a three letter code identifying the 3D imaging technique and the numbered phase of the experiment being recorded.

The three letter codes were:

- LaS: 3D Object Laser Scanning (section 6.1);
- StL: Structured Light Scanning using the Bradford Visualisation scanner (section 6.2.1);
- MSL: Macro scale Structured Light Scanning using the MechScan (section 6.2.2); and
- PtG: Photogrammetry (section 6.3).

In addition scanning electron microscopy was carried out on some samples to ascertain surface roughness and determine taphonomic changes and an additional three letter code of SEM was used in the same manner to identify the resulting imagery.

The phase numbering where:

- 001: Pre-exposure recording (or in the case of the Kenya, Schöningen and Star Carr samples in their recovered state);
- 002: Imaged after one period of exposure;
- 003: Imaged after two periods of exposure;
- 004: Imaged after three periods of exposure.

As an example, a sample number might appear as:

A0001_F02_LaS002

Indicating that this is fragment two of bone A0001 3D laser scanned after the first period of exposure.

The exception to this pattern of sample numbering were the samples from Schöningen as these already had a unique numbering system that was adequate to individualise each 3D digitised sample in the form of a small finds

number. To ensure that these were sorted together in the electronic files a prefix of “SCH” was used to identify them.

In some of the experimental and field based samples, circumstances occasionally dictated a need for flexibility within the sample numbering and labelling (e.g. high UV destroys sample labels). Where such was encountered it is covered in a short sample numbering sub-heading in the relevant experimental or field based sections below.

5.2. Experimental taphonomy samples

The central research questions of this study are concerned with postmortem changes to human bone, however, in a UK context the availability of human derived material for study is limited, thus recent human material could not provide sufficient samples to study the level of variation of taphonomic conditions required for this research. Archaeologically derived human skeletal material was available for non-destructive recording, but its use for laboratory-based degradation experiments which are destructive would be contrary to the professional ethics required for the curation of human skeletal collections, and do not accurately reflect the levels of preservation to be a viable model for the early stage chemical and biological changes occurring in the immediate postmortem interval. The selection of a non-human material that was as representative of human bone was therefore sought.

5.2.1. Use of animal analogues

The study of forensic taphonomy is an attempt to understand the effect of the introduction of animal, plant or synthetic materials on the ecology of an environment, and the effect of such changes in the environment on the introduced material (Carter & Tibbett 2008). Taphonomic pathways are dependent on a large number of variables and these result in a high degree of variance in the outcomes of taphonomic change. When modelling these pathways therefore, it is of critical importance to fully understand the nature of the materials being used and for these to be as representative of the real life scenario as possible.

When considering the selection of representative samples for the study of the taphonomic pathways for human remains, the most representative material is human remains themselves, an approach that has been pursued at several facilities in the United States utilizing donated human material (Bass & Jefferson 2007, Texas State University 2013, Sam Houston State University 2015, Southern Illinois University 2015, Western Carolina University 2015).

Within the context of the United Kingdom, the use of human remains is limited by a more tightly regulated legal framework, in particular the Human Tissue Act

(2004). The use of some human material is possible, particularly historic anatomical specimen material that is old enough to fall outside the Human Tissue Act, as well as archaeologically derived human remains; but the number of samples that are available for study are limited and their use must therefore be carefully considered to maximise the benefit gained. Limited human material can most valuably offer a mechanism to validate animal analogue studies and ensure good transferability of the results when applied to human cases.

For most taphonomic studies carried out within the UK it is therefore necessary to consider alternatives to human remains. Whilst artificial analogues are not available and *in vitro* systems of bone cell cultures do not reflect the *in vivo* changes well (Aerssens et al. 1998), animal analogues for bone taphonomy therefore offer the closest and most representative alternative.

No study to date has comprehensively examined the suitability and selection of animal analogues for non-medical uses, such as fracture modelling (Liebschner 2004, Decker et al. 2014) or forensic taphonomy, and studies in these areas have so far based their animal analogue selection on either common practice using sheep or pig, or have relied on the medical literature, taking into consideration histomorphology or bone mineral composition. In general, the selection of animal analogues is covered extensively by Davidson et al. (1987) who place the “appropriateness as an analogue” and “transferability of information” as their most significant criteria.

Within the current study these can be summarised as animal analogues that provide physical, histological and chemical properties with a close similarity to human bone.

The variety of animal analogues that have been utilised across the range of disciplines relying on them for research is broad, and even within the specific field of forensic research numerous animal analogues have been used from rodents (Janaway 1987, Amendt et al. 2004, Adlam & Simmons 2007, Widya et al. 2012), non-human primates (Sanford et al. 2012), domesticated dog (Cattaneo et al. 2009, Dominguez & Crowder 2012), wild animals such as kangaroos (Forbes et al. 2005) and domesticated livestock such as pigs (e.g. Centeno et al. 2002, Forbes et al. 2005, Calce & Rogers 2007, Smith 2014,

White & Booth 2014) and sheep (Thompson 2002, Forbes et al. 2005, Martiniaková et al. 2006).

The following sections examine a range of animal analogues and their suitability for the research study with regard to how representative they are of human skeletal remains, starting with those used commonly within medical science (non-human primates, rodents and dogs) and then considering other animals used in medical and forensic research.

The rationale for the selection of the animal analogue used throughout this research is then outlined.

5.2.1.1. Non-human primates

Non-human primates offer considerable advantages over other animal analogues due to the strong similarity of their organ systems, gastrointestinal tracts, endocrine responses, musculoskeletal anatomy and bone metabolism to humans (Newman et al. 1995). Non-human primate bone has closely comparable histology, bone mineral composition, crystal size and non-collagenous protein content to human bone.

For these reasons the use of non-human primates has proven particularly effective in skeletal related medical research. Their use in the study of osteoporosis is favoured as the hormonal skeletal interactions in ovariectomized non-human primates most closely mimics that observed in postmenopausal humans (Mann et al. 1990a). Research into the integration of surgical implants into skeletal tissues (e.g. dental implants) show a preference for non-human primates due to their similar dentition, diet and the formation of their maxillae and mandibles (Giannobile et al. 1994).

Non-human primate bone is essentially very close to human bone, with all primates (including humans) sharing a similar development of the musculoskeletal system. However, it is this very similarity that can be problematic, as the raising of primates to full adulthood in order to provide viable animals for experimental studies is slow due to the rate of bone development and the primates lifespan. For example, in the commonly used

cynomolgus monkey (*Macaca fascicularis*) peak bone mass in adults is not achieved until 9 years of age (Jerome et al. 1994, 1997). To overcome this, animals are often sourced from the wild and as such pose a significant threat as reservoirs of zoonotic diseases such as tuberculosis, Marburg virus disease or viral hepatitis (Newman et al. 1995). Consequently, the costs of using non-human primates are markedly higher than those for other animal analogues and are prohibitively costly for forensic taphonomy where live animals are not required. The use of non-human primates in forensic taphonomic research is therefore, likely to only be viable if such research is conducted in collaboration with medical studies which are already utilising non-human primates and as part of their research protocol euthanize the animals, at which point they may be available for forensic research. However, the utilisation of non-human primates is currently very limited in the UK and in 2013 only 0.078% (3,236) of all scientific procedures covered under the Animals (Scientific procedures) Act 1986 involved non-human primates, and of these only a limited number included the euthanization of the animal (Home Office Statistics 2014).

5.2.1.2. Rodents

Mice (predominantly *Mus musculus*) are the most commonly used animal analogue in medical research (Langley 2009) with 75% of all scientific procedures performed using living animals subject to the provisions of the Animals (Scientific Procedures) Act 1986, during the year 2013 (Home Office Statistics 2014). The mouse skeleton has some similarities to humans, which in conjunction with the ease with which the mouse genome can be manipulated has meant that mice are increasingly being used to investigate the effects of both bone mineralisation and growth (Di Masso et al. 1998, Voide et al. 2008) and aging and osteoporosis on bone (Jilka 2013) including methods that utilise Computed Tomography and mechanical testing of bone (Wergedal et al. 2005). However, the histology of murine bone lacks the remodelling of the secondary osteons characteristic of the cortical bone of larger mammals including humans and the weight bearing / loading factors are significantly different to humans (Jilka 2013) making mice less viable within skeletal taphonomy as human analogues.

Rats (*Rattus rattus)* are the third most commonly used animal analogue in medicine with 6% of all scientific procedures performed in 2013 (Home Office Statistics 2014) utilising rats. In analysis of the bone mineral content, it was noted that, compared to dog, pig, sheep, cow and chicken, rat bone mineral exhibited the greatest difference, whilst the bone mineral composition of canids (dogs) was closest to that of human bone (Aerssens et al. 1998). However, histologically and structurally rat bone shows strong similarities to human cortical bone, forming the basis for the use of ovariectomized rats as animal analogues for bone loss in osteoporosis studies (Thompson et al. 1995, Duque & Watanabe 2011).

Biochemically the non-collagenous proteins that drive the initiation of bone mineralisation and the regulation of mineral crystallization and crystal size (Roach 1994, Gorski 1998) have been shown to have a high level of homogeneity between rat, non-human primates, bovine species and human proteins (Sampath & Reddi 1983); although it should be noted that whilst the proteins themselves may not differ significantly, there do appear to be differences in their interaction and the biochemical response to them between different species (Sampath & Reddi 1983).

5.2.1.3. Rabbits

Rabbits are commonly used as animal analogues for human bone in periodontal research (Mapara et al. 2012) and have also seen use in taphonomic research in forensic archaeology (Adlam & Simmons 2007, Simmons et al. 2010a, 2010b, Lukasewycz & Aturaliya 1999) and forensic entomology (Amendt et al. 2004). Like rodents, they are popular due to their rapid reproduction rate, small size and the ease by which they can be raised. Whilst their value for experimental soft tissue degradation studies derives from their small size and therefore the easy production of multiple replicates, it is the disparity in the size and limb loading of rabbits that make them less representative of human skeletal remains for skeletal taphonomy research.

5.2.1.4. Domesticated dogs

Within forensic research domesticated dogs (*Canis lupus familiaris*) were one of the earliest animal analogues used, primarily through entomological investigation using naturally occurring dog carcasses in Tennessee (Reed 1958). Within medical science they are commonly used in musculoskeletal and dental research (Giannobile et al. 1994, Pearce et al. 2007) and there is a more developed literature on the comparisons of human and canine bone in relation to orthopaedics (Neyt et al. 1998, Martini et al. 2001).

In terms of their gross skeletal anatomy, the huge range in the size and shape of dog breeds means that canine bones have a considerable degree of variation and therefore animal analogue subjects must be chosen from comparable sized or individual breeds. Additionally, Mann et al. showed that in gross decomposition studies the size and weight difference between dogs and humans resulted in a marked difference in the rate of decomposition (Mann et al. 1990b).

Histologically canine and human bone both exhibit secondary osteon structures, however in canine bone this is limited to the centre of the cortical bone and is surrounded by plexiform (laminar) bone (Jee et al. 1970, Wang et al. 1998b) which imparts greater mechanical strength to canine bone. The presence of the laminar bone may also contribute to the slightly higher bone mineral density within canine bone than that of humans (Wang et al. 1998b, 1998a, Aerssens et al. 1998). In addition to comparisons of the cortical structure of canine and human bone, work by researchers such as Kuhn et al. showed that whilst the trabecular bone of both appears very similar in terms of weight, volume and complexity, the ability of canine trabeculae to withstand strain and loading is notably higher than that in humans (Kuhn et al. 1989, Goldstein et al. 1990, Ciarelli et al. 1991, Goulet et al. 1994).

5.2.1.5. Sheep

Whilst the use of canine animal analogues in orthopaedic research has seen a gradual decline since the 1970s (Pearce et al. 2007), the use of sheep (*Ovis aries*) has seen an equal rise in usage which Pearce suggests is probably due

to the “negative public perceptions of using companion animals for medical research” (Pearce et al. 2007), despite the clear indication in the literature that canid bone is a more suitable animal analogue for human bone. The size of the most commonly used dog breeds in medical research (predominantly the beagle) is significantly smaller than adult sheep, which have average weights broadly comparable to that of humans, with males ranging from 68 kg to 200 kg and females ranging from 40 kg to 135 kg (North Carolina State University 2003). The similar sizes mean that whilst the long bones of adult sheep are still notably shorter than those of the lower limb bones of humans, they are accepted as a suitable animal analogue for human bone in medical research (Newman et al. 1995).

At the histological level, ovid bone exhibits a highly comparable structure to that of human bone, albeit with some minor differences. In younger ovid bone, plexiform bone is present in conjunction with primary osteonal bone and markedly smaller osteons than humans, with average osteon diameters in young ovid bone <100 µm compared with diameters of >100 µm in humans. Indeed, osteon size and shape is a primary method for determining the species origin of fragments of bone from forensic contexts (Singh et al. 1974, Cattaneo et al. 1999, 2009, Cuijpers 2006, Dominguez & Crowder 2012). However, with age, ovid bone becomes more relevant as an animal model for human bone as the secondary osteonal remodelling (Haversian structure) begins to develop, remodelling the plexiform bone and producing a similar Haversian structure to that seen in human bone. Whilst the Haversian structure is present in human bone at an earlier age (Martin & Burr 1982), its development in sheep becomes noticeable once the animal has reached adulthood (Newman et al. 1995, Liebschner 2004) and is noted earlier in the lower portion of the limbs of the animals as a biomechanical response to load bearing in these skeletal elements.

Despite these small histological differences, ovid bone offers a material with skeletal elements of comparable size to human bone, of comparable bone mineral composition, similar histology and a material that is easily available as a by-product of the human food chain, limiting the level of legal and ethical process compliance required.

5.2.1.6. Pigs

Within medical studies domesticated pigs (*Sus scrofa*) have found considerable use due to the similarities between pig and human physiology. Pigs are omnivores of a similar size, body mass to surface area ratio to humans and it is generally accepted that their skin (Liu et al. 2010), adipose composition, cardio-pulmonary system (Smith et al. 1990, Kassab & Fung 1994, Nakakuki 1994), gastrointestinal tract (Swindle et al. 2012), and soft tissues closely resemble those of the human body (Swindle & Smith 1998).

The use of pig animal models is well established in forensic archaeology with the earliest use of them being the work of Payne who used them as a subject for the investigation of forensic entomology (Payne 1965, Payne et al. 1968b, 1968a, Payne & King 1969). Pig cadavers are the only animal model into which there has been specific research published with regard to their direct comparability to human cadavers (Haskell et al. 2002, Schoenly et al. 2007).

Pig cadavers are regularly used in taphonomic experiments both to study the gross and histological changes to the body postmortem (Abraham et al. 2008) but also as an analogue for the effect of decomposition on the environment in which the cadaver is deposited.

However, despite the regularity with which they are being used, their suitability should be carefully assessed when planning taphonomic research. Indeed, their use in some cases can be highly inappropriate and the selection of the most comparable analogue to the specific variables being examined should always be considered. For example, a recent series of research papers examining the effects of blunt force trauma and the impact of taphonomic change utilised pig's heads throughout the research (Calce & Rogers 2007, Powell et al. 2012, 2013, Jordana et al. 2013), despite very limited similarities between the gross anatomy of pig crania and that of humans. In addition to the marked differences in the morphology of pig crania, young adult male pigs have a cranial volume of c.178.7 +/-14 cm^3 (Witold 2005) compared to a study of comparable aged male students that had an average cranial volume of 1411.64 +/-118.9 cm^3 (Acer et al. 2007).

In terms of bone density, Aerssens et al. (1998) recorded bone densities and mineral content in humans and pigs as the closest match in comparison to other animal analogue species. However, Aerssens' study looked at only a small number and a later study by Ioannidou found that pigs exhibited a wide range of bone density values varying by age, but that this variance was not recorded in the lower half of the fore and hind limbs (Ioannidou 2003) suggesting that this bone mineralisation is more advanced in areas of the skeleton with the highest loadings.

Histologically a key difference between pig and human bone is the presence of highly vascularised plexiform bone in pigs which in humans is only seen in some foetal bone (Enlow 1963). In sub-adult pigs, plexiform bone is found throughout all long bones with an absence of secondary Haversian structure (Hillier & Bell 2007). The femora of adult pigs are made up of a majority of plexiform bone, with plexiform bone present throughout the rest of the skeleton as well as secondary Haversian structure similar to that of humans, the percentage of which increases with age (Hillier & Bell 2007).

5.2.2. Selection of animal analogues for experimental samples

The analogues for this research must be broadly comparable to that of human skeletal elements, and must also have sufficient cortical thickness that when fractured at the mid-shaft the resulting exposed fracture surfaces are wide enough to be digitised with the macro techniques being studied (Laser Scanning, Structured Light and Photogrammetry).

5.2.2.1. Legal and ethical considerations

The use of non-human primates, dogs, cats and horses in scientific research is subject to greater levels of protection under the Animals (Scientific Procedures) Act 1986 and EU Directive 2010/63/EU, reflecting the social perception of the use of these animals within scientific experimentation, due to either their role as pets and working companions or their perceived emotional and cognitive similarity to humans. Additionally the sourcing of skeletal elements from these animal analogues must occur post mortem and the justification of euthanization

of such animals for research is subject to an onerous and rigorous ethical approval process.

Their special protected status under the 1986 Act means that their use must therefore be justified in relation to the unsuitability of all other animal analogues; this requirement is particularly significant given the ease of sourcing skeletal material from domesticated livestock raised as part of the human food chain.

For forensic taphonomic research, where there are few direct medical benefits to humans, and other non-protected animal analogues may be sufficient to fulfil the requirements of the research, the use of non-human primates, dogs, cats and horses is difficult to justify.

The ethical approval process is considerably simplified where skeletal material can be sourced as a waste by-product of the human food chain, without requiring the euthanization of the animals specifically for research.

Additionally the regulatory framework of food safety and animal welfare monitoring in the human food chain provide reliable standards that simplify the laboratory biological health and safety requirements for such material, in comparison to the risks from wild sourced non-human primates (e.g. zoonotic disease containment).

5.2.2.2. Animal analogue chosen for use in the study

Whilst it is clear that the material properties of bone are species-dependent and obviously contribute to differences in the physical characteristics of bone, the histological and mineral composition of bone in some species has a greater resemblance to human bone composition than others (Einhorn 1992, Aerssens et al. 1998, Järvinen et al. 2005). The closest resemblance between human and non-human bone is with other primates, followed by some skeletal elements in canids (dogs).

However, the selection of non-human primates or dogs is not appropriate for this study due to the legal and regulatory requirements (section 5.2.2.1); the resultant cost and time required to obtain sufficient samples cannot be justified for a degradation study. Additionally the research need for sufficient cortical

thickness to provide digitisation of fracture surfaces, requires the use of the lower limb bones that, in dogs, have a greater component of plexiform bone making dogs less suitable.

Rodents, whilst offering cheap and easy to obtain animal bone samples, are otherwise unsuitable to a bone taphonomy study due to the poor histological, chemical and size comparability to human skeletal elements. Additionally the cortical thickness of the long bones of rodents would offer a limited fracture surface area as a target for digitisation.

Domesticated and commercially raised food animals offer considerable advantages in regards to the ease of acquisition and limited ethical and regulatory requirements. The low cost of the material permits the acquisition of a greater number of bones than required, allowing selection of a set of bones that have the least variability between samples.

Of the commercially raised (mammalian) food animals, sheep and pigs are most easily obtained. Whilst pig carcases have been used in many forensic taphonomy experiments as animal analogues for the decomposition of soft tissues, their bone histology is poorly matched to human skeletal remains. Commercially raised pigs are slaughtered whilst still young and their limb bones have a high proportion of plexiform bone which has not been remodelled by secondary osteon structures making them a poor animal analogue for human skeletal tissues.

Sheep bone is more representative of human skeletal material with similar histological structures and comparable bone mineral composition. Young sheep (lamb) bone is lacking in secondary osteon structures, however unlike pigs, the commercial demand for mutton and hogget provide a human food chain source for more mature sheep bone that displays higher levels of mineralisation and secondary remodelling, making it more comparable to human skeletal tissues.

Ovid bone therefore offers a material with skeletal elements closer in size to human bone, of comparable bone mineral composition and with similar histology. Mutton bone is easily available as a by-product of the human food chain, limiting the level of legal and ethical process compliance required.

The lower limb bones of adult sheep (mutton) show the highest level of mineralisation, with greater levels of secondary remodelling, replacing the plexiform bone with a secondary osteon structure comparable to human cortical bone. Whilst the mineralisation is highest in the tibia, the popularity of the hind-shank as a cut of meat (the proximal 2/3rds of the tibia and the surrounding musculature) means that the tibiae of sheep are harder to source whole. The femora of adult sheep (mutton) are more readily available whole and are broadly comparable in general morphology to that of humans. The cortical thickness of mutton femora offers sufficient fracture surface area to assess the quality differences of 3D digitisation methodologies.

The selected experimental sample material for the research was mutton femora acquired via a local butcher from a single farm source.

5.2.3. Bone sample preparation

The sheep (mutton) bone for the accelerated taphonomy experiments and the field based weathering experiment was sourced from a local human food chain retail outlet. Prior to its use in the taphonomy experiments the bone was defleshed, cleaned, assigned a sample number and subjected to pre-exposure recording. The following sections detail the processes followed.

5.2.4. Initial bone cleaning

The sheep bone selected for the taphonomy experiments was from freshly butchered carcasses and still had small amounts of soft tissue adhering at both the gross and micro scale.

The gross soft tissue structures were dissected from the bone by hand using a scalpel, with care being taken to avoid the incising of fine cut marks to the bone that might offer easier access to taphonomic agents (chemical or biological) and thus alter the degradation profile of the surface.

Further defleshing and removal of all small adherent soft tissues was achieved through the use of Dermestid beetles (*Dermestes maculatus*); a standard method for the removal of soft tissue from skeletal structures (Hefti et al. 1980).

Figure 5.1: The Dermestid beetle Dermestes maculatus. Larvae (left) and adult (right). Scale in mm (source: author).

Whilst the use of Dermestidae is well established, both the adults and the larvae are capable of accessing very small spaces within the bone and are difficult to remove. The presence of the beetles either in the digitisation laboratory or released onto the moorland field site was considered undesirable and posed a mild health and safety risk. Therefore, following their removal from the Dermestid colony tanks, the bones were cleaned by hand using a small soft brush to remove as many individuals or larval cases as possible. The cleaned bones were then frozen for approximately 24 hours at approximately -15°C to kill any remaining beetles within the bone. Whilst it has been shown that cycles of freeze-thaw have a negative effect on the structure of bone, a single short duration cycle at moderate temperatures, is expected not to have a significant impact on the results (Andrade et al. 2008, Ozcelikkale & Han, 2016). In order to minimise any variability introduced through this process, the duration and temperature at which the bones were stored in the freezer was logged in order to demonstrate that all bones were subject to a similar temperature regime prior to their use.

Following freezing, the cleaned bones were left for 4 hours in a fume hood at room temperature to defrost. The bones were then washed by hand with warm water and a sponge to remove any Dermestid beetle frass or other material

from the beetle colonies. No detergents were used so as to limit any chemical interactions with the bone surface.

The cleaned bones were then left for 24 hours in a fume hood at room temperature to air dry slowly.

5.2.5. Pre-exposure recording

All bone samples were digitised prior to their inclusion in either the accelerated testing experiments or the field based weathering experiment to provide a baseline dataset for later comparison.

The initial data recording using multiple techniques also facilitated the comparison of these techniques for studying green / fresh bone, with particular reference to the use of the techniques in forensic anthropological investigations and research into the remains of the recently deceased.

The pre-exposure digitisation of the bone samples was carried out in the same manner as the later phases of digitisation (sections 6.1 to 6.3)

5.3. Taphonomic degradation methodologies

In order to examine the effect of taphonomic changes to bone on the quality and refitting of digitised skeletal material the research produced experimentally degraded bone samples through four experimental approaches:

- Natural weathering at a field site location;
- Accelerated bone mineral loss utilising an acidic laboratory-based artificial weathering;
- Accelerated bone organic fraction loss utilising an alkaline laboratory-based artificial weathering; and
- Accelerated UV weathering utilising a laboratory-based high dose UV and visible light chamber.

5.3.1. Fragmentation

Fracturing of bone can occur at any point along the taphonomic pathway of a bone, therefore the research needed to produce fracture surfaces at each stage of each experimental taphonomy experiment. Therefore, following post-exposure processing and digitisation at each phase of an experiment, 2 bones were selected to be broken.

To fracture the bone samples, the samples were placed on a flat steel surface with the anterior aspect facing upwards and supported at the distal end by the posterior projection of the condyles and at the proximal end by the lesser trochanter and the intertrochanteric line. In this arrangement the diaphysis of adult sheep femora form a curved arch anteriorly. A layer of tissue paper overlying a layer of bubble wrap was placed below this arch. A 20cm tall surround made from cardboard was placed around the bone to prevent small fragments of bone being projected away and lost.

To fracture the bone, the centre of the arch of the diaphysis was struck with a medium blow using a 24 oz. ball peen hammer. In most cases the bone fragmented into 2 pieces with a fracture propagating around both sides of the

mid-shaft of the bone from the point of impact until the two fracture lines met and parted the bone into two fragments.

In a few cases fragmentation resulting in more than two fragments and where these fragments were large enough to be digitised and provide meaningful results, they were numbered, labelled and bagged. Where the fragments were too small they were cleaned and then retained in a bag labelled with the sample number, but not allocated a fragment number.

Whilst in most cases the samples were successful fractured, in one case (A0024) the distal portion or the diaphysis shattered into over 100 small fragments which could not be reconstructed. However, the proximal end was present in two refitting fragments. In this case the distal portion was not allocated a fragment number and only the two fragments representing the proximal end were used for the research (A0024_F01 & A0024_F02).

Following fragmentation, each fragment was cleaned, numbered and labelled (section 5.1.1).

5.3.1.1. Post- fragmentation cleaning.

Following fragmentation most samples still contained degraded yellow and red marrow within the medullary cavities. The presence of this material would have prevented full digitisation of the fracture surfaces and it was therefore removed.

The marrow was removed with a medium rounded end steel spatula in the laboratory before the end of the bone was washed with a soft toothbrush in a mild dishwashing detergent diluted with warm water, before being rinsed three times with clean warm water.

Following the washing process, the samples were placed on absorbent tissue paper and allowed to slowly air dry for 12 hours. The sample number and fragment number of each fragment was noted in pencil on the absorbent paper adjacent to the sample and the samples were photographed.

Once the samples were dry they were transferred to labelled plastic Ziploc sample bags, which had been perforated with small holes to prevent moisture build up and “sweating” of the samples within the bags.

The samples were then placed in a large plastic storage box to prevent damage whilst they awaited digitisation.

5.3.2. Field weathering experiment

Six bone samples were exposed on the surface on high moorland at an experimental taphonomy site to examine the taphonomic changes to bone from natural weathering and high UV light level exposure. The samples were exposed multiple times and were digitised between each exposure to document the taphonomic changes and the impact the taphonomic changes had on the digitisation process. The following sections outline the methodology used to produce the field weathering digitisation samples.

5.3.2.1. Field site location

The field weathering experiment utilised the University of Bradford’s Oxenhope Moor Field Station, situated to the north-west of the city of Bradford, West Yorkshire. The site is located at N53° 47’ 27”, W001° 59’ 3” and at approximately 430m above Ordnance Survey Datum (figure 5.2). The altitude of the site and its remote location mean the samples are exposed on high moorland and are therefore subject to high light and UV levels offering the opportunity of increased weathering rates. Additionally, the site is subject to more pronounced fluctuations in temperature, rainfall and higher wind speeds than those within more urban environments. The site therefore provides more extreme wetting-drying and freeze-thaw cycles and as noted in Chapter 3, these are known to be significant factors in the natural weathering of bone (section 3.3).

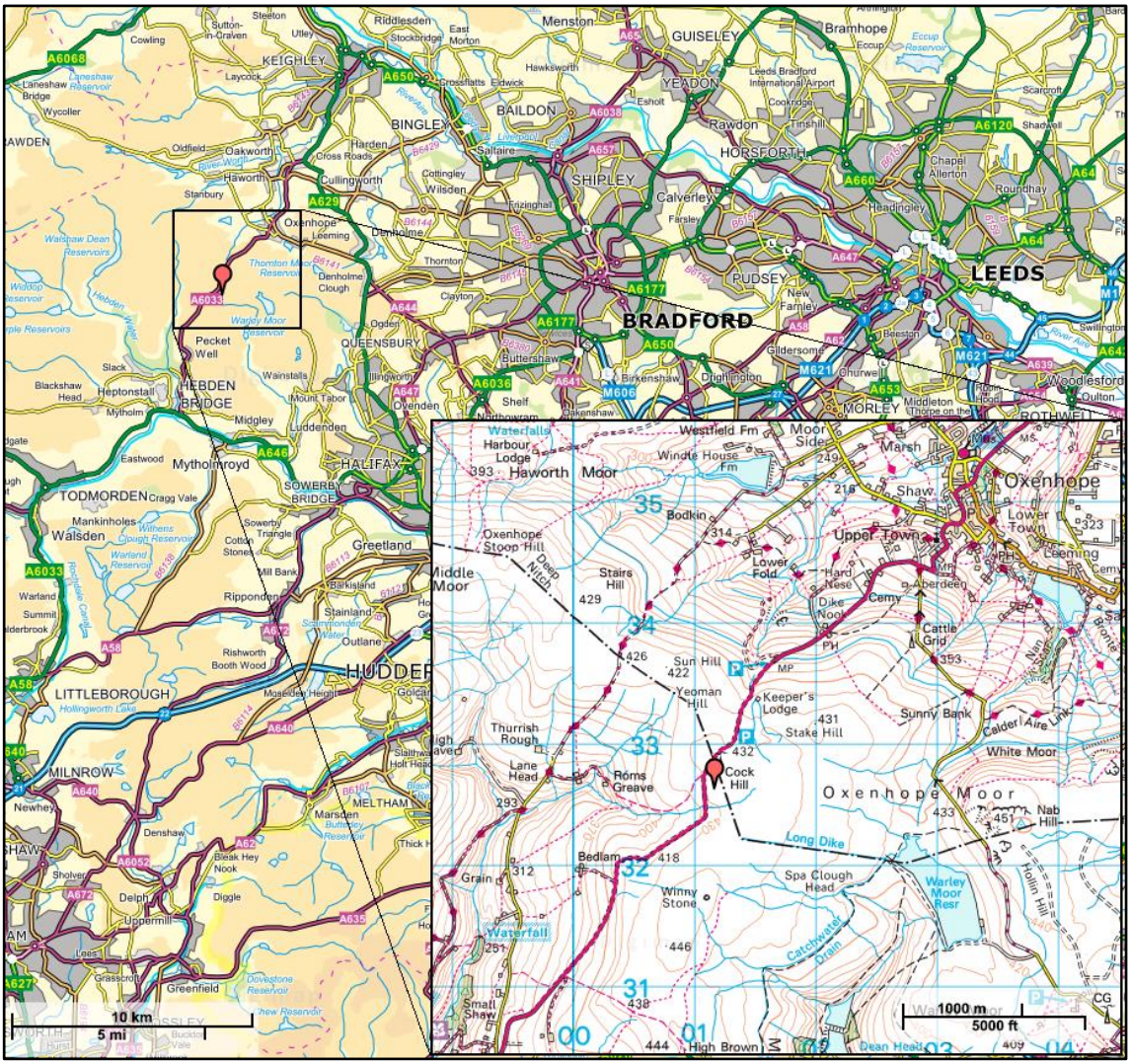

Figure 5.2: Map showing location of Oxenhope Moor Field Research Station, Cock Hill, Oxenhope (Ordnance Survey 2016a, 2016b).

The site has been utilised in a range of previous taphonomic research projects and the climate of the site is well understood (Holland 2000, Wilson et al. 2007, Janaway 2008).

5.3.2.2. Sample positioning and vegetation

The site is covered in dense clumps of purple moor grass (*Molinia caerulea*) and a variety of cotton grass species (*Eriophorum spp.)* (McCarroll et al. 2016) and the height of the vegetation varies throughout the year. The moorland site is a former RAF Navigational Aid research site and has several extant concrete surfaces previously used as the bases for radar equipment, now removed.

Plant action can produce etching of the surface, warping and even fracturing of bones (Morse et al. 1983, Nawrocki 2009) and the presence of tall vegetation cover from late spring through to autumn would introduce additional variables to the field weathering of bone samples that are outside the scope of this research.

Therefore, to both promote the development of taphonomic changes to the bone samples and to limit the effects of shading by vegetation, the experimental exposure of the samples was carried out above one of the extant concrete pads.

The light coloured concrete increased the level of reflected light exposure to the underside of the bone samples and also reduced the protection and shade that would otherwise have been provided by the micro-environment within vegetation cover. This also resulted in an increase to the rate of weathering by exposing the samples to a more rapid wetting and drying effect from wind and rain. The concrete bases were also identified as an additional variable in that they provide a thermal mass, storing radiant heat from the sun during warm days and releasing this stored heat back to the environment overnight. Whilst the effect was mild at the concrete surface it had the potential to smooth the expected diurnal temperature fluctuations. To avoid this, the samples were removed from direct contact with the concrete bases by elevating them using a wooden cargo pallet, weighted down to prevent disruption of the experiment by the frequent high wind speeds experienced at the site (figure 5.3).

5.3.2.3. Protection of the samples from scavenging

Whilst the adherent soft tissue structures were removed from the bone samples through the use of Dermestid beetles, the bone samples still represent a viable food resource for some wild scavengers (Haglund et al. 1988, 1989) likely to be present in the area of the field weathering site. The bone samples on the weathering site were therefore protected from both mammalian and avian scavengers on the site.

The site is surrounded by a fence to keep out larger mammals, as well as reduce the chance of human interference with the samples, however the fence

is not sufficient to prevent smaller scavengers and has no effect on avian scavengers, e.g. the Red Kites (*Milvus milvus*) that were regularly observed near the site.

In addition, the protection needed to be of limited impact upon the variables being measured and any minimal impact that was unavoidable needed to be uniformly distributed across the samples and the monitoring equipment.

To achieve this, the samples were surrounded by a cage made of 2.5 cm gap chicken wire suspended by supports attached to a wooden cargo pallet on which the samples were placed. The chicken wire was securely nailed to three sides of the pallet and the fourth side was attached with reusable cable ties to allow for occasional access to the samples.

The horizontal and vertical distances between the sides/top surfaces of the samples and the chicken wire was at least 30 cm, so as to prevent the beak, or limbs of avian and mammalian scavengers being able to reach the samples.

During the winter of 2015 - 2016 the site was exposed to unusually high wind speeds which blew the samples off the pallet-cage and blew the pallet-cage across the site despite the large stones placed on the base of the pallet to weigh it down. Site inspection visits shortly after the high winds recovered the pallet-cage and located the bones within the grass tussocks where they had become trapped. The samples had usually been transported distances of less than 1.5 m having fallen out of the pallet-cage after it overturned. This occurred on a number of occasions and the interval between the bone’s disturbance and their reinstatement was usually less than three days.

Figure 5.3: Weathering samples within the wire cage to protect from predation (source: author).

The samples were returned to the pallet-cage and additional stones were added to weigh it down further. The samples had become disassociated from their sample label numbers and when they were recovered for digitisation shortly afterwards the samples were given temporary labels (field_A to field_F). The sample labels were re-established by comparison of the samples to their pre-exposure digitised models which proved sufficient to individualise each sample.

5.3.2.4. Environmental monitoring

Temperature, availability of reagents such as water, ultraviolet radiation and the physical effects of freezing are all known to be factors in the weathering of materials (section 3.3), and therefore it was critical for the field weathering experiment to record these factors in relation to the exposed samples.

To maximise the number of measurements and reduce the measurement intervals, the environmental conditions that the samples were exposed to was measured through automated environment logging devices. Where feasible these devices were placed as close to the samples as possible without affecting the samples themselves by creating wind, rain or light shadows.

The environmental monitoring was carried out through two devices: A Helios Weather Station (Skye Instruments Ltd, Powys, UK) and a light intensity meter (figure 5.4).

The Helios Weather Station is a battery powered automated system that measured the minimum, maximum and average values for each measurement interval for the following variables:

- Ambient Air Temperature;
- Humidity; and
- Total rainfall for each measurement.

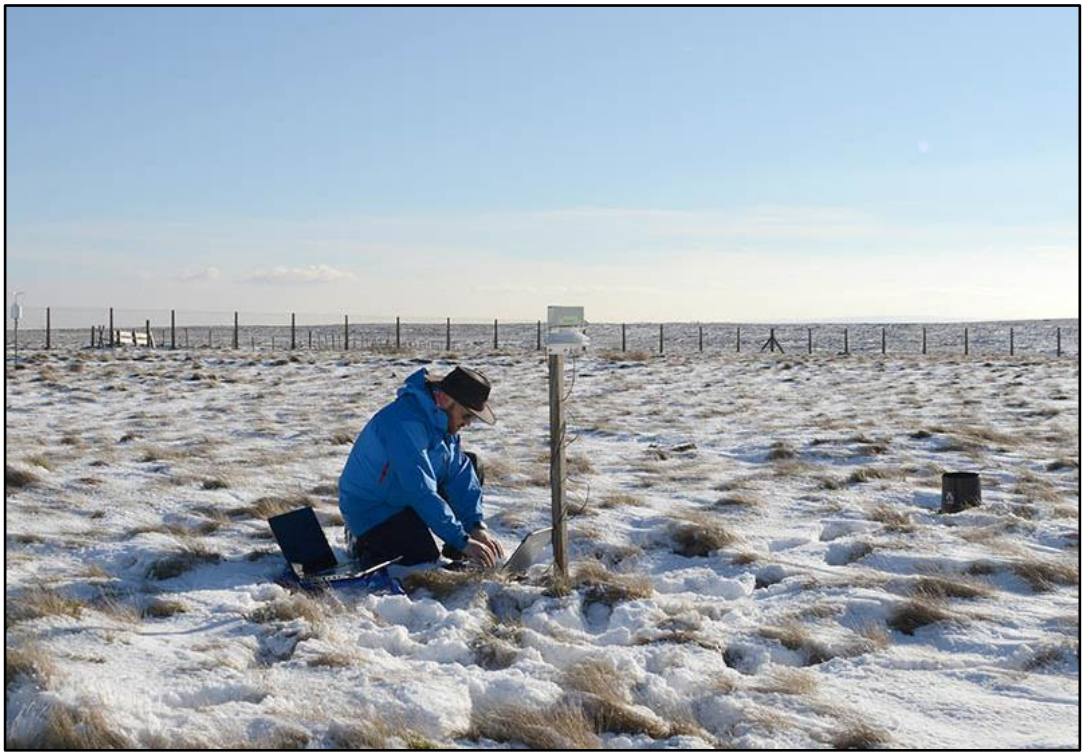

Figure 5.4: Downloading weather data from the Helios weather station in February 2015. Rainfall is measured by the black rain gauge bucket on the right of the image, all other readings are contained in the instrument's white housing atop the wooden pole (source: author).

The visible and ultraviolet light that the samples were exposed to was measured on the site through the use of an Intech Instruments Ltd. (Christchurch, NZ) general purpose HR series data logger coupled to a light intensity probe. This light intensity level instrument measured and recorded the point value, maximum, minimum and average (mean) light intensity (in lux) for each measurement interval at the site. As light intensity measurements are relative to the angle of incidence of light source to the light probe, the instrument was mounted so that the light sensitive panel was parallel to the ground and the orientation cannot be altered.

The measurement interval for both environmental monitoring systems was limited by the capacity of the small memory size on each of the two data logging systems. A measurement interval of 20 minutes was chosen as a compromise between data quality and the regularity of downloads required to free up memory for further readings. An interval of one measurement every 20 minutes provided 504 measurement intervals per week, but limiting the number of weeks which could be stored on the device's memory to approximately 5 weeks.

Whilst the environmental measurement and data loggers are environmentally sealed to IP68 rating (International Electrotechnical Commission 1999) and should therefore be capable of withstanding normal climatic conditions, the climate on the field site was sufficiently harsh that the IP68 rating was insufficient and the loggers failed on several occasions. Inspection visits to the field weathering site occurred approximately every 5 weeks to enable downloading of the data and clearing of the data logger’s memory and failures could only be detected at this point.

Where data was lost due to such failures, and whilst the instruments were dried out and resealed, environmental data for the site was approximated with reference to nearest publicly available meteorological data. The distance of publicly available meteorological data from the field site introduced inaccuracies in the data (e.g. persistence of snow to a depth of 40-50cm over the site and the samples in the winter of 2014/15 wasn’t present at the nearest weather station c. 3km away and 115m lower in elevation). Additional site visits were carried out to make manual environmental measurements at the site once a week during periods when the data loggers were being fixed.

The weather data (figure 5.5) resulted in 45,300 20 minute measurement intervals over the two exposure periods. The data was averaged over both 1 hour and 6 hour periods. Wetting and freeze-thaw events were determined on the basis of the averaged interval data. A wetting event was defined as one or more averaged time intervals during which precipitation was recorded and separated from other wetting events by at least one averaged time interval with no recorded precipitation. Freeze-thaw events were defined similarly where the averaged time intervals had an average air temperature of 0°C or less followed by at least one averaged time interval with an average air temperature greater than 0°C.

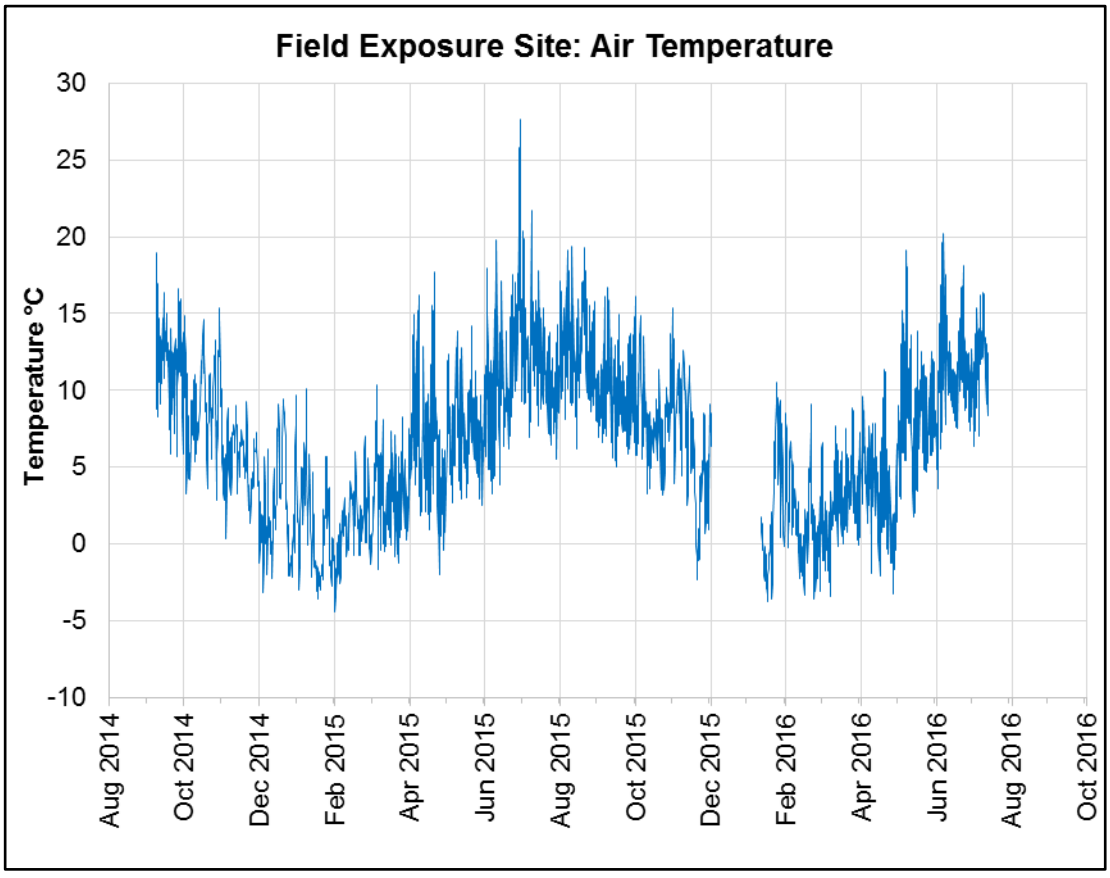

Figure 5.5: Plot of air temperature at the field weathering site during the exposure two exposure periods. Data averaged to 6 hour intervals (source: author).

The 1 hour averaged data recorded 123 freeze-thaw events and 785 wetting events over the 630 days total exposure for the field weathering samples. The 6 hour averaged data recorded 80 freeze-thaw events and 308 wetting events over the 630 days total exposure for the field weathering samples.

The variation in temperature and moisture content are important taphonomic factors in surface weathered bone (sections 3.3.33.3.4) however, the bone samples were anticipated to require a time interval to dry or thaw and therefore the 6 hour averaged time interval data was used when considering the impact of exposure of the bone samples to weather conditions.

The full 1 hour and 6 hour averaged weather data for the site are included in appendix A (on the SD data card attached to the back cover of this thesis).

5.3.2.5. Exposure intervals

The rate of taphonomic change to adult bone in field environments is initially slow, with the lipid content of the bone providing initial protection from rain wetting and the associated damage of wet - dry and freeze-thaw cycles. In order to provide a long enough time interval to produce observable taphonomic changes to the bone samples, the field weathering experiment at the Oxenhope Moor Field Station was therefore the earliest to be established within the project.

The exact onset of observable taphonomic changes to the bone samples at the site was anticipated as being difficult to predict due to the variability of the weather at the site. Instead of setting a specific timescale for the initial exposure period, which may not have produced measurable changes, the experimental design outlined an initial exposure period that would be determined by regular observation of the bone samples in situ with one or more additional exposure periods of between a half and a third the length of the initial exposure.

The bone samples were exposed over two exposure periods, the first for 448 days (64 weeks) from mid-2014 onwards, and then, following digitisation of the samples, a second exposure period of 182 days (26 weeks) finishing in July 2016. The length of the second exposure period was extended from the planned 21 weeks (one third of the initial exposure period) to 26 weeks (i.e. two fifths of the initial exposure period) to maximise the changes that might be observed and to better fit into the digitisation schedule of the other concurrent experiments. The resulting second exposure period was therefore exactly between one third and a half of the initial exposure period.

5.3.2.6. Sample numbering

As the environmental conditions at the weathering field site have been documented to significantly degrade organic materials as well as synthetic materials through a combination of biological activity and photo degradation, the sample labelling needed to be robust enough to both survive and remain readable. Inks used to write labels on the site have been noted during previous research (e.g. (Janaway et al. 2003, Wilson et al. 2007) to photo-degrade and fade beyond readability over a relatively short period of time. Therefore, additional labels for the samples assigned to the field based weathering experiment were made from c.0.5mm brass sheet and acid etched with the unique sample number through a photo acid etching process. Etched numbers were chosen over engraving as the later promotes corrosion through cold working around the engraved figures and around the cut edges rendering engraved brass labels less durable (Edeleanu & Forty 1960).

5.3.3. Chemical weathering

As shown in chapter 3, the taphonomic changes that alter bone once it is deposited within the burial environment are hugely variable with a wide array of influencing factors. The wide spectrum of taphonomic changes that bone can undergo when buried in real burial conditions therefore introduces too many variables to the quality and response of 3D digitisation systems when recording bone. In order to control this variance in samples and thereby limit the number of replications needed to a level within the scope of a Doctoral research program, the research utilised an accelerated laboratory taphonomy approach. The use of accelerated testing conditions within the laboratory to simulate particular variables associated with burial conditions is established in forensic archaeology (e.g. Stokes et al. 2009a, 2009b, 2013, Schotsmans et al. 2012, Ueland et al. 2014).

Three accelerated taphonomy methodologies were employed to create taphonomically altered bone samples for comparison and research into the response of 3D digitisation techniques to bone:

- Low pH (mineral loss) conditions;
- High pH (protein loss) conditions; and
- High ultraviolet dose.

5.3.4. Low pH (mineral loss) experiment

The mineral loss experiment aimed to induce dissolution and subsequent loss of biological apatite from the bone samples over an accelerated timescale within the laboratory to simulate the taphonomic changes that occur naturally in acidic depositional environments (section 3.4.4.1) such as those found in highly anoxic conditions in waterlogged peat. Similar conditions are noted from archaeological deposits and the results of this experiment should therefore be comparable to the burial conditions at Star Carr (Boreham et al. 2011, Milner et al. 2011), from which archaeological demineralised bones have been selected for comparison.

As covered in greater detail in chapter 3, the burial conditions at sites such as Star Carr have been shown to be highly acidic containing high humic acid levels as well as having increased concentrations of sulphur within the peat that produce a highly reducing environment. To produce experimental bone samples for digitisation, these conditions were mimicked within a controlled laboratory setting.

5.3.4.1. Demineralisation methodology

Bone collagen's long term survival due to the protection of the surrounding bioapatite (section 2.5) makes it a valuable target biomolecule in both radiocarbon dating of bone, as well as the analysis of stable isotopes from skeletal remains. However, the protection that bioapatites offer to collagen within bone also prevent its unprocessed use in these analyses and therefore the laboratory demineralisation of bone has become an established sample preparation process to facilitate collagen's use in such analyses.

The experimental methodology was adapted from these sample preparation protocols, most of which are based on the protein extraction methods of Longin (1971). Whilst there are more recent updates to the Longin method, these are generally variations of the process aimed at minimising contaminating factors such as humic acids, fatty acids etc. (Lidén et al. 1995, Nielsen-Marsh & Hedges 2000, Garvie-Lok et al. 2004, Brown et al. 2006, Brock et al. 2010) that would otherwise have a negative effect on the quality of the resultant C^{14} or stable isotope measurements (Jørkov et al. 2007).

Whilst these variations are key to good sample preparation and cleaning ahead of radiocarbon or isotopic analysis, they are all steps applied after the initial demineralisation of the bone and are therefore of little utility in the methodology design of the current research project.

Longin's original protocol, on which the later refinements are based, exposes the bone to a weak acid solution (usually HCl) to dissolve the bone mineral and then lyophilises the collagen that remains, with additional treatments such as the use of sodium hydroxide to remove any remaining humic acid contamination from the burial environment (Deniro & Epstein 1981, Jørkov et al. 2007).

The grinding and lyophilisation of the samples to increase the reaction surface area and thus the speed of the sample preparation (e.g. Collins & Galley 1998) were counterproductive to the purposes of the research and were therefore not followed. The timescales of the collagen extraction protocols such as that first used by Longin (1971) are optimised for the shortest sample preparation time whilst limiting damage to the extracted collagen. The protocols therefore provide an upper limit to the acidic concentration for the experiment of no greater than a 1M HCl solution commonly used within these and other related protocols (e.g. Deniro & Epstein 1981, Richards & Hedges 1999).

The experiments aimed to reduce the timescales for demineralisation observed in the burial environment but not to the extent of that within the collagen extraction protocols. A designed longer timescale was preferred to offer a spectrum of taphonomic demineralisation at multiple recording intervals and a lower concentration of HCl was therefore selected. The HCl was diluted from the 37% stock solution with distilled water to the desired molar strength solution.

Figure 5.6: Sample number A0020 in the reaction jar of HCl solution during the second exposure period of the mineral loss experiment (source: author).

During a short pilot study two concentrations of 0.5M and 0.2M HCl were used in order to assess their suitability to the methodology. In both cases, useful results were derived from the pilot study, however the bone demineralisation progressed at a higher rate than was desirable and a lower concentration of 0.1M HCl was therefore used for the main experiments offering a slower speed of reaction.

The reaction jars were placed on a thermostatically controlled heated sand tray in the archaeological chemistry laboratory to maintain their temperature at a constant 30°C; the temperature of the solutions and of the ambient air temperature adjacent to the jars was monitored for consistency through the use of a temperature data logger.

5.3.4.2. Prevention of microbial degradation

Whilst the loss of bone mineral is not unusual in acidic conditions, the accompanied preservation of the collagenous structure of the bone is unusual, as within the burial environment the unprotected collagen structure is normally compromised, promoting its chemical oxidation and subsequent microbial digestion (chapter three).

To limit the oxidation and loss of the collagen structure within the experimental methodology, the sample bones were placed into 4.5 litre glass reaction jars (large pickle jars) filled with the 0.1M hydrochloric acid solution. The reaction jars were then sealed airtight (with tight fitting screw top lids) to deny oxygen to the reactions. In addition, the pH of hydrochloric acid (below pH 5) prevented greater degradation of the remaining bone protein structure of the demineralised samples as below pH 5 microbial growth is inhibited.

5.3.4.3. Exposure intervals

Following initial cleaning and pre-exposure recording (section 5.2.4 and 5.2.5) the samples were placed in the reaction jars for an exposure period of 28 days. Following exposure, the samples were cleaned and then digitised before being returned to the reaction jars for the next exposure period. The acid (mineral loss) samples were subject to three exposure cycles, each of 28 days in duration.

5.3.4.4. Post - exposure processing

After each exposure period the samples were carefully removed from the sealed reaction jars and soaked in water for 12 hours to dilute and then wash out the acid solution from within the internal spaces of the bones. The water was refreshed at least 4 times throughout the cleaning process.

Following the washing process, the samples were placed on absorbent tissue paper and allowed to slowly air dry for a further 12 hours. The sample number of each bone was noted in pencil on the absorbent paper adjacent to the sample and the samples were photographed.

Once the samples were dry they were transferred to labelled plastic Ziploc sample bags, which had been perforated with small holes to prevent moisture build up and “sweating” of the samples within the bags.

The samples were then placed in a large plastic storage box to prevent damage whilst they awaited digitisation.

5.3.5. High pH (protein loss) experiment

The protein loss experiment aimed to induce breakdown and subsequent loss of the organic fraction from the bone samples over an accelerated timescale within the laboratory to simulate the taphonomic changes that occur naturally in alkaline depositional environments (section 3.4.4.2) such as those found in burial environments in areas of chalk or limestone geologies where the high alkaline conditions induce hydrolysis of the polypeptide chains in collagen and other proteins within bone.

As covered in greater detail in chapter three, such burial conditions also result in swelling of the collagen fibrils and may disrupt the bone mineral structure. To produce experimental bone samples for digitisation, these conditions were mimicked within a controlled laboratory setting.

5.3.5.1. Methodology

As with the mineral loss samples, the timescales required for the loss of the organic fraction from bone as observed in the burial environment was reduced through the use of laboratory accelerated testing. The experiment aimed to be comparable to that of the low pH mineral loss experiment (section 5.3.4) and to therefore produce a spectrum of taphonomic change that could be digitised at multiple recording intervals. To achieve this sample bones were placed in 4.5 litre glass reaction jars (large pickle jars) filled with a sodium hydroxide (NaOH) solution made up from sodium hydroxide beads dissolved in distilled water to achieve the desired molar strength solution

During a short pilot study two concentrations of 0.5M and 0.2M NaOH were used in order to assess their suitability to the methodology. In both cases,

useful results were derived from the pilot study, however the bone taphonomy progressed at a higher rate than was desirable and a lower concentration of 0.1M NaOH was therefore used for the main experiments offering a slower speed of reaction and a direct comparison to the mineral loss experimental samples.

The reaction jars were placed on a thermostatically controlled heated sand tray in the archaeological chemistry laboratory to maintain their temperature at a constant 30°C; the temperature of the solutions and of the ambient air temperature adjacent to the jars was monitored for consistency through the use of a temperature data logger.

The reaction jars were sealed airtight (with tight fitting screw top lids) to limit oxygen to the reactions. In addition, the high pH of sodium hydroxide also inhibited microbial alterations to the bone structure of the samples.

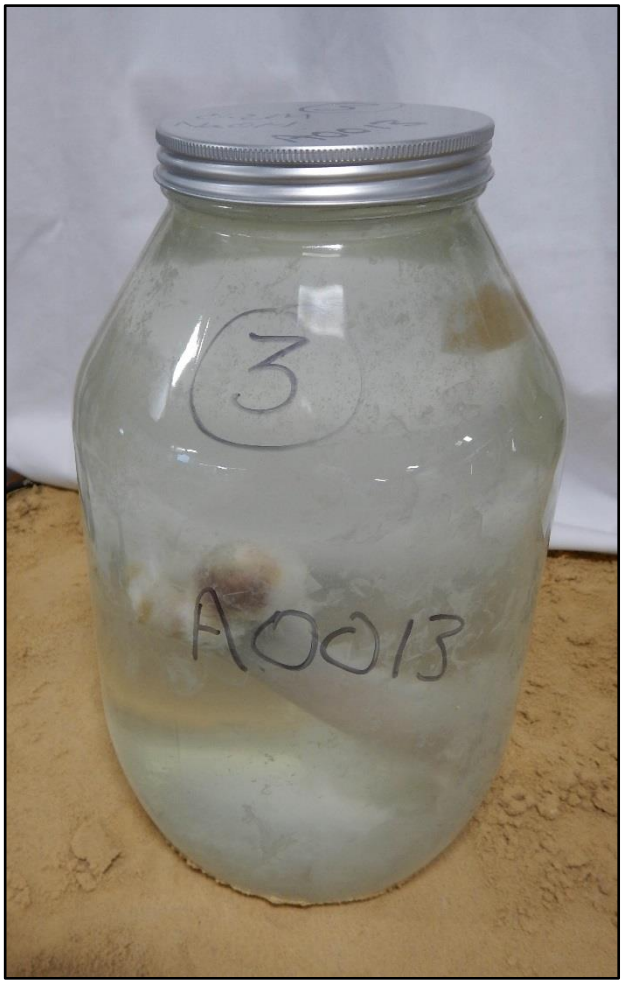

Figure 5.7: Sample number A0013 in the reaction jar of NaOH solution during the second exposure period of the protein loss experiment (source: author).

5.3.5.2. Exposure intervals

Following initial cleaning and pre-exposure recording (section 5.2.4 and 5.2.5) the samples were placed in the reaction jars for an exposure period of 28 days. After exposure the samples were cleaned and digitised before being returned to the reaction jars for the next exposure period. The alkaline (protein loss) samples were subject to three exposure cycles, each of 28 days in duration.

5.3.5.3. Post - exposure processing

After each exposure period the samples were carefully removed from the sealed reaction jars and soaked in water for 12 hours to dilute and then wash out the sodium hydroxide solution from within the internal spaces of the bones. The water was refreshed at least 4 times throughout the cleaning process.

Following the washing process, the samples were placed on absorbent tissue paper and allowed to slowly air dry for a further 12 hours. The sample number of each bone was noted in pencil on the absorbent paper adjacent to the sample and the samples were photographed.

Once the samples were dry they were transferred to labelled plastic Ziploc sample bags, which had been perforated with small holes to prevent moisture build up and “sweating” of the samples within the bags.

The samples were placed in a large plastic storage box to prevent damage whilst they awaited digitisation.

5.3.6. High UV dose experiment

During surface weathering photo degradation causes damage to the bone and produces changes to the surface optical properties that were anticipated to be significant in the digitisation of the bone. To examine this interaction, an accelerated testing experiment was designed to expose sheep bone to high doses of visible and ultraviolet light using a standard testing procedure used in materials science. This was completed in collaboration with Edwards Analytical,

a company specialising in the materials testing for the pharmaceutical, healthcare and food industries.

5.3.6.1. Methodology

Bone samples were placed in a Heraeus Suntest CPS (Atlas Material Testing Technology GmbH, Altenhaßlau) UV and visible light exposure unit at Edwards Analytical in Co. Durham. The bone was exposed continuously following the standard testing procedure outlined in the unit's operation manual (Atlas Material Testing Solutions 2003 p. 22).

Figure 5.8: Heraeus Suntest CPS benchtop xenon UV and visible light exposure unit (source: author).

The Heraeus Suntest CPS is a xenon lamp based testing unit that is the most widely used benchtop instrument for materials testing of UV and light degradation of materials (Atlas Material Testing Solutions 2015). The unit contains a 1500 W air-cooled xenon lamp that exposes the 560 cm^2 stainless steel exposure plate to a spectra of UV and visible light between 300 and 800 nm in wavelength (figure 5.9) at an irradiance that can be manually set between 250 and 765 W/m^2 (Atlas Material Testing Solutions 2003).

The peak irradiance of the Heraeus Suntest CPS unit was set via the adjustable exposure control to 500 W/m^2 using a calibrated light intensity meter using the standard formula:

$$P_{(W)} = E_{v(lx)} \times A_{(m^2)} / \eta_{(lm/W)}$$

Where P is the peak irradiance power (in watts), Ev is the luminous flux (in lumens) measured by the light intensity meter, A is the area of the light intensity meter's detector and η is the luminous efficacy of the light intensity meter (in lumens per watt).

The xenon lamp within the unit produces heat and the unit was placed within a fume extraction cupboard to provide a constant flow of air to cool the lamp and minimise sample heating. The test chamber temperature (TCT) within the Heraeus Suntest CPS unit was monitored through the use of a digital temperature data logger with a consistent temperature of 32°C +/- 3°C throughout both exposure periods (section 5.3.6.2).

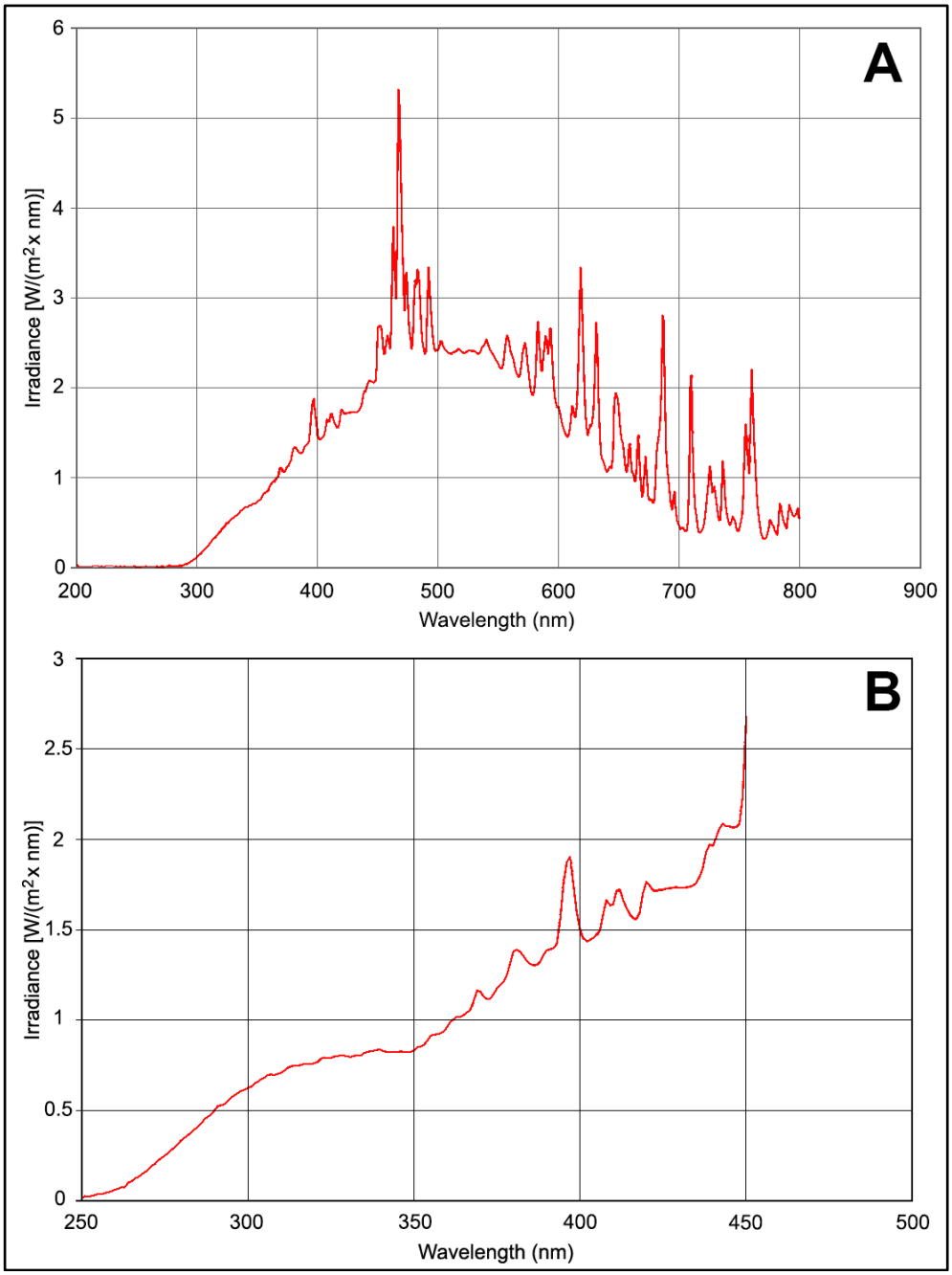

Figure 5.9: Spectral distribution of the Heraeus Suntest CPS. A: Spectral distribution across UV and visible wavelengths. B: Spectral distribution for UV wavelengths (after Atlas Material Testing Solutions 2003).

5.3.6.2. Exposure intervals

Following initial cleaning and pre-exposure recording (sections 5.2.4 and 5.2.5) the samples were placed on the stainless steel exposure tray of the Heraeus Suntest CPS (figure 5.10) and exposed to the high dose UV source for a constant period of 28 days.

Figure 5.10: Bone samples placed on the stainless steel exposure tray prior to exposure (top) and with the exposure tray inside the Heraeus Suntest CPS unit (bottom) (source: author).

5.3.6.3. Sample numbering

As the primary use in industrial testing for the Heraeus Suntest CPS is to test colour fastness of inks and dyes and the UV degradation of materials, it was anticipated that written labels could not be relied upon. Therefore, all the samples were photographed prior to exposure and the layout of the samples on the stainless steel exposure tray was recorded in a sketch drawing and photographs for later reference.

After each period of exposure, the layout of the samples was photographed and the samples were then removed one at a time, photographed and identified by reference to the initial drawing and photographs. The samples were cleaned and processed (section 5.3.6.4) and digitised. Following digitisation, the samples were returned to the Heraeus Suntest CPS for the next exposure period. The UV exposure samples were subject to two exposure cycles, each of 28 days in duration.

5.3.6.4. Post - exposure processing

After each exposure period the samples were carefully removed from the Heraeus Suntest CPS unit and identified and recorded as already outlined. In some instances, the warm airflow within the unit had liquefied some of the lipid component of the bone samples and this had flowed to the underside of the bone samples coating some or all of the downward facing surfaces. The bone samples were therefore wiped gently with an absorbent paper tissue to remove the surface film of grease and then the samples were transferred to labelled plastic Ziploc sample bags, which had been perforated with small holes to prevent moisture build up and “sweating” of the samples within the bags.

The samples were placed in a large plastic storage box to prevent damage during transportation back to the digitisation suite at the University of Bradford.

5.4. Archaeological and palaeontological samples

Samples from three field locations with contrasting taphonomic profiles were included in the project for comparison to the main experimentally degraded samples. The sites cover both archaeological and palaeontological timescales. Forensic case examples were not available for study due to the nature of such samples, however the short timescales in forensic cases results in lower levels of taphonomic change in bone, similar to the field weathering (section 5.3.2) and UV exposure samples (section 5.3.6). The sites and the samples in this research were selected so that they would complement the research of the wider *Fragmented Heritage* project (section 1.3), and in one case the research has already contributed to a collaborative publication (Little et al. 2016). The three sites selected were:

- Turkana Basin, Kenya;
- Schöningen 13, Lower Saxony, Germany; and
- Star Carr, UK.

Each of the three sites and the samples selected is summarised in the following sections.

5.4.1. Turkana Basin, Kenya

The area around Lake Turkana in Northern Kenya is widely known for the density of fossiliferous remains weathering out on the surface of the deep sedimentary strata representing a time depth from the Cretaceous onwards. The rich fossiliferous record is the result of a succession of fluvial and lacustrine systems associated with the Omo River and its lake phases forming sediments throughout the Plio-Pleistocene and spread over an area of 131,000km^2 (Feibel 2011).

The *Fragmented Heritage* project has been collaborating with the Turkana Basin Institute as a project partner on research into new approaches to the identification of fossiliferous material and artefacts (section 1.3), from the sedimentary stratigraphy of the Koobi Fora formation, near to the Turkana Basin

Institute's Ileret field research centre at the north-east end of Lake Turkana in Northern Kenya (figures 5.11 & 5.12).

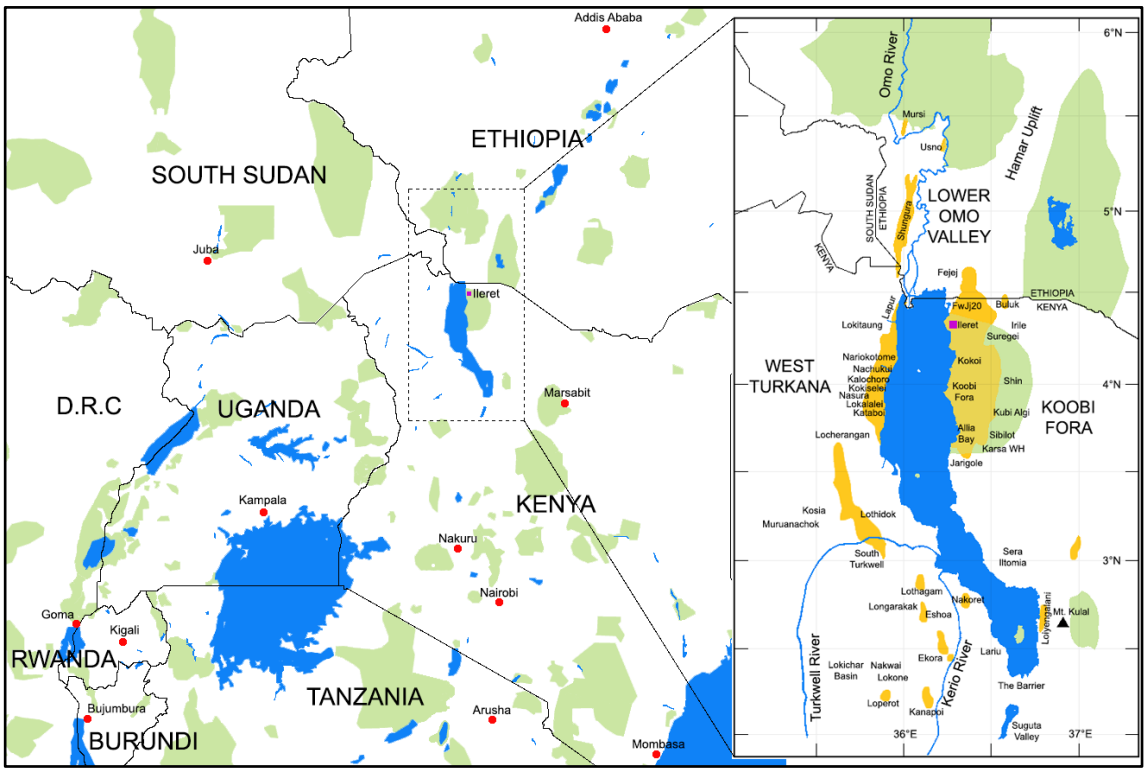

Figure 5.11: Map of East Africa showing location of Ileret field research centre on the north-east end of Lake Turkana (source: author). Inset map of the Lake Turkana system showing local geographic terms, fossil sites, archaeological sites and the fossiliferous beds (yellow) and the national parks (green) (modified from Feibel 2011).

As part of this research, ground truthing and digitisation fieldwork was carried out in February and March 2016 at the Ileret field research centre where samples for this project were also identified and digitised by the author.

5.4.1.1. Site description

The Ileret field research centre of the Turkana Basin Institute is located on the north-east side of Lake Turkana adjacent to the Ethiopian border near to where the present-day Omo river flows into the northern end of the lake (figure 5.11). The Turkana basin forms a hydrographic and sedimentary system of approximately 131,000km^2 in the Central African Rift System in northern Kenya and southern Ethiopia (Feibel 2011) which over the last 4.2 million years has alternated between a river floodplain of the palaeo-Omo river and a series of lacustrine systems within the basin. The lacustrine phase (between 2.0 and 1.5

million years ago) formed a basin wide lake (Lorenyang Lake), the sediments of which formed the Upper Burgi Member stratigraphic deposits of the Koobi Fora formations (Scholz & Glaubrecht 2013). The Upper Burgi Member deposits are directly overlain and capped by the KBS tuff (named after the FxJj1 site nicknamed “Kay Behrensmeyer Site” in area 105 where it was first identified) and are therefore readily identifiable in the field. All the samples included within this study were from the Upper Burgi Member deposits, and in general were eroded out onto the surface.

The period represented by the Upper Burgi Member deposits is of importance to palaeo-anthropology, in that they span the emergence of several early Homo taxa (Wood & Leakey 2011) and the first use of stone tools resulting in their extensive study (Fleagle & Leakey 2011).

5.4.1.2. Sample selection

The samples selected for digitisation at the Ileret field research centre were taken from both field ground truthing of associated research work by the Fragmented Heritage project, as well as material within the Kenyan National Museum collections held at the field research centre.

Within the wider Fragmented Heritage project, a research programme was established under the name *Fossil Finder* to examine the use of “Citizen Science” (the collection and processing of data by members of the public in collaboration with scientists) for investigating fossil hominid research. Georeferenced aerial imagery of long transects of the ground surface at Ileret was collected at very high spatial resolution; this imagery was then uploaded to a website where members of the public were asked to identify material on the surface and their mouse clicks were recorded. By tying the mouse click coordinates on each image to the georeferenced longitude and latitude co-ordinates, the exact location of each identified item could be established. A team returned to the Turkana basin to ground truth these locations and investigate the level of surface movement of material. Fossil bone material was identified in many photos and material which exhibited fracture surfaces was identified by the author as target samples for the research within this thesis.

The fossiliferous bearing deposits on the east side of Lake Turkana are divided into palaeontological collecting areas to make documentation of finds easier. The samples identified from the Fossil Finder data (section 1.3) were from areas 3 and 6. Additional material already held at the Ileret Field Research Centre was from areas 10 and 105 (figure 5.12).

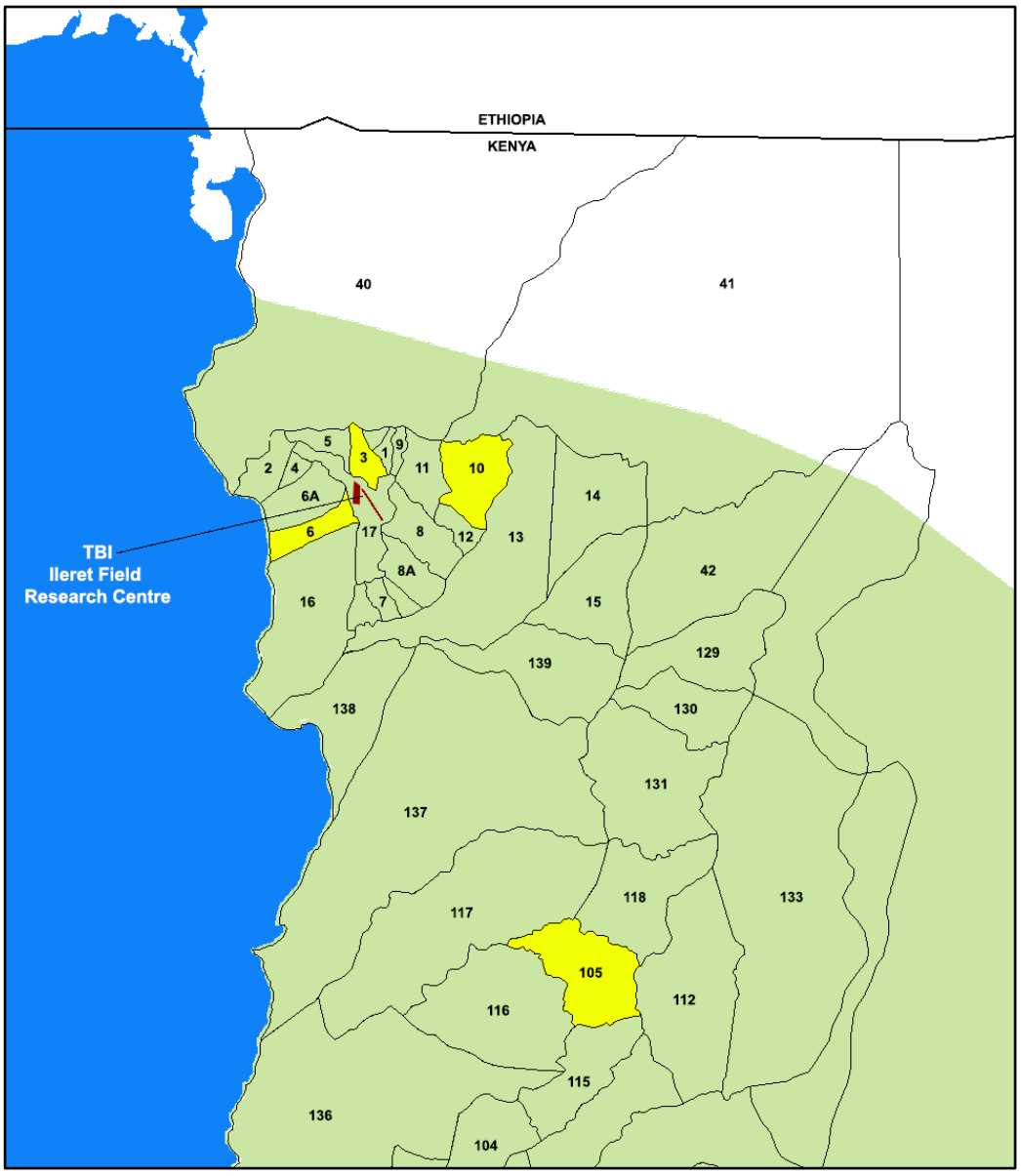

Figure 5.12: Map showing a selection of the numbered palaeontological collecting areas in the Koobi Fora and Ileret areas of the Turkana Basin, Kenya highlighting the areas where samples were sourced (yellow) and the boundary of the national park (green) (adapted from Leakey 2016a pers. comm., Joordens et al. 2013).

The fossilised bone eroded out of the surface at the site was, with the exception of very small animal and fish bone, fragmentary. As such most large fossil bone material included fracture surfaces, but in most cases the corresponding bone

fragment that would refit at the fracture surface was not present, or not identifiable.

Of those fossil bone samples identified from the Fossil Finder data, 35 fragments were shown to refit together forming 6 refit groups. A further 6 fossil bone fragments forming two refit groups were selected from the Kenya National Museum collections held at the field research centre. In addition, a Holocene bone harpoon point (not fossilised) was identified from the Fossil Finder data and was included in the samples selected for digitisation.

All the samples of refitting fossilised bone identified from the fossil finder data were identified as cortical fragments of the diaphysis of long bones from large mammals, either ungulates or hippopotamidae (Fortelius 2016 pers. comm., Leakey 2016b pers. comm.). The samples sourced from the Kenya National Museum collection had previously been identified as rib fragments from two individuals of *aff. Hippopotamus karumensis* (Coryndon 1977) an extinct ancestor species to modern hippopotami.

The colour of the samples varied from dark grey and black, often with a white outer coating of carbonate based material derived from the depositional sediments.

A list of the samples from Kenya is outlined in Appendix B.

5.4.1.3. Sample numbering

As the samples selected for inclusion within the data set of this research were from varied contexts they had a range of sample labels which did not have any clear consistency. The items identified from the fossil finder data were associated with the image ID numbers for the aerial image that they were present in, however, where multiple items were present in the same image, sample numbers were not unique. In addition, where fragmentary fossil bone was identified within an aerial image ground truthing occasionally located refitting fragmentary fossil material in close proximity, but not within the aerial imagery. In these cases, the additional digitised material was of significant value for this research but lacked any specific image ID number.

Additional pre-recovered material, already within the collection of the Turkana Basin Institute's Ileret field centre, was utilised and these samples had a Kenya National Museum accession number (e.g. KNM-ER 62866) which was very different to the image ID numbers.

To provide a clear record of all samples, the sample labelling system used for the experimental taphonomy samples (section 5.1.1) was adopted. The Kenyan samples were distinguished from the experimental taphonomy samples by substituting the initial letter 'A' in the sample number with 'K'. As with the experimental taphonomy samples, where fossil material was fragmentary, or where several samples were shown to have refitting surfaces, they were allocated the same sample number (e.g. K0003) with the addition of "_F##" where "_F" indicates a fragment and ## represents a two figure serial number unique to each fragment. Each fragment could therefore be uniquely identified and the relationship of one fragment to the others in its refit group was clear (figure 5.13).

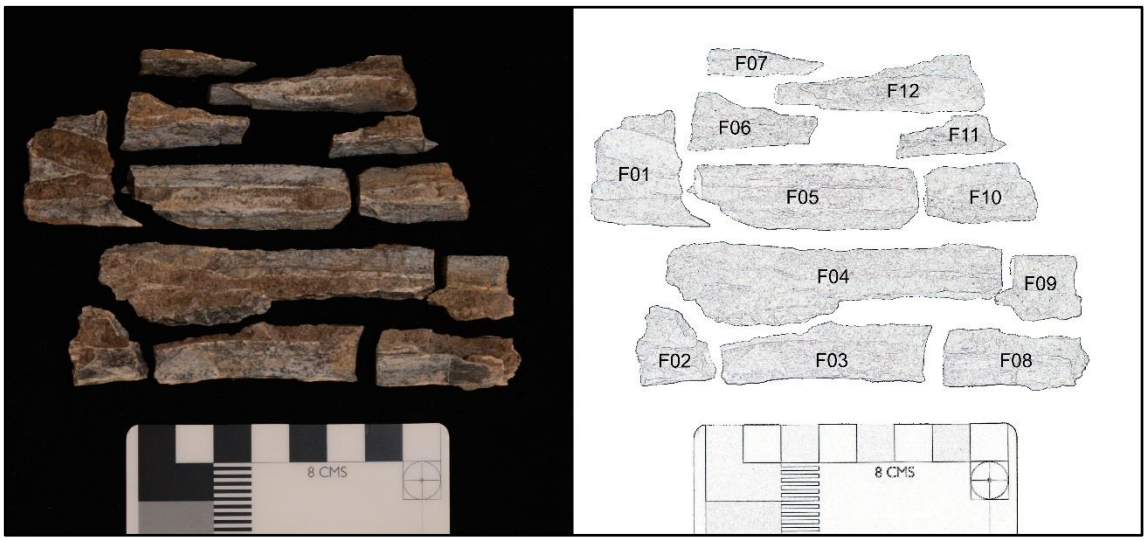

Figure 5.13: Photo of fragmented fossil bone sample K0003 and drawing identifying each fragment number (source: author).

5.4.1.4. Sample preparation

Due to the high temperatures and arid environment in the Turkana Basin, the samples were all dry and relatively free of soil / deposit. A small dry toothbrush was used to brush off the adhering deposits and to remove surface dust prior to digitisation and photography.

5.4.1.5. Sample digitisation

The Turkana Basin samples from Ileret were digitised using a MechInnovations Ltd (Leamington Spa, UK) MechScan macro scale structured light scanner (section 6.2.2) over the three week duration of the 2016 *Fragmented Heritage* field trip to the Turkana Basin Institute's Ileret field research centre (figure 5.14)

Figure 5.14: MechInnovations MechScan macro structured light scanner as set up in the Turkana Basin Institute's Ileret field centre laboratory (source: author).

Due to the limitations of equipment transport to Northern Kenya, as well as the requirement for a stable scanning system in the high temperatures of the remote bush location, only one scanner could be transported to Ileret to record the samples, however, basic photogrammetry was also attempted utilising the photographic equipment available (section 6.3).

Additionally, the Turkana Basin Institute provided access to their Artec Spider and Artec Eva scanners (Artec3D, Luxembourg) in conjunction with the Artec Studio 11 software suite that they currently use at the field centre to digitise material for publication on the African fossils website (www.africanfossils.org).

A range of field of view sizes was used on the MechScan, dependant on the size of the sample being digitised. Exposure times on the MechScan's machine vision cameras were altered to obtain the least noisy digitisations. The ambient light levels within the field centre laboratory used for digitisation varied considerably during the day. Where possible the ambient light levels within the laboratory were limited, and samples with high levels of reflectance (shiny) or very dark coloured samples were reserved for scanning at, or after, dusk where the light on the samples being digitised could be limited to that from the projector element of the scanner, resulting in better structured light pattern recognition within the machine vision element of the scanner and thus improved scan quality.

Samples were placed on the rotary table of the scanner for scanning. In some cases, the samples were placed on supports made from red plasticine sculpting clay which allowed the samples to be scanned without movement or to hold the samples in orientations that they would not otherwise maintain.

5.4.2. Schöningen 13, Germany

The Schöningen lignite extraction mine in Germany has yielded large assemblages of organic materials deposited in anaerobic lacustrine silt sediments during the Middle Pleistocene (781kya to 126kya). The preservation of the remains is exceptional and offers detailed information about organic material, hunting weapons, prey carcases and evidence of their butchery, making the site of Schöningen of prime importance to our understanding of the behavioural, social and economic patterns of hominins in the Lower Palaeolithic of the Middle Pleistocene in Europe.

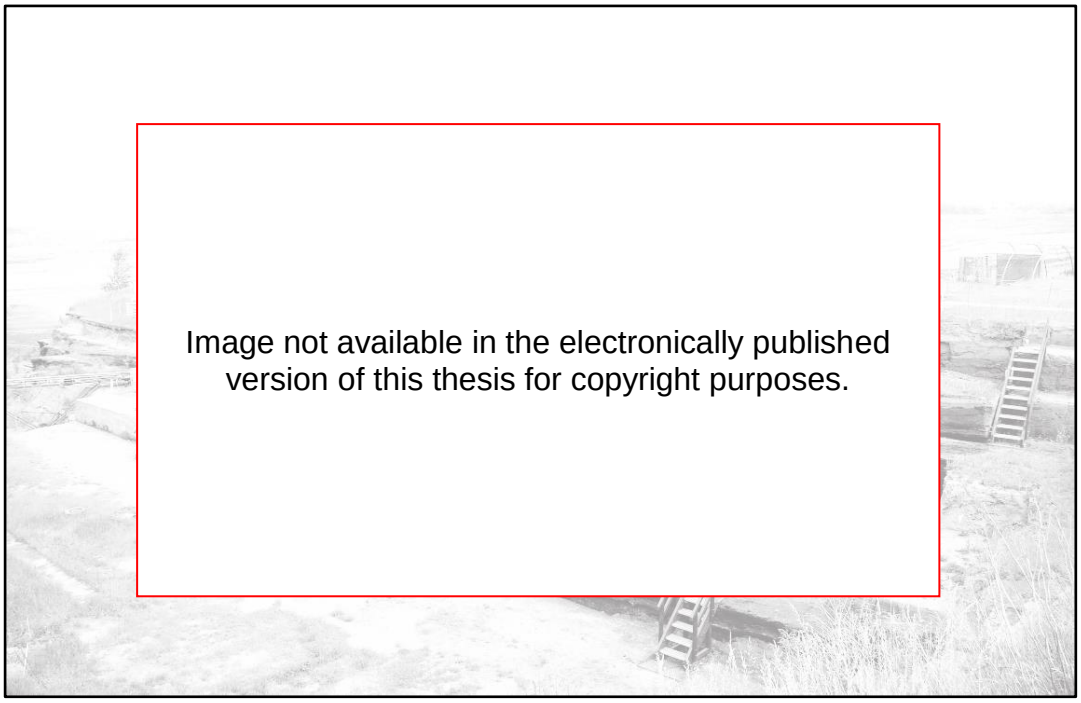

Figure 5.15: Schöningen 13 site preserved within the southern quarry of the Schöningen lignite extraction mine (after Balter 2014).

The primary prey species at the site were large equids which represented between 85% and 95% of the individuals (Starkovich & Conard 2015). This imprecise estimate reflects the fragmentary nature of the remains following their perimortem processing to extract the marrow (Voormolen 2008a, 2008b, Van Kolfschoten et al. 2015). The number of fragments of equine bone within the deposits offers a refit analysis problem comparable to that of lithic refit analysis on other butchery sites such as Boxgrove (Rees 2000, Ashton 2007); a manual refit process, comparing each surface to every other surface in the assemblage, would be prohibitively time consuming. Yet refitting the bone fragments is important to produce accurate numbers for the minimum number of skeletal elements (MNE), which is key to the calculation of measures of abundance such as minimum number of individuals (MNI). These in turn are used to assess the taphonomic histories of the faunal assemblage and the human behaviours associated with its formation (García-Moreno et al. 2015, Villaluenga et al. 2015).

The wider *Fragmented Heritage* project aims to demonstrate how the power of computer aided automation can be applied to the problem of refit analysis for lithics. The osseous remains from Schöningen 13 therefore offered an opportunity to extend computer based refit to skeletal material from a similar

context to that of the lithic material already being analysed by the *Fragmented Heritage* project. This thesis explores some of the factors that can inform the adaption of the *Fragmented Heritage* digital refit system to the refitting of fragmentary osseous material. As such, digitisation of the complete Schöningen 13 faunal assemblage was not considered to be appropriate until the refit methodology had reached a more mature form, but an initial study of a subsample of the faunal remains would form an ideal case study. A subsampling strategy (section 5.4.2.3) for the faunal remains was developed and the author carried out digitisation of the fragmentary skeletal material whilst it was being studied at the MONREPOS Archaeological Research Centre and Museum for Human Behavioural Evolution in Neuwied, Germany.

5.4.2.1. Site description

The archaeological deposits at Schöningen were located within a large open cast lignite extraction mine to the east of the village of Schöningen near Helmstedt in Lower Saxony, Germany (figure 5.16). The site is divided into two large quarries (northern and southern).

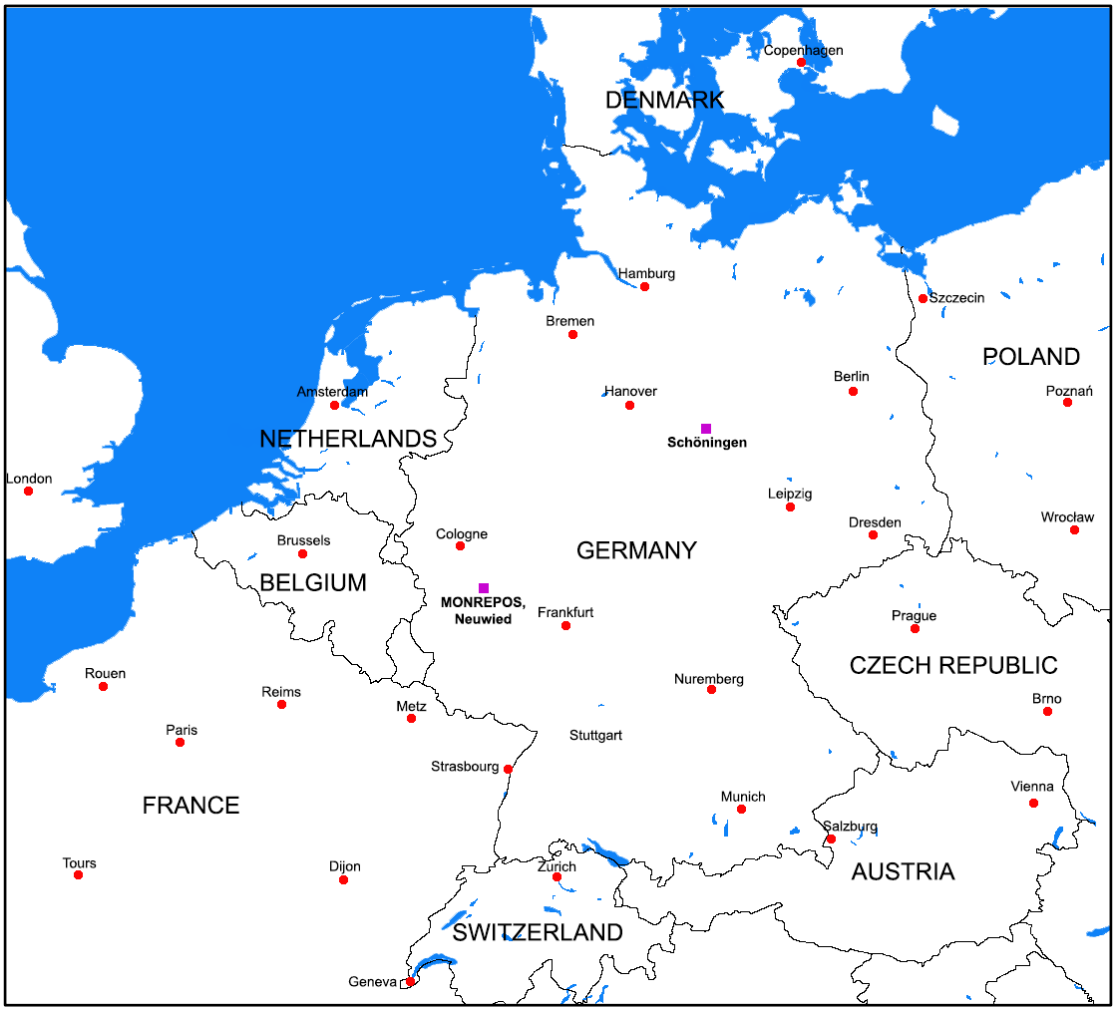

Figure 5.16: Map showing location of Schöningen, Germany (source: author).

From 1994 onwards removal of the quaternary deposits overlying the Palaeogene lignite in the southern quarry exposed a series of waterlogged Middle Pleistocene deposits in which significant archaeological material was identified (figure 5.17).

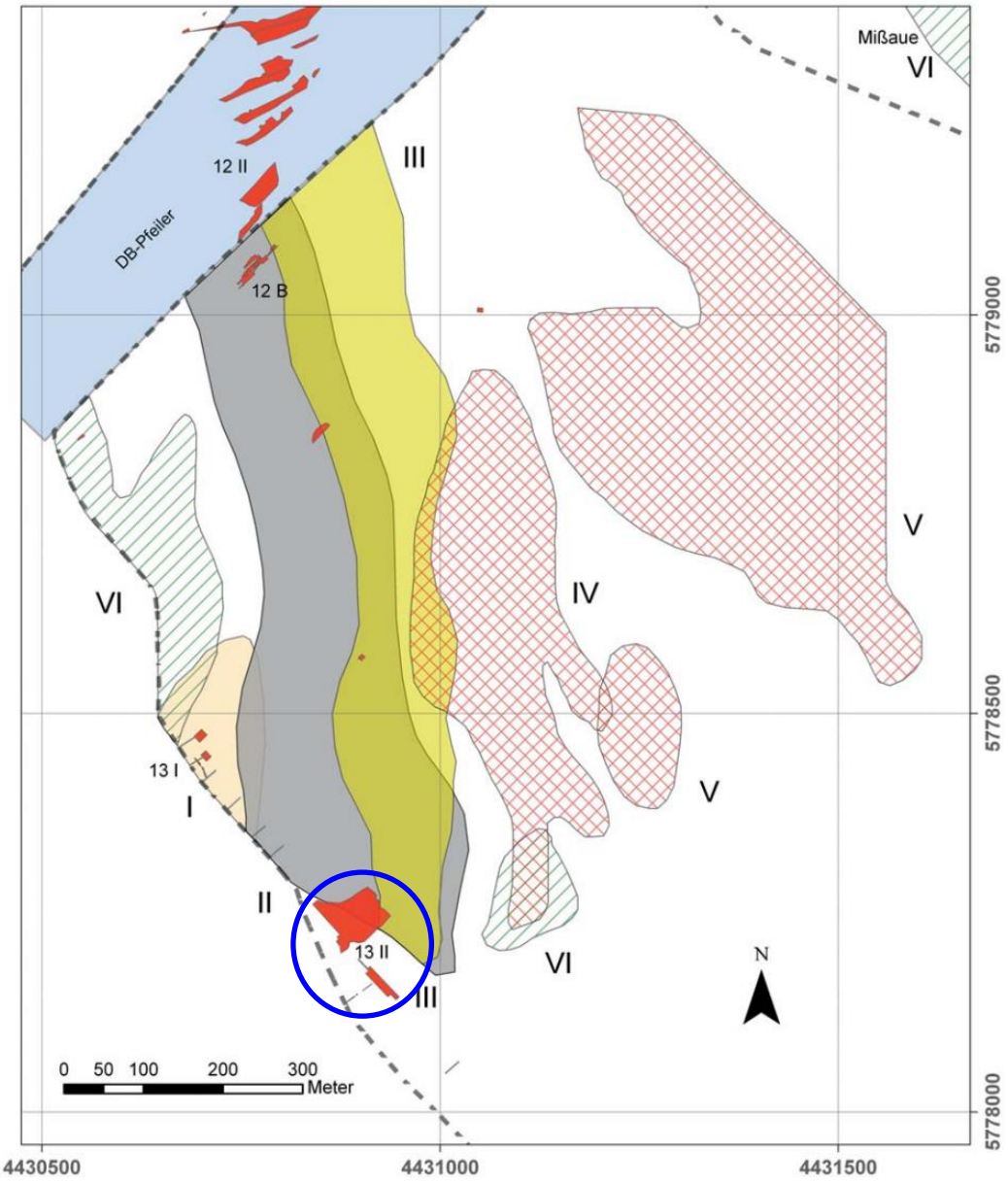

Figure 5.17: General site plan for the southern quarry of the Schöningen lignite extraction mine including Schöningen 13-II (circled) (after Serangeli et al. 2012).

Schöningen site 13 within the southern quarry was comprised of a sequence of six palaeochannels eroded into the glacial till deposits associated with the Elsterian glaciation (figure 5.18) which in turn overlie the Palaeogene lignite deposits that were being extracted. The six channels, numbered I to VI, intercut each other (with channel I being the stratigraphically earliest) and are filled with lacustrine silts, with later complete silting of the channels and peat formation. The six channels therefore represent a sequence of laterally stacked shallow channels of an interglacial lake forming a deltaic littoral wetland environment (Mania 1995, Thieme 1999, Lang et al. 2012).

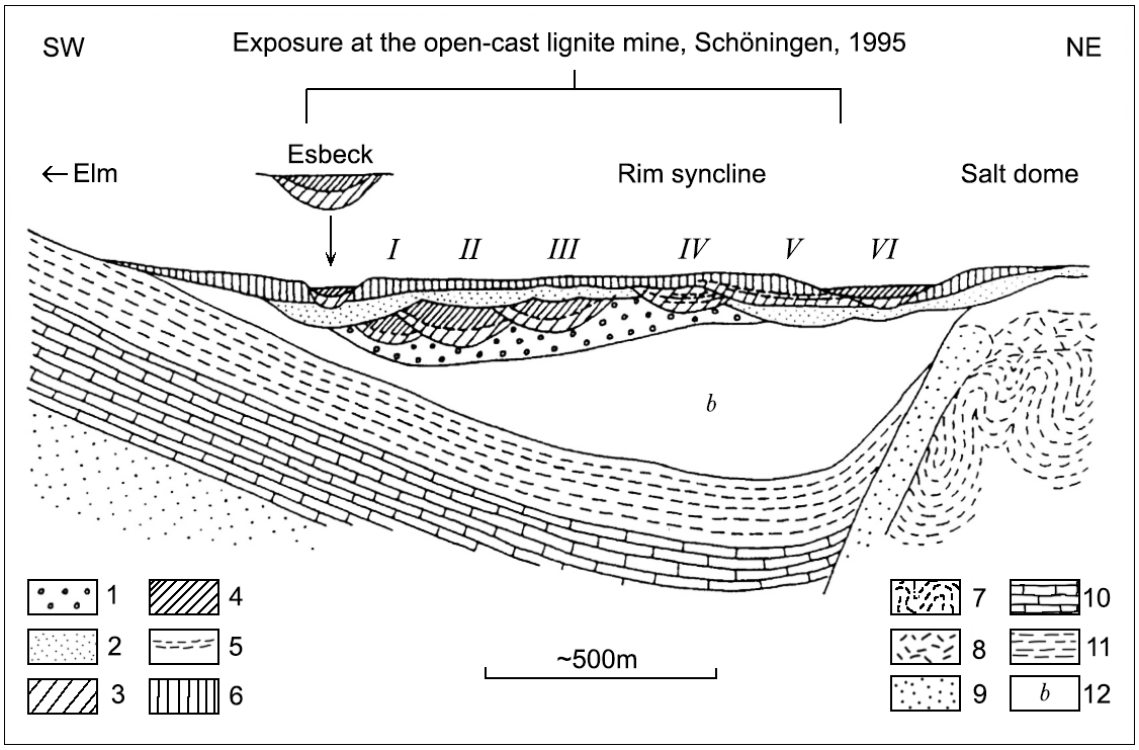

Figure 5.18: Reconstructed section drawing of the deposits of Schöningen 13 in the southern quarry of the Schöningen lignite extraction mine. Key: 1. Elsterian glacial tills; 2. Saalian glacial deposits; 3. Lacustrine deposits; 4. Limnic telmatic sequences; 5. Soil complexes; 6. Loess deposits; 7. Evaporites; 8. Gypsum cap-rock; 9. Buntsandstein; 10. Triassic limestone (Muschelkalk); 11. Triassic deposits (Keuper); 12 Palaeogene deposits (Mania 1995).

Layer 4 of channel II (Schöningen 13 II - 4) produced eight wooden throwing spears made of spruce and pine. These were dated through U/Th dating to 290+/- 5 KaBP (Marine Isotope Stage 9) (Sierralta et al. 2012, Urban & Sierralta 2012) and representing the earliest throwing spears recorded anywhere to date (Thieme 1997). In association with them is a very large assemblage of faunal remains (c. 15,000 elements). The faunal remains from the site are dominated by a large equine species (*Equus mosbachensis*) although large bovids and cervids are also present within the assemblage in smaller numbers (van Kolfschoten 2012, 2014, García-Moreno et al. 2015).

5.4.2.2. Taphonomy

Preservation of the organic materials from the Middle Pleistocene layers of the Schöningen 13 site is exceptional due to the wet anaerobic nature of the lacustrine silt sediments into which they were deposited. Additionally, the underlying limestone geology imparts a high carbonate concentration to the

pore water environment, producing stable, reducing conditions which have limited the dissolution of bone mineral (Serangeli et al. 2015) and inhibited access to the underlying collagen structure (Kuitems et al. 2015).

Consequently, the surfaces of the equine bone from Schöningen 13 II - 4 were very well preserved, allowing the marks of carcass processing to be assessed against evidence for pre- and post- depositional taphonomic change (Starkovich & Conard 2015). 98% of the equine remains are ascribed to weathering stage A (i.e. “not to slightly weathered”) (Voormolen 2008b) indicating that the bones were rapidly deposited within the silt. Furthermore 95% of the bones show no sign of post-depositional taphonomic damage to the bone surface with only 2.8% of the specimens showing slight rounding of the fracture surfaces.

Fluvial transport and erosion of the surface of the bone is not a significant factor in the assemblage with only 1.5% of bone fragments exhibiting sediment friction striation damage to the bone surfaces (Voormolen 2008a, Starkovich & Conard 2015).

The surfaces of the bones are stained mid to dark brown in colour from the surrounding organic rich silt and peat sediments.

In terms of the fracture patterns, green bone fractures occur in a large percentage of the assemblage; these are associated with impact notches and scarring, indicating that the bone was intentionally fractured close to the animal's death, a pattern that has been linked to marrow extraction (Voormolen 2008a). Whilst dry bone fractures were also identified within the assemblage, these fractures occur almost exclusively (82.6% of dry bone fractures) on fragile osseous structures particularly in the axial skeleton (vertebral processes, ribs etc.) and are associated with sediment compaction and deformation from the weight of overlying sediments (Voormolen 2008b).

5.4.2.3. Sample selection

As part of the post excavation analysis and documentation of the Schöningen 13 II - 4 faunal assemblage at the MONREPOS, a number of fracture refits had been manually identified. The research for this thesis aimed to examine if

refitting fracture surfaces could be identified from digitised fragmentary skeletal material. In order to test this the sub-sample needed to include material that was known to refit. The sub-sample of material considered for scanning therefore included all those fragments where manual refits had been already identified (21 fragments). Additionally, in order to demonstrate that digitised material did not generate false positive results for otherwise non-refitting fracture surfaces, a further two fragments that were known from manual refit testing not to match any of the surfaces within those in the sub-sample were also included.

Initially the criteria for the sub-sample included both green bone fractures and dry bone fractures in order to further examine the effect of taphonomic change on digitisation and the resultant digital refit. However, the dry bone fractures within the assemblage occurred on small and fragile osseous structures meaning that manual refit had not identified any refitting bone fracture pairs by the date of digitisation, therefore the sub-sample was limited to green bone fractures.

A list of the samples from Schöningen is outlined in appendix C.

5.4.2.4. Sample numbering

Each bone fragment was already ascribed a find number within the assemblage. To distinguish this number from other samples recorded within this thesis, the assemblage find number was prefixed with the letters SCH. In one instance a sample had post excavation damage in the form of the completion of a fracture line that, from the evidence of the taphonomic staining, had been initiated prior to deposition or within the depositional environment. In this instance a suffix of “a” and “b” was added to the sample numbers to distinguish the two resultant fragments.

5.4.2.5. Sample preparation

The samples had been cleaned and dried during the post-excavation processing of the site archive. The samples were dry but some had

accumulated a fine coating of dust in the interim, which was gently removed with a soft brush prior to digitisation.

5.4.2.6. Sample digitisation

The Schöningen 13 II - 4 samples were digitised with the MechScan macro scale structured light scanner (MechInnovations Ltd, Leamington Spa, UK) on an 8cm field of view (section 6.2.2) over a week at MONREPOS in Germany. Due to the limited access and time constraints of an international research visit, only one scanner could be transported to Germany to record the samples. The dark brown surface colour of the Schöningen samples introduced digitisation challenges due to the changing ambient light within the digitisation room throughout the day. To mitigate this, black-out curtains were used to limit the light on the samples during scans, resulting in better structured light pattern recognition within the machine vision element of the scanner and thus improving scan quality.

5.4.3. Star Carr, UK

Collaborative work was carried out with the Star Carr project based at the Universities of York and Manchester on the digitisation of culturally altered deer frontlets (frontal bones of deer with the antlers still attached), probably used for ritual purposes (Conneller 2004). This collaboration resulted in publication of the deer frontlets as the world's earliest example of shamanistic costume (Little et al. 2016). Whilst the wider cultural implications of the material are covered in the published paper, the digitisation of the material formed part of the preliminary work for this thesis and informed methodological development of the current project. The results of the digitisation are therefore included within chapter 6.

5.4.3.1. Site description

The site of Star Carr is a Mesolithic site situated on the edge of a system of postglacial palaeo lakes (Lake Flixton) which formed at the eastern end of what is now the Vale of Pickering in North Yorkshire, UK (figure 5.19) at around

11,000 BP (Mellars 1990); occupation at the site has been dated to about 9,600 BP (Mellars 1990, Day & Mellars 1994, Mellars & Dark 1998, Dark et al. 2006).

The site is considered to be one of the most important Mesolithic sites in the UK and is noted for the level of organic preservation, including artefacts made of red deer (*Cervus elaphus*) and elk (*Alces alces*) bone and antler.

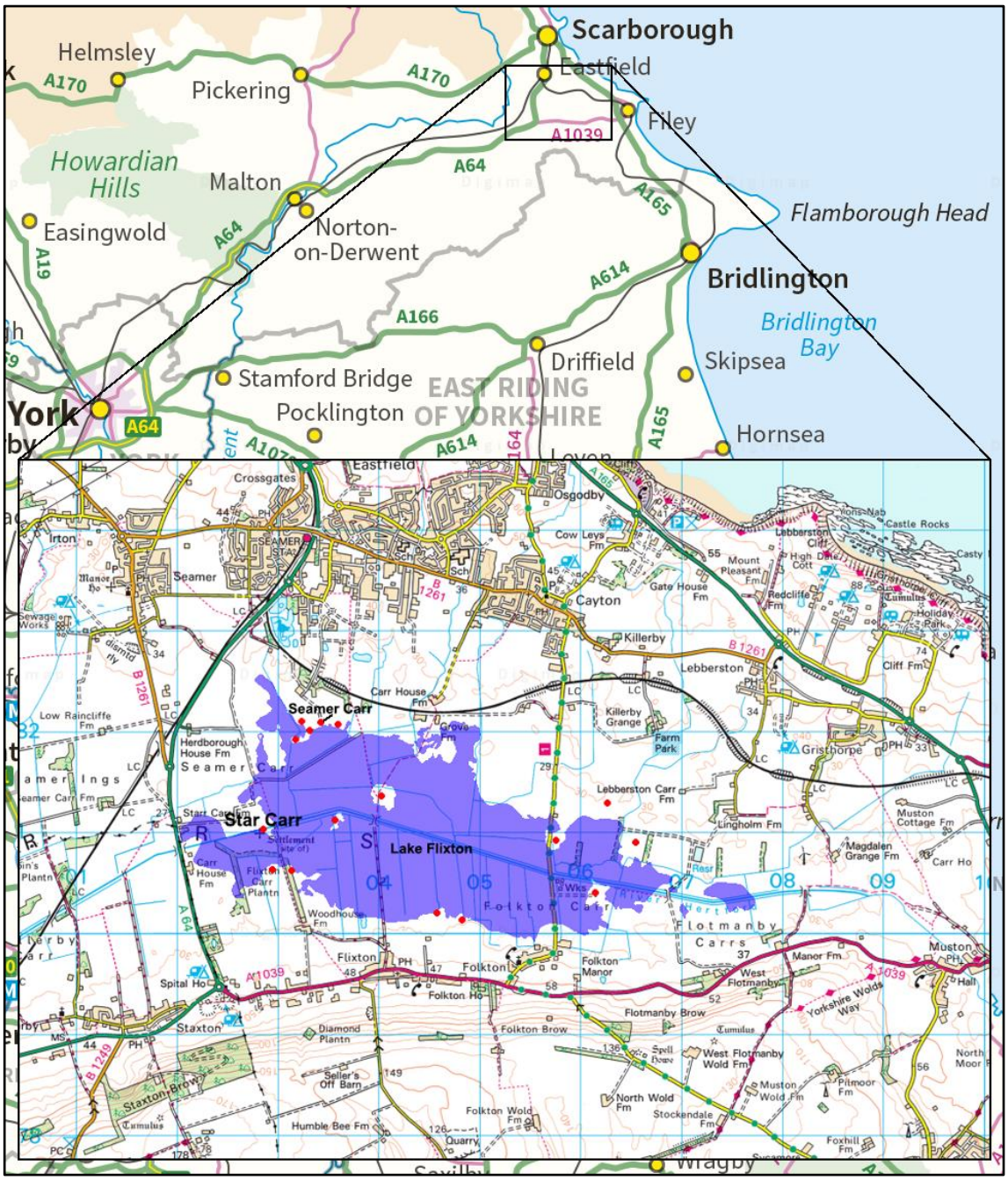

Figure 5.19: Map showing location of the Mesolithic site of Star Carr and the outline (purple) of the palaeolake Lake Flixton in the Vale of Pickering and the location of nearby Mesolithic sites (red dots) (adapted from Milner et al. 2013, Ordnance Survey 2016a, Robson et al. 2016).

5.4.3.2. Taphonomy

The preservation of the organic material from Star Carr is as a result of low anoxic acidic conditions within the depositional environment. Following the formation of Lake Flixton in the late-glacial/post-glacial period about 11,000 BP a series of Mesolithic detritus muds, reed peat, wood peat and lake marls (Boreham et al. 2011) continued to accumulate in the lake throughout the period the site was in use and continuing until at least 7,000 BP (Cloutman 1988a, 1988b, Cloutman & Smith 1988). These peat-like sediments have been shown to exhibit very acidic conditions between pH 3.0 and pH 4.0, elevated sulphur content and high moisture content (Boreham et al. 2011). This provides the highly anoxic and acidic conditions that produce extensively demineralised bone sometimes referred to as 'jelly bone' because of the modified physical properties and distortion brought about by the leaching of bone mineral whilst the collagen and other proteins survive (van der Sanden 1996).

5.4.3.3. Sample selection

A single red deer (*Cervus elaphus*) frontlet broken in the depositional environment into multiple fragments was identified from the material excavated from Star Carr for digitisation.

The sample was made up of bone and antler exhibiting intermediate to high levels of bone mineral dissolution and loss, leaving a semi degraded soft and flexible "jelly bone" but which retains its histological structure (Milner et al. 2011).

5.4.3.4. Sample Preparation

The samples had been gently washed following their excavation and were being wet stored in low temperature conditions in order to prevent further degradation. Their shape was supported through the use of aluminium foil wrappings and protected from further physical damage inside a sealed plastic storage box. The samples were therefore removed from the aluminium foil immediately prior to scanning and wetted with a fine water spray. On some fragments the moist conditions had promoted a thin fungal growth on the surface of the material

which was removed prior to scanning through repeated irrigation of the sample with the fine mist water spray.

5.4.3.5. Sample digitisation

Due to the need to scan the samples prior to conservation treatment (which would have introduced additional dimensional changes to the material) the samples were kept in a wet state throughout the scanning by periodic spraying with a fine water spray. The magnet and rubber supports used in both laser and structured light scans to elevate the samples above the laser bench / structured light turntable (sections 6.1 and 6.2) were not used for these samples as the samples were not strong or rigid enough to prevent them sagging between the supports.

The samples were scanned with the Faro Quantum Arm and Laser Line Probe as well as the Bradford Visualisation custom structured light scanner.

5.5. Technique comparison standards

Based on the research experience of the author three significant factors in the quality of 3D digitisation results have been identified:

- The colour of the material being digitised;
- The opacity of the material being digitised; and
- The surface roughness of the material being digitised.

The impact on 3D digitisation techniques of these factors as they are exhibited in bone samples is the main focus of this research. In order to understand the results of differing digitisation methods on bone samples, the research identified a need to examine the baseline variation in response to these factors between differing digitisation techniques. To facilitate this, the design and development of measurement standards for each of these factors was explored.

The samples that were developed were labelled following the pattern of sample labels used with the experimental taphonomy samples (section 5.1.1) and distinguished from them by substituting the initial letter ‘A’ with ‘S’.

5.5.1. Colour technique comparison standards

Within photography the colour temperature of the light source significantly impacts the recorded image and requires the photographer to adjust the “white balance” and “colour balance” of the image. Prior to digital photography this was achieved by matching the properties of the light sensitive emulsion on the film to a specific type of light source. The introduction of digital photography, has significantly simplified this process of white and colour balancing as the recorded RAW image can be processed to produce an adjusted output image that compensates for the colour temperature of the light source. To further improve this, colour standards have been developed to ensure high quality colour reproduction and their use is now a standard practice within photographic illustration and recording. These colour calibration guides (figure 5.20) are produced to ISO standards (International Organisation for Standardization

2006) and therefore are ideal for testing the response of 3D digitisation techniques to colour variation within the target material.

Figure 5.20: Five different colour calibration standards used for accurate colour correction and reproduction within photography (source: author).

5.5.1.1. Digitisation of the colour technique comparison standards

A set of Danes-Picta BST-13 (Danes-Picta Ltd, Prague) colour calibration boards were used as targets for digitisation by each of the 3D digitisation techniques (sections 6.1 to 6.3) and the response by each instrument was assessed and were used to white balance the photographs of the bone samples.

5.5.2. Opacity

The opacity of a material is a measure of how well the material blocks light from passing through the surface, and in the case of completely opaque materials all the light is reflected off the surface. Its corollary is transparency in which light can pass through the surface and either completely through the material, or is

reflected one or more times within the material resulting in sub-surface scattering (figure 5.21).

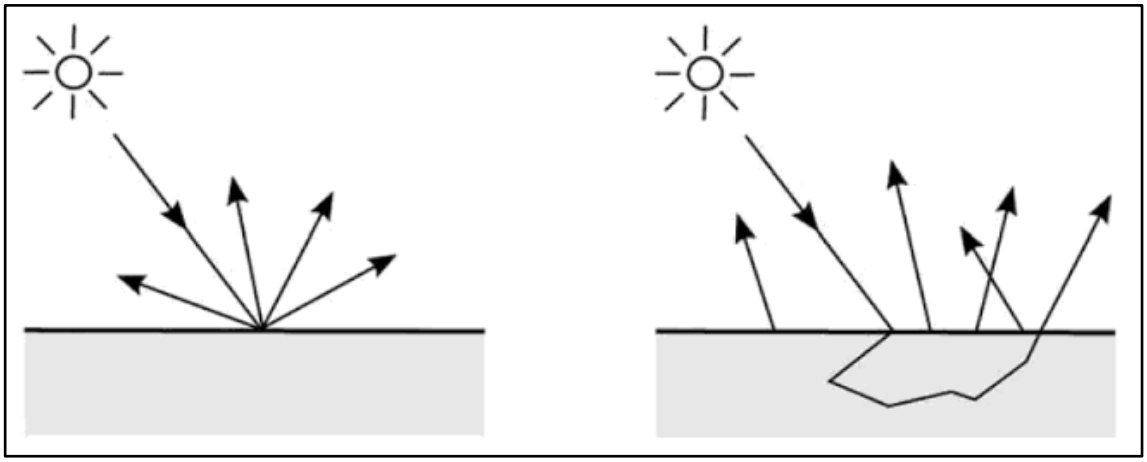

Figure 5.21: Model of a flat opaque material (left) and a translucent material exhibiting sub-surface light scattering (right) (after Stanco et al. 2011 p. 189).

Experience from previous digitisation projects by the author has shown that some biological hard tissues can provide a poor response to digitisation due to the degree of opacity / translucency. However, there are not currently any available standards aimed at 3D digitisation to assess the response of digitisation techniques to semi-opaque / translucent materials.

5.5.2.1. Opacity technique comparison standards production

To assess the response of a digitisation technique to a semi-opaque material, duplicate items with identical dimensions and properties, varying only in their level of opacity were created. It was anticipated that by measuring each of the duplicates under the same settings any variation in the recorded dimensions, levels of noise or surface roughness would therefore be attributable to the variation in opacity.

A precision machined acrylic right rectangular parallelepiped with polished flat faces (used as a display stand for high end retail displays of jewellery) was selected as a master from which to create duplicate items. The master was used to create several two part RTV (Room Temperature Vulcanization) silicone moulds of the master (figure 5.22).

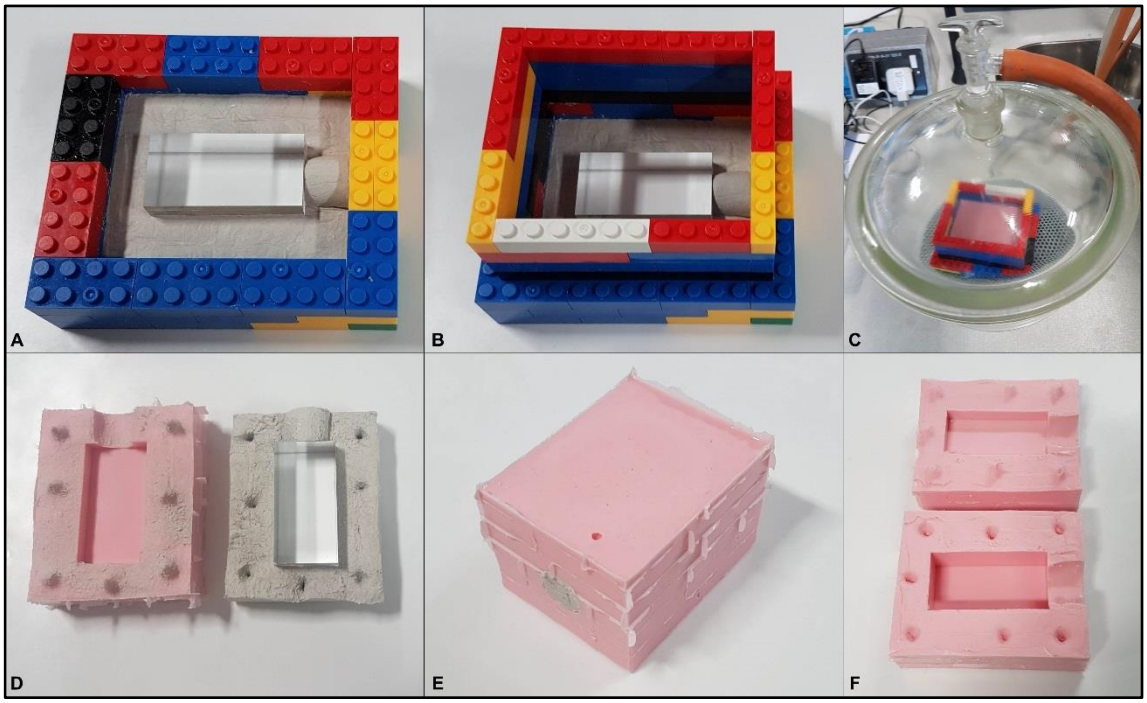

Figure 5.22: Sequence showing the process of producing the opacity technique comparison standards. The acrylic master was half embedded in modelling clay (A) and the walls of the dam were built up and coated with release agent (B). The upper part of the mould was filled with a (degassed) two part RTV silicone rubber (C) and left to set. The Lego™ dam was then removed and the modelling clay was separated from the master and upper half of the mould (D). The process was repeated for the lower half leaving a modelling clay plug for filling the mould (E). The two mould halves were then cleaned and dried in a 40°C oven to remove moisture (F) (source: author).

Copies of the master were then cast in a water clear polyester casting resin mixed with a white pigment polyester colour paste. The specification for the white pigment polyester colour paste indicated that a mix of between 5% and 10% would provide a completely opaque resin. To produce copies of the master at varying levels of opacity, mixes of between 0.25% and 10% of white pigment polyester colour paste were prepared (table 5.1). The proportions were mixed thoroughly to ensure an even distribution of the colour paste, and the methyl ethyl ketone catalyst, throughout the resin, before the resin was degassed in a vacuum chamber and poured into the RTV silicone moulds to produce targets of differing opacities.

Figure 5.23: Casting the opacity technique comparison standards with 5% and 10% opacifier into the RTV silicone moulds (source: author).

Sample	Resin (g)	Opacifier (g)	Catalyst (g)	Opacifier %
S0011	195.51	0.49	4	0.25
S0012	195.02	0.98	4	0.5
S0013	194.53	1.47	4	0.75
S0014	97.02	0.98	2	1
S0015	96.04	1.96	2	2
S0016	46.55	2.45	1	5
S0017	44.1	4.9	1	10

Table 5.1: Resin, opacifier and catalyst proportions for the production of the opacity technique standards.

Once the opacity technique comparison standards were fully set, they were removed from the mould, cleaned and allocated a sample label (figure 5.24).

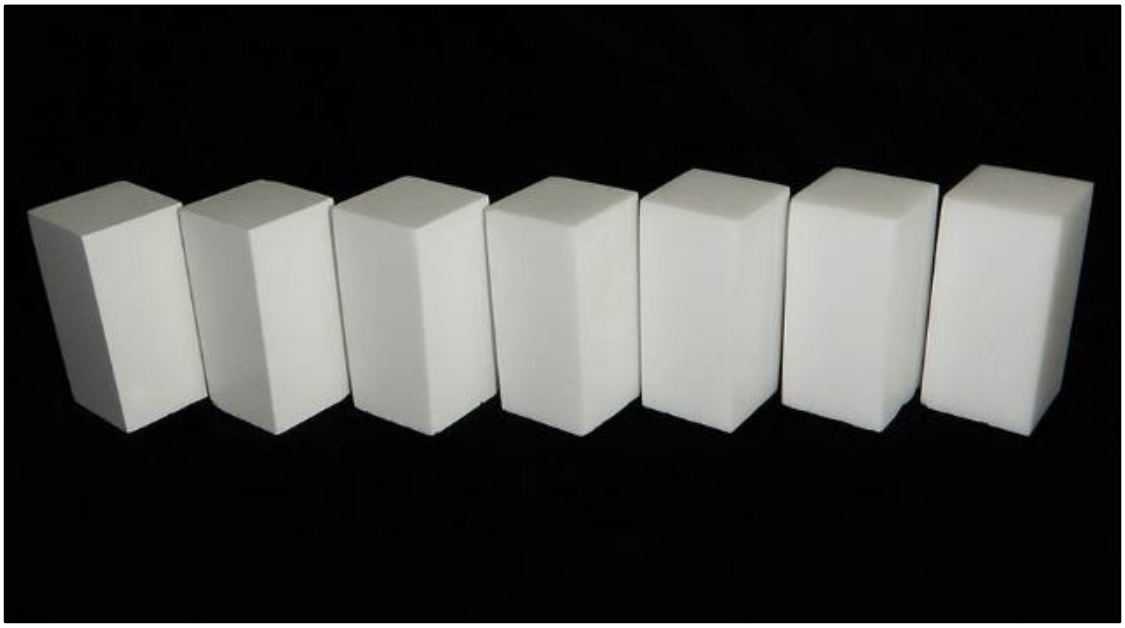

Figure 5.24: The completed opacity standard samples (S0011 (right) to S0017 (left)) (source: author).

To aid identification of the samples and each face of the block so as to ensure the digitised models could be identified in the same orientation the samples were glued to a 1mm thick rectangle of white plastic card. The sample label was written on the underside of the plastic card base and the percentage of opacifier was written on the upper surface in one corner to act as a reference point in the digitised models (figure 5.27).

5.5.2.2. Measuring the opacity of the opacity standards

During production of the opacity technique comparison standards, a small amount of each resin mix was poured into a plastic mini petri dish to a depth of between 2 – 3 mm and the dishes were marked with the sample number on the outside. The mini petri dishes were spray coated with release agent prior to the addition of the resin to prevent the resin from bonding with the plastic. Once set the resin within the petri dishes formed thin discs of material, 34 mm in diameter with the same opacity properties as the standards. The discs were removed from the petri dishes and the meniscus around the top was removed by wet sanding the discs on increasing grades of engineering grade abrasive papers. The discs were reduced in thickness to a uniform 1.5 mm (measured with a 0.01 mm resolution digital sliding calliper) and then polished on a thin section

polishing machine using a 6 µm and then 1 µm diamond polishing liquid to produce a uniform and consistent finish to all the discs.

The discs were then rinsed and dried before their final thickness was checked and they were placed in sample bags labelled with their sample number and percentage opacifier.

To measure the opacity of sample discs and the bone samples, an opacity meter was built using a focusable high output, single LED light source integrated into a black light proof box (figure 5.25). The fixed light was focused onto a circular LED collimating lens, fixed into a subdivision within the box, which collected the light from a flat 20 mm diameter circle onto an Adafruit TSL2561 digital light sensor board (Adafruit, New York). The TSL2561 board was connected via the Inter-Integrated Circuit (I^2C) bus, to a Raspberry Pi2 model B mini computer (Raspberry Pi Foundation, Cambridge) running Raspbian (Raspberry Pi Foundation, Cambridge), an open-source Debian-based operating system derived from Unix.

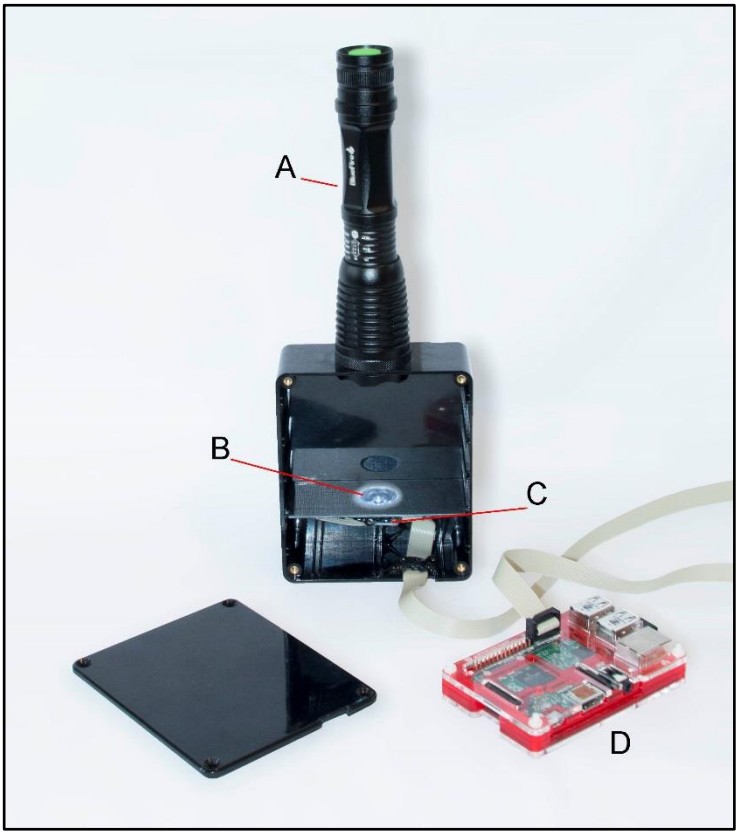

Figure 5.25: Opacity meter. A. High lumen LED torch with a single LED light source. B. Collimating lens mounted flush with compartment divide. C. Adafruit TSL2561 light intensity meter breakout board. D. Raspberry Pi2 Model B (source: author).

By using a fixed focused light the distance and intensity of the light was maintained at a constant level, with variation in the output of the light being limited to battery charge and circuit based fluctuations. To compensate for these fluctuations, a Python script was written to automate the recording of 50 measurements of the light intensity without the sample in the opacity meter, and then with the sample.

The data from the opacity meter was written by the Python script to a text file and later imported into Microsoft Excel where the data was averaged, the attenuation coefficient was calculated and the opacity and transmittance were calculated.

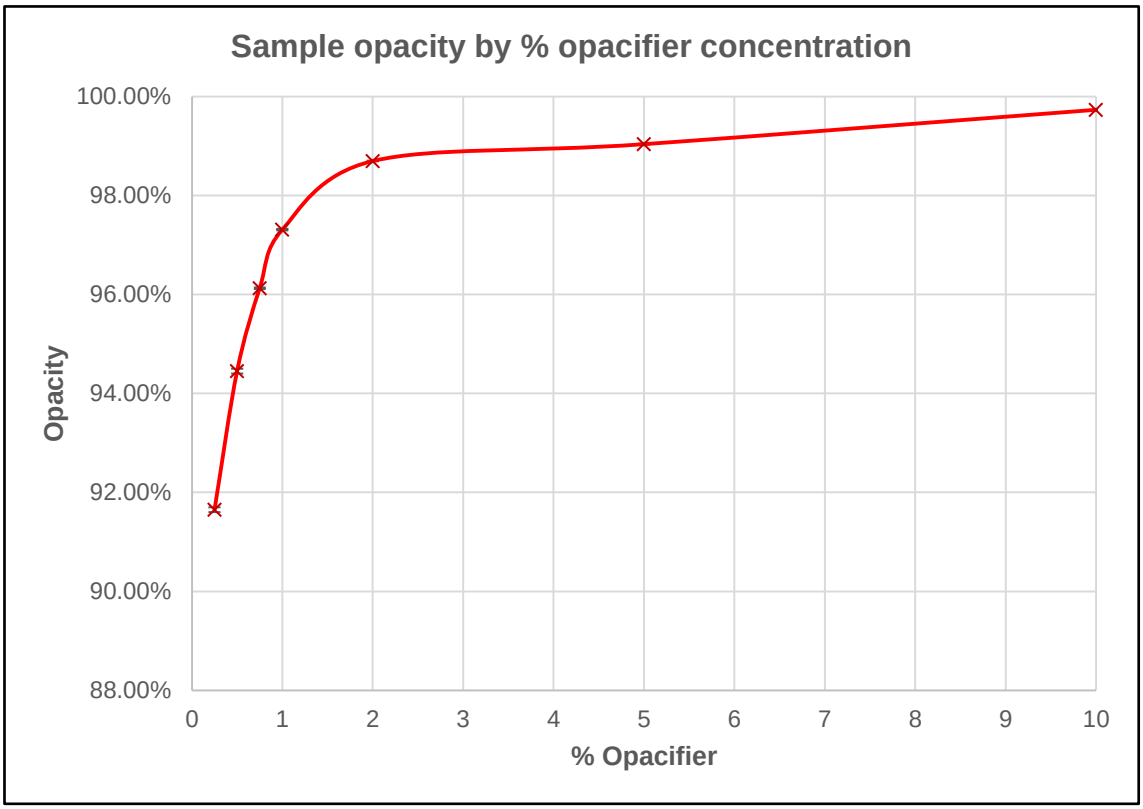

Figure 5.26: Plot of measured opacity against percentage opacifier for the opacity technique comparison standards (source: author).

The measured data for the opacity technique comparison standards is included in appendix E.

5.5.2.3. Measurement of dimensions of the opacity technique comparison standards

Experience of digitisation by the author during this research and during the previous research projects indicated that variations in opacity might impact dimensional accuracy of digitised materials. To test this the physical dimensions of the opacity technique comparison standards were recorded for comparison to the digitised measurements (section 6.9.3).

A common set of measurements was defined to aid comparison (figure 5.27). The horizontal measurement of the distance between each parallel face taken at the top corners, and vertical measurements from the top surface at each corner to the surface of the plastic card base were measured using a micrometer and a digital sliding caliper both with a resolution of 0.01 mm.

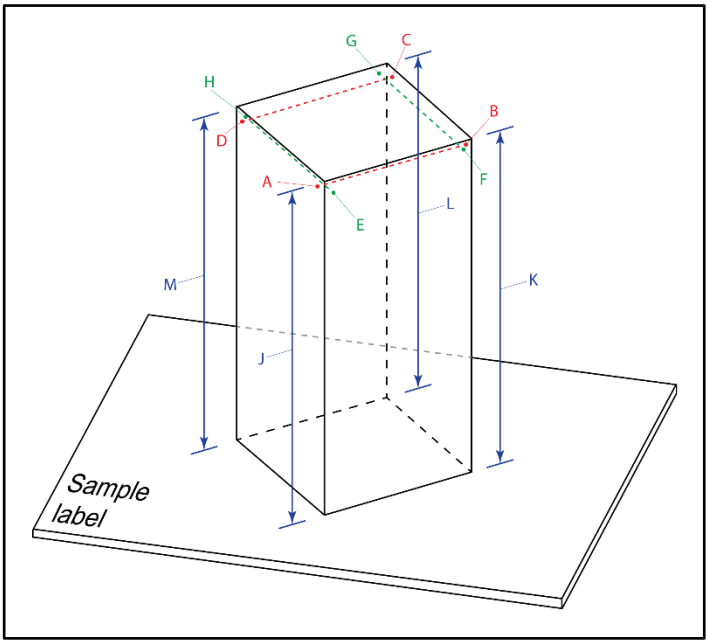

Figure 5.27: 3D drawing showing the location of the measurements used on the opacity technique comparison standards (source: author).

The same measurements were made on the 3D models for each instrument type and the difference was calculated (appendix E).

5.5.3. Surface roughness technique comparison standards

The left of figure 5.21 shows a standard model for reflection of light from a surface, however, at the microscopic scale, most apparently flat surfaces are not flat but exhibit a degree of roughness. As surfaces reflect light rays relative to the angle of incidence to the surface (section 4.2.3.2) surfaces that have very varied micro topography will tend to disperse light from 3D digitisation equipment to a greater extent compared to flatter and less varied surfaces. As most 3D digitisation techniques rely on reflecting of a light or pattern of light onto a surface and recording the light rays reflected back to a camera or other light detector, the degree to which an object reflects or disperses (diffuses) light rays is therefore expected to impact the quality of 3D digitisation results.

To assess the response of each 3D digitisation technique to this requires a set of consistent known roughness materials which are otherwise similar in chemical composition, colour etc. Abrasive polishing cloths / papers were identified as a potential material for the assessment of the impact of surface roughness on 3D digitisation.

5.5.3.1. Abrasive polishing cloth and paper.

Abrasive polishing materials used in engineering are made from silicon carbide or aluminium carbide bonded to a cloth or paper carrier. The average diameter of the silicon / aluminium carbide grains is rated by size and therefore area distribution of the grains per square inch or centimetre (the grit or grade). In order for polishing abrasives to be effective they are available from low grit counts (with large diameter grains) to high grit counts (with small diameter grains) in the same manufacturer range (figure 5.29). The determination of the grit count is standardised under the Federation of European Producers of Abrasives “P” grading system as specified by ISO 6344 (International Organisation for Standardization 1998a, 1998b, 2013).

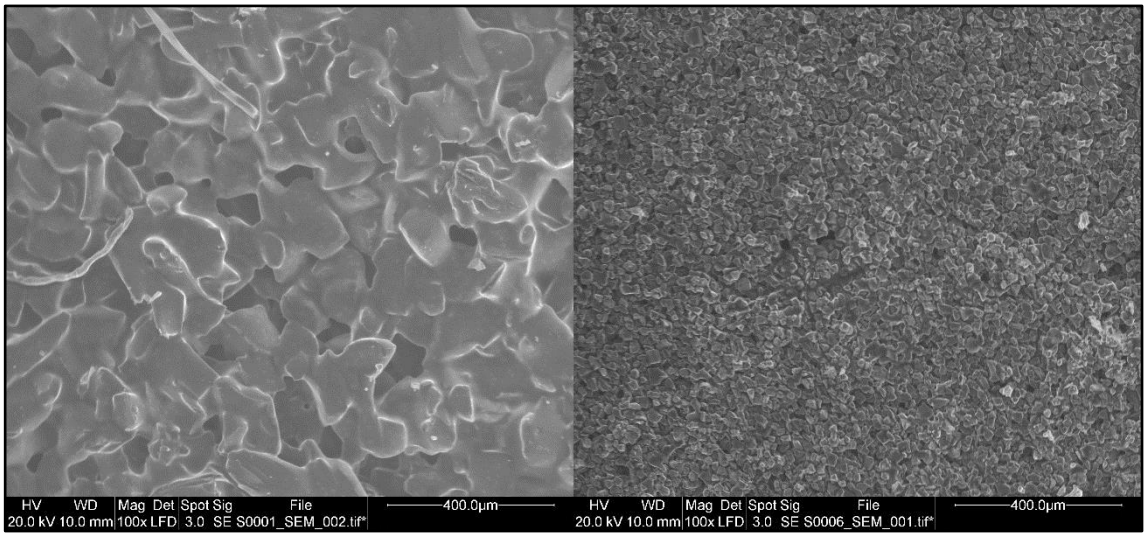

Figure 5.28: Scanning electron microscopy images of MicroMesh 1500 grade (left) and 4000 grade (right) silicon carbide abrasive cloth at x100 magnification (source: author).

Just as the diameter of the grains limits the number of grains that can occupy a set area (and hence the P grade) the diameter also determines how far above the carrier paper and bonding material the grain protrudes. Therefore, as the average grain diameter decreases the roughness of the surface also decreases.

This quality, along with the consistent chemical composition (silicon carbide) makes engineering abrasive polishing cloths and papers an appropriate model for comparing surface roughness.

5.5.3.2. Selected material

Micro-Mesh (Micro-Surface Finishing Products Inc. Iowa) polishing cloths were selected in 1500, 1800, 2400, 3200, 3600, 4000, 6000, 8000, and 12000 grades.

Whilst these grades give an indication of the relative fineness of the polishing provided by each cloth, they are not sufficient to calculate the roughness of the abrasive surfaces. To do so a small circular sample of each abrasive cloth was mounted on a 12.5 mm diameter aluminium sample stub and imaged in a FEI Quanta 400 Scanning Electron Microscope (SEM) using a secondary electron detector in low vacuum mode (figure 5.28). The SEM images were used to measure the silicon carbide particle dimensions and to determine the following surface roughness measures:

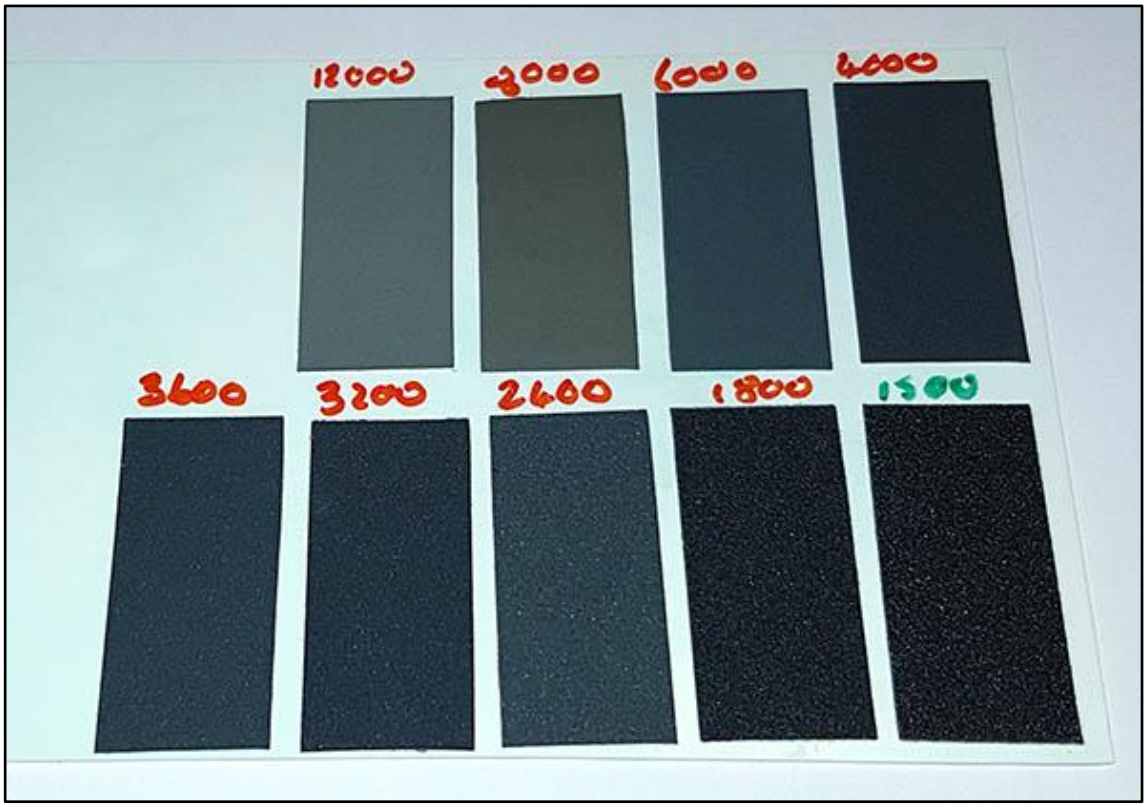

Figure 5.29: The surface roughness technique comparison standards (source: author).

Sample	Average surface roughness (microns)	Manufacturer stated grade (particles/area)
S0001	118.04	1500
S0002	100.6	1800
S0003	53.94	2400
S0004	43.67	3200
S0005	36.16	3600
S0006	27.64	4000
S0007	16.65	6000
S0008	7.076	8000
S0009	4.32	12000

Table 5.2: Average surface variation size of the surface roughness technique comparison standards.

5.5.3.3. Measuring response to surface roughness

A sample rectangle of each grade of the abrasive material was glued to a flat plastic board with spray mount and the board was labelled using permanent marker with the sample number adjacent to the sample. The samples were digitised by each of the 3D digitisation techniques (sections 6.1 to 6.3) and the response by each instrument was assessed.

Chapter 6. Methods 2: Digitisation

The technique comparison standards, experimental bone samples and the archaeological and palaeontological samples for this thesis were digitised using 3D laser scanning, structured light scanning and photogrammetry. The digital models produced from this data were analysed using a selection of software packages. The following section outlines the three methods used to digitise the samples and the software that were applied to the resultant 3D models to analyse the data. The results of these analyses are presented in chapter seven and discussed in chapter eight.

6.1. Laser scanning

As already discussed (section 4.3.1.2) higher quality laser scanning is best achieved through the combination of a coordinate measuring machine (CMM) and the laser line probe (van Gestel et al. 2009, Bešić et al. 2011, Boeckmans et al. 2014, Xie et al. 2014).

The research utilised a FARO Quantum Arm with V3 Laser Line Probe (FARO, Lake Mary, FL, USA). This laser scanning system was mounted on a bespoke Bradford Visualisation steel-topped metrology instrument bench (figure 6.1), designed and built by the author as part of the Digitised Diseases project to eliminate errors caused by the relative movement at the micron scale of the laser scanner and the subject being scanned.

The laser scanning was carried out in Bradford Visualisation's digitisation suite located in the School of Archaeological Sciences, University of Bradford.

Figure 6.1: FARO Quantum Arm with V3 Laser Line Probe mounted on a Bradford Visualisation metrology instrument bench (source: author).

The FARO arm was developed as a coordinate measuring machine for engineering utilising an articulated arm providing seven degrees of freedom, in a sphere of measurement 2.4m in diameter around the origin point at the base of the articulated arm. The use of an arm-based coordinate measuring machine laser scanner such as the FARO instrument allows the laser probe at the end of the arm to be moved around the object being digitised. This feature offered flexibility and ease of digitisation of the surface morphology of the samples which was particularly useful for degraded and fragile material that is vulnerable during movement.

The FARO V3 Laser Line Probe projects a line of 640 points of laser light which it alters at 30 frames per second allowing the scanner to capture 19,200 points per second. All scans were carried out in ‘high accuracy mode’ where the spacing of these points is reduced along the laser line, increasing the resolution of the laser line.

6.1.1. Laser scan calibration

Through the use of the fixed ball probe at the end of the articulated arm, the FARO system can compare direct fixed probe measurements of object surfaces with the laser line probe measurements. This feature was utilised within this research project to measure the white calibration target used to calibrate the laser probe.

During calibration the laser arm was positioned on the Bradford Visualisation metrology instrument bench so as to align the Y axis encoded by the arm with the long axis of the benchtop. This facilitated easier alignment of samples in the post-processing stage. The calibration data was saved to a Microsoft Excel spreadsheet.

6.1.2. Laser scan software

Laser scan and fixed probe measurements were recorded using the IMAlign module of the Polyworks 2014 software suite (InnovMetric, Québec, Canada) and the FARO Laser Line Probe plugin.

All scans were carried out in high accuracy mode. The exposure and noise filtering threshold levels were set before each sample was scanned using the auto function in the scanner control dialogue window (figure 6.2). This function requires that the FARO arm is held so as to maintain the laser line in a fixed position perpendicular to the sample surface, at a distance in the middle of the ideal range (as indicated by the on screen rangefinder). The function then varies the exposure and noise filtering levels measuring the intensity and variation in the line thickness of the laser light returned to the camera. The setting with the best return and the least variation (best precision) is selected by the software. The exposure and noise filter threshold settings selected were recorded for each sample.

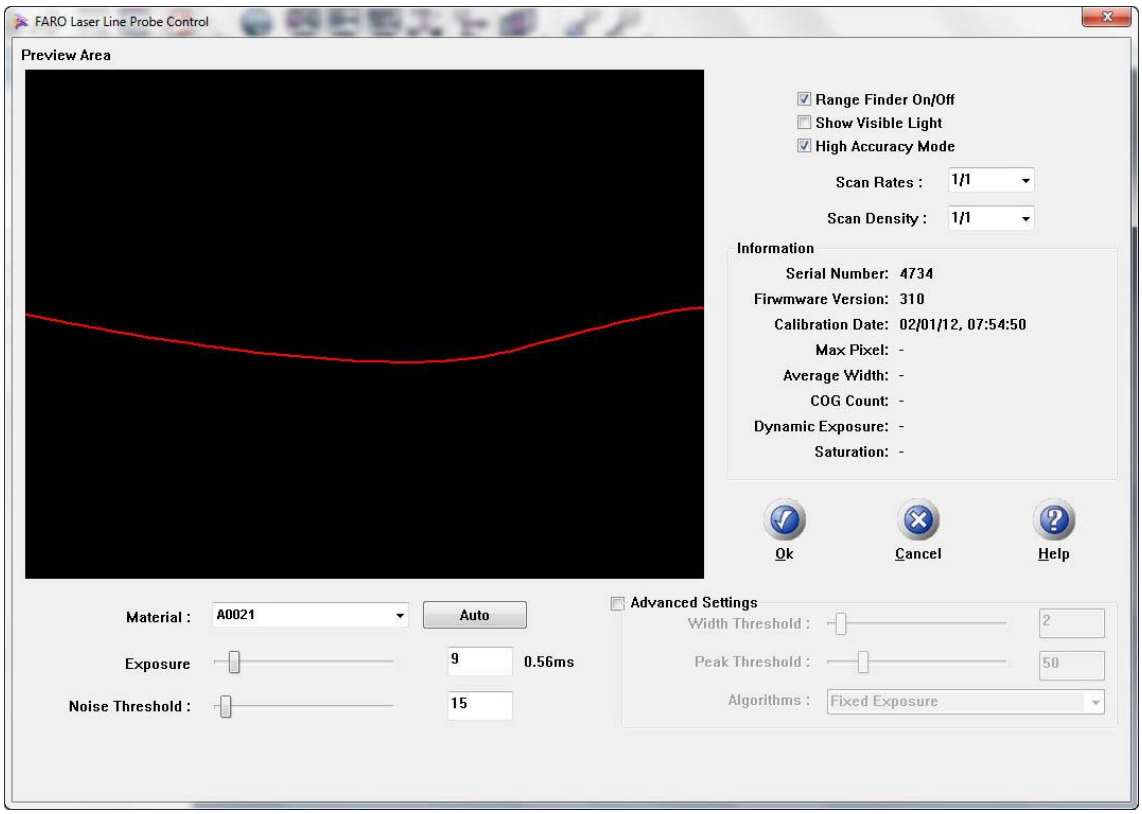

Figure 6.2: Using the auto function to set the exposure and noise filter threshold values in the FARO Laser Line Probe Control dialogue window (source: author).

Prior to each sample being scanned, the interpolation step was set to 0.1 mm and the maximum angle set to 75° in the FARO laser line probe settings dialogue window (figure 6.3). The interpolation step setting defines the spacing of returned data points along the laser line by averaging the values in 0.1 mm groups. This results in a pseudo-regular grid interpolation to the point cloud of each scan pass. Polyworks IMAlign meshes the point cloud as the scan pass is being captured and this per scan interpolation aids scan speed and visualisation of the scan progress to the user. Meshing of the final 3D model however, is based on the merged point clouds from multiple overlapping scans passes (see below) and not on this initial interpolation grid. The maximum angle setting filters laser reflections from surfaces with an incidence angle of more than the set value to reduce incidence angle noise.

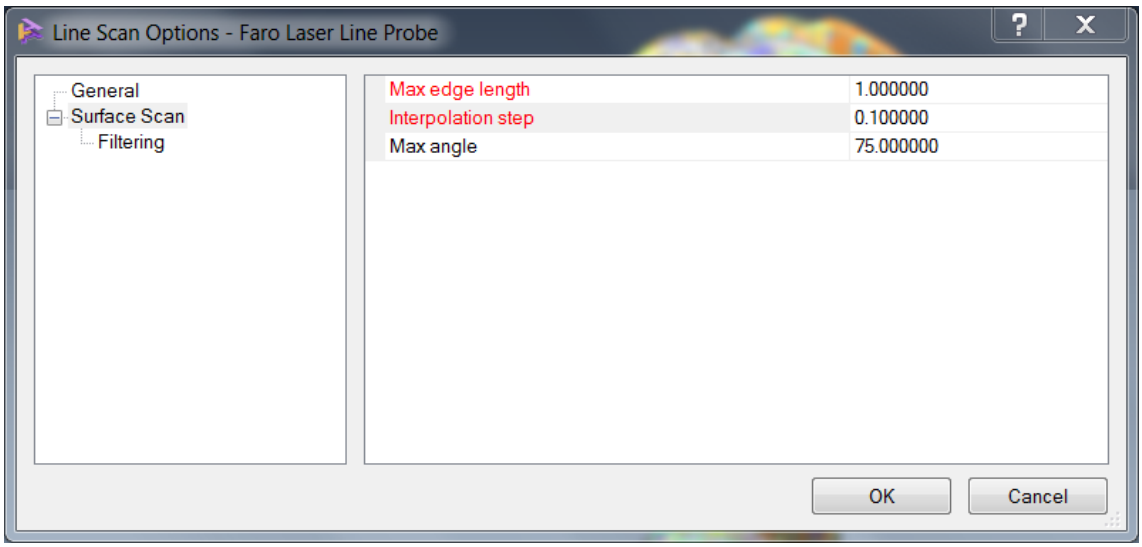

Figure 6.3: FARO Laser Line Probe plugin surface scan settings (source: author).

The samples were positioned to align the long axis of the scanning bench and the long axis of the bone; this aids the post-processing stage. Samples were scanned in two orientations: anterior view and posterior view. The samples were raised above the scanning bench on custom made magnetic rubber scanning stands, affording a greater level of overlap between scan passes in the upper and lower orientations. Individual scan passes were orientated to ensure some overlap between passes to aid alignment. The scan passes from the posterior orientation were manually rotated in the instrument coordinate system to align with the anterior view using the Split View Alignment tool.

A best fit alignment algorithm was then applied to all scan passes. The best fit alignment algorithm uses an iterative least squares method to reach a selected convergence of 0.000001 (figure 6.4) where zero is the optimum convergence. This value represents the difference between the point clouds of individual scan passes and therefore the degree of convergence of each point cloud.

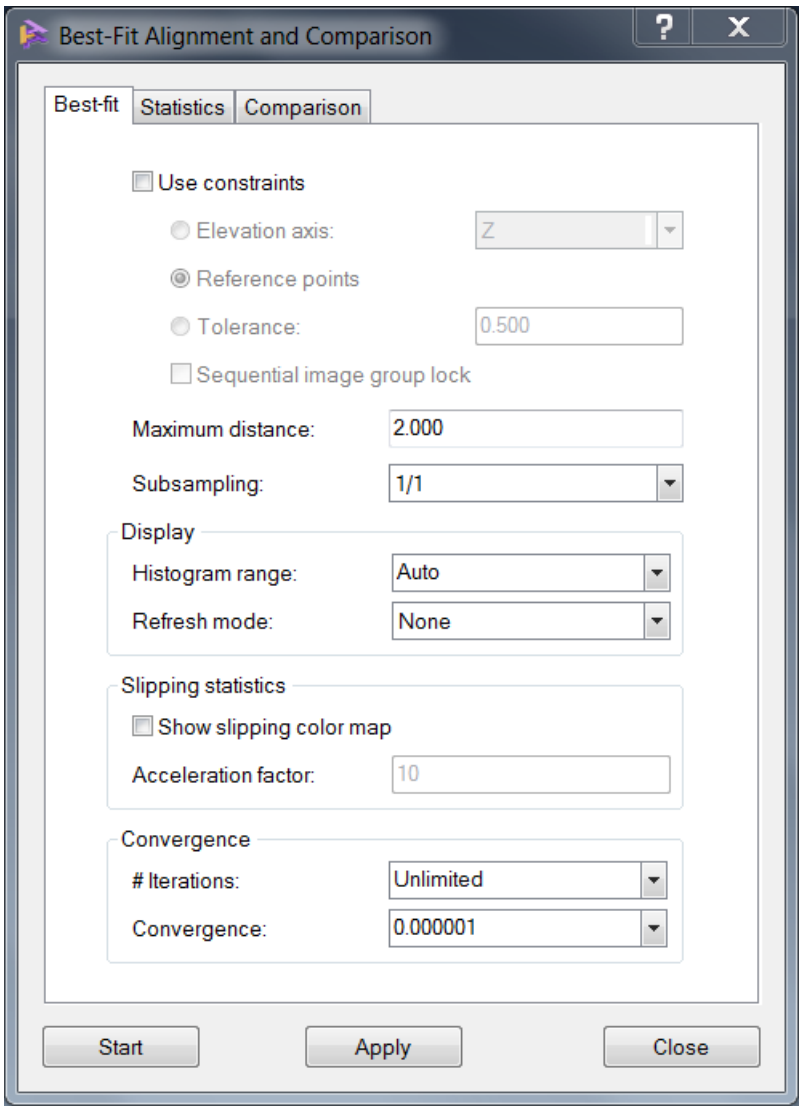

Figure 6.4: Applying a Best Fit Alignment to scan passes in Polyworks IMAlign (source: author).

The resultant point cloud for each sample was rendered out to a 3D mesh surface model in IMMerge module of the Polyworks 2014 software suite (InnovMetric, Québec, Canada), using a 0.1 mm surface sampling step and a low smoothing pass. The IMMerge meshing algorithm sub-samples the point cloud and averages the points within each 0.1 mm domain. The point cloud is then meshed using a Delaunay triangulation method to produce the 3D surface model (figure 6.5).

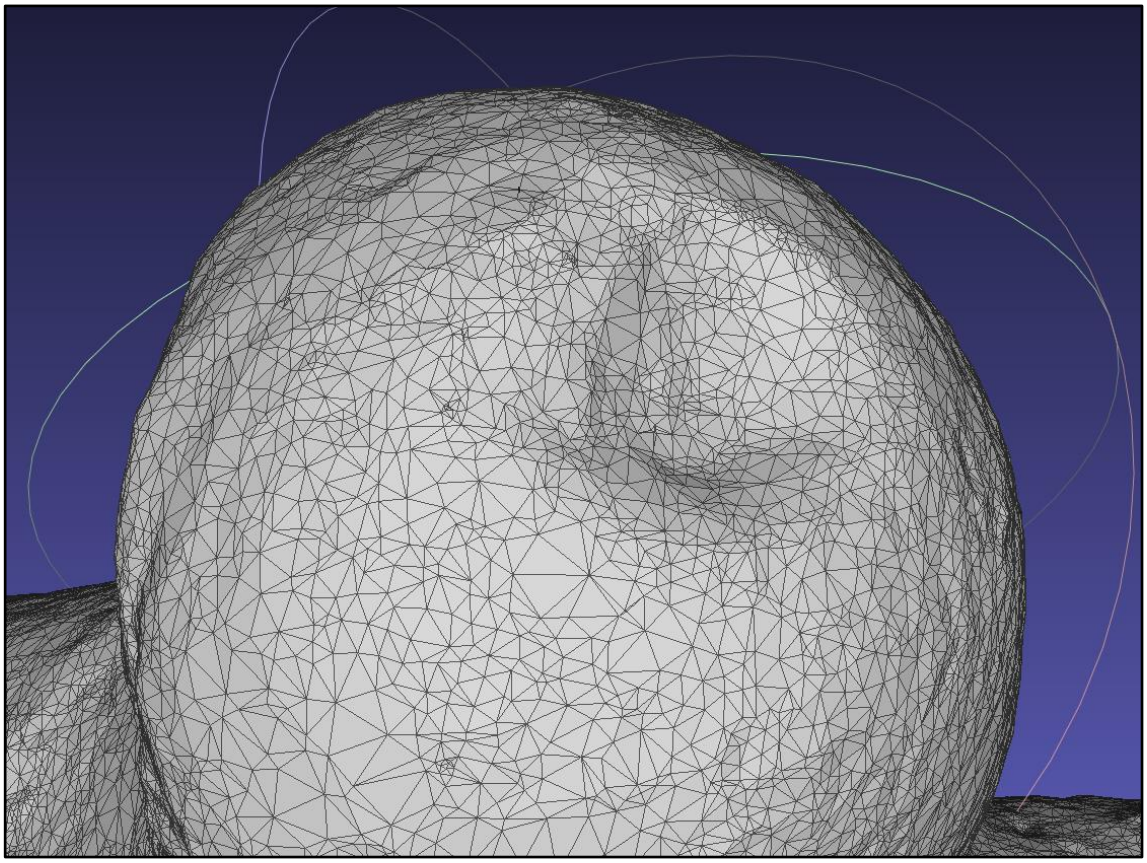

Figure 6.5: Irregular triangular network meshing of the surface of the femoral head of sample A0024_LaS01 (source: author).

The final model was exported, using the sample and fragment numbering system in the filename (section 5.1.1), to both an .obj and an .stl file format for later analysis.

6.2. Structured light scanning

The project utilised two different scale structured light scanners: a general scale structured light scanner; and a macro scale structured light scanner for recording more detailed surface characteristics.

The general scale structured light scanning was carried out in the Bradford Visualisation digitisation suite and the macro scale structured light scanning was carried out in the Fragmented Heritage workroom, both of which are located in the School of Archaeological Sciences, University of Bradford.

Both scanners were controlled by the same software package and the processes of scanning were identical beyond the field of view range and calibration of the two scanners.

6.2.1. General scale structured light scanner

General scale structured light scanning was undertaken using a custom built scanner, designed within Bradford Visualisation at the University of Bradford (figure 6.6). The Bradford Visualisation structured light scanner combines a GS3-U3-28S5C-C colour machine vision camera and a GS3-U3-28S5M-C monochrome camera, both of which are produced by Point Grey Cameras (Point Grey Research Inc., Richmond, Canada). The cameras were set to the same focal distance as the projector and set at a fixed lens aperture of f/8. The digital fringe projection is provided by an Acer P1206P white light projector (Acer Inc., New Taipei, Taiwan). The projector and cameras were held in fixed relative positions, via custom-made machined aluminium mounts and extruded aluminium profile sections. The scanner was mounted on a Manfrotto tripod (Lino Manfrotto and Co, Cassola, Italy) with a three axis heavy duty pan and tilt head used for film applications.

Figure 6.6: The Bradford Visualisation structured light scanner system (source: author).

A high precision computer controlled turntable produced by MechInnovations (MechInnovations Ltd, Leamington Spa, UK) was used to mount all the samples, and the samples were scanned in two orientations: anterior view and posterior view (figure 6.7). Using the turntable to automate the scanning, individual scans were recorded every 30° of rotation. Additional, manually oriented scans, were added as required to ensure full coverage of the sample's surface.

Figure 6.7: Sample A0021 on the structured light scanner turntable in anterior (left) and posterior (right) orientation (source: author).

6.2.1.1. Bradford Visualisation scanner calibration

The Bradford Visualisation scanner was calibrated using a high resolution printed calibration target with grid spacing of 10 mm bonded to a flat glass plate (figure 6.8). The calibration target was mounted on a custom made stand so that the plate was held at an angle close to perpendicular to the axis of view of the scanner.

During the calibration process pairs of images from the left and right cameras of the scanner were taken of the calibration target, allowing the scanning software to identify the corners of the grid squares and calculate the calibration parameters (figure 6.8) (LMI Technologies 2015).

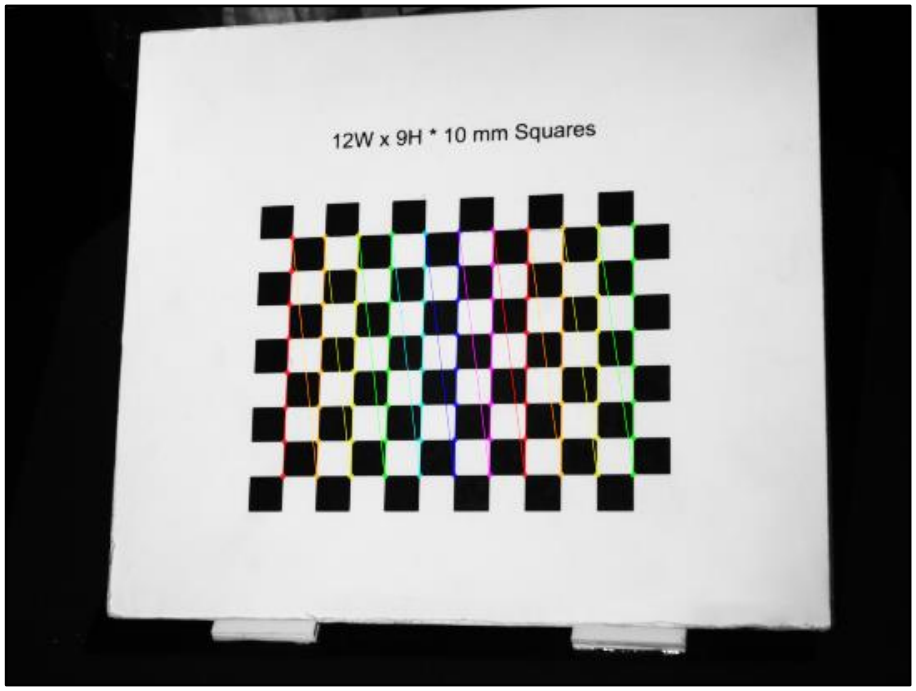

Figure 6.8: Identification of the corner points on a single camera image of the calibration board during calibration in FlexScan3D (source: author).

To ensure good coverage of calibration points the scanner head and the calibration target were moved incrementally to give pairs of images throughout the scanning volume. A minimum of 60 pairs of images were collected to ensure reliable calibration which was carried out in FlexScan3D (LMI Technologies Inc., Delta, BC, Canada). The rotation angle of the turntable was calibrated using the same 10 mm grid square calibration target used for the main scanner calibration.

The Bradford Visualisation scanner has a wide range of field of views from 180 mm to 540 mm. A ~300 mm field of view was used this research. For all calibrations over the period of the research (n = 22), the scanner had an average accuracy of 18.6 µm at a precision of +/- 13.3 µm and an average point to point distance (resolution) of 145 µm.

6.2.2. Macro scale structured light scanning

For recording fine surface taphonomic changes to the bone samples a MechInnovations MechScan (MechInnovations Ltd, Leamington Spa, UK) macro structured light scanner was used (figure 6.9). The principles of the scanner are identical to the general scale structured light system (section 6.2.1)

but the field of view and the fineness of the projected pattern image are all maximised for fields of view between 20 mm and 150 mm. The MechScan uses two GS3-U3-28S5M-C monochrome cameras produced by Point Grey Cameras (Point Grey Research Inc., Richmond, Canada).

The cameras were set to the same focus distance as the projector and set at a fixed lens aperture of f/8.

Figure 6.9: MechInnovations MechScan structured light scanner (source: author).

The scanner was mounted on a Manfrotto tripod (Lino Manfrotto and Co, Cassola, Italy) with a three axis heavy duty pan and tilt head used for film applications.

A high precision computer controlled turntable produced by MechInnovations (MechInnovations Ltd, Leamington Spa, UK) was used to mount all the samples, and the samples were scanned in two orientations: anterior view and posterior view (figure 6.7). The samples were scanned using 80 mm and 60 mm fields of view, with some small fragments being scanned at a 20 mm field of view when required. Using the turntable to automate the scanning, individual

scans were recorded every 30° of rotation. Additional, manually oriented scans were added as required to ensure full coverage of the sample's surface. The scanner was recalibrated each time the field of view was changed.

6.2.2.1. MechScan macro scanner calibration

The MechInnovation MechScan macro scanner was calibrated using a high resolution calibration target with a grid spacing of 1.3 mm, photo-chemically printed on high tolerance flat glass. The calibration target was mounted on a custom 3D printed stand so that the plate was held at an angle close to perpendicular to the axis of view of the scanner (figure 6.10).

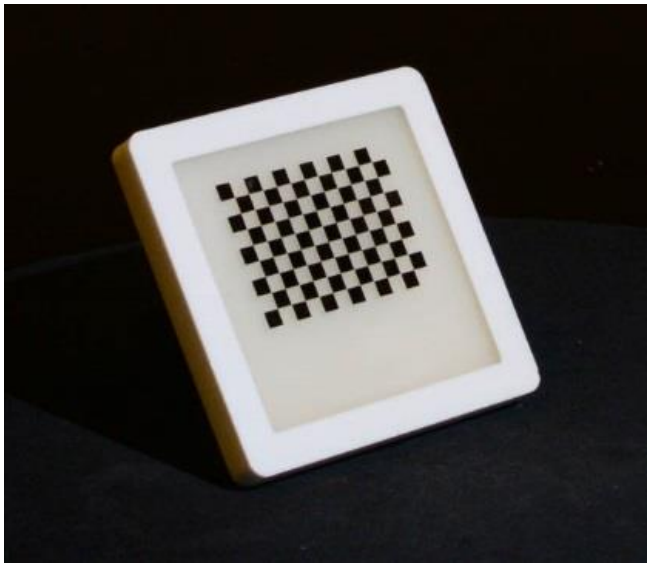

Figure 6.10: The MechScan calibration target during scanner calibration (source: author).

During the calibration process pairs of images from the left and right cameras of the scanner were taken of the calibration target, allowing the scanning software to identify the corners of the grid squares and calculate the calibration parameters (figure 6.8) (LMI Technologies 2015). To ensure good coverage of calibration points the scanner head and the calibration target were moved incrementally to give pairs of images throughout the scanning volume. A minimum of 60 pairs of images were collected to ensure reliable calibration which was carried out in FlexScan3D (LMI Technologies Inc., Delta, BC, Canada). The rotation angle of the turntable was calibrated using the 1.3 mm grid square calibration target used for the main scanner calibrations.

The MechScan macro scanner has a wide range of field of views from 20 mm to 150 mm (MechInnovation 2013) with manufacturer stated accuracies of 1 µm and 10 µm (respectively), however, these are determined in ideal conditions on a calibration subject designed in sympathy with the scanner's maximum capabilities.

For all calibrations at a field of view of 60 mm over the period of the research, the scanner had an average accuracy of 4.7 µm at a precision of +/- 1.7 µm and an average point to point distance (resolution) of 26 µm. This average was biased by calibrations carried out during the field research trip to the Turkana Basin Institute's Ileret Field Research Centre, Kenya, where the values were poorer quality, likely due to the environmental factors (i.e. high temperatures and dust). For all calibrations at a field of view of 20 mm over the period of the research, the scanner had an average accuracy of 3.4 µm at a precision of +/- 1.7 µm and an average point to point distance (resolution) of 13 µm.

6.2.3. Structured light scanning software

Both scanners were controlled and captured scan data using FlexScan3D version 3.3 (LMI Technologies Inc., Delta, BC, Canada) software system.

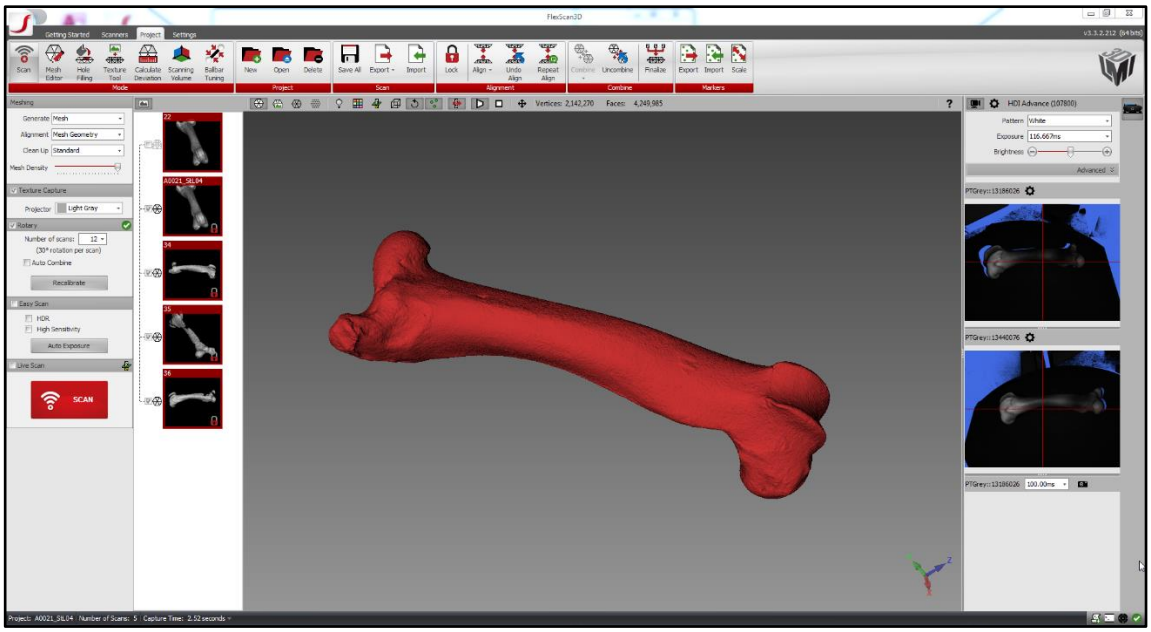

Figure 6.11: The FlexScan3D project user interface used for structured light scanning (source: author).

Following scanner calibration, each sample was placed on the rotary turntable and scanned for one rotation with scan passes at 30° intervals (12 scan passes) per orientation (total 24 scan passes). After each full rotation FlexScan3D calculates the 3D points from the fringe pattern images of the two cameras and produces a point cloud for each scan pass. Noise filtering is applied based on a user determined level and FlexScan3D temporarily meshes the point clouds from each scan pass with a triangulated irregular network meshing. All the samples were scanned using the 'standard' noise filtering level. FlexScan3D attempts to automatically align all the scan passes using a basic mesh geometry matching algorithm. As the number of scan passes increases, both the number of possible solutions to the mesh to mesh matching, and the level of uncertainty due to imprecision resulting from mesh variation increases (figure 6.12). The mesh to mesh alignment therefore often failed at this stage and manual alignment was performed to overcome this challenge.

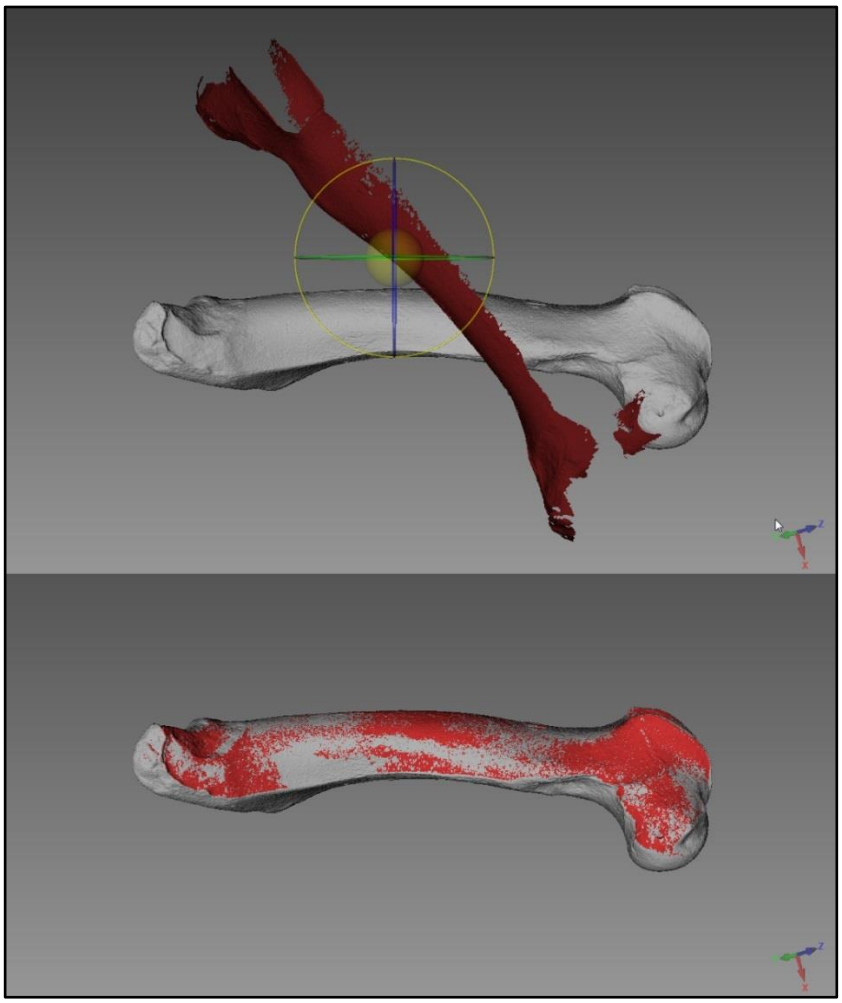

Figure 6.12: A failed mesh geometry alignment of a scan pass (the selected scan pass is coloured red in FlexScan3D) (top) and successful mesh geometry alignment of the same scan pass after manual reorientation (bottom).

One or more scan pass meshes (those that had aligned) were locked in position with the lock function and the misaligned individual scan passes were manipulated using the manual rotation and translation controls until their positions and orientations were close to the locked scan passes. The mesh geometry matching alignment algorithm was then run again. Once all the scan passes from both sample orientations were aligned any areas with missing data were targeted using additional scans, manually orientating the samples on the turntable to maximise the data return. The mesh geometry alignment was then repeated to align the resulting scan pass.

The mesh geometry alignment algorithm provides a basic alignment, but the temporary meshing of the scan passes introduces imprecision that results in larger mesh to mesh distances. To overcome this, FlexScan3D includes a fine alignment algorithm. The fine alignment algorithm was applied to all the scan passes once scanning was complete and applies an iterative least squares alignment on the underlying point cloud data for each scan pass, this produces a mesh to mesh distance statistic which is an indicator of model and scan quality. This mesh to mesh distance figure was recorded along with the total number of vertices and faces for the scan passes.

To create a single model the scan passes were combined and finalised (figure 6.13). During the finalise operation the point clouds of the scan passes were merged into a single reconstructed model using either a precise merge or a smoothed merge; the resulting point cloud was

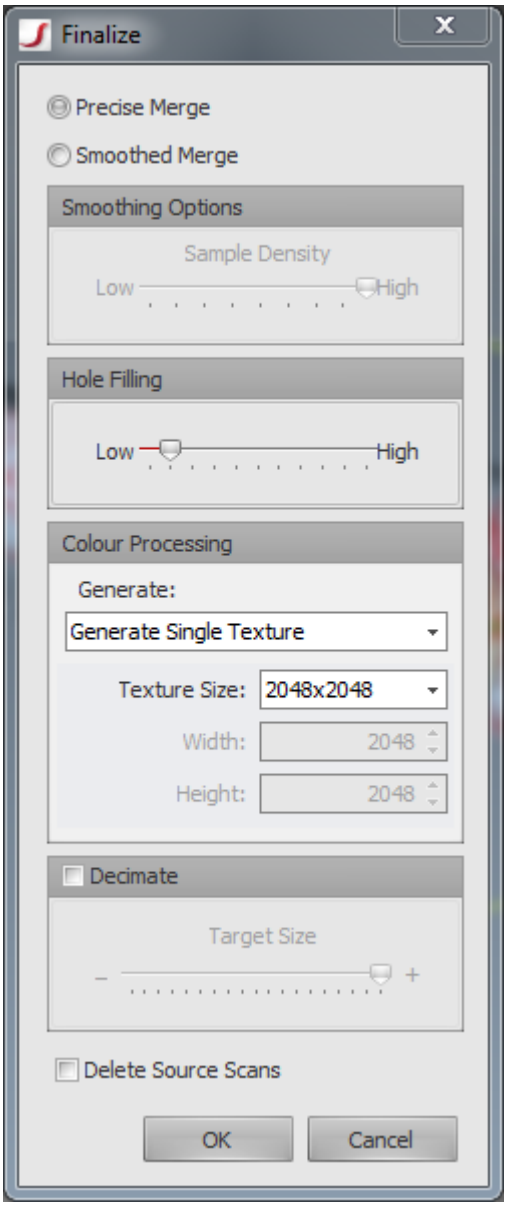

Figure 6.13: The finalize operation dialogue window with precise and smooth merged options (source: author).

meshed with an irregular triangulated network meshing operation (section 4.1.1). The precise merge option retained the exact point positions, including any sudden surface angle changes, whilst the smoothed merge applied a user determined level of resampling of the point cloud which results in smoothing of the model. The precise merge therefore produced a more accurate record of the scanned surface, but which included areas of high triangle densities caused by scanning errors or difficult to scan surface properties. These inconsistencies in the data could cause the merge to fail, especially on larger objects with big data sizes. Smoothing removed these inconsistencies but degraded the exactitude of the surface representation. The precise merge operation was applied to the scans of all the samples within this research. Where the precise merge failed, the smooth merge was applied.

During merging, a hole filling option is available to fill small holes in the surface based on a user defined variable from 0 to 100. As the scanning included additional, manually orientated, scan passes to ensure full surface coverage the samples were subject to a minimal level of hole filling at level 10. This level provided filling of very small holes in the mesh surface without introducing surface topography that was not based on the scanned sample's surface. UV unwrapping and texturing are integral to the finalise operation; texture files were generated to 2048 x 2048 pixel .jpeg images for all samples. The finalised models were exported, using the sample and fragment numbering system in the filename, to both an .obj and an .stl file format for later analysis.

6.3. Photogrammetry

Photogrammetry was carried out in the photographic suite of Bradford Visualisation in the University of Bradford's School of Archaeological Sciences.

6.3.1. Photographic equipment

All the samples were photographed using a Nikon D600 digital single lens reflex camera with a Nikon Nikkor 105 mm f/2.8 G AF-S VR IF ED Micro (Macro) lens (Nikon Corporation, Shinegawa, Tokyo, Japan). The camera was mounted on a Manfrotto tripod with a three axis pan and tilt head (Lino Manfrotto and Co, Cassola, Italy) which provided stability to the camera allowing the use of slower shutter speeds (figure 6.14). The slower shutter speed provided for smaller lens apertures of approximately f/13 producing a deeper depth of field and better feature recognition (section 4.3.3.2) but without inducing vignetting, fringe chromatic aberration or loss of sharpness normally associated with small aperture settings (Ang 2013).

Lighting was provided by the suite's fluorescent tube room lights with additional flat diffuse light panels above, in front-below and to both sides of the photographic scene, providing evenly diffused flat lighting across the samples. White balance and exposure settings were maintained in these mixed colour temperature lighting conditions through the use of an 18% grey card and white balance target card.

The photographic scene was dressed with black velvet cloth which has a very low specular reflection and provides a flat black background. The samples were placed on a rotating turntable which provides accurate rotations through the incorporation of a Nodal Ninja RD16 rotator base (Nodal Ninja, Chandler, Arizona, USA). The turntable was set to one rotation every 20 degrees resulting in 18 images per rotation. The circular top of the turntable was covered in a fitted covering of black velvet to match the background. The bone samples were raised off the circular top of the turntable with small stands custom-made from discs of black felt.

Figure 6.14: Composite image showing the three camera positions used in the photogrammetric recording within the Bradford Visualisation photographic suite (source: author).

The samples were photographed in two orientations: anterior view and posterior view (figure 6.15). Each orientation was photographed through a full rotation with the tripod set at three different heights to produce camera to turntable plane angles of 10°, 30° and 60° (figure 6.14) resulting in at least 108 photos per sample or fragment. Additional viewpoints were photographed when needed to ensure full overlapping surface coverage.

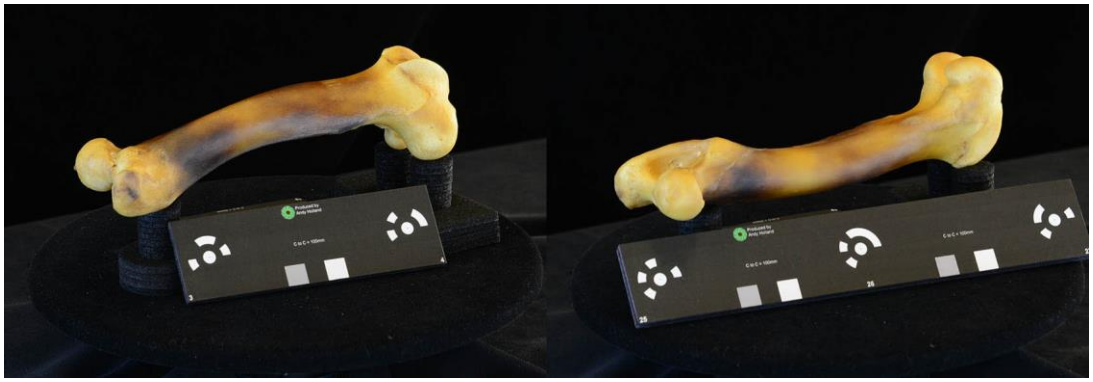

Figure 6.15: Two images of sample A0021 in anterior view (left) and posterior view (right) (source: author).

The camera recorded full frame images in Nikon's native raw format (.NEF) and 24 bit depth .jpeg format images of 3008 x 2008 pixels. A photographer's hand-

held whiteboard and marker was used to identify the sample numbers in the first photograph of each sample.

6.3.2. Photogrammetric coded markers and photo scales

Size information in photogrammetry is determined from collinearity equations, which produce a degree of uncertainty in the Z direction (i.e. depth along the focal axis). Known size scale bars can improve the size precision when photographed at the same time as the subject object (Cultural Heritage Imaging 2015). In machine vision systems, coded markers can be understood by the instrument and identified with a machine encoded label; this removes the need to manually apply markers and speeds up processing time. These markers can also be used to supplement tie point features and improve the accuracy of image alignment.

12 bit circular black and white number encoded markers for use in photogrammetry were generated in Agisoft PhotoScan (Agisoft LLC, St. Petersburg, Russia). The markers were incorporated into custom-made photogrammetry specific photo scales using Adobe Illustrator (Adobe Systems Inc, San Jose, California, USA), printed on a high resolution colour printer and spray mounted to black dense foam mount board to provide rigidity. A range of scales were created with point centre distances of between 50 mm and 200 mm (figure 6.16). The accuracy of the photo scale point centre distances were checked with a set of digital sliding callipers with a point accuracy 0.05 mm. Black, white and 18% grey white balance squares were also added to the scales to aid colour correction.

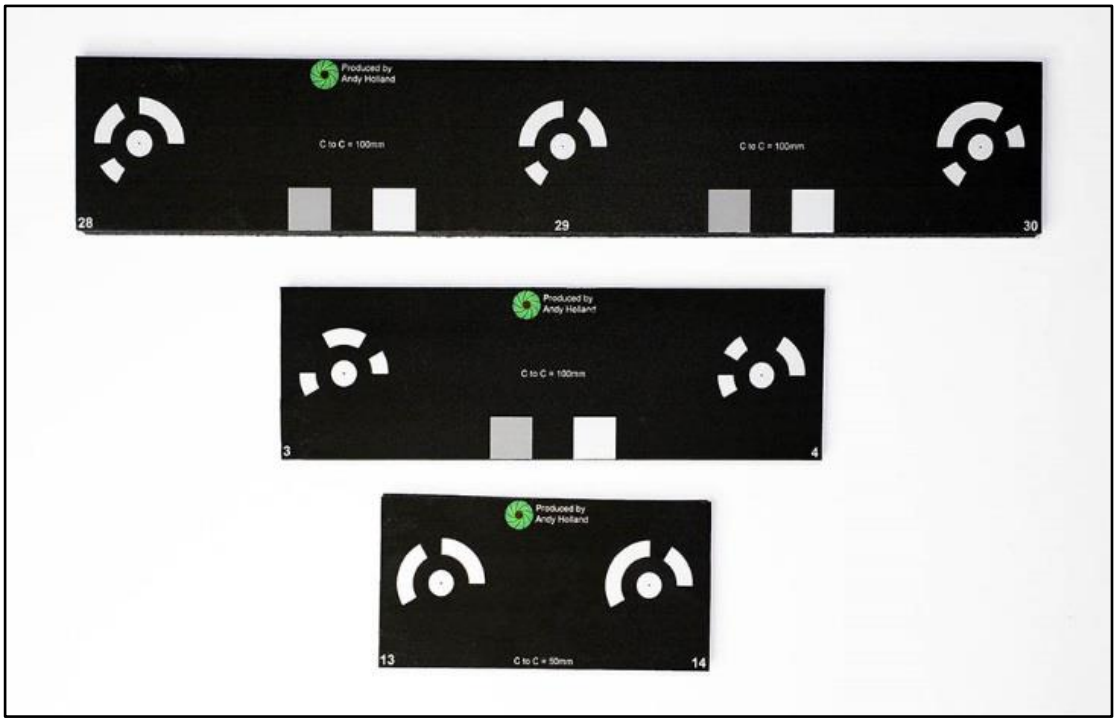

Figure 6.16: 12 bit circular encoded photogrammetry photo scales custom made for the research (source: author).

Photo scales were initially included in all the photos taken during the photogrammetric recording, however, during the first tranche of post processing in PhotoScan, movement in the scales was noted. The movement occurred through centripetal force on the rotating turntable and the scales were so light that the small movement of the turntable was sufficient to displace them radially in small increments making the markers on the photo scales inaccurate. The use of photos scales was therefore no longer included in all photographs. The centre distances were still of value in calculating some metric parameters within PhotoScan. An additional photograph per rotation was therefore included with a marker to facilitate better error calculations.

6.3.3. Camera and lens calibration

All camera lenses have some level of distortion inherent in their design. The level of this distortion, and that of the camera body itself, must be accounted for through camera calibration when calculating interior and exterior orientations of the cameras in order to accurately calculate the collinearity equations for each point.

Within the Agisoft PhotoScan software (Agisoft LLC, St. Petersburg, Russia) photogrammetry workflow, camera and lens calibration is automated within the alignment and optimisation stage (section 6.3.4.2) (Agisoft 2016). The lens and camera data are extracted from each photographs metadata (EXIF or XML) and the calibration parameters, including skew transform, radial and tangential distortion coefficients are calculated using the Brown model of lens distortion (Brown 1966, Hugemann 2010).

6.3.4. Photogrammetric reconstruction

Photogrammetric 3D reconstructions of the samples were created using Agisoft PhotoScan Professional version 1.2.3 (Agisoft LLC, St. Petersburg, Russia). This program provides a full workflow from image import to 3D reconstructed model export. The photogrammetric processing workflow was:

- Import of photos;
- Masking;
- Alignment and optimisation;
- Dense point cloud calculation;
- Meshing and texturing; and
- Export.

6.3.4.1. Photo import and masking

The photos of both posterior and anterior view orientations of bone specimens were imported into Agisoft PhotoScan. Each photo had a plain black background, although some detail of the black felt sample supports remained visible. Prior experience with Agisoft PhotoScan showed that slight variations within the black background and the edges of the supports can be erroneously identified as tie point features and thus result in failed photo alignment. Alignments (and feature identification) can be constrained to specific regions of the photos through the application of an image mask, eliminating the identification of false tie points in the backgrounds (Agisoft 2016). The image masks for each photo were created through a Boolean difference operation

between an empty scene photograph and each image, using a difference threshold value of 35.

The resultant mask occasionally masked off dark areas of a bone samples or included highlight reflections within the background. The masks were manually edited to correct these errors. The earliest processed samples included encoded marker photo scales in the images. The coloured areas of these were not masked off and also had to be manually added to the masking once the movement of the markers was identified as a source of error (section 6.3.2).

6.3.4.2. Alignment and optimisation

Following photo masking the “Align Photos” function was applied. This function applies several processes to build a sparse point cloud of tie points identified within the images.

The camera and lens calibration was calculated and applied (section 6.3.3), before the images were analysed and feature points on the images identified and characterised relative to the surrounding pixels. The interior and exterior orientations for each feature point were calculated using bundled collinearity equations (section 4.3.3.1), and the distribution of feature points in each image was compared during the alignment process. The alignment uses an iterative least squares method to refine camera positions in the object coordinate system. The threshold for the iterations of the alignment were determined by the user set accuracy setting. For the alignment of the models in this research the accuracy setting was set to high.

Once complete the sparse point cloud made of tie points was displayed with the reconstructed position of each of the images (termed ‘cameras’ in PhotoScan). The photographic setup used to photograph the samples was then expressed in the spherical shape of the collective image positions in the 3D object coordinate system space (figure 6.17).

The sphere arrangement of the images occurs where the photogrammetric reconstruction is successful. However, in some instances the alignment could not distinguish between the photos of the samples in the anterior view and the

posterior view orientations. In these instances the reconstructed image positions appear as two superimposed hemispheres of images (figure 6.18).

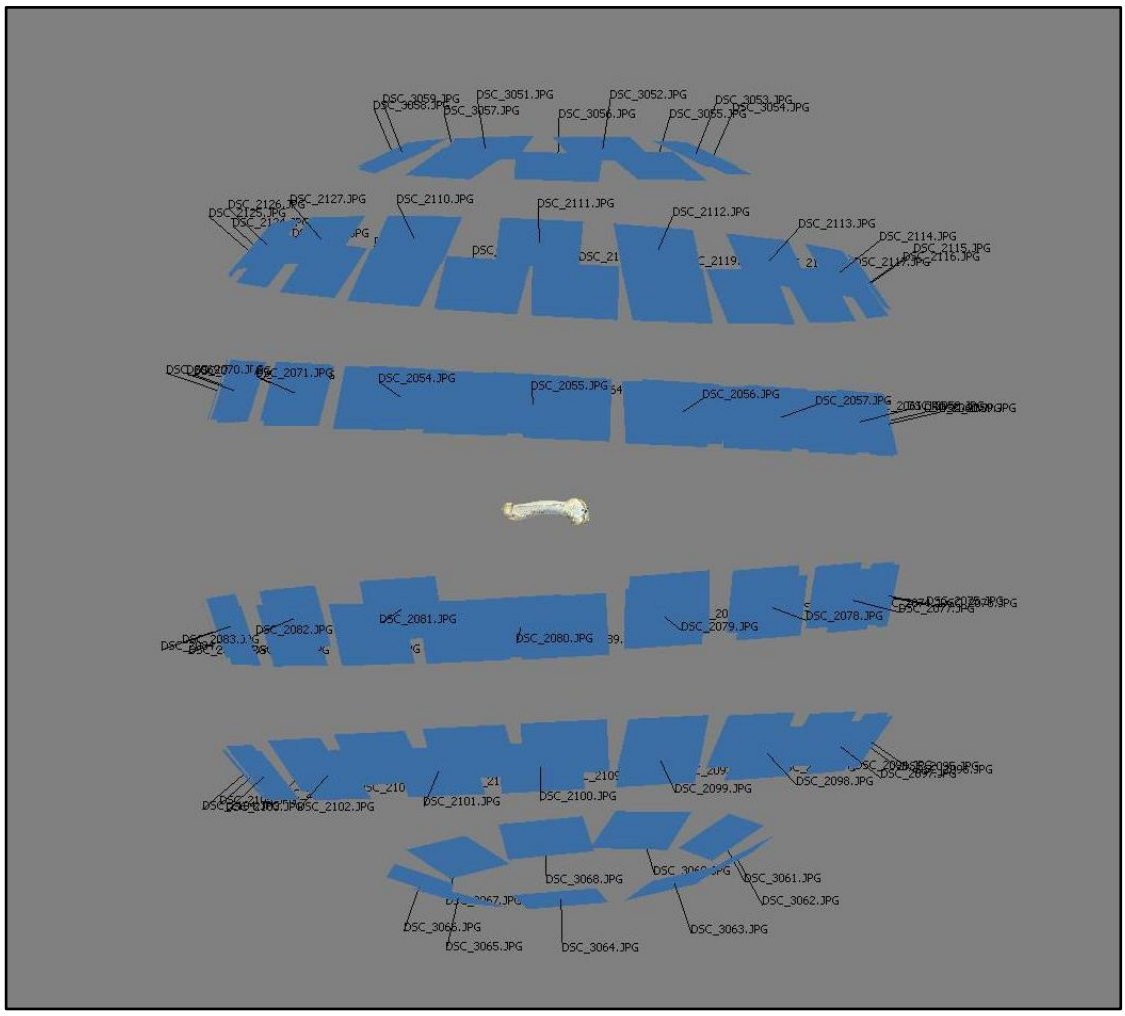

Figure 6.17: The camera positions used in the photographic recording of samples results in a sphere of image positions in the reconstructed 3D object coordinate system space (source: author).

Two approaches were used to rectify this: manual tie point markers common to both orientations were identified and added to the images and the alignment re-run; or the images from each orientation were divided into separate 3D objects which PhotoScan refers to as “chunks”. These chunks were then treated separately for the dense cloud calculations (section 6.3.4.3) and the dense cloud geometry was used to align and then merge the two chunks. Alignment of the two orientations relied on the identification of common tie points between the images of each and therefore failure to align was derived from a poor feature density within the images. The need to “chunk” the images is an indicator of the qualities of either the photography or the object surface.

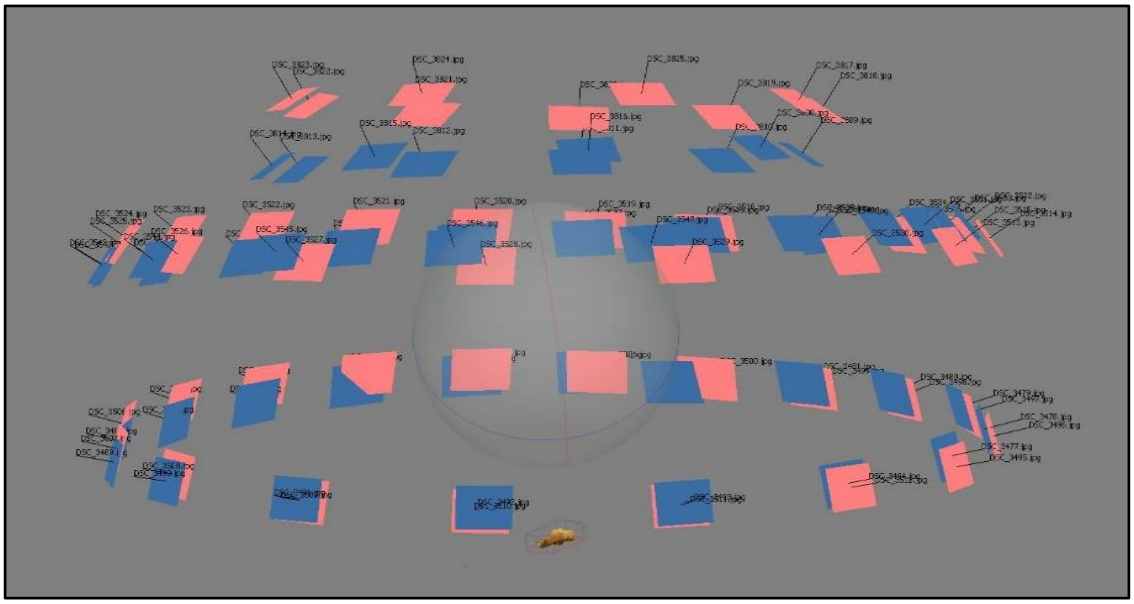

Figure 6.18: Failure to distinguish images photographed in different orientations results in two superimposed hemispheres. Anterior orientation images highlighted in pink, posterior orientation images in blue (source: author).

The alignment process produces a sparse cloud of tie points that exhibit some misaligned areas. Photographic images that had poor alignment appeared to be out of position in the spherical pattern and were individually realigned. Additional incorrect tie points (figure 6.19) were manually selected within the sparse cloud and deleted to improve the quality of the dense point cloud calculation.

Figure 6.19: Incorrect tie points in the sparse cloud appear as noise (source: author).

In some instances despite significant amounts of this user intervention to manually realign and edit the sparse cloud, the photogrammetric reconstruction of the bone sample failed to produce an alignment of cameras that resulted in sufficient tie points. After chunking and further user intervention the resulting dense cloud still had significant errors which prevented successful realignment of the chunks and production of a full 3D model. After several attempts, photogrammetric reconstruction of these samples was deemed to have failed.

6.3.4.3. Dense point cloud calculation

Once the alignment was complete and the sparse cloud had been manually cleaned of incorrect points, the ‘Build Dense Cloud’ function was applied to the sparse cloud (or to each chunk sequentially in the case of chunked models). This function builds a dense point cloud by extrapolation of the pixels between tie points in the sparse point cloud (figure 6.20). Imprecisely plotted points were manually selected within the outputted dense cloud and deleted to improve the quality of the meshing.

Figure 6.20: The dense cloud for sample A0029_PtG01 (source: author).

For those models that were reconstructed in two chunks (section 6.3.4.2) the “align chunks” function was applied. Where this alignment was successful the

chunks were merged before meshing. Where the alignment failed, additional common tie points were identified and used to align the chunks.

6.3.4.4. Meshing and texturing

Meshing of the dense point cloud into a 3D surface meshed object was carried out using the arbitrary mesh generation option which uses a triangulated irregular network meshing system using Delaunay triangle calculation to produce a mesh. The meshes were automatically UV unwrapped and textured to produce a complete 3D model of the sample (figure 6.21). The final model was exported, using the sample and fragment numbering system in the filename, in .obj format with a single 4096 x 4096 pixel merged texture file in .png format.

Figure 6.21: A meshed and textured model of A0029_PtG01 (source: author).

6.4. Post processing and comparison

The results of the digitisation of the experiments at each phase, recorded by each of the instruments, were output to 3D mesh .obj models with units defined in millimetres. To analyse the models and to assess the variation in the quality and response of the instruments to each taphonomic change, the analysis of the models was carried out in MeshLab version 1.3.3 (ISTR/CNR, Pisa / Rome) and CloudCompare V2 version 2.6.1 (CloudCompare.org, Paris).

MeshLab is an open source programme suite of 3D graphical and computational mathematics tools for the processing of 3D meshed objects. MeshLab was developed specifically for research into 3D data and therefore offers advanced research tools over commercial 3D graphical programme suites (Cignoni et al. 2008; Ranzuglia et al. 2013).

CloudCompare V2 is an open source programme suite of 3D graphical and computational mathematics tools for the analysis and comparison of 3D data. Whilst it is most commonly used for analysing point cloud data (e.g. such as that from terrestrial laser scanning) many of the tools can be applied to the surfaces of meshed 3D objects, or to point clouds sub-sampled from those 3D meshed object surfaces.

Like MeshLab, CloudCompare V2 was developed for research and a number of tools were common to multiple analyses. The common tools are described in more detail below and referenced in the analysis sections that used them.

6.4.1. Point-Pair Registration tool

The Point-Pair Registration tool is used to align two 3D models through the manual selection of pairs of equivalent points on the two models (figure 6.22). One 3D model is set as the reference to which the other model is aligned. The tool requires the identification of a minimum of three equivalent pairs of points on the model's' surfaces and then uses the angle and distances between points on the surface to align and match the two models together. The tool applies the alignment to both mesh and point cloud 3D models. For point clouds the user selects corresponding points directly, and for meshes the position of a user

identified point is projected onto the surface of the polygon within the mesh surface rather than the position being estimated to the nearest neighbouring vertex. The tool only calculates distances between the corresponding points and not the underlying mesh or point cloud geometry. Where the distances and angles between the three corresponding points is not exactly the same and a perfect match cannot be made, the tool determines the best fit between the selected pairs of points through the application of a least squares calculation.

The positional accuracy of the placement of the pairs of points by the user is therefore the limiting factor to the accuracy of the alignment; the tool is best suited as an initial alignment between meshes or for aligning identical (i.e. cloned) meshes. The result of the alignment of the two models is expressed as a Root Mean Square (RMS) distance measure for the selected points from those of the reference model (CloudCompare.org 2015).

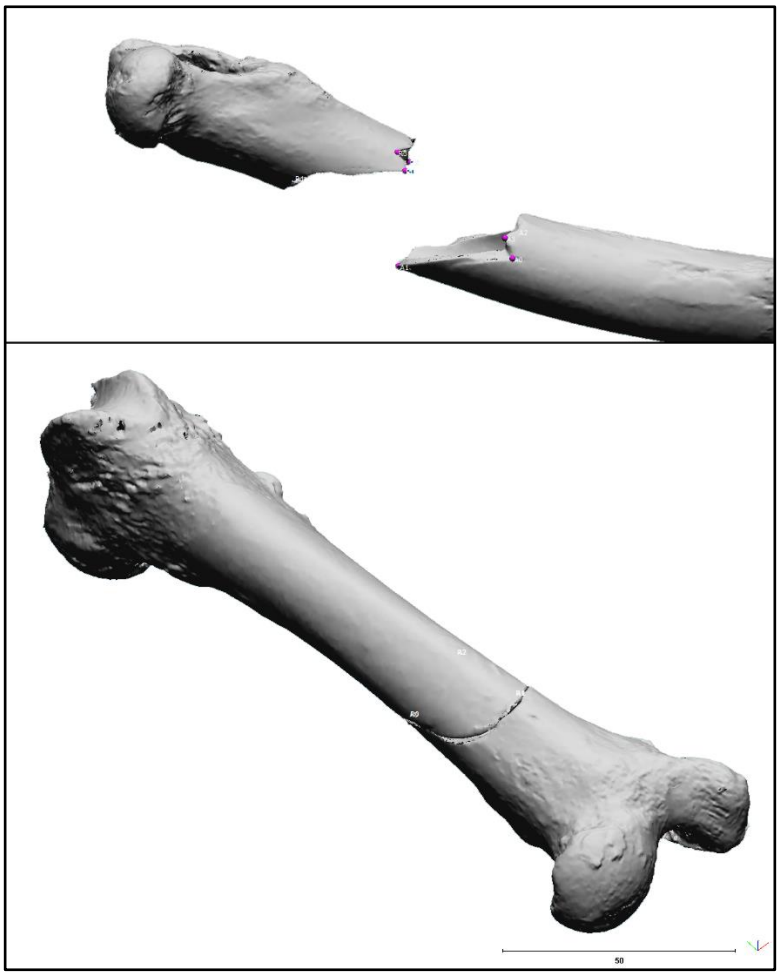

Figure 6.22: Using the Point-Pair Registration tool to select pairs of corresponding points on the refitting fracture surfaces to two fragments of sample A0013 (top) to initially align the fragments (bottom). Scale bar in mm (source: author).

6.4.2. Iterative Closest Point Fine Registration tool

The Iterative Closest Point Fine Registration tool is used to carry out fine alignment between two mesh or point cloud objects by minimizing the total difference between them. Whilst the Iterative Closest Point algorithm on which the tool is based was designed to be applied to point clouds (Chen and Medioni 1992; Besl and McKay 1992), CloudCompare applies it to meshes by automatically sampling the meshes in the back end of the application and creating a temporary point cloud for each mesh on which the Iterative Closest Point algorithm can be applied (CloudCompare.org 2015).

The tool is an iterative process starting with matching each point in the cloud of the surface being aligned to a nearest neighbour in the reference cloud. The distance between all the neighboured points is determined, outlier points are rejected and the translation and rotation that produces the nearest distance between all the points (by means of a least squares calculation) is estimated. The transformation is then applied and the root mean square distance and total surface overlap is calculated. The sequence is then repeated (iterated) until an iteration achieves the user defined thresholds for the alignment.

In CloudCompare V2 the user defined thresholds are the difference in root mean square distance between successive iterations and the surface overlap between the two surfaces measured as a percentage of the total surface of the aligning surface.

The result of the fine alignment of the two models is expressed as a root mean square (RMS) distance measure for the selected points from those of the reference model (CloudCompare.org 2015).

6.4.3. Point Sampling on Mesh tool

Some operations within CloudCompare V2 require point cloud data as an input; However, the 3D models for experimental and site based samples were imported as surface meshed .obj 3D models. The easiest method to convert a mesh to a point cloud is to remove all the faces and use the vertices as the

point cloud, however, this results in a lower density point cloud that limits the resolution of most analysis tools.

CloudCompare V2 provides the *Point Sampling on Mesh* tool to provide higher density conversion of a mesh to a point cloud. A user defined number of points (or a point density) are evenly distributed over the surface of the mesh object resulting in a point cloud that conforms to the surface topography of the original mesh and with a greater density than the vertices of the original (figure 6.23). Normals are then generated either independently on a per point basis or inherited from the source mesh.

The number of points selected for all experiments was set at 1,000,000.

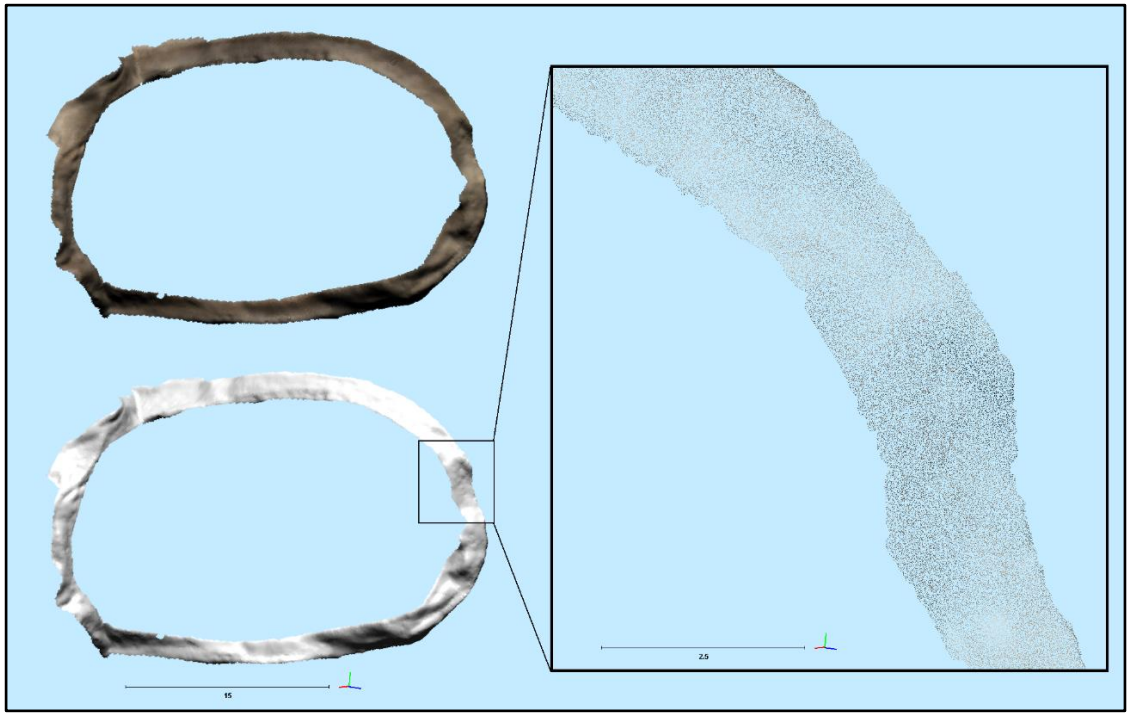

Figure 6.23: Point Sampling on Mesh in CloudCompare V2. The refiting fracture surface across the cortical thickness of the diaphysis of sample A0013_F02_StL04 after being isolated from the rest of full fragment model using the Segment tool (top left); a dense point cloud derived using the Point Sampling on Mesh tool from the isolated fracture surface (bottom left); close-up of point cloud showing high point density within the point cloud of the samples isolated fracture surface (right). Scale in mm (source: author).

6.4.4. Distance analysis

The distance between point clouds, a point cloud and a reference mesh, or between a point cloud and a mathematically defined flat plane, provides the data for analysis of both refit quality and the effect of influencing factors (colour, opacity etc.) on surface variation. CloudCompare V2 calculates the distance through the *Cloud to Cloud Distance* or *Cloud to Mesh Distance* analysis tools. The *Cloud to Cloud Distance* tool calculates the Euclidean distance between each point and its nearest neighbour within a spherical neighbourhood domain of the reference cloud, whilst the Cloud to Mesh Distance tool calculates the distance from a point to the intersect with the reference mesh (figure 6.24). The distance between a point and its nearest neighbour, which may be offset to one side, does not provide the true distance between the two clouds and therefore introduces small imprecision error to the overall results. Cloud to Mesh Distance analysis overcomes this as the distance is calculated to the mesh surface rather than a point that might be offset and therefore Cloud to Mesh Distances provide more accurate results (figure 6.24).

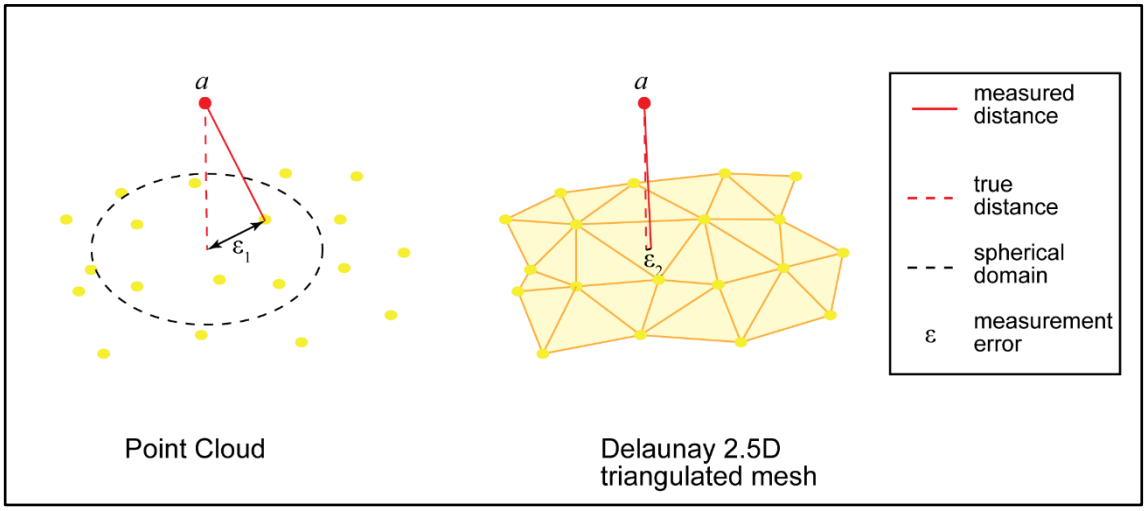

Figure 6.24: Comparison of Cloud to Cloud and Cloud to Mesh Distance analysis methods. Measured distances between a point and its nearest neighbour in Cloud to Cloud Distance analysis may not as accurately reflect the true distance (left); Cloud to Mesh Distance analysis produces a measurement from the point to the nearest mesh surface resulting in more accurate data (i.e. $\varepsilon_1 > \varepsilon_2$*)* (adapted from CloudCompare.org 2015, page 30).

6.5. Volume and Area

The computation of surface area and volume in 3D models is a non-trivial computational mathematics problem in itself, with considerable variation between differing methods for their calculation. Variations in the implementation of the computational mathematics occur between programme applications including between MeshLab and CloudCompare V2. Therefore to ensure comparability, the determination of the surface area and total model volume for all samples was calculated in MeshLab using the *Compute Geometric Measures* tool from the *Quality Measure and Computations* filter. The volume and area calculations were carried out prior to the noise calculation and therefore variations in volume and area will reflect both digitisation quality and the level of noise within the 3D data.

For an in-depth discussion of the complexity of accurately calculating volume and surface area in 3D models see Zhang and Chen (2001).

The volume and area data for the whole bones is included in appendix G. Volume and area data was not relevant or appropriate for the fragmented bones as the digitisation of those samples included the additional fracture surfaces and internal bone surfaces.

6.6. Noise

The level of noise in the 3D digitised samples was calculated from the change in the total number of vertices and faces within the model before and after a standardised set of noise clean-up operations were performed in MeshLab.

The .obj files for each instrument's model of each sample were opened in MeshLab and the volume and area (section 6.5) were calculated. The total number of vertices and faces were then recorded and the following sequence of clean-up operations from the *Cleaning and Repair* filters menu were applied:

- Remove duplicate faces;
- Remove duplicated vertices;
- Remove zero area faces;
- Remove unreferenced vertices;
- Select self-intersecting faces;
- Select non-manifold edges; and
- Select non-manifold vertices.

Following each of the "Select" operations the *Delete Current Set of Selected Faces and Vertices* operation was executed. Each of these operations removed small numbers of noise derived faces or vertices within the 3D mesh and therefore the total number removed faces and vertices represents the level of noise within the 3D meshed object from each instrument. These operations cover the main categories of noise within meshed 3D data excluding edge noise. The difficulties of quantifying edge noise and its impact on 3D object mesh quality are discussed in chapter eight.

The total number of vertices and faces remaining in the 3D mesh was recorded and the reduction in the number of vertices and faces was calculated in Microsoft Excel as a percentage of the original number, representing the level of noise present in the data. The measured noise data is included in appendix G.

6.7. Surface roughness and surface variation analysis

The variation of recorded points forming the surface of a digitised object reflects both the true surface roughness of the object as well as the colour, noise, and opacity qualities of that surface. Distinguishing between the influences of these three factors on surface variation is important to understand the challenge they pose to the quality of fracture surface refitting in fragmentary bone. To examine the impact of each of these factors on digitised materials and therefore consider how they interact, surface patches of known surface roughness (section 5.5.3.2) were digitised; their surface variation (section 6.7.1) was compared to surface patches digitised from flat planar samples, with variations in colour (section 6.8.3) or opacity (Section 6.9.3). To ensure that the measured values were comparable, a common surface variation measurement process was used (section 6.7.2).

6.7.1. Roughness technique comparison standards

The nine surface roughness samples (section 5.5.3.2) were glued to a backing sheet of white plastic card to hold them in a flat plane. They were digitised with each of the techniques and segmented in the capture software to produce a single .obj model file for each of the samples. The models were imported into CloudCompare V2 and upon import the models were aligned in a row reflecting their relative positions during scanning. The *Translate-Rotate* tool was used to move each of the samples to the centre of the virtual space and then to orientate each of them to the local x,y,z axes.

The macro structured light scan for the lowest numbered sample (S0011_MLS01) was used as a reference and the *Point-Pair Registration* tool was used to initially align all the other samples to it. The dimensions of the abrasive cloth samples were equal and the corners of the samples could be used as the common points for the alignment.

The *Segment* tool was used on all the samples simultaneously to produce an exactly equal sized surface patch, removing the digitised plastic card backing and a small boundary at the edges of the abrasive cloth samples where there was greater variation in the flatness and adhesion.

A flat plane was fitted to the surface patch from sample S0011_MSL01 using the *Fit - Plane* operation from the *Tools* menu. The plane was used as a reference to refine the alignment of the other sample surface patches utilising the *ICP Fine Registration* tool. The *Point Sampling on Mesh* tool was used to convert each of the patches to a point cloud and the surface variation was determined using the common methodology for surface variation outlined in section 6.7.2.

The measured data for the surface variation of the samples was recorded in Excel (appendix F) and compared to the SEM measured values of surface roughness described in section 5.5.3.2 (table 5.2).

6.7.2. Common surface variation analysis

The analysis of surface variation of the opacity, colour and surface roughness samples was carried out following a common process outlined in this section to avoid duplication in other sections.

Prior to this process, each of the samples from the three types of technique comparison standards had been segmented into surface patches, aligned to a common fitting plane in the front orientation in CloudCompare V2 and converted to a point cloud (sections 6.7.1, 6.8.3 and 6.9.3).

The response of each digitisation instrument to the surface roughness patches showed full digitisation of the surface of all samples. None of the samples had any gross noise artefacts or holes within the mesh. Whilst the samples were glued to a flat piece of plastic card, some showed responses due to deviations from a flat plane. In these instances the non flat areas (at the edge of the sample patch) were removed with the Segment tool in CloudCompare V2.

The fitting plane is a mathematically flat surface that acts like a single polygon mesh. The use of it as the reference for the fine alignment for each of the surface patches aligned them such that the plane intersected them at approximately the mean point of the surface variation (figure 6.25).

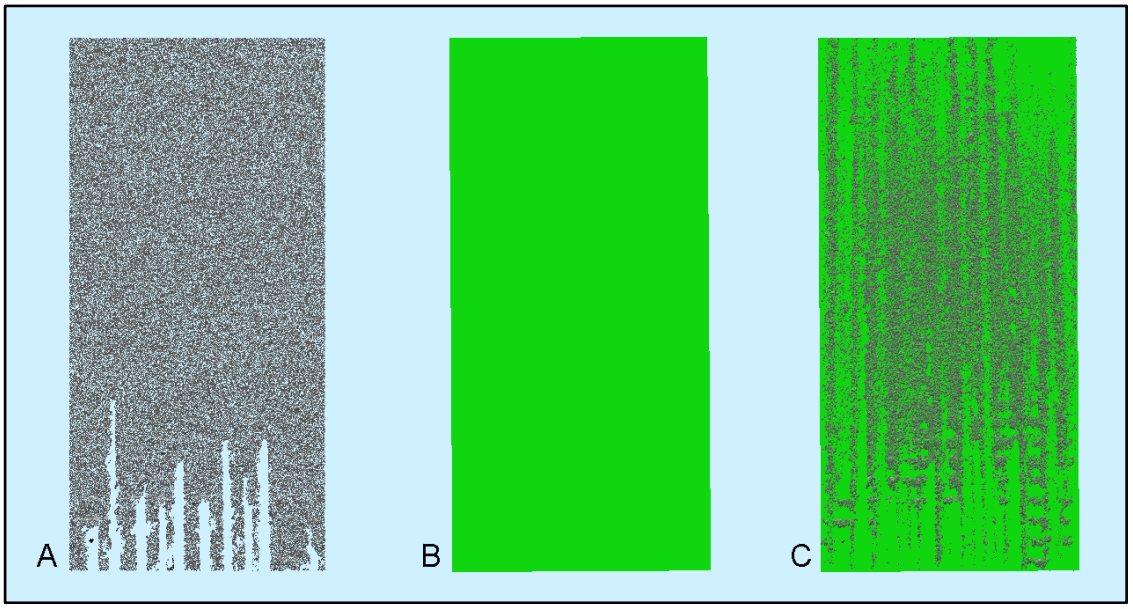

Figure 6.25: Fitting a plane to a sample surface variation patch. A. The surface variation patch for S0011_MSL01; B. The fitting plane matching the dimensions of the patch; C. The surface variation patch aligned to the fitting plane. The plane intersects the sample at the approximate mean point of surface variation resulting in some of the point cloud protruding above the plane and some protruding behind the plane and therefore hidden by it in this view (source: author).

The Cloud to Mesh Distance tool was used to calculate the surface variation of the sample surface patches above and below the flat fitting plane (section 06.4.4) and therefore equates to the surface roughness of the sample. The statistical analysis produced both mean and standard deviation signed distances between the cloud points and the fitting plane and applied them as a symmetrical scalar field colour scale to the surface of the point cloud with the colour thresholds set at plus and minus 0.1 mm (figure 6.26).

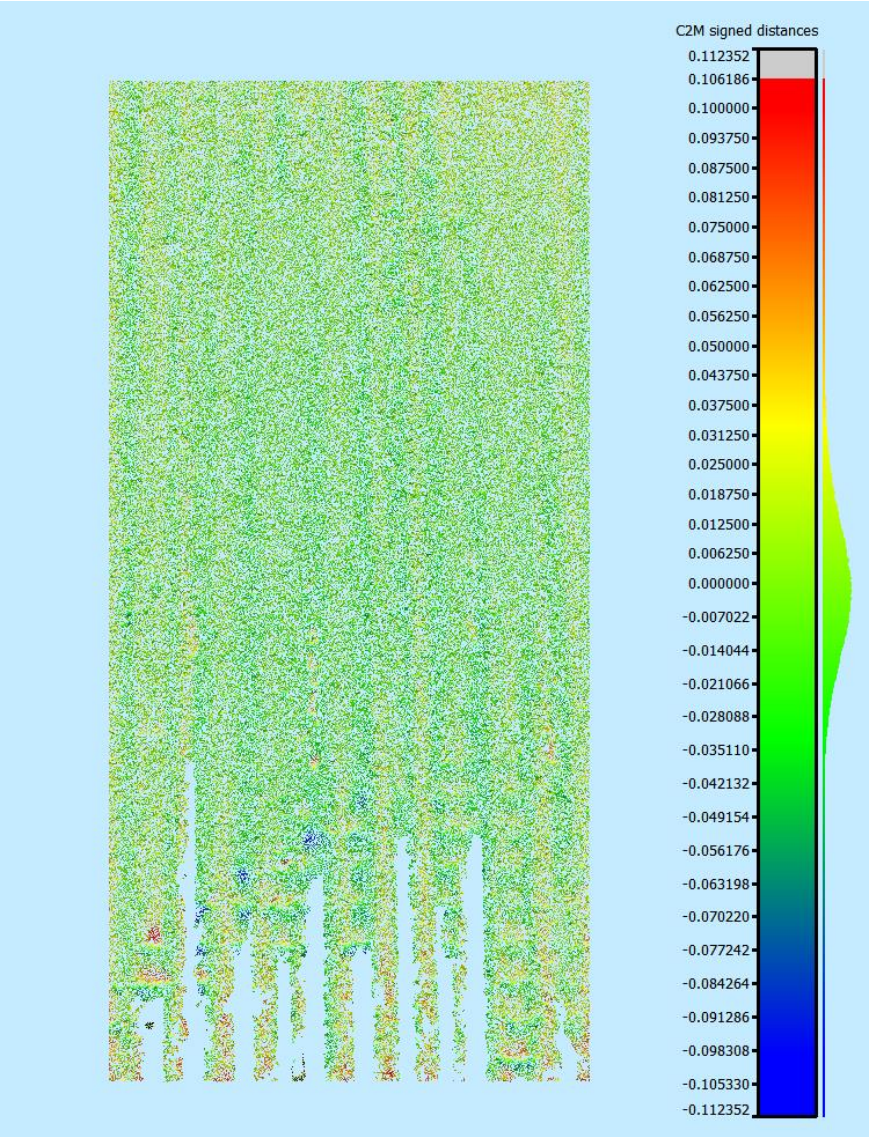

Figure 6.26: A symmetrical scalar field blue-green-yellow-red colour scale of the signed cloud to mesh distance for a surface variation patch of sample S0011_MSL01 (source:author).

In some samples the fitting did not fully overlap the extreme edge of the point cloud resulting in a maximum high or low value for the variation. These outliers for the distance distributions were removed from the data through the *Filter Points by Value* tool. The calculated mean and standard deviation of the distances between the patch and the fitting plane were recorded in Excel (appendices D, E and F).

6.8. Colour

Colour theory and the recording of the colour of objects in absolute terms is a complex problem with a wide and detailed literature and is beyond the scope of this thesis. Colours are described in digital systems in regards to the mixing of the three primary colours (red, green and blue) usually in 8 bit values (i.e. 0 to 255). Colour in physical objects is the interaction of light with the chemical and physical structure of the surface of the object and is hugely variable by the range of wavelengths in the incident light, the angle of the light, the angle of the observer, temperature and a wide array of other variables. Additionally, the colour recorded in a digital instrument can have an infinite number of solutions to the mix of colour wavelengths of light that produced that colour response from an object.

A final complication is that human vision does not perceive all wavelengths in the visible spectrum equally. The digital sensors we build to record images of the world incorporate these same variations in colour perception so that the produced images look natural. Therefore, measurement of the colour of a sample for comparison of the colour value to the response of a digitisation instrument to the sample is complicated by these factors.

To address this the colour of the samples was considered in relation to the variation in the lightness of the colour between black and white and a general description of the response of the digitisation instrument to sample colour variation.

6.8.1. Colour lightness calculation

Lightness can be described as a point on a scale between black and white. However, colour values are defined in a three dimensional colour space. In r,g,b colour spaces, the three dimensions are defined by axes for each of the three primary colours with values from 0 to 255. The resulting cube of three dimensional colour space places black at the origin (0,0,0) and white at the opposite corner (255,255,255) (figure 6.27).

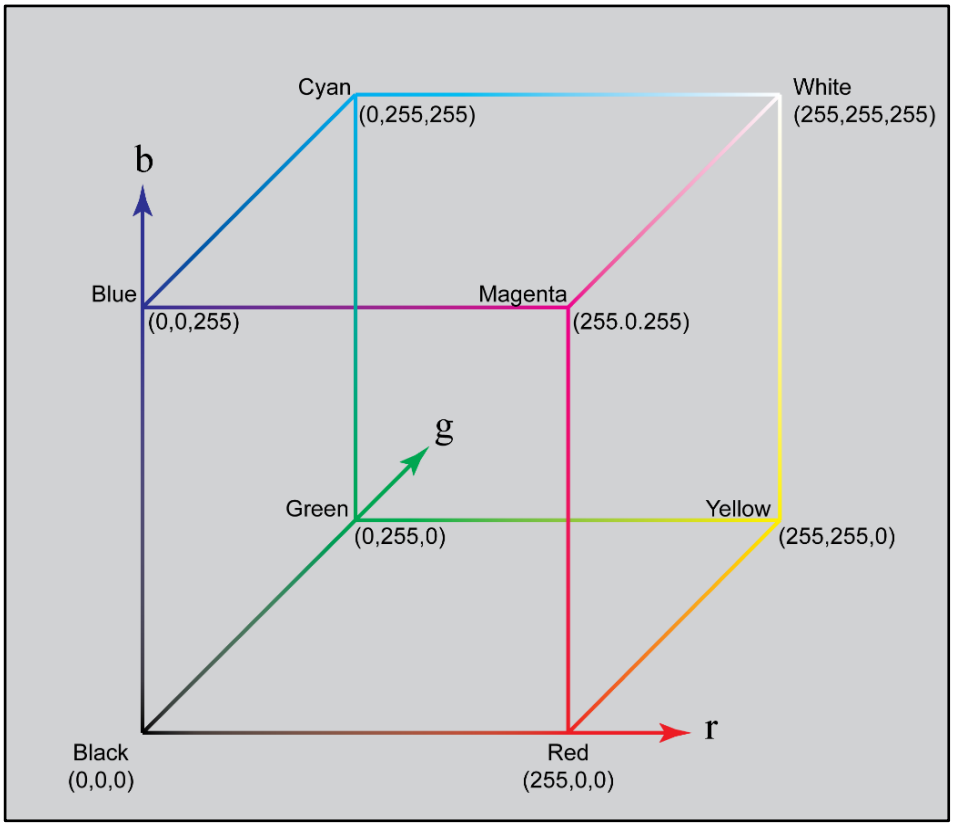

Figure 6.27: Three dimensional r,g,b, colour space with black at the origin and white at the maximum value of all axes (source: author).

The lightness of a colour value is therefore described by the Euclidean distance between the measured value plotted in 3D colour space and the black point.

The measured r,g,b values in camera systems have a gamma 2.2 correction applied to them to make the colours appear correctly on emissive devices such as computer screens (Sonka et al. 2015). This correction results in a gamma compressed r,g,b colour space which must be converted back to uncompressed values before the lightness can be calculated. The gamma correction was reversed for all the r,g,b values by multiplying them by 0.4545455 (the reciprocal value for 2.2) (Sonka et al. 2015).

The intensity to lightness conversion in camera sensors (based on the sensitivity curves for the r,g,b elements in each sensor pixel) for the three primary colours is not uniform (reflecting the tristimulus colour perceptions in human vision) and therefore the linear distances within each of the dimensions of the 3D colour space must be calculated with reference to a weighting factor based on colour perception variations for the visible spectrum (Nixon & Aguado 2012; Petrou & Petrou 2010).

The Euclidean distance from the black point for each r,g,b colour point in uncompressed gamma r,g,b, colour space was therefore calculated as:

$$\text{Lightness} = \sqrt{(r^2 \times 0.299) + (g^2 \times 0.587) + (b^2 \times 0.114)}$$

The resulting value was divided by 255 to scale the values to a range of 0 to 1 with 0 designating no lightness (i.e. black) and 1 being fully light (i.e. white).

6.8.2. Colour variation in the experimental samples

For the experimental bone samples colour varied across the surfaces of the bone. To measure the colour variation, the samples were photographed under fixed and controlled lighting conditions using a copy stand. The camera's exposure was set based on the exposure of an 18% grey card and the white balance was set using a white colour balance card.

The photographs of each bone were imported into Adobe Photoshop (Adobe Systems Inc, San Jose, California, USA) and the colour and exposure were refined using white, grey and black droppers within the *Levels Adjustment* tool. A gamma correction of 0.4545455 was applied and the image was desaturated using the *Black and White* operation in the *Image-Adjustments* menu. The red, green and blue levels could only be defined in Photoshop in terms of integer values and the weighting factors in the lightness calculation were rounded up to r = 30%, g = 59% and b = 11%.

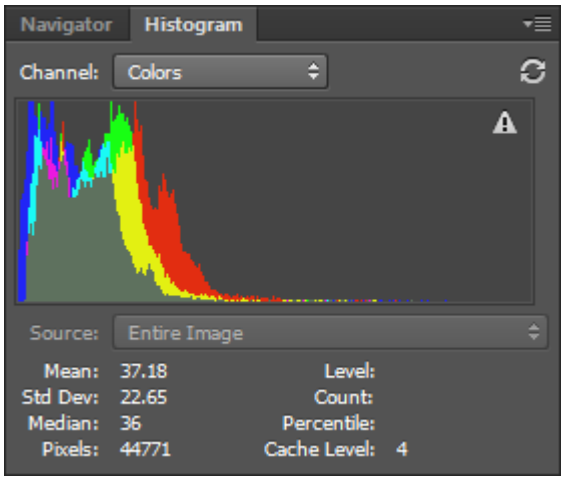

Figure 6.28: The histogram window in Adobe Photoshop showing the tonal range histogram and related statistical analysis (source: author).

The *Magic Wand* select tool was used to select the grey background and the selection then inversed so that only the bone was selected. The Photoshop histogram window (figure 6.28) calculates the tonal range of the selected area of the image and displays both a histogram of the range and the statistical analysis of the tonal range. The mean, median and standard deviation of the tonal range were recorded in Microsoft Excel for each sample.

The measured data are included in appendix H.

6.8.3. Surface variation of the colour technique comparison standards

The Danes-Picta BST13 colour separation guide (section 5.5.1, figure 6.29) was digitised with each of the techniques as a single sample number (S0010). The colour separation guide is made up of two rows of rectangular colour targets with full saturation colours on the bottom row and 25% lightness equivalent colours on the top row (figure 6.29).

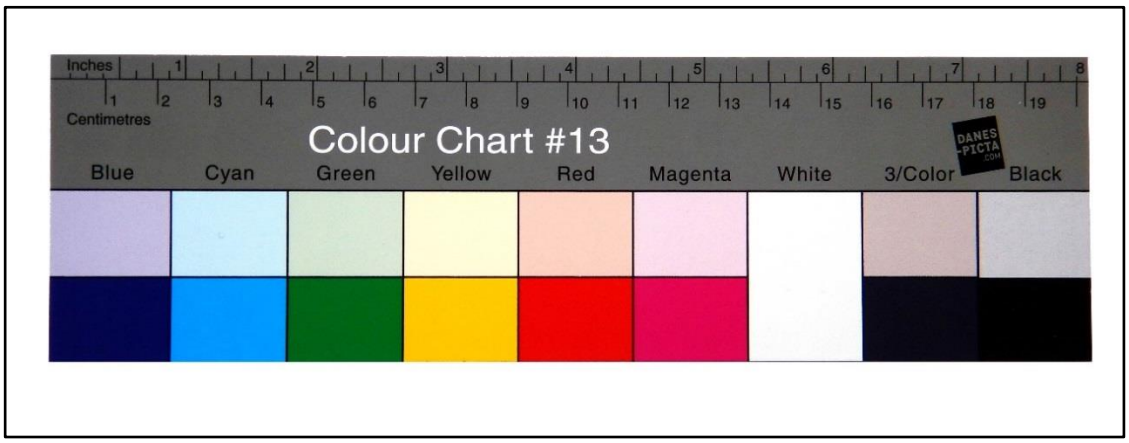

Figure 6.29: The Danes Picta BST-13 colour separation guide used as the technique comparison standard for colour (sample S0010) (source: author).

The digitised versions of the colour separation guide from each instrument were imported into CloudCompare V2 as .obj meshed models. The *Translate-Rotate* tool was used to move each of the samples to the centre of the virtual space and then to orientate each of them to the local X,Y,Z axes. The *Segment* tool was used to separate a uniform size rectangular surface patch from each of the colour targets and the separated surface patches were labelled. The first

surface patch (blue) from the macro structured light scan was used as a reference and the *Point-Pair Registration* tool was used to initially align all the other surface patches to it, using the corners of the patch as the common points for the alignment.

A flat plane was fitted to the first surface patch (blue) of the macro structured light sample using the *Fit - Plane* operation from the *Tools* menu. The plane was used as a reference to refine the alignment of the other sample surface patches utilising the *ICP Fine Registration* tool. The *Point Sampling on Mesh* tool was used to convert each of the patches to a point cloud and the surface variation was determined using the common methodology for surface variation outlined in section 6.7.2.

The measured data for the surface variation of the samples was recorded in Excel (appendix D) and compared to the measured values of their colour and lightness (section 6.8.1 and 6.8.2).

6.8.3.1. Colour - wavelength correlation

The colour technique comparison standard (S0010) used a Danes-Picta BST13 colour separation guide (section 5.5.1). The colours included in the colour separation guide included both primary colours found within the spectrum of visible wavelengths of light and colours that are composed of a mixture of the primary colours. Whilst the potential solutions of the regression of the *r,g,b* values for some of the mixed colours to the wavelengths of light that generated each colour response at the colour patch surface are infinite and therefore impossible to regress, the primary colours (red, green and blue) and those colours that are an equal mix of the primary colours (i.e. cyan and yellow) could be correlated to wavelengths of light within the visible light spectrum. These values were used to describe the general response of the digitisation instruments to colour.

The measured data is included in appendix D.

6.9. Opacity

The 3D digitisation techniques examined in this research measure the response of light to the surface of an object. To assess the response of the instruments in each technique to the variation in the penetration of light into the samples, the opacity of the samples was measured throughout the experiments and compared to a set of known opacity technique comparison standards (section 5.5.2).

6.9.1. Opacity calculations

The opacity (*O*) of a material is defined by the amount of light that it absorbs or scatters, and is the inverse of the transmittance (*T*), the amount of light that the material allows to pass through. The Beer-Lambert law describes the relationship of the transmittance (and hence the opacity) and the optical depth ($\boldsymbol{\tau}$) and the absorbance (*A*) of a material as:

$$T = \phi_e^t / \phi_e^i = e^{-\tau} = 10^{-A}$$

Where ϕ_e^i and ϕ_e^t are the radiant flux received by and transmitted by the sample (Calloway 1997). Additionally, the Beer-Lambert law defines the relationship of the thickness of the sample (*l*) and its attenuation coefficient ($\boldsymbol{\alpha}$) to the optical depth ($\boldsymbol{\tau}$) as:

$$\boldsymbol{\tau} = \boldsymbol{\alpha} l$$

By integrating and rearranging these equations for the measured samples, the attenuation coefficient was determined and could be used to normalise the opacity and transmittance values to a uniform sample thickness by:

$$-\ln(\phi_e^t / \phi_e^i) = (\boldsymbol{\alpha} l)^{-1}$$

The thickness of all samples was measured with a calibrated digital sliding calliper with a resolution of 0.01mm.

6.9.2. Opacity of experimental samples

The opacity of the experimental samples was measured at each of the stages of the experimental taphonomy. For the early phases, prior to the availability of the opacity meter (section 5.5.2.2), small fragments that resulted from fragmentation of the bone samples were retained for later measurement of their opacity without further exposure to the experimental taphonomy conditions.

Opacity was measured through the cortical thickness of the diaphysis of the bones utilising the flattest part of the bone available. The bone was placed in the opacity meter so that the surface was as flat and perpendicular to the direction of the light and to cover the 20mm collimating lens.

Whilst the opacity technique comparison standards were produced to a uniform thickness, the experimental taphonomy bone samples varied naturally in cortical thickness. Taphonomic alterations to the bone then added to, or reduced, the cortical thickness of the bone samples to a range of 1.4 mm to 4.4 mm and introduced differential surface staining and colour change. To compensate for this and to make the results comparable, the bone samples were normalised via the Beer-Lambert law calculations in section 6.9.1.

The measured data of the experimental samples opacity are included in appendix I.

6.9.3. Opacity technique comparison standards

Each of the opacity technique comparison standards was digitised with laser scanning and the two different scale structured light scanners. The standards were photographed for photogrammetry alongside photogrammetry scales and markers fixed in place to the rotary turntable base board (section 6.3.2) following the same method as that used for the experimental samples (section 6.3). The requirement for a uniform smooth surface which eliminated variables other than opacity in the standards, also eliminated surface imperfections or colour variations useable as feature identification points in the photogrammetric reconstruction of the samples. PhotoScan was unable to identify tie points to reconstruct the models (section 6.3.4) and there were insufficient points that

could be manually identified. In all the opacity samples the photogrammetry process failed, producing a dispersed cloud of white points (figure 6.30).

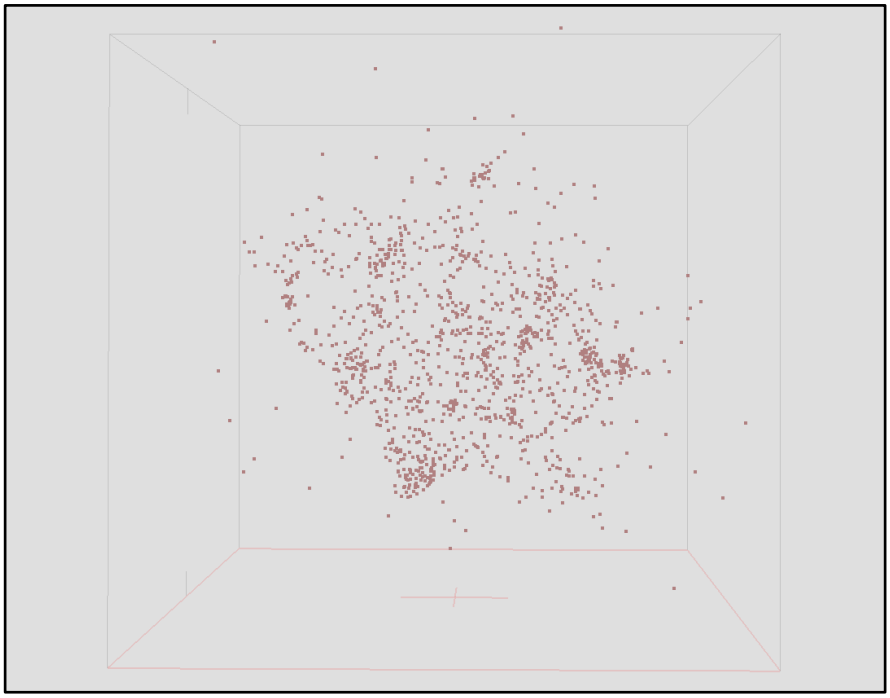

Figure 6.30: Failed photogrammetric reconstruction of the opacity technique comparison standards sample due to a lack of identifiable surface features (source: author).

The 3D mesh models from laser scanning, structured light and macro structured light for each sample were imported into MeshLab and CloudCompare V2.

In MeshLab the dimensions of the samples for each digitisation instrument were measured using the *Measuring* tool from the toolbar. The samples were measured at the same points as the physical samples described in section 5.5.2.3 (figure 5.27) and the measurements recorded in Excel for comparison to the physical measurements (appendix E).

In CloudCompare V2, upon import, each model was located in a different part of the 3D coordinate space and the *Translate-Rotate* tool was used to move each of the samples to the centre of the virtual space and then to orientate each of them to the local X,Y,Z axes.

The macro structured light scan for the lowest numbered sample (S0011_MLS01) was used as a reference and the *Point-Pair Registration* tool was used to initially align all the other samples to it using the top corners as the common points.

Each sample had been mounted on a plastic card base with the opacifier percentage in one corner in black marker pen (section 5.5.2.1) and the sharp contrast between the black pen and the white plastic card produced clearly identifiable variation or holes in the 3D mesh of the models. The marks were used to ensure that all samples were equally orientated. The *ICP Fine Registration* tool was used to refine the alignment between all models and the selected reference model (S0011_MSL01).

The plastic card bases varied in size and needed to be removed from the 3D data to prevent them from influencing the measured values for the response of the instruments to the varied opacity samples. The *Segment* tool was used on all the models to remove the digitised plastic card bases (figure 6.31). The samples were all segmented at the same time slightly above the join to the base and removing a short distance at the bottom of each sample to produce a uniform and consistently sized set of samples. Any variation in the calculated volume or area of the samples would therefore be limited to the instrument's response to the sample opacity.

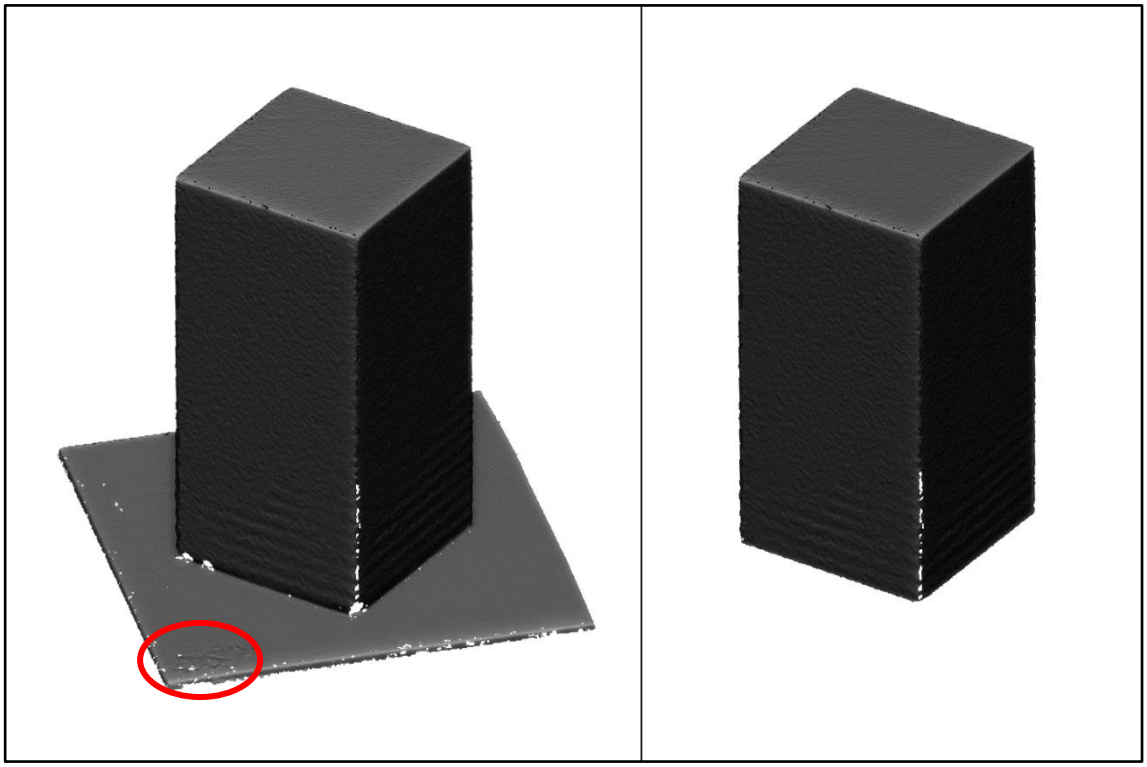

Figure 6.31: Removal of the opacity technique comparison standards base plate with CloudCompare V2 Segment tool from sample S0011_StL01. Sample with plastic card base including the corner marked with the percentage opacifier (red circle) used to orient and identify samples (left); sample with the base removed (right) (source: author).

The CloudCompare V2 workspace was saved at this point and the samples were exported as .obj models and imported into MeshLab. The MeshLab *Compute Geometric Measures* tool from the *Quality Measure and Computations* filter was used to determine the total surface area and volume. The surface area and volume of the samples were recorded and the variation between samples was calculated in Excel (see appendix E).

The CloudCompare V2 workspace was reloaded and the Segment tool was used to cut the sides of the parallelepiped blocks into equal sized surface patches. A flat plane was fitted to the front patch (i.e. that aligned with the front view in CloudCompare V2) from sample S0011_MSL01 using the *Fit - Plane* operation from the *Tools* menu.

The plane acted as a reference to align the other sample surface patches into a common alignment utilising the *Point-Pair Registration* tool using the corners as the corresponding points. The *ICP Fine Registration* tool was used to refine the alignment of the patches to the fitting plane. The *Point Sampling on Mesh* tool was used to convert each of the patches to a point cloud and the surface variation was determined using the common methodology for surface variation outlined in section 6.7.2.

The measured data for the surface variation of the samples was recorded in Excel (appendix E).

6.10. Refit analysis

The analysis of refit quality for refitting fragments of bone was carried out on experimental samples from each of the taphonomy experiments and for the samples from the three archaeological or palaeoanthropological sites.

The meshed 3D models of the refitting fragments were imported into the CloudCompare V2 software package. Normals were recalculated for the models of each fragment on a per-triangle basis using the *Compute Normals* function. The per-triangle calculation preserves a hard tessellated appearance which aids feature identification and later alignment. If a fragment model did not have an associated colour texture (i.e. Laser scan models etc.) a mid-grey (r = 172, g = 172, b =172) colour material was applied to the fragment to further aid feature identification.

6.10.1. Orientation and alignment

The *Translate-Rotate* tool was used to move each of the fragments to the centre of the virtual space in CloudCompare V2 and orientate each of them to the local X,Y,Z axes. The fragment with the lowest fragment number was chosen to be the reference fragment (i.e. to remain in a fixed position) and the other fragment(s) were orientated using the *Translate-Rotate* tool so that their refitting surface was roughly aligned to the corresponding surface on the reference fragment.

Three corresponding pairs of points were selected on each of the refitting surfaces using the *Point-Pair Registration* tool (section 6.4.1) to produce an initial alignment to the reference fragment (figure 6.22) and the RMS distance was recorded for each refitting pair of models (“Point Pair Alignment RMS” column in appendix J). The aligned fragment models were duplicated using the *Clone* tool and the originals hidden for later reference by unselecting their visibility check box.

6.10.2. Segmentation

Computer modelling systems are poor at characterising refitting fracture surfaces and distinguishing them from surrounding bone. In the wider Fragmented Heritage project this problem is currently the subject of extensive research in computer modelling theory and 3D computational mathematics (section 4.5.2). Due to this computational challenge, the computer programmes cannot yet determine which areas of two 3D models to compare to produce a refit analysis. The presence of large digitised areas of the external cortical surfaces of the bone fragments within the scans dominate alignment calculations over the smaller fracture surfaces and confuse the alignment algorithms (figure 6.32).

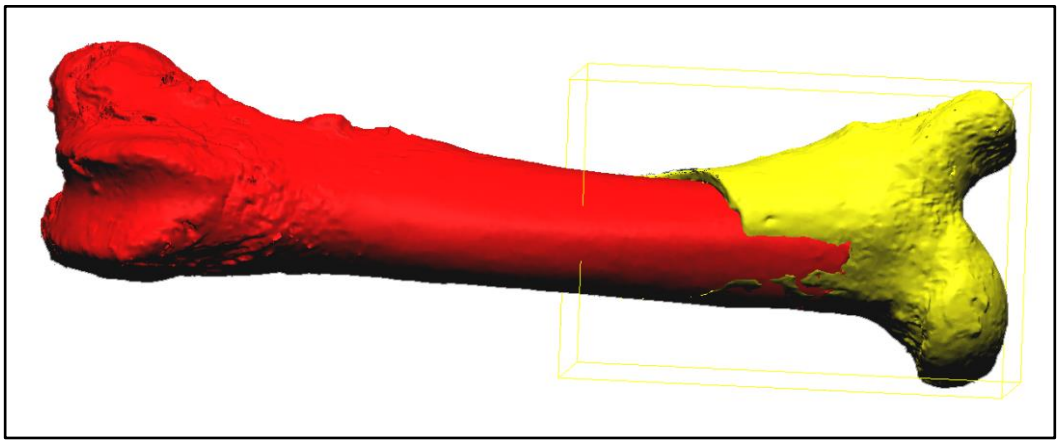

Figure 6.32: Failed Iterative Close Point registration of two fragments of sample A0013. The computer does not distinguish between fracture surfaces and outer cortical surfaces resulting in the outer cortical surfaces of the aligning mesh (red) overlapping those of the reference mesh (yellow). (source: author).

To overcome this, the 3D models of the fragments were manually edited using the *Segment* tool to remove the external and internal cortical surfaces and leave only the fracture surfaces. The edge of the fracture surface was determined by comparison of the models to the physical bone fragment, based on experience.

6.10.3. Fine alignment

Following segmentation of both fragments refitting fracture surfaces, an Iterative Closest Point (ICP) alignment algorithm was applied using the *ICP Fine Registration* tool (section 6.4.2) to produce a fine alignment with a Root Mean Square difference between iterations of less than $10e^{-6}$ and a final overlap

between the refitting surfaces of at least 75%. Where small fragments of bone were lost during the fragmentation, gaps between the two refitting surfaces could produce inaccurate alignment. A furthest point removal option was included in the Iterative Closest Point alignment to eliminate areas of the fracture surfaces without corresponding refitting surface matches from the alignment calculation. The result of the *ICP Fine Registration*, expressed as a Root Mean Square distance, for the refit between the two fracture surfaces was recorded in Excel ("Segmented fine alignment RMS" column in appendix J).

6.10.4. Comparison and assessment of refit distance

A statistical analysis of the distances between the two fracture surfaces was carried out using the *Cloud to Mesh Distance* analysis tool (section 6.4.4). To facilitate this, the segmented surface of the fragment with the higher fragment number was converted to a cloud point using the *Points Sampling on Mesh* tool (section 6.4.3). The tool produced a regularly distributed high density point cloud with point positions corresponding to the surface of the source mesh.

The statistical analysis produced both mean and standard deviation signed distances between the cloud points and the mesh surface, and applied them as a symmetrical scalar field colour scale to the surface of the point cloud, with the colour thresholds set at +/- 0.1 mm (figure 6.34 (left)).

The long tails of outliers for the distance distributions were removed from the data using the *Filter Points by Value* tool. The upper and lower bounds for the outlier removal were calculated based on the outlier data labelling rule with a g value of 2.2, and the calculated mean and standard deviation of the distances between the two surfaces were recorded (see appendix J) (figure 6.33).

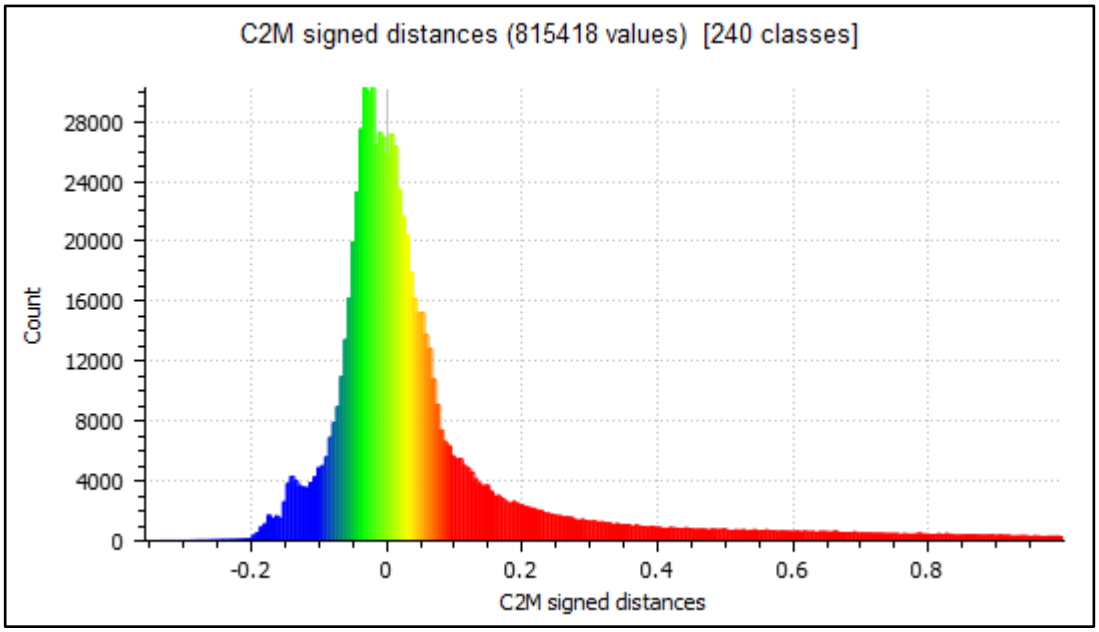

Figure 6.33: Histogram of signed cloud to mesh distances for the segmented fracture surfaces of fragments A0013_F01_StL04 and A0013_F02_StL04 with an applied symmetrical scalar field blue-green-yellow-red colour scale. Values in mm (source: author).

The original full 3D model of the fragment with the highest fragment number was aligned to its segmented fracture surface using the *Point-Pair Registration* tool to allow the results of the distance analysis to be overlain on the full model of the fragment and make interpretation of the result easier (figure 6.34 (right)).

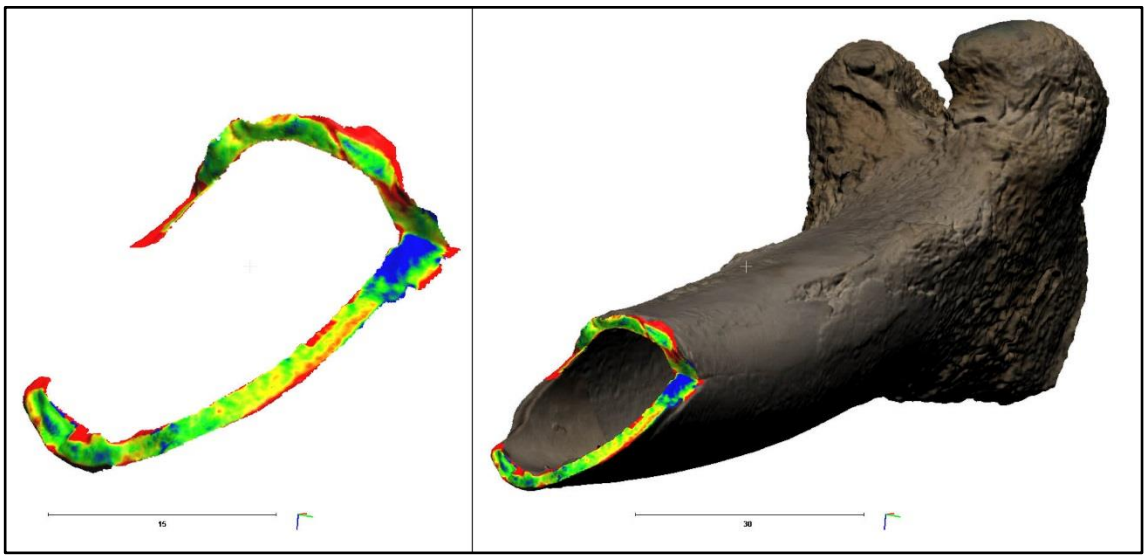

Figure 6.34: A symmetrical scalar field blue-green-yellow-red colour scale applied to the fracture surface of fragment A0013_F02_StL04 (left) and shown with the original fragment model aligned to the fracture surface using the Point-Pair Registration tool (right). Scale bars in mm (source: author).

As a further quality measure for the refit of the fracture surfaces, the percentage of the refitting surface at a distance from the corresponding fracture surface within a range of +/-0.1 mm was calculated. Surface area calculations can only be reliably applied to meshed surfaces, as point clouds do not have any surface dimensions. Two clones of the point cloud produced in the *Cloud to Mesh Distance* analysis (figure 6.34) were made using the *Clone* tool. One of the cloud points was filtered using the *Filter Points by Value* tool to remove all values outside of the -0.1 mm to 0.1 mm range. Both clouds were meshed using the *Delaunay 2.5D (Best Fitting Plane)* tool from the *Mesh Tools* menu. This produced two comparable surfaces meshed using the same Delaunay triangulation process (section 4.1.1), applied to the 3D point cloud which had been projected on the best fitting plane, determined through a least squares process.

The resultant surfaces were exported as .obj models and imported into MeshLab. The MeshLab *Compute Geometric Measures* tool from the *Quality Measure and Computations* filter was used to determine the total surface area of each mesh in order to allow comparison of the results with those for the whole bone samples (section 6.5). The surface areas were recorded and the percentage calculated in Excel (see appendix J).

6.11. Chapter Summary

The digitisation of the samples described in the first half of this chapter resulted in an .obj model for each digitisation technique for each of the samples. These .obj models are included in appendix K on the memory card at the back of this thesis. The results of the analysis of these models are presented in chapter seven and discussed in chapter eight.

Examining the taphonomic challenges to the 3D digitisation of fragmented bone.

Volume II of II

Andrew David HOLLAND

Submitted for the Degree of

Doctor of Philosophy

School of Archaeological and Forensic Sciences

University of Bradford

2017

Chapter 7. Results

In this chapter, the results for the technique comparison standards and experimental taphonomy whole bone samples are presented, as well as the refit analysis for both the fragmented experimental samples and the archaeological and palaeontological samples. The data tables are located in appendices D to J. These results are considered further in the chapter eight discussion.

7.1. Technique comparison standards

The results from the technique comparison standards allow for the comparison of the response of each digitisation technique to specific variables and create a baseline for the specific instruments used in this study.

The standards provided a baseline against which the factors influencing the digitisation techniques could be considered. The complex interaction of these factors within the taphonomically altered bone could then be considered with respect to its 3D digitisation and the refitting of fragmentary bone.

7.1.1. Effect of colour on digitisation methods

The response of the techniques to surface colour was assessed using the difference in cloud point surface variation from a least squares plane, statistically fitted to the digitised colour patches (section 6.8.3). As the colour patches were printed onto the Danes-Picta colour separation guide they have a uniform level of surface variation (i.e. flatness); the difference in the surface variation in the 3D digitised colour patches was therefore an indicator of the response of the instrument to the colour surface.

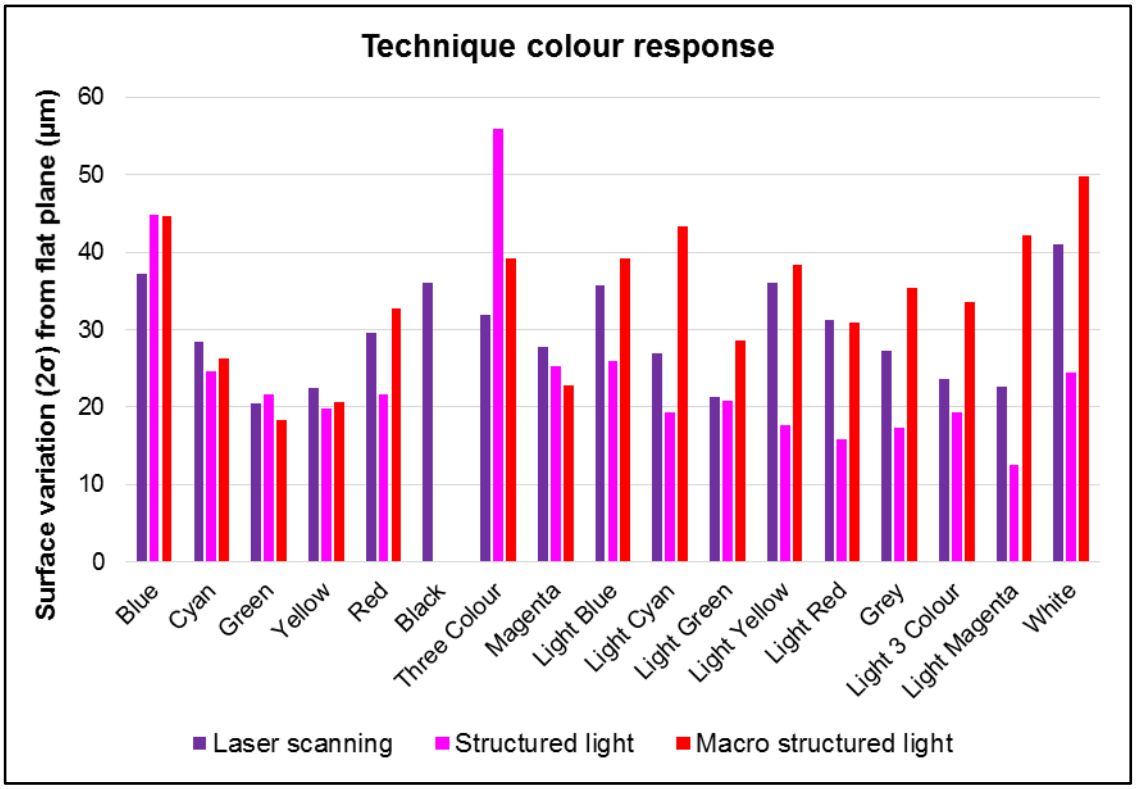

Figure 7.1: Histogram of surface variation from fitted plane for 3D digitised colour patch samples (source: author).

Figure 7.1 shows the response from all three instruments to all the colour patches from the photographic colour target used as the technique comparison standard (figure 6.29). The variation in response to the colour patches is not easily discernible within the overall data for the colour patches (figure 7.1). As outlined in section 4.2.3, experience has shown that the instrument response to variably coloured surfaces is determined by the lightness of the surface and the interaction of the object surface colour and the colour of the instrument source light, together with other optical properties. The description of colours by their red, green and blue colour components results in a three dimensional colour space (figure 6.27) and this is difficult to display on a single axis to allow plotting against the colour response. Therefore the following sections examine the results in terms of colour lightness (section 6.8.1) and estimated colour wavelength of the colour patches (section 6.8.3.1), both of which can be shown on a linear 2D axis.

7.1.1.1. Effect of surface colour lightness on surface variation

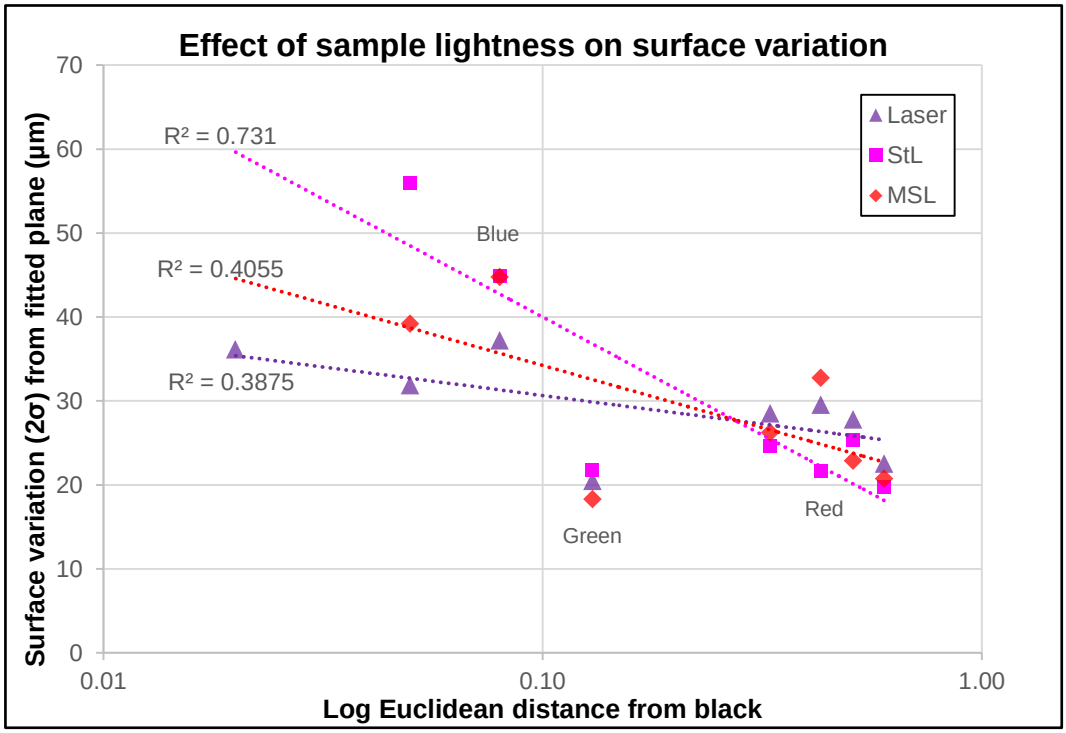

Figure 7.2: Plot showing the effect of sample colour lightness on the surface variation from a fitted plane for colour samples digitised with three 3D digitisation techniques (source: author).

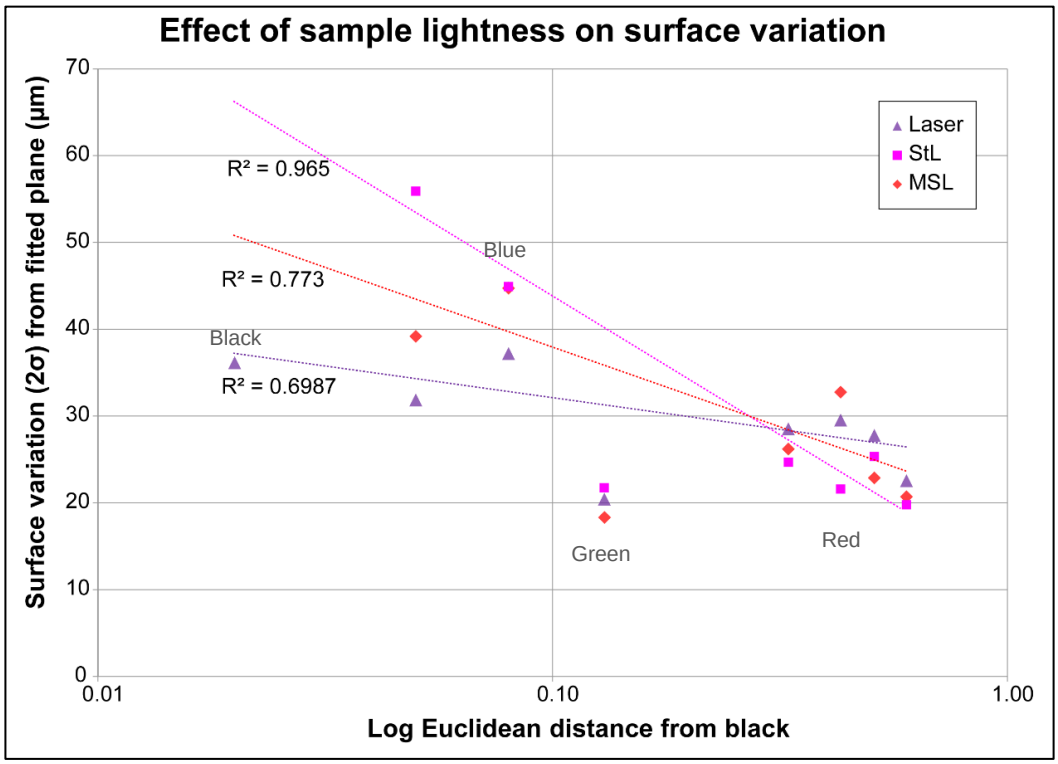

Figure 7.3: Plot showing the effect of sample colour lightness on the surface variation from a fitted plane for colour samples digitised with three 3D digitisation techniques. The data points for the green colour patch have been excluded from the trend line calculations (source: author).

Figure 7.2 displays the surface variation from a plane fitted to the colour patches digitised by the three different techniques. The data is presented on a logarithmic scale with the lightest colour patches furthest to the right and trend lines for each technique with R^2 values describing the quality of the trend line fit to the data. The data points for the green samples are tightly grouped and plot significantly below from the trend lines, distorting the trends. Green lightness values are known to be problematic, as the weighting factor for the green component in the lightness conversion formula (section 6.8.1) is over twice that of the other colours to ensure correct conversion of the green component in mixed colours. For colours with a high green component, slight variations in lighting when measuring the colour values are disproportionately amplified by the green weighting factor resulting in incorrect lightness conversions. Figure 7.3 therefore presents the same data with the green data point removed from the trend line fit calculation, and the resulting trend lines have significantly better fit to the data (i.e. higher R^2 values).

All three techniques showed clear trends of lower surface variation from the fitted flat plane for lighter colours than for darker colours. Both the structured light scanners did not produce a digitised model for the black colour patch, have a higher surface variation for the darker colours than laser scanning and comparable responses for the lighter colours. The laser scanner response to the blue colour patch produced a surface variation that was elevated above the response predicted from the other data.

The response of all three instrument techniques converged for the lighter colours producing surface variations that were all within the precision for the instruments.

7.1.1.2. Effect of estimated surface colour wavelength on surface variation

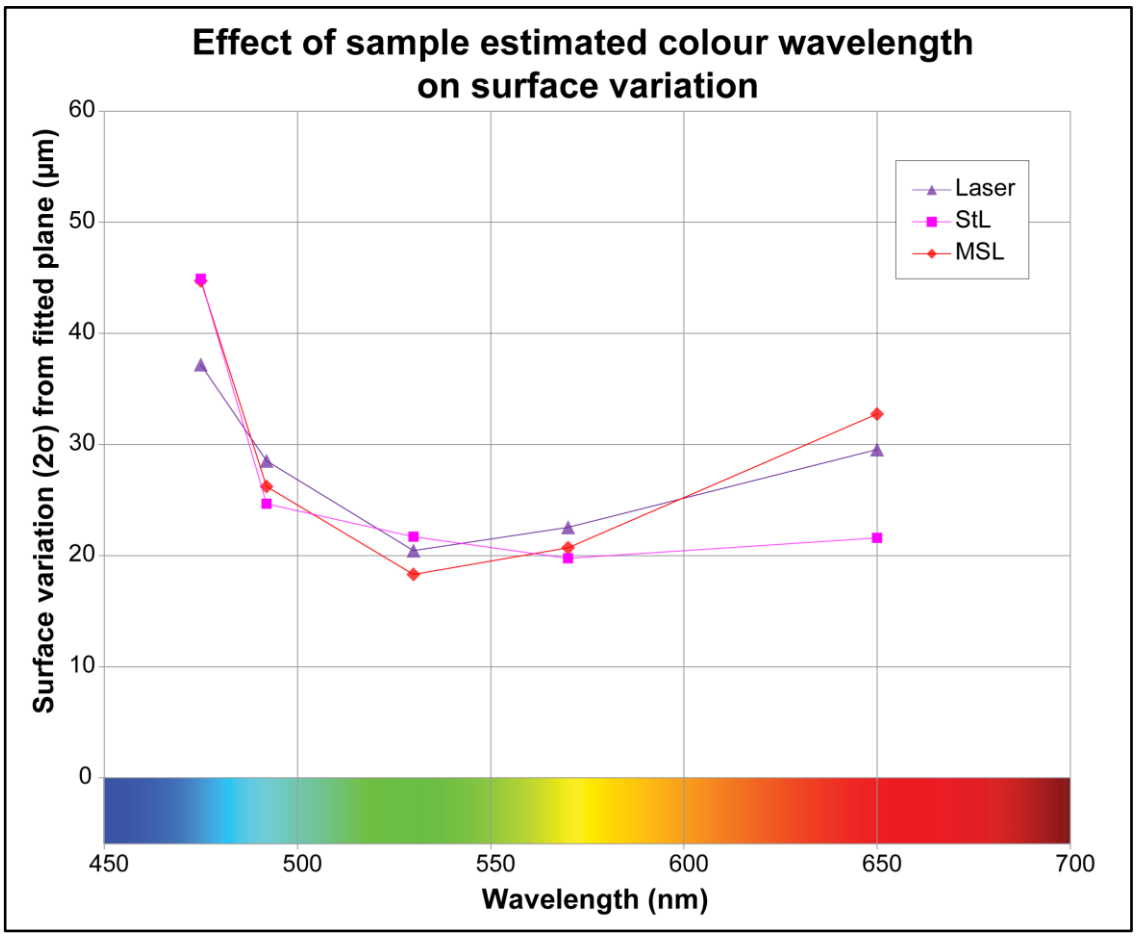

Figure 7.4: Plot showing the effect of sample colour wavelength on the surface variation from a fitted plane for colour samples digitised with three 3D digitisation techniques (source: author).

Figure 7.4 displays the surface variation from a flat plane fitted to the colour patches digitised by the three different techniques, compared against the estimated wavelengths for the primary colour patches and the 1:1 primary mixed colour patches (section 6.8.3.1). The data is presented with a representation of the visible spectrum on the x axis for ease of reference.

The data exhibited very similar trends for all three techniques. All the techniques showed the poorest quality responses at the blue end of the spectrum, with least variation (best quality response) in the middle of the spectrum and a slight increase in variation towards the red end of the spectrum.

7.1.2. Effect of sample opacity on digitisation

The responses of the digitisation techniques to the variable opacity technique comparison standards were assessed with regard to the impact of opacity on surface variation, on volume and area calculations, and on the dimensional accuracy of the resulting 3D models.

The impact of opacity on photogrammetry could not be assessed as the smooth uniform white surfaces of the technique comparison standards did not provide any features that could be identified by PhotoScan during the photogrammetric 3D reconstruction (section 6.3.4.2). Laser scanning, structured light and macro structured light all produced 3D models which could be assessed.

7.1.2.1. Effect of sample opacity on surface variation

The surfaces of the opacity standards were polished flat during their production, and for each technique, the samples were all scanned at the same time and in the same conditions. The base instrument precision (which leads to a base level of surface variation) should be consistent across all samples, therefore, any variation in the meshed surfaces of the 3D digitised models should reflect the response of the instrument to varying surface opacity.

The results shown in figure 7.5 show that in all three digitisation techniques there was an overall reducing trend in 3D surface variation as opacity was increased. The data shows that laser scanning was most susceptible to sample opacities below approximately 97% and that in all three techniques the response was comparable above 97%.

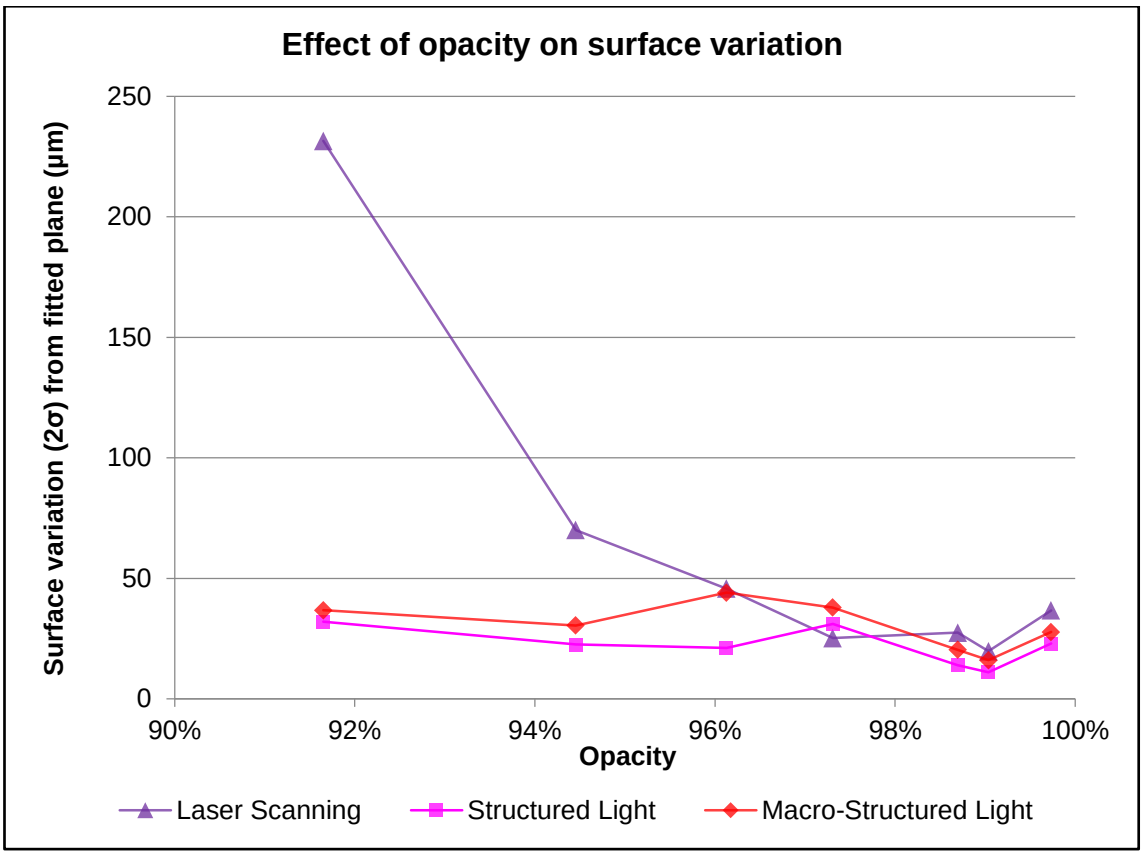

Figure 7.5: Plot showing the effect of increasing sample opacity on the variation of the resulting 3D digitised surface (source: author).

7.1.2.2. Effect of sample opacity on area and volume measurement

The results displayed in figure 7.6 show that structured light techniques underestimated the true volume of samples with opacities below c.98.5% and show a linear trend of improving volume estimation accuracy as sample opacity increased. The laser scanner results exhibited a non-linear relationship between volume measurement accuracy and sample opacity with over-estimation of volume over 92.5% followed by a rapid reduction in estimated volume as opacity increased to 97.5%. Over 97.5% opacity the volume estimates more closely resembled those of the structured light techniques.

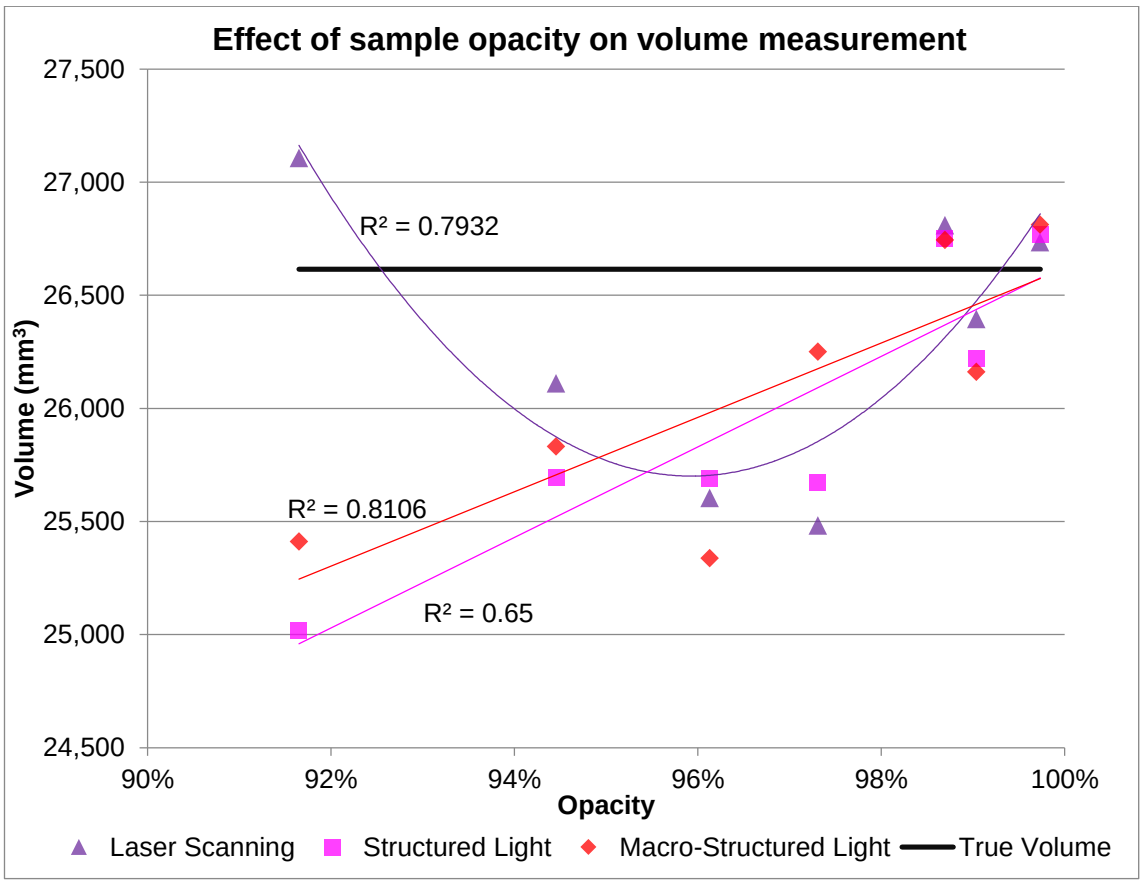

Figure 7.6: Plot showing the effect of increasing sample opacity on the variation in the volume calculation of the resulting 3D digitised models (source: author).

Laser scanning also showed a contrasting response to the structured light methods with regard to the area measurements, with high area measurements at lower opacity followed by a linear decrease as opacity rose. Additionally figure 7.7 shows that structured light methods underestimated the area of a 3D digitised object at lower opacities. In all three techniques area estimation improved with increasing opacity.

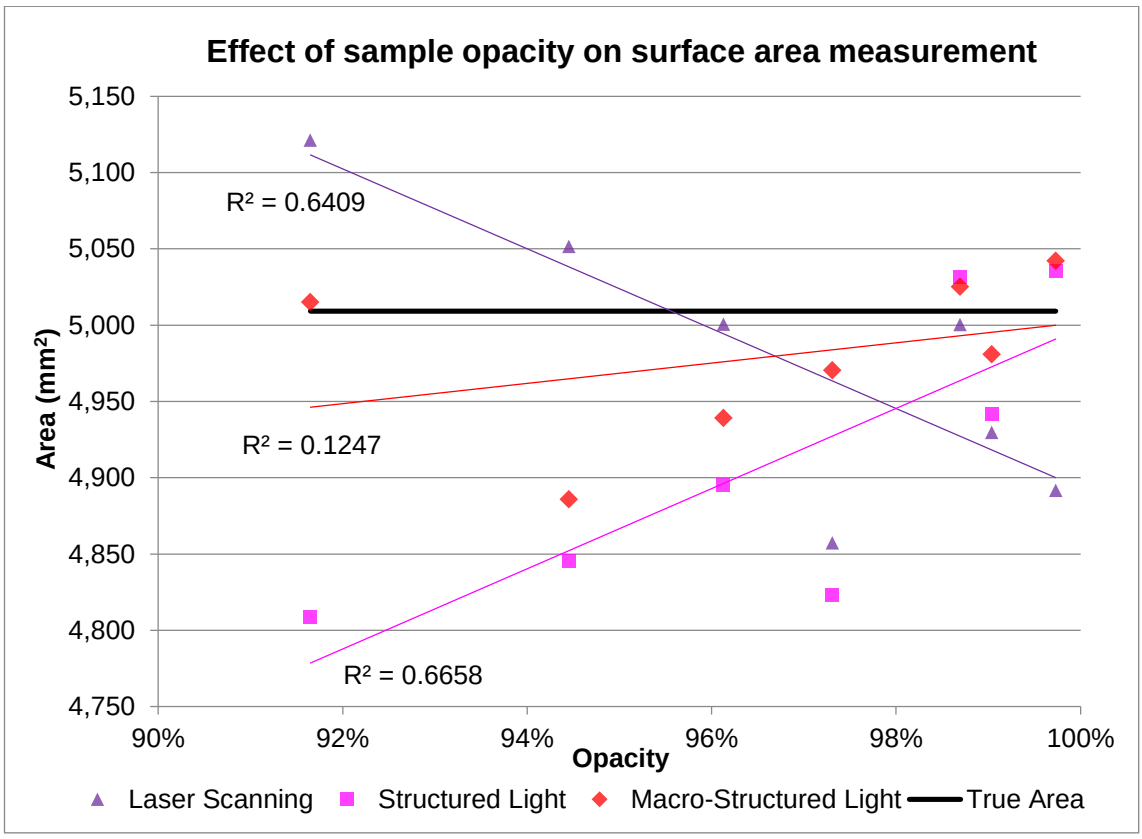

Figure 7.7: Plot showing the effect of increasing sample opacity on the variation in the area calculation of the resulting 3D digitised models (source: author).

The first data point for macro structured light in figure 7.7 (sample S0011_MSL) shows a poor correlation with the trend for the rest of the results. The digitised sample included positional errors for the surface that corresponded with the phase pattern from the scanner (figure 7.8).

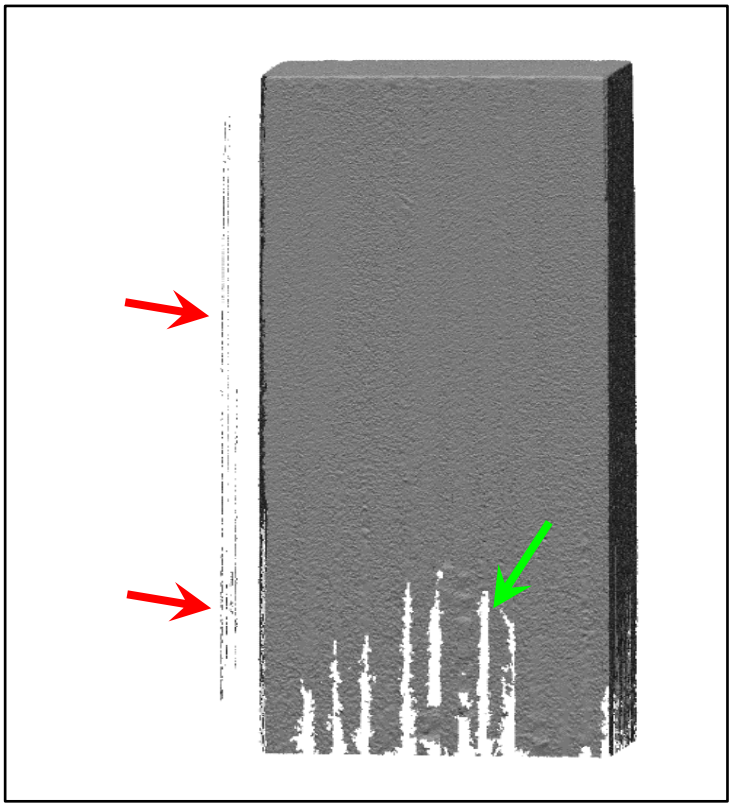

Figure 7.8: Loss of data due to noise in macro-structured light scanning at lower opacities (sample S0011). Note the inaccurate mesh construction to the left of the standards block resulting in meshed points "floating" (red arrows) above the surface and the striped pattern of holes in the mesh surface (green arrow) (source: author).

These errors resulted in inaccurate assessment of the surface and produced small areas of the mesh that "float" above the actual surface of the mesh and distorted the data. The floating mesh areas seen to the left side of the sample in figure 7.8 were removed with the segment tool in CloudCompare V2 before the mesh was re-exported from CloudCompare V2 into MeshLab where the area analysis was re-run. The corrected data in figure 7.9 shows a higher correlation with the trend for the rest of the macro structured light data with a higher R^2 value.

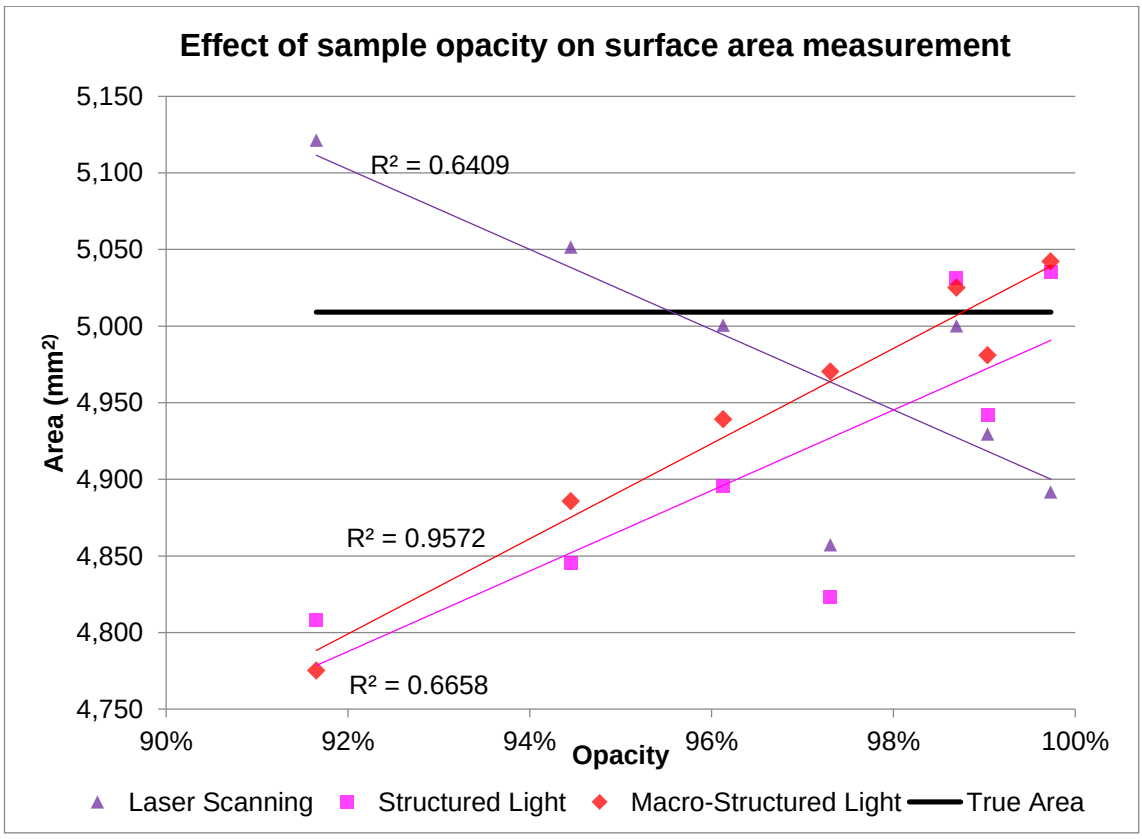

Figure 7.9: Plot showing the effect of increasing sample opacity on the variation in the area calculation of the resulting 3D digitised models with corrected data for S0011_MSL (source: author).

7.1.2.3. Effect of sample opacity on dimensional accuracy

A comparison of the measurement of the opacity standards dimensions from the physical block against the same points measured on the 3D digitised models for each digitisation technique showed clear differences. The difference for each dimension were averaged to provide mean differences between the physical measurements and the digitised model measurements (figure 7.10). The plot shows that the digitised models resulted in an underestimate of the value compared to the physical measures and that with increasing opacity the mean measurement differences converge for all three techniques to within +/- 0.1 mm of each other by 98% and with a consistent 0.2 mm underestimate for fully opaque materials. Laser scanning shows the greatest underestimate of dimensions whilst the macro structured light data shows a generally flat trend.

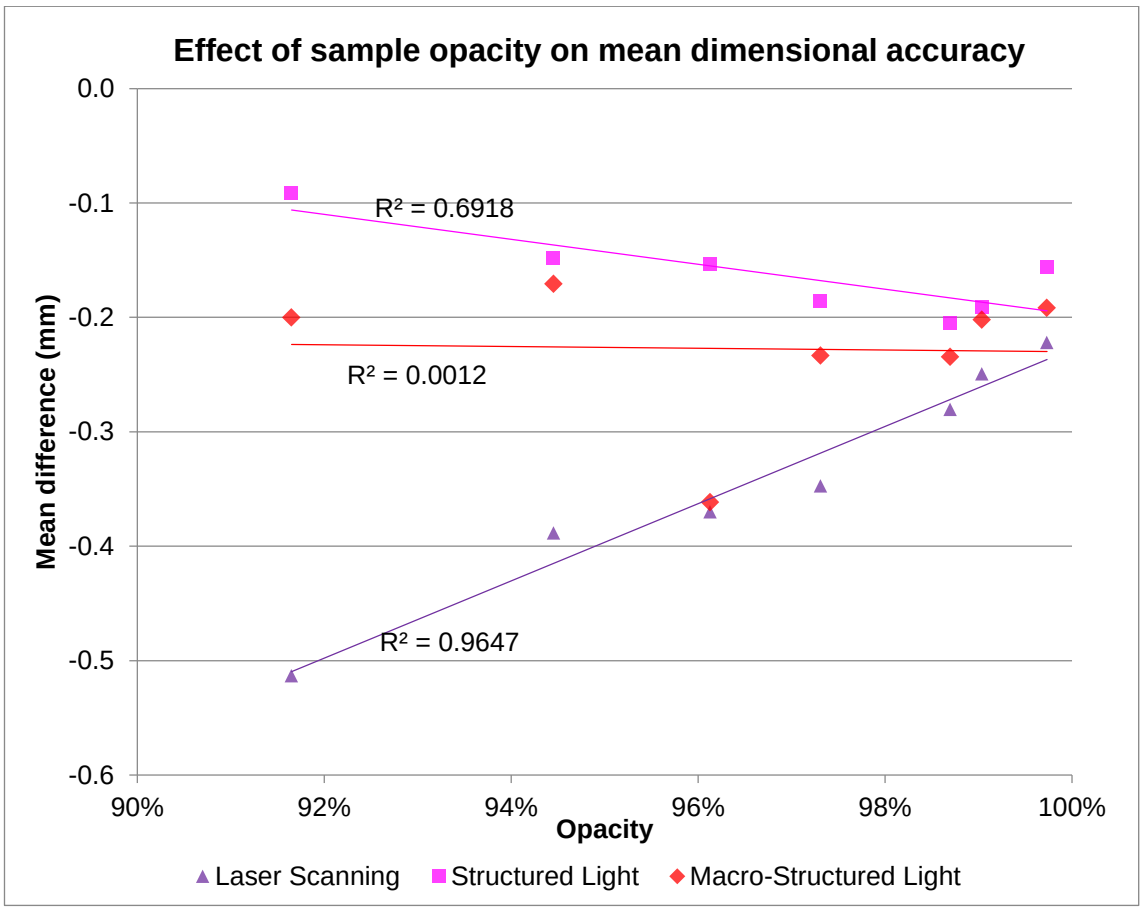

Figure 7.10: Plot showing the effect of sample opacity on the mean difference between sample dimensions measured physically and those from the 3D digitised models (source: author).

The difference between the physical and digital measurements was based on multiple measurements and the standard error between the measurements for each sample is shown in figure 7.11. Structured light scanning was the most consistent technique for measurements with c. +/-0.1 mm variation in measurements for each sample. Again, the laser scan data showed the poorest response and at the lowest opacity the measurements on the digitised mesh were over 1 mm different (+/- 0.547).

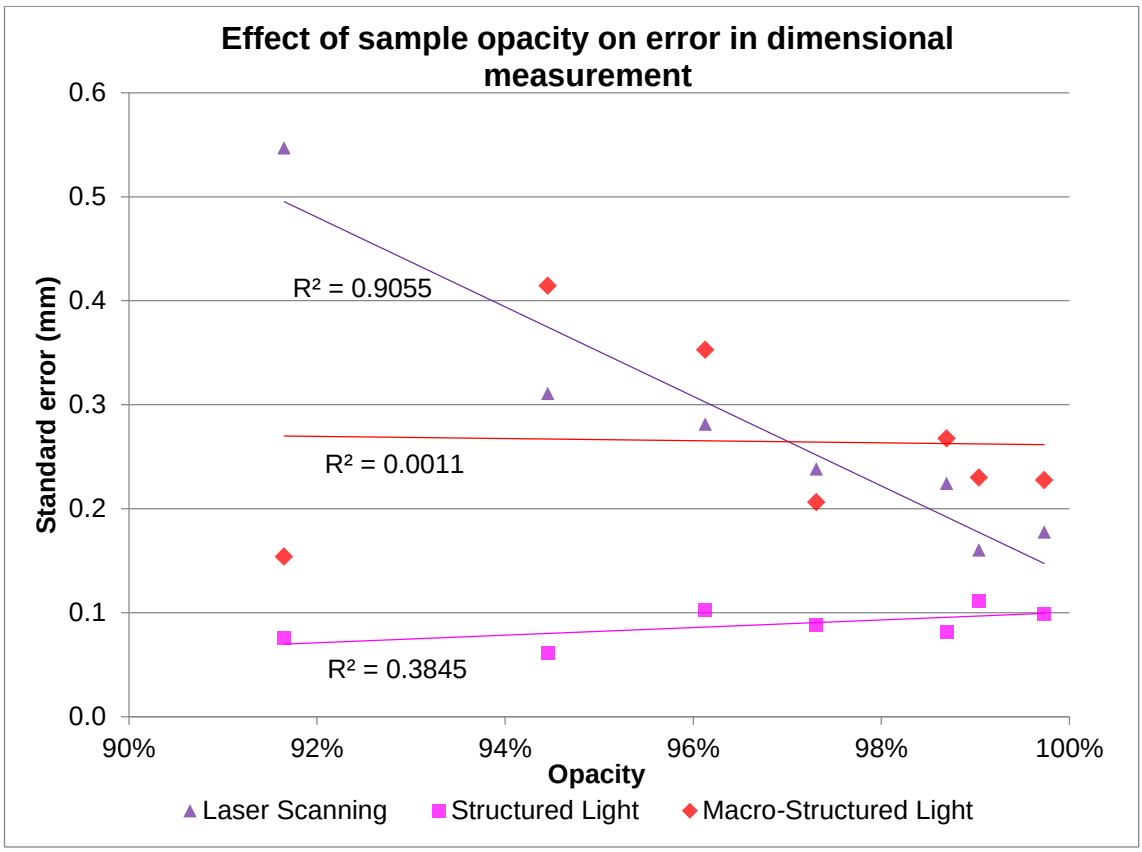

Figure 7.11: Plot showing the effect of sample opacity on standard error between measurements of sample dimensions measured physically and those from the 3D digitised models (source: author).

The macro structured light data again showed poor correlation due to sample S0011_MSL (92%). When the data for this sample was excluded from the trend line calculation the macro structured light trend closely follows that of the laser scan data (figure 7.12).

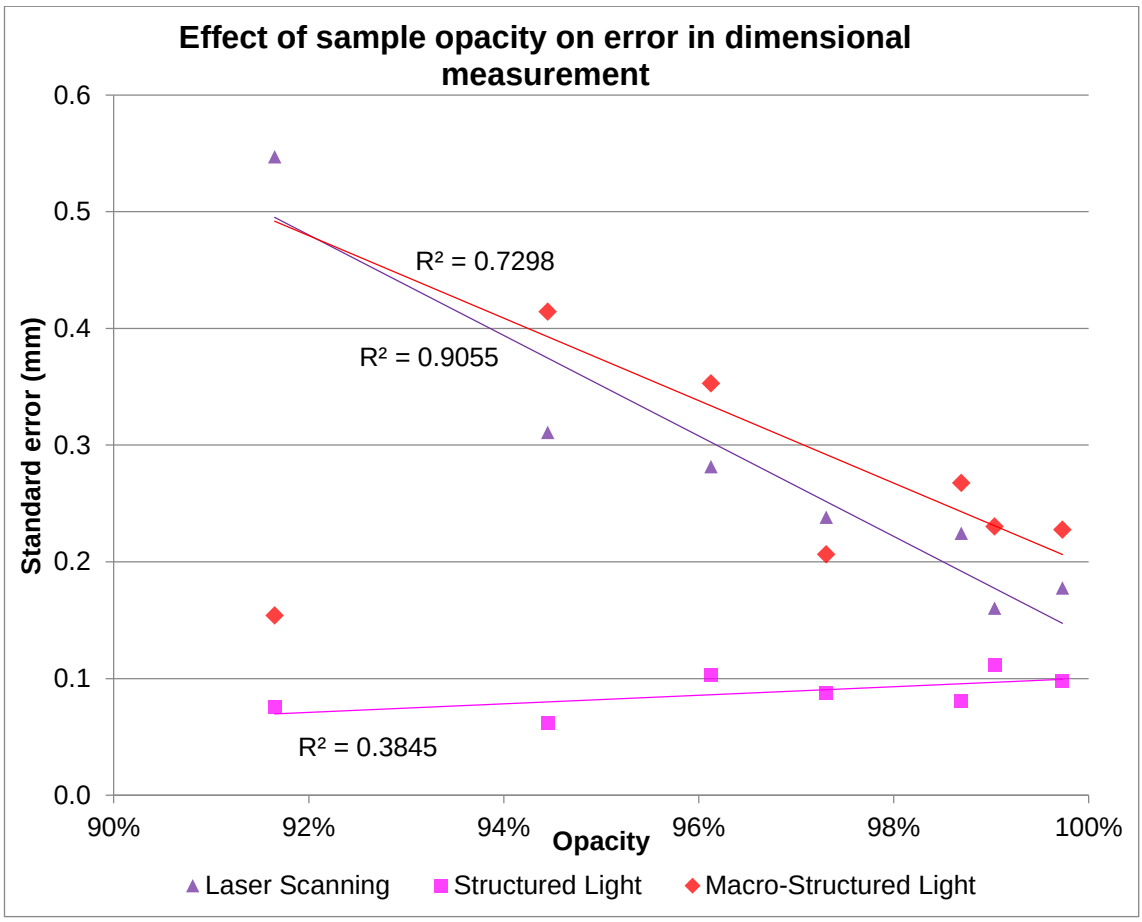

Figure 7.12: Plot showing the effect of sample opacity on standard error between measurements of sample dimensions measured physically and those from the 3D digitised models (outlier removed) (source: author).

7.1.3. Effect of sample surface roughness on digitisation

The responses of the digitisation techniques to the variable surface roughness technique comparison standards were assessed by comparing the measured surface variation of the 3D digitised patches and the known values for surface roughness determined through measurement using the scanning electron microscope (section 5.5.3.2 & table 5.2).

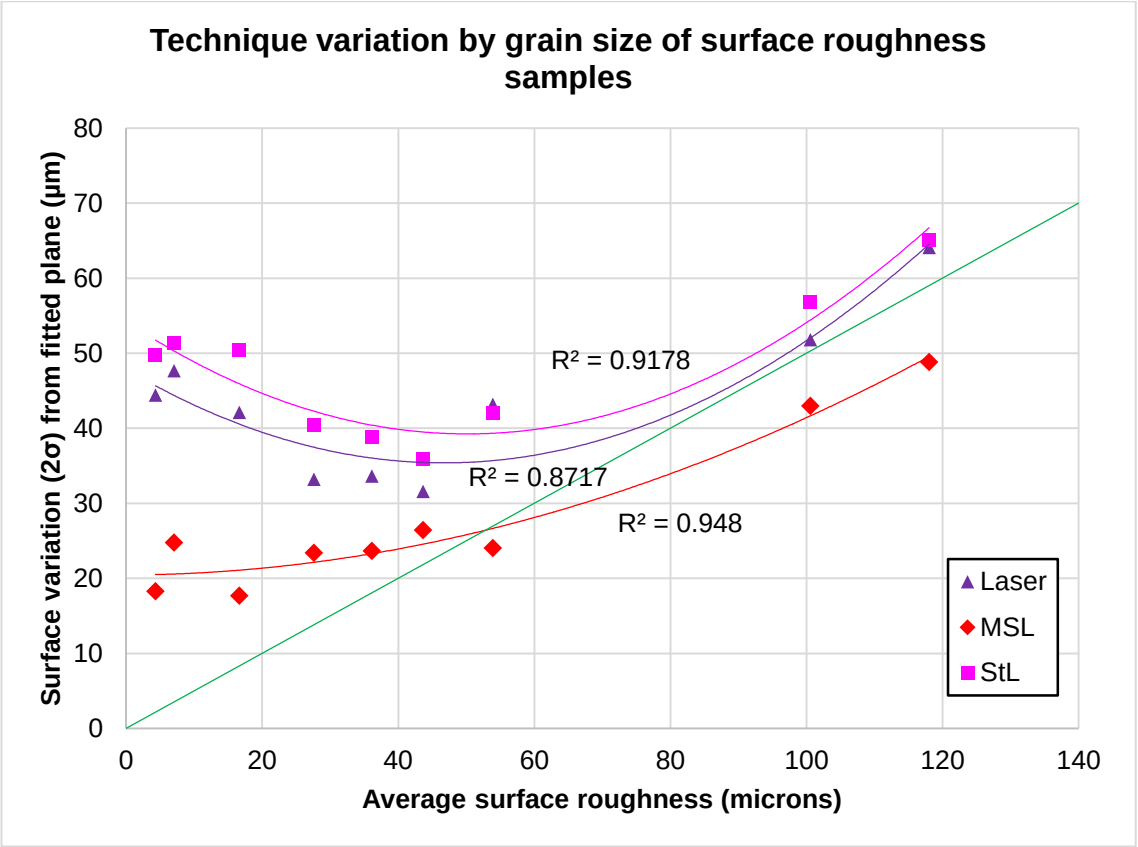

*Figure 7.13: Plot of the variation in point distances from a fitted plane for 3D digitised surface roughness technique comparison standards compared to the known values of surface roughness for the samples. The green line represents the ideal match between 3D and known values (source: author).*If the 3D digitisations were perfect then figure 7.13 would show an exact 2:1 relationship between surface roughness and surface variation from a flat plane fitted to the resultant point cloud (figure 7.13 green line). For surfaces with greater levels of surface roughness, the instrument response converges on the ideal line as the digitisation instruments are able to resolve the individual elements of the surface variation. However, as the surface roughness decreases in size the gaps between the individual surface features become smaller and reach a point where they cannot be distinguished by the instrument. After this point, the data shows the instrument's responses diverging with the highest resolution instrument (macro structured light) maintaining the closest relationship to the ideal line, and the lowest resolution instrument (structured light) exhibiting the greatest level of divergence.

7.2. Qualitative gross changes to the experimental bone samples

The bone samples in the four taphonomic experiments underwent taphonomic change at the gross level. The gross changes are initially described in a qualitative approach highlighting specific taphonomic changes that may significantly impact the digitisation of the bone and the digital refit of bones fragmented at each stage. Gross changes to the bone samples that could be measured in a quantitative manner are described in section 7.3. The results in this section are referred to in the results of the digitisation results for both the whole bone (section 7.4) and the fragmentary bone refit analysis (section 7.5) and in the discussion (chapter eight).

Prior to exposure in the taphonomic experiments the bones had already undergone some taphonomic change due to the method of slaughter of the animals and the cleaning and preparation of the bone for use in the study (section 5.2.4).

Figure 7.14: Bone sample showing the appearance following cleaning and prior to exposure. Note the pink colour from deeper in the bone indicating the greater transluscency/lower opacity and high specularity indicated by the white highlights even under the controlled diffuse lighting conditions of a photographic studio setting (source: author).

Figure 7.14 shows an example bone sample prior to use in the taphonomic experiments. The bone samples were greasy due to the presence of bone lipid (section 2.4.3) and were a yellow cream colour, with an underlying pink tone. The pink colour was due to the presence of clotted blood trapped within the

vascular channels of both the Haversian system (section 2.2.4) and the red, haematopoietic bone marrow (section 2.1.2) following hypostasis. The surface of the bone was smooth and the articular surfaces retained the layer of articular cartilage. The surfaces of the bone were therefore highly specular as can be seen in the white light reflections along the length of the bone in figure 7.14 despite the controlled and diffuse lighting used in the photographic studio to facilitate good photogrammetric images.

Following each period of exposure the experimental samples were photographed and the gross changes were recorded. Most of the photographs were taken for the purposes of photogrammetric reconstruction and are therefore lacking photographic scales, the uniform appearance of which would otherwise have introduced incorrect tie points to the photogrammetry. All the bones were of similar size, being sourced from sheep of a similar age and size for commercial slaughter as mutton (section 5.2.2), and are presented in comparable positions with regard to the camera (usually lateral or medial views) except where the subject illustrated required an alternate view.

Following manual fracture of the bone samples, the fracture surfaces of the bone fragments were recorded for comparison to the digital refit analysis results (section 7.4.1).

7.2.1. Low pH experimental bone samples

Following the first period of exposure in the low pH reaction jars the bone samples were pliable enough to gently bend the bones along their length. The bones resisted the bending force and returned to their original shape when the force was removed (i.e. elastic deformation see section 3.6.2).

Figure 7.15: Gross appearance of low pH exposed bone after the first period of exposure showing the darkening of the surface colour of the bone and a small reduction in the specularity of the surface. The articular (e.g the femoral head) ends appear rougher and less specular (source: author).

The bone samples had greater variation in surface colour compared to the pre-exposure appearance with the ends of the bone being lighter in colour and more yellow-cream than the diaphysis which usually had a lighter yellow area at mid-shaft and dark red-brown staining at the end of the diaphysis (figure 7.15). The cortical surfaces of the bone samples were smooth although they no longer had the greasy texture of the pre-exposure samples. The surfaces retained some specular response, although it was no longer as distinct as that of the glossy pre-exposure surfaces. The articular surfaces had lost most of the glossy articular cartilage compared to the pre-exposure samples, resulting in a matt appearance, with some specular areas of the articular cartilage remaining in small patches.

Figure 7.16: Gross appearance of low pH exposed bone after two periods of exposure showing lightening of the colour surface compared to the first exposure period and lower specularity (source: author).

Figure 7.16 displays an example of the gross taphonomic changes that had occurred after two periods of exposure in the low pH solution. The samples were soft and elastically deformed between forefinger and thumb when handled. The bone colour was dominated by yellow areas in the diaphysis and the articular ends of the bone, and a dark red-brown staining to the bone between the diaphysis and the epiphyses. The surface of the bone was more translucent and the samples were no longer greasy, but retained a smooth surface with less specular reflectivity than the previous stage. The articular surfaces had lost all their articular cartilage covering and were entirely matt with a fine surface roughness.

After the third period of exposure (figure 7.17) in the low pH conditions, the yellow colour tone of the bone samples had darkened and the samples continued to show dark areas of staining at the end of the diaphysis, although this staining had darkened from a red brown to a dark brown.

Figure 7.17: Gross appearance of low pH exposed bone after three periods of exposure. N/B the photo was taken after fragmentation (source: author).

The bone samples were very pliable whilst still wet and bent under their own weight. When air dried slowly the bones hardened with smooth cortical surfaces which reflected light in a more diffuse pattern. The articular surfaces had a greater degree of surface roughness with a rough crazed surface on the femoral head and the distal condyles.

7.2.1.1. Gross changes to the fracture surfaces

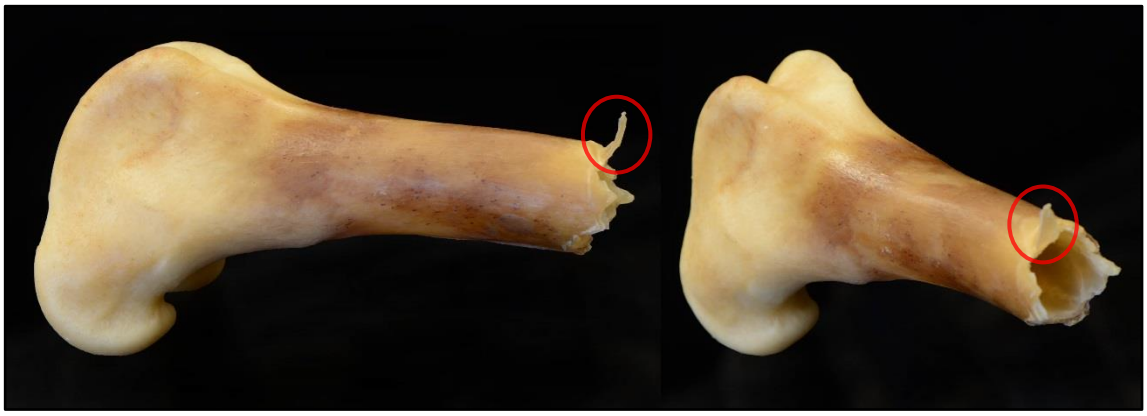

Figure 7.18: Fracture surface of the distal fragment of a low pH sample fractured after the first exposure period showing the sharp projections in the fracture surface and a V shape tear out plastically deformed during fragmentation so that it protrudes anteriorly (red circle). Medial view (left) and a rotated view to show detail of the fracture surface (right) (source: author).

After the first period of exposure to the low pH conditions the fracture of the bone produced very ragged fracture surfaces with sporadic sharp V shaped projections (figure 7.18). The margins of the fractures included buckling and delamination of the outer layers of the cortical bone as well as some "tear out" where V shaped lengths of the outer circumferential lamellae layers were torn away from the surrounding bone and plastically deformed at the base (circled in figure 7.18). The tear out pieces occurred closest to where the bending force was applied during fragmentation at the point where the propagating fracture plane completed.

The outer cortical surface was darker in colour and more translucent than the inner surface which was an opaque creamy colour in all samples. The yellow and red marrow were both still intact and were manually removed to aid digitisation (section 5.3.1.1).

Following the second period of exposure in the low pH conditions the bone samples that were fractured displayed thinning of the cortical thickness and loss of the creamy white colouring to the bone (figure 7.19). The extent of loss of the bone mineral had penetrated much further into the cortex of the bone samples with only a thin layer of bone on the internal cortical surface that remained opaque, with the opacity remainder of the cortical bone significantly decreased.

The marrow was still intact in the samples accounting for some of the protection of the inner surfaces.

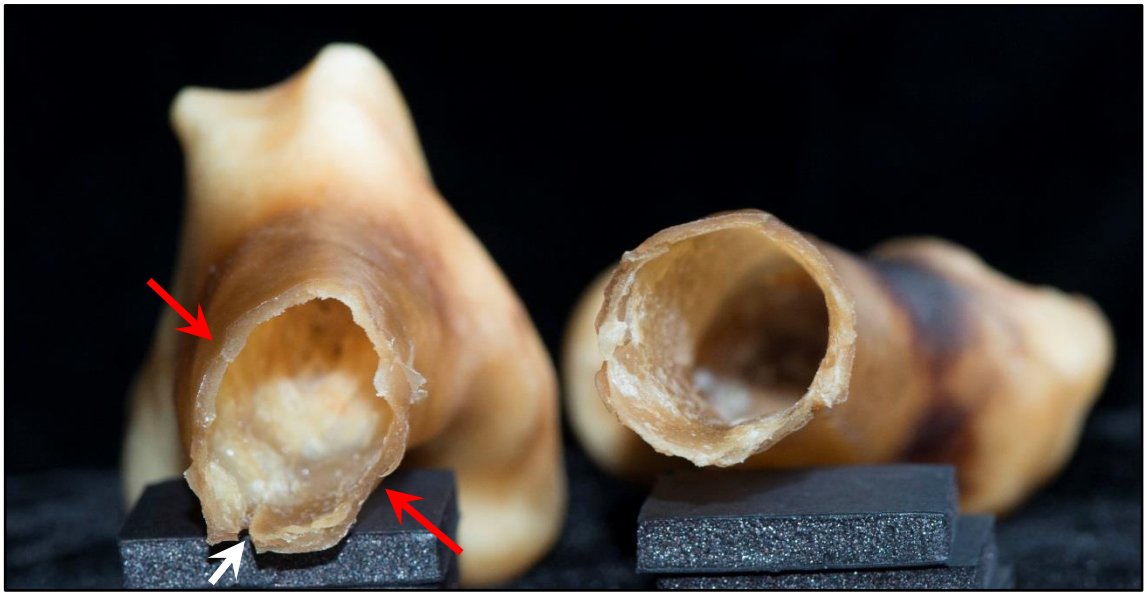

Figure 7.19: Fracture surfaces proximal and distal fragments of the same low pH sample fractured after two exposure periods showing the differential distortion in the distal fragment (left) with anterolateral-posteromedial flattening of the distal diaphysis (red arrows) and associated longitudinal cracks (white arrow). Note the lack of distortion at the fracture surface of the corresponding proximal fragment (right) (source: author).

The fracture surfaces were ragged with some sharp projections and the fracture margins exhibited sharp oblique angles, with multiple tear off pieces at the surface circumferential lamellae, as well as peeling back and distortion. Additionally, the samples exhibited distortion of the cross section of the cortical mid shaft and tension splits radiating longitudinally, perpendicular to the fracture plane.

Figure 7.19 illustrates an example of the distortion and splitting observed in the fragments fractured at this stage. The figure includes the two corresponding fracture surfaces of the same sample. The distal fragment (left) has distorted with anterolateral-posteromedial flattening (red arrows) and a longitudinal split (white arrow) runs distally along the bone from the fracture surface but is not present in the proximal fragment (right), demonstrating that the split formed during fragmentation.

Samples that had been fractured after the previous period of exposure and placed back in solution, exposing the internal cortical surfaces after the removal

of the yellow marrow, demonstrated the greatest degree of thinning of the cortical thickness of the bone in the diaphysis and were semi-transparent.

Figure 7.20: Photo of a bone sample following the second period of exposure after having been fractured and digitised after the first period of exposure to low pH conditions. Changes in cortical thickness and opacity of bone in low pH exposed bone samples were most extreme in samples subject to further exposure after fragmentation (source: author).

After the third period of exposure in the low pH conditions the bone samples were difficult to fracture; they bent and deformed plastically before failing, resulting in a torn and ragged fracture surface with very thin sharp angled fracture margins (figure 7.21), splits and significant alterations to the profile of the bone at the point of fracture (usually mid shaft).

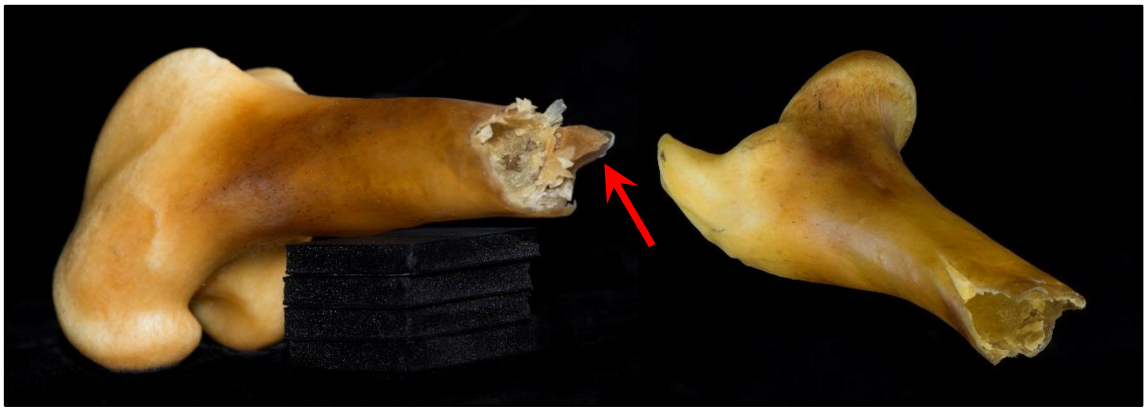

Figure 7.21: Fracture surface of low pH sample fractured after three exposure periods. Red arrow indicates a very thin translucent tear out protrusion from the fracture surface (source: author).

The samples showed a further reduction in opacity and the thin sharp projections from the fracture surface and the peeled tear outs at the margins were transparent at their edges (figure 7.21 red arrow). The marrow was still

intact within the medullary cavity and the inner cortical surface had patches of high opacity cream coloured bone.

7.2.2. High pH experimental bone samples

After the first period of exposure in high pH conditions the bone samples were no longer greasy, and had a soapy texture when first removed from the reaction jars. The solution in the reaction jar was cloudy white with fine fragments of surface bone held in suspension.

On slow drying the bone sample surfaces remained smooth with some crazing of the outermost bone layer, had lost their specular reflective properties and had a diffuse matt appearance (figure 7.22).

Figure 7.22: Gross appearance of a high pH exposed bone after the first period of exposure with reduced surface colour variation and surface specularity (source: author).

The colour of the bone samples appeared lighter and less yellow than the pre-exposure samples. The pink had been replaced with a dark, grey brown discolouration at the ends of the diaphysis. The surface of the bone exhibited less colour variation than the pre-exposure samples.

The articular surfaces remained intact and smooth although the articular cartilage had yellowed and was beginning to craze in places reducing the specular reflectivity of the surface.

Following the second period of exposure in high pH conditions the surfaces of the bone samples were much whiter in colour, but still with some yellow tone

with the articular surfaces displaying the strongest yellow tone. The darker internal staining at the ends of the diaphysis were less clear as the increasing opacity of the surface obscured the darker material deeper in the bone.

Figure 7.23: High pH exposed bone sample after being washed following the second period of exposure. The outer layers of the bone cortex have swollen resulting in small cracks and exfoliation of the surface (source: author).

On initial removal from the reaction jars the surfaces of the samples were soapy and slightly soft to the touch. The bone samples had swollen and the outer lamellae had expanded (figure 7.23) resulting in small cracks and loss of bone surface into the reaction solution. The solution in the reaction jar was more opaque due to a greater amount of fine bone fragments in suspension. A thin layer of white bone material had settled out at the bottom of the reaction jar.

When air dried (figure 7.24), the surface of the bone samples displayed fine cracks and areas of flaking bone, especially in the epiphyses of the bone, resulting in an increase in the surface roughness of the samples. Individual layers of the circumferential lamellae were discernible at the surface as they flaked away, resulting in a highly diffuse matt surface. Small flakes of bone that had not fully detached from the surface protruded from the surface of the bone, further roughening the appearance of the surface.

Figure 7.24: Gross appearance of a high pH exposed bone after the two periods of exposure showing the loss of some of the yellow tone and surface colour variation. The increased surface roughness and diffuse surface are clearly evident (source: author).

The articular cartilage on the distal condyles, femoral head and the patella surfaces exhibited fine cracks and crazing on the surface resulting in the loss of small patches of the outer layer.

Following the final period of exposure in high pH conditions the bone samples had a bleached white appearance, with only limited areas of yellower tone (figure 7.25), usually associated with articular surfaces and the attachments for their articular capsules.

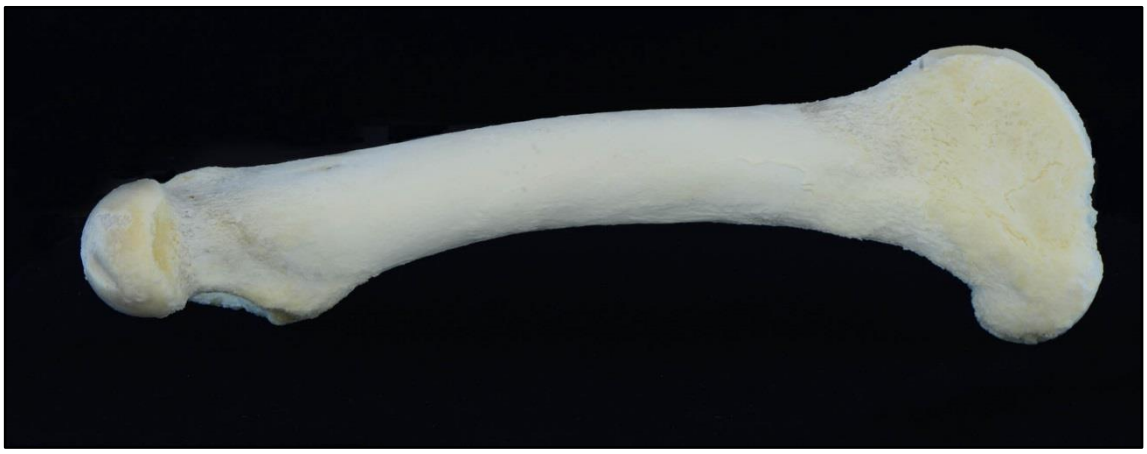

Figure 7.25: Gross appearance of a high pH exposed bone sample after the three periods of exposure showing the bleached white diffuse surface with increased surface roughness (source: author).

Upon removal from the reaction jars, the outer surfaces of the bone samples were very soft to the touch with a soapy texture. Multiple layers of the circumferential lamellae of the bone cortex had swelled resulting in more

extensive cracking and exfoliation of the surfaces. The reaction jars had large amounts of suspended material and the reaction solution was entirely opaque. The bottom of the reaction jars had a thick layer of settled out bone material exfoliated from the surface of the samples.

After slow air drying the surfaces of the bone samples had a rough powdery texture, with multiple layers of bone exfoliating in places. The small cracks and fissures in the surface of the samples observed after the second period of exposure had expanded and joined together to form larger cracks. The surfaces had high degrees of surface roughness resulting in a highly diffuse matt appearance.

The distal articular surfaces of the samples had lost all their smoothness and were missing the surface layer. The femoral heads had patches of exfoliation that were at least one layer deep.

As the bone dried some samples developed long deep longitudinal cracks, following the line of cracks on the surface and extending deeper into the cortical thickness.

7.2.2.1. Gross changes to the fracture surfaces

After the first period of exposure to high pH conditions the fracture of the bone samples produced smooth fracture surfaces (figure 7.26). The fracture surfaces had sharp edges to the fracture margins with acute and oblique angles. On the anterior of the bone samples (i.e. nearest to the point of loading during fragmentation where the bone was under compression) the fracture margins were usually thin with sharp protruding bone with surfaces that curved around the bone. Additionally very small fragments of bone spalled from the outer margins of the fracture surface during the fracture sequence.

Figure 7.26: Fracture surface of a high pH sample fractured after the first exposure period showing the sharper fracture margins and the variation of colour and opacity across the exposed cortical thickness (source: author).

The fracture of the bone allowed the extent of the loss of collagen from the bone cortex to be assessed. As can be seen in figure 7.26, the collagen loss after the first exposure period resulted in a limited thin whitening of the outer layers of the cortex of the bone samples, beyond which the cortical bone remained comparable to its pre-exposure colour. Within the medullary cavity, the marrow was still intact limiting access of the sodium hydroxide solution and protecting the internal surface of the cortical bone.

A greater degree of collagen loss from the cortical bone was evident within the fracture surfaces of the samples fractured after the second period of high pH exposure (figure 7.27). The whitened layer extended through approximately a quarter of the cortical thickness and was strongly contrasted with the pink colouration of the remaining cortical bone thickness.

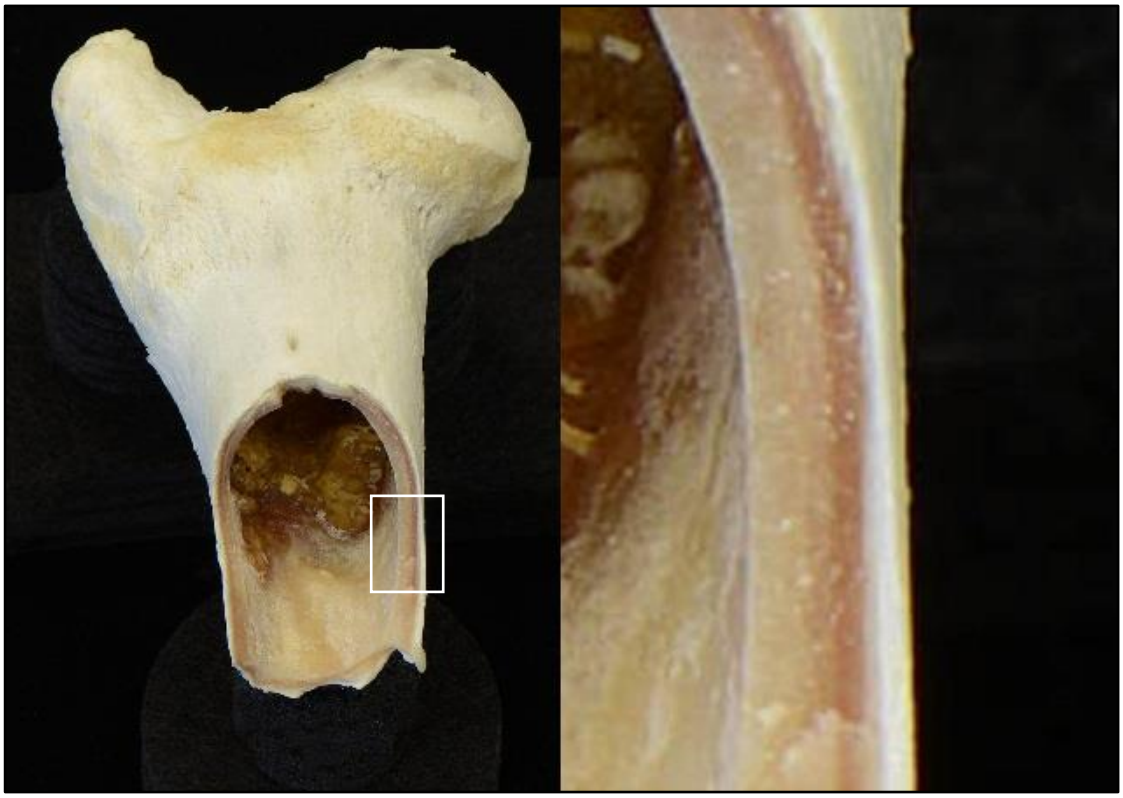

Figure 7.27: Proximal fragment of a high pH sample fractured after two exposure periods (left) and close up of the fracture surface (right) showing the variation in opacity and colour across the thickness of the cortical bone (source: author).

The bone marrow remained intact in the bone samples and continued to protect the inner surface from the high pH conditions in the reaction jar. Additionally the internal surfaces within the medullary cavities of the bone samples still had a greasy texture, although they were slightly lighter in colour suggesting some loss of collagen had started to occur.

The bone margins of samples fractured at this stage were sharp with slightly curved profiles towards the margins. There were less sharp individual projections of bone than occurred within the samples fractured after the first exposure period, with fewer small fragments spalled off the fracture surface margins.

The fracture surfaces of the samples fractured after the third period of exposure to high pH conditions showed rougher fracture surfaces with fracture surface angles closer to 90 degrees with respect to the cortical surfaces (figure 7.28).

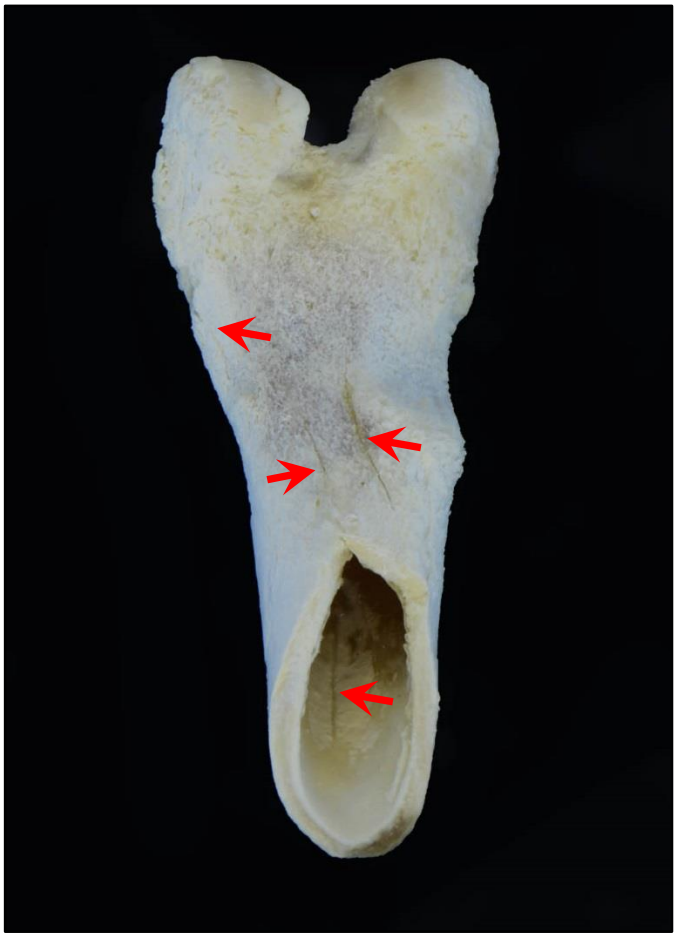

Figure 7.28: Fracture surface of a high pH sample fractured after three exposure periods showing the reduced variation in the fracture surface through the cortical bone and the presence of large cracks (red arrows) on both the external and internal cortical surfaces (source: author).

The fracture surfaces exhibit lines of lighter colour and greater opacity associated with the loss of bone collagen in cortical bone on both the internal and external fracture margins, with a thin band of less affected bone in the centre of the cortex. This central band was yellower in colour than the surrounding bone and had a smoother surface. The longitudinal cracks and splits observed on the outer surfaces of the bone samples were also present on the internal surfaces (arrowed in figure 7.28).

7.2.3. High UV experimental bone samples

Figure 7.29 and figure 7.30 show the same high UV exposure sample before and after the first period of exposure. Following the first period of high UV exposure the bone samples exhibited a fading of the pink staining of the bone and a bleaching of the surface layer of the bone, resulting in a mottled white colouration to the surface. The greasy texture to the surfaces of the bones observed in the pre-exposure samples was reduced after the first exposure and bone lipid had collected in small patches in the bottom of the steel exposure tray (section 5.3.6). The reduced surface bone lipid and the bleaching of the bone samples resulted in a small reduction in the specular appearance of the surface.

Figure 7.29:Gross appearance of a high UV exposure bone sample prior to the first period of exposure (source: author).

Figure 7.30: Gross appearance of high UV exposed bone after the first period of exposure showing the white mottling of photodegradation of the outer layers of the cortical bone (source: author).

The surface properties of the bone samples after the second period of high UV exposure displayed a continuation of the changes observed after the first period (figure 7.31). The bleaching of the surface had resulted in further fading of the pink staining of the bone and further whitening of the outer layers of the bone cortex. The bone samples exhibited a further loss of lipid content from the surface. The bleaching of the bone, combined with the reduction in the greasy texture of the surface, resulted in a further reduction in the specular properties of the surface of the bone samples.

Figure 7.31: Gross appearance of high UV exposed bone after the second period of exposure with a whitened and less specular surface due to photodegradation (source: author).

7.2.3.1. Gross changes to the fracture surfaces

The fracture surfaces of the bone samples fragmented after the first period of high UV exposure (figure 7.32) exhibited smooth surfaces and the fracture planes had propagated in a curved path around the bone rather than perpendicular to the axis. The fracture surfaces included sharp projections and the fracture surfaces had curved profiles across the cortical thickness resulting in fracture margins that exhibited oblique angles with respect to the cortical surface.

The limited extent of photodegradation and bleaching of the cortical surface was visible as a thin line of lighter bone at the margins of the fracture surface. The penetrative effects of photodegradation were sufficiently limited by the attenuation of the UV light that the internal surfaces of the bone samples did not appear to display any physical change.

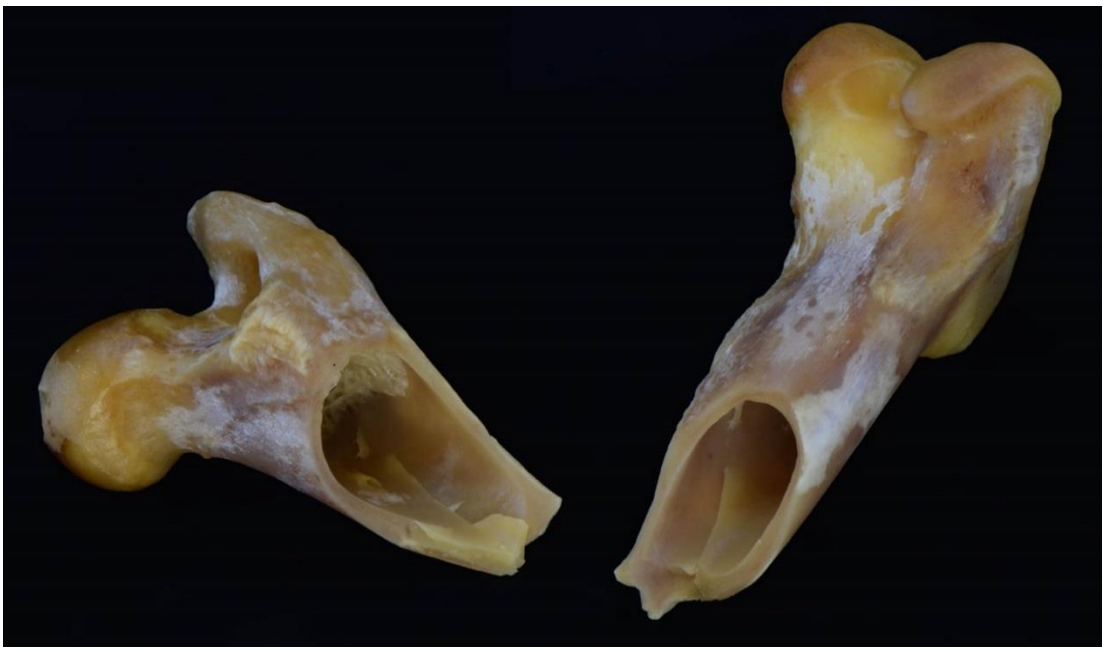

Figure 7.32: Fracture surface of high UV sample fractured after the first exposure period showing initial increase in the outermost layers of the cortical bone due to photodegradation (source: author).

The bone samples fractured after the second period of high UV exposure exhibited a greater degree of bleaching and photodegradation across the cortical bone thickness (figure 7.33). The penetration effects were still restricted by the attenuation of the UV light, such that the internal surface remained unaffected and the fracture surfaces displayed a similar pattern to those from the first period of exposure.

Figure 7.33: Fracture surface of high UV sample fractured after the second exposure period showing the increased opacity from photodegradation of the outermost layers of the cortical bone in the fracture surface outer margins (source: author).

7.2.4. Field weathering experimental bone samples

The field weathering experimental bone samples were exposed to natural surface weathering at the field weathering site for two exposure periods of 448 days and 182 days (630 days total exposure). Throughout the first exposure the samples were regularly inspected in situ to note any surface changes and to ensure that the samples were not disturbed or predated (section 5.3.2). Figure 7.34 illustrates that gross changes began to occur after only one month of exposure; black spots and staining from the growth of fungal colonies were present on the bone samples. The pink colouration remained and the surfaces showed a white mottling representing photodegradative change similar to that seen in the high UV samples.

Figure 7.34: Gross appearance of a bone sample in situ after surface exposure for one month showing small black spots from fungal colonies and slight whitening of the bone surface due to photodegradation (source: author).

By the end of the first exposure period changes to the bone samples were more advanced with large areas of black fungal surface staining, particularly around the epiphyses of the bone where the bone density was lower and where the presence of the hyaline articular cartilage provided an initial nutrition source (figure 7.35). The hyaline cartilage of the articular surfaces was no longer present in the bone samples having been consumed by the fungal colonies. The colour of the bone samples was much whiter, with only small areas retaining the yellow colour tone of pre-exposure bone, although the invasion of the fungal colonies into the cortical bone had added a grey mottling to the bone samples. The pink staining from the haemolysis of the blood within the Haversian system

and the areas of haematopoietic (red) marrow were reduced in area and the colour had darkened to a red brown.

Figure 7.35: Gross appearance of a bone sample after the first period of surface weathering rotated from the standard view to show the black fungal staining on the distal end (source: author).

The surfaces of the bone samples were dry and had completely lost the greasy texture of the pre-exposure samples. The loss of the bone lipid from the surface was also noted in the increased surface opacity of the samples and the loss of surface specularity. The surfaces of the bone samples exhibited very fine cracks and were less smooth compared to the pre-exposure samples, with a less specular appearance.

Larger longitudinal cracking and splits occurred on the bone samples, most commonly on the upper surfaces.

Figure 7.35 and figure 7.36 show the same bone after the first and the second period of field exposure respectively. The bone samples after the second period of exposure were bleached white with a grey mottling to the bone. The large areas of fungal staining had also been bleached and a faint green staining to some areas of the surface was present from the establishment of colonies of mosses on the surface (in figure 7.36 these can appear as a slight green tint to

the bone on the posterior aspect of the femoral head, on the lesser trochanter and superior of the adductor tubercle). The combination of differential bleaching and the colonisation of the shaded areas of the bone by mosses resulted in the greatest variation in colour at the ends of the bone, particularly on the underside and regions of greater surface topography.

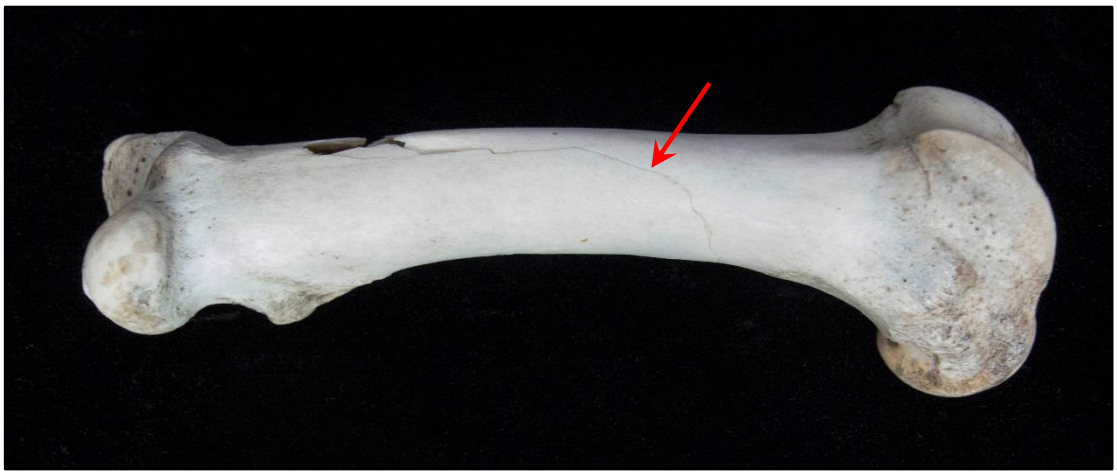

Figure 7.36: Gross appearance of a bone sample after the second period of field weathering showing the bleaching of both the bone surface and the fungal staining seen in the earlier stage. N.B. The sample was photographed after fragmentation and this image includes the fracture line between the two fragments (red arrow) (source: author).

The large cracks seen in figure 7.36 (red arrow) resulted from the experimental fragmentation of the bone rather than taphonomic change due to field weathering, however all bone samples exhibited larger amounts of surface cracking and longitudinal cracks than after the first period of exposure. The interaction of these with the experimental fragmentation is described below.

The increase in fine surface cracking and further loss of the bone lipid and collagen gave the bone samples a very fine surface roughness and a more diffuse appearance than the bone samples from the first period of exposure.

7.2.4.1. Gross changes to the fracture surface

Figure 7.37: Gross appearance of a bone sample fragmented after the first exposure period. The outer margins are opaque and whitened whilst the inner margins still retain some yellow colour indicating surviving protein content (source: author).

The bone samples fractured after the first period of exposure demonstrated the depth of the photo bleaching into the cortical bone. Loss of the yellow colour tone and the increase in opacity continued through approximately 75% of the cortical thickness, with the internal surfaces remaining yellow (figure 7.37). The marrow was intact within the medullary cavity and continued to protect the internal surface of the bone demonstrating that photodegradation had not penetrated all the way into the bone at this stage.

The fracture surfaces of the bone samples were smooth near the internal margin, but rougher towards the external margin and the fracture planes had propagated in a path close to perpendicular to the bone axis. The external

margins of the fracture surface had some sharp protrusions of bone, often following lines of surface cracking.

Figure 7.38 shows a bone sample fractured after the second period of field weathering exposure. The whitening of the bone is consistent across the full thickness of the cortical bone in the diaphysis. The marrow in the medullary cavities was dried and degraded indicating that there was little lipid content left. The staining on the internal cortical and trabecular structures was mid brown at the end of the bone in the haematopoietic marrow areas and lighter in the centre of the diaphysis.

Figure 7.38: Whitening of the bone is uniform all the way through the cortex of the bone after two exposure periods. Red arrow indicates an oblique angled protrusion in the fracture surface (source: author).

The fracture surfaces of the bone samples were roughened and generally had fracture margins with angles of approximately 90 degrees with respect to the cortical surfaces, although there were oblique angles where the fracture plane had terminated (red arrow in figure 7.38). The surface of the bone exhibited large cracks (section 3.3.2) and the fracture of the bone followed these weaknesses resulting in fractures that were oblique to the axis of the bone, and producing sharp angled protrusions where the fracture jumped from a one crack to another. The fracture plane had propagated in straight lines in contrast to the curved fracture path of first exposure bone.

7.3. Quantitative gross changes to the experimental bone samples

The gross changes to the experimental samples that could be measured using a quantitative approach to demonstrate specific taphonomic changes, that may significantly impact the digitisation of the bone and the digital refit of bones fragmented at each stage, are described in this section. These results are discussed in chapter eight in more detail.

7.3.1. Experimental sample opacity

The opacity of the bone samples at each period of exposure was measured using the same method used for the opacity standards (section 5.5.2.2). Due to varying bone thickness the measured values were normalised to a fixed width to make the measurements comparable (section 6.9.1). The normalised results for all the experimental taphonomy experiments are presented in figure 7.39.

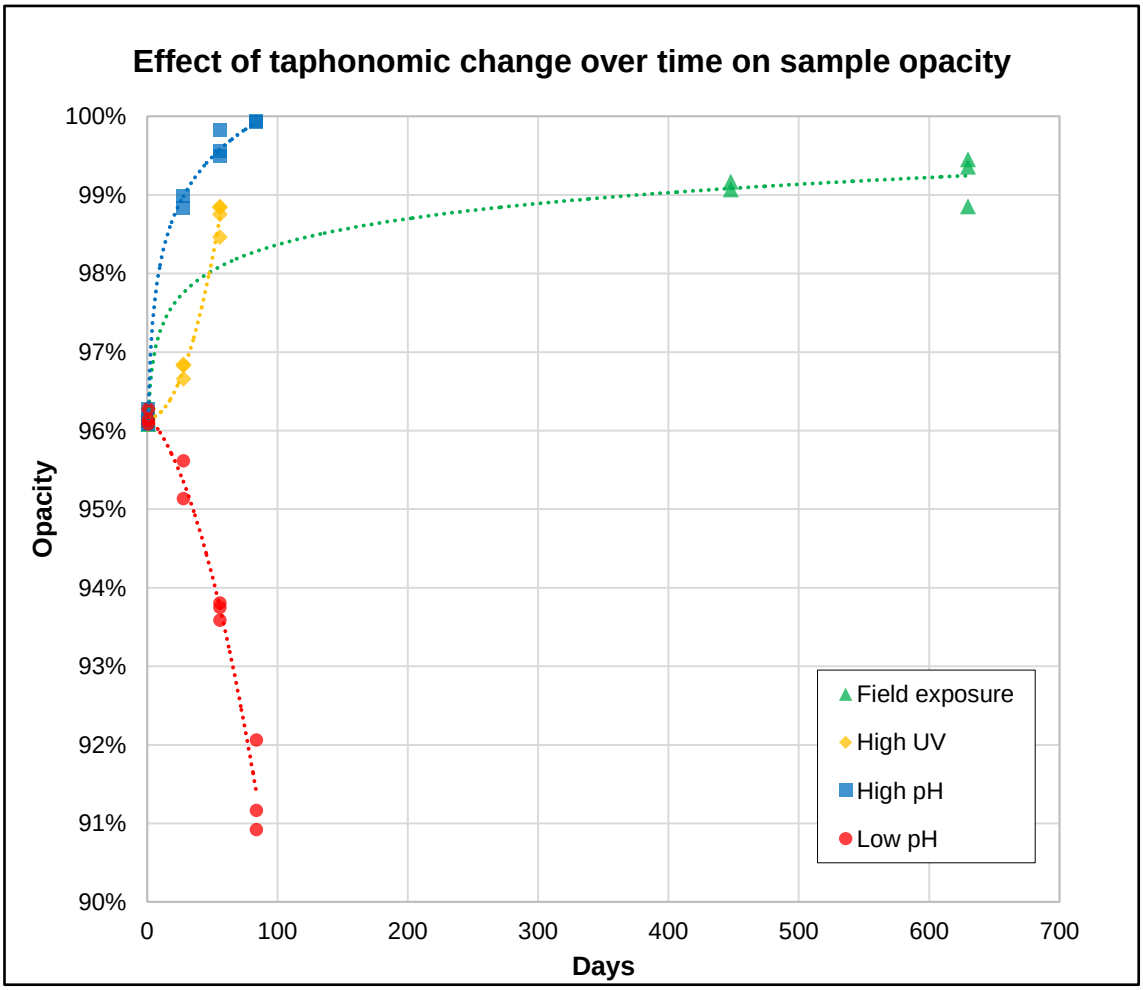

Figure 7.39: Plot of sample opacity change over time for the four taphonomy experiments (source: author).

All of the accelerated testing experiments in the laboratory were carried out on 28 day exposure periods, whilst the field weathering experiment, being a natural weathering, occurred over two periods totalling 630 days; the scale of the accelerated experiments is therefore compressed. The field weathering shows the expected increase in opacity from pre-exposure levels of c. 96% to highly opaque samples over 99%. Figure 7.40 displays the same data, excluding the field weathering in order to compare the accelerated testing experiments directly.

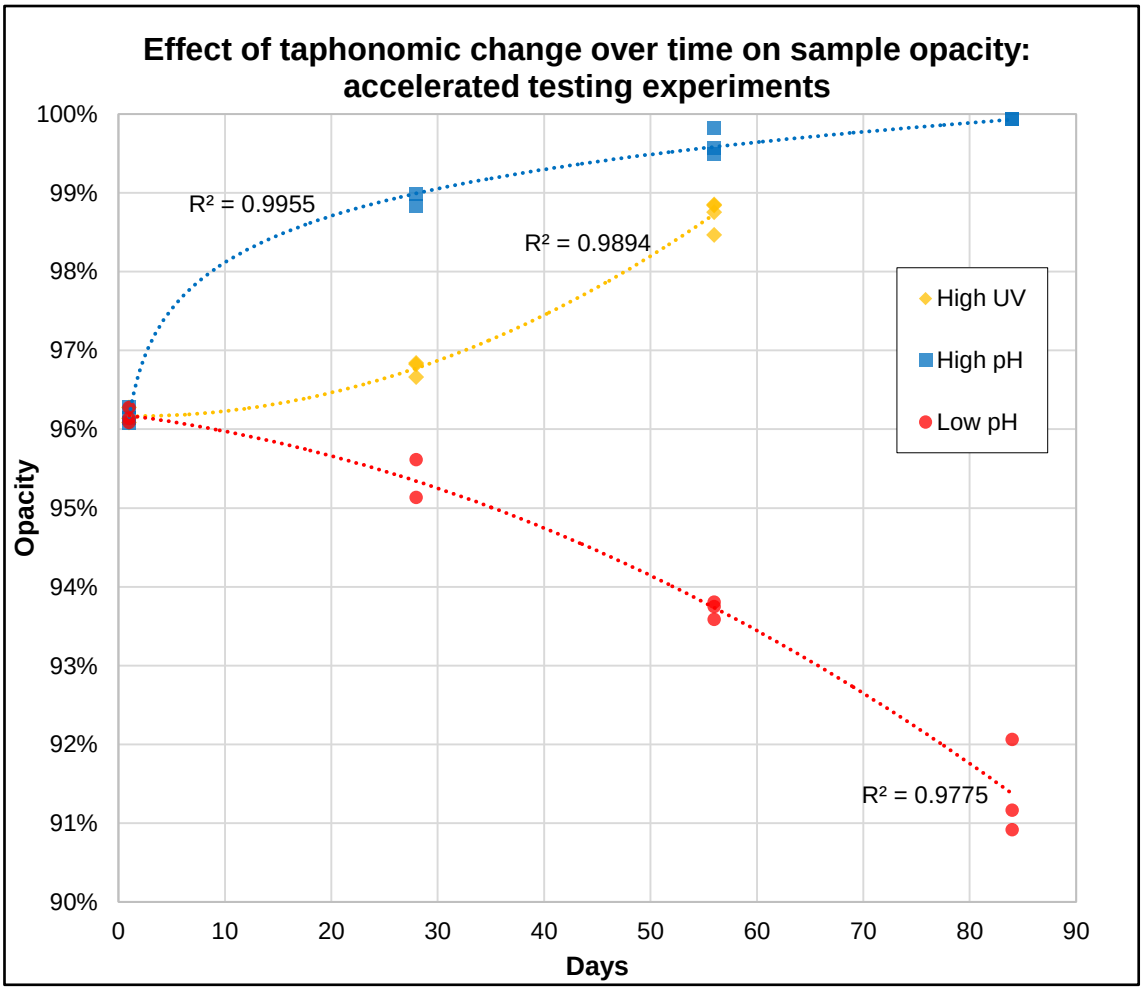

Figure 7.40: Plot of sample opacity change over time for the three accelerated taphonomy experiments (source: author).

The high pH samples display a logarithmic pattern to the opacity change over time with initial rapid increase followed by a tailing off as the rate of change slowed. The values for the high UV show a general increase in opacity over the two exposure periods. The low pH values show a rapid decrease in opacity over time. These results mirror those observed visually in the gross changes to whole and fragmentary bone samples (section 7.2.1).

7.3.2. Experimental sample colour lightness

The surface variation with respect to colour and colour lightness of the experimental samples were measured and normalised to a 0 to 1 range to make the measurements comparable (section 6.8.2), where 0 indicates no variation and 1 indicates a maximum variation (i.e. for colour lightness the variation between white and black).

The variation in surface lightness plotted against length of exposure in each of the taphonomic conditions is shown in figure 7.41.

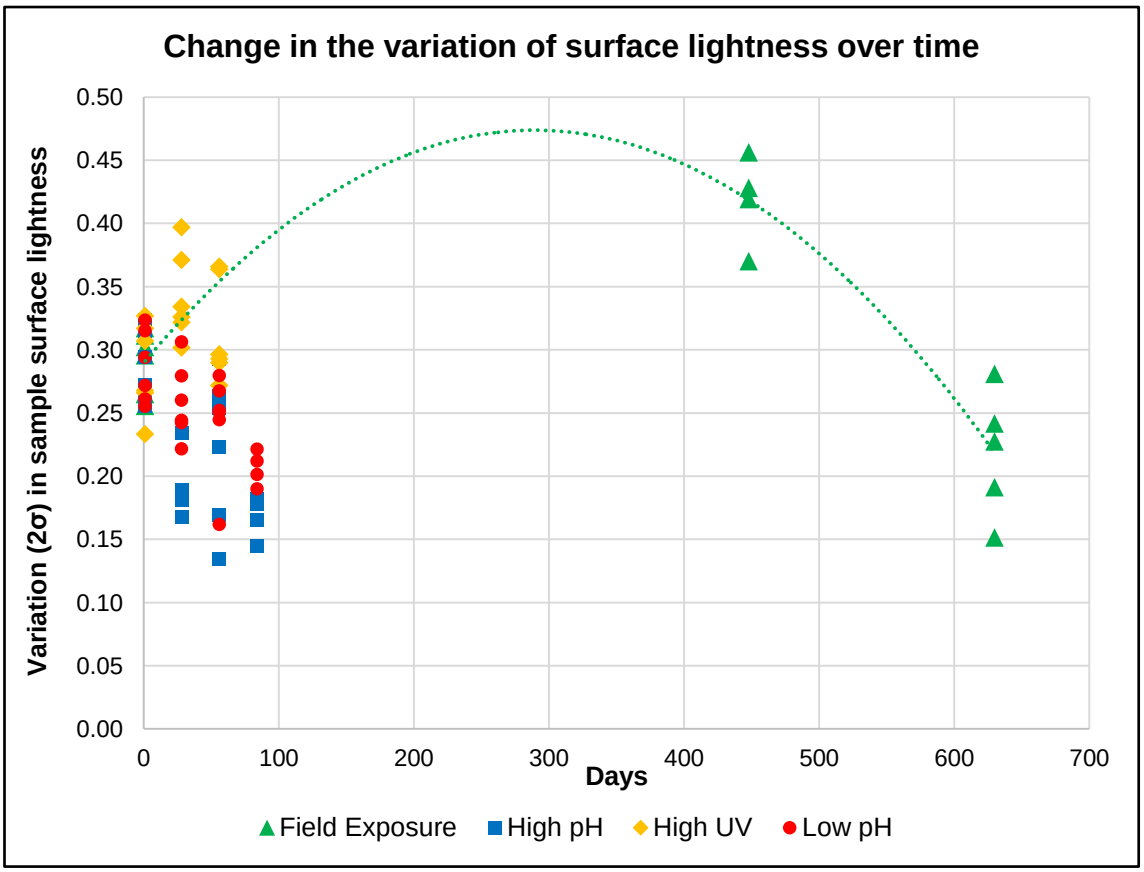

Figure 7.41: Plot of change in the variation of surface lightness over time for each of the four taphonomy experiments (source: author).

As with the measurement of the other variables, the pattern of data in the accelerated testing experiments is masked by the difference in timescale compared to the natural field weathering and the same data is therefore presenting in figure 7.42 without the field weathering data.

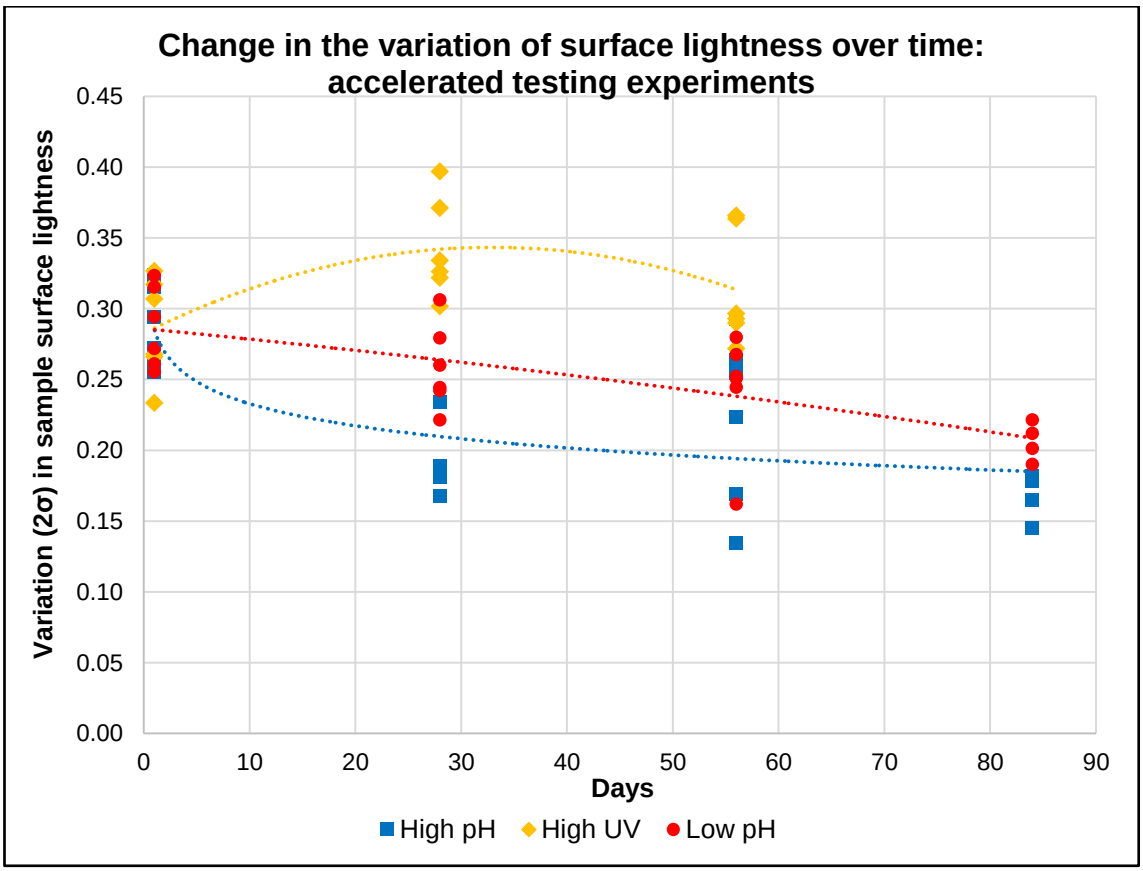

Figure 7.42: Plot of change in the variation of surface lightness over time for each of the three accelerated testing taphonomy experiments (source: author).

The data for the field weathering in figure 7.41 displays a pattern of marked increase in the variation in surface lightness on the samples after the first period of exposure, followed by a rapid decrease in the variation.

Within the accelerated testing data shown in figure 7.42, the high pH samples exhibited an initial reduction in the level of colour lightness followed by a further more gradual decrease. The high UV data shows a slight increase in the variation followed by a return to a similar level of lightness variation after the second period of exposure. The low pH data followed a gradual decrease in the level of colour lightness variation on the surface of the samples.

7.4. Results for the 3D digitised whole bone samples

After each period of exposure the whole bone samples from each of the taphonomic experiments were digitised in line with the methodology outlined in chapter six and the resultant 3D models were processed to produce measures of digitisation quality.

The following sections describe the quantitative results from the 3D digitised models of the whole bone samples.

7.4.1. Effect of the taphonomic changes of low pH exposure on the digitisation of whole bone samples

The whole bone samples in the low pH experiment displayed a large decrease in measured volumes over the three exposure periods (figure 7.43). The decrease in volume was greatest after the first exposure with a levelling off of volume change during the second exposure periods followed by a further decrease after the third period of exposure. The laser scan results show consistently higher volumes than the corresponding structured light results for the same whole bone sample.

Figure 7.43 Illustrates the change in volume for each of the 3D digitised whole bone samples over the three periods using lines to link the digitised results at each period of exposure for the same whole bone sample.

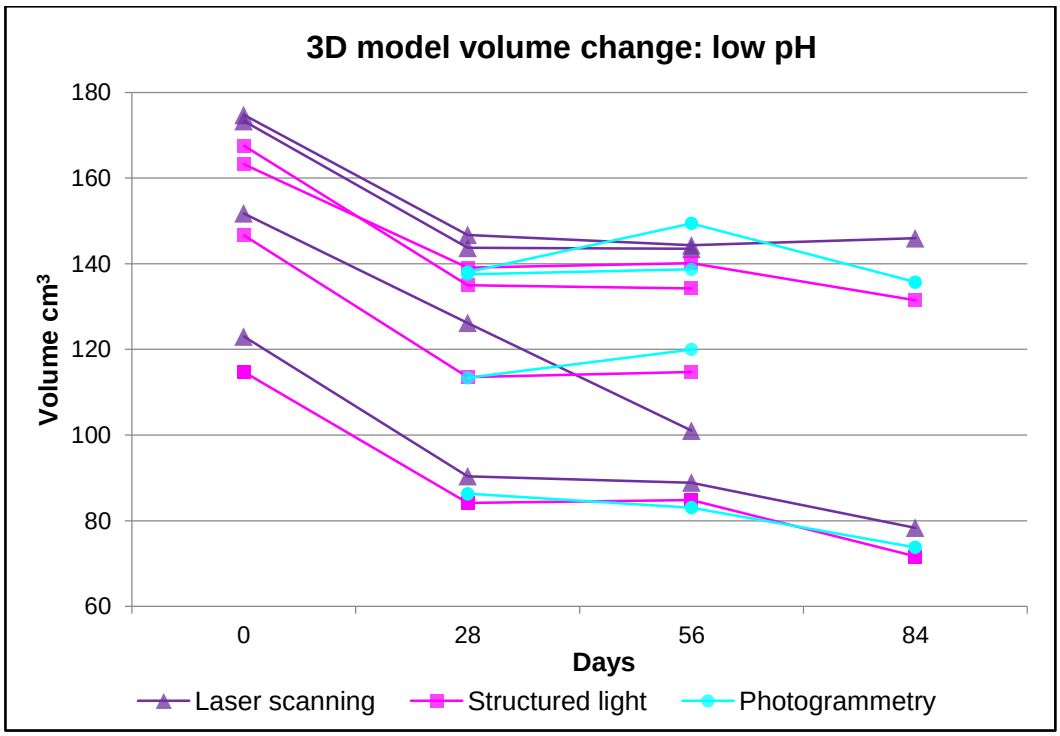

Figure 7.43: Plot of the measured change in 3D digitised model volumes for whole bone samples subject to three periods of low pH exposure (source: author).

Figure 7.44 plots the variation in volume measurement between laser scanning and structured light scanning (as a percentage of the pre-exposure sample volume) averaged over all samples at each exposure period. Laser scanning measured a smaller volume change than structured light scanning. Whilst photogrammetry volumes followed the general trend seen in the other instrument techniques (figure 7.43), the lack of pre-exposure digitised models prevented their inclusion in figure 7.44.

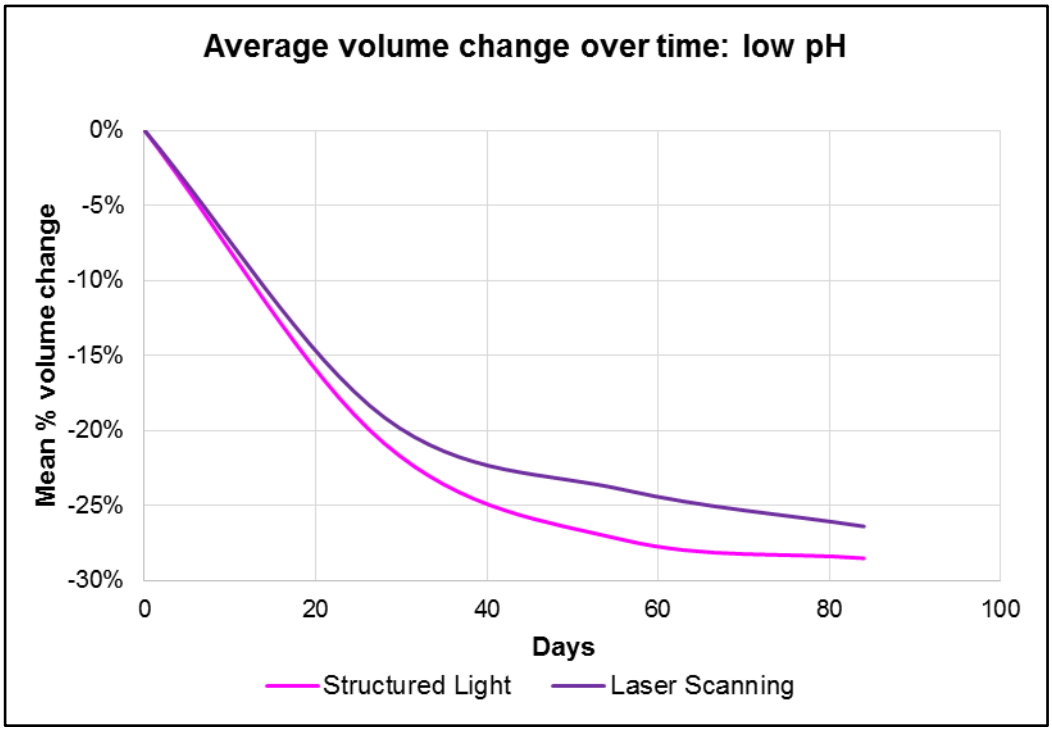

Figure 7.44: Plot of mean volume change as a percentage of starting volume for the structured light and laser scanned low pH samples (source: author).

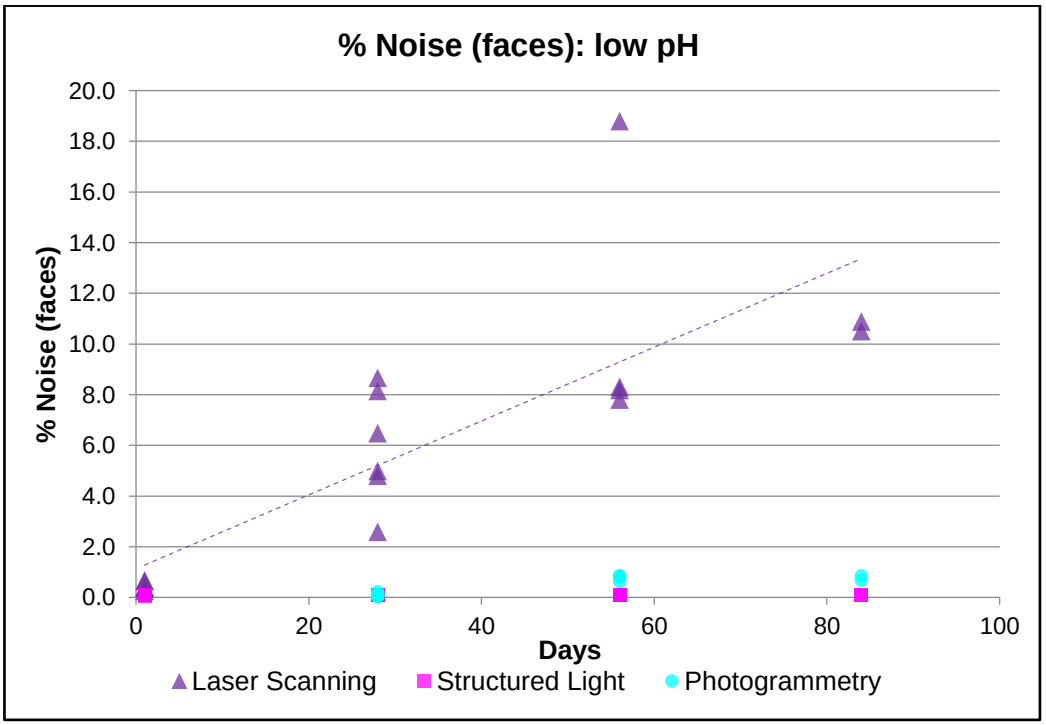

Figure 7.45: Plot comparing the percentage of mesh faces identified as noise within the low pH whole bone experimental samples for each of the digitisation techniques over time (source: author).

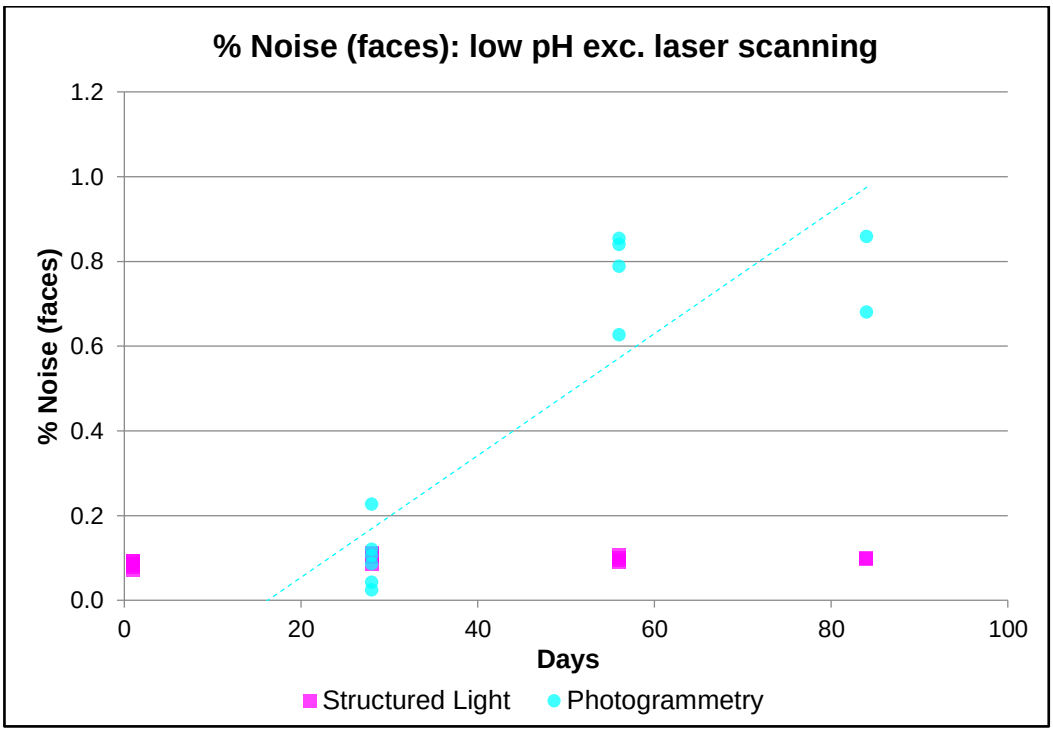

Figure 7.46: Plot comparing the percentage of mesh faces identified as noise within the low pH whole bone experimental samples for structured light and photogrammetry techniques over time (source: author).

The noise levels for laser scanning and photogrammetry in the low pH conditions displayed a greater percentage of face noise than in other taphonomy experiments; the scale of noise in relation to laser scanning (figure 7.45) was notably higher than for other taphonomy experiments and the y axis values reflect this.

Photogrammetry displayed an increase in the percentage of face noise over the exposure periods. The levels of noise for structured light scanning remained constant at around 0.1% at which level they probably reflect the inherent instrument noise of the scanner rather than the response of the scanner to the optical surface properties of the samples.

7.4.2. Effect of the taphonomic changes of high pH exposure on the digitisation of whole bone samples

The whole bone samples in the high pH experiment displayed a pattern of decreased volume across all samples for all techniques over the entire length of the experiment (figure 7.47).

Figure 7.47 illustrates the change in volume for each of the 3D digitised whole bone samples over the three periods using lines to link the digitised results at each period of exposure for the same whole bone sample.

Whilst there is a general decrease in volume over the duration of the experiment, there is also an increase in volume for some samples after the second period of exposure. In laser scanning and structured light scanning this increase is small and the two techniques are generally consistent. Photogrammetry displayed the greatest variation in volume measurements; whilst the measured volumes followed the general trend seen in the other instruments, the variation between photogrammetry and the other techniques was inconsistent.

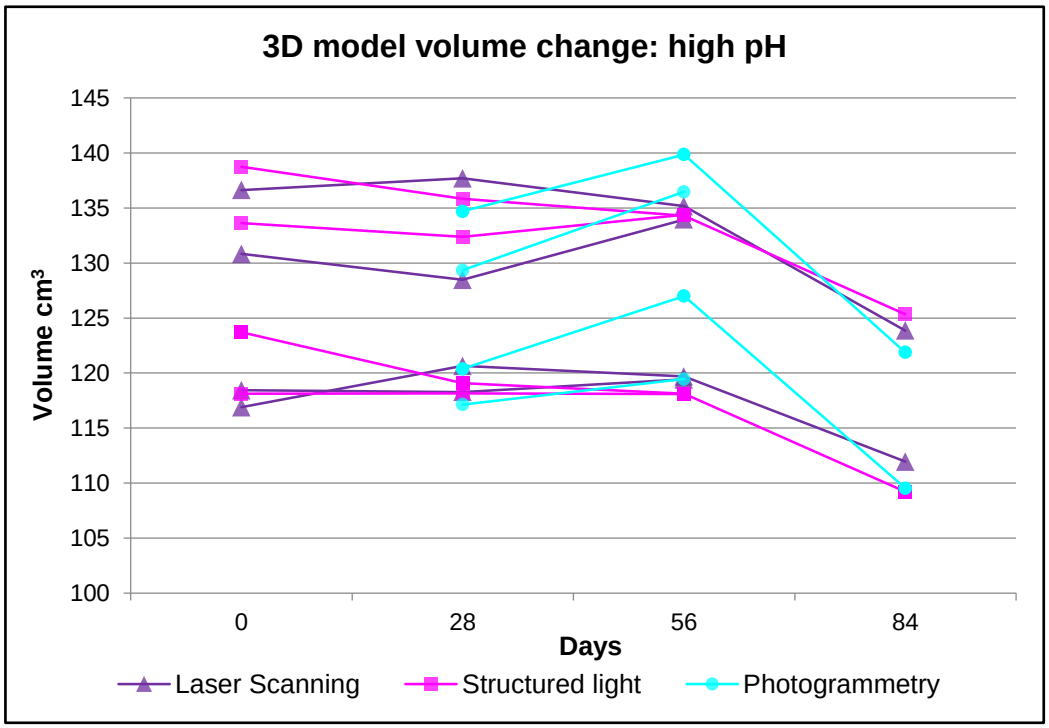

Figure 7.47: Plot of the measured change in 3D digitised model volumes for whole bone samples subject to three periods of high pH exposure (source author).

Figure 7.48 plots the variation in volume measurement between laser scanning and structured light scanning (as a percentage of the pre-exposure sample volume) averaged over all samples at each exposure period. Laser scanning measured a smaller volume change over the three high pH exposure periods than structured light scanning with overall percentage loss of volume over the length of the experiment of -6.8% and -10.7% respectively (figure 7.48).

Whilst photogrammetry volumes followed the general pattern seen in the other instrument techniques (figure 7.47), the lack of pre-exposure digitised models prevented their inclusion in figure 7.48.

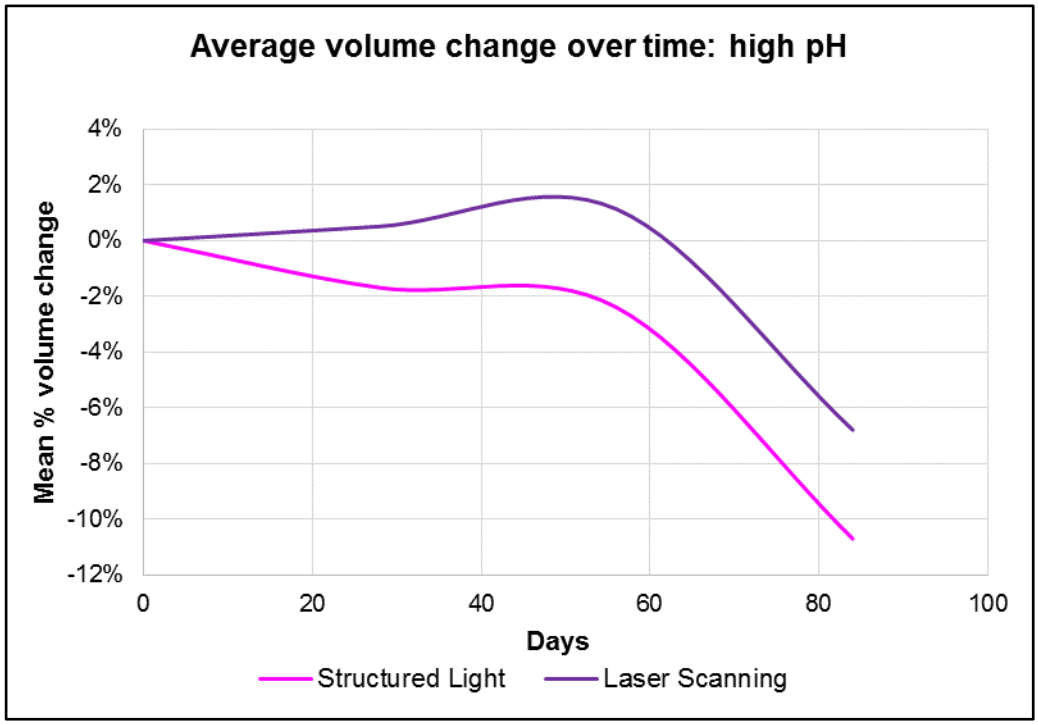

Figure 7.48: Plot of mean volume change as a percentage of starting volume for the structured light and laser scanned high pH samples (source: author).

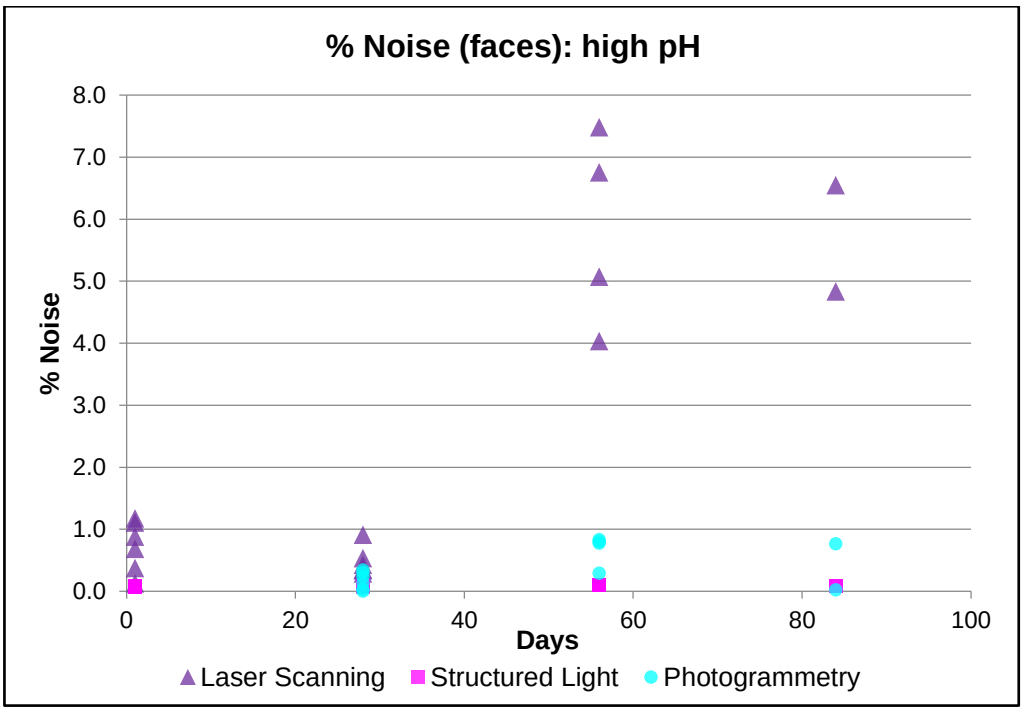

Figure 7.49: Plot comparing the percentage of mesh faces identified as noise within the high pH whole bone experimental samples for each of the digitisation techniques over time (source: author).

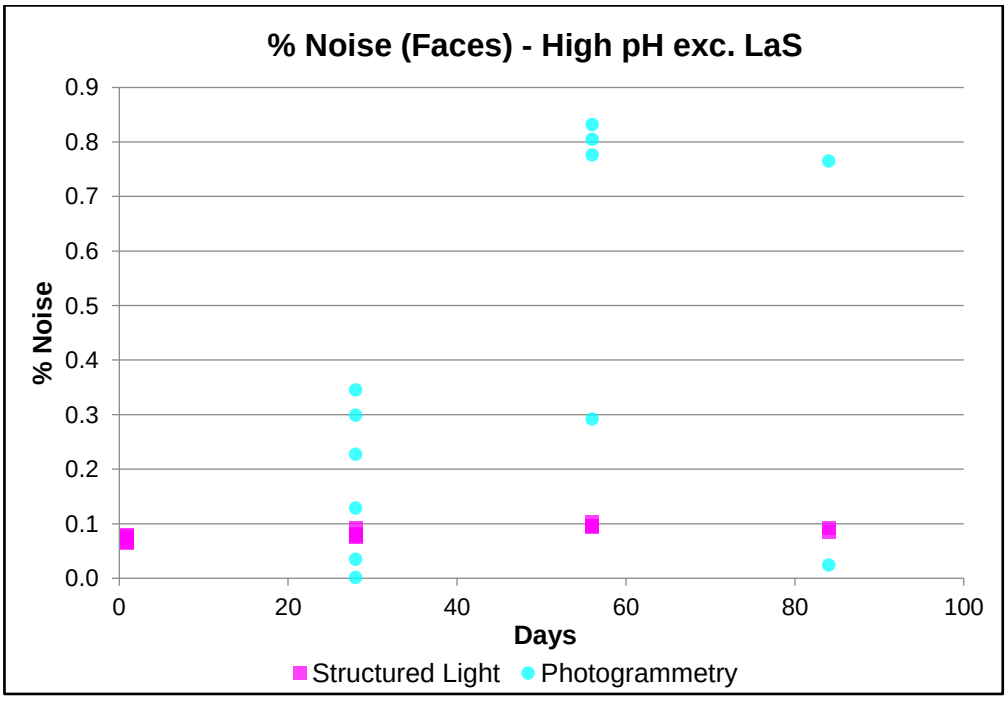

Figure 7.50: Plot comparing the percentage of mesh faces identified as noise within the high pH whole bone experimental samples for structured light and photogrammetry techniques over time (source: author).

The noise levels show an increase over the experimental timescale for laser scanning and photogrammetry, although the increase is significantly greater from the second period of exposure onwards (figure 7.50). Laser scanning

produced the highest percentage of face noise compared to the other techniques with the highest levels of noise after the second exposure period (max. 7.48%).

Photogrammetry showed a pattern of increased noise over the exposure periods with a sharp rise between the first and second periods, followed by a slight reduction after the final exposure period. The highest values were recorded after the second period of exposure (max. 0.8%).

The levels of noise for structured light scanning remained constant at around 0.1% at which level they probably reflect the inherent instrument noise of the scanner rather than the response of the scanner to the optical surface properties of the samples.

7.4.3. Effect of the taphonomic changes of high UV exposure on the digitisation of whole bone samples

The whole bone samples in the high UV experiment displayed some limited variation in the measured model volumes for the techniques with the exception of photogrammetry which shows highly inconsistent volume changes (figure 7.51).

Figure 7.51 illustrates the change in volume for each of the 3D digitised whole bone samples over the two periods using lines to link the digitised results at each period of exposure for the same whole bone sample.

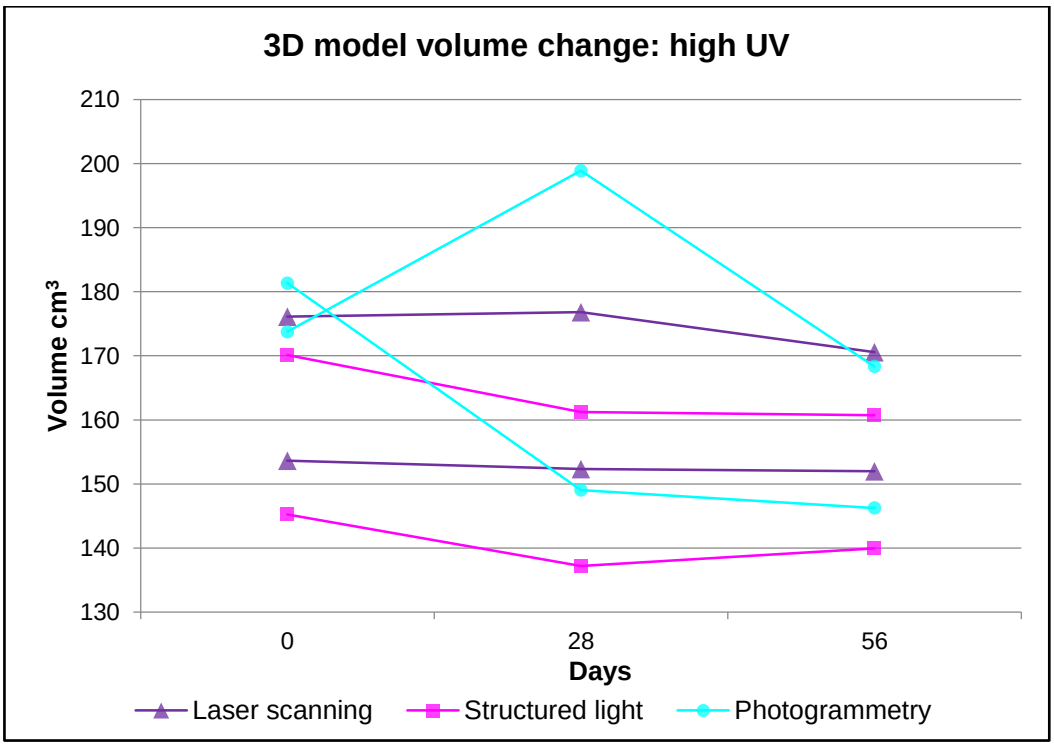

Figure 7.51: Plot of the measured change in 3D digitised model volumes for two whole bone samples subject to two periods of high UV exposure (source: author).

Figure 7.52 plots the variation in volume measurement for the techniques (as a percentage of the pre-exposure sample volume) averaged over all samples at each exposure period. Laser scanning measured a smaller volume change over the two high UV exposure periods than structured light scanning with overall percentage loss of volume over the length of the experiment of -2.1% and -4.6% respectively. Photogrammetry shows a much larger decrease in volume (-11.2% overall) although this is mainly due to the inconsistency of the photogrammetry data after the first and second exposure periods.

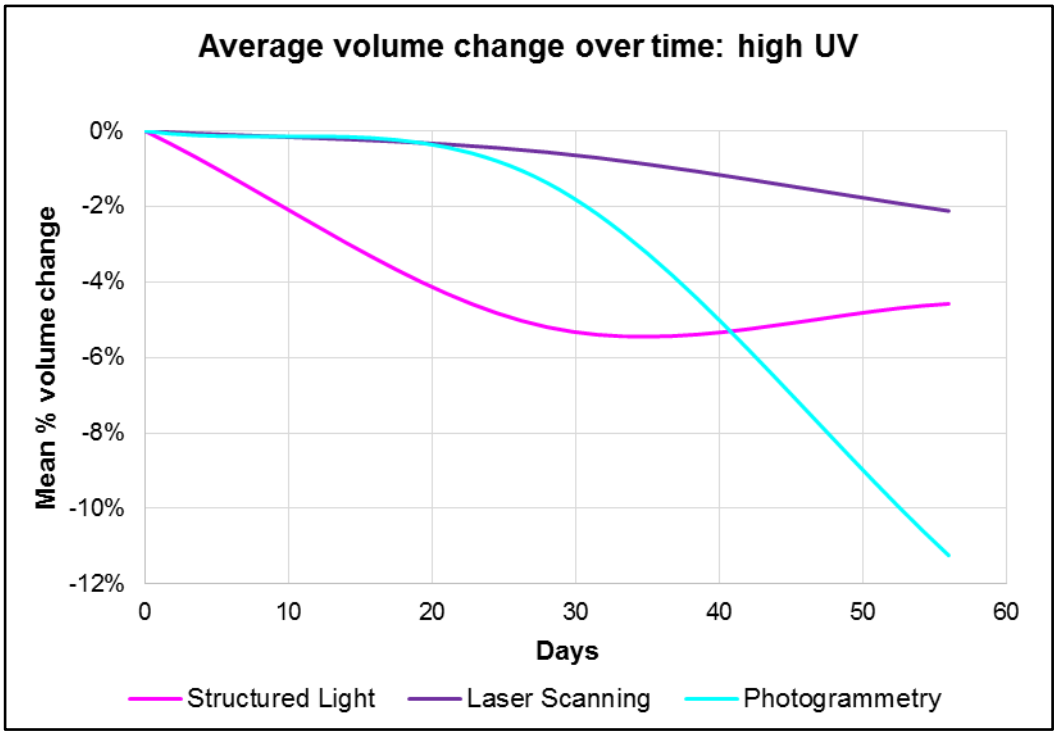

Figure 7.52: Plot of mean volume change as a percentage of starting volume for the structured light and laser scanned high UV samples (source: author).

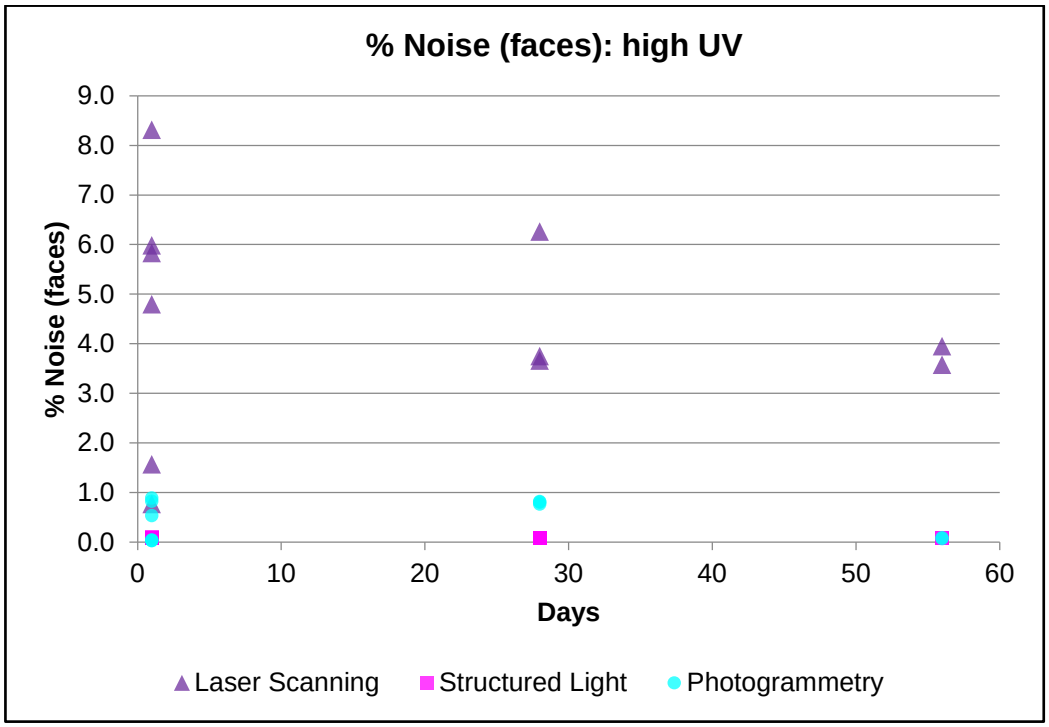

Figure 7.53: Plot comparing the percentage of mesh faces identified as noise within the high UV exposure whole bone experimental samples for each of the digitisation techniques over time (source: author).

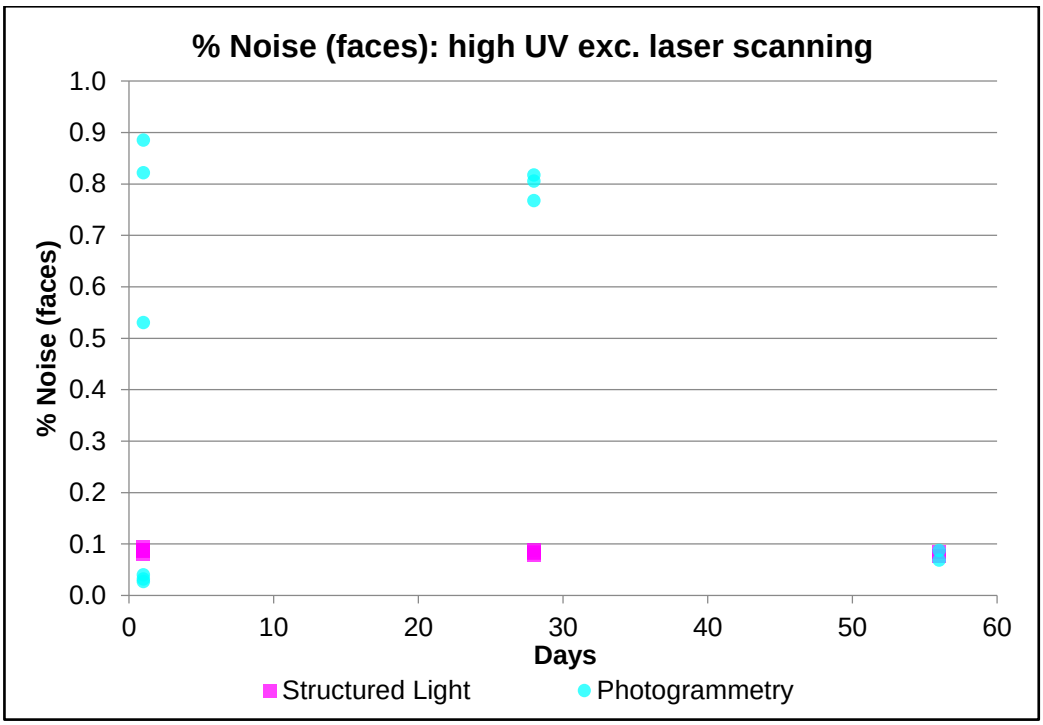

Figure 7.54: Plot comparing the percentage of mesh faces identified as noise within the high UV exposure whole bone experimental samples for structured light and photogrammetry techniques over time (source: author).

The noise levels show a clear reduction from the pre-exposure levels for both laser scanning and photogrammetry (figure 7.53). Laser scanning had the highest percentage of face noise compared to the other techniques and the decrease in noise levels was the largest of the techniques from max values of 8.3% prior to exposure to 3.9% following the second exposure period.

The decrease in noise values for the photogrammetry models was greatest after the second exposure period where they fell to below 0.1%, with only limited reductions after the first exposure (figure 7.54).

The levels of noise for structured light scanning remained constant at around 0.1% at which level they probably reflect the inherent instrument noise of the scanner rather than the response of the scanner to the optical surface properties of the samples.

7.4.4. Effect of the taphonomic changes of field weathering on the digitisation of whole bone samples

The measured volumes of the bone samples (figure 7.55) exhibited a limited degree of variation over the length of the experiment.

Whilst photogrammetry data wasn't collected for the earlier stages, the later stage data shows consistent volume estimates to laser scanning and structured light scanning.

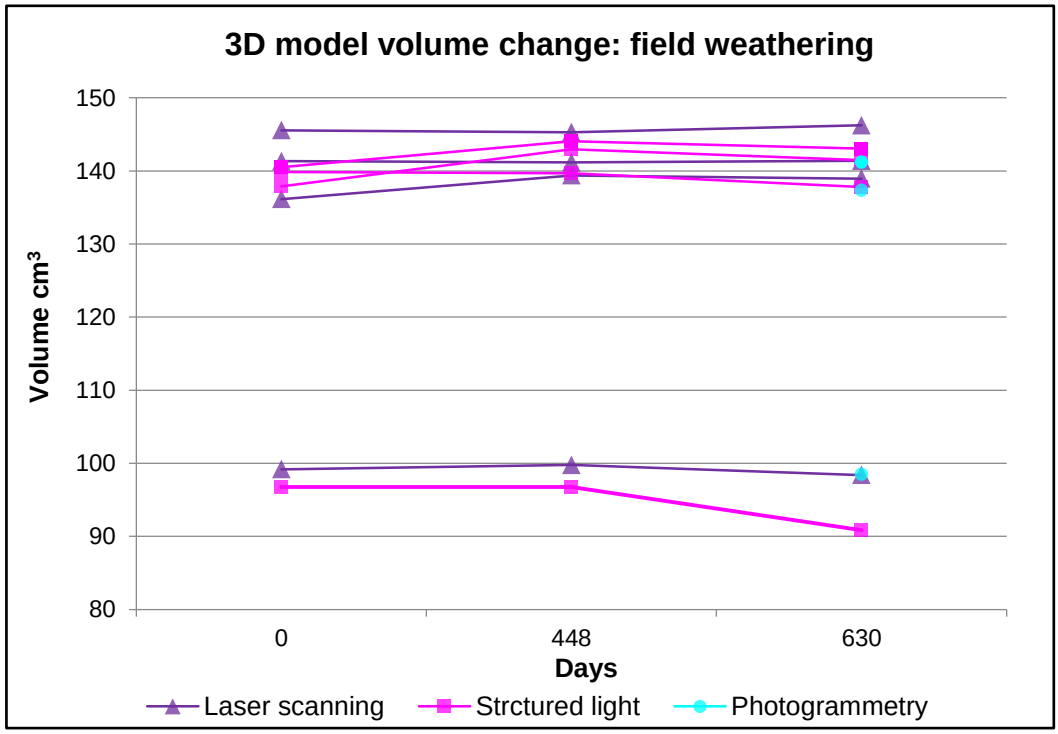

Figure 7.55: Plot of the measured change in 3D digitised model volumes for whole bone samples subject to two periods of field weathering exposure (source: author).

Figure 7.56 plots the variation in volume measurement between laser scanning and structured light scanning (as a percentage of the pre-exposure sample volume) averaged over all samples at each exposure period. Laser scanning and structured light had similar measured volumes and the variation between them is too small to be significant, representing variation in instrument noise (figure 7.57).

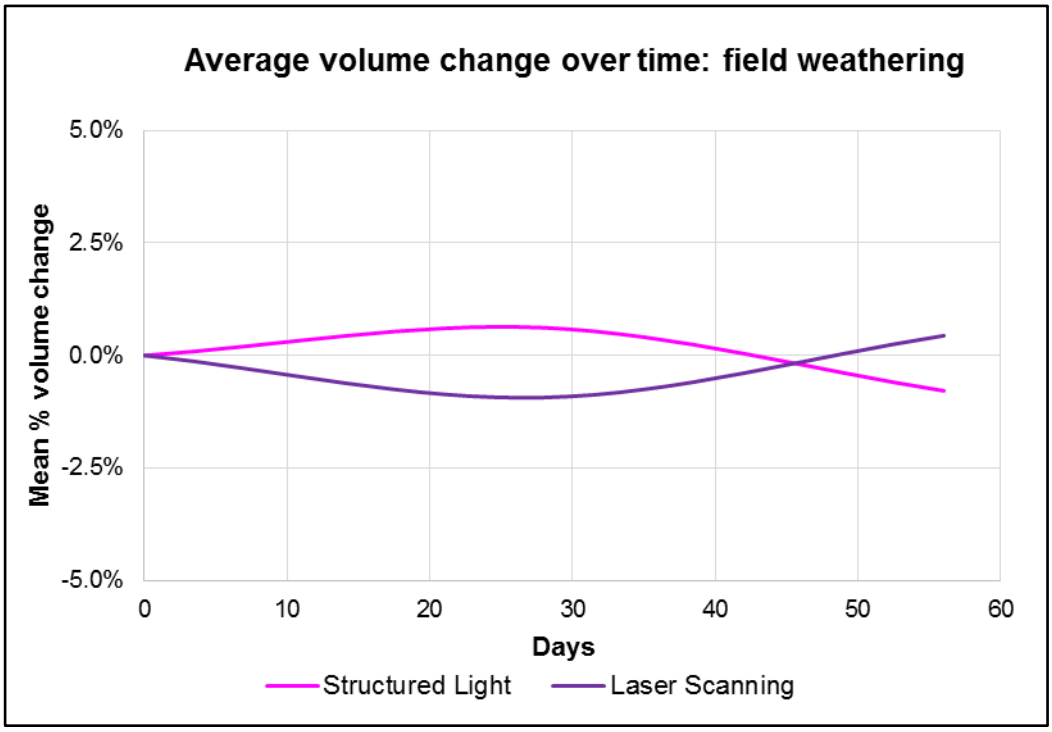

Figure 7.56: Plot of mean volume change as a percentage of starting volume for the structured light and laser scanned field weathering samples (source: author).

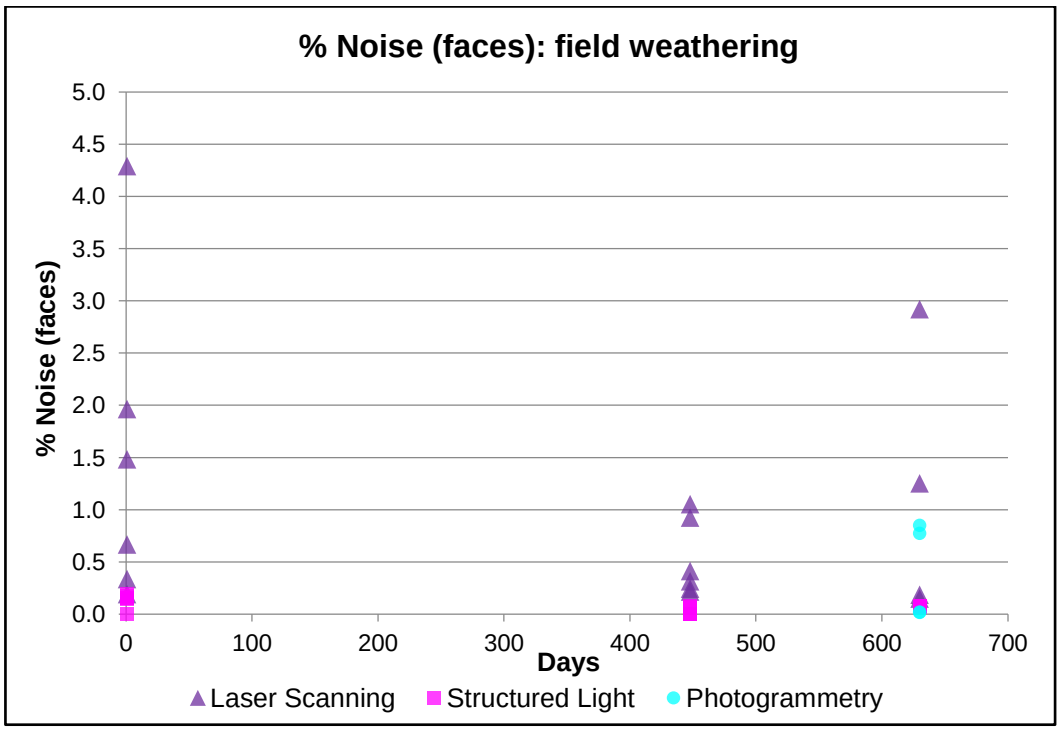

Figure 7.57: Plot comparing the percentage of mesh faces identified as noise within the field weathering whole bone experimental samples for each of the digitisation techniques over time (source: author).

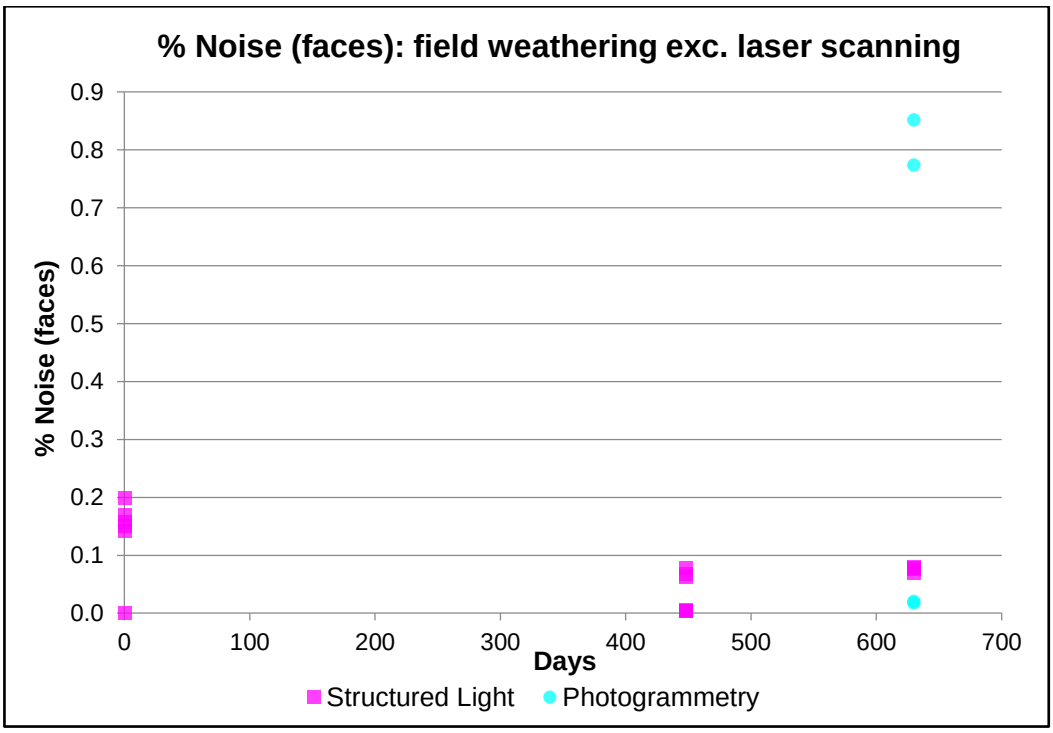

Figure 7.58: Plot comparing the percentage of mesh faces identified as noise within the field weathering whole bone experimental samples for structured light and photogrammetry techniques over time (source: author).

The levels of face noise exhibit a reduction in values for both laser scanning and structured light over the pre-exposure values (figures 7.57 and 7.58). The laser scanning values displayed the highest initial values and the largest reduction over the two exposure periods. The reduction was greatest after the first exposure period with maximum face noise values of 0.9%, although after the second exposure period the level of noise increased again to a maximum of 2.9%.

The photogrammetry values are only available for the final exposure period at a max value of 0.85%.

The levels of noise for structured light scanning demonstrated a small reduction from 0.2% to below 0.1%. The pre-exposure samples for the field weathering experiment were the first to be prepared over a year prior to the samples used in the other experiments and this change probably represents reduced instrument noise associated with increased user experience with the structured light scanner rather than a response to taphonomic change in the samples. Considerable prior user experience with the equipment negates this factor in the laser scanner and photogrammetry data.

7.5. Refit analysis of fragmented bone samples

The refit analysis was undertaken for bone fragmented at each period of exposure in all taphonomic experiments in line with the methodology outlined in section 6.10.

The following sections describe the results of the refit analysis of the fragmented bone samples. The refit analysis methodology described in section 6.10.4 produced cloud to mesh distances for the two corresponding surfaces of each fragmented bone sample. The distances were expressed as a mean distance averaged for all points on the two corresponding fracture surfaces. The variation in the distances within each pair of corresponding fracture surfaces was expressed by the two sigma standard deviation of the distances from the mean.

The percentage of the surface area of the two corresponding fracture surfaces refitting to a refit distance of within +/- 0.1 mm is used as a comparative quality indicator.

A pre-exposure sample was fragmented and subject to the same refit analysis to provide a baseline comparator. The refit analysis of the 3D digital models from the fragmented pre-exposure bone sample demonstrated that the two corresponding surfaces were digitally refit to within +/- 0.1 mm distance for 50.11% to 55.49% of the fracture surface area across all three techniques and showed consistent results for the mean distance and distance variation.

7.5.1. Effect of the taphonomic changes of low pH exposure on the digital refit of bone

The mean refit distance between the two corresponding surfaces for each sample shows wide and inconsistent variation for all three exposure periods and all three techniques (figure 7.59). There is no clearly defined pattern to the data within either exposure period or technique. The distance variation within each refit demonstrates a lower level of distance variation for structured light than for photogrammetry and laser scanning (figure 7.60).

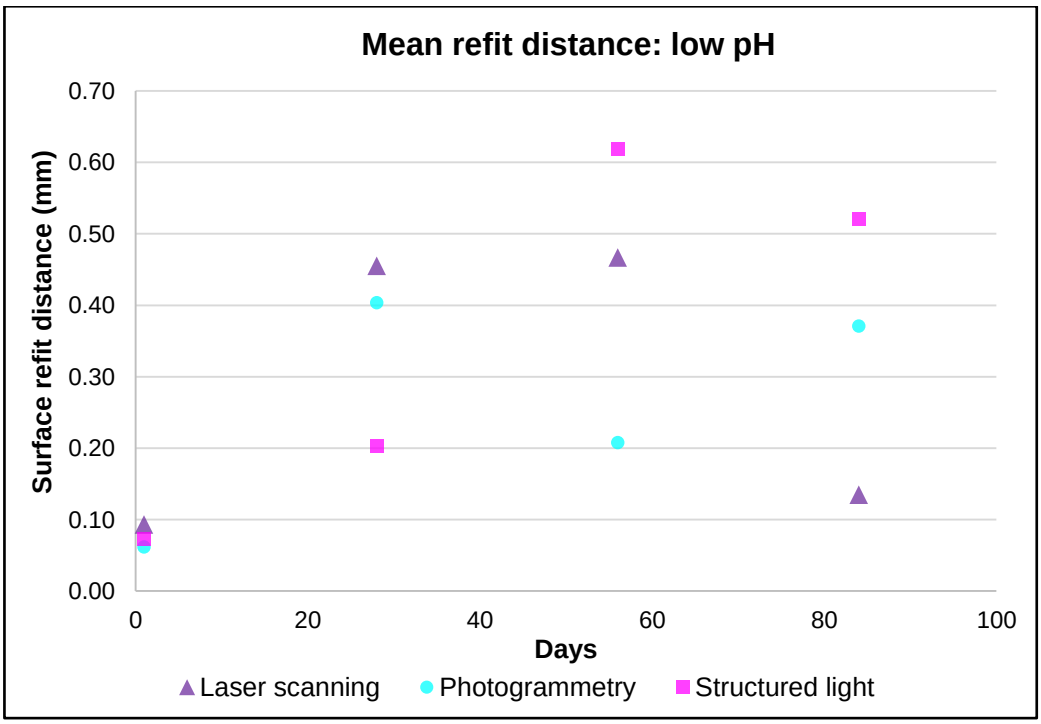

Figure 7.59: Plot of the mean distance between the refitting surfaces of the fragmented low pH experimental samples (source: author).

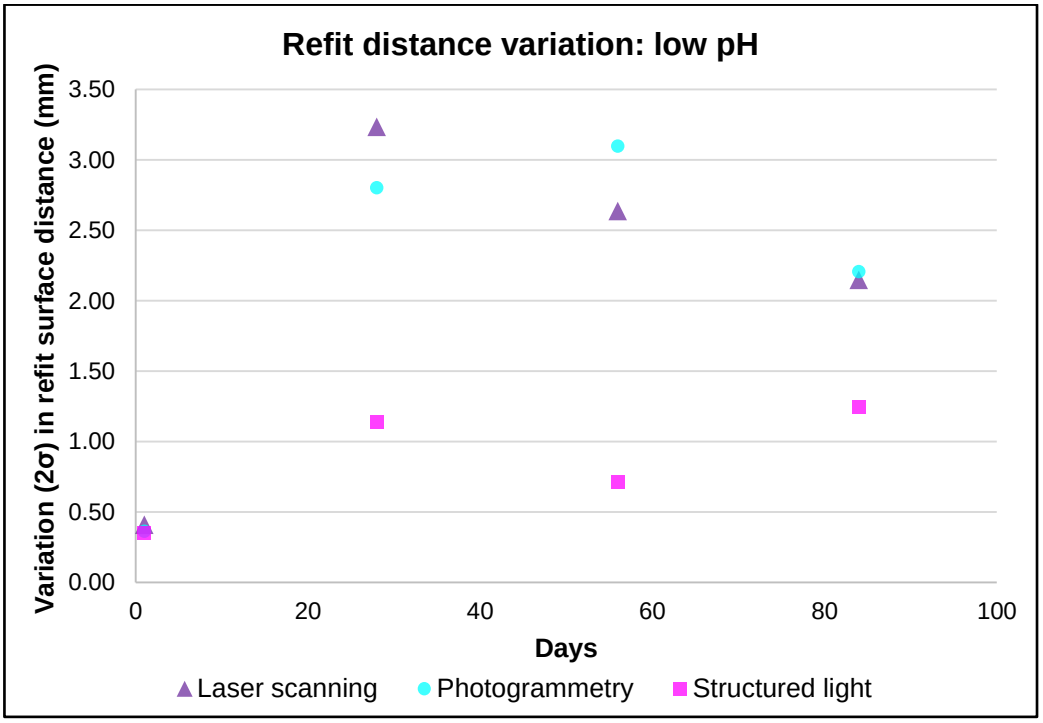

Figure 7.60: Plot of the variation in distance between the refitting surfaces of the fragmented low pH experimental samples (source: author).

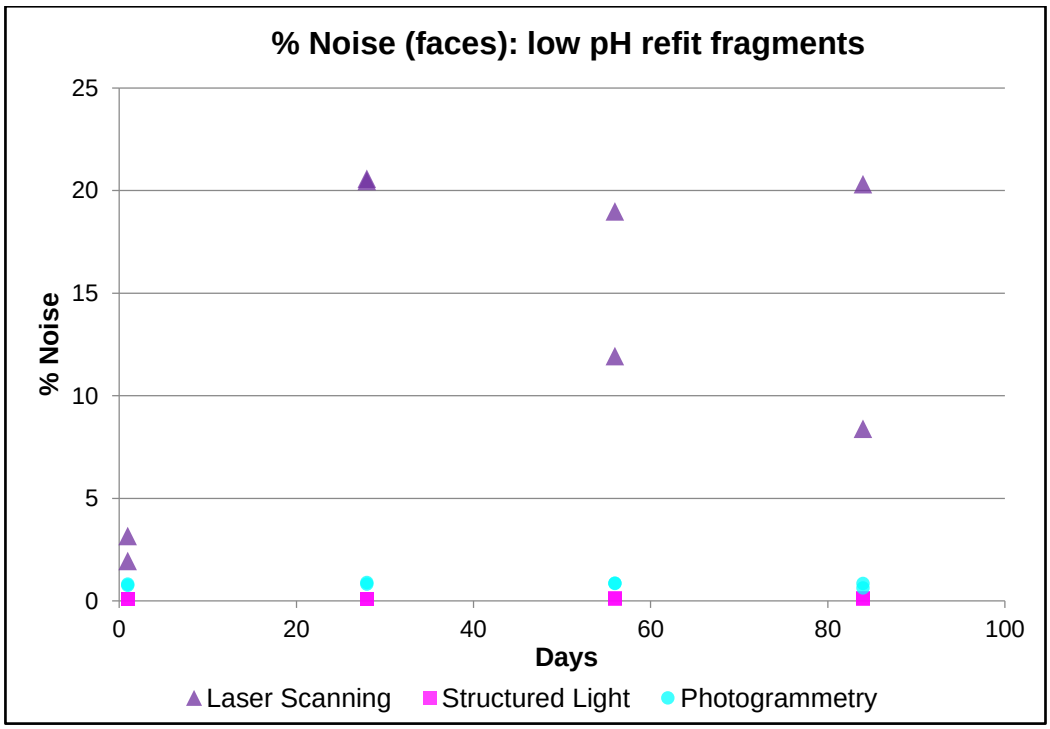

Figure 7.61: Plot comparing the percentage of mesh faces identified as noise within the fragmented low pH experimental samples for each of the digitisation techniques over time (source: author).

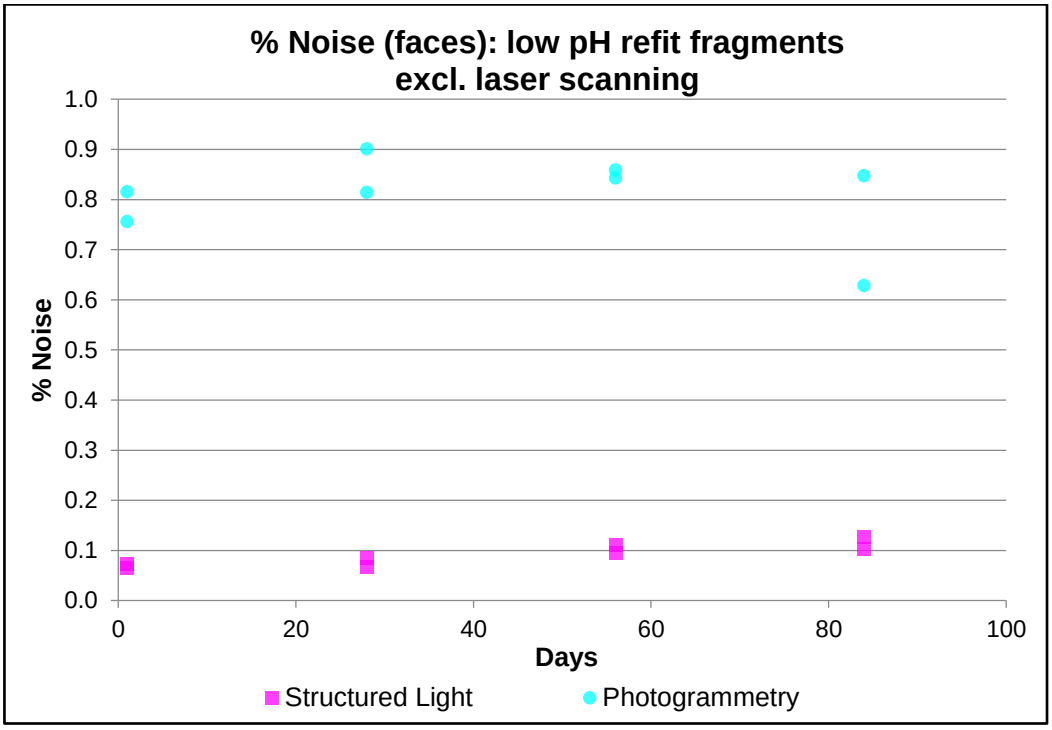

Figure 7.62: Plot comparing the percentage of mesh faces identified as noise within the fragmented low pH experimental samples for structured light and photogrammetry techniques over time (source: author).

The percentage of face noise in the low pH samples showed a very high level of noise for laser scanning across all three exposure periods (figure 7.61); the

noise affected up to 20% of the digital model mesh. The noise associated with the photogrammetry models ranged from 0.6% to 0.9% of the digital model mesh, whilst the percentage of noise associated with structured light was considerably less at c. 0.05 to 0.15% with a very gradual increase over the three exposure periods (figure 7.62).

Following the first exposure period the percentage of the refitting fracture surfaces within +/- 0.1 mm had decreased to less than 18% for all three techniques compared to the c. 50% for the pre-exposure sample. Further exposure periods resulted in additional reduction in this quality indicator to between 5.08% and 7.55% after the final exposure period (figure 7.63).

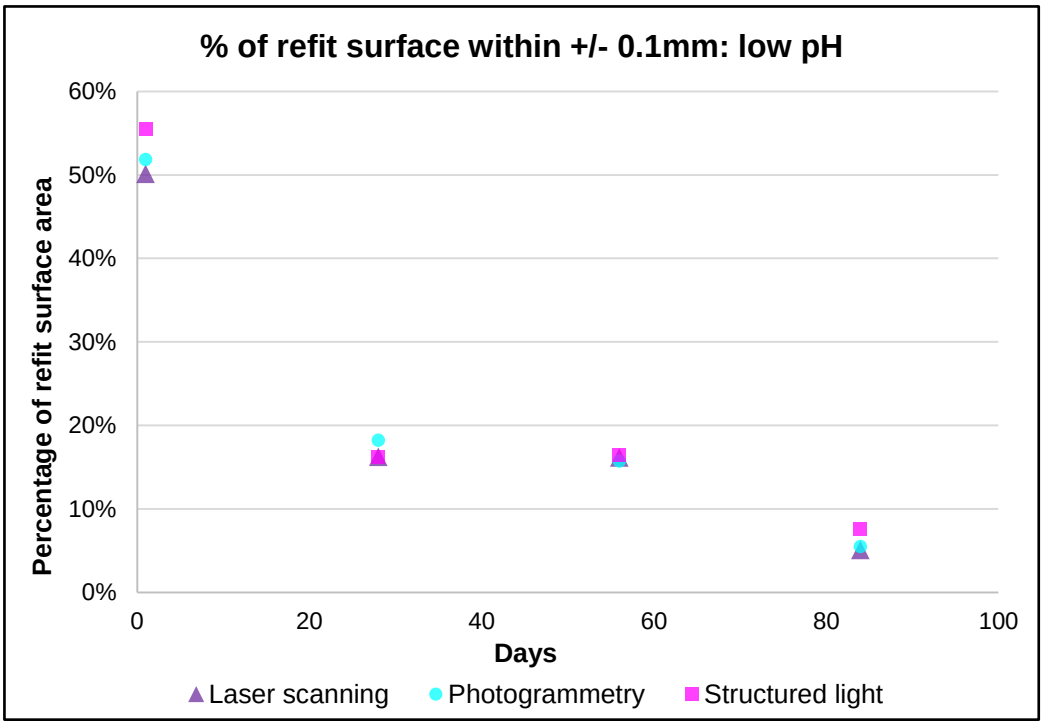

Figure 7.63: Plot showing the percentage of the refitting surface area between the fragments of the low pH experimental samples within a +/- 0.1 mm distance (source: author).

7.5.2. Effect of the taphonomic changes of high pH exposure on the digital refit of bone

The mean refit distance between the two surfaces for each sample displayed a consistent decrease across the three exposure periods for all techniques (figure 7.64). The photogrammetry model following the third exposure period exhibits as an outlier to this trend and the reasons are included in the discussion in chapter eight.

The distance variation within each refit demonstrated an initial increase compared to the pre-exposure samples. After subsequent exposure periods the variation in the refit distances decreased returning to the pre-exposure level. The photogrammetry results exhibited a consistently higher level of variation in the refit distances than the other techniques which were broadly comparable (figure 7.65).

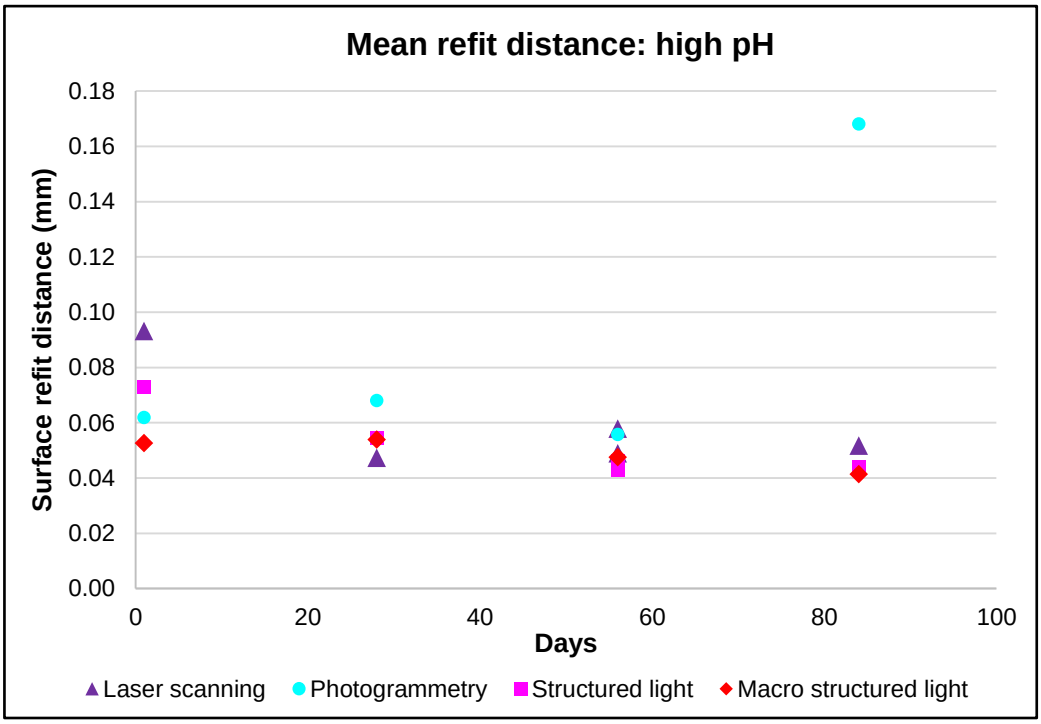

Figure 7.64: Plot of the mean distance between the refitting surfaces of the fragmented high pH experimental samples (source: author).

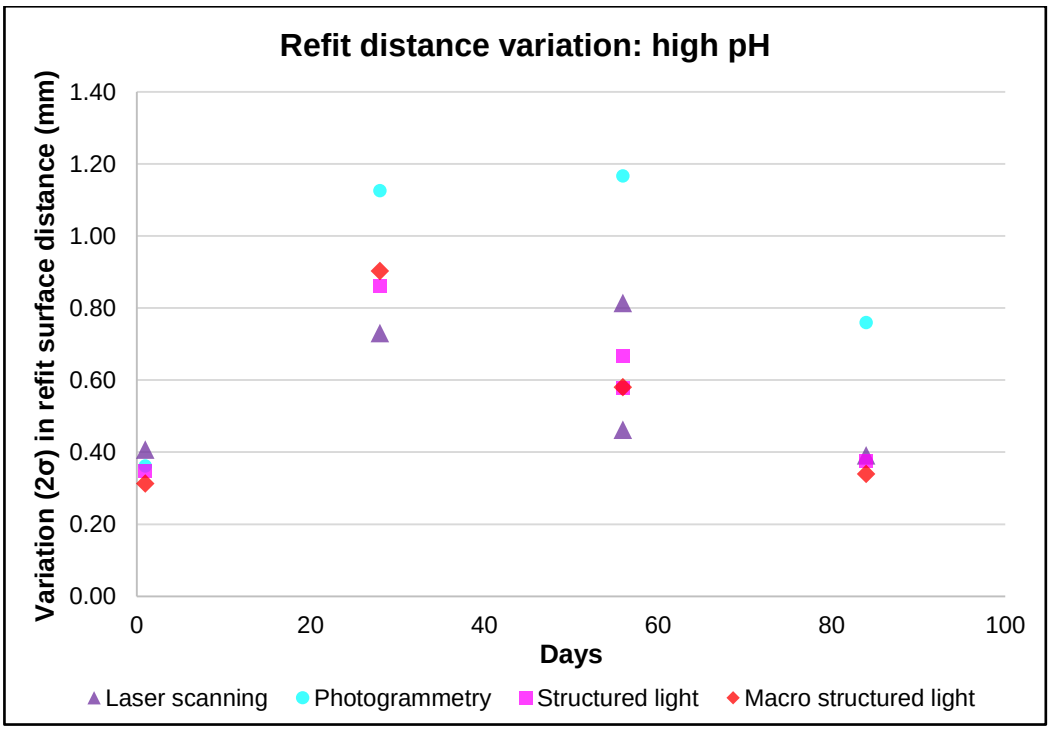

Figure 7.65: Plot of the variation in distance between the refitting surfaces of the fragmented high pH experimental samples (source: author).

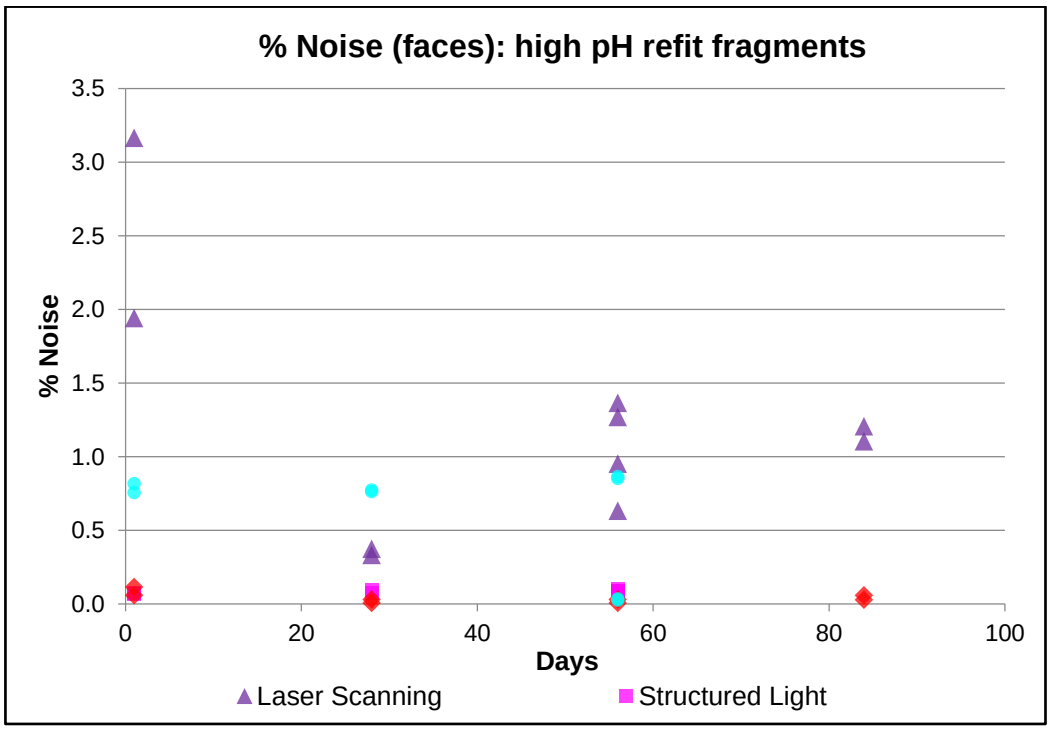

Figure 7.66: Plot comparing the percentage of mesh faces identified as noise within the fragmented high pH experimental samples for each of the digitisation techniques over time (source: author).

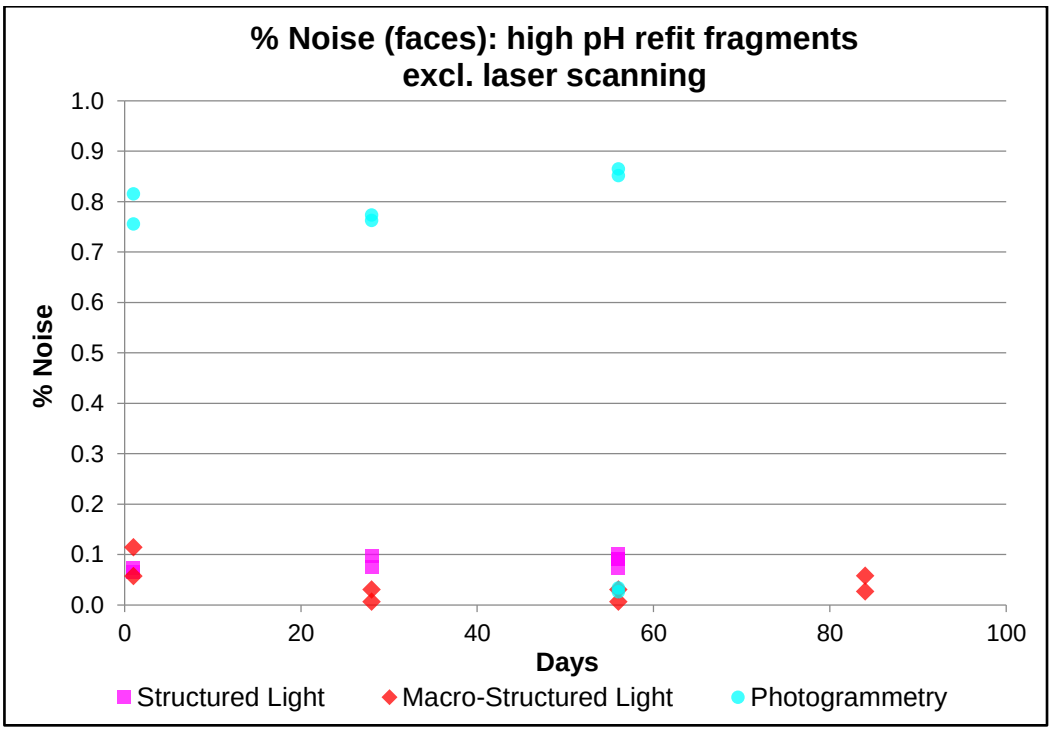

Figure 7.67: Plot comparing the percentage of mesh faces identified as noise within the fragmented high pH experimental samples for structured light, macro structured light and photogrammetry techniques over time (source: author).

The percentage of face noise in the high pH samples showed a higher level of noise for laser scanning (max. 1.37%) and photogrammetry (max. 0.87%) across all three exposure periods (figure 7.66); the percentage of noise associated with structured light and macro structured light was considerably less at values below 0.1% (figure 7.67).

The percentage of the refitting fracture surfaces within +/- 0.1 mm for structured light scanning remained broadly consistent at over 50% over all three exposure periods (figure 7.68). Macro structured light and laser scanning both displayed a decrease in the percentage of the refitting surfaces within +/- 0.1 mm over the first two exposure periods to c. 35%, but showed a noticeable improvement after the third period with values comparable with structured light scanning. Photogrammetry followed a similar pattern with an initial reduction in quality, followed by an improvement after the third exposure period. However, the quality of the refit was considerably lower than for the other techniques with a minimum value of 14.3% after the second exposure period.

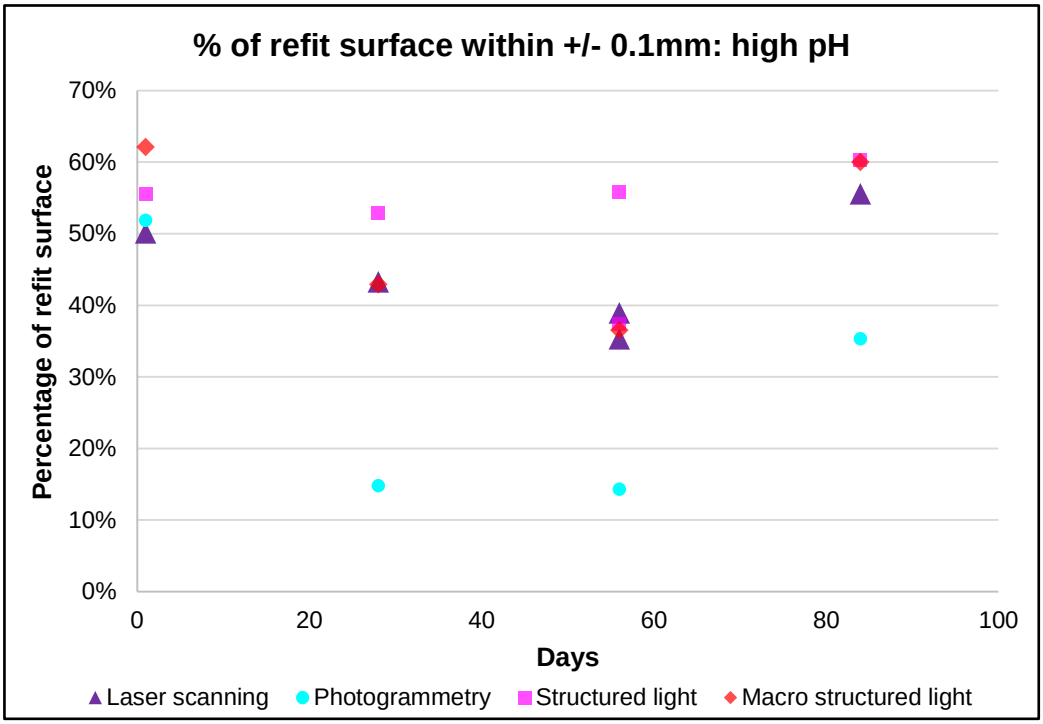

Figure 7.68: Plot showing the percentage of the refitting surface area between the fragments of the high pH experimental samples within a +/- 0.1 mm distance (source: author).

7.5.3. Effect of the taphonomic changes of high UV exposure on the digital refit of bone

The mean refit distance between the two surfaces for each sample displayed a decrease across the two exposure periods for all techniques (figure 7.69).

The distance variation within each refit demonstrated a minor increase over the two exposure periods. The photogrammetry results exhibited a higher level of variation in the refit distances than the other techniques which were broadly comparable (figure 7.70).

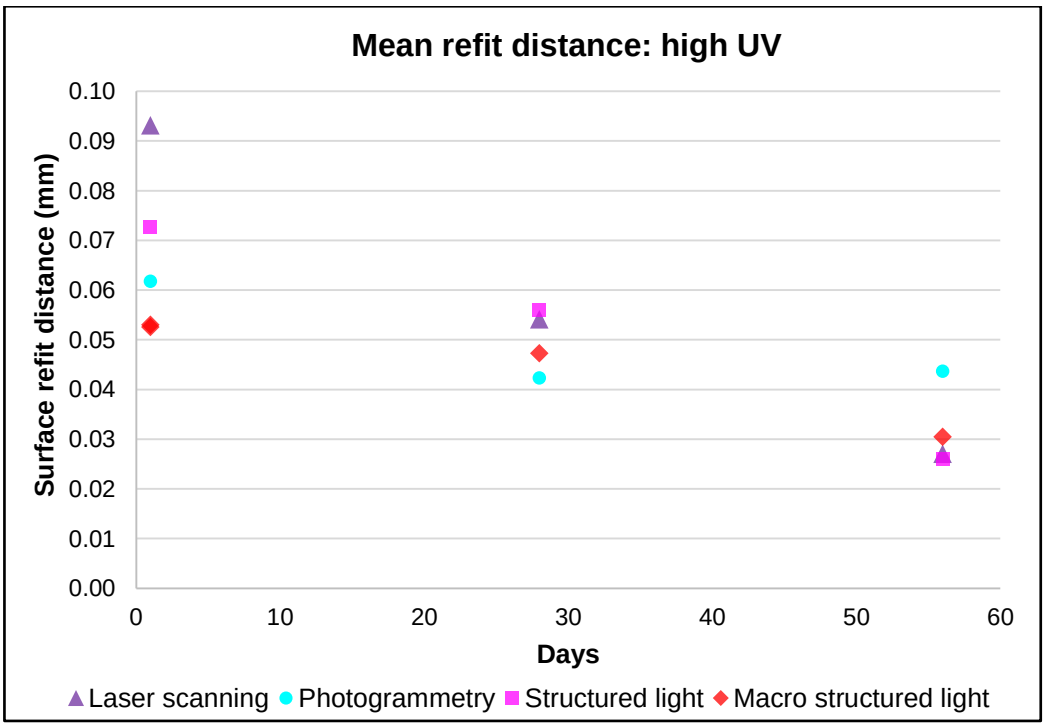

Figure 7.69: Plot of the mean distance between the refitting surfaces of the fragmented high UV experimental samples (source: author).

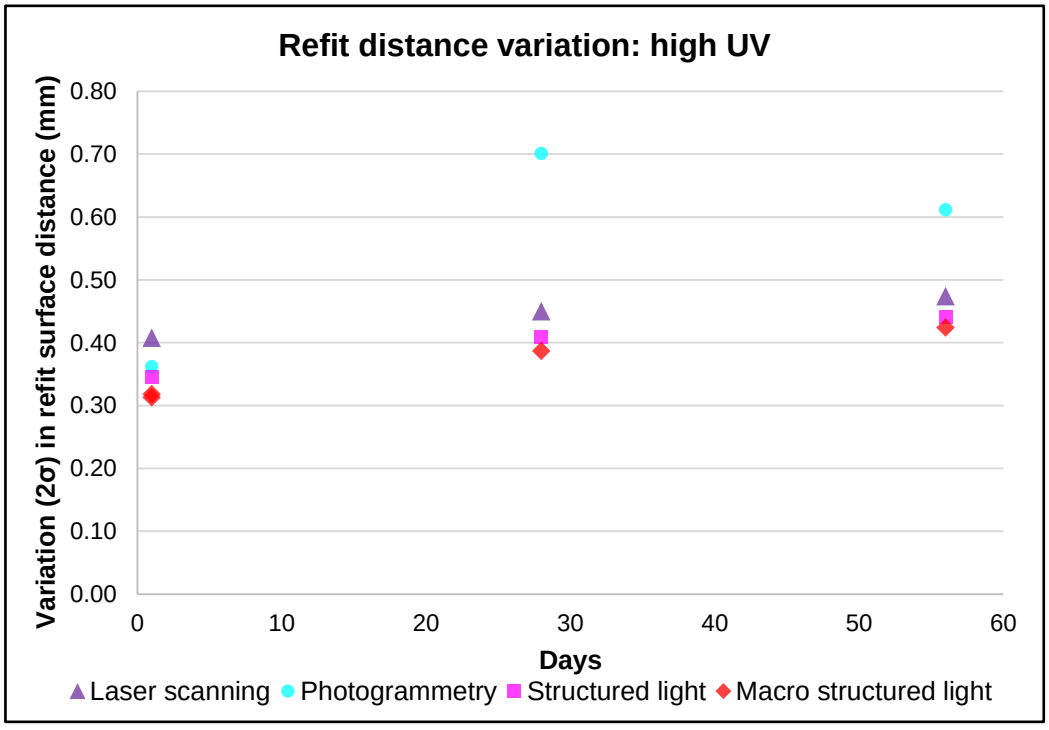

Figure 7.70: Plot of the variation in distance between the refitting surfaces of the fragmented high UV experimental samples (source: author).

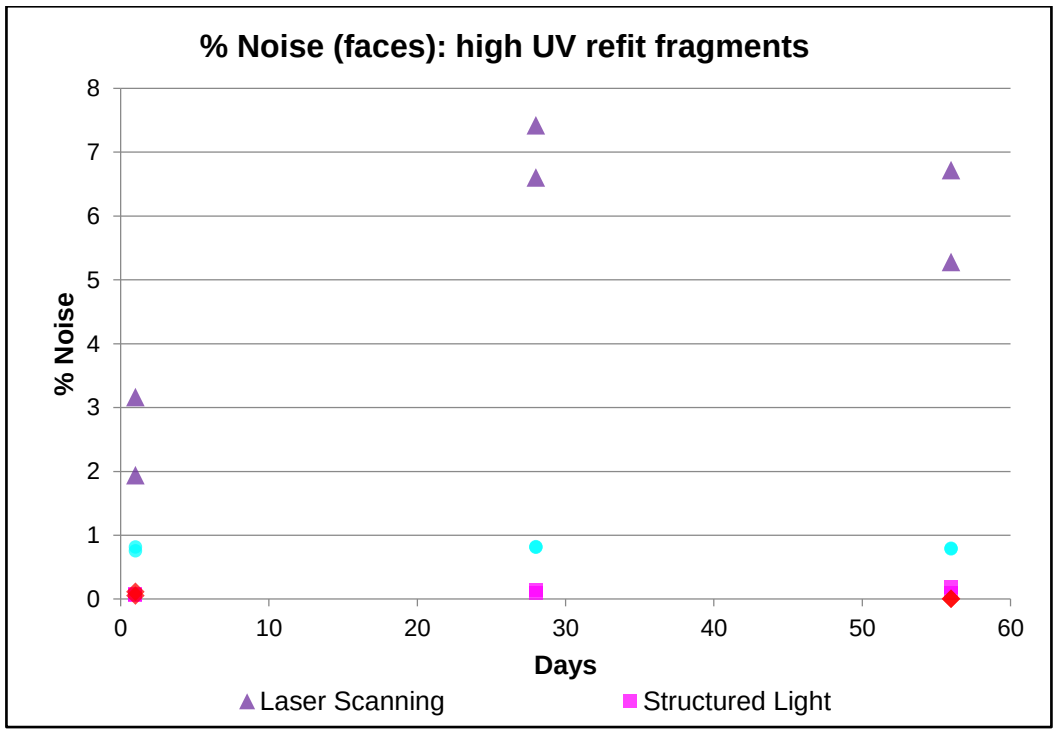

Figure 7.71: Plot comparing the percentage of mesh faces identified as noise within the fragmented high UV experimental samples for each of the digitisation techniques over time (source: author).

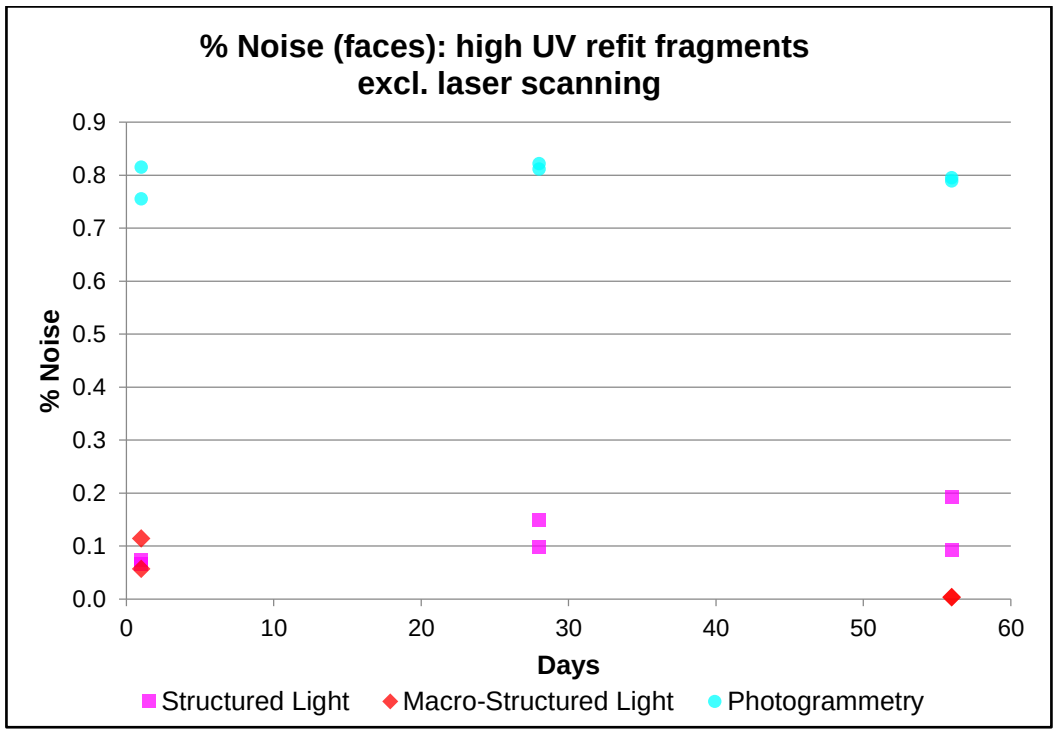

Figure 7.72: Plot comparing the percentage of mesh faces identified as noise within the fragmented high UV experimental samples for structured light, macro structured light and photogrammetry techniques over time (source: author).

The percentage of face noise in the high UV exposure samples showed a high level of noise for laser scanning across both exposure periods (figure 7.71); the noise affected up to 7.4% of the digital model mesh. The noise associated with the photogrammetry models remained comparable across both exposure periods with the pre-exposure samples at approximately 0.8% (figure 7.72). The structured light and macro structured light scanning noise levels show a minimal rise in values over the duration of the experiment.

The percentage of the refitting fracture surfaces within +/- 0.1 mm for structured light and macro structured light scanning displayed a comparable reduction over the two exposure periods. Laser scanning had an initial greater decrease with minimal change for the second exposure period. Photogrammetry was comparable for the pre-exposure and second exposure period, but showed a far greater reduction in quality after the first exposure period (figure 7.73).

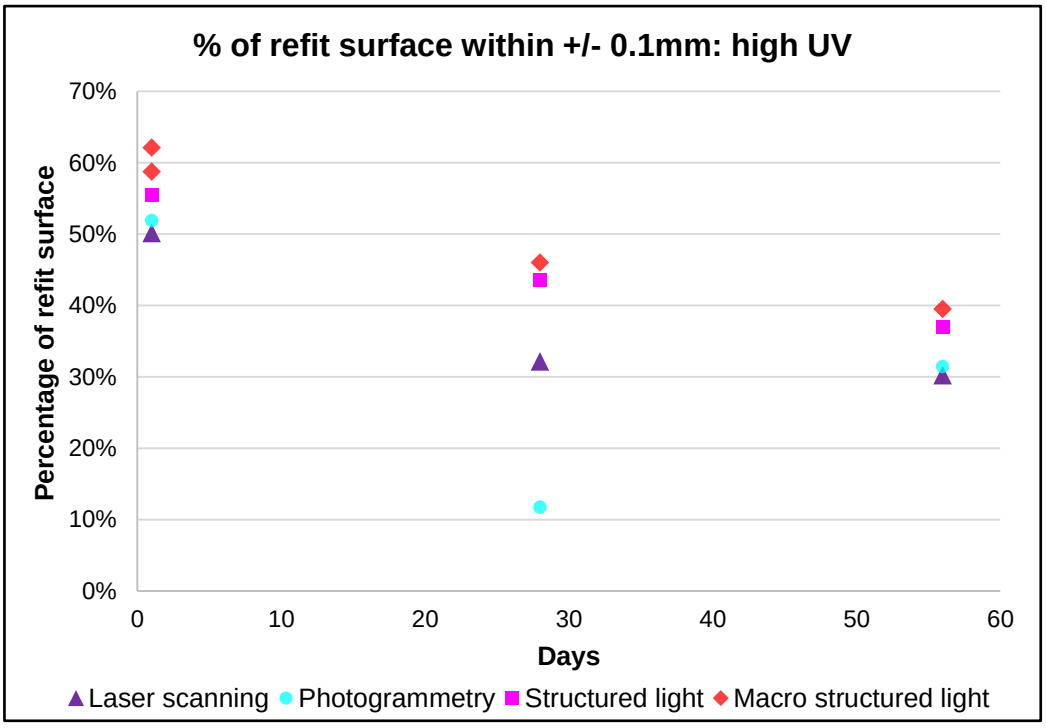

Figure 7.73: Plot showing the percentage of the refitting surface area between the fragments of the high UV experimental samples within a +/- 0.1 mm distance (source: author).

7.5.4. Effect of the taphonomic changes of field weathering on the digital refit of bone

The mean refit distance between the two surfaces for each sample displayed a consistent decrease across the exposure periods for all techniques (figure 7.74).

The distance variation within each refit demonstrated a slight decrease over the two exposure periods for all three techniques which were broadly comparable (figure 7.75).

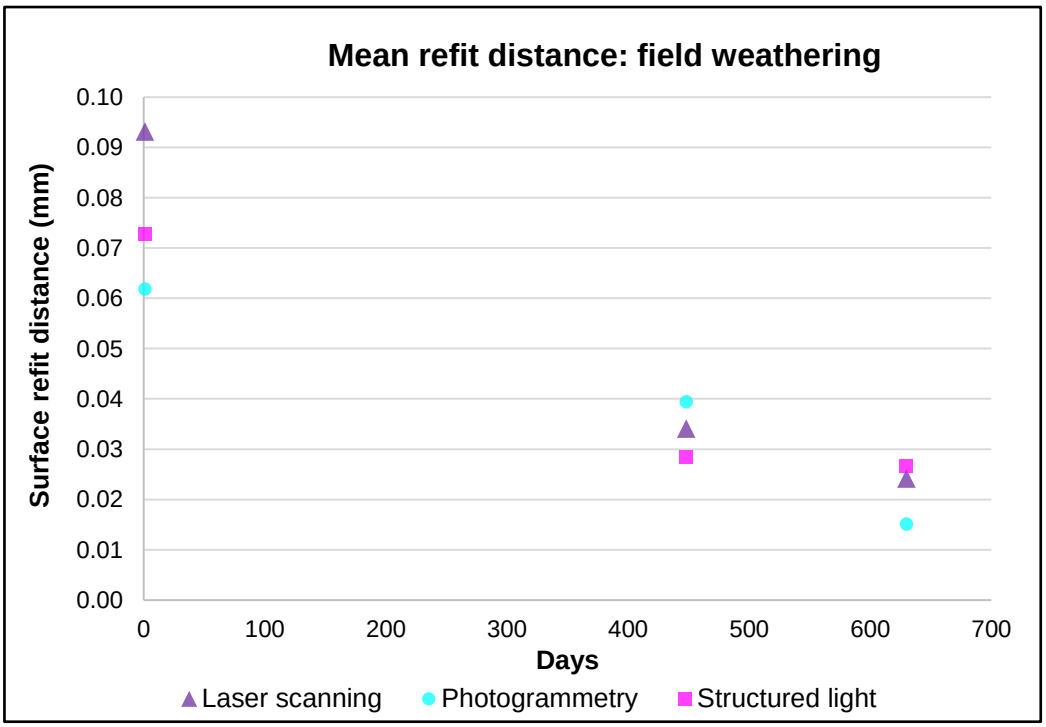

Figure 7.74: Plot of the mean distance between the refitting surfaces of the fragmented field weathering samples (source: author).

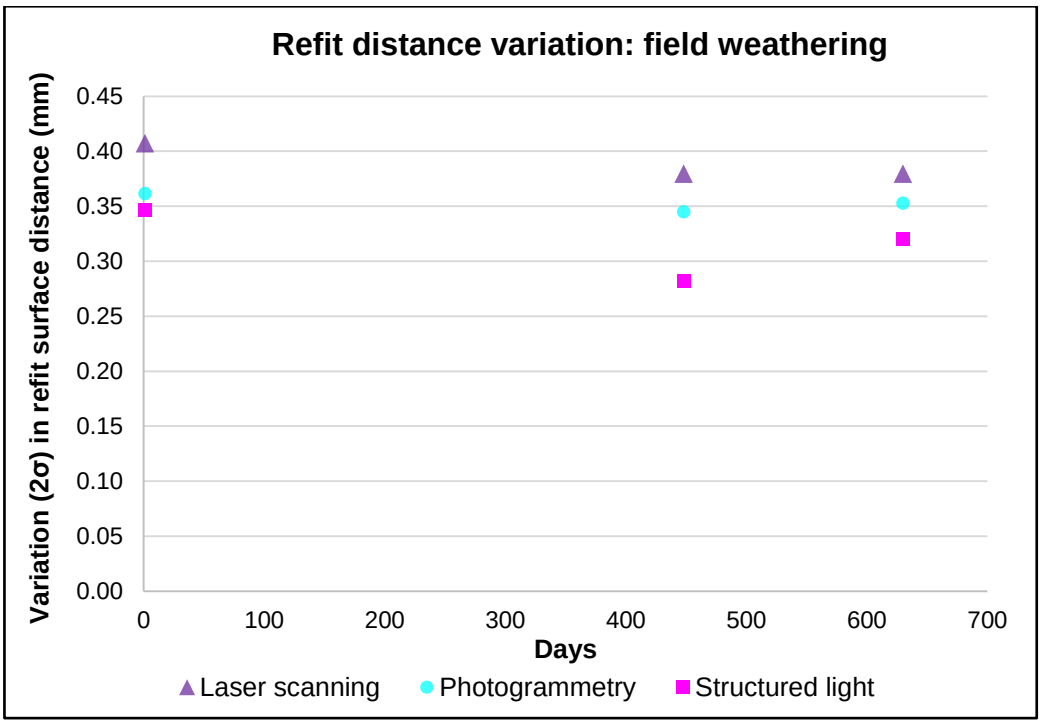

Figure 7.75: Plot of the variation in distance between the refitting surfaces of the fragmented field weathering samples (source: author).

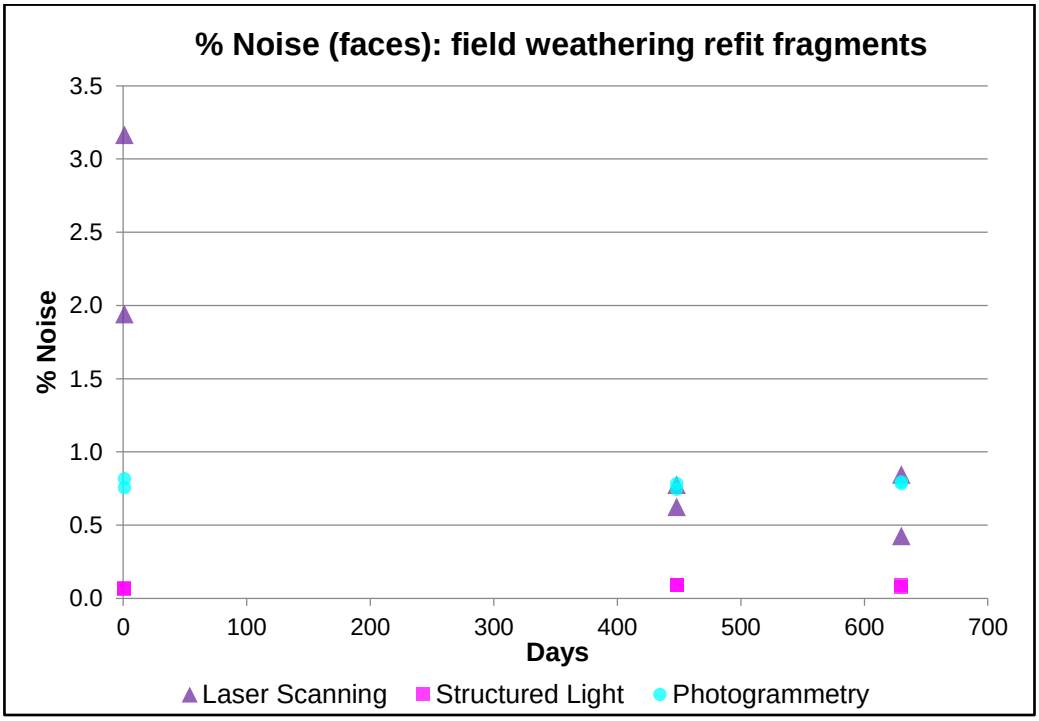

Figure 7.76: Plot comparing the percentage of mesh faces identified as noise within the fragmented field weathering samples for each of the digitisation techniques over time (source: author).

The percentage of face noise in the field weathering samples showed a higher level of noise for laser scanning (max. 0.84%) and photogrammetry (max.

0.79%) across both exposure periods (figure 7.77); the percentage of noise associated with structured light was less at values below 0.1%.

The percentage of the refitting fracture surfaces within +/- 0.1 mm increased for all three techniques over the two exposure periods (figure 7.76).

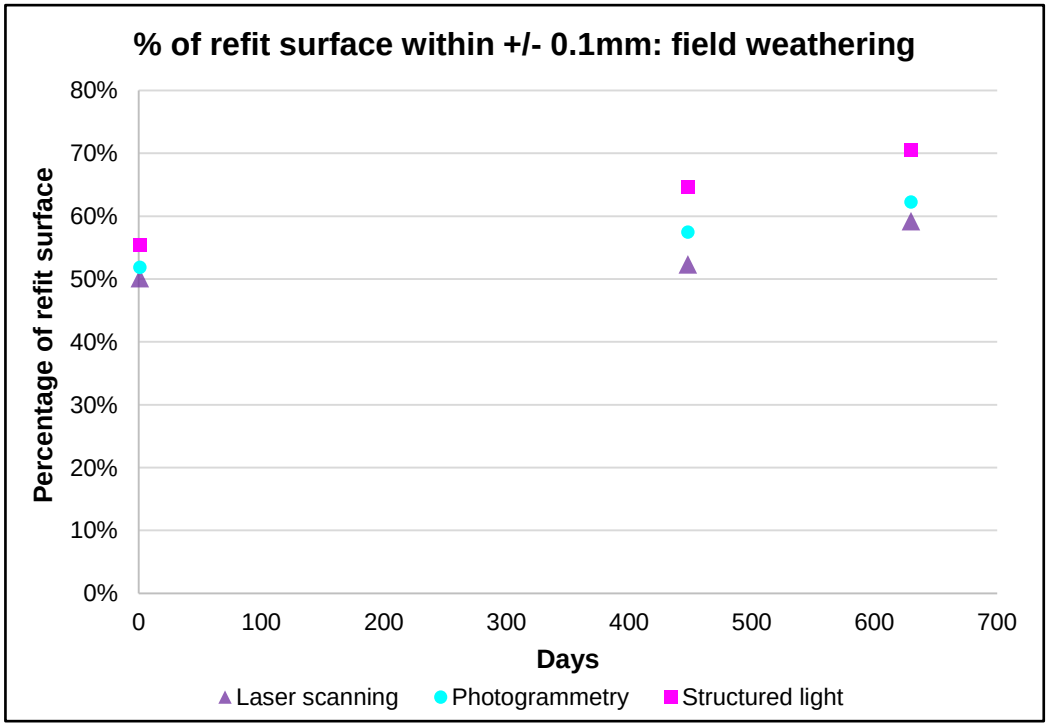

Figure 7.77: Plot showing the percentage of the refitting surface area between the fragments of the field weathering samples within a +/- 0.1 mm distance (source: author).

7.6. Refit analysis of the archaeological and palaeontological samples

The 3D models for a selection of refitting bone material from three sites were assessed for digital refit using the same method used for the fragmented experimental bone samples (section 6.4). In all the sites some digital refit was achieved, although a number of refitting pairs failed to refit.

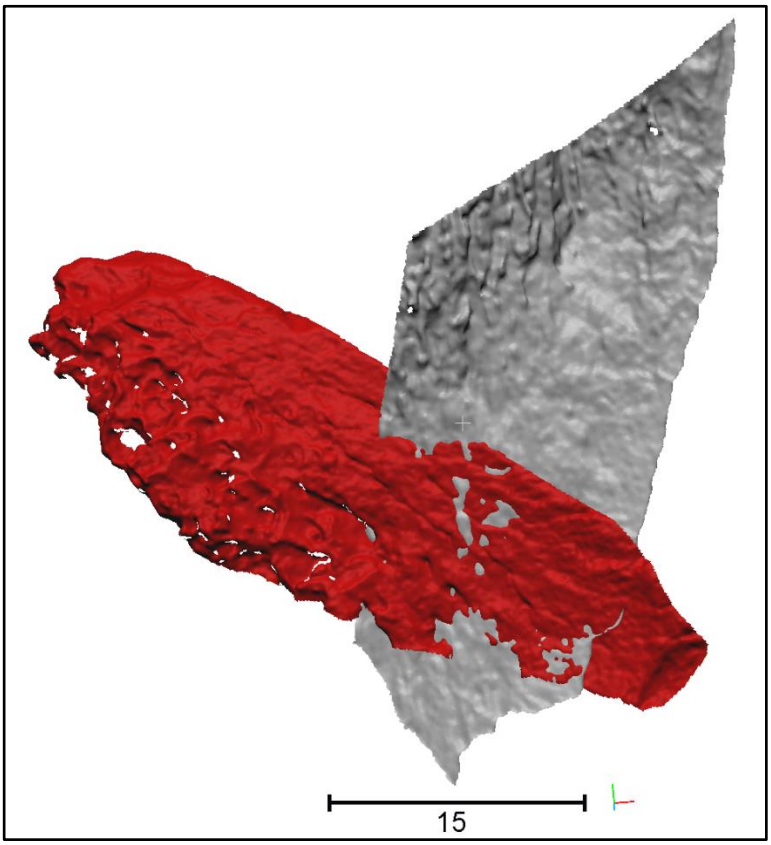

Figure 7.78: Example of a failed refit using the ICP Fine Registration tool in CloudCompareV2; one surface has been coloured red to distinguish the two surfaces. Scale in mm (source: author).

A refit was determined to have failed at either the initial rough alignment stage if the two bone fragments could not be manually aligned into a physically viable arrangement, or, following rough alignment and segmentation of the fracture surfaces, the *ICP Fine Registration* tool (section 6.4.2) did not produce a result. The latter was determined if the *ICP Fine Registration* tool ran for more than two minutes without producing a result (normal alignments took between 2 and 20 seconds), or where the result placed the meshes outside of any probable arrangement (figure 7.78). Manually refitting pairs that resulted in failed digital refits were reset to their starting positions using the *Point-Pair Registration* tool

and the refit analysis was attempted again. Up to three attempts to refit the 3D models were undertaken, if after three failed attempts the pair was recorded as having a failed refit in the results.

7.6.1. Star Carr

The samples were dark brown in colour and highly specular from the water sprayed on them to prevent them drying out prior to conservation. Some of the samples had thin white fungal growth on the surface from the aerated and wet storage conditions.

The 3D digital models of the nine samples Star Carr were digitised using laser scanning as part of a wider research project that has since been published (Little et al. 2016) and comprised eight manual refit pairs. The scans produced 3D models which exhibited some noise including surface artefacts. The digital refit analysis failed for six of the refit pairs (table 7.1).

Reference model	Compared Model	Mean refit distance (mm)	Refit distance variation (2σ)	% of fracture surface within +/-0.1mm
BV001	BV002	Refit failed		
BV001	BV003	Refit failed		
BV001	BV004	Refit failed		
BV001	BV005_F02	Refit failed		
BV002	BV006_F01	Refit failed		
BV002	BV006_F02	Refit failed		
BV005_F01	BV005_F02	0.61	1.69	16.03%
BV005_F02	BV005_F03	Refit failed		
BV006_F01	BV006_F02	0.08	1.77	13.28%

Table 7.1: Refit analysis results for the Star Carr samples with known refits from manual refit analysis.

The data for the remaining two pairs exhibited good mean refit distances of but very large variations in refitting surface distance.

The percentage of the refitting surfaces within +/-0.1mm for the two pairs of samples that produced digital refits were also very low (16.03% and 13.28%).

7.6.2. Schöningen 13 II-4

The 3D digital models of the 21 selected bone samples from the Schöningen 13 II – 4 faunal assemblage that were known to have 11 pairs of refitting fracture surfaces were subject to refit analysis. The macro structured light scans produced high quality 3D models which exhibited very little noise. In three cases the refitting pairs, known from manual refitting, failed to digitally refit (table 7.2).

Reference model	Compared Model	Mean refit distance (mm)	Refit distance variation (2σ)	% of fracture surface within +/-0.1mm
SCH_7574	SCH_7707	0.13	1.11	26.08%
SCH_7094	SCH_5167	Refit failed		
SCH_6056	SCH_6540	Refit failed		
SCH_6726	SCH_12487	0.44	1.38	28.33%
SCH_2926	SCH_3058	0.05	0.42	47.43%
SCH_2499	SCH_3134	0.02	0.64	26.82%
SCH_2525	SCH_1158	0.11	0.45	60.16%
SCH_5140	SCH_4283	0.06	0.47	39.71%
SCH_6835	SCH_4772	0.12	1.08	19.70%
SCH_6880	SCH_6599	0.17	0.95	31.44%
SCH_6599	SCH_6599_b	Refit failed		
Mean		0.139	0.812	34.96%
Standard Deviation		0.132	0.365	13.35%

Table 7.2: Refit analysis results for Schöningen samples with known refits from manual refit analysis.

The data for the remaining eight pairs showed an average mean refit distance of 0.139 mm and a variation in refitting surface distance of 0.81 mm.

The average percentage of the refitting surface within +/-0.1mm was 34.96% but the range of values was broad with a maximum value of 60.16% and a minimum value of 19.7%.

Multiple fracture surfaces were segmented from the two bone fragments known not to refit, and included to provide a control, were tested for refit using the same process as the main samples. None of the fracture surfaces matched and all produced failed refits as expected. One pair of surfaces could be roughly

aligned to a physically feasible match, but failed at the *ICP Fine Registration tool* stage.

7.6.3. Turkana Basin, Kenya

All the samples from the Turkana Basin, Kenya digitised during the field trip to the Ileret field research centre in northern Kenya were scanned using macro structured light and produced high quality 3D models which exhibited very little noise. All of the samples with known manual refits produced digital refits with an average mean refit distance of 0.06 mm and variation in refitting surface distance of 0.31 mm (table 7.3).

Reference model	Compared Model	Mean refit distance (mm)	Refit distance variation (2σ)	% of fracture surface within +/-0.1mm
K0001_F01	K0001_F02	0.04	0.29	70.04%
K0004_F01	K0004_F02	0.01	0.27	65.83%
K0003_F03	K0003_F04	0.29	0.31	88.67%
K0003_F03	K0003_F08	0.00	0.13	90.03%
K0003_F04	K0003_F05	0.07	0.37	82.19%
K0003_F04	K0003_F09	0.01	0.16	91.22%
K0003_F05	K0003_F06	0.04	0.33	85.49%
K0005_F01	K0005_F02	0.11	0.41	69.15%
K0005_F02	K0005_F03	0.04	0.23	82.75%
K0005_F03	K0005_F04	0.03	0.23	86.74%
K0007_F01	K0007_F02	0.10	0.50	36.93%
K0008_F01	K0008_F02	0.09	0.61	24.41%
K0008_F02	K0008_F03	0.07	0.43	62.70%
K0006_F01	K0006_F02	0.02	0.21	90.85%
K0006_F06	K0006_F07	0.06	0.28	79.15%
K0006_F08	K0006_F09	0.03	0.23	87.81%
K0006_F09	K0006_F06	0.02	0.21	91.65%
K0006_F05	K0006_F08	0.04	0.31	90.68%
K0006_F05	K0006_F06	0.03	0.22	89.71%
K0006_F02	K0006_F05	0.07	0.42	57.31%
Mean		0.06	0.31	76.16%
Standard Deviation		0.063	0.120	18.91%

Table 7.3: Refit analysis results for Kenya samples with known refits from manual refit analysis.

The average percentage of the refitting surface within +/-0.1mm was 76.16% and the majority of the results were above 55% with only two refit pairs producing poorer results.

Multiple fracture surfaces were segmented from sample K0002 and refit analysis was carried out between it and samples K0001_F01 and K0001_F02 which were similar in appearance and found in close proximity. Manual refit attempts in the field had shown that K0002 did not refit with the other samples and K0002 was included to provide a control. None of the fracture surfaces matched and all produced failed refits as expected.

Chapter 8. Discussion

The aim of this research was to examine the effect of taphonomic changes to mammalian bone on the quality of 3D digitisation techniques and explore how those changes impact the refit of fragmentary bone materials.

To achieve this aim the research had six objectives. Chapters two, three and four addressed the first objective by providing a survey of existing literature on both taphonomic change to mammalian bone and 3D digitisation techniques appropriate to the recording of mammalian bone.

The sections of the following chapter discuss the remaining objectives with reference to the results described in chapter seven as follows:

- Create technique comparison standards to assess the response of 3D digitisation techniques to the colour, opacity and surface roughness properties of objects (section 8.1);
- Use accelerated laboratory degradation and natural field-based exposure methods to simulate taphonomic change to mammalian bone (section 8.2);
- Assess the impact of the taphonomically induced changes to bone on the quality of 3D digitisation techniques (section 8.3);
- Carry out a comparison of 3D digitisation techniques by recording the same experimentally degraded bone samples with each technique and comparing their response (section 8.3); and
- Examine the impact of taphonomic changes on the digital refitting of fractured experimentally degraded bone samples and compare it to similar fragmentary material from archaeological and palaeontological examples (section 8.4).

8.1. Technique comparison standards

The following sections discuss the creation of technique comparison standards in relation to the results in chapter seven (section 7.1) and their use to assess the response of the 3D digitisation techniques to the colour, opacity and surface roughness properties of objects.

8.1.1. Discussion of the colour technique comparison standards

As described in section 4.2.3.3 the colour of an object surface corresponds to the absorption or reflectance of the various wavelengths within the light falling on it and the intensity (brightness) of that light.

The results described in section 7.1.1 showed that the amount of light reflected from a surface back to a 3D digitisation instrument's sensor has a direct impact on the quality of the data. Lighter surfaces absorbed less light and therefore reflected more of the instrument source light back to the instrument sensor giving a greater number of point measurements for sensor to object distance. The larger number of point estimates for the lighter surfaces produced a greater point density to the point cloud for the surface and, when meshed, the averaging of the point cloud surface was more precise (section 4.2.3.3). The data showed that lighter coloured surfaces produced 3D meshed surfaces that had lower levels of surface variation.

Darker colour surfaces resulted in reduced density for the point cloud; noise and outliers within the distribution of points therefore have a greater effect, producing greater variation in the estimated values for sensor to object distance and a degradation of the instrument's point accuracy. This mirrors effects seen more widely in terrestrial scanners (Clark & Robson, 2004, Coşarcă et al. 2009). When the point clouds were meshed this poorer point accuracy (i.e. imprecision) was expressed as mesh surfaces that had a greater level of surface variation than the true object surface. The data (figure 7.3) illustrated that the response of 3D digitisation techniques is, in general, expressed as an increase in the roughness of the final digitised surface in objects with darker colour surfaces.

For objects with both light and dark colour areas on their surface (such as bone), 3D digitisation will produce a meshed 3D object with surfaces that vary in their surface roughness in response to surface colour lightness rather than representing the objects true surface roughness. This can affect the quantitative analysis (e.g. volume and surface area) and the refit analysis where surface roughness can adversely affect surface to surface matching and distance.

When compared the three techniques had varying susceptibility to colour lightness. The lack of return by both the structured light scanners for the black colour patch illustrates the susceptibility of structured light to darker surfaces and lower lighting levels. The machine vision element of structured light relies on the contrast between the white and black patterned light projected onto the targets surface in order to determine 3D shape. The absorption of light by dark colours significantly reduces the contrast within the projected pattern. This poorer contrast leads to poorer definition of the edges of the stripes in the pattern and the reconstruction of the 3D surface is based on fewer returns resulting in greater point uncertainty and surface variation. The impact of poor phase pattern contrast has been noted in archaeology (Gernat et al. 2008, McPherron et al. 2009) and is known more widely in engineering (Nayar & Gupta 2012, Gupta et al. 2013, Van der Jeught & Dirckx 2016) this research provides direct measurement of its effect in relation to archaeological and palaeontological materials.

The lower surface variation for the macro structured light scanner compared to the standard scale structured light scanner is a consequence of the higher resolution of the macro structured light instrument. The macro structured light scanner achieves higher resolution by limiting the scanning volume to a narrow field of view. The width of the projector in the scanner is limited using custom optics and therefore concentrates the same light as the standard structured light scanner into a much smaller scanning volume. The intensity of light per mm^2 of object surface is therefore considerably higher, producing greater contrast on darker surfaces. Whilst the macro structured light scanner has proportionally greater sensitivity and improved response over the standard structured light scanner, its response remains poorer than the single wavelength light source of the laser scanner.

The laser scanner's use of a single wavelength light source, combined with the incorporation of a narrow bandpass filter on the scanner's optical sensor, means that the scanner filters all reflected light, other than the wavelength of the light source. This produces a binary toned image where only the laser line is visible and all other surrounding detail is black, resulting in a sharp contrast line for all colours except blue. In the results in figure 7.3 this is expressed by lower surface variations in the surface of the dark colour patches when compared to the full spectrum light of the structured light scanners.

The exception was for the blue colour patch, which exhibited an increased level of surface variation above the trend line for the other laser scan responses. The red wavelength of the laser scanner (λ = 655nm) is absorbed by surfaces of the corresponding wavelength blue colour. As the blue colours of most surfaces are rarely a single wavelength response pigment, most blue surface colours will disproportionately absorb some of the red light of the laser compared to other equally dark colours, but will still provide a limited contrast return to the instrument sensor. Blue colours therefore respond as darker surfaces than their true colour lightness value. This has limited influence on bone as in most taphonomic pathways there is little blue component in the colour of bone.

Whilst this response was seen only in the laser data in this study, the same response would be expected of any digitisation system using a narrow band of the spectrum. In structured light scanning blue light scanners are used to address the effects of semi-translucent materials (see section 8.1.2) (Coşarcă et al. 2009). The results suggest that such scanners will show a poor response to red coloured surfaces, which combined with demonstrated poorer response from darker surfaces would make structured blue light scanners a poor choice for the digitisation of objects with a larger red component to their surface colour. As will be discussed in later sections, this is relevant for bone as red and pink colours are evident in the initial stages of degradation from the breakdown of blood within the Haversian system.

In the estimated wavelength data (figure 7.4) the red laser should produce a greater surface variation for the laser scan data of the blue colour patch than for the two structured light scanning instruments which utilise full colour spectrum white light. However, whilst the laser scan data for the blue colour patch had a

higher surface variation than the adjacent colour patches, the blue colour patch values for all three instruments do not show significant variation.

This discrepancy is due to the two separate factor acting on the results. The blue colour patch is the darkest colour in figure 7.4 and the lightness graph (figure 7.3) shows that all the other colour patches included in figure 7.4 are grouped at the light end of the colour lightness scale. In the structured light techniques the poorer surface contrast provided by the dark blue surface of the colour patch produced poorer responses for both instrument types than would have been predicted. Whilst the laser scan data has elevated levels of surface variation due to absorption of the red laser light. This results in a similar surface variation responses from laser scanning and the two structured light techniques but with different underlying causes.

Whilst the response of 3D digitisation to surface colour in heritage objects has had little study, these results correspond well with experimental data on range and surface variation in terrestrial laser scanning by Clark & Robson (2004) who also showed disproportionately poorer responses to blue colour patches in terrestrial laser scanners with red wavelength light sources and showed poorer point precision in darker colours (Clark & Robson, 2004).

The results show that the use of readily available photographic colour calibration targets was an appropriate approach as a standard comparator for the measurement of the response of 3D digitisation systems to colour variation. The results were limited by the complexity of characterisation of colour and the potential for further work utilising more direct measurement of true colour values is discussed in the further work section of chapter nine.

8.1.2. Discussion of the opacity technique comparison standards

The Beer-Lambert law equations describe the interaction of light with a semi opaque material. Light penetrates into the material and is transmitted through it, whilst attenuating in proportion to both the concentration of absorbing or diffracting material in a given volume. The attenuation of the original signal is therefore a distance function, with a negative logarithmic relationship to the length of the light path through the material (section 6.9.1).

The mixture of the resin and opacifier used to produce the opacity methodology comparison standards was uniform throughout each sample block producing a homogenous material with equally distributed particles of opacifier held in suspension of the resin whilst it set. The attenuation coefficient of light should therefore be uniform throughout each of the samples.

Reflections of light occur within a material when it is reflected at crystalline boundaries, internal microstructure, imperfections (e.g. bubbles) or adjacent surfaces. Lower opacity materials have a lower attenuation coefficient and the light can travel further within the material before being fully absorbed offering greater probability that the light will be reflected back towards the source from within the material where in digitisation instruments it can be recorded as an erroneous surface reflection.

In 3D digitisation there is a baseline level of surface variation related to the instrument precision. The random variation in precision for recorded points leads to a normal distribution in the estimated instrument to object distance for the points in a 3D model's surface point cloud. In calibrated instruments the mean distance for the surface point cloud should reflect the true instrument to object distance to within the accuracy and resolution of the instrument's sensor (figure 8.1 top). When meshed this point cloud produces a surface that is not planar, but has a small degree of variation about the true value.

In addition to the baseline variation provided by the instrument precision, in semi-opaque materials the penetration of light from the instrument into the surface and the reflection of light back to the instrument at varying depths produces an increased level of variation within the point cloud for the estimated surface.

However, as the reflections can only occur within the sample material, the widening of the distribution of the points in the point cloud can only occur in one direction. The increase in the points below the surface results in greater mean instrument to object distances (figure 8.1 bottom).

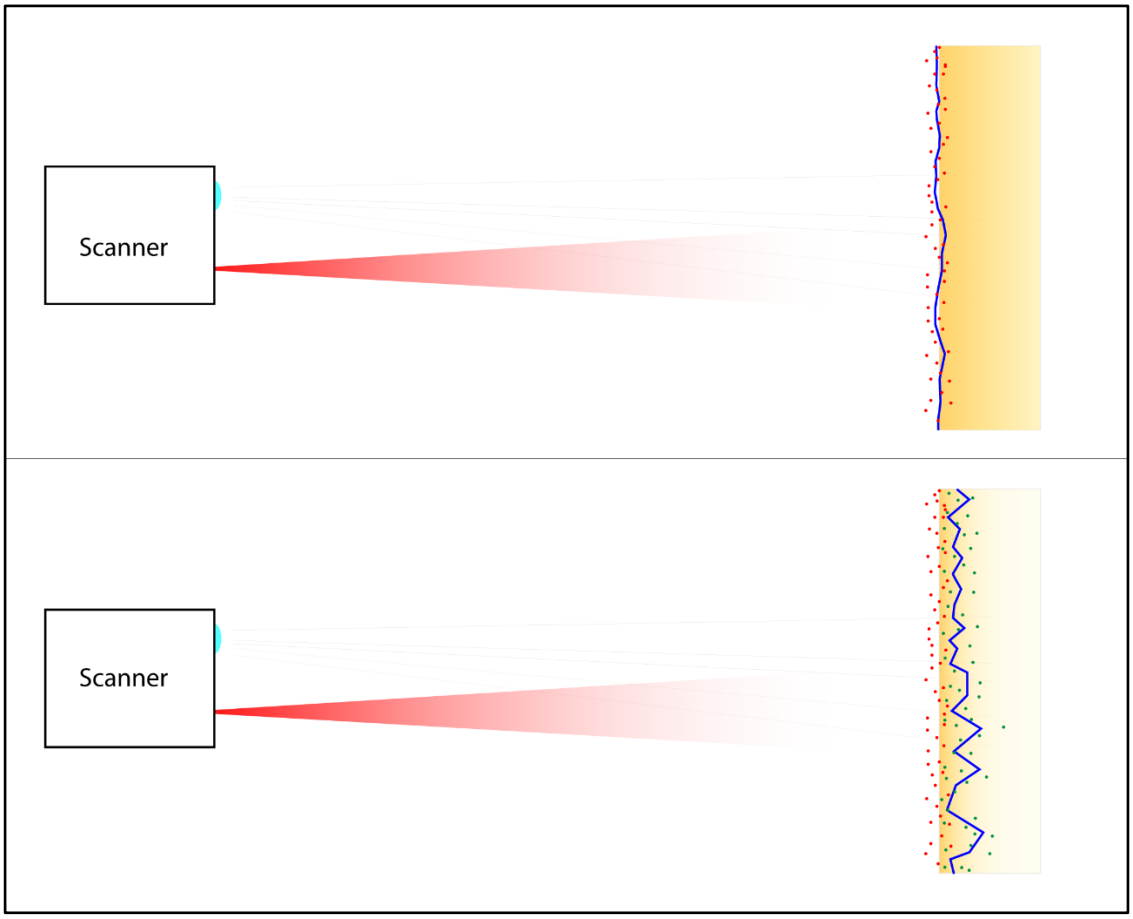

Figure 8.1: Illustration showing the effect of opacity on the scanner to object distance for a fully opaque sample (top) and semi-opaque sample (bottom). The recorded points for the surface of the opaque sample are distributed about the true surface and vary due to the instrument precision (red points). The reconstructed surface (blue line) therefore closely resembles the true surface. In semi-opaque samples this distribution of points is expanded into the sample by sub-surface reflected light (green points). The resulting reconstructed surface is therefore further from the instrument than the true surface leading to underestimates of volume, area and dimensions and increasing the surface variation (source: author).

When meshed the point cloud therefore produces a surface with greater levels of surface variation than the instrument precision and the mesh surface is offset away from the instrument resulting in the smaller volume and area values and greater standard variation in the measured values. As opacity decreases the impact of this effect should be greater resulting in increasing underestimates of the size of 3D digitised objects. Additionally, at lower angles of incidence specular surface reflection reduces the amount of light penetrating into the object further varying the effect.

This model of the interaction of digitisation with varying levels of object opacity broadly corresponds to the data in the three parts of the opacity technique comparison experiment.

The results for the structured light scan data in figure 7.5 showed gradual decreases in the surface variation as opacity increased broadly in line with this model. For laser scan data however, the level of surface variation at lower opacities was markedly greater than structured light. The results showed that laser scanning was more susceptible to the level of surface opacity than structured light methods and produced much larger surface variations.

For structured light scans the volume and area calculations demonstrated the predicted pattern of inaccurate estimation of the object surface position due to reflections below the surface, producing increased estimates of instrument to object surface distance and therefore inaccurate positioning of the reconstructed surface. Both structured light systems demonstrated a linear relationship between increasing opacity and improvements in volume or area accuracy.

In laser scanning this relationship was more complex. For area estimation the laser scan data follows a linear trend in opposition to those of the structured light data and does not fit with the suggested pattern. At higher opacities the relationship was similar to that in structured light, but below 97.5% opacity the laser scanned objects showed an increase in 3D mesh volume in opposition to the structured light trends suggesting that there were multiple factors influencing the laser scan results and that these became less significant as opacity increased.

The differences between laser scanning and structured light can best be explained by the presence of higher levels of edge noise in the laser scan data, and its underlying mechanism. Only limited levels of edge noise were observed directly in the structured light scanning 3D models, but examination of the laser scan derived models showed large increases in the level of edge noise as opacity was decreased (figure 8.2).

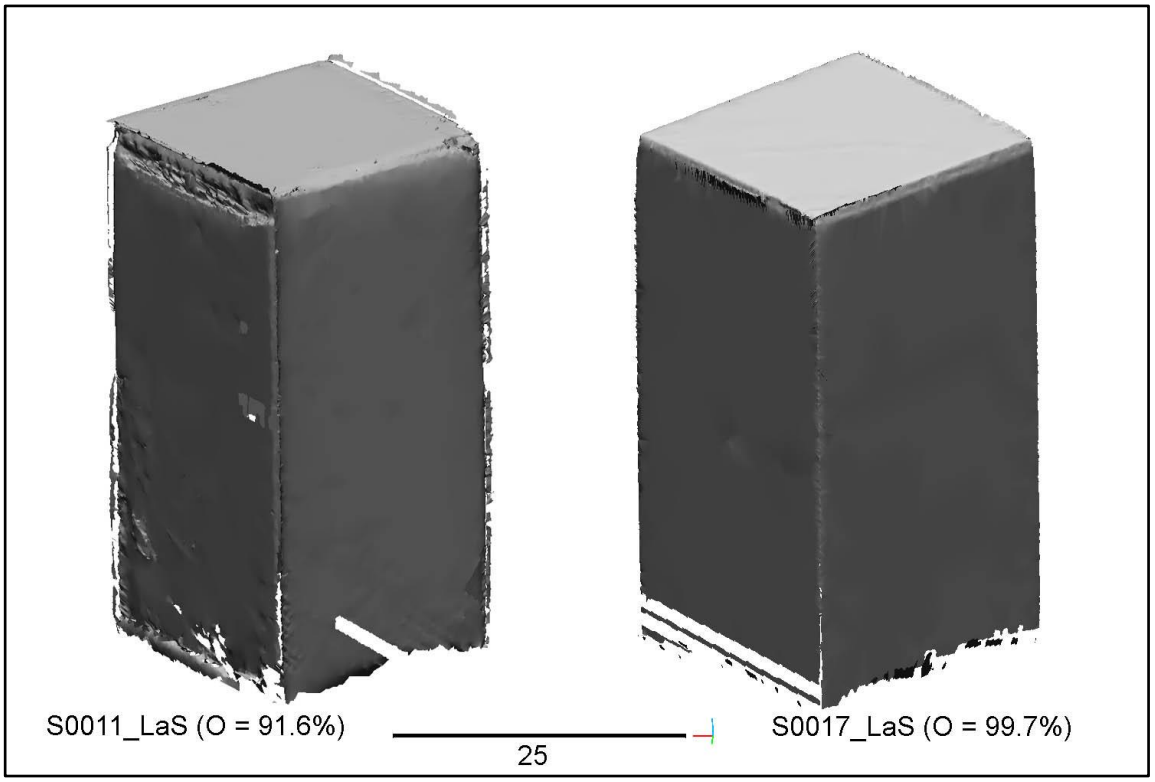

Figure 8.2: Edge noise in two laser scanned technique comparison standards samples with differing opacities. Comparison of the 3D digitised models for the lowest opacity sample S0011_LaS (O = 91.6%) (left) and highest opacity sample S0017_LaS (O = 99.7%) (right) both displayed in the same orientation (scale in mm) (source: author).

Edge noise can occur in all light based 3D digitisation techniques and is exacerbated by lower opacity. Where two or more flat surfaces meet at the corners and edges of the blocks, the thickness is at its lowest and light from the instrument can penetrate and reflect back from the adjacent surface (figure 8.3). For lower opacity blocks, this effect is greater due to the lower attenuation of light.

Figure 8.3: Photo of edge transmittance of light in opacity sample S0011 photographed during structured light scanning lit from behind by the structured light scanner as the light source (source: author).

The attenuation of light in a material surface is wavelength dependant, with longer wavelengths penetrating deeper into a material surface than light of shorter wavelengths. Instruments with a red single wavelength light source, such as the laser scanner (655nm red laser), are therefore more susceptible to lower opacity, and this effect will be most notable in the thinnest areas of the scanned object.

In addition, the light in the laser scanner is focussed into a laser line, the thickness of which when projected onto a sharp edge on the surface of a scanned object, results in only part of the laser line being reflected back to the scanner. The part of the laser light line that is not reflected by the object is projected beyond the edge and may reflect back from other surfaces within the scanning volume. The recorded point in laser scanning is calculated for the centre of the line thickness and therefore where only part of the line is reflected, or where the line width is increased due to variable angles of reflectance, the point position is inaccurately calculated. These result in phantom point artefacts along the edge of the object (figure 8.4) and when meshed these produce phantom mesh surfaces.

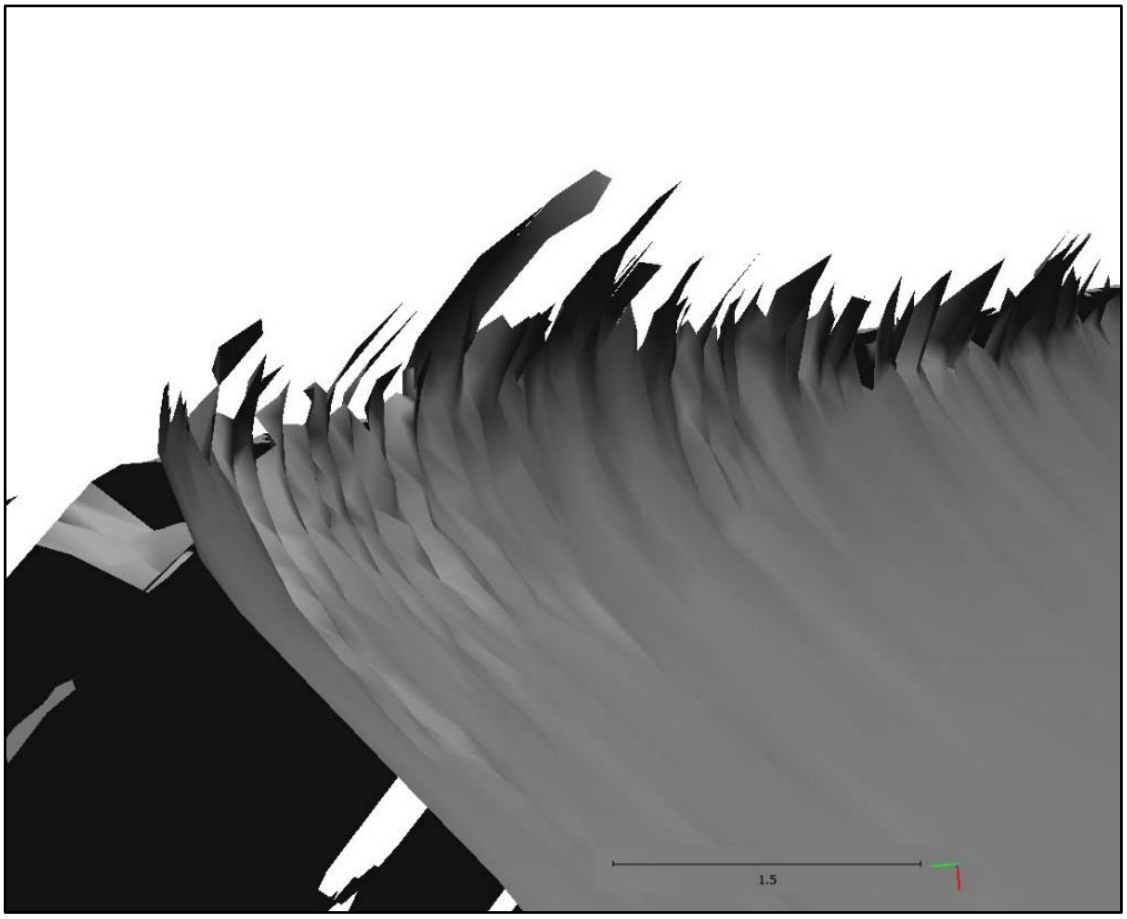

Figure 8.4: Close up showing the outward curving mesh from edge noise derived phantom points at the edge of opacity sample S0011 digitised by laser scanning (source: author).

In lower opacity objects, these artefacts are exacerbated as the part of the laser line not reflected back to the instrument can penetrate into the material and be reflected back, via multiple light paths within the material, from adjacent surfaces. The multiple reflected returns diffuse the thickness of the line, degrading the point accuracy.

Furthermore, the multiple reflections of light all have slightly varying light path distances and therefore when they are reflected back to the instrument the wavelengths are out of phase with each other resulting in interference patterns and a higher occurrence of speckle (section 4.2.3.1). The Gaussian distribution of speckle noise within the recorded image at the instruments sensor further reduces the quality of the scan data by broadening the spatial distribution of recorded points and further increasing surface variation.

The greater penetration of the laser's red wavelength light is seen in the significant increase in the level of surface variation (figure 7.5) at lower opacities

and the increased standard error in the dimensional measurement data (figure 7.12). In the area and volume data this error is increased by the presence of phantom points forming additional mesh surfaces at the edges of the blocks which increase the total area of the mesh. As opacity increases the reduction in edge noise present in the 3D digitised object results in the downward trend seen in the laser scan data in figure 7.9.

Whilst the position of the dimensional accuracy measurement points on each sample were located on the flat faces, away from the edges of the block (figure 5.27) and therefore the dimensional accuracy was not significantly affected by the errors directly associated with edge noise, other speckle and sub surface reflection based errors remain present in the results.

The production of edge noise artefacts in the laser scan data also prevents the production of surface mesh at the corners of the blocks leaving holes in the mesh. During the estimation of volume, holes within the mesh surface of a 3D digitised object require the software to estimate the probable shape of the missing surface in order to separate internal from external volumes in 3D space. This surface estimation is a common source of error and can be influenced by the shape of the mesh at the edge of the hole. The boundary of the object described by the mesh surface is calculated by extrapolation of the mesh surface at the edges of a hole until they intersect. For simple holes in the mesh, this method produces a good estimation of the probable surface. However in the laser scanning samples, the edge noise errors are present as outwardly curving surfaces at each of the corners and a gap between these mesh edges (figure 8.4). The curved surfaces are the result of phantom point creation described above and do not reflect the true surface of the mesh. The outward curvature of this edge noise results in expansion of the estimated mesh surface and overestimation of the volume calculation observed at lower opacities in the results (figure 7.6). As edge noise decreases with increased opacity the impact on volume calculation is reduced. The reduction in this edge noise associated volume error is coupled with a general increase in the accuracy of volume measurement due to the reduced surface variation with increasing opacity, producing the non-linear trend between volume calculation and opacity seen in figure 7.6. Blue laser based laser scanners such as the Faro Edge Scan Arm HD (Faro Technologies, 2013b) will still produce some edge noise, however the

reduced penetration of the shorter wavelength blue light will improve the response at lower opacities. However, as discussed in 8.1.1, in bone this may be offset by the greater absorption of blue light by the higher red colour component of bone surfaces.

The full breadth spectrum of the structured light scanners includes red wavelengths that can penetrate further into semi-opaque surfaces, but the effect is outweighed by the surface reflections of shorter wavelengths, and the lower intensity of the red wavelengths within the light source reduce the impact of speckle for structured light scanners. Structured light scanners that use a narrow band of the visible spectrum such as blue light scanners will be subject to some speckle effects, however the shorter wavelengths of the blue end of the spectrum penetrate less into semi-opaque materials explaining their suggested use for lower opacity objects (Bernal et al. 2013; Jeon et al. 2015; Logozzo et al. 2011).

Additionally, structured light data has a degree of averaging inherent in the data acquisition process which acts to filter the distribution of points. Numerous images of the same object are taken with different phased patterns of light projected over them. The boundary of the white and black stripes should, in highly opaque surfaces, return a well-defined line to the software. As the varying patterns are phase shifted across the surface of the object, a single point on the surface is measured multiple times. The result of these multiple measurements is then used to produce the averaged 3D shape. Some inconsistency in the position of each measured point is expected due to the instrument precision and this leads to a background level of surface variation in the meshed data. However, in lower opacity materials multiple reflected light paths within the surface of the material produce a higher degree of inconsistency of measured point position (i.e. noise). To aid in surface reconstruction in structured light scanning, the software can filter out points from the raw data which have high positional variation. At its maximum setting the threshold for the filter is based on the value of the instrument's precision, filtering all points that have a positional variation greater than that which would be achieved from digitising an ideal surface in perfect scanning conditions.

However, most object surfaces are not ideal and scanning conditions vary resulting in the point data for large areas of the object surface being discarded by the filter. The filter therefore lets the user increase the allowable level of positional variation retained in the surface reconstruction of a digitised object by applying a multiplier to the value of the measured instrument precision. In FlexScan this filter is the “cleanup” setting in the scanning menu and ranges from the relaxed cleanup filtering to the high cleanup filtering (figure 8.5) with an extreme cleanup for very small precision objects.

Figure 8.5: Comparison of the surface quality of the same subject scanned with filter set to high (left) and relaxed (right) (LMI Technologies 2015, page 115).

The levels for the filter are relative to the measured precision of the instrument. The smaller scale instruments, such as the macro structured light scanner used in this study, reduce the size of the scanning area to achieve the high resolution sought. Whilst these smaller scale scanners have smaller absolute values of measured point variation, the built-in instrument noise that contributes to the precision values is not altered and macro scanners have a slightly higher level of point imprecision proportional to their resolution.

During digitisation of all the samples, filtering was minimised to allow the effect of sample surface properties to be demonstrated. The “standard” cleanup level

was used as below this filtering threshold (i.e. relaxed or no cleanup) the scanned data included considerable additional points from the scanning background, and environmental factors such as ambient light and dust.

The variation in results between the two structured light methods and laser scanning was influenced by this inherent filtering and was particularly noticeable in the noise data for each of the taphonomic experiments (e.g. figure 7.53).

Within the wider field of research into 3D digitisation it is widely noted that surface scanning methods are only appropriate for opaque materials (Gu et al. 2008, Barsanti et al. 2013, Wilson et al. 2017) and semi-transparent materials are generally avoided or are digitised through the application of a “matting spray” to the surface which provides an opaque response for the surface scanner (Díaz-Marín et al. 2016, Skabek & Kowalski 2009). For cultural heritage objects this may be problematic due to the matting spray’s impact on conservation of the object. For porous materials such as bone matting sprays are rarely appropriate as once applied they are difficult to remove and introduce additional material that may influence further analysis (e.g. stable isotope measurement) or conservation. It is therefore difficult to remove or reduce issues associated with opacity in digitisation of bone through the use of matting sprays.

Whilst in both engineering and cultural heritage the 3D digitisation of semi-transparent materials where matting sprays cannot be used are avoided, solutions to the digitisation of glass and other fully transparent objects are being proposed through the fabrication of devices specific to the material that take advantage of its optical properties in near infra-red or ultraviolet spectra (Mériaudeau et al. 2012; Stanco et al. 2011; Ihrke et al. 2010; Osorio et al. 2012). The drawback of these techniques is their specificity to their target material which are generally uniform in composition; they are therefore less applicable to the wide variety of materials from archaeological contexts. The histological variation in bone and its mixed opacity values make the application of these new approaches less feasible for bone and other animal hard tissues.

Very little work has been carried out into the digitisation of near opaque materials, or sought to explore the threshold at which each digitisation method

becomes less viable. A single paper on the response of semi-transparent materials to terrestrial laser scanning (Voegtle et al. 2008) demonstrated significantly increasing noise at lower opacities which broadly correspond to the laser scanning results in this research, however the differences between terrestrial and laser scanning ranges and limited detail on the target materials make further comparison of the results difficult.

The results for the technique comparison standards for opacity showed that 3D digitisation techniques can be extended into less opaque materials, albeit with some degradation in dimensional accuracy (figures 7.6. & 7.8). The results demonstrate there is a threshold of opacity at approximately 97.5% for the application of red wavelength laser scanning at which point the quantification of volume and area becomes problematic; structured light and macro structured light scanning remains applicable below this, at least to the lowest opacity measured (91.65%). The level of a similar threshold for the structured light methods requires further study and the potential of structured light in lower opacities will be discussed in the further work section of chapter nine.

The results showed that the use of the resin cast opacity targets were an appropriate approach as a standard comparator for the measurement of the response of laser scanning and structured light 3D digitisation techniques to varying opacity. However, the failure of the photogrammetric reconstructions for all the opacity targets (irrespective of opacity level) demonstrated the problem of developing a standard target for examining the impact of object opacity on the quality of photogrammetry whilst also providing sufficient surface features to enable photogrammetric reconstruction (section 6.9.3). The potential for extending research in this area is discussed in the further work section of chapter nine.

These results are relevant to the study of bone where taphonomic change induces alterations to their opacity. Whilst these samples were made from a uniform resin material and therefore do not simulate the histological structure of bone, they provide a baseline of instrument response to changing opacity against which the more complex opacity light interactions in bone can be considered.

8.1.3. Discussion of the surface roughness technique comparison standards

The results show that the use of high quality abrasive cloths as a standard target to compare the response of 3D digitisation techniques to surface roughness proved effective.

The laser scanner had a resolution comparable to the macro structured light scanner, yet the quality of the data for lower levels of surface roughness are unexpectedly poor for the laser scanners resolution. For all scanners, once the surface roughness was smaller in size than the resolution of the scanner, the scanner should have returned a flat surface with low levels of variation derived from the precision of the instrument. However, the data showed that the recorded surface variation increased in opposition to the decreasing known surface roughness for the samples, and relative to the resolution of the scanners.

For surfaces with lower levels of surface roughness, the interaction of light at the surface became more diffuse (figure 4.12) and the path of light was directed back to the instrument sensor through multiple reflections off the surface variations (section 4.2.3.1). In these conditions, single wavelength scanners such as the laser scanner are more susceptible to speckle which produces interference patterns and widens the variation in point accuracy for the recorded surface resulting in an overestimate of the total surface variation of the sample. In figure 7.13 this results in the higher surface variation than expected for the resolution of the laser scanner.

Additionally, the increased susceptibility of single wavelength laser scanners to diffuse surface generated interference in the form of speckle (section 4.2.3.1) was reflected in the higher levels of variation in the point cloud of surfaces below the resolution threshold of the laser scanner. These results correspond with the expected effects speckle pattern described within the literature (e.g. Feng et al. 2001, Gåsvik 2002, Marom et al. 2003, Rak & Wozniak 2012).

These results are relevant to the study of bone as the surface roughness of samples is affected by taphonomic change. The degree of surface roughness affected digitisation quality leading to variation in measured parameters (area,

volume). Furthermore, the digitisation of surface roughness is likely to affect the results of digital refitting of fragmented bone where greater digitised surface variation will impact alignment of refitting surfaces, and reduce quality indicators such as the percentage of surfaces refitting within +/- 0.1 mm (section 8.4).

8.2. Accelerated testing and natural weathering of mammalian bone

The following discussion considers the results in chapter seven (sections 7.2, 7.3 & 7.4) and specifically the use of accelerated and natural field weathering methods to simulate degradation to mammalian bone.

8.2.1. Taphonomic change to bone in low pH conditions

Low pH conditions dissolve the mineral fraction from bone and, where the burial environment is anoxic, preserve the gross protein structure (section 3.4.4.1). The loss of the rigid bone mineral softens the bone to the point that the bone can be flexed and bent. The gross changes observed in the experimental bone samples exposed to low pH conditions illustrates this demineralisation and were soft to the touch and flexible whilst wet (section 7.2.1). The flexibility of the bone increased over the three exposure periods as the mineral content in the bone samples decreased.

Upon air drying, the bone samples stiffened, fixing any alterations of the bone's shape that had occurred through bending, and allowed the samples to be fragmented. The samples shrank whilst drying. These changes are consistent with the dehydration of the collagen protein structure in dry bone described by Currey (2006). Whilst in archaeological bone from less acidic environments the contraction of the collagen fibrils is opposed by the compression strength of the surviving bone mineral, in highly acidic environments dissolution of bone mineral allows the collagen fibrils to freely contract, resulting in the dimensional changes both in terms of overall volume and the thinning of the cortical thickness observed in the experimental bone samples.

The loss of bone mineral in the low pH samples removed the opaque white hydroxyapatite, resulting in a significant reduction in the opacity of the bone (section 7.2.1). This gross observation was confirmed in quantitative results for sample opacity (section 7.3.1) where the bone samples exhibited a steady decrease in opacity as dissolution of bone mineral increased. Following the third exposure period the measured opacity of the bone samples had reduced to less than 92% (figure 7.40). This was below the threshold level of opacity at which

the assessment of technique comparison standards for laser scanning ceased to be effective (97.5%) and close to the lowest opacity technique standard (section 8.1.2).

These experimental taphonomy changes correlate well with the distortion and translucency in bone samples exposed to pH 1 conditions described in the visual analysis results in High et al. (2015). Whilst High et al. describe disintegration of their modern bone samples after only three days exposure to acid solution, the results in this research showed less distortion. The difference may be accounted for by their use of 3 mm sheep rib sections with correspondingly thinner cortical thicknesses. In contrast the complete sheep femora used in this research slowed taphonomic change. When fragmented samples were returned to the reaction jars without the protective effects of the marrow, the demineralisation of the samples and increased translucency (figure 7.20) was closer to that seen by High et al. (2015).

The loss of the white bone mineral from the bone allowed the yellow coloured collagen to dominate as described in the gross changes and this is reflected in the reduction in measured values of surface colour lightness variation (figure 7.42). The colour change mirrors that seen in bone samples demineralised in the laboratory prior to isotopic analysis (Richards & Hedges, 1999), where the colour staining from humic acids in acidic burial environments, such as that seen at Star Carr (Milner et al. 2011), are not present.

The loss of specularity and rougher surface appearance of the articular surfaces of the bone are associated with the loss of the hyaline cartilage through chemical hydrolysis. As the smooth outer layer of the hyaline cartilage was removed it exposed the underlying cartilage to bone junction which has a rougher texture (section 2.1.3) (Hoemann et al. 2012).

8.2.2. Taphonomic change to bone in high pH conditions

The bone samples subjected to high pH exposure primarily exhibited gross change in the surface roughness, opacity and colour of the bone. These qualitative observations are borne out by the rapid increase in opacity in the quantitative data (figure 7.40) to 98.8% after the first period of exposure and full

opacity by the end of the third exposure period. The measured data (figure 7.42) for colour lightness showed a rapid reduction in surface lightness variation after the first exposure period continuing to gradually reduce over the following exposure periods.

As described in section 3.4.4.2 alkaline conditions result in loss of bone collagen preserving the gross mineral structure. The removal of the bone collagen from the experimental bone samples left behind the opaque white bone mineral, accounting for the observed increase in opacity and whitening of the colour, whilst also reducing the visibility of the pink colouring from the postmortem haemolysis of the blood within the Haversian system and the areas of haematopoietic (red) marrow.

The high pH environment led to the chemical hydrolysis of the collagen to produce random coil gelatine. The hydrophilic gelatine swelled adding to the swelling of the triple polypeptide collagen chain fibrils, further promoting the chemical hydrolysis of the collagen (section 3.4.3). The swelling of the collagen in the outer layers of the circumferential lamellae of the bone samples resulted in the expansion of these layers adding tensional loads across the layers. The chemical hydrolysis of the collage fibrils reduced the ability of the bone to resist tension, and formation of small cracks in the surface layers and the loss of structural strength. At the same time, the chemical hydrolysis of the collagen bonding the layers of circumferential lamellae together resulted in their delamination, which in association with the cracking within the outer layers promoted flaking of small fragments from the surface and exfoliation (figure 8.6) which could then be lost into the sodium hydroxide solution in the reaction jars. The gross changes observed follow those predicted from the gelatinisation of collagen reported by Pfretzshner (2006) and are similar to the gross changes described in avian bones submerged in alkaline lake waters in Tanzania (Prassack, 2011).

Figure 8.6: Increasing exfoliation of the surface of the bone over time in high pH exposed samples. Initial loss of collagen from the surface layers of bone after one period of exposure (left). Crazing and flaking of outer layers of bone exposing further layers after two periods of exposure (middle). Loss of areas of bone surface after three periods of exposure (right) (source: author).

Additionally the formation of small cracks promoted access to deeper layers of bone, the formation of larger cracks and split lines, as well as greater roughness of the surface of the bones (figure 8.7). These changes resulted in outer cortical surfaces that had an overall greater surface roughness and this accounts for the more diffuse appearance.

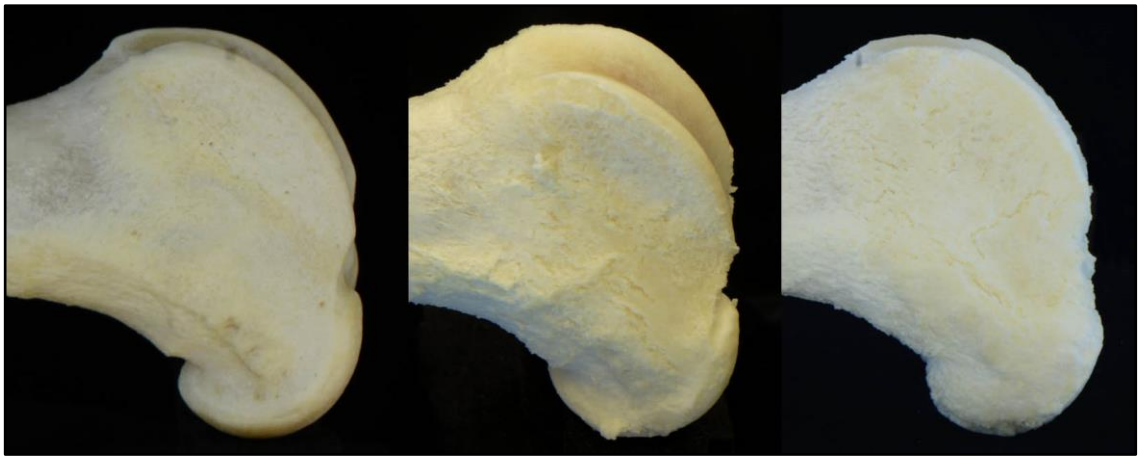

Figure 8.7: Increasing surface roughness due to taphonomic damage of the bone over time in high pH exposed samples. Initial loss of collagen from the surface with limited change to surface roughness after one period of exposure (left). Crazing and cracking of outer layers of bone after two periods of exposure increases the surface roughness (middle). Expansion of cracks with increased flaking and loss of bone surface after three periods of exposure results in increased surface roughness (right) (source: author).

Chemical hydrolysis of the bone lipid into individual fatty acid residues with greater solubility also accounts for the loss of the bone lipid from the cortical

surfaces of the bone samples. Bone lipid within the surface of bone contributes to the translucency of bone and therefore the reduction of bone lipid content from the surface of the bone samples further increased the bone sample opacity (section 3.3.5.1).

8.2.3. Taphonomic change to bone in high UV conditions

The bone samples subjected to high UV exposure exhibited limited gross physical changes beyond the photodegradation and bleaching of the outer cortical surface and the reduction in bone lipid on the surface.

The loss of lipid content can be partially explained by the warming of the bone associated with the high intensity UV lamp within the UV exposure testing unit (section 5.3.6.1). Additionally, exposure to high doses of UV radiation results in photolytic and photooxidative degradation of the molecular chains within the bone lipid, reducing their length and promoting their loss from the bone surface (section 3.3.5) (Zayat et al. 2007, Dupras & Schultz 2013). Bone lipid within the surface of bone contributes to the translucency of bone and therefore the reduction of bone lipid content from the surface of the bone samples results in increasing opacity (section 3.3.5.1) and increases the reflectivity index (Beary 2005, Dupras & Schultz 2013, Byers 2015).

Photooxidative change also damaged the collagen within the bone surface, leading to bleaching of the bone samples and the pattern of white mottling observed. The visual observations of gross appearance were supported by the measured change to the variation of surface lightness (figure 7.42) where the initial increase in bleaching created contrasting colours with the darker red and pink stained bone. Further bleaching began to reduce the level of contrast on the surface producing a more uniform light surface. Additionally, this second period saw a reduction in the red/pink staining of bone as photolytic degradation broke down the haemolysis products within the Haversian system which are photodegraded more rapidly than collagen (Huculak & Rogers 2009). These results for colour change in response to high UV exposure support the conclusions of Beary (2005) who noted that even short duration exposure to UV produced measurable surface bleaching.

The measured opacity of the bone samples displayed a greater increase in opacity than either the gross visual changes or the measured lightness variation on the surface of the bone samples indicated (figure 7.40). These results suggest that the taphonomic change is altering the attenuation coefficient of light at both the surface of the bone and deeper into the cortex. This effect heightens the attenuation and diffusion of light at the boundaries between histological structures, in particular the boundaries between the circumferential lamellae. This scattering of light corresponds with the results on the scattering properties of bone by Matousek et al. (2005) and that of Golcuk et al. (2006) and shows that the opacification through photodegradation is not limited to the surface layers, but penetrates into the cortex and interacts with the boundaries between deeper histological structures.

The changes to the volume of UV exposed bone (figure 7.52) can be explained by the long term heating of the bone in the UV exposure instrument (section 5.3.6). The high intensity lamp of the instrument produced heat and used a fan to cool the lamp. The exposure of the bone samples to elevated temperatures and increased air movement over the 56 days of the combined exposure periods accelerated the effects of dehydration of the samples. The dehydration of bone reduces the spacing between the collagen fibrils and the hydroxyapatite platelet surfaces resulting in shrinkage of the bone (Currey 2006, Lievers et al. 2010, Rai & Sinha 2011).

8.2.4. Taphonomic change to bone resulting from field weathering

The bone samples subjected to exposure on the field weathering site exhibited gross physical changes in line with those expected for the environment (section 3.3). All the bone samples exhibited limited surface change within weathering stages 0 or 1 (Behrensmeyer, 1978) and were comparable to surface weathered bone in forensic contexts where the duration of exposures are often similar (Cunningham et al. 2011, Wilson-Taylor 2012, Junod & Pokines 2013).

The results showed the most significant factor affecting the gross appearance of the bone samples was the effect of solar radiation resulting in photodegradation and bleaching (section 3.3.5). This increased the opacity, whitened the bone and faded the pink colouring from the postmortem haemolysis of the blood

within the Haversian system and the areas of haematopoietic (red) marrow. Additionally the photodegradation of bone lipid from the bone samples further increased the opacity and reduced the specularity of the surface. These changes are consistent with the taphonomic changes described in the high UV discussion (section 8.2.3). The extent of bleaching after the second period of exposure was more pronounced than for the high UV samples reflecting the longer exposure period in this experiment. The results of the colour variation and description of the gross changes didn't show variation between the upper and lower exposed surfaces suggested in the literature (Behrensmeyer 1978a, Miller 2009). This is probably due to the elevation of the samples over the concrete pad, the light colour of which reflected light onto the lower surfaces evening out the impact of photodegradation. The concrete pad also prevented vegetation growth near the bone samples resulting in continued exposure of the bone samples when the sun was lower in the sky (figure 5.3). These low angles of light allowed greater illumination of the lower surfaces of the bone which would, in more natural weathering experiments, have been blocked by the surrounding vegetation. Whilst differences in surface degradation are not apparent in these samples, extended exposure intervals may have allowed greater variation between upper and lower surfaces to emerge.

The exposure of the bones to natural weathering resulted in the bone samples being subject to fungal and plant colonisation. The location of black staining on the surface of the bone indicates that fungal activity was concentrated at the articular surfaces and their associated capsule attachments. This suggests that unmineralised hyaline cartilage at the surface provided an easily accessible food source in the early stages. Fernández-Jalvo et al. (2010) note that fungal attack on bone is associated with the histological damage at the surface of bone in the form of Wedl type I tunnelling which produces increased surface porosity. Furthermore fungal attack can result in cortical exfoliation breaking down and removing thin layers of surface bone which in the samples would account for some of the increased surface roughness and the more diffuse appearance observed in the samples. Additionally stripping of the hyaline cartilage exposed the underlying rougher bone (Hoemann et al. 2012) contributing to the more diffuse appearance bone surface.

By the end of the second exposure period, the surface staining was no longer present and suggests that once all the surface accessible hyaline cartilage had been lost, fungal activity declined allowing photodegradation to bleach the black staining revealing the taphonomically-altered bone underneath. The staining from the fungal colonies coloured the surface of the bone black during the early stages of exposure, and in association with the photodegradation led whitening of the bone significantly increased the surface colour variation of the samples. This pattern of surface exploitation of cartilage followed by photobleaching is also expressed in the surface colour lightness variation data shown in figure 7.41 (section 7.3.2).

During surface weathering fungal penetration into the cortical bone can also occur via the Haversian system into the lamellae of the osteons (i.e. type II Wedl tunnelling) (section 3.3.7) (Trueman & Martill 2002). Such fungal penetration may explain the grey mottling to the bone observed in the samples after the second period of exposure where a combination of the breakdown of the haemolysis products (Huculak & Rogers 2009) and the black fungal staining within the Haversian system discolours the surrounding white bone. In this case the intensity of the grey mottling of the bone should be limited by both the 500 µm spacing of osteon structures (Cuijpers 2009) derived from the diffusion characteristics of nutrients *in vivo*, and the continued photobleaching of staining within the cortical bone.

The presence of surface cracking and the development of the fine surface roughness over the diaphysis of the bone produced a diffuse appearance by the end of the second period of exposure; this is due to a combination of photodegradation and physical weathering through fluctuations in temperature and moisture on the field weathering site. Freeze-thaw and wetting-drying damage set up cycles of tensional loading in the bone resulting in the fine cracking and surface damage observed. However, based on the limited surface change in other similar exposure experiments in temperate settings (e.g. Andrews & Armour-Chelu 1998) the samples displayed greater taphonomic change after the short duration possible within the timescale available for this research than was predicted. The presence of some fine cracking and surface damage and its resultant diffuse optical surface properties, was therefore greater than anticipated. The temperature and precipitation data for the site

(see section 5.3.2), characterised in 6 hour periods, showed that the samples were subject to a total of 80 freeze-thaw events and 308 wetting events over the duration of the experiment, demonstrating that the elevation and exposed location of the field weathering site produced more extreme variations in weather conditions in comparison to most temperate locations in the UK and explaining the greater level of surface change compared to other studies. Boutros et al. (2000) showed that as few as four cycles of freeze-thaw could induce small amounts of surface change to bone, with incremental damage occurring after each subsequent cycle. The damage to the samples within this study corroborated limited freeze-thaw can induce observable change at levels likely to have an impact on the 3D digitisation response.

8.3. Effect of taphonomic changes on the quality of 3D digitisation

The following discussion draws on the results in chapter seven (sections 7.2, 7.3 & 7.4) to assess the impact of the taphonomically-induced changes to bone (section 8.2) on the quality of 3D digitisation techniques and compares the response of each technique.

8.3.1. Digitisation of low pH taphonomically-altered bone

For laser scanning of the low pH samples, the large decrease in opacity dominated the quality of the digitisation. The decrease in opacity was a direct result of the taphonomic change discussed in section 8.2.1. The technique comparison standards for opacity demonstrated the relationship of lower opacity to the increased effects of noise, as the light from the laser is reflected at multiple depths within the cortex of the bone (section 8.1.2). This resulted in laser scan models that displayed greater levels of surface variation (figure 8.8 red arrow) than observed in the physical samples (figure 7.17).

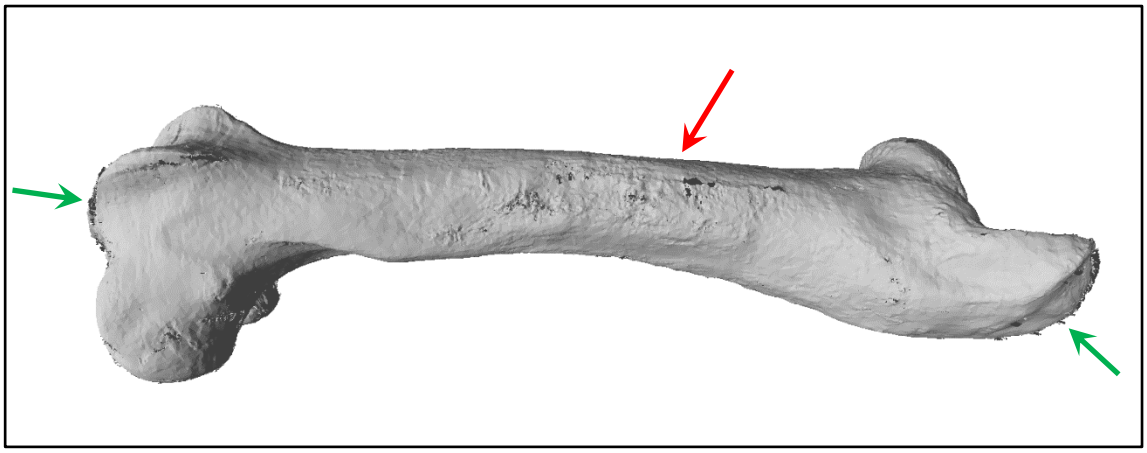

Figure 8.8: 3D model of low pH taphonomically-altered bone sample laser scanned after the third period of exposure. The diaphysis of the bone shows greater levels of surface variation (red arrow) than observed in the physical samples for this exposure period (compare to figure 7.17). The model also exhibits edge noise (green arrows) (source: author).

The laser scanning results displayed consistently larger levels of noise in the 3D models (section 7.4.1) than the other techniques. This noise comprises errors due to opacity derived point position inaccuracy on all surfaces of the bone and edge noise at points where the sample surface topography has greater variation (figure 8.8 green arrow). The lower opacity of the low pH exposed samples

amplifies the effect of edge noise in the 3D models as discussed in the section 8.1.2. The higher noise response results from the greater susceptibility of the single red wavelength (λ = 655 nm) used in the FARO laser scanner to lower opacities. The measured opacity of the low pH samples (figure 7.40) are consistently below the 97.5% opacity threshold for the quality response of laser scanning determined in the technique comparison standards (section 7.1.2, figure 7.5).

The presence of higher noise levels within laser scanned 3D models explains the consistently larger measured volume over structured light scanning for the same samples at each stage in figure 7.43. The pattern of higher volumes for laser scanning are consistent with the volume measurements within the opacity technique comparison standards (section 7.1.2.2). The lower opacity in the low pH samples exacerbates variation in volume measurement consistent with the model proposed in section 8.1.2 (figure 8.1).

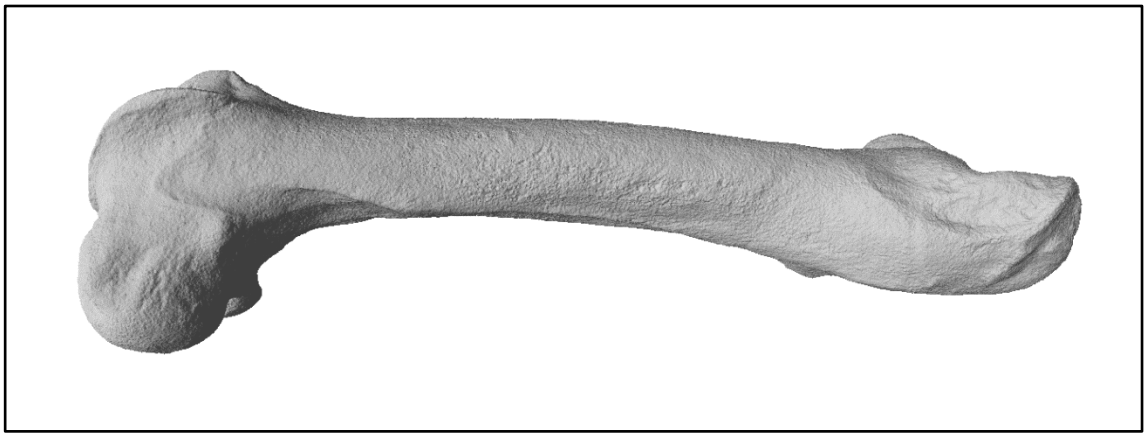

Figure 8.9: 3D model of low pH taphonomically-altered bone sample structured light scanned after the third period of exposure. The surface of the bone shows greater levels of surface variation than observed in the physical samples for this exposure period (compare to figure 7.17). The model does not exhibit edge noise compared to figure 8.8 (source: author).

The structured light 3D models of low pH taphonomically-altered bone samples showed a degree of surface variation across the whole bone that was greater than the level of surface roughness seen in the physical samples. This surface variation was not as great as that seen in laser scanning (figure 8.8). The technique comparison standards showed that structured light produced a larger surface variation than laser scanning when digitising the same surface roughness (figure 7.13), however the opacity technique comparison standards

showed lower opacity produces significantly greater noise in laser scanning resulting in greater surface variation. In the 3D models from low pH conditions, the surface variation is dominated by opacity induced noise and therefore structured light scanning produced better quality models.

The lower noise levels for structured light reflect the lower susceptibility of the full spectrum light source used in the instrument, and the inherent filtering of extraneous points through the averaging of multiple images with differing phase patterns for each scan (section 4.3.2) as described by Zhang (2010). Whilst blue structured light scanners may mitigate some of the quality impacts of lower opacity in low pH altered bone (Bernal et al. 2013) (section 8.1.2), the presence of red and pink colouration of the bone observed in the gross changes (section 7.2.1) would be expected to offset any improvement due to the increased blue wavelength absorption of these surface colours.

A comparison of the 3D models from laser scanning and structured light demonstrated that colour variation was not a significant factor in the quality of models for these techniques. The lightness of the bone samples surfaces was sufficient provide good contrast between the black and white phase patterns within structured light and in laser scanning the lack of significant blue colour component to the surface resulted in good reflectance of the red laser line.

The quality of the photogrammetry models was consistently poorer than laser scanning and structured light techniques. The noise levels recorded from the finalised models shown in figure 7.46 underestimate the level of noise as they present post processed values. The low pH samples showed very high levels of noise within the sparse clouds during photogrammetric reconstruction and required a substantially higher level of user intervention (section 6.3.4.2) than the other experimental samples removing greater quantities of noise prior to meshing. Additionally some photogrammetric reconstructions failed (section 6.3.4.2) for the low pH samples despite the high level of user intervention, and noise levels for the failed samples are not included in the data shown in figure 7.46.

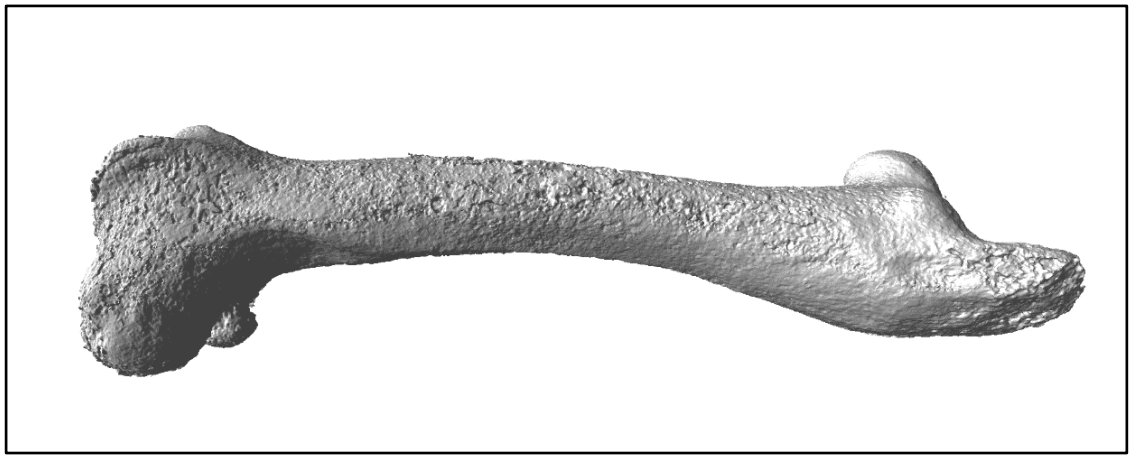

Figure 8.10: 3D model of low pH taphonomically-altered bone sample produced through photogrammetric reconstruction after the second period of exposure. The surface of the bone shows significant errors and greater surface variation than observed in the physical samples for this exposure period (compare to figure 7.16) (source: author).

Photogrammetry lacks an integral scale reference within the data capture process; this is in contrast to laser scanning and structured light which have calibration built in through the coordinate measuring machine basis of the arm mounted laser scanner or the known dimensions of the projected phase patterns in structured light scanning. The reconstruction process in photogrammetry therefore relies on the identification of tie points from image features; where there is poor tie point identification the 3D reconstruction is often poorly aligned and the sparse and dense clouds both exhibit high levels of point position uncertainty (Wenzel et al. 2012) (figure 8.11). These manifest as erroneously positioned points and successful creation of a 3D model relies on significant user input to identify, select and delete incorrectly positioned points. This results in a high degree of subjective selection reliant on user experience.

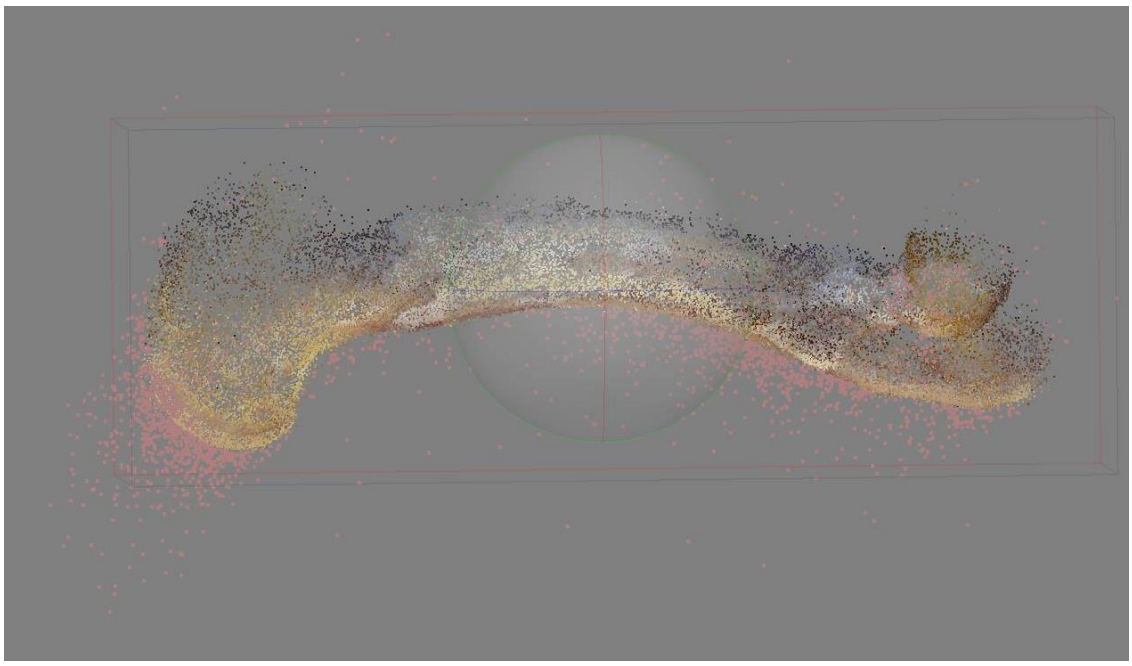

Figure 8.11: Poor tie point alignment in the sparse cloud of experimental bone sample showing poorly aligned points highlighted in pink (source: author).

In the low pH conditions the lower opacity of surfaces in the bone samples allowed sub-surface colour changes within the bone to be recorded in the 2D photographic image and thus identified as surface features used as tie points in the 3D reconstruction (section 4.3.3.2). When the same sub-surface colour change was captured in the 2D image at the next camera position, the position of the feature identified as if on the surface, was not consistent. Because the 3D reconstruction relies on calculations of collinearity between pairs of identified surface features in multiple images (Remondino 2014) this inconsistency of position resulted in significant errors in the point position reconstruction (section 4.3.3.1) and therefore poorer quality responses in photogrammetry.

All three techniques produced 3D models of relatively poor quality with high levels of noise or surface errors. Structured light scanning displayed the best response to taphonomic changes in samples from low pH conditions as the technique least affected by decreased opacity.

8.3.2. Digitisation of high pH taphonomically-altered bone

The bone samples subjected to high pH exposure primarily exhibited gross change in the surface roughness, opacity and colour of the bone. The lighter colour of the bone samples observed over the three periods of exposure and the reduction in colour variation (figure 7.42) produced surfaces that absorbed less of the instrument source light and provided a greater return to the instrument sensors in both laser scanning and structured light. This resulted in larger numbers of point estimates within the point clouds for these surfaces and therefore reduced surface variation from the true values. The response of laser scanning and structured light for high pH exposed samples corresponded with that predicted in the technique comparison standards for colour (section 8.1.1).

The increased opacity of the bone samples (figure 7.40) resulted in higher quality 3D digitised models in laser scanning and structured light techniques. This directly reflects the results as predicted by the opacity technique comparison standards (section 8.1.2) due to the reduction in sub-surface scattering of light and therefore greater point precision (figure 8.1). This was also reflected in the lower face noise values for the first exposure period (figure 7.50) where opacity had increased in the samples but other taphonomic changes were not yet impacting the results.

Following the second period of exposure the swelling, cracking, exfoliation and flaking of bone, associated with the chemical hydrolysis of collagen discussed in section 8.2.2, impacted the quality of 3D digitisation of the samples. Where larger flakes continued to adhere to the surface they protruded from the surface producing very small thin edges. These resulted in an associated increase in edge noise (section 8.1.2), exacerbating the effects of surface roughness due to the increased speckle-derived noise seen in the technique comparison standards (section 7.1.3) and literature (Rak & Wozniak 2012).

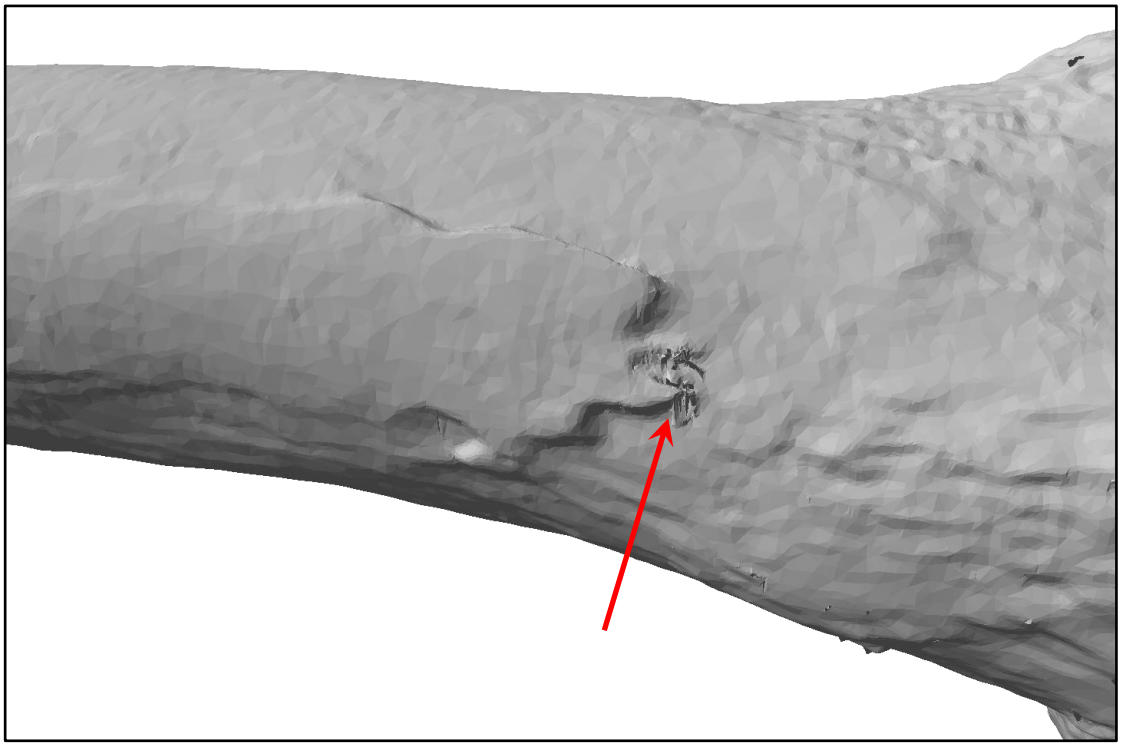

Figure 8.12: Edge noise shown in a close up of 3D model of high pH taphonomically-altered bone sample laser scanned after the third period of exposure. Flaking and exfoliation of the outer layers of cortical lamellae produced increased noise response in laser scanning (red arrow) (source: author).

Laser scanning produced the highest percentage of face noise compared to the other techniques, reflecting the greater susceptibility of laser scanning to both edge noise (figure 8.12) and speckle. In addition the elevated noise levels in laser scanning impacted the volume measurement from the 3D model. Whilst the majority of the volume loss can be attributed to the physical loss of surface flakes of bone through flaking and exfoliation, the difference in response between laser scanning and structured light (figure 7.48) can partially be attributed to the response of these instruments to surface roughness factors (section 7.1.3).

For laser scanning the higher estimation of volume seen in figure 7.48 can be attributed to the greater edge noise. The over estimation of volume in laser scanned 3D models through the creation of phantom points and mesh surfaces at edges has been demonstrated in the technique comparison samples for opacity (section 8.1.2). Whilst lower opacity exacerbates edge noise, edge noise is not a function of opacity and occurs on all samples with thin edges and remains a notable challenge in opaque samples.

For structured light scanning edge noise was limited by the inherent filtering of extraneous points through the averaging of multiple images with differing phase patterns for each scan. Structured light recorded the increased surface roughness and accurately modelled the surface flakes of bone in the second and third exposure periods (figure 8.13). These results correlate with those seen in the methodology comparison standards for surface roughness (section 7.1.3).

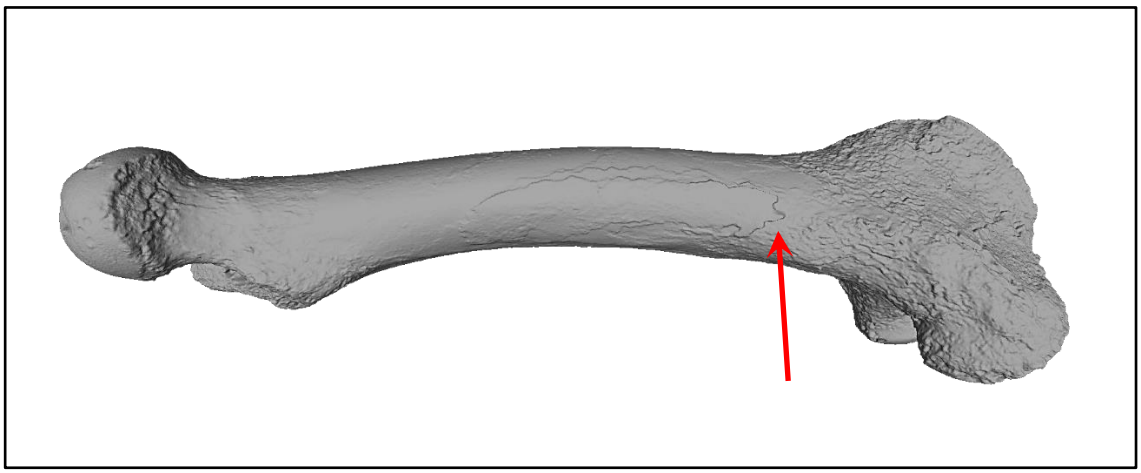

Figure 8.13: 3D model of high pH taphonomically-altered bone sample structured light scanned after the third period of exposure. Flaking, exfoliation and cracking of the outer layers of cortical lamellae produced increased surface roughness particularly at the distal end of the bone. Note the same flake of bone seen in figure 8.12 without edge noise (red arrow) (source: author).

The photogrammetry models from high pH taphonomically-altered bone samples demonstrated similar levels of poor quality surface reconstruction associated with poor feature identification as those from the low pH experiment (section 8.3.1). Whilst the underlying reasons for the poor feature identification vary between the high pH and low pH exposed samples, the resulting poor tie point alignment is similar.

The low levels of surface colour variation seen in the high pH taphonomically-altered bone (figure 7.42) reduced the number of identifiable image features within photogrammetric imagery leading to poor tie point identification (Wenzel 2012). The high pH models for the second and third periods of exposure required significantly more user intervention during photogrammetric model reconstruction (section 6.3.4.2). This resulted in the introduction of subjective removal of data that affected the quality of the quantitative measures.

The extent of face noise for photogrammetry models increased over the exposure periods with a noticeable increase after the second period of exposure; this correlates with the taphonomic changes to the bone surface. This higher noise after the second exposure period was exhibited within the reconstructed models as a significant increase in surface variation compared to the laser scan and structured light models producing poor surface modelling with misaligned areas of mesh which floated above the surrounding surface (figure 8.14 red arrows).

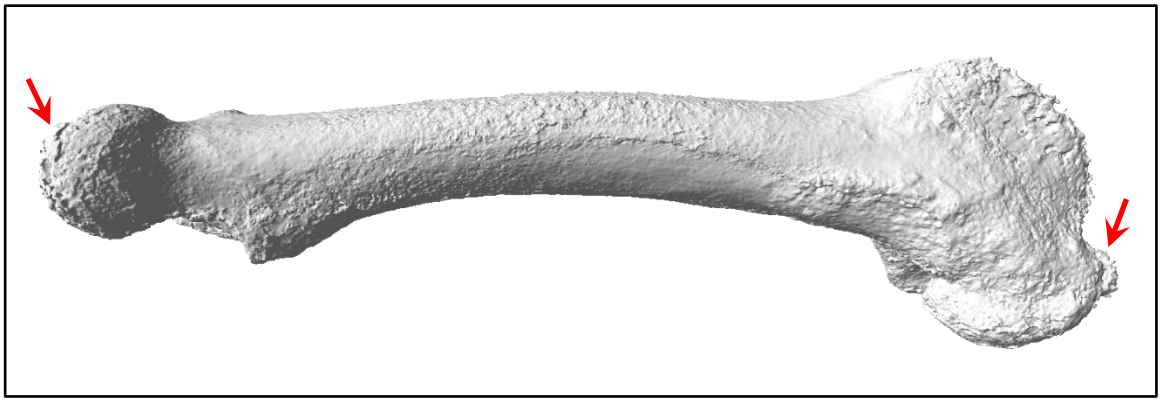

Figure 8.14: 3D model of high pH taphonomically-altered bone produced through photogrammetric reconstruction after the second period of exposure. Flaking, exfoliation and cracking of the outer layers of cortical lamellae produced increased surface roughness which is poorly digitised. Misaligned areas of mesh float above the surrounding surface (red arrows) (source: author).

Following the third exposure the increased whiteness of the samples further reduced the number of identifiable surface features and the reconstructed dense clouds had lower point density. Meshing of the dense cloud therefore exhibited smoothing as the more widely spaced points were averaged, resulting in an effective reduction in the resolution of the model. The models therefore fail to accurately resolve surface features on the high pH exposed samples, as shown by the smoothing of the cortical surface flake on the distal diaphysis of the illustrated example in figure 8.15 (red arrow) in comparison to the well-defined flake in laser scanning (figure 8.12) and structured light (figure 8.13).

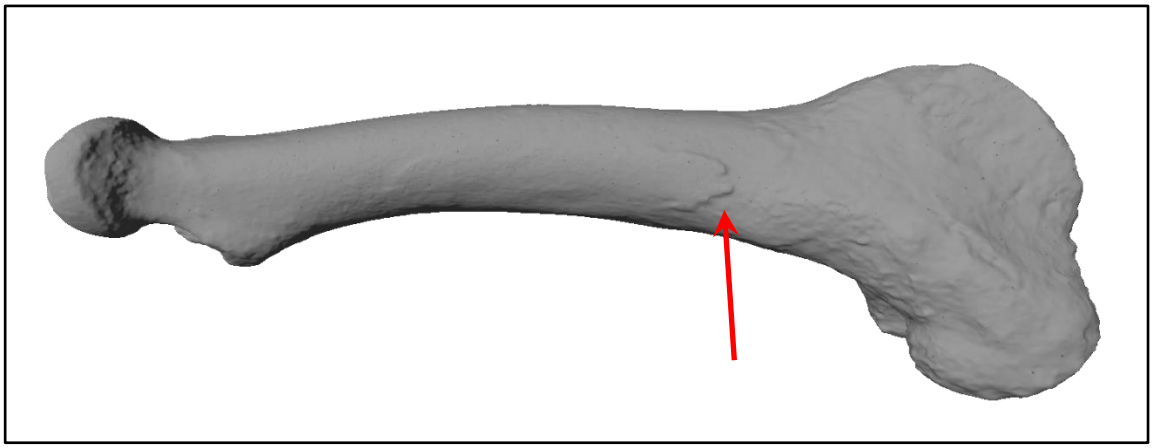

Figure 8.15: 3D model of high pH taphonomically-altered bone produced through photogrammetric reconstruction after the third period of exposure. Note the failure of photogrammetry to resolve the surface flake of bone seen in the laser scan and structured light models (figures 8.12 and 8.13) (red arrow) (source: author).

The response to the taphonomic change in high pH altered bone was poorest in photogrammetry. Structured light and laser scanning both produced accurate models of the taphonomically-altered surface of the bone samples, however, the response to thin bone flakes was poorer in laser scanning resulting in greater edge noise.

8.3.3. Digitisation of high UV taphonomically-altered bone

The primary taphonomic changes in the high UV exposed bone samples were induced by photodegradative processes resulting in increased opacity, an initial increase in colour surface variation followed by bleaching and loss of bone lipid which reduced specularity of the surface.

The increase in the surface colour lightness variation recorded in figure 7.42 for the samples and the increased opacity shown in figure 7.40 can be observed in the surface variation of the laser and structured light 3D models. The darker areas of colour on the surface of samples coincided with the less opaque areas of the surface (figure 8.16) and therefore the digitisation response displays effects from both of these variables. The technique comparison standards predict that laser scanning is more susceptible to opacity (section 8.1.2), whilst structured light scanning is more susceptible to darker colours (section 8.1.1).

Figure 8.16: 3D model of high UV taphonomically-altered bone showing the surface colour and opacity variation after the second exposure period (source: author).

The change in response to the high UV exposed sample surfaces in laser scanning and structured light between the first and second exposures allowed these two factors to be differentiated. The laser scan models showed limited change in the surface variation (figure 8.17), although there was a slight decrease in the level of edge noise observed. The structured light models for the two exposures (figure 8.18) demonstrated an improvement in surface variation. Therefore the reduction of surface lightness variation in the samples after the second exposure period has a greater impact on the quality of the 3D models than the improving opacity.

There was no observable variation in laser scan and structured light model quality as a result of decreasing specularity arising from lipid loss as might be expected (Rak & Wozniak 2012); the effects on model quality arising from opacity and colour lightness variation of the sample surfaces mask any minor changes that may be present.

The reduction in model volumes (figure 7.52) correspond with dehydration of the bone samples in the high UV instrument discussed in section 8.2.3. The presence of edge noise in the laser scan data produced the same elevated volume calculations observed in the other experiments. The structured light volume data may therefore be more representative of the true volume changes in the samples.

Figure 8.17: 3D model of high UV taphonomically-altered bone sample laser scanned after the first (top) and second (bottom) period of exposure showing limited change in the surface variation (source: author).

Figure 8.18: 3D model of high UV taphonomically-altered bone sample structured light scanned after the first (top) and second (bottom) period of exposure showing a decrease in the surface variation after the second period (source: author).

Figure 8.19: 3D model of high UV taphonomically-altered bone sample produced through photogrammetric reconstruction after the first (top) and second (bottom) period of exposure showing significantly improved quality of model reconstruction after the second exposure period (source: author).

Within the photogrammetry models improved point certainty produced greater precision in the reconstructed 3D models as opacity increased following the second exposure period. The observed increase in surface opacity (figure 7.40) reduced the visibility of sub-surface colour variations that were incorrectly identified as tie points after the first period of exposure (as discussed in the low pH experiment (section 8.3.1)). In the high UV exposed samples sufficient colour variation on the surface remained after the second period of exposure to allow feature identification and tie point alignment. The greater specularity, due to the higher lipid content present at the earlier stage, also contributed to the poorer response through the creation of white highlights which were misidentified as feature points in the photogrammetric images (section 04.3.3.3). This is illustrated in figure 8.19 where the quality of the model produced after the second period of exposure is significantly better, and by the reduction in the noise recorded in figure 7.54.

8.3.4. Digitisation of field weathered bone

The bone samples subjected to field weathering primarily exhibited gross change in the surface roughness, opacity and colour of the bone; the pattern of change reflects a more advanced change to that seen in the high UV experiment, but with a lesser degree of difference between the laser scanner and structured light scanner. This is due to the greater increase in opacity over the longer exposure periods of the field weathering experiment compared to the shorter higher UV exposure periods (section 5.3.6).

The opacity technique comparison results indicated a convergence of response for the techniques at higher opacities over c.98.5% (section 7.1.2.2). The measured opacity of the field weathering samples (section 7.3.1) demonstrated that by the end of the first exposure period sample opacity was already c.99% therefore the digitised models of the field weathering samples from the three techniques were expected to show similar levels of surface response. The low levels of noise and consistent volume measurements in the data bear out this prediction, suggesting that taphonomic changes within short periods of field weathering contribute to good 3D digitisation results.

The colour technique comparison standard results for the black colour patches predicted that the black fungal staining after the first period of exposure (figure 7.35) would produce a poorer response in structured light surface, that would be expressed as surface variation in the model with an improvement after the second period of exposure once the staining had been bleached via photodegradation. The surface variation in the structured light models (figure 8.20) did vary but the variation observed was less than that predicted. This indicated that the extent of mottling of the black fungal staining and the lower saturation of the black colour on the surface were sufficient to return a contrast response.

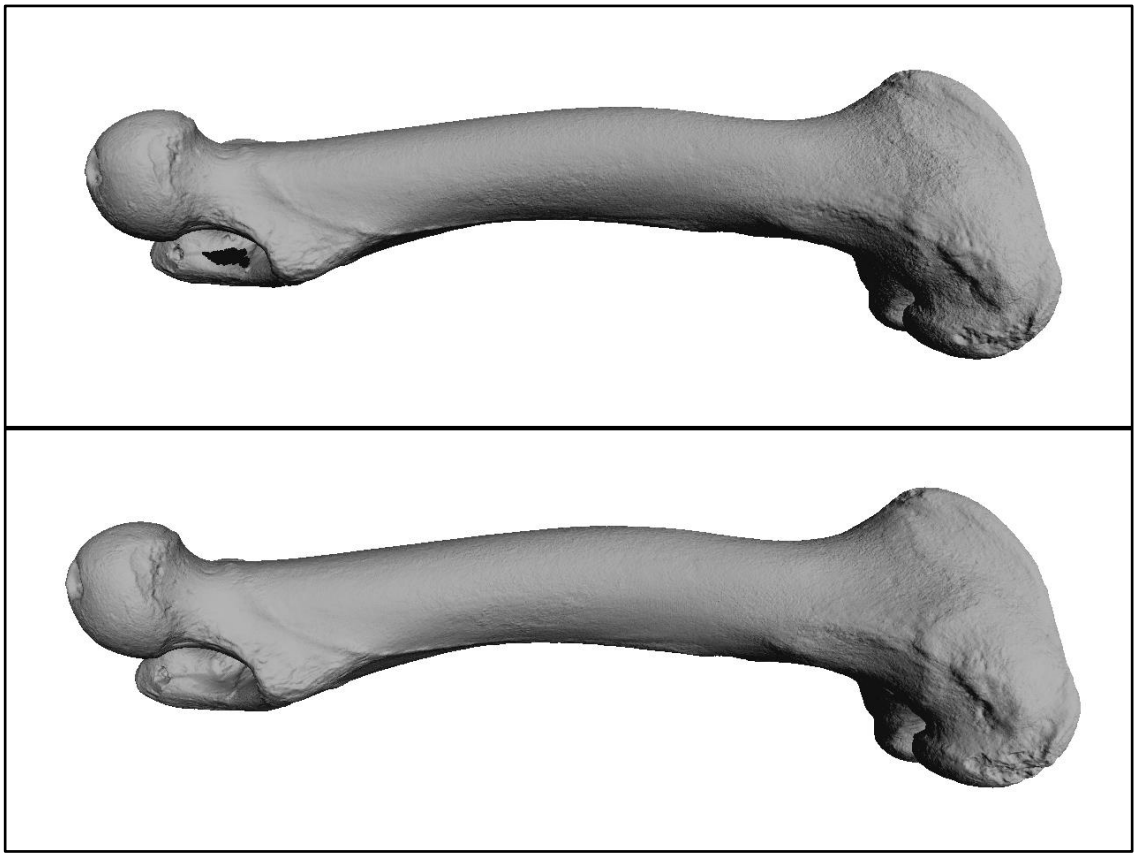

Figure 8.20: 3D models of field weathered bone sample structured light scanned after the first (top) and second (bottom) period of exposure showing limited change in the surface variation (source: author).

The laser scanned models showed the greatest level of noise in the data, although the field weathering samples showed the lowest noise levels of all the taphonomic conditions. The higher noise level results at the pre-exposure period result from the increased penetration of the single red wavelength light into the less opaque and specular bone surface of unaltered bone. This effect was removed after field weathering exposure due to the highly opaque bone surface resulting from photodegradation.

Laser scanning showed a small rise in the level of noise after the second period of exposure (figure 7.57) associated with the increased surface roughness in the form of fine cracking of the surface layers and the more diffuse appearance. The surface roughness technique comparison standards predict that laser scanning has a greater susceptibility to finely diffuse surfaces in the form of speckle noise (section 07.1.3) and the greater noise response in the laser scanned field weathering samples corresponds with this prediction; the effect of this can be seen in the 3D models (figure 8.21).

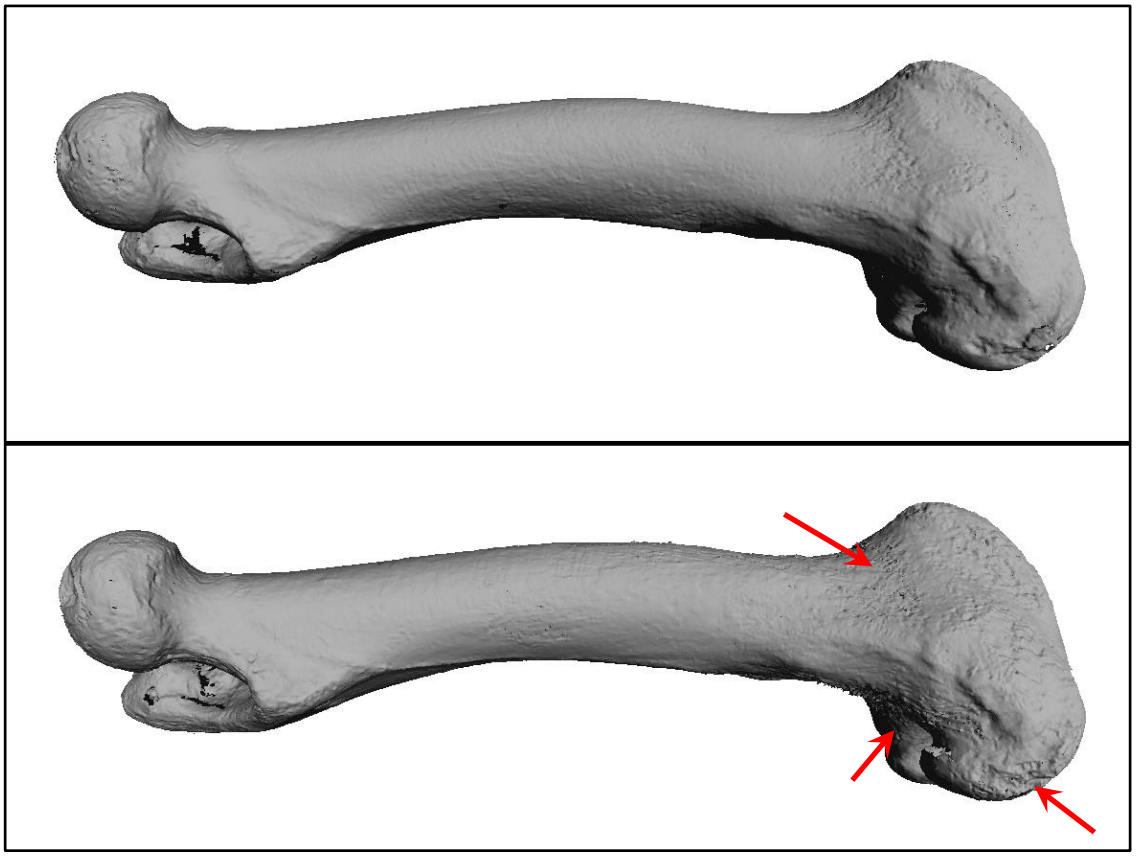

Figure 8.21: 3D models of field weathered bone sample laser scanned after the first (top) and second (bottom) period of exposure showing a small increase in noise after the second period of exposure exhibited as greater surface variation (red arrows) (source: author).

Whilst photogrammetry data wasn't collected for the earlier stages, the later stage data shows consistent volume estimates to laser scanning and structured light scanning. This reflects the improvement in tie point identification from image features in more opaque samples. The increase in opacity and bleaching of the bone was initially predicted to limit the number of surface features that could be used as tie points during model reconstruction similar to that seen in the high pH results. However, taphonomically-induced cracking and the presence of moss staining on the surface of the bone samples provided identifiable features, whilst the highly opaque low specularity surface removed the lower opacity impacts on photogrammetry seen in the low pH and high UV experiments. The better photogrammetric response was illustrated by the comparatively easier production of the photogrammetric models which required less user intervention and time for the field weathering samples than the other taphonomic experiments. The resultant models (figure 8.22) show few errors and result in good quality digitisation in short duration field weathered bone.

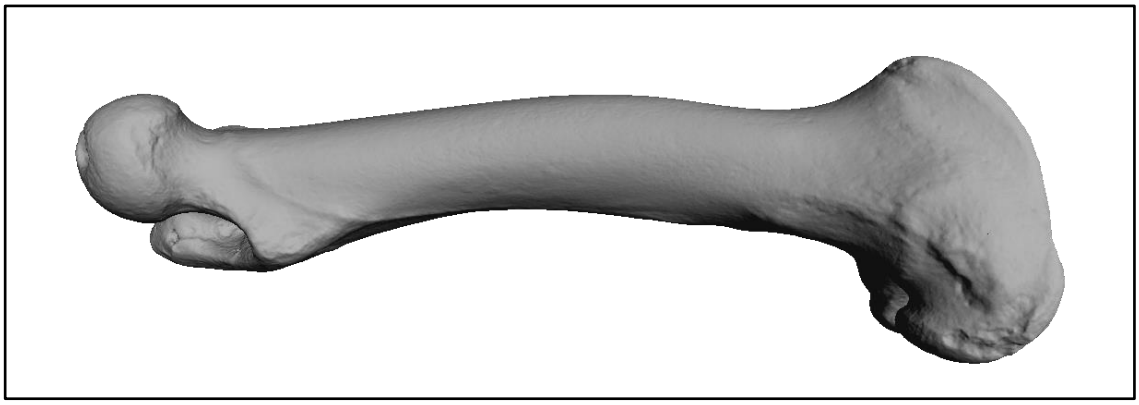

Figure 8.22: 3D model of field weathered bone sample produced through photogrammetric reconstruction after the second period of exposure showing good reconstruction and alignment (source: author).

The response to the taphonomic change in field weathering altered bone was good for all three techniques. The smooth but diffuse surfaces, low opacity and lighter colours are all conducive to accurate data collection and hence high quality 3D models. The single wavelength light source of laser scanning was more susceptible to speckle noise from the increasing surface roughness produced through taphonomic degradation of the outer layers of bone, although the levels of noise were lower than in other taphonomic conditions. The colour variation due to fungal staining was not strong enough to induce significant degradation of the structured light response and the development of small cracks and other surface changes aided photogrammetric reconstruction.

8.4. Effect of taphonomic changes on the quality of digital refit of bone

The following discussion centres on the results of refit in chapter seven (sections 7.5 and 7.6), to examine the impact of taphonomic changes on the quality of digital refitting of fractured experimental bone samples. The discussion compares these results to those from similar fragmentary material from archaeological and palaeontological examples of bone and other animal hard tissues.

8.4.1. Discussion of the effect of low pH taphonomic change on bone refit analysis

The gross taphonomic changes observed in the fragmented bone samples are described in section 7.2.1. The thinning of the cortical bone and the loss of the brittle bone mineral resulted in a significantly increased post-yield area (section 3.6.2), where plastic deformation of the bone resulted in distortions of the cross sectional profile of the bone during fracture (figure 7.19). The fracture patterns of the later stages of exposure were characterised by tearing and ripping of the bone producing very ragged and thin edges. Tear out spurs or “hinged” fragments occurred as the fracture path completed around the bone from the initial failure, resulting in protruding pieces of the outer layers of the cortex which were no longer aligned with the corresponding bone fragment. These fracture patterns are comparable to some of the features in wet bone and green stick fractures (section 3.6.3) (Currey 2006, Schmuck et al. 2010, Berteau et al. 2015).

The drying of the flexible bone observed in the gross changes to the whole bone samples (section 7.2.1) resulted in significant shrinkage and distortion. These dimensional changes were exacerbated in the fragmentary samples due to the thinner cortical bone and the additive effect of the plastic post-yield deformation during fragmentation. These changes resulted in corresponding fragments with differing patterns of distortion (figure 7.19). The two fragments displayed poor manual refit prior to digitisation and therefore the potential for refit of the resultant digital models was considerably reduced.

In addition to the effects of physical distortion of the bone, the taphonomic alteration to the samples discussed in section 8.2.1 also impacted the quality of the 3D digital models of the fragmentary samples; these introduced further challenges to the digital refit of low pH exposed bone. The most significant of these factors in the low pH experiment was the large decrease in opacity over the three exposure periods (section 7.4.1). The effect of lower opacity on the quality of 3D models seen in the whole bone samples (greater noise and positional inaccuracy) was heightened for the digitisation of the fracture surfaces, where the combination of the thinning of the cortical bone and the tear out spurs at the fracture margins produced sharp translucent edges. These resulted in levels of edge noise which were significantly higher than those in the other taphonomic conditions studied (figure 8.23).

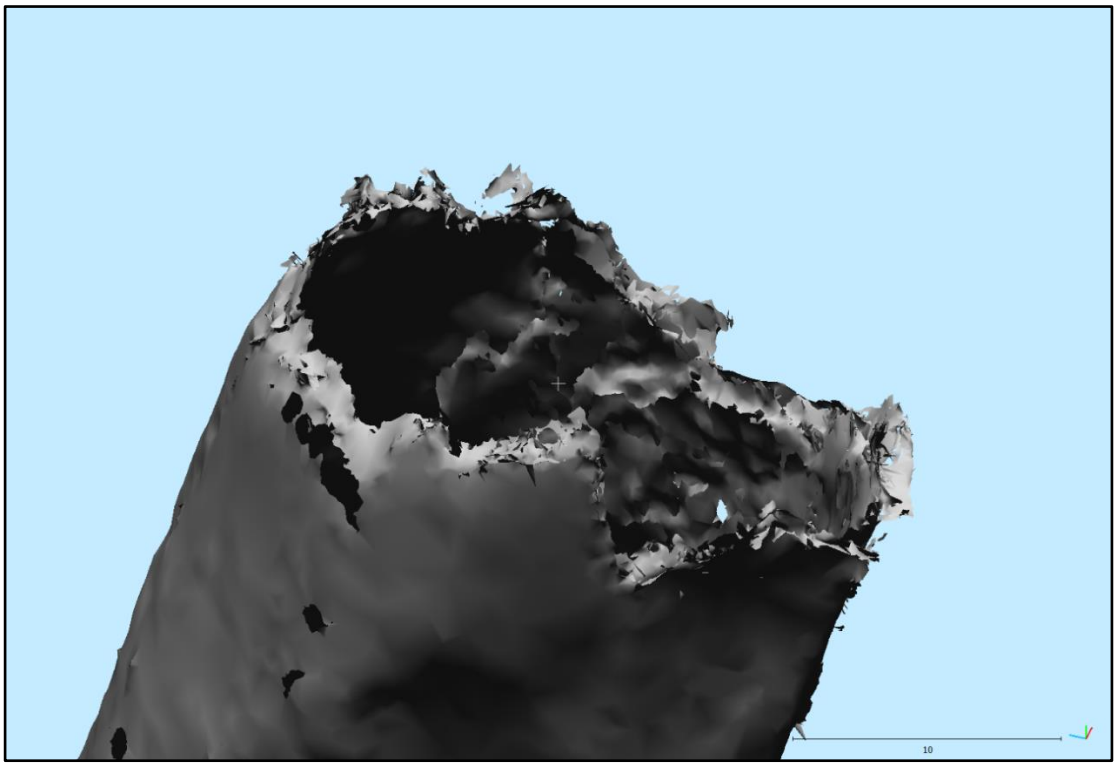

Figure 8.23: High levels of edge noise in the laser scanning digitisation of the fracture surfaces from low pH taphonomically-altered bone. Scale in mm (source: author).

In some circumstances where edge noise occurs, the addition of phantom mesh surfaces within the 3D model can be removed by manual segmentation of the edge noise derived areas of mesh (e.g. using the Segmentation tool in CloudCompare V2 (section 6.10.2)). This manual editing relies on the clear differentiation by the user of true mesh surface from the noise derived areas of

mesh. However, the loss of bone mineral in low pH conditions resulted in cortical bone thicknesses which, as illustrated in figure 8.23, produced digitised surface and edge noise that were difficult to differentiate. The taphonomic alteration to the bone therefore not only induced poor digitisation but also noise effects that made the feasibility of refit of fragmented bone highly problematic. Although a refitting match was produced in the CloudCompare V2 software, the quality of the refit was very poor and was only achieved through significant user intervention.

These factors explain the very large values for variation in the refit distances seen in figure 7.60 which varied by more than +/- 0.7 mm for structured light scanning and up to +/- 3.3 mm for laser scanning and photogrammetry. The scale of these variations and the low percentage matches between the surfaces (figure 7.63) indicates that refit analysis of fractured bone in these low pH conditions does not provide reliable refits. These results were gained using known corresponding fracture surfaces, therefore the application of digital refit analysis to identify refits not previously identified manually or to automate the identification of refits in a larger assemblage, is not likely to be successful.

8.4.2. Discussion of the effect of high pH taphonomic change on bone refit analysis

The gross taphonomic changes observed in the fragmented bone samples for samples from high pH conditions are described in section 7.2.2. The loss of collagen from the bone progressed initially from the outside of the bone inwards with the lipid rich marrow protecting the inner surface of the bone samples until the second period of exposure, when hydrolysis of the lipid in the marrow allowed access to the internal bone surface by the sodium hydroxide. The resultant fracture surfaces had mixed qualities, with higher opacity white bone at the margins of the fracture surface and more translucent pink bone at the centre of the fracture surface.

During the first two periods of exposure the fracture surfaces exhibited variable optical properties across the thickness of the cortical bone exposed on the fracture surfaces (section 7.2.2.1). The variation in optical properties (opacity and colour) resulted in 3D digital models that displayed greater levels of noise

and point position uncertainty induced by the interaction of these variables (section 7.4.2). The reduced quality of the digitised fracture surfaces, therefore resulted in a wider variation and greater range of mean surface refit distances (figures 7.64 and 7.65).

Following the second period of exposure the breakdown in the marrow allowed access of the high pH solution to the medullary cavity resulting in high pH taphonomic alteration to the inner cortical surface of the bone samples (section 7.2.2.1). This resulted in a reduction in the variation of colour and opacity across the cortical thickness exposed during fragmentation, with a consequent improvement in digitisation quality. By the third exposure period the variation in the optical properties of the fracture surface had been minimised and this was reflected in the improved quality refit distances seen in figure 7.64 and in figures 8.24 and 8.25.

These varied optical properties had the greatest impact on the laser scan models due to the previously documented effects of edge noise and single wavelength susceptibility to lower opacities (section 8.1.2). This was reflected in the reduced quality of the laser scan models in comparison to structured light, which was less susceptible to these factors due to the full spectrum light source and inherent filtering. The increased noise within the laser scan models can be seen in the sharp colour contrasts displayed on the false colour scalar field of refit distances in figure 8.24. The better quality of digital 3D models led to an increase in the quality of refit analysis undertaken from the structured light models, as visualised in figure 8.24, where there is less variation in refit distances compared to the laser scan models.

The macro structured light scanner had a higher intensity of projected light resulting in an increased amount of light reflected from within the less opaque surfaces, producing a model with greater point inaccuracy and therefore higher levels of variation in the refit surfaces for lower opacity bone from the initial exposure periods.

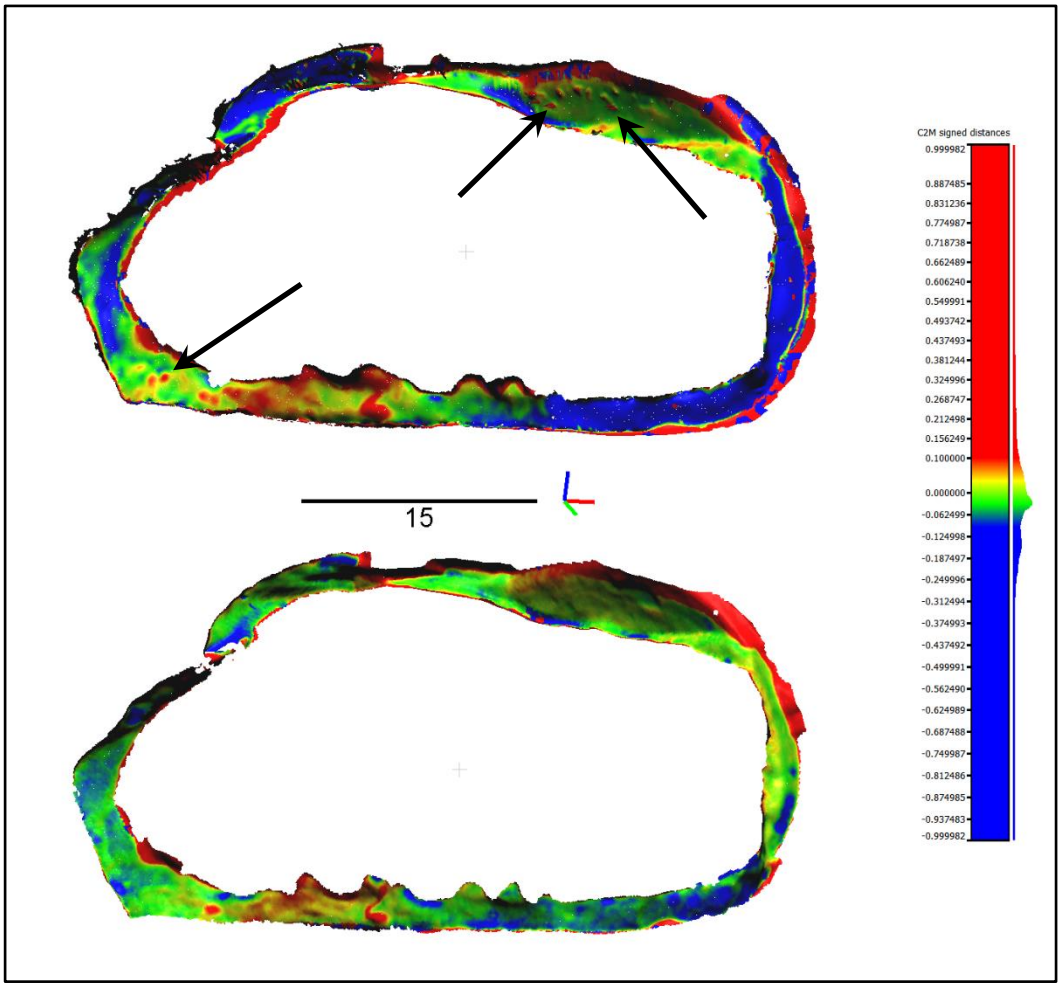

Figure 8.24: False colour scalar field of refit distances applied to the refitting fracture surface of high pH bone sample after the second period of exposure showing the better quality refit in structured light (bottom) compared to laser scanning (top). Greater variation in colour reflects greater variation in refit distance centred on green. Noise is apparent in the laser scan data due to sharp changes in colour (arrowed). Scale in mm (source: author).

The observed variation in optical properties across exposed fracture surfaces was in contrast to the improvement seen in whole bone, which reflected only the surface changes associated with taphonomic high pH exposure (section 07.4.2). This resulted in digitised models for fragmented bone which did not show the improvement in digital quality as rapidly as the whole bone samples. The increase in digitisation quality for fragmented bone after the third exposure period implies that the digitisation response for whole and fragmentary bone should converge as the taphonomic changes extend to the full cortical thickness.

In addition, following the third exposure period the loss of bone collagen and the reduction in the yield strength of the bone samples was indicated in the gross

observation by the change in the shape of the fracture patterns, from curving edges with sharp margins, to flatter fracture profiles with rougher surfaces as the bone fractured across histological structures rather than propagating along them (section 3.6.2). When digitised the rougher surface afforded a larger number of topographical features which aided in surface alignment and therefore improved the quality of the refit process (figure 8.25).

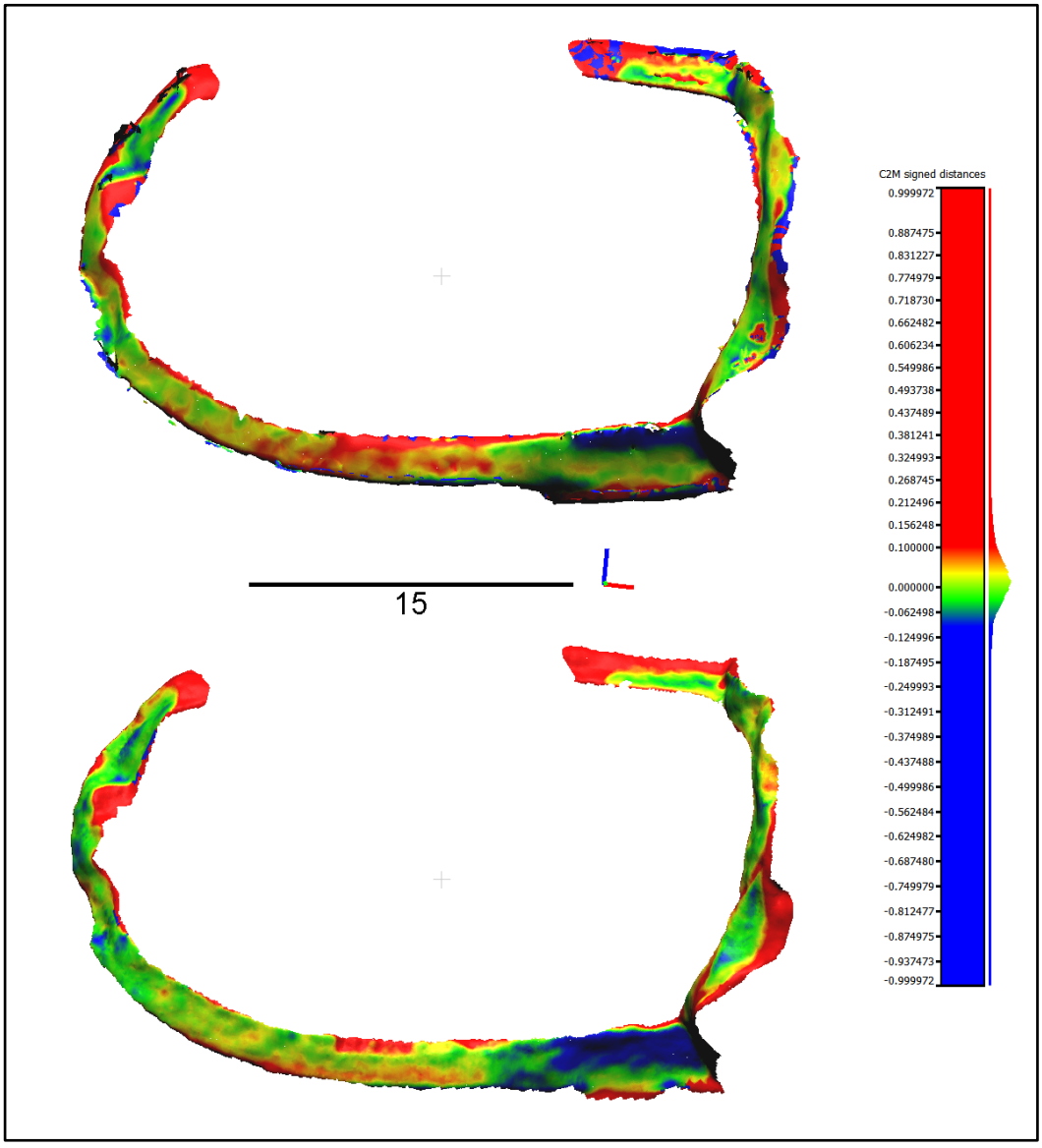

Figure 8.25: False colour scalar field of refit distances applied to the refitting fracture surface of high pH bone sample after the third period of exposure showing the better quality refit in structured light (bottom) compared to laser scanning (top). Greater variation in colour reflects greater variation in refit distance centred on green. Scale in mm (source: author).

The swelling, exfoliation and increase in surface roughness observed in the external surfaces of whole bone (section 7.2.2) were not reflected in the freshly fractured surfaces used in the refit analysis.

The response of photogrammetry to opacity, previously described for the whole bone (section 7.4.2), was reflected in the pattern of reduced quality in the refit data for the first and second exposure periods, where the lower opacity of the inner portions of the cortical bone resulted in a poor quality digital model. This effect was reduced by the third exposure period as bone opacity increased.

The overall quality of refit for photogrammetry models was driven by the lower resolution of the digital models. This resulted from the photo data capture of whole fragments and therefore limited pixel resolution distributed across fracture surfaces. This resulted in lower accuracy of the reconstructed fracture surface as minor topographic variations in the fracture surface were not resolved by the sensor at a pixel level and therefore not reflected in the reconstructed 3D mesh. The requirement for greater user intervention in the reconstruction of fragmentary bone photogrammetry models with poor tie point alignment, introduced subjective selection of points which further reduced the dimensional accuracy of the models and hence the lower refit quality (figure 8.26).

Consistent with the results for the digitisation of whole bone samples, structured light produced the best quality models for the taphonomic changes observed in the high pH experiment. This resulted in structured light yielding the best refit results. Laser scanning and macro structured light 3D models also resulted in successful refit analysis although at lower quality levels than structured light. Photogrammetry resulted in a significantly poorer refit due to the inherent introduction of dimensional errors from the model reconstruction process. The quality of refit improved for all techniques as the opacity of the samples increased throughout the experiment.

This analysis indicates that samples exposed to high pH conditions over archaeological timescales have potential for successful digital refit. This reflects the limited number of manual refit studies undertaken on bone from

archaeological sites in alkaline burial conditions (e.g. Morin et al. 2005, Rosell et al. 2012).

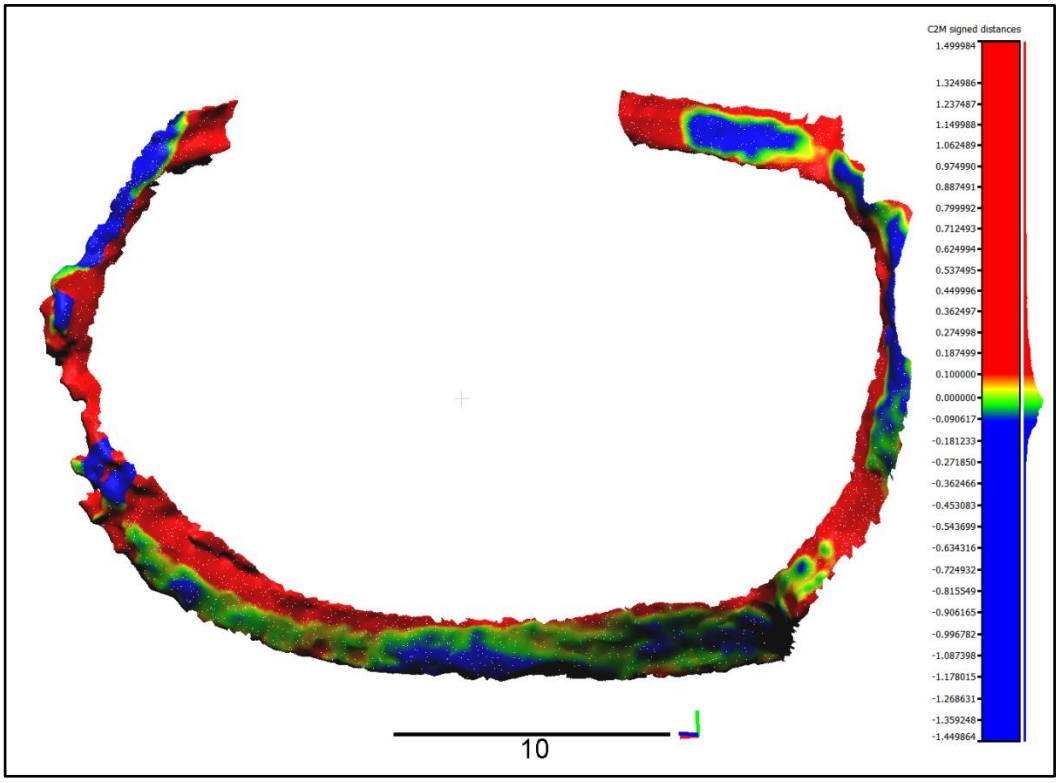

Figure 8.26: False colour scalar field of refit distances applied to the refitting fracture surface of high pH bone sample produced through photogrammetric reconstruction after the third period of exposure showing the lower quality refit in photogrammetry models. Greater variation in colour reflects greater variation in refit distance centred on green. Scale in mm (source:author).

8.4.3. Discussion of the effect of high UV exposure taphonomic change on bone refit analysis

The gross taphonomic changes observed in the high UV fragmented bone samples are described in section 7.2.3.1. The limited gross physical alteration to the structure of the bone led to fracture properties for both periods of exposure that were largely unaltered from that of green bone (section 3.6.3) (Currey 2006).

During both periods of exposure the fracture surfaces exhibited variable optical properties across the thickness of the cortical bone exposed on the fracture surfaces (section 7.2.3.1). However, the increase in opacity was limited to the outer margins of the fracture surface corresponding with the photodegradation of the outer most layers of the cortical bone surface. The extent of change in

opacity over the timescale of the high UV experiment was not sufficient to result in increased opacity across the full thickness of the cortical bone and therefore the general improvement in digitisation associated with increased opacity (section 8.3.3) was not seen for fragmented bone within the timescale of the experiment. The macro structured light scans of the fracture surfaces illustrate the variation in opacity and colour across the thickness of the bone cortex (figure 8.27) where the higher resolution and the greater intensity of the light in the scanning volume make macro structured light more sensitive to changes in colour and opacity.

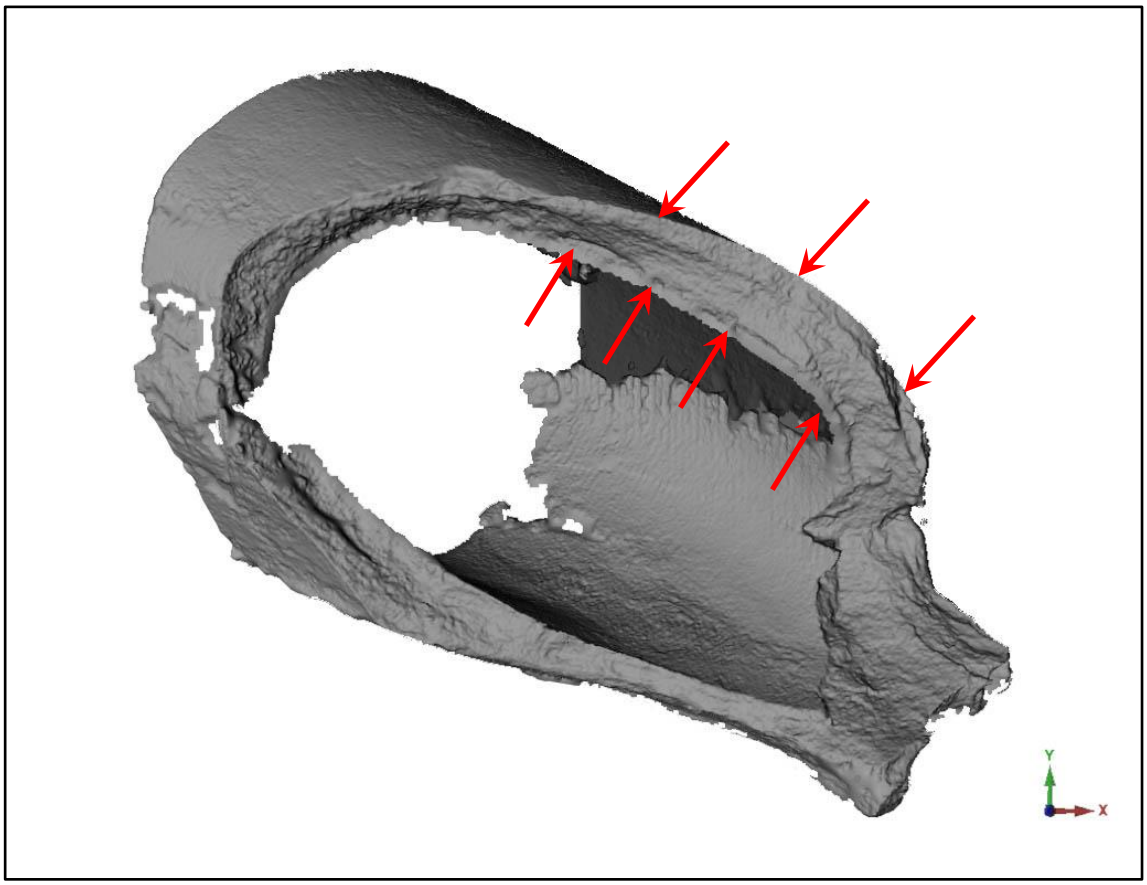

Figure 8.27: 3D model of high UV taphonomically-altered bone fragment macro structured light scanned after the first period of exposure showing banding of response on the fracture surface due to variable bands of opacity (arrowed) seen in figure 7.32(source: author).

The variation in optical properties (opacity and colour) resulted in digitisation models that displayed greater levels of noise and point position uncertainty across all techniques, induced by the interaction of these variables (section 7.4.3). The reduced quality of the digitised fracture surfaces, therefore resulted in a wider variation and greater range of mean surface refit distances (figures

7.69 and 7.70). These effects mirror those initially seen in the high pH fracture surfaces (section 7.5.2), although the cause of the increased taphonomic opacity differs.

These varied optical properties had the greatest impact on the quality of the laser scan models due to the known effects of edge noise and single wavelength susceptibility to lower opacities (section 8.1.2). This was reflected in the reduced quality of the laser scan data in comparison to structured light and macro structured light, which were less susceptible to these factors due to the full spectrum light source and inherent filtering reflected in the low noise data (figure 7.72).

The quality of refit for photogrammetry models was driven by the lower resolution of the instrument and therefore the fewer number of pixels recording the narrow fracture surfaces. The taphonomic alteration to the bone exhibited in the fracture surfaces further limited the identification of image features within the surfaces and therefore led to poor tie point alignment. The poor expression of the fracture surfaces within the digital models consequently led to fewer topographical features to aid the refit.

8.4.4. Discussion of the effect of field weathering taphonomic change on bone refit analysis

The gross taphonomic changes observed in the field weathered fragmented bone samples are described in section 7.2.4. The fragmentation of the bone samples produced fracture surfaces that exhibited increasing opacity and loss of the organic content over the two exposure periods. After the first exposure period the loss of collagen and bone lipid had not extended across the full thickness of the cortical bone.

After the second exposure period the loss of collagen and lipid had progressed and the fracture surfaces of the bone samples exhibited brittle fractures with straighter fracture paths. These produced fracture surfaces with a diffuse appearance, greater surface roughness and opacity than those fractured after the first period of weathering (section 3.6.3.2).

At both exposure periods the fragmented bone samples exhibited significantly increased opacity (section 7.3.1) and surface roughness compared to pre-exposure bone. As evidenced in the whole bone samples, this resulted in good digitisation response from all techniques (figure 8.28). Despite the internal surface of the bone still displaying some translucency, taphonomic alteration of the opacity had progressed sufficiently to produce the increased digitisation quality over the pre-exposure samples seen in figure 7.77. These changes resulted in a reduction in the mean refit distance (figure 7.74) compared to pre-exposure samples and an overall increase in the quality of the refit as shown by the increase in the percentage of the refit surface within +/- 0.1 mm (figure 7.77).

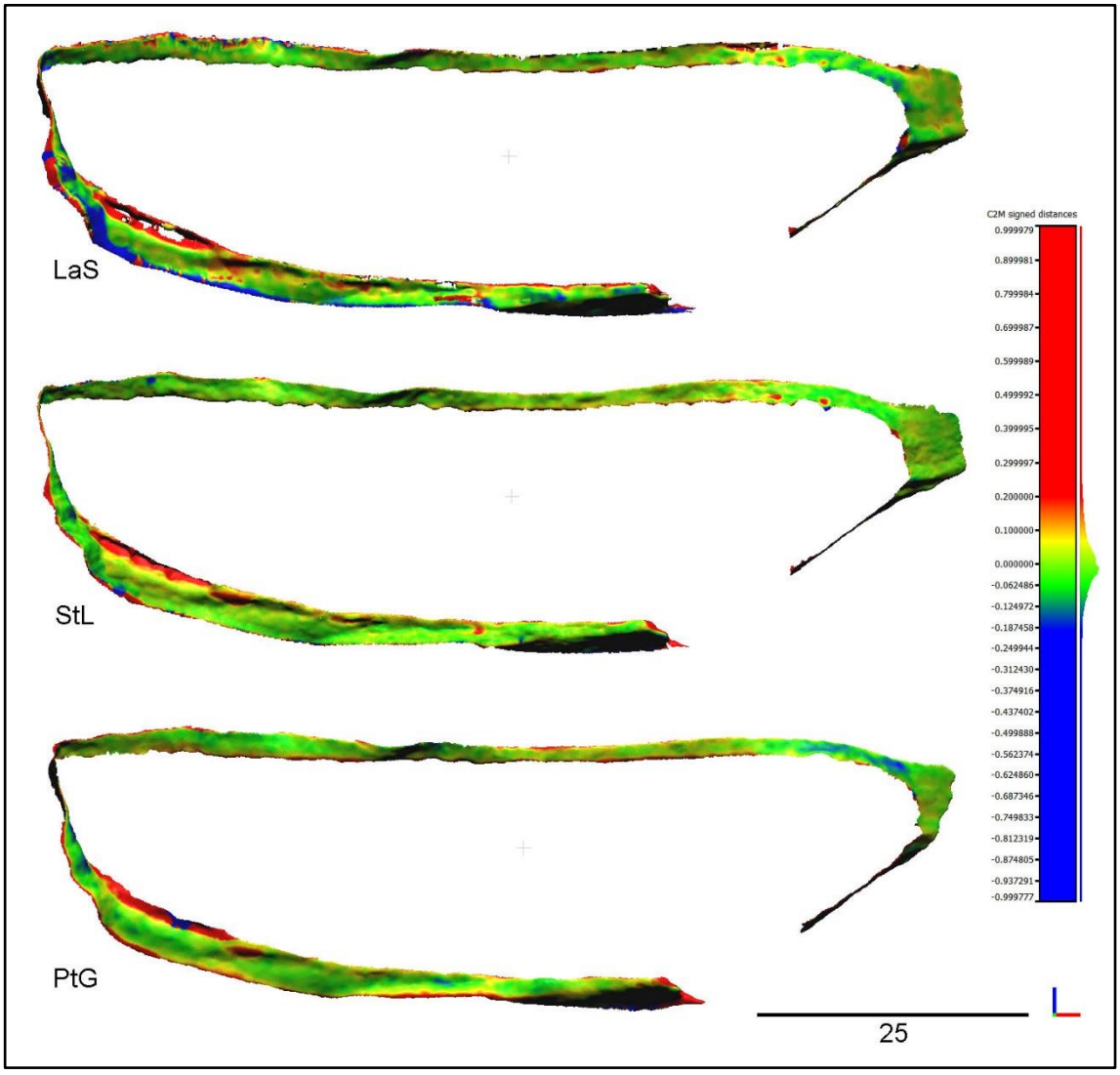

Figure 8.28: False colour scalar field of refit distances applied to the refitting fracture surface of field weathered bone samples after the first period of exposure showing the high quality refits for laser scanning (top), structured light (middle) and photogrammetry (bottom). The slightly elevated levels of edge

noise in laser scanning compared to the other techniques is apparent in the red speckling around the margins of the fracture surface. Greater variation in colour reflects greater variation in refit distance centred on green. Scale in mm (source: author).

The penetration of the taphonomic change across the cortical thickness for the second period of exposure led to consistent fracture surface characteristics which reduced the variability in digitisation quality across the fracture surface. There was therefore a consequent increase in the quality of the digital refit compared to the first period of exposure across all three techniques (figure 8.29).

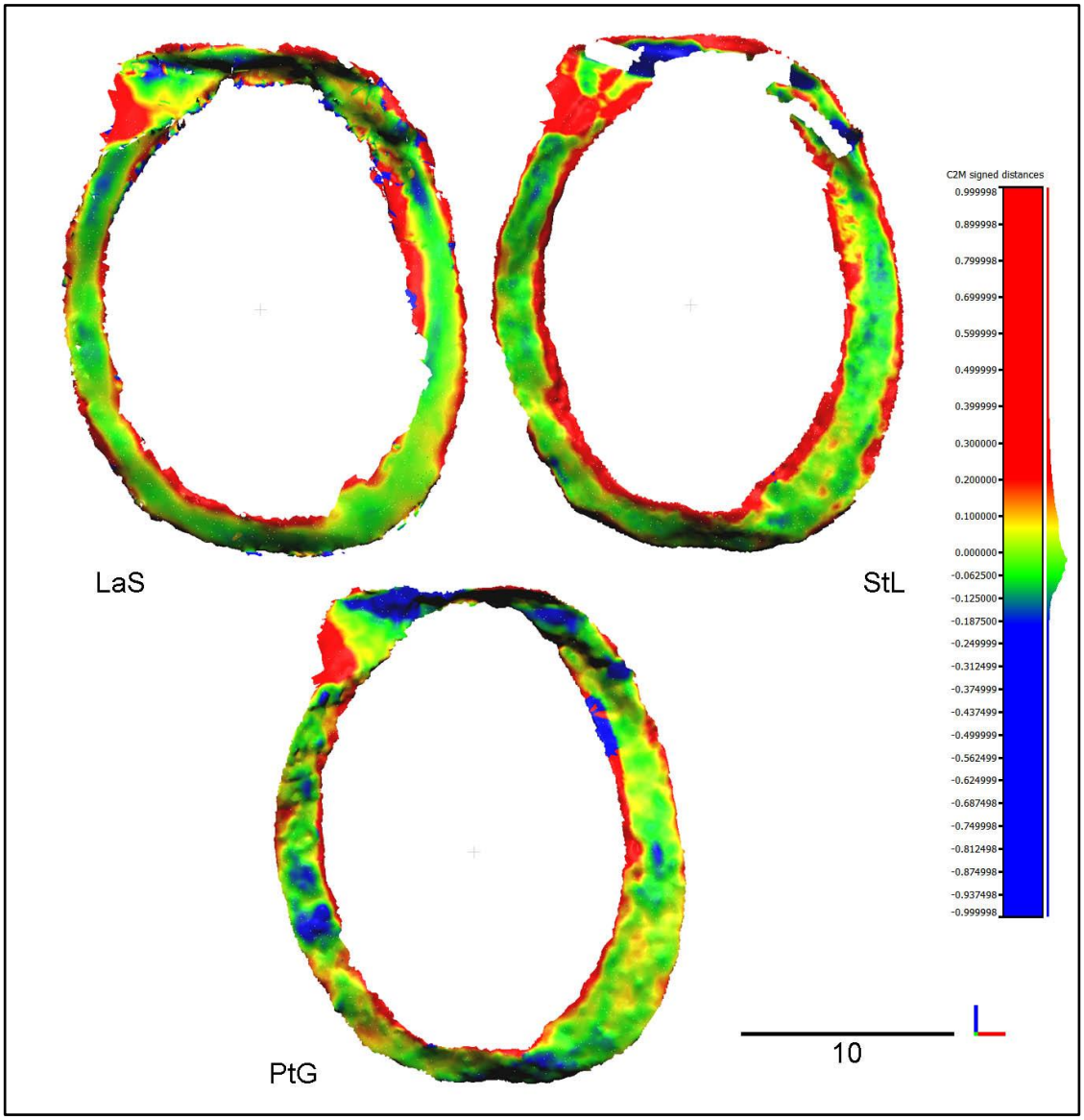

Figure 8.29: False colour scalar field of refit distances applied to the refitting fracture surface of field weathered bone samples after the second period of exposure showing the high quality refits for laser scanning (top left), structured light (top right) and photogrammetry (bottom). Greater variation in colour

reflects greater variation in refit distance centred on green. Scale in mm (source: author).

In contrast to the photogrammetry results associated with other taphonomic experiments, the field weathering results for photogrammetry were comparable to the other digitisation techniques. The improved digitisation response can be attributed to the increased surface roughness, which provided more surface features that could be used as tie points within the reconstruction (section 4.3.3.2) low specular response and increased opacity (section 7.3.1). Additionally, the opaque fracture surface eliminated the identification of sub-surface colour changes as tie points. Finally, the diffuse appearance of the weathered bone had a low specular response, eliminating white highlights in the photogrammetric imagery that would otherwise be incorrectly identified as tie points (section 4.3.3.3).

The field weathered bone produced high quality refits for all three techniques. The high opacity and lighter colours on the fracture surfaces were conducive to accurate data collection and hence high quality 3D models. The loss of bone collagen from the cortical bone resulted in brittle fractures without post-yield plastic deformation and distortions. These brittle properties also resulted in bone fracture across histological structures (e.g. osteons) producing a varied fracture surface with good topographical variation that aided alignment of the refitting surfaces. This analysis indicates that samples exposed to shorter duration surface weathering conditions have potential for successful digital refit. These timescales are comparable to those seen in forensic archaeology (Cunningham et al. 2011, Wilson-Taylor 2012, Junod & Pokines 2013) and digital refit would therefore be appropriate to the analysis of fragmentary skeletal material from these contexts.

8.4.5. Discussion of the archaeological and palaeontological sample refit results

The refit analysis results from the archaeological and palaeontological samples showed a range of responses, from the poor quality and low refit success of the Star Carr samples with only two refits out of nine, to the Kenya samples, which produced higher quality models and the best refitting results of the research with a maximum value of 91.22% of the surface area between two samples refitting within +/-0.1mm.

The Kenya and Schöningen 13 II-4 samples were both deposited in alkaline anoxic silt conditions which promoted fossilisation. The results for these samples should therefore be comparable. The taphonomic histories of the samples differ in the point at which the samples were fractured; the fractured surfaces, and the refit quality should therefore reflect these taphonomic histories.

Voormolen (2008a, 2008b) and Van Kolfschoten et al. (2015) have identified that the Schöningen 13 II-4 samples were intentionally fragmented to extract marrow from the bones and therefore the fragmentation occurred at or around the point that the animals were killed. Their rapid incorporation into the alkaline silts resulted in alkaline taphonomic alteration to the fracture surfaces in burial conditions that aided their fossilisation (section 3.5) (Serengeli et al. 2015, Kuitems et al. 2015).

By contrast the Kenya samples exhibited fracture surfaces that occurred in the burial environment and during the erosion and weathering of the samples from the palaeontological deposits. The fracture of these samples was therefore a natural taphonomic process rather than an anthropogenic one and occurred to already fossilised bone. The difference between these taphonomic histories is expressed in the refit data where the Schöningen samples have poorer mean refit distances and greater variance within the surface to surface refit distances.

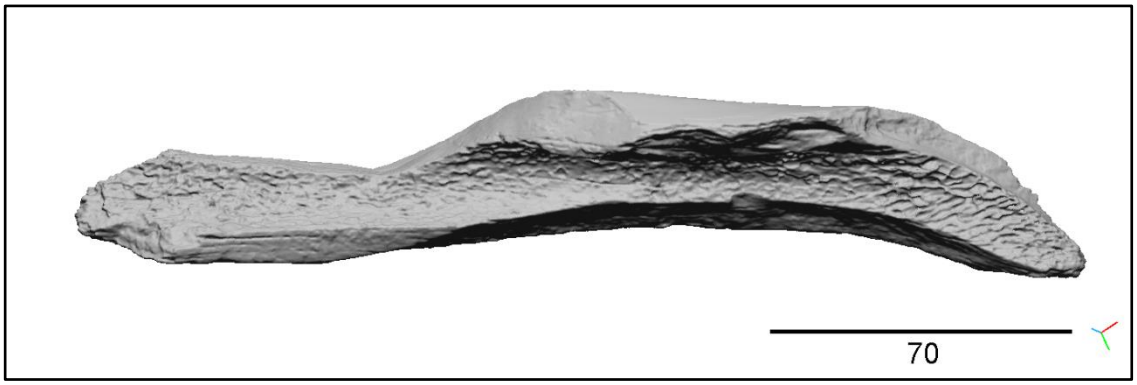

Figure 8.30: 3D macro structured light model of Schöningen bone sample showing curved fracture surfaces resulting from fragmentation of the bone whilst it was still fresh. Scale in mm. (source: author).

The fragmentation of the Schöningen material occurred whilst the bones were still fresh and this can be seen in the curving smooth fracture surfaces of the samples (figure 8.30). The morphology of these fracture surfaces are similar to those seen in the high UV experiment and all of the pre-exposure fractured samples (section 7.2.3).

The fracture of fresh bone can result in distortion of the fracture surface at the point of fracture as the stress on the bone exceeds the yield strength and the bone deforms plastically prior to fracture (section 3.6.2) (Currey 2006). The robust nature of the equine bones required the application of a fast loading of stress to the bone in order to fracture the bone to access the marrow. As discussed in section 3.6.2, bones that are loaded at a higher rate have reduced post-yield areas and therefore undergo lower levels of distortion (Hansen et al. 2008, Ural et al. 2011). The samples from Schöningen were therefore expected to display less distortion during fracturing than the experimental samples which are less robust elements with thinner cortical thicknesses.

Whilst the lower distortion and wider fracture surfaces would be expected to yield an improved digital refit, the fracture surfaces were exposed to the burial environment from initial deposition and therefore taphonomic change will have taken place directly to the fracture surfaces as well as the outer cortical bone. The post deposition transportation in the wetland environment of Schöningen resulted in the wide distribution of corresponding bone fragments (van Kolfschoten 2012, 2014, García-Moreno et al. 2015) and therefore the refitting fracture surfaces were subject to different degrees of taphonomic change. This

results in surface level changes to the fracture surfaces which impacted the quality of the refit.

The outer cortical surface of the Schöningen samples exhibited taphonomic change similar to that seen in the high pH experimental samples, including cracking and exfoliation (figure 8.31).

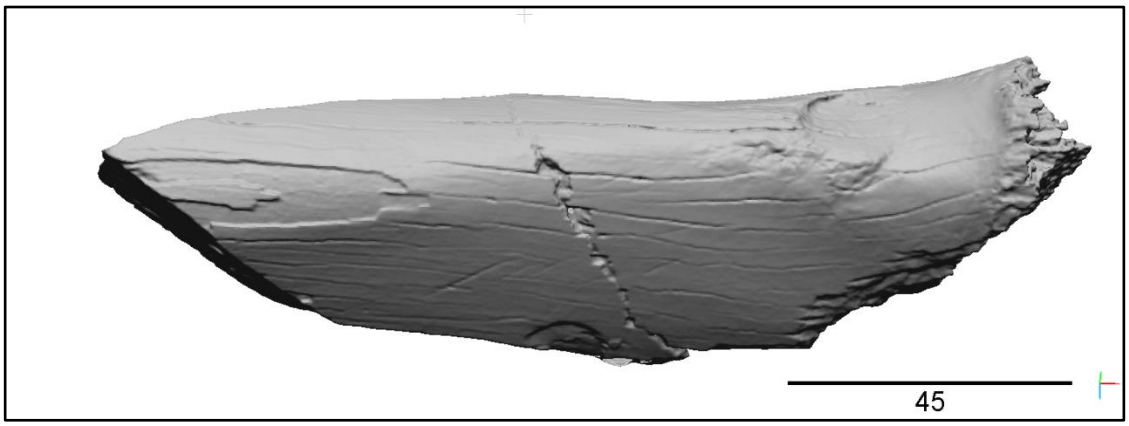

Figure 8.31: 3D macro strucutured light model of Schöningen bone sample showing cracking and exfoliation to the outer cortical bone surface similar to the changes seen in the high pH experimental samples. Scale in mm (source: author).

The Schöningen samples exhibited refit results that were comparable to the first two periods of exposure in the high pH experimental samples showing similar results for refit distance, variance and the percentage of the refit surface within +/- 0.1 mm.

The samples from Kenya demonstrated high levels of refit. The taphonomic change from the initial burial environment resulted in levels of surface exfoliation and cracking similar to that seen in the Schöningen samples (figure 8.32) and the high pH experimental samples. There was an overall loss of a larger proportion of the outer cortical surface of the bone within the samples, which was anticipated given the greater age of the Upper Burgi Member deposits in Kenya compared to the deposits at Schöningen (Sierralta et al. 2012, Urban & Sierralta 2012).

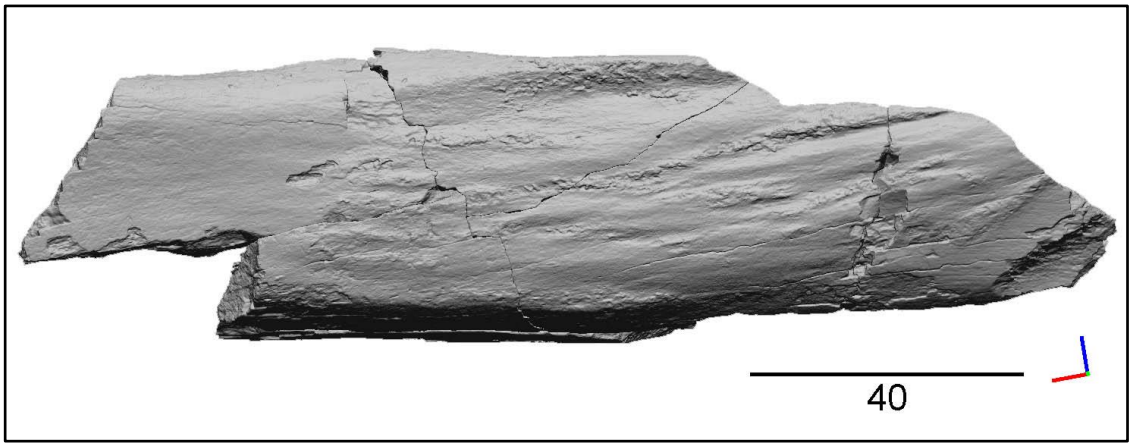

Figure 8.32: Refitting 3D macrostructured light models of six fragments of sample K0006 from Kenya showing similar levels of taphonomic damage to the outer cortical bone to the Schöningen samples (figure 8.31). Scale in mm (source: author).

The fragmentation of the samples from Kenya occurred after fossilisation, within the burial environment or once the samples were weathered out of their deposits. The fracture characteristics of these samples mirror those of brittle material, such as dry bone, with straight fracture paths in contrast to the curved surfaces of the Schöningen samples (figure 8.33). The fracture margins of many of the samples were observed to be eroded and rounded suggesting that the fractures follow the lines of surface cracks that developed in the early diagenesis of the samples prior to their fossilisation.

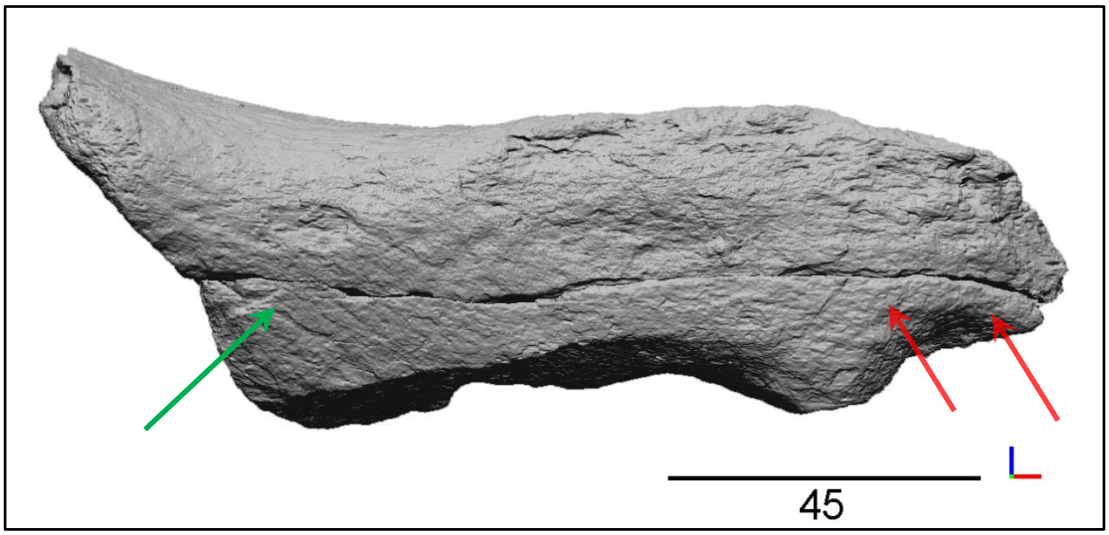

Figure 8.33: Refitting 3D macro structured light models of the two fragments of K0001 from Kenya showing the rounding of the margins of the fracture surface on the right hand side of the image (red arrows). The fracture margins on the left (green arrow) are sharper indicating that the erosion of the margins did not occur post-fragmentation. Scale in mm (source: author).

Whilst the weathering out of the samples onto the surface exposed the samples to surface weathering, these effects would have been limited in lithified fossil bone compared to the surface weathered experimental samples. The fracture of the Kenya samples after fossilisation resulted in fracture surfaces that were therefore not subject to significant further taphonomic change, resulting in corresponding fractures surfaces which closely mirrored each other. This explains the very high quality of digital refit in the Kenya samples with very close refit distances, low refit distance variance and a high percentage of the refit surface that was within +/- 0.1 mm.

The refit analysis of the archaeological samples from Star Carr demonstrated very poor response. Only two of the nine samples could be refitted and the analysis data associated with these refits have refit distances and variances that are too poor to be viewed as reliable.

The taphonomic change from the acidic peat burial environment resulted in dark stained samples which were flexible with poorly defined fracture surfaces. The samples were digitised when wet and this added a translucent refracting layer, adding further noise to the digitisation process (figure 4.16). The flexibility of the samples was similar to that of the low pH samples when wet although the humic acid staining and recrystalisation of minerals was expected to have increased the opacity of the Star Carr samples. Prior to digitisation manual refit was attempted and whilst a match could be visualised, the soft condition of the samples and their fragile, pre-conservation state precluded a close match.

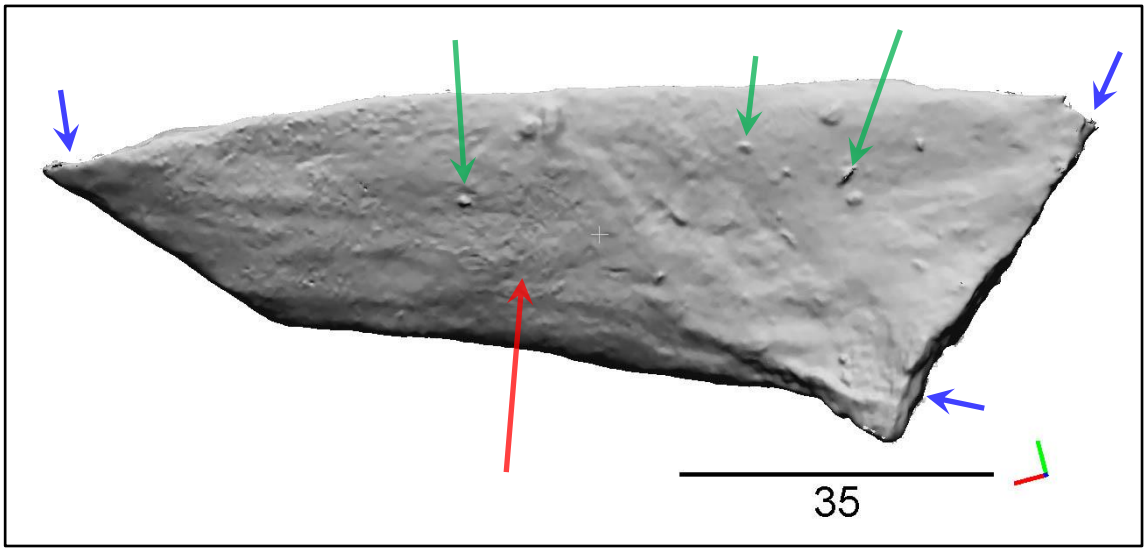

Figure 8.34: 3D laser scanned model of a Star Carr sample showing poor surface quality. Surface variation is not uniform due to the use of water to hydrate the samples during scanning (red arrows) and there are large noise spikes in the data (green arrows) as well as edge noise (blue arrows). Scale in mm (source: author).

The 3D digitised models of the sample fragments illustrate the eroded margins of fracture surfaces were rounded and poorly defined resulting in lower refit potential (figure 8.35).

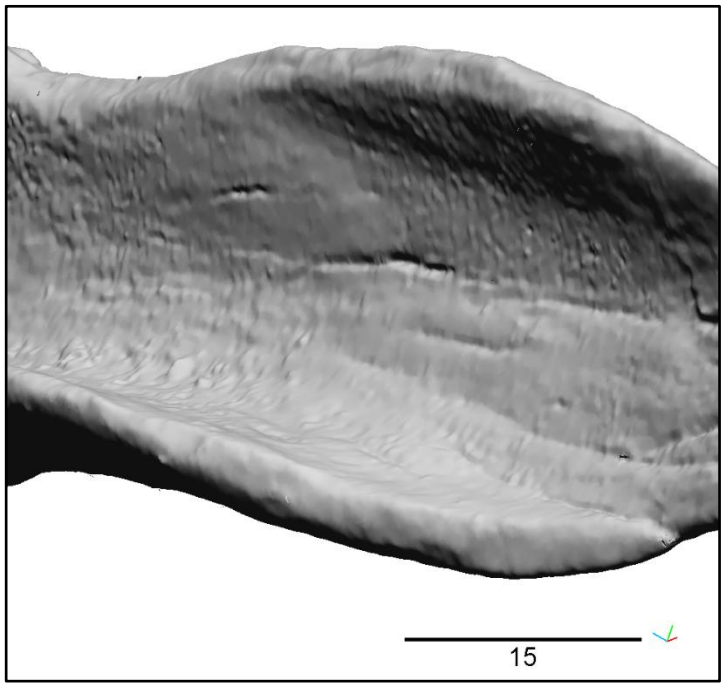

Figure 8.35: 3D laser scanned model of a Star Carr sample showing rounded fracture surfaces. Scale in mm (source: author).

The distortion and flexibility of the samples was apparent during the initial alignment of the digital refit process and corresponding surfaces, identified in the manual refit, were distorted at differing angles making digital refit unfeasible for most samples.

The alignment of fragments could be approximated digitally to produce a visualisation of the original artefact however, mathematical refit and therefore any subsequent quantitative analysis was not possible due to the taphonomic changes to the samples. A general visualisation of the Star Carr fragments was carried out using the digitised models and used to illustrate research into the ritual use of the material (Milner et al. 2016). Therefore whilst digitisation remains an useful illustrative technique in cultural heritage formats (e.g. museums), the digital refit analysis of taphonomically-altered samples from low pH anoxic environments is of limited value.

Digital refit of fossilised bone is a valuable technique to be utilised in further research allowing reconstruction of fragmentary material to facilitate further analysis. The taphonomic conditions that facilitate fossilisation also provide the long term preservation required to produce good digital refit. The Schöningen samples showed refit analysis still provided useful results from fracture surfaces that had undergone taphonomic change in the burial environment. Additionally the comparison with the Kenya samples showed that taphonomic information could be determined from the refit data. The Kenya samples illustrate digital refit is highly suited to fossilised material and particularly where fractures occur post-fossilisation. The quality of the data for both sets of palaeontological samples suggests the potential for automated refit.

Chapter 9. Conclusions and further research

9.1. Summary

This research aimed to examine the effect of taphonomic changes to mammalian bone on the outcome of 3D digital recording methods and the digital refit of fragmentary bone. To achieve this aim, current levels of understanding and methods were critically reviewed for the structure and properties of mammalian bone, taphonomy of bone, digitisation techniques and influences on data quality.

A series of technique comparison standards were created to elucidate the response of multiple 3D digitisation techniques to variations in the colour, opacity and surface roughness properties of bone. The use of standards allowed a comparison of these factors within each technique to be considered against a common baseline.

Experimental work then sought to simulate taphonomic changes to mammalian bone through the use of natural field based surface weathering and laboratory-based accelerated testing in a range of taphonomic conditions. These experimental samples were digitised using multiple techniques and an assessment of the effects of each of the taphonomic changes on the quality of 3D digitised models was undertaken with reference to the predicted results based on the technique comparison standards. This approach was adopted to also examine fragmentary bone samples after each period of exposure.

The 3D digitised models of the fragmentary experimental bone samples were subject to digital refit analysis. The quality of the digital refits were critically examined in relation to the taphonomic change with further reference to the technique comparison standards. The response between different techniques for each taphonomic experiment was compared with reference to the quality of digital refit. Archaeological and palaeontological fragmentary samples were digitised and the subject to digital refit analysis; the results of these analyses were compared to the experimental refit results to assess whether evidence of taphonomic change observed in the experimental samples could be identified.

9.2. Research evaluation

Evaluation of the research can be carried out in terms of the project objectives in section 1.2. The objectives of this research are to:

Survey existing literature and manufacturers documentation for differing 3D digital recording techniques and assess their potential for recording degraded mammalian bone.

This was achieved by the critical literature reviews in chapters two, three and four, which provided the necessary background knowledge for subsequent research.

Create technique comparison standards to assess the response of 3D digitisation techniques to the colour, opacity and surface roughness properties of objects.

A series of defined measurable standards were created which varied the component being considered. These standards allowed the baseline response of each technique to be assessed in isolation from other variables. This allowed the effect of each variable to be quantified in terms of each techniques response to the factor under consideration and allowed development of a model of response to be formulated based on the physical properties of the target samples and the critical literature review. The development of these models provided information that could be used for comparison with the experimental, archaeological and palaeontological samples.

The standards could not be used for the assessment of photogrammetry as this technique relies on variation in the surface of the target object to provide feature points to be identified in multiple images which are used to calculate the 3D positions of these points. The technique comparison standards by their nature of excluding variables meant that photogrammetric reconstruction could not be achieved. Further work is required to develop suitable standards for photogrammetry to quantify the impact of the variables considered by the technique comparison standards.

Colour. The colour technique comparison standards provided useful and appropriate data with regard to the techniques response to variation in colour wavelength and surface colour lightness. The lack of direct colour measurement of the target patches meant that an element of simplification was required to compare the results and further work would benefit from the use of spectrophotometry measurement of the specific colour values during further development of the colour standards.

The technique comparison standards demonstrate that structured light techniques do not respond to black due to lack of contrast in the phase pattern; this also results in a poorer response in darker colours. Lighter colours all gave greater contrast to both the phase pattern and the laser line and therefore produced the best responses in both techniques.

Instruments that use a single wavelength light source do not provide a good response to the correlating colour due to absorption, and therefore the colour of the digitisation target object in relation to the instrument light source must be considered when selecting appropriate digitisation techniques. The red wavelength of the laser scanner was predicted to be appropriate for bone digitisation as except in rare taphonomic conditions, bone does not exhibit a significant blue component.

Opacity. The opacity technique comparison standards provided useful and appropriate data with regard to the techniques response to variation in the opacity of digitised surfaces.

Lower opacity materials adversely affected all the techniques through a digitised response that recorded a greater level of surface variation than exhibited in the physical surface due to sub-surface scattering and reflection of light; laser scanning was the most susceptible due to the exacerbation of edge noise through sub-surface scattering and reflections.

Both techniques displayed lower volume and poorer dimensional accuracies at lower opacities and a model of the cause of this variation was developed. Laser

scanning was most affected by opacity due to the greater penetration of the longer wavelength of red light into semi-opaque surfaces.

Surface roughness. The surface roughness technique comparison standards provided useful and appropriate data with regard to the techniques response to variation in the roughness of target surfaces. The manufacturer stated grade of the target samples was not sufficiently accurate and therefore the use of abrasive cloths relied on further measurement with Scanning Electron Microscopy.

All instruments showed a response to surface roughness that corresponded to the instrument precision. The lower level of instrument response was dictated by the instrument resolution and the effects of light scattering and speckle became more pronounced at smaller surface roughness. Laser scanning was more susceptible to speckle noise from these diffuse surfaces.

Use accelerated laboratory degradation and natural field-based exposure methods to simulate taphonomic change to mammalian bone.

The four simulated taphonomic condition experiments demonstrated observable and measureable taphonomic changes to the bone samples consistent with those predicted from critical literature review. The timescale of the research required the assessment of extremes of taphonomic conditions to produce measurable change. The further research would benefit from examining more nuanced variations within these taphonomic conditions over longer timescales, however the research has provided a framework within which this further research can be designed.

Assess the impact of the taphonomically induced changes to bone on the quality of 3D digitisation techniques.

The assessment of taphonomic change, considered through observation and the 3D models:

Low pH. Taphonomic change resulting from loss of bone mineral resulted in shrinkage of the samples and distortion of their morphology. This was coupled with a decrease in opacity which, as the technique comparison standards had demonstrated, resulted in a consequent decrease in the quality of the 3D models.

High pH. The loss of bone collagen and bone lipid resulted in an increase in opacity. The hydrolysis of the collagen led to swelling of the bone producing cracking and exfoliation of the surface with a consequent loss of volume. The loss of bone from the surface and the development of small cracks in the surface produced greater surface roughness and a more diffuse surface. The increased opacity and lighter coloured surface generally resulted in better quality 3D models although the effects of increased surface roughness resulted in greater noise in the 3D data.

High UV exposure. The high UV exposure demonstrated a limited increase in opacity as a result of photodegradation and a reduction in the surface specularity through the loss of bone lipid. Photodegradation also produced an initial increase in the colour variation on the surface of the bone followed by a decrease as bleaching occurred. These factors resulted in an increase in digitisation quality over the pre-exposure bone.

Field Weathering. The field weathering exposure resulted in an increased opacity, surface roughness and cracking as a results of freeze-thaw and wet-dry cycles. An initial increase in the colour variation on the surface of the samples was observed due to black fungal staining, although this reduced and bleaching of the samples occurred after the surface cartilage had been lost. These resulted in the best 3D digitisation response from all techniques.

Carry out a comparison of 3D digitisation techniques by recording the same experimentally degraded bone samples with each technique and comparing their response.

The 3D digitisation techniques were compared through consideration of the quality of the 3D models created for each of the experimental samples.

Laser scanning was most susceptible to lower opacities due to its use of a single wavelength light source and the penetration of the longer red wavelength. Edge noise was a significant quality factor in the 3D models and this was further exacerbated by lower opacities and the expression of this edge noise within the mesh surface of the models.

Structured light methods benefitted from the broad spectrum light source and the inherent level of filtering of outlier point positions through the use of multiple phase patterns with a resulting consistency of low noise responses. Structured light produced good quality models for each of the experimental conditions, with the exception of low pH where the much lower opacities were sufficient to be reflected in the quality of the data.

Photogrammetry produced poor quality models for all the experiments with the exception of field weathering. The technique was susceptible to lower opacities where sub-surface colour variations affected tie point calculations, although at higher opacities where this effect was removed, the lower surface colour variation also resulted in poor feature identification. Photogrammetry required a larger amount of user time and input in the creation of the models and introduced subjective selection and removal of tie points which limits the use of the models for quantitative analysis.

For low pH conditions all three techniques produced poor quality models that can are of limited use for quantitative analysis but may have value as illustrative aids. In high pH conditions the effects of edge noise from surface swelling and exfoliation adversely affected the laser scanning quality despite the increase in opacity. Structured light provided the best quality models and would be the most appropriate technique for samples from these conditions.

As with the low pH experimental samples, those exposed to high UV conditions also displayed evidence of the effects of lower opacity. The degree of lower opacity meant these effects were limited in structured light although they remained a significant factor in laser scanning and photogrammetry techniques.

All three techniques produced good quality models for the field weathering experiment. The effects of high opacity and reduced colour variation resulted in the improvements predicted by the technique comparison standards. In addition

the increase in surface roughness within the field weathering samples did not display the surface flakes seen in the high pH conditions leading to better edge noise response in the laser scan models.

Examine the impact of taphonomic changes on the digital refitting of fractured experimentally degraded bone samples and compare it to similar fragmentary material from archaeological and palaeontological examples.

The effects of taphonomic change on the whole bone samples was reflected in the fragmentary samples subject to digital refit. The quality of the digital refit was closely related to the quality of the 3D digital models which provided surfaces for the matching of points.

The digital refit of fragmentary samples was most effective for the field weathered samples where the loss of collagen within the cortical bone resulted in brittle fracture of the bone and coupled with the taphonomic change resulting in higher opacity, low colour variation and diffuse surface roughness, produced conditions conducive to good 3D digital models and topographical variation within the fracture surfaces. This resulted in high levels of matching between corresponding fracture surfaces and hence good digital refit quality.

High UV and high pH samples demonstrated that digital refitting holds some potential as an analysis tool, although the taphonomic changes restricted the quality of the digital models.

The very poor digitisation response of the low pH samples allied with the significant dimensional distortions at a gross level limit the potential of digital refit for samples from these conditions. This was reflected in the poor quality results for the Star Carr archaeological samples.

The analysis of palaeontological samples from Kenya and Schöningen demonstrated good digital refit and the taphonomic conditions prior to fossilisation contributed to surface properties conducive to good quality digital models. The taphonomic conditions that promote long term survival of bone and its fossilisation also provide the greatest potential for digital refit.

The different taphonomic histories of the samples from Kenya and Schöningen demonstrated that fracture post-fossilisation was likely to lead to high levels of digital refit quality due to the reduced potential for taphonomic alteration to the fracture surface.

9.3. Further work

The research has demonstrated that production of 3D digital models from taphonomically-altered bone can provide useable quantitative and qualitative data. Whilst there are challenges to the production of models and the subsequent implications for digital refit further research can lead to further improvements and mitigation of these factors. Areas of potential further research are outlined below.

As highlighted in the research evaluation there is potential for development of the experimental methodology to encompass the creation of technique comparison standards for photogrammetry and the assessment of subtle variations in taphonomic conditions over longer timescales. The field weathering and high UV experiments identified that the effects of photodegradation are complex and the existing published literature contains little research into the quantification of these changes. The data from the field weathering site identified freeze-thaw events, however the effect on surface characteristics of the samples cannot be isolated and the effect on 3D digital models determined. Whilst the timescales in this research reflect those seen in forensic surface weathering cases all of the changes observed remained within weathering stages 0 and 1. The application of this research to archaeological and palaeontological samples would benefit from consideration of longer time periods with greater variety of sample weathering.

The identification of corresponding features on fracture surfaces is likely to be in part driven by the width of the cortical surfaces limiting the number of potential features. The effect of differing cortical bone thickness on fracture surfaces may therefore provide further data for development of models for refit analysis.

The automated refit of fracture surfaces is an ongoing area of research in a variety of archaeological materials. The research in this thesis has identified potential for digital refit to be productive for taphonomies other than low pH conditions. The challenges for automated refit of bone samples include overcoming the time consuming digitisation and post processing of bone samples. Additionally the automation of refit relies on the accurate segmentation of digital models to identify and separate fracture surface and

significant challenges remain to the identification of fracture margins particularly where edge noise is present. Computer algorithms for digital refit are not sufficiently refined to undertake this accurately and further development will be required to realise the benefits of automation over manual refit by an experienced osteoarchaeologist or zooarchaeologist.

The increased adoption of blue light scanners within 3D digitisation requires further examination to provide a comparative baseline to other structured light scanners and digitisation techniques. The influence of the properties of blue light scanners and their interaction with taphonomic changes remains an area yet to be explored.

The potential of macro-photography to improve the resolution of photogrammetric imagery needs further exploration to assess whether this could mitigate the effects of poor feature identification and tie point alignment in photogrammetric models. The potential of near infrared and ultraviolet photogrammetry to overcome opacity in fresh bone and low pH taphonomic altered samples also provides opportunities for further research.

This research has demonstrated that taphonomic conditions have a significant influence on the quality of 3D digital models. It is therefore critically important to understand the taphonomic histories of objects being digitised. This encompasses the deposition environment and subsequent post excavation taphonomy and conservation. At present this data is poorly and inconsistently recorded limiting the effectiveness of 3D digital models for future analysis. Cultural heritage would benefit from the development and adoption of metadata standards to record document and archive this information.

References

3D Systems. (2015) *Geomagic capture: integrated, industrial-grade 3D scanner and software systems*. Rock Hill, South Carolina: 3D Systems.

Abraham, E., Cox, M. and Quincey, D. (2008) Pig-mentation: postmortem iris color change in the eyes of *Sus scrofa*. *Journal of forensic sciences*. **53** (**3**), 626–631.

Acer, N., Usanmaz, M., Tugay, U. and Erteki'n, T. (2007) Estimation of cranial capacity in 17-26 years old university students. *International journal of morphology*. **25** (**1**), 65–70.

Adlam, R. E. and Simmons, T. (2007) The effect of repeated physical disturbance on soft tissue decomposition: are taphonomic studies an accurate reflection of decomposition? *Journal of forensic sciences*. **52** (**5**), 1007–1014.

Aerssens, J., Boonen, S., Lowet, G. and Dequeker, J. (1998) Interspecies differences in bone composition, density, and quality: potential implications for *in vivo* bone research. *Endocrinology*. **139** (**2**), 663–670.

African Fossils. (2016) *African fossils 3D models fossil collection*. http://africanfossils.org/search Accessed August 11, 2016.

Agisoft. (2016) *Agisoft PhotoScan user manual. Professional edition version 1.2*. St. Petersburg: Agisoft LLC.

Ahmadabadian, A. H., Robson, S., Boehm, J., Shortis, M., Wenzel, K. and Fritsch, D. (2013) A comparison of dense matching algorithms for scaled surface reconstruction using stereo camera rigs. *ISPRS journal of photogrammetry and remote sensing*. **78**, 157–167.

Ai-Aql, Z. S., Alagl, A. S., Graves, D. T., Gerstenfeld, L. C. and Einhorn, T. A. (2008) Molecular mechanisms controlling bone formation during fracture healing and distraction osteogenesis. *Journal of dental research*. **87** (**2**), 107–118.

Aiello, L., Wood, B., Key, C. and Wood, C. (1998) Laser scanning and paleoanthropology. In Strasser, E.,Fleagle, J. G.,Rosenberger, A. L. and McHenry, H. M. (editors). *Primate locomotion*. New York: Springer. 223–236.

Akcil, A. and Koldas, S. (2006) Acid Mine Drainage (AMD): causes, treatment and case studies. *Journal of cleaner production*. **14** (**12–13**), 1139–1145.

Albertz, J. and Wiggenhagen, M. (2009) *Taschenbuch zur photogrammetrie und fernerkundung*. 5th edition. Heidelberg: Wichmann Herbert.

Allard, T. T., Sitchon, M. L., Sawatzky, R. and Hoppa, R. D. (2005) Use of hand-held laser scanning and 3D printing for creation of a museum exhibit. In Mudge, M.,Ryan, N. and Scopigno, R. (editors). *Proceedings of the 6th international symposium on virtual reality, archaeology and cultural heritage (VAST 2005)*. 97–101.

Amendt, J., Krettek, R. and Zehner, R. (2004) Forensic entomology. *Die Naturwissenschaften*. **91** (**2**), 51–65.

Andrade, M. G. S., Sá, C. N., Marchionni, A. M. T., de Bittencourt, T. C. B. dos S. C. and Sadigursky, M. (2008) Effects of freezing on bone histological morphology. *Cell and tissue banking*. **9** (**4**), 279–287.

Andrady, A. L., Hamid, S. H., Hu, X. and Torikai, A. (1998) Effects of increased solar ultraviolet radiation on materials. In UNEP (editor). *Environmental effects of ozone depletion: 1998 assessment*. Nairobi: United Nations Environmental Programme. 160–174.

Andrews, P. (1990) *Owls, caves and fossils*. Chicago: University of Chicago Press.

Andrews, P. (1995) Experiments in taphonomy. *Journal of archaeological science*. **22** (**2**), 147–153.

Andrews, P. and Armour-Chelu, M. (1998) Taphonomic observations on a surface bone assemblage in a temperate environment. *Bulletin de la Societe Geologique de France*. **169** (**3**), 433–442.

Andrews, P. and Cook, J. (1985) Natural modifications to bones in a temperate setting. *Man*. **20** (**4**), 675–691.

Andrews, P. and Fernández-Jalvo, Y. (2003) Cannibalism in Britain: taphonomy of the Creswellian (Pleistocene) faunal and human remains from Gough's Cave (Somerset, England). *Bulletin of the Natural History Museum: Geology series*. **58** (**S1**), 59–81.

Andrews, P. and Whybrow, P. (2005) Taphonomic observations on a camel skeleton in a desert environment in Abu Dhabi. *Palaeontologia electronica*. **8** (**1**), 1–17.

Ang, T. (2013) *Digital photography masterclass*. 2nd edition. London: Dorling Kindersley Ltd.

Artec 3D. (2016) *Professional 3D scanning solutions*. Luxembourg: Artec 3D.

Ashton, N. M. (2007) Refitting and technology in the British Lower Palaeolithic: where are we? In Schurmans, U. and De Bie, M. (editors). *Fitting rocks: lithic refitting examined*. Oxford: 45–53.

Atlas Material Testing Solutions. (2003) *Suntest CPS / CPS+: Operating manual*. Atlas Material Testing Technology GmbH.

Atlas Material Testing Solutions. (2015) *Suntest CPS*. http://atlas-mts.com/products/product-detail/pid/237/ Accessed March 13, 2016.

Aung, S. C., Ngim, R. C. and Lee, S. T. (1995) Evaluation of the laser scanner as a surface measuring tool and its accuracy compared with direct facial anthropometric measurements. *British journal of plastic surgery*. **48** (**8**), 551–558.

Bain, B. J., Clark, D. M. and Wilkins, B. S. (2009) *Bone marrow pathology*. 4th edition. Sussex: Wiley-Blackwell.

Balter, M. (2014) The killing ground: clues from a German coal mine show how early hunters lived, 300,000 years ago, and how their prey died. *Science*. **344** (**6188**), 1080–1083.

Barou, O., Mekraldi, S., Vico, L., Boivin, G., Alexandre, C. and Lafage-Proust, M. H. (2002) Relationships between trabecular bone remodelling and bone vascularization: a quantitative study. *Bone*. **30** (**4**), 604–612.

Barsanti, S. G., Micoli, L. L. and Guidi, G. (2013) Quick textured mesh generation for massive 3D digitization of museum artifacts. *2013 Digital heritage international congress*. 197–200.

Bass, B. and Jefferson, J. (2007) *Beyond the body farm: a legendary bone detective explores murders, mysteries, and the revolution in forensic science*. New York: William Morrow.

Bathow, C., Breuckmann, B. and Scopigno, R. (2010) Verification and acceptance tests for high definition 3D surface scanners. *Proceedings of the 11th international conference on virtual reality, archaeology and cultural heritage*. Aire-la-Ville, Switzerland: Eurographics Association. 9–16.

Beary, M. O. (2005) *Estimation of bone exposure duration through the use of spectrophotometric analysis of surface bleaching and its application in forensic taphonomy*. MSc Thesis, Mercyhurst University.

Beary, M. O. (2016) A priori postulates, immanent properties, diluted inferential confidence and unexplainable residues: a consideration of the scientific basis of taphonomic theory. *The 85th Annual Meeting of the American Association of Physical Anthropologists, Atlanta, GA*.

Beary, M. O. and Lyman, R. L. (2012) The use of taphonomy in forensic anthropology: past trends and future prospects. In Dirkmaat, D. (editor). *A companion to forensic anthropology*. Chichester: John Wiley & Sons Ltd. 499–527.

Beaubien, H. F. R. (2008) Documentation of Mongolia's deer stones - 2007 field season. *Arctic Studies Center newsletter*. (**15**), 30–31.

Behrensmeyer, A. K. (1978) Taphonomic and ecologic information from bone weathering. *Paleobiology*. **4** (**2**), 150–162.

Behrensmeyer, A. K. and Kidwell, S. M. (1985) Taphonomy's contributions to paleobiology. *Paleobiology*. **11** (**1**), 105–119.

Behrensmeyer, A. K. and Miller, J. H. (2012) Building links between ecology and paleontology using taphonomic studies of recent vertebrate communities. In Louys, J. (editor). *Paleontology in ecology and conservation*. Berlin: Springer-Verlag. 69–91.

Bell, L. S. (1990) Palaeopathology and diagenesis: an SEM evaluation of structural changes using backscattered electron imaging. *Journal of archaeological science*. **17** (**1**), 85–102.

Bell, L. S., Skinner, M. F. and Jones, S. J. (1996) The speed of post mortem change to the human skeleton and its taphonomic significance. *Forensic science international*. **82** (**2**), 129–140.

Benazzi, S., Maestri, C., Parisini, S., Vecchi, F. and Gruppioni, G. (2008) Sex assessment from the acetabular rim by means of image analysis. *Forensic science international*. **180** (**1**), 58.e1–3.

Benazzi, S., Maestri, C., Parisini, S., Vecchi, F. and Gruppioni, G. (2009) Sex assessment from the sacral base by means of image processing. *Journal of forensic sciences*. **54** (**2**), 249–254.

Benjamin, M., Toumi, H., Ralphs, J. R., Bydder, G., Best, T. M. and Milz, S. (2006) Where tendons and ligaments meet bone: attachment sites ('entheses') in relation to exercise and/or mechanical load. *Journal of anatomy*. **208** (**4**), 471–490.

Bennett, M. R., Falkingham, P., Morse, S. A., Bates, K. and Crompton, R. H. (2013) Preserving the impossible: conservation of soft-sediment hominin footprint sites and strategies for three-dimensional digital data capture. *PloS one*. **8** (**4**), e60755.

Bennett, M. R., Harris, J. W. K., Richmond, B. G., Braun, D. R., Mbua, E., Kiura, P., Olago, D., Kibunjia, M., Omuombo, C., Behrensmeyer, A. K., Huddart, D. and Gonzalez, S. (2009) Early hominin foot morphology based on 1.5-

million-year-old footprints from Ileret, Kenya. *Science*. **323** (**5918**), 1197–1201.

Bent, D. V. and Hayon, E. (1975) Excited state chemistry of aromatic amino acids and related peptides. II. Phenylalanine. *Journal of the American Chemical Society*. **97** (**10**), 2606–2612.

Bernal, C., de Agustina, B., Marín, M. M. and Camacho, A. M. (2013) Performance evaluation of optical scanner based on blue LED structured light. *Procedia engineering*. **63**, 591–598.

Berteau, J.-P., Gineyts, E., Pithioux, M., Baron, C., Boivin, G., Lasaygues, P., Chabrand, P. and Follet, H. (2015) Ratio between mature and immature enzymatic cross-links correlates with post-yield cortical bone behavior: an insight into greenstick fractures of the child fibula. *Bone*. **79**, 190–195.

Bešić, I., Van Gestel, N., Kruth, J.-P., Bleys, P. and Hodolič, J. (2011) Accuracy improvement of laser line scanning for feature measurements on CMM. *Optics and lasers in engineering*. **49** (**11**), 1274–1280.

Besl, P. J. and McKay, N. D. (1992) A method for registration of 3-D shapes. *IEEE transactions on pattern analysis and machine intelligence*. **14** (**2**), 239–256.

Bhatia, G., Vannier, M. W., Smith, K. E., Commean, P. K., Riolo, J. and Young, V. L. (1994) Quantification of facial surface change using a structured light scanner. *Plastic and reconstructive surgery*. **94** (**6**), 768–774.

Biological Anthropology Research Centre. (2014) *From cemetery to clinic: digitised pathological data from archaeological leprous skeletons*. http://www.barc.brad.ac.uk/FromCemeterytoClinic/index.php Accessed February 23, 2014.

Bish, D. L. and Chipera, S. J. (1988) Problems and solutions in quantitative analysis of complex mixtures by X-ray powder diffraction. In Barrett, C. S.,Gilfrich, J. V.,Jenkins, R.,Russ, J. C.,Richardson, J. W. and Predecki, P. K. (editors). *Advances in X-ray analysis*. Boston, MA: Springer US. 295–308.

Blackburn, J. and Mansell, J. P. (2012) The emerging role of lysophosphatidic acid (LPA) in skeletal biology. *Bone*. **50** (**3**), 756–762.

Blasco, R., Fernández Peris, J. and Rosell, J. (2010) Several different strategies for obtaining animal resources in the late Middle Pleistocene: the case of level XII at Bolomor Cave (Valencia, Spain). *Comptes rendus. Palevol*. **9** (**4**), 171–184.

Boeckmans, B., Zhang, M., Welkenhuyzen, F., Dewulf, W. and Kruth, J.-P. (2014) Comparison of aspect ratio, accuracy and repeatability of a laser line scanning probe and a tactile probe. *10th IMEKO symposium: laser metrology for precision measurement and inspection in industry (LMPMI) 2014*. Dusseldorf: IMEKO.

Böhler, W. and Marbs, A. (2004) 3D scanning and photogrammetry for heritage recording: a comparison. *Proceedings of the 12th international conference on geoinformatics*. Citeseer. 291–298.

Böhm, J. and Pateraki, M. (2006) From point samples to surfaces-on meshing and alternatives. *International archives of photogrammetry and remote sensing*. **36** (**5**), e1–e6.

Booth, T. J. (2016) An investigation into the relationship between funerary treatment and bacterial bioerosion in European archaeological human bone. *Archaeometry*. **58** (**3**), 484–499.

Booth, T. J., Chamberlain, A. T. and Pearson, M. P. (2015) Mummification in Bronze Age Britain. *Antiquity*. **89** (**347**), 1155–1173.

Booth, T. J. and Madgwick, R. (2016) New evidence for diverse secondary burial practices in Iron Age Britain: A histological case study. *Journal of archaeological science*. **67**, 14–24.

Borderie, Q., Torguet, P., Subsol, G., de Lumley, H., Mafart, B. and Jessel, J. P. (2004) 3D modeling of Palaeolithic tools. *Workshop on archaeology and computers, Vienna, Austria*. foveaproject.free.fr.

Boreham, S., Conneller, C., Milner, N., Taylor, B., Needham, A., Boreham, J. and Rolfe, C. J. (2011) Geochemical indicators of preservation status and site deterioration at Star Carr. *Journal of archaeological science*. **38** (**10**), 2833–2857.

Boskey, A. L. (1989) Noncollagenous matrix proteins and their role in mineralization. *Bone and mineral*. **6**, 111–123.

Bouaziz, S., Tagliasacchi, A. and Pauly, M. (2013) Sparse iterative closest point. *Computer graphics forum: journal of the European Association for Computer Graphics*. **32** (**5**), 113–123.

Boutros, C. P., Trout, D. R., Kasra, M. and Grynpas, M. D. (2000) The effect of repeated freeze-thaw cycles on the biomechanical properties of canine cortical bone. *Veterinary and comparative orthopaedics and traumatology*. **13** (**2**), 59–64.

Bouxsein, M. L. (2013) Overview of bone structure and strength. In Thakker, R. V.,Whyte, M. P.,Eisman, J. A. and Takashi, I. (editors). *Genetics of bone biology and skeletal diseases*. London: Academic Press. 25–34.

Bradford Visualisation. (2014) *Visualising animal hard tissues*. http://www.3dbones.org/visual/index.html Accessed February 23, 2015.

Bretzke, K. and Conard, N. J. (2012) Evaluating morphological variability in lithic assemblages using 3D models of stone artifacts. *Journal of archaeological science*. **39** (**12**), 3741–3749.

Breuckmann, B. (2008) High-tech und hohe kunst: anwendungen von high defiinition 3D-scannern in kunst und kultur. *Inspect*. **9**, 68–70.

Briers, J. D. (2001) Laser doppler, speckle and related techniques for blood perfusion mapping and imaging. *Physiological measurement*. **22** (**4**), R35–66.

British Standards Institution. (2015) *BS 5930:2015 Code of practice for ground investigations*. British Standards Institution.

Brock, F., Higham, T., Ditchfield, P. and Bronk Ramsey, C. (2010) Current pretreatment methods for AMS radiocarbon dating at the Oxford Radiocarbon Accelerator Unit (ORAU). *Radiocarbon*. **52** (**1**), 103–112.

Bromage, T. G., McMahon, J. M., Thackeray, J. F., Kullmer, O., Hogg, R., Rosenberger, A. L., Schrenk, F. and Enlow, D. H. (2008) Craniofacial architectural constraints and their importance for reconstructing the early Homo skull KNM-ER 1470. *The Journal of clinical pediatric dentistry*. **33** (**1**), 43–54.

Brothwell, D. (2012) Tumors: problems of differential diagnosis in palaeopathology. In Grauer, A. L. (editor). *A companion to palaeopathology*. Oxford: Wiley-Blackwell. 420–433.

Brown, D. C. (1966) Decentering distortion and the definitive calibration of metric cameras. *Photogrammetric engineering and remote sensing*. **32** (**3**), 444–462.

Brown, M. and Lowe, D. G. (2006) Automatic panoramic image stitching using invariant features. *International journal of computer vision*. **74** (**1**), 59–73.

Brown, T. A., Nelson, D. E., Vogel, J. S. and Southon, J. R. (1988) Improved collagen extraction by modified Longin method. *Radiocarbon*. **30** (**2**), 171–177.

Bruce Martin, R., Burr, D. B., Sharkey, N. A. and Fyhrie, D. P. (2015) Mechanical properties of bone. *Skeletal tissue mechanics*. New York: Springer New York. 355–422.

Brudnicki, W. (2005) Comparison of craniometric features and cranial cavity volume in domestic pig (*Sus scrofa forma domestica*) and wild boar (*Sus scrofa*) in view of development. *Folia biologica*. **53** (**4**), 25–30.

Buckberry, J. (2000) Missing, presumed buried? Bone diagenesis and the under-representation of Anglo-Saxon children. *Assemblage*, 1–17.

Buckwalter, J. A., Glimcher, M. J., Cooper, R. R. and Recker, R. (1995) Bone biology. Part 1: structure, blood supply, cells matrix and mineralization. *Journal of bone and joint surgery*. **77-A** (**8**), 1256–1275.

Burr, D. B. and Akkus, O. (2014) Basic bone biology and physiology. In Burr, D. B. and Allen, M. R. (editors). *Basic and applied bone biology*. London: Academic Press. 3–26.

Burr, D. B. and Guillot, G. M. (2012) Almost invisible, often ignored: periosteum and living lace of bone. *Medicographia*. **34** (**2**), 221–227.

Burr, D. B., Schaffler, M. B. and Frederickson, R. G. (1988) Composition of the cement line and its possible mechanical role as a local interface in human compact bone. *Journal of biomechanics*. **21** (**11**), 939–945.

Büster, L. S., Evans, A. A., Armit, I. and Kershaw, R. (2016) Developing the 3D imaging of Iron Age art in the ENTRANS Project. In Armit, I.,Potrebica, H.,Črešnar, M.,Mason, P. and Büster, L. (editors). *Cultural encounters in Iron Age Europe*. Budapest: Archaeolingua. 23–38.

Byers, S. N. (2015) *Introduction to forensic anthropology*. 4th edition. London: Taylor & Francis.

Cahen, D. (1987) Refitting stone artefacts: why bother. In Sieveking, G. D. G. and Newcomer, M. H. (editors). *Proceedings of the Fourth International Flint Symposium Held at Brighton Polytechnic 10–15 April 1983*. Cambridge: Cambridge University Press. 1–9.

Calce, S. E. and Rogers, T. L. (2007) Taphonomic changes to blunt force trauma: a preliminary study. *Journal of forensic sciences*. **52** (**3**), 519–527.

Calloway, D. (1997) Beer-Lambert law. *Journal of chemical education*. **74** (**7**), 744.

Caple, C. (1996) Parameters for monitoring anoxic environments which preserve archaeological organic materials. In Corfield, M.,Hinton, P.,Nixon, T. and Pollard, A. M. (editors). *Preserving archaeological remains in situ*. London: Museum of London Archaeology Service. 113–123.

Carter, D. O. and Tibbett, M. (2008) Cadaver decomposition and soil: processes. In Tibbett, M. and Carter, D. O. (editors). *Soil analysis in forensic taphonomy: chemical and biological effects of buried human remains*. Boca Raton: CRC Press. 29–45.

Carter, D. R., Mikić, B. and Padian, K. (1998) Epigenetic mechanical factors in the evolution of long bone epiphyses. *Zoological journal of the Linnaean Society*. **123** (**2**), 163–178.

Cattaneo, C., DiMartino, S., Scali, S., Craig, O. E., Grandi, M. and Sokol, R. J. (1999) Determining the human origin of fragments of burnt bone: a comparative study of histological, immunological and DNA techniques. *Forensic science international*. **102** (**2-3**), 181–191.

Cattaneo, C., Porta, D., Gibelli, D. and Gamba, C. (2009) Histological determination of the human origin of bone fragments. *Journal of forensic sciences*. **54** (**3**), 531–533.

Centeno, N., Maldonado, M. and Oliva, A. (2002) Seasonal patterns of arthropods occurring on sheltered and unsheltered pig carcasses in Buenos Aires Province (Argentina). *Forensic science international*. **126** (**1**), 63–70.

Chen, Y. and Medioni, G. (1992) Object modelling by registration of multiple range images. *Image and vision computing*. **10** (**3**), 145–155.

Child, A. M. (1995)(a) Towards an understanding of the microbial decomposition of archaeological bone in the burial environment. *Journal of archaeological science*. **22**, 165–174.

Child, A. M. (1995)(b) Microbial taphonomy of archaeological bone. *Studies in conservation*. **40** (**1**), 19–30.

Child, A. M., Gillard, R. D. and Pollard, A. M. (1993) Microbially-induced promotion of amino acid racemization: isolation of the microorganisms and the detection of their enzymes. *Journal of archaeological sciences*. **20** (**2**), 159–168.

Chinsamy-Turan, A. (2005) *The microstructure of dinosaur bone: deciphering biology with fine-scale techniques*. Chichester: John Wiley & Sons.

Chiotti, L., Dibble, H. L., Olszewski, D. I., McPherron, S. P. and Schurmans, U. A. (2013) Middle Palaeolithic lithic technology from the western High Desert of Egypt. *Journal of field archaeology*. **34** (**3**), 307–318.

Chipera, S. J. and Bish, D. L. (1991) Applications of X-ray diffraction crystallite size/strain analysis to *Seismosaurus* dinosaur bone. In Barrett, C. S.,Amara, M.,Huang, T. C.,Bernard, N. and Knorr, D. (editors). *Advances in X-ray analysis*. Boston MA: Springer US. 473–482.

Cho, T.-J., Gerstenfeld, L. C. and Einhorn, T. A. (2002) Differential temporal expression of members of the transforming growth factor beta superfamily during murine fracture healing. *Journal of bone and mineral research*. **17** (**3**), 513–520.

Chua, D. C. K., Chou, S. M., Ng, W. S., Chow, K. Y., Lee, S. T., Aung, S. C. and Seah, C. S. (1998) An integrated experimental approach to link a laser digitiser, a CAD/CAM system and a rapid prototyping system for biomedical applications. *International journal of advanced manufacturing technology*. **14** (**2**), 110–115.

Chung, L., Dinakarpandian, D., Yoshida, N., Lauer-Fields, J. L., Fields, G. B., Visse, R. and Nagase, H. (2004) Collagenase unwinds triple-helical collagen prior to peptide bond hydrolysis. *The EMBO journal*. **23** (**15**), 3020–3030.

Ciarelli, M. J., Goldstein, S. A., Kuhn, J. L., Cody, D. D. and Brown, M. B. (1991) Evaluation of orthogonal mechanical properties and density of human trabecular bone from the major metaphyseal regions with materials testing and computed tomography. *Journal of orthopaedic research*. **9** (**5**), 674–682.

Cignoni, P., Callieri, M., Corsini, M., Dellepiane, M., Ganovelli, F. and Ranzuglia, G. (2008) Meshlab: an open-source mesh processing tool. *Eurographics Italian chapter conference*. 129–136.

Claes, L., Recknagel, S. and Ignatius, A. (2012) Fracture healing under healthy and inflammatory conditions. *Nature reviews. Rheumatology*. **8** (**3**), 133–143.

Clarke, B. (2008) Normal bone anatomy and physiology. *Clinical journal of the American Society of Nephrology*. **3 Suppl 3**, S131–S139.

Clarke, M. A., Worrell, M. B. and Pless, J. E. (1997) Postmortem changes in soft tissues. In Haglund, W. D. and Sorg, M. H. (editors). *Forensic taphonomy: the postmortem fate of human remains*. Boca Raton: CRC Press. 151–164.

Clark, J. M. and Huber, J. D. (1990) The structure of the human subchondral plate. *Journal of bone and joint surgery. British volume*. **72** (**5**), 866–873.

Clark, J. and Robson, S. (2004) Accuracy of measurements made with a Cyrax 2500 laser scanner against surfaces of known colour. *Survey review*. **37** (**294**), 626–638.

CloudCompare.org. (2015) *CloudCompare version 2.6.1: user manual*. Paris: Cloudcompare.org.

Cloutman, E. W. (1988)(a) Palaeoenvironments in the Vale of Pickering. Part 1: stratigraphy and palaeogeography of Seamer Carr, Star Carr and Flixton Carr. *Proceedings of the Prehistoric Society*. **54**, 1–19.

Cloutman, E. W. (1988)(b) Palaeoenvironments in the Vale of Pickering. Part 2: environmental history at Seamer Carr. *Proceedings of the Prehistoric Society*. **54**, 21–36.

Cloutman, E. W. and Smith, A. G. (1988) Palaeoenvironments in the Vale of Pickering. Part 3: environmental history at Star Carr. *Proceedings of the Prehistoric Society*. **54**, 37–58.

Coe, M. (1978) The decomposition of elephant carcasses in the Tsavo (East) National Park, Kenya. *Journal of arid environments*. **1**, 71–86.

Collier, O. (2002) The impact of topographic mapping on developments in land and air survey: 1900 - 1939. *Cartography and geographic information science*. **29** (**3**), 155–174.

Collins, M., Buckley, M., Grundy, H. H., Thomas-Oates, J., Wilson, J. and van Doorn, N. (2010) ZooMS: the collagen barcode and fingerprints. *Spectroscopy Europe*. **22**, 2–2.

Collins, M. J. and Galley, P. (1998) Towards an optimal method of archaeological collagen extraction: the influence of pH and grinding. *Ancient biomolecules*. **2** (**2/3**), 209–223.

Collins, M. J., Nielsen-Marsh, C. M., Hiller, J., Smith, C. I., Roberts, J. P., Prigodich, R. V., Wess, T. J., Csapò, J., Millard, A. R. and Turner-Walker, G. (2002) The survival of organic matter in bone: a review. *Archaeometry*. **44** (**3**), 383–394.

Collins, M. J., Riley, M. S., Child, A. and Turner Walker, G. (1995) A basic mathematical simulation of the chemical degradation of ancient collagen. *Journal of archaeological science*. **22** (**2**), 175–183.

Confavreux, C. B. (2011) Bone: from a reservoir of minerals to a regulator of energy metabolism. *Kidney international. Supplement*. **79** (**121**), S14–S19.

Conneller, C. (2004) Becoming deer. Corporeal transformations at Star Carr. *Archaeological dialogues*. **11** (**1**), 37–56.

Contri, A., Bourdet, P. and Lartigue, C. (2002) Quality of 3D digitised points obtained with non-contact optical sensors. *CIRP annals - manufacturing technology*. **51** (**1**), 443–446.

Cooke, R. C. (1963) Succession of nematophagous fungi during the decomposition of organic matter in the soil. *Nature*. **197** (**4863**), 205.

Cooper, J. R. and Laughlin, J. P. (2006) Testing a computerized model for lithic refitting: an example from Barger Gulch Locality B. *71st annual meeting of the Society for American Archaeology, Puerto Rico*.

Cooper, J. R. and Qiu, F. (2006) Expediting and standardizing stone artifact refitting using a computerized suitability model. *Journal of archaeological science*. **33** (**7**), 987–998.

Copp, D. H. and Shim, S. S. (1963) The homeostatic function of bone as a mineral reservoir. *Oral surgery, oral medicine, and oral pathology*. **16**, 738–744.

Coryndon, S. C. (1977) The taxonomy and nomenclature of the Hippopotamidae (Mammalia, Artiodactyla) and a description of two new fossil species. *Proceedings of the Koninklijke Nederlandse Akademie van Wetenschappen. Series C. Biological and medical sciences*. **B80**, 61–88.

Coşarcă, C., Jocea, A. and Savu, A. (2009) Analysis of error sources in terrestrial laser scanning. *Journal of geodesy and cadastre*. **9** (**1**), 115–124.

Cowin, S. C. (1999) Bone poroelasticity. *Journal of biomechanics*. **32** (**3**), 217–238.

Creaform 3D. (2015) *Optical CMM 3D scanner: MetraScan 3D*. https://www.creaform3d.com/en/metrology-solutions/optical-3d-scanner-metrascan Accessed March 2, 2016.

Creaform 3D. (2016)(a) *Portable 3D scanners: HandySCAN 3D*. https://www.creaform3d.com/en/metrology-solutions/portable-3d-scanner-handyscan-3d Accessed January 6, 2017.

Creaform 3D. (2016)(b) *Portable 3D scanners: Go!Scan 3D*. https://www.creaform3d.com/en/metrology-solutions/handheld-portable-3d-scanner-goscan-3d Accessed January 6, 2017.

Creed, D. (1984)(a) The photophysics and photochemistry of the near-UV absorbing amino acids–I. Tryptophan and its simple derivatives. *Photochemistry and photobiology*. **39 (4)**. 537–562.

Creed, D. (1984)(b) The photophysics and photochemistry of the near-UV absorbing amino acids–II. Tyrosine and its simple derivatives. *Photochemistry and photobiology*. **39 (4)**. 563–575.

Crow, P. (2008) Mineral weathering in forest soils and its relevance to the preservation of the buried archaeological resource. *Journal of archaeological science*. **35** (**8**), 2262–2273.

Cruess, R. L. and Clark, I. (1965) Alterations in the lipids of bone caused by hypervitaminosis A and D. *Biochemical journal*. **96**, 262–265.

Cuijpers, A. G. F. M. (2006) Histological identification of bone fragments in archaeology: telling humans apart from horses and cattle. *International journal of osteoarchaeology*. **16** (**6**), 465–480.

Cuijpers, A. G. F. M. (2009) *The application of bone histology for species identification in archaeology; with photo catalogue*. PhD Thesis, Vrije Universiteit Amsterdam.

Cultural Heritage Imaging. (2015) *Photogrammetry*. http://culturalheritageimaging.org/Technologies/Photogrammetry/ Accessed January 14, 2017.

Cunningham, S. L., Kirkland, S. A. and Ross, A. H. (2011) Bone weathering of juvenile-sized remains in the North Carolina Piedmont. In Ross, A. H. and Abel, S. M. (editors). *The juvenile skeleton in forensic abuse investigations*. Humana Press. 179–196.

Currey, J. D. (2006) *Bones: structure and mechanics*. New edition. Princeton, New Jersey: Princeton University Press.

Currey, J. D. (2012) The structure and mechanics of bone. *Journal of materials science*. **47** (**1**), 41–54.

Cziesla, E. (1990) On refitting of stone artefacts. In Cziesla, E. (editor). *The big puzzle: international symposium on refitting stone artefacts, MONREPOS, 1987.* Bonn: Holos. 9–44.

Dall'Asta, E. and Roncella, R. (2014) A comparison of semiglobal and local dense matching algorithms for surface reconstruction. *ISPRS - international archives of the photogrammetry, remote sensing and spatial information sciences*. **XL-5**, 187–194.

Dark, P., Higham, T. F. G., Jacobi, R. and Lord, T. C. (2006) New radiocarbon accelerator dates on artefacts from Star Carr, North Yorkshire. *Archaeometry*. **48**, 185–200.

Dauphin, Y., Kowalski, C. and Denys, C. (1994) Assemblage data and bone and teeth modifications as an aid to paleoenvironmental interpretations of

the open-air Pleistocene site of Tighenif (Algeria). *Quaternary research*. **42** (**3**), 340–349.

Dauphin, Y., Williams, C. T., Andrews, P., Denys, C. and Fernández-Jalvo, Y. (1999) Diagenetic alterations of micromammal fossil bones from Olduvai Bed I of the lower Pleistocene sequence at Olduvai Gorge, Tanzania. *Journal of sedimentary research*. **69** (**3**), 612–621.

David 3D. (2015) *SLS-2 structured light 3D scanning system*. David 3D.

Davidson, M. K., Lindsey, J. R. and Davis, J. K. (1987) Requirements and selection of an animal model. *Israel journal of medical sciences*. **23** (**6**), 551–555.

Dawson, G., Mackintosh, M. and Anand, P., editors. (2006) *Economics and economic change: microeconomics*. Milton Keynes: The Open University.

Dawson, P. C. and Levy, R. M. (2005) A three-dimensional model of a Thule Inuit whale bone house. *Journal of field archaeology*. **30** (**4**), 443–455.

Day, A. D. and Ludeke, K. L. (1993) Soil alkalinity. In Day, A. D. and Ludeke, K. L. (editors). *Plant nutrients in desert environments*. Berlin Heidelberg: Springer. 35–37.

Day, S. P. and Mellars, P. A. (1994) “Absolute” dating of Mesolithic human activity at Star Carr, Yorkshire: new palaeoecological studies and identification of the 9600 BP radiocarbon “plateau.” *Proceedings of the Prehistoric Society*. **60**, 417–422.

Decker, S., Reifenrath, J., Omar, M., Krettek, C. and Müller, C. W. (2014) Non-osteotomy and osteotomy large animal fracture models in orthopedic trauma research. *Orthopedic reviews*. **6** (**4**), 168–174.

Deecke, W. (1923) *Die fossilisation*. Berlin: Gebrüder Borntraeger.

Deen, S. (2014) Musculoskeletal system. In Orchard, G. and Nation, B. (editors). *Cell structure & function*. Oxford: Oxford University Press. 296–322.

De La Cruz, B., V. (2001) *Studies on the state of preservation of archaeological bone*. PhD Thesis, University of Bradford.

De Loera, J., Rambau, J. and Santos, F. (2010) *Triangulations: structures for algorithms and applications (algorithms and computation in mathematics)*. London: Springer.

DeLuca, H. F. (1979) The vitamin D system in the regulation of calcium and phosphorus metabolism. *Nutrition reviews*. **37** (**6**), 161–193.

Deniro, M. J. and Epstein, S. (1981) Influence of diet on the distribution of nitrogen isotopes in animals. *Geochimica et cosmochimica acta*. **45** (**3**), 341–351.

Dent, B. B., Forbes, S. L. and Stuart, B. H. (2003) Review of human decomposition processes in soil. *Environmental geology*. **45** (**4**), 576–585.

Depetris, P. J., Pasquini, A. I. and Lecomte, K. L. (2014) Chemical weathering processes on the earth's surface. In Depetris, P. J.,Pasquini, A. I. and Lecomte, K. L. (editors). *Weathering and the riverine denudation of continents*. London: Springer. 33–46.

De Ricqles, A., Meunier, F. J., Castanet, J. and Francillon-Vieillot, H. (1991) Comparative microstructure of bone. In Hall, B. K. (editor). *Bone, volume 3: Bone matrix and bone specific products.* Boca Raton: CRC Press. 1–78.

Derkx, P., Nigg, A. L., Bosman, F. T., Birkenhäger-Frenkel, D. H., Houtsmuller, A. B., Pols, H. A. and van Leeuwen, J. P. (1998) Immunolocalization and quantification of noncollagenous bone matrix proteins in methylmethacrylate-embedded adult human bone in combination with histomorphometry. *Bone*. **22** (**4**), 367–373.

Díaz-Marín, C., Aura-Castro, E., Sánchez-Belenguer, C. and Vendrell-Vidal, E. (2016) Cyclododecane as opacifier for digitalization of archaeological glass. *Journal of cultural heritage*. **17**, 131–140.

Digitised Diseases. (2014) *Digitised diseases: informing clinical understanding of chronic conditions affecting the skeleton using archaeological and*

historical exemplars. http://www.digitiseddiseases.org/alpha/ Accessed February 23, 2015.

Di Masso, R. J., Celoria, G. C. and Font, M. T. (1998) Morphometric skeletal traits, femoral measurements, and bone mineral deposition in mice with agonistic selection for body conformation. *Bone*. **22** (**5**), 539–543.

Dimitriou, R., Tsiridis, E. and Giannoudis, P. V. (2005) Current concepts of molecular aspects of bone healing. *Injury*. **36** (**12**), 1392–1404.

Dirckx, N., van Hul, M. and Maes, C. (2013) Osteoblast recruitment to sites of bone formation in skeletal development, homeostasis, and regeneration. *Birth defects research. Part C, embryo today*. **99** (**3**), 170–191.

Doblaré, M., García, J. M. and Gómez, M. J. (2004/9) Modelling bone tissue fracture and healing: a review. *Engineering fracture mechanics*. **71** (**13–14**), 1809–1840.

Dobson, J. (1952) Pioneers of osteogeny: Clopton Havers. *Journal of bone and joint surgery*. **34** (**4**), 702–707.

Dominguez, V. M. and Crowder, C. M. (2012) The utility of osteon shape and circularity for differentiating human and non-human Haversian bone. *American journal of physical anthropology*. **149** (**1**), 84–91.

Dumas, A., Brigitte, M., Moreau, M. F., Chrétien, F., Baslé, M. F. and Chappard, D. (2009) Bone mass and microarchitecture of irradiated and bone marrow-transplanted mice: influences of the donor strain. *Osteoporosis international*. **20** (**3**), 435–443.

Dupras, T. L. and Schultz, J. J. (2013) Taphonomic bone staining and color changes in forensic contexts. In Pokines, J. T. and Symes, S. A. (editors). *Manual of forensic taphonomy*. Boca Raton: CRC Press. 315–340.

Duque, G. and Watanabe, K. (2011) *Osteoporosis research: animal models*. London: Springer-Verlag.

Durán-Domínguez, G., Felicísimo, A. M. and Polo, M. E. (2014) 3D study of cultural heritage for conservation: reliability of portable 3D laser scanner.

In Rogerio-Candelera, M. Á. (editor). *Science, technology and cultural heritage: proceedings of the 2nd international congress on science and technology for the conservation of cultural heritage, Sevilla, Spain, 24 - 27 June 2014*. London: Taylor & Francis Group. 357–361.

Dury, M., Brown, S., McCarthy, M. and Woodward, S. (2015) Blowing hot and cold: temperature sensitivities of 3D optical scanners. *Proc. of the 15th international conference of the European Society for Precision Engineering and Nanotechnology*. academia.edu. 161–162.

Dwek, J. R. (2010) The periosteum: what is it, where is it, and what mimics it in its absence? *Skeletal radiology*. **39** (**4**), 319–323.

Edeleanu, C. and Forty, A. J. (1960) Some observations on the stress-corrosion cracking of α-brass and similar alloys. *Philosophical magazine*. **5** (**58**), 1029–1040.

Eeckhout, Y. (1990) Possible role and mechanism of action of dissolved calcium in the degradation of bone collagen by lysosomal cathepsins and collagenase. *Biochemical journal*. **272** (**2**), 529–532.

Efremov, I. A. (1940) Taphonomy: a new branch of paleontology. *Pan-American geologist*. **74**, 81–93.

Einhorn, T. A. (1992) Bone strength: the bottom line. *Calcified tissue international*. **51** (**5**), 333–339.

Eisenberg, D. and Kauzmann, W. (2005) *The structure and properties of water*. Oxford: Oxford University Press.

Ekstrand, L., Wang, Y., Karpinsky, N. and Zhang, S. (2013) Superfast 3D profilometry with digital fringe projection and phase shifting techniques. In Zhang, S. (editor). *The handbook of 3D machine vision: optical metrology and imaging*. Boca Raton: CRC Press. 233–251.

Elliott, J. C. (1973) The problems of the composition and structure of the mineral components of the hard tissues. *Clinical orthopaedics and related research*. (**93**), 313–345.

English Heritage. (2011) *3D laser scanning for heritage: advice and guidance to users on laser scanning in archaeology and architecture*. 2nd edition. Swindon: English Heritage.

Enlow, D. H. (1963) *Principles of bone remodelling*. Springfield, Illinois: Charles C Thomas.

ePHOTOzine. (2007) *Digital camera sales - film camera sales*. http://www.ephotozine.com/article/digital-camera-sales---film-camera-sales-3716 Accessed February 23, 2015.

Evans, S., Jones, C. and Plassmann, P. (2010) 3D imaging in forensic odontology. *Journal of visual communication in medicine*. **33** (**2**), 63–68.

Evans, T. (2013) Fluvial taphonomy. In Pokines, J. T. and Symes, S. A. (editors). *Manual of forensic taphonomy*. Boca Raton: CRC Press. 115–141.

Fadda, C., Faggiani, F. and Corti, M. (1997) A portable device for the three dimensional landmark collection of skeletal elements of small mammals. *Mammalia*. **61** (**4**), 622–627.

Falk, D., Cheverud, J., Vannier, M. W. and Conroy, G. C. (1986) Advanced computer graphics technology reveals cortical asymmetry in endocasts of rhesus monkeys. *Folia primatologica; international journal of primatology*. **46** (**2**), 98–103.

Fan, K.-C. (1997) A non-contact automatic measurement for free-form surface profiles. *Computer integrated manufacturing systems*. **10** (**4**), 277–285.

Farhi, D. C. (2009) *Pathology of bone marrow and blood cells*. 2nd edition. Philadelphia: Lippincott, Williams and Wilkins.

Farlow, J. O. and Argast, A. (2006) Preservation of fossil bone from the Pipe Creek Sinkhole (Late Neogene, Grant County, Indiana, USA). *Journal of the Paleontological Society of Korea*. **22** (**1**), 51–75.

FARO Technologies. (2009) *FARO Laser ScanArm V3*. Lake Mary, Florida: FARO Technologies Inc.

FARO Technologies. (2013)(a) *FARO Edge and ScanArm ES: non-contact measurement with enhanced scanning technology*. Lake Mary, Florida: FARO Technologies Inc.

FARO Technologies. (2013)(b) *FARO Edge and ScanArm HD: features, benefits and technical specifications*. Lake Mary, Florida: FARO Technologies Inc.

Feibel, C. S. (2011) A geological history of the Turkana Basin. *Evolutionary anthropology*. **20** (**6**), 206–216.

Feng, H.-Y., Liu, Y. and Xi, F. (2001) Analysis of digitizing errors of a laser scanning system. *Precision engineering*. **25** (**3**), 185–191.

Fernández-Jalvo, Y., Andrews, P., Pesquero, D., Smith, C., Marín-Monfort, D., Sánchez, B., Geigl, E.-M. and Alonso, A. (2010) Early bone diagenesis in temperate environments: Part I: Surface features and histology. *Palaeogeography, palaeoclimatology, palaeoecology*. **288** (**1–4**), 62–81.

Fernández-López, S. R. (1984) Nuevas perspectivas de la tafonomía evolutiva: tafosistemas y asociaciones conservadas. *Estudios geológicos*. **40** (**1983**), 215–224.

Fernández-López, S. R. (1988) La tafonomía: un subsistema conceptual de la paleontología. *Coloquios de paleontología*. **41** (**1986 - 1987**), 9–34.

Fernández López, S. R. (1989) La materia fósil. Una concepción dinamicista de los fósiles. In Aguirre, E. (editor). *Nuevas tendencias: Paleontología*. Madrid: Consejo Superior de Investigaciones Científicas. 22–45.

Fernández-López, S. R. (2000) *Temas de tafonomía*. Madrid: University of Madrid.

Fernández, P. J., Holowka, N. B., Demes, B. and Jungers, W. L. (2016) Form and function of the human and chimpanzee forefoot: implications for early hominin bipedalism. *Scientific reports*. **6**, 30532.

Fink, M., Medelnik, J., Strobel, K. and Hirschfelder, U. (2014) Metric precision via soft-tissue landmarks in three-dimensional structured-light scans of human faces. *Journal of orofacial orthopedics*. **75**, 133–143.

Finks, R. M. (1979) Fossils and fossilization. In Fairbridge, R. W. (editor). *Paleontology*. Berlin: Springer-Verlag. 327–332.

Finlay, J. B. and Hardie, W. R. (1994) Anisotropic contraction of cortical bone caused by dehydration of samples of the bovine femur *in vitro*. *Proceedings of the Institution of Mechanical Engineers. Part H, Journal of engineering in medicine*. **208** (**1**), 27–32.

Fleagle, J. G. and Leakey, M. (2011) The Turkana Basin. *Evolutionary anthropology*. **20** (**6**), 201.

Fleet, M. E. and Liu, X. (2008) Location of carbonate ions in structure of biological apatite. *Advances in bioceramics and porous ceramics*. **29** (**7**), 63–76.

Floss, H. and Terberger, T. (1990) The Magdalenian of Andernach: analysis of camp structures by refitting stone artefacts. In Cziesla, E. (editor). *The big puzzle: international symposium on refitting stone artefacts, MONREPOS, 1987.* Bonn: Holos. 339–362.

Fogel, M. L., Noreen, T., Johnson, B. J. and Miller, G. H. (1997) Biogeochemical record of ancient humans. *Organic geochemistry*. **27** (**5-6**), 275–287.

Forbes, S. L., Stuart, B. H., Dent, B. B. and Fenwick-Mulcahy, S. (2005) Characterization of adipocere formation in animal species. *Journal of forensic sciences*. **50** (**3**), 633–640.

Förstner, W. (1986) A feature based correspondence algorithm for image matching. *International archives of photogrammetry and remote sensing*. **23** (**3**), 150–166.

Fortelius, M. (2016), *Laboratory discussion on the species identification of fragmentary fossil remains*. [Personal communication] 26 February.

Fragmented Heritage. (2013) *The project*. http://www.fragmentedheritage.com/ Accessed November 11, 2016.

Francillon-Vieillot, H., de Buffrénil, V., Castanet, J., Géraudie, J., Meunier, F. J., Sire, J. Y., Zylberberg, L. and de Ricqlès, A. (1989) Microstructure and mineralization of vertebrate skeletal tissues. In Carter, J. G. (editor). *Skeletal biomineralization: patterns, processes and evolutionary trends*. Washington, D. C.: American Geophysical Union. 175–234.

Frankel, V. H. and Nordin, M. (1980) *Basic biomechanics of the skeletal system*. Philadelphia: Lea and Febiger.

Freundorfer, S., Grupe, G. and Weickmann, D. (1995) Mineral-bound noncollagenous proteins in archaeological human skeletons. *Electrophoresis*. **16** (**5**), 817–819.

Friess, M. (2012) Scratching the surface? The use of surface scanning in physical and paleoanthropology. *Journal of anthropological sciences*. **90**, 7–31.

Friess, M., Marcus, L. F., Reddy, D. P. and Delson, E. (2002) The use of 3D laser scanning techniques for the morphometric analysis of human facial shape variation. In Mafart, B. and Delingette, H. (editors). *Three-dimensional imaging in paleoanthropology and prehistoric archaeology*. BAR International Series 1049. Oxford: BAR Publishing. 31–35.

Galloway, A., Zephro, L. and Wedel, V. L. (2013) Diagnostic criteria for the determination of the timing and fracture mechanism. In Wedel, V. L. and Galloway, A. (editors). *Broken bones: anthropological analysis of blunt force trauma*. 2nd edition. Springfield: Charles C. Thomas. 47–58.

García-Moreno, A., Hutson, J. M., Villaluenga, A., Turner, E. and Gaudzinski-Windheuser, S. (2015) Counting sheep without falling asleep: using GIS to calculate the minimum number of skeletal elements (MNE) and other archaeozoological measures at Schöningen 13II-4 “Spear Horizon.” In Giligny, F.,Djindjian, F.,Costa, L.,Moscati, P. and Robert, S. (editors). *CAA 2014 - 21st century archaeology: Concepts, methods and tools. Proceedings of the 42nd annual conference on computer applications and*

quantitative methods in archaeology. Oxford: Archaeopress Archaeology. 407–412.

Garland, A. N. (1987) A histological study of archaeological bone decomposition. In Boddington, A.,Garland, A. N. and Janaway, R. C. (editors). *Death, decay, and reconstruction: approaches to archaeology and forensic science*. Manchester: Manchester University Press. 109–126.

Garland, A. N. (1989) Microscopical analysis of fossil bone. *Applied geochemistry*. **4** (**3**), 215–229.

Garvie-Lok, S. J., Varney, T. L. and Katzenberg, M. A. (2004) Preparation of bone carbonate for stable isotope analysis: the effects of treatment time and acid concentration. *Journal of archaeological science*. **31** (**6**), 763–776.

Gåsvik, K. J. (2002) *Optical metrology*. 3rd edition. Chichester: John Wiley & Sons, Ltd.

Geneser, F. (1989) *Textbook of histology*. New Jersey, USA: Wiley-Blackwell.

Gernat, T., McPherron, S. P., Dibble, H. and Hublin, J. J. (2008) An application of structured light scanning to documenting excavated surfaces and in situ finds: examples from the Middle Paleolithic sites of Jonzac and Roc de Marsal, France. *Layers of perception: proceedings of the 35th international conference on computer applications and quantitative methods in archaeology*. Kolloquien zur Vor-und Frühgeschichte. 51–57.

Ghyme, S. W., Brian, A. and Chae, W. S. (2008) *Method and system for texturing of 3D model in 2D environment*. US Patents Office. Patent number: US 12/048,495.

Giannobile, W. V., Finkelman, R. D. and Lynch, S. E. (1994) Comparison of canine and non-human primate animal models for periodontal regenerative therapy: results following a single administration of PDGF/IGF-I. *Journal of periodontology*. **65** (**12**), 1158–1168.

Gifford-Gonzalez. (1989) Ethnographic analogues for interpreting modified bones: some cases from East-Africa. In Bonnichsen, R. and Sorg, M. H.

(editors). *Bone modification*. Orono, Maine: Center for the study of the first Americans, Orono, University of Maine. 179–246.

Giraud-Guille, M. M. (1988) Twisted plywood architecture of collagen fibrils in human compact bone osteons. *Calcified tissue international*. **42** (**3**), 167–180.

Glimcher, M. J. (1987) The nature of the mineral component of bone and the mechanism of calcification. *Instructional course lectures*. **36**, 49–69.

Golcuk, K., Mandair, G. S., Callender, A. F., Sahar, N., Kohn, D. H. and Morris, M. D. (2006) Is photobleaching necessary for Raman imaging of bone tissue using a green laser? *Biochimica et biophysica acta*. **1758**, 868–873.

Goldstein, S. A., Hollister, S. J., Kuhn, J. L. and Kikuchi, N. (1990) The mechanical and remodeling properties of trabecular bone. In Mow, V. C.,Ratcliffe, A. and Woo, S. L.-Y. (editors). *Biomechanics of diarthrodial joints*. New York: Springer New York. 61–81.

Gomez, S. (2002) Crisóstomo Martinez, 1638-1694: the discoverer of trabecular bone. *Endocrine*. **17** (**1**), 3–4.

Gordon, C. C. and Buikstra, J. E. (1981) Soil pH, bone preservation, and sampling bias at mortuary sites. *American antiquity*. **46** (**3**), 566–571.

Goring-Morris, A. N., Marder, O., Davidzon, A. and Ibrahim, F. (1998) Putting Humpty together again: preliminary observations on refitting studies in the eastern Mediterranean. In Milliken, S. (editor). *From raw material procurement to tool production: the organization of lithic technology in late glacial and early postglacial Europe.* BAR International Series 700. Oxford: BAR Publishing. 149–182.

Gorski, J. P. (1998) Is all bone the same? Distinctive distributions and properties of non-collagenous matrix proteins in lamellar vs. woven bone imply the existence of different underlying osteogenic mechanisms. *Critical reviews in oral biology and medicine*. **9** (**2**), 201–223.

Goulet, R. W., Goldstein, S. A., Ciarelli, M. J., Kuhn, J. L., Brown, M. B. and Feldkamp, L. A. (1994) The relationship between the structural and

orthogonal compressive properties of trabecular bone. *Journal of biomechanics*. **27** (**4**), 375–389.

Grévin, G., Bailet, P., Quatrehomme, G. and Ollier, A. (1998) Anatomical reconstruction of fragments of burned human bones: a necessary means for forensic identification. *Forensic science international*. **96** (**2-3**), 129–134.

Grosman, L., Sharon, G., Goldman-Neuman, T., Smikt, O. and Smilansky, U. (2011) Studying post depositional damage on Acheulian bifaces using 3-D scanning. *Journal of human evolution*. **60** (**4**), 398–406.

Grosman, L., Smikt, O. and Smilansky, U. (2008) On the application of 3-D scanning technology for the documentation and typology of lithic artifacts. *Journal of archaeological science*. **35** (**12**), 3101–3110.

Grupe, G. (2007) Taphonomic and diagenetic processes. In Henke, W. and Tattersall, I. (editors). *Handbook of paleoanthropology: Volume III phylogeny of hominids*. Berlin: Springer-Verlag. 241–259.

Grussenmeyer, P., Landes, T., Doneus, M. and Lerma, J. L. (2016) Basics of range-based modelling techniques in cultural heritage 3D recording. In Stylianidis, E. and Remondino, F. (editors). *3D recording, documentation and management of cultural heritage*. Dunbeath: Whittles Publishing. 305–368.

Guadelli, J.-L. and Ozouf, J.-C. (1994) Etudes expérimentales de l'action du gel sur les restes fauniques: premiers résultats: Actions climatique et édaphique. *Artefacts*. **9**, 47–56.

Guanchang, J. and Guanchang, N. (1990) Automated 3-d profilometry and its application to human face measurements. *Acta Anthropologica Sinica*. **9** (**2**), 164–167.

Gu, J., Nayar, S., Grinspun, E., Belhumeur, P. and Ramamoorthi, R. (2008) Compressive structured light for recovering inhomogeneous participating media. *Computer vision – ECCV 2008*. Springer, Berlin, Heidelberg. 845–858.

Gupta, M., Yin, Q. and Nayar, S. K. (2013) Structured light in sunlight. *Proceedings of the IEEE International Conference on Computer Vision*. cv-foundation.org. 545–552.

Hackett, C. J. (1981) Microscopical focal destruction (tunnels) in exhumed human bones. *Medicine, science, and the law*. **21** (**4**), 243–265.

Haglund, W. D., Reay, D. T. and Swindler, D. R. (1988) Tooth mark artifacts and survival of bones in animal scavenged human skeletons. *Journal of forensic sciences*. **33** (**4**), 985–997.

Haglund, W. D., Reay, D. T. and Swindler, D. R. (1989) Canid scavenging/disarticulation sequence of human remains in the Pacific Northwest. *Journal of forensic sciences*. **34** (**3**), 587–606.

Hammond, A. S., Plavcan, J. M. and Ward, C. V. (2013) Precision and accuracy of acetabular size measures in fragmentary hominin pelves obtained using sphere-fitting techniques. *American journal of physical anthropology*. **150** (**4**), 565–578.

Han, D., Chimienti, A. and Menga, G. (2013) Improving calibration accuracy of structured light systems using plane-based residual error compensation. *Optical engineering*. **52** (**10**).

Hansen, U., Zioupos, P., Simpson, R., Currey, J. D. and Hynd, D. (2008) The effect of strain rate on the mechanical properties of human cortical bone. *Journal of biomechanical engineering*. **130** (**1**), 011011.

Harcourt-Smith, W. E. H., Tallman, M., Frost, S. R., Wiley, D. F., James Rohlf, F. and Delson, E. (2008) Analysis of selected hominoid joint surfaces using laser scanning and geometric morphometrics: a preliminary report. In Sargis, E. J. and Dagosto, M. (editors). *Mammalian evolutionary morphology*. Netherlands: Springer. 373–383.

Harcourt-Smith, W. E. H., Throckmorton, Z., Congdon, K. A., Zipfel, B., Deane, A. S., Drapeau, M. S. M., Churchill, S. E., Berger, L. R. and DeSilva, J. M. (2015) The foot of *Homo naledi*. *Nature communications*. **6**, 8432.

Harris, C. and Stephens, M. (1988) A combined corner and edge detector. *Proceedings of the 4th Alvey Vision Conference*. 147–151.

Hartman, S. E. (1989) Stereophotogrammetric analysis of occlusal morphology of extant hominoid molars: phenetics and function. *American journal of physical anthropology*. **80** (**2**), 145–166.

Haskell, N. H., Schoenly, K. G. and Hall, R. D. (2002) *Testing reliability of animal models in research and training programs in forensic entomology, part II, final report*. Washington DC: U.S. Department of Justice, National Criminal Justice Reference Service (NCJRS).

Hassan, A. A., Termine, J. D. and Haynes, C. V. (1977) Mineralogical studies on bone apatite and their implications for radiocarbon dating. *Radiocarbon*. **19**, 364–74.

Hawkins, C. L. and Davies, M. J. (2001) Generation and propagation of radical reactions on proteins. *Biochimica et biophysica acta*. **1504** (**2-3**), 196–219.

Hedges, R. E. M. (2002) Bone diagenesis: an overview of processes. *Archaeometry*. **44** (**3**), 319–328.

Hedges, R. E. M. and Law, I. A. (1989) The radiocarbon dating of bone. *Applied geochemistry*. **4** (**3**), 249–253.

Hedges, R. E. M. and Millard, A. R. (1995) Bones and groundwater: towards the modelling of diagenetic processes. *Journal of archaeological science*. **22** (**2**), 155–164.

Hedges, R. E. M., Millard, A. R. and Pike, A. W. G. (1995) Measurements and relationships of diagenetic alteration of bone from three archaeological sites. *Journal of archaeological science*. **22** (**2**), 201–209.

Hefti, E., Trechsel, U., Rüfenacht, H. and Fleisch, H. (1980) Use of Dermestid beetles for cleaning bones. *Calcified tissue international*. **31** (**1**), 45–47.

Hennessy, R. J. and Stringer, C. B. (2002) Geometric morphometric study of the regional variation of modern human craniofacial form. *American journal of physical anthropology*. **117** (**1**), 37–48.

Hesse, B. C. and Wapnish, P. (1985) *Animal bone archaeology: from objectives to analysis*. Washington DC: Taraxacum.

Hexagon Metrology. (2014) *HP-L-20.8: laser scanner for ROMER Absolute Arm*. Cobham, Surrey: Hexagon Manufacturing Intelligence.

Hexagon Metrology. (2015) *ROMER Absolute Arm and RS3*. Cobham, Surrey: Hexagon Manufacturing Intelligence.

Hietala, H. J. (1983) Boker Tachtit: intralevel and interlevel spatial analysis. *Prehistory and paleoenvironments in the Central Negev, Israel*. **3**, 217–281.

High, K., Milner, N., Panter, I. and Penkman, K. E. H. (2015) Apatite for destruction: investigating bone degradation due to high acidity at Star Carr. *Journal of archaeological science*. **59**, 159–168.

High, K., Milner, N., Panter, I., Demarchi, B. and Penkman, K. E. H. (2016) Lessons from Star Carr on the vulnerability of organic archaeological remains to environmental change. *Proceedings of the National Academy of Sciences of the United States of America*. **113** (**46**), 12957–12962.

Hildebolt, C. F. and Vannier, M. W. (1988) Three-dimensional measurement accuracy of skuII surface landmarks. *American journal of physical anthropology*. **76**, 497–503.

Hillier, M. L. and Bell, L. S. (2007) Differentiating human bone from animal bone: a review of histological methods. *Journal of forensic sciences*. **52** (**2**), 249–263.

Hinkes, M. J. (2008) Migrant deaths along the California–Mexico border: an anthropological perspective. *Journal of forensic sciences*. **53** (**1**), 16–20.

Historic England (2016) *Preserving archaeological remains. Decision-taking for sites under development.* Swindon: Historic England.

Hoemann, C. D., Lafantaisie-Favreau, C.-H., Lascau-Coman, V., Chen, G. and Guzmán-Morales, J. (2012) The cartilage-bone interface. *The journal of knee surgery*. **25** (**2**), 85–97.

Holden, J., West, L. J., Howard, A. J., Maxfield, E., Panter, I. and Oxley, J. (2006) Hydrological controls of in situ preservation of waterlogged archaeological deposits. *Earth-Science reviews*. **78** (**1–2**), 59–83.

Holland, A. D. (2000) *An investigation into the effect of soft tissue decomposition on short term degradation of associated textiles, using pig cadavers as an analogue for human remains*. MSc Dissertation, University of Bradford.

Home Office Statistics (2014) *Annual statistics of scientific procedures on living animals Great Britain 2013*. London: Her Majesty's Stationary Office.

Huculak, M. A. and Rogers, T. L. (2009) Reconstructing the sequence of events surrounding body disposition based on color staining of bone. *Journal of forensic sciences*. **54** (**5**), 979–984.

Hugemann, W. (2010) *Correcting lens distortions in digital photographs*. Leverkusen, Germany: Ingenieurbüro Morawski.

Huiskes, R., Ruimerman, R., van Lenthe, G. H. and Janssen, J. D. (2000) Effects of mechanical forces on maintenance and adaptation of form in trabecular bone. *Nature*. **405** (**6787**), 704–706.

Human Tissue Act. (2004) London: Her Majesty's Stationary Office.

Igarashi, T. and Cosgrove, D. (2001) Adaptive unwrapping for interactive texture painting. *Proceedings of the 2001 symposium on interactive 3D graphics*. New York, USA: ACM. 209–216.

Ihrke, I., Kutulakos, K. N., Lensch, H. P. A., Magnor, M. and Heidrich, W. (2010) Transparent and specular object reconstruction. *Computer graphics forum: journal of the European Association for Computer Graphics*. **29** (**8**), 2400–2426.

Inokuchi, S., Sato, K. and Matsuda, F. (1984) Range imaging system for 3-D object recognition. *Proceedings of the international conference on pattern recognition*. 806–808.

International Electrotechnical Commission. (1999) *IEC 60529: Degrees of protection provided by enclosures (IP Code)*. Geneva, Switzerland: International Electrotechnical Commission.

International Organisation for Standardization. (1998)(a) *ISO 6344-1: Coated abrasives: grain size analysis - part 1: grain size distribution test*. International Organisation for Standardization.

International Organisation for Standardization. (1998)(b) *ISO 6344-2: Coated abrasives: grain size analysis - part 2: determination of grain size distribution of macrogrits P12 to P220*. International Organisation for Standardization.

International Organisation for Standardization. (2006) *ISO 2846-1: Graphic technology - colour and transparency of printing ink sets for four-colour printing - part 1: sheet-fed and heat-set web offset lithographic printing*. International Organisation for Standardization.

International Organisation for Standardization. (2013) *ISO 6344-3: Coated abrasives: grain size analysis - part 3: determination of grain size distribution of microgrits P240 to P2500*. International Organisation for Standardization.

International Organization for Standardization. (1992) *Solar energy - Reference solar spectral irradiance at the ground at different receiving conditions. Part 1: direct normal and hemispherical solar irradiance for air mass 1,5. ISO 9845-1*. International Organization for Standardization.

Ioannidou, E. (2003) Taphonomy of animal bones: species, sex, age and breed variability of sheep, cattle and pig bone density. *Journal of archaeological science*. **30** (**3**), 355–365.

Irving, J. T. (1958) A histological stain for newly calcified tissues. *Nature*. **181** (**4610**), 704–705.

Islam, A., Glomski, C. and Henderson, E. S. (1990) Bone lining (endosteal) cells and hematopoiesis: a light microscopic study of normal and pathologic

human bone marrow in plastic-embedded sections. *The anatomical record*. **227** (**3**), 300–306.

Jacques, S. L. (2013) Optical properties of biological tissues: a review. *Physics in medicine and biology*. **58** (**11**), R37–61.

Janaway, R. C. (1987) The preservation of organic materials in association with metal artefacts deposited in inhumation graves. In Boddington, A.,Garland, A. N. and Janaway, R. C. (editors). *Death, decay and reconstruction: approaches to archaeology and forensic science.* Manchester: Manchester University Press. 127–148.

Janaway, R. C. (1996) The decay of buried human remains and their associated materials. In Hunter, J.,Roberts, C. and Martin, A. (editors). *Studies in crime: an introduction to forensic archaeology*. London: Routledge. 58–85.

Janaway, R. C. (2008) The decomposition of materials associated with buried cadavers. In Tibbett, M. and Carter, D. O. (editors). *Soil analysis in forensic taphonomy: chemical and biological effects of buried human remains*. Boca Raton: CRC Press. 154–199.

Janaway, R. C., Wilson, A. S., Holland, A. D. and Baran, E. N. (2003) Taphonomic changes to the buried body and associated materials in an upland peat environment: experiments using pig carcasses as human body analogues. In Lynnerup, N.,Andreasen, C. and Berglund, J. (editors). *Mummies in the new millennium*. Copenhagen: Greenland National Museum and Archives & Danish Polar Center. 56–59.

Janjua, M. A. and Rogers, T. L. (2008) Bone weathering patterns of metatarsal v. femur and the postmortem interval in Southern Ontario. *Forensic science international*. **178** (**1**), 16–23.

Jans, M. M. E. (2008) Microbial bioerosion of bone: a review. In Wisshak, M. and Tapanila, L. (editors). *Current developments in bioerosion*. Berlin Heidelberg: Springer. 397–413.

Jans, M. M. E. (2013) Microscopic destruction of bone. In Pokines, J. T. and Symes, S. A. (editors). *Manual of forensic taphonomy*. Boca Raton: CRC Press. 19–35.

Jans, M. M. E., Nielsen-Marsh, C. M., Smith, C. I., Collins, M. J. and Kars, H. (2004) Characterisation of microbial attack on archaeological bone. *Journal of archaeological science*. **31** (**1**), 87–95.

Janssen, W. (1984) *Forensic histopathology*. Berlin: Springer-Verlag.

Järvinen, T. L., Sievänen, H., Jokihaara, J. and Einhorn, T. A. (2005) Revival of bone strength: the bottom line. *Journal of bone and mineral research*. **20** (**5**), 717–720.

Jee, W. S. S., Bartley, M. H., Cooper, R. R. and Dockum, N. L. (1970) Bone structure. In Andersen, A. C. (editor). *The beagle as an experimental dog*. Ames: Iowa State University Press. 162–188.

Jeon, J.-H., Choi, B.-Y., Kim, C.-M., Kim, J.-H., Kim, H.-Y. and Kim, W.-C. (2015) Three-dimensional evaluation of the repeatability of scanned conventional impressions of prepared teeth generated with white and blue-light scanners. *The journal of prosthetic dentistry*. **114** (**4**), 549–553.

Jerome, C. P., Carlson, C. S., Register, T. C., Bain, F. T., Jayo, M. J., Weaver, D. S. and Adams, M. R. (1994) Bone functional changes in intact, ovariectomized, and ovariectomized, hormone-supplemented adult cynomolgus monkeys (*Macaca fascularis*) evaluated by serum markers and dynamic histomorphometry. *Journal of bone and mineral research*. **9** (**4**), 527–540.

Jerome, C. P., Turner, C. H. and Lees, C. J. (1997) Decreased bone mass and strength in ovariectomized cynomolgus monkeys (Macaca fascicularis). *Calcified tissue international*. **60** (**3**), 265–270.

Jilka, R. L. (2013) The relevance of mouse models for investigating age-related bone loss in humans. *The journals of gerontology. Series A, biological sciences and medical sciences*. **68** (**10**), 1209–1217.

Johnson, E. (1985) Current developments in bone technology. *Advances in archaeological method and theory*. **8**, 157–235.

Joint Committee for Guides in Metrology. (2008) *International vocabulary of metrology: basic general concepts and associated terms (VIM)*. 3rd edition. Sevres, France: Joint Committee for Guides in Metrology.

Joordens, J. C. A., Dupont-Nivet, G., Feibel, C. S., Spoor, F., Sier, M. J., van der Lubbe, J. H. J. L., Nielsen, T. K., Knul, M. V., Davies, G. R. and Vonhof, H. B. (2013) Improved age control on early Homo fossils from the Upper Burgi Member at Koobi Fora, Kenya. *Journal of human evolution*. **65** (**6**), 731–745.

Jordana, F., Colat-Parros, J. and Bénézech, M. (2013) Diagnosis of skull fractures according to postmortem interval: an experimental approach in a porcine model. *Journal of forensic sciences*. **58 Suppl 1**, S156–62.

Jørkov, M. L. S., Heinemeier, J. and Lynnerup, N. (2007) Evaluating bone collagen extraction methods for stable isotope analysis in dietary studies. *Journal of archaeological science*. **34** (**11**), 1824–1829.

Jungers, W. L., Harcourt-Smith, W. E. H., Wunderlich, R. E., Tocheri, M. W., Larson, S. G., Sutikna, T., Due, R. A. and Morwood, M. J. (2009) The foot of *Homo floresiensis*. *Nature*. **459** (**7243**), 81–84.

Junod, C. A. (2013) *Subaerial bone weathering and other taphonomic changes in a temperate climate*. MSc Dissertation, Boston University.

Junod, C. A. and Pokines, J. T. (2013) Subaerial weathering. In Pokines, J. T. and Symes, S. A. (editors). *Manual of forensic taphonomy*. Boca Raton: CRC Press. 287–314.

Junqueira, L. C. and Carneiro, J. (2005) *Basic histology: text and atlas*. London: Appleton and Lange.

Kaasalainen, S., Ahokas, E., Hyyppa, J. and Suomalainen, J. (2005) Study of surface brightness from backscattered laser intensity: calibration of laser data. *IEEE geoscience and remote sensing letters*. **2** (**3**), 255–259.

Kanz, F. and Grossschmidt, K. (2006) Head injuries of Roman gladiators. *Forensic science international*. **160** (**2-3**), 207–216.

Kappelman, J. (1998) Advances in three-dimensional data acquisition and analysis. In Strasser, E.,Fleagle, J. G.,Rosenberger, A. L. and McHenry, H. M. (editors). *Primate locomotion*. New York: Springer US. 205–222.

Karasik, A. and Smilansky, U. (2008) 3D scanning technology as a standard archaeological tool for pottery analysis: practice and theory. *Journal of archaeological science*. **35** (**5**), 1148–1168.

Karsenty, G., Kronenberg, H. M. and Settembre, C. (2009) Genetic control of bone formation. *Annual review of cell and developmental biology*. **25**, 629–648.

Kassab, G. S. and Fung, Y. C. (1994) Topology and dimensions of pig coronary capillary network. *The American journal of physiology*. **267** (**1 Pt 2**), H319–25.

Kibblewhite, M., Tóth, G. and Hermann, T. (2015) Predicting the preservation of cultural artefacts and buried materials in soil. *The science of the total environment*. **529**, 249–263.

Kim, D.-I., Lee, U.-Y., Park, D.-K., Kim, Y.-S., Han, K.-H., Kim, K.-H. and Han, S.-H. (2006) Morphometrics of the hyoid bone for human sex determination from digital photographs. *Journal of forensic sciences*. **51** (**5**), 979–984.

Kini, U. and Nandeesh, B. N. (2012) Physiology of bone formation, remodelling, and metabolism. In Fogelman, I.,Gnanasegaran, G. and van der Wall, H. (editors). *Radionuclide and hybrid bone imaging*. Berlin: Springer-Verlag. 29–57.

van Klinken, G. J. (1999) Bone collagen quality indicators for palaeodietary and radiocarbon measurements. *Journal of archaeological science*. **26** (**6**), 687–695.

Knüsel, C. J. and Outram, A. K. (2006) Fragmentation of the body: comestibles, compost, or customary rite? In Gowland, R. and Knüsel, C. J. (editors). *Social archaeology of funerary remains*. Oxford: Oxbow books. 253–278.

van Kolfschoten, T. (2012) The Schöningen mammalian fauna in biostratigraphical perspective. In Behre, K.-E. (editor). *Die pleistozänen Fundstellen in Schöningen - eine Einführung*. Mainz: Römisch-Germanischen Zentralmuseums. 113–124.

van Kolfschoten, T. (2014) The Palaeolithic locality Schöningen (Germany): a review of the mammalian record. *Quaternary international*. **326-327**, 469–480.

Kontopoulos, I., Nystrom, P. and White, L. (2016) Experimental taphonomy: post-mortem microstructural modifications in *Sus scrofa domesticus* bone. *Forensic science international*. **266**, 320–328.

Koutsoudis, A., Vidmar, B. and Arnaoutoglou, F. (2013) Performance evaluation of a multi-image 3D reconstruction software on a low-feature artefact. *Journal of archaeological science*. **40** (**12**), 4450–4456.

Kress, T. A., Porta, D. J., Snider, J. N., Fuller, P. M., Psihogios, J. P., Heck, W. L., Frick, S. J. and Wasserman, J. F. (1995) Fracture patterns of human cadaver long bones. *Proceedings of the International Research Council on the Biomechanics of Injury conference*. International Research Council on Biomechanics of Injury. 155–169.

Kuhn, J. L., Goldstein, S. A., Ciarelli, M. J. and Matthews, L. S. (1989) The limitations of canine trabecular bone as a model for human: a biomechanical study. *Journal of biomechanics*. **22** (**2**), 95–107.

Kuitems, M., van der Plicht, J., Drucker, D. G., Van Kolfschoten, T., Palstra, S. W. L. and Bocherens, H. (2015) Carbon and nitrogen stable isotopes of well-preserved Middle Pleistocene bone collagen from Schöningen (Germany) and their paleoecological implications. *Journal of human evolution*. **89**, 105–113.

Kukko, A., Kaasalainen, S. and Litkey, P. (2008) Effect of incidence angle on laser scanner intensity and surface data. *Applied optics*. **47** (**7**), 986–992.

Kuz'mina, M. A., Zhuravlev, S. V. and Frank-Kamenetskaya, O. V. (2014) The effect of medium chemistry on the solubility and morphology of brushite crystals. *Geology of ore deposits*. **55** (**8**), 692–697.

Lacroix, M. N. (2013) *A study of the impact of weathering upon the minimal force required to fracture bone*. M.S. thesis, Boston University.

Lang, J., Winsemann, J., Steinmetz, D., Polom, U., Pollok, L., Böhner, U., Serangeli, J., Brandes, C., Hampel, A. and Winghart, S. (2012) The Pleistocene of Schöningen, Germany: a complex tunnel valley fill revealed from 3D subsurface modelling and shear wave seismics. *Quaternary science reviews*. **39**, 86–105.

Langley, G (2009) The validity of animal experiments in medical research. *Revue Semestrielle de Droit Animalier*. **1**,161-168.

Larsen, C. S. (2002) Bioarchaeology: the lives and lifestyles of past people. *Journal of archaeological research*. **10** (**2**), 119–166.

Larson, S. G., Jungers, W. L., Tocheri, M. W., Orr, C. M., Morwood, M. J., Sutikna, T., Awe, R. D. and Djubiantono, T. (2009) Descriptions of the upper limb skeleton of *Homo floresiensis*. *Journal of human evolution*. **57** (**5**), 555–570.

Lartigue, C., Contri, A. and Bourdet, P. (2002) Digitised point quality in relation with point exploitation. *Measurement*. **32**, 193–203.

Laughlin, J. P. and Kelly, R. L. (2010) Experimental analysis of the practical limits of lithic refitting. *Journal of archaeological science*. **37** (**2**), 427–433.

Lawrence, D. R. (1968) Taphonomy and information losses in fossil communities. *Geological Society of America bulletin*. **79** (**10**), 1315–1330.

Lawrence, D. R. (1971) The nature and structure of paleoecology. *Journal of paleontology*. **45** (**4**), 593–607.

Lawrence, D. R. (1979) Biostratinomy. In Fairbridge, R. W. (editor). *Paleontology*. Berlin: Springer-Verlag. 99–102.

Leakey, L. N. (2016a) *Laboratory discussion identifying the find locations for material in the Illeret field research centre and the numbering of the palaeontological collecting areas in the Koobi Fora and Ileret areas of the Turkana Basin, Kenya on Joordens et al. 2013 map.* [Personal communication] 19 February.

Leakey, M. (2016b) *Laboratory discussion on the species identification of fragmentary fossil remains*. [Personal communication] 26 February.

Lees, S. (1989) Sonic velocity and the ultrastructure of mineralised tissues. In Hukins, D. L. (editor). *Calcified tissue*. London: Macmillan Press. 121–152.

Lees, S., Bonar, L. C. and Mook, H. A. (1984) A study of dense mineralized tissue by neutron diffraction. *International journal of biological macromolecules*. **6** (**6**), 321–326.

Lee–Thorp, J. (2002) Two decades of progress towards understanding fossilization processes and isotopic signals in calcified tissue minerals. *Archaeometry*. **44** (**3**), 435–446.

Lee-Thorp, J. A. and van der Merwe, N. J. (1991) Aspects of the chemistry of modern and fossil biological apatites. *Journal of archaeological science*. **18** (**3**), 343–354.

Lee, W. and Jasiuk, I. (2014) Effects of freeze–thaw and micro-computed tomography irradiation on structure–property relations of porcine trabecular bone. *Journal of biomechanics*. **47** (**6**), 1495–1498.

Lennox, F. G., King, M. G., Leaver, I. H., Ramsay, G. C. and Savige, W. E. (1971) Mechanism, prevention, and correction of wool photo-yellowing. *Applied polymer symposia*. **18**. 353-369.

Lichti, D. D. and Harvey, B. R. (2002) The effects of reflecting surface material properties on time-of-flight laser scanner measurements. *Geomatics research australasia*. **76**, 1–9.

Liden, K., Takahashi, C. and Erle Nelson, D. (1995) The effects of lipids in stable carbon isotope analysis and the effects of NaOH treatment on the composition of extracted bone collagen. *Journal of archaeological science*. **22**, 321–326.

Liebschner, M. A. K. (2004) Biomechanical considerations of animal models used in tissue engineering of bone. *Biomaterials*. **25** (**9**), 1697–1714.

Lievers, W. B., Poljsak, A. S., Waldman, S. D. and Pilkey, A. K. (2010) Effects of dehydration-induced structural and material changes on the apparent modulus of cancellous bone. *Medical engineering & physics*. **32** (**8**), 921–925.

Linder, W. (2006) *Digital photogrammetry: a practical course*. 2nd Edition. Berlin: Springer Verlag.

Lindsay, W. L. (1979) *Chemical equilibria in soils*. New York: John Wiley & Sons.

Little, A., Elliott, B., Conneller, C., Pomstra, D., Evans, A. A., Fitton, L. C., Holland, A. D., Davis, R., Kershaw, R., O'Connor, S., O'Connor, T., Sparrow, T., Wilson, A. S., Jordan, P., Collins, M. J., Colonese, A. C., Craig, O. E., Knight, R., Lucquin, A. J. A., Taylor, B. and Milner, N. (2016) Technological analysis of the world's earliest shamanic costume: a multi-scalar, experimental study of a red deer headdress from the Early Holocene Site of Star Carr, North Yorkshire, UK. *PloS one*. **11** (**4**), e0152136.

Littleton, J. (2000) Taphonomic effects of erosion on deliberately buried bodies. *Journal of archaeological science*. **27** (**1**), 5–18.

Liu, D., Wagner, H. D. and Weiner, S. (2000) Bending and fracture of compact circumferential and osteonal lamellar bone of the baboon tibia. *Journal of materials science. Materials in medicine*. **11** (**1**), 49–60.

Liu, Y., Chen, J.-Y., Shang, H.-T., Liu, C.-E., Wang, Y., Niu, R., Wu, J. and Wei, H. (2010) Light microscopic, electron microscopic, and

immunohistochemical comparison of Bama minipig (*Sus scrofa domestica*) and human skin. *Comparative medicine*. **60** (**2**), 142–148.

LMI Technologies. (2015)(a) *HDI 100 series: advanced 3D scanners*. Delta, British Columbia, Canada: LMI Technologies Inc.

LMI Technologies. (2015)(b) *FlexScan3D user manual*. Delta, British Columbia: LMI Technologies.

LMI Technologies. (2016) *HDI Advance: advanced 3D scanners*. Delta, British Columbia, Canada: LMI Technologies Inc.

Loe, L. (2011) Perimortem trauma. In Blau, S. and Ubelaker, D. H. (editors). *Handbook of forensic archaeology and anthropology*. Walnut Creek, California: Left Coast Press Inc. 263–283.

Logozzo, S., Franceschini, G., Kilpelä, A., Caponi, M., Governi, L. and Blois, L. (2011) A comparative analysis of intraoral 3D digital scanners for restorative dentistry. *The internet journal of medical technology*. **5** (**1**), 1–18.

Longin, R. (1971) New method of collagen extraction for radiocarbon dating. *Nature*. **230** (**5291**), 241–242.

Lowe, D. G. (2004) Distinctive image features from scale-invariant keypoints. *International journal of computer vision*. **60** (**2**), 91–110.

Lubarda, V. A., Novitskaya, E. E., McKittrick, J., Bodde, S. G. and Chen, P.-Y. (2012) Elastic properties of cancellous bone in terms of elastic properties of its mineral and protein phases with application to their osteoporotic degradation. *Mechanics of materials*. **44** (**January**), 139–150.

Lucas, B. D. and Kanade, T. (1981) An iterative technique of image registration and its application to stereo. *Proceedings of the international joint conference on artificial intelligence*.

Luebke, K. (2014) Coordinate measuring machine. In Laperrière, L.,Reinhart, G. and The International Academy for Production Engineering (editors). *CIRP*

encyclopedia of production engineering. Berlin Heidelberg: Springer. 285–289.

Lukasewycz, A. and Aturaliya, S. (1999) Experimental forensic and bioanthropological aspects of soft tissue taphonomy: 1. Factors influencing postmortem tissue desiccation rate. *Journal of forensic sciences*. **44** (**5**), 893–896.

Lyell, C. (1833) *Principles of geology: Being an attempt to explain the former changes of the Earth's surface, by reference to causes now in operation*. London: Murray.

Lyman, R. L. (1994) *Vertebrate taphonomy*. Cambridge: Cambridge University Press.

Lyman, R. L. and Fox, G. L. (1989) A critical evaluation of bone weathering as an indication of bone assemblage formation. *Journal of archaeological science*. **16** (**3**), 293–317.

Lyman, R. L. and Fox, G. L. (1996) A critical evaluation of bone weathering as an indication of bone assemblage formation. In Haglund, W. D. and Sorg, M. H. (editors). *Forensic taphonomy: the postmortem fate of human remains*. Boca Raton: CRC Press. 223–247.

Lynnerup, N. (2010) Medical imaging of mummies and bog bodies - a mini-review. *Gerontology*. **56** (**5**), 441–448.

Macaluso, P. J., Jr. (2010) Sex discrimination potential of permanent maxillary molar cusp diameters. *The journal of forensic odonto-stomatology*. **28** (**1**), 22–31.

Macaluso, P. J., Jr. (2011)(a) Sex discrimination from the acetabulum in a twentieth-century skeletal sample from France using digital photogrammetry. *Homo: internationale Zeitschrift fur die vergleichende Forschung am Menschen*. **62** (**1**), 44–55.

Macaluso, P. J., Jr. (2011)(b) Sex discrimination from the glenoid cavity in black South Africans: morphometric analysis of digital photographs. *International journal of legal medicine*. **125** (**6**), 773–778.

Madgwick, R. and Mulville, J. (2012) Investigating variation in the prevalence of weathering in faunal assemblages in the UK: a multivariate statistical approach. *International journal of osteoarchaeology*. **22** (**5**), 509–522.

Manferdini, A. M., Gasperoni, S., Guidi, F. and Marchesi, M. (2016) Unveiling Damnatio Memoriae. The use of 3D digital technologies for the virtual reconstruction of archaeological finds and artefacts. *Virtual archaeology review*. **7** (**15**), 9–17.

Mania, D. (1995) Die geologischen Verhältnisse im Gebiet von Schöningen. In Thieme, H. and Maier, R. (editors). *Archäologische Ausgrabungen im Braunkohlentagebau Schöningen*. Hannover: Hahnsche Buchhandlung. 33–43.

Mann, D. R., Gould, K. G. and Collins, D. C. (1990)(a) A potential primate model for bone loss resulting from medical oophorectomy or menopause. *The journal of clinical endocrinology and metabolism*. **71** (**1**), 105–110.

Manning, D. A. C. (2000) Carbonates and oxalates in sediments and landfill: monitors of death and decay in natural and artificial systems. *Journal of the Geological Society*. **157** (**1**), 229–238.

Mann, R. W., Bass, W. M. and Meadows, L. (1990)(b) Time since death and decomposition of the human body: variables and observations in case and experimental field studies. *Journal of forensic sciences*. **35** (**1**), 103–111.

Mapara, M., Thomas, B. S. and Bhat, K. M. (2012) Rabbit as an animal model for experimental research. *Dental research journal*. **9** (**1**), 111–118.

Maples, W. R. (1998) Trauma analysis by the forensic anthropologist. In Reichs, K. (editor). *Forensic osteology: advances in the identification of human remains*. Springfield: Charles C Thomas. 218–228.

Marean, C. W., Abe, Y., Nilssen, P. J. and Stone, E. C. (2001) Estimating the minimum number of skeletal elements (MNE) in zooarchaeology: a review and a new image-analysis GIS approach. *American antiquity*. **66** (**2**), 333–348.

Marean, C. W. and Spencer, L. M. (1991) Impact of carnivore ravaging on zooarchaeological measures of element abundance. *American antiquity*. **56** (**4**), 645–658.

Marom, E., Krešić-Jurić, S. and Bergstein, L. (2003) Speckle noise in bar-code scanning systems—power spectral density and SNR. *Applied optics*. **42** (**2**), 161–174.

de Marsico, M., Nappi, M. and Riccio, D. (2013) Biometrics using 3D vision techniques. In Zhang, S. (editor). *The handbook of 3D machine vision: optical metrology and imaging*. Boca Raton: CRC Press. 361–386.

Martiniaková, M., Grosskopf, B., Omelka, R., Vondráková, M. and Bauerová, M. (2006) Differences among species in compact bone tissue microstructure of mammalian skeleton: use of a discriminant function analysis for species identification. *Journal of forensic sciences*. **51** (**6**), 1235–1239.

Martini, L., Fini, M., Giavaresi, G. and Giardino, R. (2001) Sheep model in orthopedic research: a literature review. *Comparative medicine*. **51** (**4**), 292–299.

Martinón-Torres, M., Bastir, M., Bermúdez de Castro, J. M., Gómez, A., Sarmiento, S., Muela, A. and Arsuaga, J. L. (2006) Hominin lower second premolar morphology: evolutionary inferences through geometric morphometric analysis. *Journal of human evolution*. **50** (**5**), 523–533.

Martin, R. B. and Burr, D. B. (1982) A hypothetical mechanism for the stimulation of osteonal remodelling by fatigue damage. *Journal of biomechanics*. **15** (**3**), 137–139.

Martin, R. E. (1999) *Taphonomy: a process approach*. Cambridge: Cambridge University Press.

Matousek, P., Clark, I. P., Draper, E. R. C., Morris, M. D., Goodship, A. E., Everall, N., Towrie, M., Finney, W. F. and Parker, A. W. (2005) Subsurface probing in diffusely scattering media using spatially offset Raman spectroscopy. *Applied spectroscopy*. **59** (**4**), 393–400.

Mays, S. (2010) *The archaeology of human bones*. 2nd edition. London: Routledge.

McCarroll, J., Chambers, F. M., Webb, J. C. and Thom, T. (2016) Informing innovative peatland conservation in light of palaeoecological evidence for the demise of *Sphagnum imbricatum*: the case of Oxenhope Moor, Yorkshire, UK. *Mires and peat*. **18**, 1–24.

McFarlin, S. C., Terranova, C. J., Zihlman, A. L., Enlow, D. H. and Bromage, T. G. (2008) Regional variability in secondary remodeling within long bone cortices of catarrhine primates: the influence of bone growth history. *Journal of anatomy*. **213** (**3**), 308–324.

McPherron, S. P., Gernat, T. and Hublin, J.-J. (2009) Structured light scanning for high-resolution documentation of in situ archaeological finds. *Journal of archaeological science*. **36** (**1**), 19–24.

MechInnovation. (2013) *MechScan: high resolution 3D macro scanner*. Leamington Spa: MechInnovation Ltd.

Mellars, P. (1990) A major “plateau” in the radiocarbon time-scale at c. 9650 BP: the evidence from Star Carr (North Yorkshire). *Antiquity*. **64** (**245**), 836–841.

Mellars, P. and Dark, P., editors. (1998) *Star Carr in context: new archaeological and palaeoecological investigations at the Early Mesolithic site of Star Carr, North Yorkshire,*. Cambridge: McDonald Institute for Archaeological Research.

Mériaudeau, F., Rantoson, R., Fofi, D. and Stolz, C. (2012) Review and comparison of non-conventional imaging systems for three-dimensional digitization of transparent objects. *Journal of electronic imaging*. **21** (**2**), 021105–1–021105–5.

Michel, V., Veronique, M., Philippe, I. and Guillaume, M. (1995) Chemical and structural changes in *Cervus elaphus* tooth enamels during fossilization (Lazaret cave): a combined IR and XRD Rietveld analysis. *Applied geochemistry*. **10** (**2**), 145–159.

Mikolajczyk, K., Krystian, M. and Krystian, M. (2004) Scale & affine invariant interest point detectors. *International journal of computer vision*. **60** (**1**), 63–86.

Mikolajczyk, K., Tuytelaars, T., Schmid, C., Zisserman, A., Matas, J., Schaffalitzky, F., Kadir, T. and Van Gool, L. (2005) A comparison of affine region detectors. *International journal of computer vision*. **65** (**1-2**), 43–72.

Miles, C. A., Sionkowska, A., Hulin, S. L., Sims, T. J., Avery, N. C. and Bailey, A. J. (2000) Identification of an intermediate state in the helix-coil degradation of collagen by ultraviolet light. *The Journal of biological chemistry*. **275** (**42**), 33014–33020.

Miller, J. H. (2009) *The large-mammal death assemblage of Yellowstone National Park: historical ecology, conservation biology, paleoecology*. PhD Thesis, University of Chicago.

Milner, N., Conneller, C., Elliott, B., Koon, H., Panter, I., Penkman, K., Taylor, B. and Taylor, M. (2011) From riches to rags: organic deterioration at Star Carr. *Journal of archaeological science*. **38** (**10**), 2818–2832.

Milner, N., Taylor, B., Conneller, C. and Schadla-Hall, T. (2013) *Star Carr: life in Britain after the Ice Age*. York: Council for British Archaeology.

Milz, S., Eckstein, F. and Putz, R. (1995) The thickness of the subchondral plate and its correlation with the thickness of the uncalcified articular cartilage in the human patella. *Anatomy and embryology*. **192** (**5**), 437–444.

Moraitis, K., Eliopoulos, C. and Spiliopoulou, C. (2009) Fracture characteristics of perimortem trauma in skeletal material. *The internet journal of biological anthropology*. **3** (**2**), 585.

Moravec, H. P. (1983) The Stanford Cart and the CMU Rover. *Proceedings of the IEEE*. **71** (**7**), 872–884.

Morin, E., Tsanova, T., Sirakov, N., Rendu, W., Mallye, J.-B. and Lévêque, F. (2005) Bone refits in stratified deposits: testing the chronological grain at Saint-Césaire. *Journal of archaeological science*. **32** (**7**), 1083–1098.

Morse, D., Duncan, J. and Stoutamire, J. (1983) *Handbook of forensic archaeology and anthropology*. Tallahassee: Bills Bookstore.

Moss, J. P., Linney, A. D., Grindrod, S. R., Arridge, S. R. and Clifton, J. S. (1987) Three-dimensional visualization of the face and skull using computerized tomography and laser scanning techniques. *European journal of orthodontics*. **9** (**4**), 247–253.

Moyle, D. D. and Bowden, R. W. (1984) Fracture of human femoral bone. *Journal of biomechanics*. **17** (**3**), 203–213.

Mullender, M. G., van der Meer, D. D., Huiskes, R. and Lips, P. (1996) Osteocyte density changes in aging and osteoporosis. *Bone*. **18** (**2**), 109–113.

Müller, A. H. (1951) Grundlagen der biostratonomie. *Abhandlungen der Deutsche Akademishe Wissenschaft*. **1950**, 1–147.

Müller, A. H. (1963) *Lehrbuch der paläozoologie: 1 allgemeine grundlagen*. Jena: Gustav Fischer Verlag.

Müller, A. H. (1979) Fossilization (taphonomy). In Robinson, R. A. and Teichert, C. (editors). *Treatise on invertebrate paleontology: part A, introduction*. Boulder: Geological Society of America & University of Kansas Press. A2–A78.

Murao, H., Yamamoto, K., Matsuda, S. and Akiyama, H. (2013) Periosteal cells are a major source of soft callus in bone fracture. *Journal of bone and mineral metabolism*. **31** (**4**), 390–398.

Museums and Galleries Scotland. (2009) *Temperature and humidity: advice sheet*. Museums and Galleries Scotland.

Nakakuki, S. (1994) Bronchial tree, lobular division and blood vessels of the pig lung. *The Journal of veterinary medical science / the Japanese Society of Veterinary Science*. **56** (**4**), 685–689.

Nanci, A. (1999) Content and distribution of noncollagenous matrix proteins in bone and cementum: relationship to speed of formation and collagen packing density. *Journal of structural biology*. **126** (**3**), 256–269.

Nawrocki, S. P. (2009) Forensic taphonomy. In Blau, S. and Ubelaker, D. H. (editors). *Handbook of forensic anthropology and archaeology*. Walnut Creek: Left Coast Press. 284–294.

Nayar, S. K. and Gupta, M. (2012) Diffuse structured light. *2012 IEEE international conference on computational photography (ICCP)*. 1–11.

Neves-Petersen, M. T., Gajula, G. P. and Petersen, S. B. (2012) UV light effects on proteins: from photochemistry to nanomedicine. In Saha, S. (editor). *Molecular photochemistry: various aspects*. InTech Open. 125–158.

Newesely, H. (1989) Fossil bone apatite. *Applied geochemistry*. **4** (**3**), 233–245.

Newman, E., Turner, A. S. and Wark, J. D. (1995) The potential of sheep for the study of osteopenia: current status and comparison with other animal models. *Bone*. **16** (**4 Suppl**), 277S–284S.

NextEngine Inc. (2010) *NextEngine 3D scanner ultra HD*. NextEngine

Neyt, J. G., Buckwalter, J. A. and Carroll, N. C. (1998) Use of animal models in musculoskeletal research. *The Iowa orthopaedic journal*. **18**, 118–123.

Nielsen-Marsh, C. M., Gernaey, A. M., Turner-Walker, G., Hedges, R. E. M., Pike, A. W. G. and Collins, M. J. (2000) The chemical degradation of bone. In Cox, M. and Mays, S. (editors). *Human osteology: in archaeology and forensic science*. Cambridge: Cambridge University Press. 439–454.

Nielsen-Marsh, C. M. and Hedges, R. E. M. (1999) Bone porosity and the use of mercury intrusion porosimetry in bone diagenesis studies. *Archaeometry*. **41** (**1**), 165–174.

Nielsen-Marsh, C. M. and Hedges, R. E. M. (2000) Patterns of diagenesis in bone II: effects of acetic acid treatment and the removal of diagenetic CO_3. *Journal of archaeological science*. **27** (**12**), 1151–1159.

Nielsen-Marsh, C. M., Smith, C. I., Jans, M. M. E., Nord, A., Kars, H. and Collins, M. J. (2007) Bone diagenesis in the European Holocene II: taphonomic and environmental considerations. *Journal of archaeological science*. **34** (**9**), 1523–1531.

Nitsch, E. J. (2008) *When pigs fly: a study of computer generated paper folding*. PhD thesis, Texas A&M University.

Niven, L., Steele, T. E., Finke, H., Gernat, T. and Hublin, J.-J. (2009) Virtual skeletons: using a structured light scanner to create a 3D faunal comparative collection. *Journal of archaeological science*. **36** (**9**), 2018–2023.

Nixon, M. S. and Aguado, A. S. (2012) *Feature extraction and image processing for computer vision*. Oxford: Academic Press.

Noble, B. S. (2008) The osteocyte lineage. *Archives of biochemistry and biophysics*. **473** (**2**), 106–111.

North Carolina State University. (2003) *Sheep Facts*. http://www.cals.ncsu.edu/an_sci/extension/animal/4hyouth/sheep/sheepfacts.htm Accessed February 18, 2015.

Ntim, M., Bembey, A., Ferguson, V. and Bushby, A. (2005) Hydration effects on the viscoelastic properties of collagen. *MRS online proceedings library archive*. **898**, 2–7.

van Oers, R. F. M., Ruimerman, R., Tanck, E., Hilbers, P. A. J. and Huiskes, R. (2008) A unified theory for osteonal and hemi-osteonal remodelling. *Bone*. **42** (**2**), 250–259.

d' Orbigny, A. (1849) *Cours élémentaire de paléontologie et de géologie stratigraphiques*. Paris: Masson.

Ordnance Survey. (2016)(a) *East Yorkshire*. Ordnance Survey.

Ordnance Survey. (2016)(b) *Bradford and Huddersfield*. Ordnance Survey.

Ordnance Survey. (2016)(c) *Bradford*. Ordnance Survey.

Osorio, M. F., Salazar, A., Prieto, F., Boulanger, P. and Figueroa, P. (2012) Three-dimensional digitization of highly reflective and transparent objects using multi-wavelength range sensing. *Machine vision and applications*. **23** (**4**), 761–772.

Ozcelikkale, A. and Han, B. (2016) Thermal destabilization of collagen matrix hierarchical structure by freeze/thaw. *PloS one*. **11** (**1**), 1–18.

Özkaya, N., Nordin, M., Goldsheyder, D. and Leger, D. (2012) *Fundamentals of biomechanics: equilibrium, motion, and deformation*. New York: Springer Science & Business Media.

Paine, G. (1937) Fossilization of bone. *American journal of science*. **34** (**200**), 148–157.

Pal, S. and Saha, S. (1989) Coefficient of thermal expansion of bone. In Sahay, K. B. and Saxena, R. K. (editors). *Biomechanics*. New York: John Wiley & Sons. 52–60.

Payne, J. A. (1965) A summer carrion study of the baby pig *Sus scrofa linnaeus*. *Ecology*. **46** (**5**), 592–602.

Payne, J. A. and King, E. W. (1969) Lepidoptera associated with pig carrion. *Journal of the Lepidopterists' society*. **23** (**3**), 191–195.

Payne, J. A., King, E. W. and Beinhart, G. (1968)(a) Arthropod succession and decomposition of buried pigs. *Nature*. **219** (**5159**), 1180–1181.

Payne, J. A., Mead, F. W. and King, E. W. (1968)(b) Hemiptera associated with pig carrion. *Annals of the Entomological Society of America*. **61** (**3**), 565–567.

Pearce, A. I., Richards, R. G., Milz, S., Schneider, E. and Pearce, S. G. (2007) Animal models for implant biomaterial research in bone: a review. *European cells & materials*. **13**, 1–10.

Pechníková, M., Porta, D. and Cattaneo, C. (2011) Distinguishing between perimortem and postmortem fractures: are osteons of any help? *International journal of legal medicine*. **125** (**4**), 591–595.

Petrou, M. and Petrou, C. (2010) *Image processing: the fundamentals*. 2nd edition. Chichester: John Wiley & Sons.

Pfretzschner, H. U. (2000) Microcracks and fossilization of Haversian bone. *Neues jahrbuch fur geologie und palaontologie abhandlungen*. **216** (**3**), 413–432.

Pfretzschner, H.-U. (2004) Fossilization of Haversian bone in aquatic environments. *Comptes rendus. Palevol*. **3** (**6–7**), 605–616.

Pfretzschner, H.-U. (2006) Collagen gelatinization: the key to understand early bone-diagenesis. *Palaeontographica Abteilung A*. **278** (**1-6**), 135–148.

Pidaparti, R. M. and Turner, C. H. (1997) Cancellous bone architecture: advantages of nonorthogonal trabecular alignment under multidirectional joint loading. *Journal of biomechanics*. **30** (**9**), 979–983.

Piepenbrink, H. (1986) Two examples of biogenous dead bone decomposition and their consequences for taphonomic interpretation. *Journal of archaeological science*. **13** (**5**), 417–430.

Piepenbrink, H. (1989) Examples of chemical changes during fossilisation. *Applied geochemistry*. **4** (**3**), 273–280.

Pike, A., Nielsen-Marsh, C. M. and Hedges, R. E. (2001) Modelling bone dissolution under different hydrological regimes. In Millard, A. (editor). *Proceedings of Archaeological Sciences 1997: Proceedings of the conference held at the University of Durham, 2nd-4th September 1997*. BAR International Series 939. Oxford: BAR publishing. 127–132.

Plavcan, J. M., Hammond, A. S. and Ward, C. V. (2014) Brief communication: calculating hominin and nonhuman anthropoid femoral head diameter from acetabular size. *American journal of physical anthropology*. **155** (**3**), 469–475.

Pokines, J. T. (2016) Taphonomic alterations to terrestrial surface-deposited human osseous remains in a New England environment. *Journal of forensic identification*. **66** (**1**), 59–78.

Pokines, J. T. and De La Paz, J. S. (2016) Recovery rates of human fetal skeletal remains using varying mesh sizes. *Journal of forensic sciences*. **61 Suppl 1**, S184–9.

Pokines, J. T., King, R. E., Graham, D. D., Costello, A. K., Adams, D. M., Pendray, J. M., Rao, K. and Siwek, D. (2016/4) The effects of experimental freeze-thaw cycles to bone as a component of subaerial weathering. *Journal of archaeological science: reports*. **6**, 594–602.

Polhemus. (2011) *FastSCAN Cobra C1: handheld laser scanner user manual*. Colchester, Vermont: Polhemus.

Pollard, A. M. and Heron, C. (2008) *Archaeological chemistry*. 2nd edition. Cambridge: Royal Society of Chemistry.

Pollefeys, M., Nistér, D., Frahm, J.-M., Akbarzadeh, A., Mordohai, P., Clipp, B., Engels, C., Gallup, D., Kim, S.-J., Merrell, P., Salmi, C., Sinha, S., Talton, B., Wang, L., Yang, Q., Stewénius, H., Yang, R., Welch, G. and Towles, H. (2007) Detailed real-time urban 3D reconstruction from video. *International journal of computer vision*. **78** (**2-3**), 143–167.

Porter, S. T., Huber, N., Hoyer, C. and Floss, H. (2016) Portable and low-cost solutions to the imaging of Paleolithic art objects: a comparison of photogrammetry and reflectance transformation imaging. *Journal of archaeological science: reports*. **10**, 859–863.

Powell, B. J., Passalacqua, N. V., Baumer, T. G., Fenton, T. W. and Haut, R. C. (2012) Fracture patterns on the infant porcine skull following severe blunt impact. *Journal of forensic sciences*. **57** (**2**), 312–317.

Powell, B. J., Passalacqua, N. V., Fenton, T. W. and Haut, R. C. (2013) Fracture characteristics of entrapped head impacts versus controlled head drops in infant porcine specimens. *Journal of forensic sciences*. **58** (**3**), 678–683.

Prassack, K. A. (2011) The effect of weathering on bird bone survivorship in modern and fossil saline-alkaline lake environments. *Paleobiology*. **37** (**04**), 633–654.

Pribanić, T., Mrvoš, S. and Salvi, J. (2010) Efficient multiple phase shift patterns for dense 3D acquisition in structured light scanning. *Image and vision computing*. **28** (**8**), 1255–1266.

Proffitt, T. and de la Torre, I. (2014) The effect of raw material on inter-analyst variation and analyst accuracy for lithic analysis: a case study from Olduvai Gorge. *Journal of archaeological science*. **45**, 270–283.

Rabotyagova, O. S., Cebe, P. and Kaplan, D. L. (2008) Collagen structural hierarchy and susceptibility to degradation by ultraviolet radiation. *Materials science & engineering. C, materials for biological applications*. **28** (**8**), 1420–1429.

Rai, R. K. and Sinha, N. (2011) Dehydration-induced structural changes in the collagen–hydroxyapatite interface in bone by high-resolution solid-state NMR spectroscopy. *Journal of physical chemistry C*. **115** (**29**), 14219–14227.

Rak, M. and Woźniak, A. (2012) The influence of properties of a measured object on the surface digitalization performed by a laser scanner integrated with measuring arm. *Pomiary, Automatyka, Robotyka*. **16**, 76–81.

Ranzuglia, G., Callieri, M., Dellepiane, M., Cignoni, P. and Scopigno, R. (2013) MeshLab as a complete tool for the integration of photos and color with high resolution 3D geometry data. In Earl, G.,Sly, T.,Chrysanthi, A.,Murrieta-Flores, P.,Papadopoulos, C.,Romanowska, I. and Wheatley, D. (editors). *Archaeology in the digital era. Papers from the 40th annual conference of computer applications and quantitative methods in archaeology (CAA), Southampton, 26-29 March 2012.* Amsterdam: Computer applications and quantitative methods in archaeology (CAA). 406–416.

Reed, H. B. (1958) A study of dog carcass communities in Tennessee, with special reference to the insects. *The American midland naturalist*. **59** (**1**), 213–245.

Rees, D. A. (2000) The refitting of lithics from unit 4C, area Q2/D excavations at Boxgrove, West Sussex, England. *Lithic technology*. **25** (**2**), 120–134.

Rees, W. (1990) *Physical principles of remote sensing*. Cambridge: Cambridge University Press.

Reiche, I., Vignaud, C. and Menu, M. (2002) The crystallinity of ancient bone and dentine: new insights by transmission electron microscopy. *Archaeometry*. **44** (**3**), 447–459.

Reilly, D. T. and Burstein, A. H. (1975) The elastic and ultimate properties of compact bone tissue. *Journal of biomechanics*. **8** (**6**), 393–405.

Reilly, D. T., Burstein, A. H. and Frankel, V. H. (1974) The elastic modulus for bone. *Journal of biomechanics*. **7** (**3**), 271–275.

Remondino, F. (2014) Photogrammetry: basic theory. In Remondino, F. and Campana, S. (editors). *3D recording and modelling in archaeology and cultural heritage*. Oxford: Archaeopress. 63–86.

Remondino, F. and Fraser, C. (2006) Digital camera calibration methods: considerations and comparisons. *International archives of photogrammetry, remote sensing and spatial information sciences*. **36** (**5**), 266–272.

Rey, C., Renugopalakrishnan, V., Shimizu, M., Collins, B. and Glimcher, M. J. (1991) A resolution-enhanced Fourier transform infrared spectroscopic study of the environment of the CO_3^{2-} ion in the mineral phase of enamel during its formation and maturation. *Calcified tissue international*. **49** (**4**), 259–268.

Rho, J. Y. and Pharr, G. M. (1999) Effects of drying on the mechanical properties of bovine femur measured by nanoindentation. *Journal of materials science. Materials in medicine*. **10** (**8**), 485–488.

Richards, M. P. and Hedges, R. E. M. (1999) Stable isotope evidence for similarities in the types of marine foods used by Late Mesolithic humans at sites along the Atlantic coast of Europe. *Journal of archaeological science*. **26** (**6**), 717–722.

Riel-Salvatore, J., Bae, M., McCartney, P. and Razdan, A. (2002) Palaeolithic archaeology and 3D visualization technology: recent developments. *Antiquity*. **76** (**294**), 929–930.

Riley, M. S. and Collins, M. J. (1994) The polymer model of collagen degradation. *Polymer degradation and stability*. **46** (**1**), 93–97.

Riso, E.-M., Kaasik, P. and Seene, T. (2016) Remodelling of skeletal muscle extracellular matrix: effect of unloading and reloading. In Travascio, F. (editor). *Composition and function of the extracellular matrix in the human body*. InTech Open Science. 45–68.

Roach, H. I. (1994) Why does bone matrix contain non-collagenous proteins? The possible roles of osteocalcin, osteonectin, osteopontin and bone sialoprotein in bone mineralisation and resorption. *Cell biology international*. **18** (**6**), 617–628.

Roberts, W. E., Smith, R. K., Zilberman, Y., Mozsary, P. G. and Smith, R. S. (1984) Osseous adaptation to continuous loading of rigid endosseous implants. *American journal of orthodontics*. **86** (**2**), 95–111.

Robson, H. K., Little, A., Jones, A. K. G., Blockley, S., Candy, I., Matthews, I., Palmer, A., Schreve, D., Tong, E., Pomstra, D., Fletcher, L., Hausmann, N., Taylor, B., Conneller, C. and Milner, N. (2016) Scales of analysis: evidence of fish and fish processing at Star Carr. *Journal of Archaeological Science: Reports*.

Rolfe, W. D. I. and Brett, D. W. (1969) Fossilization processes. In Eglinton, G. and Murphy, M. T. J. (editors). *Organic geochemistry: methods and results*. Berlin: Springer. 231–244.

Rosell, J., Blasco, R., Fernández-Laso, M. C., Vaquero, M. and Carbonell, E. (2012) Connecting areas: faunal refits as a diagnostic element to identify synchronicity in the Abric Romaní archaeological assemblages. *Quaternary international: the journal of the International Union for Quaternary Research*. **252**, 56–67.

Ross, A. H. and Cunningham, S. L. (2011) Time-since-death and bone weathering in a tropical environment. *Forensic science international*. **204** (**1-3**), 126–133.

de la Roza, G. and Damron, T. A. (2016) *Mature trabecular bone exhibits lamellae and osteocytes between the lamellae.* Digital Image. http://emedicine.medscape.com/article/1254517-overview#a2. Accessed: July 1, 2016

RSI 3D systems. (2013) *PicoScan optical 3D digitizer*. http://www.rsi-3dsystems.de/content/en/picoscan Accessed September 22, 2016.

Rudakova, T. E. and Zaikov, G. E. (1987) Degradation of collagen and its possible applications in medicine. *Polymer degradation and stability*. **18** (**4**), 271–291.

Rusinkiewicz, S. and Levoy, M. (2001) Efficient variants of the ICP algorithm. *Proceedings third international conference on 3-D digital imaging and modelling*. 145–152.

Salarashayeri, A. F. and Siosemarde, K. M. (2012) Prediction of soil hydraulic conductivity from particle-size distribution. *International journal of environmental, chemical, ecological, geological and geophysical engineering*. **6** (**1**), 16–20.

Salvi, J., Fernandez, S., Pribanic, T. and Llado, X. (2010) A state of the art in structured light patterns for surface profilometry. *Pattern recognition*. **43** (**8**), 2666–2680.

Salvi, J., Pagès, J. and Batlle, J. (2004) Pattern codification strategies in structured light systems. *Pattern recognition*. **37** (**4**), 827–849.

Sam Houston State University. (2015) *Southest Texas Applied Forensic Science Faculty*. http://www.shsu.edu/~stafs/ Accessed February 17, 2015.

Sampath, T. K. and Reddi, A. H. (1983) Homology of bone-inductive proteins from human, monkey, bovine, and rat extracellular matrix. *Proceedings of*

the National Academy of Science of the United States of America. **80** (**21**), 6591–6595.

van der Sanden, W. (1996) *Through nature to eternity. The bog people of Northwest Europe*. Assen: Drents Museum.

Sanford, K. R., Farmerie, M. R. and Pastorial, R. G. (2012) Friction ridge skin: preliminary study of nonhuman primates. In Jamieson, A. and Moessons, A. (editors). *Wiley encyclopedia of forensic science*. Wiley Online Library. http://onlinelibrary.wiley.com/doi/10.1002/9780470061589.fsa1018 . Accessed May 3, 2015.

Santolaria, J., Pastor, J. J., Brosed, F. J. and Aguilar, J. J. (2009) A one-step intrinsic and extrinsic calibration method for laser line scanner operation in coordinate measuring machines. *Measurement science & technology*. **20** (**4**), 045107.

Sarmiento, A. and Latta, L. L. (1995) *Functional fracture bracing: tibia, humerus, and ulna*. Berlin: Springer-Verlag.

Savara, B. S., Steen, J. C. and Vannier, M. W. (1986) Applications of biostereometrics to biomedical and anthropological research. *1985 international technical symposium/Europe*. International Society for Optics and Photonics. 148–155.

Schäfer, H., Prus, M., Meyer, Q., Süß, J. and Stamminger, M. (2012) Multiresolution attributes for tessellated meshes. *Proceedings of the ACM SIGGRAPH symposium on interactive 3D graphics and games*. New York, USA: ACM. 175–182.

Scheuer, L. and Black, S. (2004) *The juvenile skeleton*. London: Elsevier Academic Press.

Schindler, K. (2015) Mathematical foundations of photogrammetry. In Freeden, W.,Nashed, M. Z. and Sonar, T. (editors). *Handbook of geomathematics*. 2nd edition. Berlin: Springer - Verlag. 3087–3103.

Schmuck, T., Altermatt, S., Büchler, P., Klima-Lange, D., Krieg, A., Lutz, N., Muermann, J., Slongo, T., Sossai, R. and Hasler, C. (2010) Greenstick

fractures of the middle third of the forearm. A prospective multi-centre study. *European journal of pediatric surgery*. **20** (**5**), 316–320.

Schoenly, K. G., Haskell, N. H., Hall, R. D. and Gbur, J. R. (2007) Comparative performance and complementarity of four sampling methods and arthropod preference tests from human and porcine remains at the Forensic Anthropology Center in Knoxville, Tennessee. *Journal of medical entomology*. **44** (**5**), 881–894.

Scholz, H. and Glaubrecht, M. (2013) Shell and operculum taphonomy of the Bithyniid gastropod *Gabbiella* in the Pleistocene Turkana Basin, North Kenya. *Journal of paleontology*. **87** (**1**), 84–90.

Schotsmans, E. M. J., Denton, J., Dekeirsschieter, J., Ivaneanu, T., Leentjes, S., Janaway, R. C. and Wilson, A. S. (2012) Effects of hydrated lime and quicklime on the decay of buried human remains using pig cadavers as human body analogues. *Forensic science international*. **217** (**1-3**), 50–59.

Schultz, M. (2001) Paleohistopathology of bone: a new approach to the study of ancient diseases. *American journal of physical anthropology*. **Suppl 33**, 106–147.

Schwarcz, H. P., Hedges, R. E. M., Ivanovich, M., Pate, F. D., Hutton, J. T. and Norrish, K. (1989) Ionic exchange between soil solution and bone: toward a predictive model. *Applied geochemistry*. **4** (**3**), 303–316.

Schwiedrzik, J., Raghavan, R., Bürki, A., LeNader, V., Wolfram, U., Michler, J. and Zysset, P. (2014) In situ micropillar compression reveals superior strength and ductility but an absence of damage in lamellar bone. *Nature materials*. **13** (**7**), 740–747.

Seilacher, A. (1973) Biostratinomy: the sedimentology of biologically standardized particles. In Ginsburg, R. N. (editor). *Evolving concepts in sedimentology*. Baltimore: John Hopkins University Press. 159–177.

Seilacher, A. (1984) Sedimentary structures tentatively attributed to seismic events. *Marine geology*. **55** (**1984**), 1–12.

Seilacher, A. (1992) Event stratigraphy: a dynamic view of the sedimentary record. In Brown, G.,Hawkesworth, C. and Wilson, C. (editors). *Understanding the Earth*. Cambridge: Cambridge University Press. 375–385.

Serangeli, J., Böhner, U., Haßmann, H. and Conard, N. J. (2012) Die Pleistozänen Fundstellen in Schöningen - eine Einführung. In Behre, K.-E. (editor). *Die chronologische Einordnung der Paläolithischen Fundstellen von Schöningen*. Mainz: Römisch-Germanischen Zentralmuseums. 1–22.

Serangeli, J., Böhner, U., Van Kolfschoten, T. and Conard, N. J. (2015) Overview and new results from large-scale excavations in Schöningen. *Journal of human evolution*. **89**, 27–45.

Shape Analysis. (2012) *Shape analysis*. www.shapeanalysis.com Accessed April 20, 2015.

Shipman, P. (1990) *Life history of a fossil: an introduction to taphonomy and palaeoecology*. Cambridge, USA: Harvard University Press.

Shipman, P. L. (1977) *Paleoecology, taphonomic history, and population dynamics of the vertebrate fossil assemblage from the Middle Miocene deposits exposed at Fort Ternan, Kenya*. PhD Thesis, New York: New York University.

Sholts, S. B., Wärmländer, S. K. T. S., Flores, L. M., Miller, K. W. P. and Walker, P. L. (2010) Variation in the measurement of cranial volume and surface area using 3D laser scanning technology. *Journal of forensic sciences*. **55** (**4**), 871–876.

Sierralta, M., Frechen, M. and Urban, B. (2012) 230Th/U dating results from opencast mine Schöningen. In Behre, K.-E. (editor). *Die pleistozänen Fundstellen in Schöningen - eine Einführung*. Mainz: Römisch-Germanischen Zentralmuseums. 143–154.

Sillen, A. (1989) Diagenesis of the inorganic phase of cortical bone. In Price, T. D. (editor). *The chemistry of prehistoric human bone.* Cambridge: Cambridge University Press. 211–229.

Simmons, T., Adlam, R. E. and Moffatt, C. (2010)(a) Debugging decomposition data: comparative taphonomic studies and the influence of insects and carcass size on decomposition rate. *Journal of forensic sciences*. **55** (**1**), 8–13.

Simmons, T., Cross, P. A., Adlam, R. E. and Moffatt, C. (2010)(b) The influence of insects on decomposition rate in buried and surface remains. *Journal of forensic sciences*. **55** (**4**), 889–892.

Singh, I. J., Tonna, E. A. and Gandel, C. P. (1974) A comparative histological study of mammalian bone. *Journal of morphology*. **144** (**4**), 421–437.

Sisk, M. L. and Shea, J. J. (2008) Intrasite spatial variation of the Omo Kibish Middle Stone Age assemblages: artifact refitting and distribution patterns. *Journal of human evolution*. **55** (**3**), 486–500.

Skabek, K. and Kowalski, P. (2009) Building the models of cultural heritage objects using multiple 3D scanners. *Theoretical and applied informatics*. **21** (**2**), 115–129.

Skedros, J. G., Holmes, J. L., Vajda, E. G. and Bloebaum, R. D. (2005) Cement lines of secondary osteons in human bone are not mineral-deficient: new data in a historical perspective. *The anatomical record. Part A, discoveries in molecular, cellular, and evolutionary biology*. **286** (**1**), 781–803.

Slizewski, A., Friess, M. and Semal, P. (2010) Surface scanning of anthropological specimens: nominal-actual comparison with low cost laser scanner and high end fringe light projection surface scanning systems. *Quartär*. **57**, 179–187.

Smith, A. C. (2014) The effects of sharp-force thoracic trauma on the rate and pattern of decomposition. *Journal of forensic sciences*. **59** (**2**), 319–326.

Smith, A. C., Spinale, F. G. and Swindle, M. M. (1990) Cardiac function and morphology of Hanford miniature swine and Yucatan miniature and micro swine. *Laboratory animal science*. **40** (**1**), 47–50.

Smith, C. (2002) *Modelling diagenesis in archaeological bone*. PhD thesis, University of Newcastle-upon-Tyne.

Smith, C. I., Nielsen-Marsh, C. M., Jans, M. M. E. and Collins, M. J. (2007) Bone diagenesis in the European Holocene I: patterns and mechanisms. *Journal of archaeological science*. **34** (**9**), 1485–1493.

Smith, J. W. (1960) Collagen fibre patterns in mammalian bone. *Journal of anatomy*. **94** (**Pt 3**), 329–344.

Smith, M. J., Allen, M. J., Delbarre, G., Booth, T., Cheetham, P., Bailey, L., O'Malley, F., Pearson, M. P. and Green, M. (2016) Holding on to the past: Southern British evidence for mummification and retention of the dead in the Chalcolithic and Bronze Age. *Journal of Archaeological Science: Reports.* **10**, 744–756.

Smith, N. E. and Strait, S. G. (2008) PaleoView3D: from specimen to online digital model. *Palaeontologia Electronica*. **11** (**2**), 1-17.

Smith, W. A. P. and Hancock, E. R. (2006) Recovering facial shape using a statistical model of surface normal direction. *IEEE transactions on pattern analysis and machine intelligence*. **28** (**12**), 1914–1930.

Smithsonian Institute. (2016) *Smithsonian X 3D*. http://3d.si.edu/ Accessed May 25, 2016.

Snavely, N., Seitz, S. M. and Szeliski, R. (2007) Modeling the world from internet photo collections. *International journal of computer vision*. **80** (**2**), 189–210.

Sonka, M., Hlavac, V. and Boyle, R. (2015) *Image processing, analysis, and machine vision*. 4th edition. Andover, Hampshire: Cengage Learning.

Soudarissanane, S., Van Ree, J., Bucksch, A. and Lindenbergh, R. (2007) Error budget of terrestrial laser scanning: influence of the incidence angle on the scan quality. *Proceedings 3D-NordOst*., 1–8.

Southern Illinois University. (2015) *Complex for Forensic Anthropology Research*. http://cola.siu.edu/anthro/cfar/ Accessed February 17, 2015.

Sparrow, T., Ugail, H., Holland, A.D., Evans, A., and Wilson, A.S. (In Prep) Automated digital refit of fragmentary archaeological materials: technical challenges to computer characterisation and segmentation of fracture surfaces in bone and lithics.

Spencer, M. A. and Spencer, G. S. (1995) Technical note: video-based three-dimensional morphometrics. *American journal of physical anthropology*. **96** (**4**), 443–453.

Sponheimer, M. and Lee-Thorp, J. A. (1999) Alteration of enamel carbonate environments during fossilization. *Journal of archaeological science*. **26** (**2**), 143–150.

Stackelbeck, K. L. (2000) *Big Eddy site: Lithic refit analysis, site structure, and late Paleoindian settlement patterns*. publisher not identified.

Stackelbeck, K. L. (2010) Maximizing the research potential of refit analysis without replicating Pincevent: a case study from the Big Eddy site in Southwest Missouri. *Lithic technology*. **35** (**1**), 37–62.

Stanco, F., Battiato, S. and Gallo, G. (2011)(a) *Digital imaging for cultural heritage preservation: analysis, restoration, and reconstruction of ancient artworks*. Boca Raton: CRC Press.

Stanco, F., Tanasi, D. and Gallo, G. (2011)(b) Virtual restoration of fragmented glass plate photographs of archaeological repertoires. *Virtual archaeology review*. **2** (**3**), 141–144.

Starkovich, B. M. and Conard, N. J. (2015) Bone taphonomy of the Schöningen “Spear Horizon South” and its implications for site formation and hominin meat provisioning. *Journal of human evolution*. **89**, 154–171.

Stephens, B. G. and Heglar, R. (1989) Use of glue gun in forensic anthropology and pathologic bone reconstruction cases. *Journal of forensic sciences*. **34** (**2**), 454–457.

Stevens, W. P. (1997) Reconstruction of three-dimensional anatomical landmark coordinates using video-based stereophotogrammetry. *Journal of anatomy*. **191 (Pt 2)**, 277–284.

Stokes, K. L., Forbes, S. L., Benninger, L. A., Carter, D. O. and Tibbett, M. (2009)(a) Decomposition studies using animal models in contrasting environments: evidence from temporal changes in soil chemistry and microbial activity. *Criminal and environmental soil forensics*. Springer Netherlands. 357–377.

Stokes, K. L., Forbes, S. L. and Tibbett, M. (2009)(b) Freezing skeletal muscle tissue does not affect its decomposition in soil: evidence from temporal changes in tissue mass, microbial activity and soil chemistry based on excised samples. *Forensic science international*. **183** (**1-3**), 6–13.

Stokes, K. L., Forbes, S. L. and Tibbett, M. (2013) Human versus animal: contrasting decomposition dynamics of mammalian analogues in experimental taphonomy. *Journal of forensic sciences*. **58** (**3**), 583–591.

Stoessel, A., David, R., Gunz, P., Schmidt, T., Spoor, F. and Hublin, J.-J. (2016) Morphology and function of Neandertal and modern human ear ossicles. *Proceedings of the National Academy of Sciences of the United States of America*. **113** (**41**), 11489–11494.

Stone, S. (2015), *An in depth discussion on the calibration standards, error propagation and new scanner development during the BABAO annual conference 2015*. [Personal communication] 18 September

Stone, T. T., Dickel, D. N. and Doran, G. H. (1990) The preservation and conservation of waterlogged bone from the Windover site, Florida: a comparison of methods. *Journal of field archaeology*. **17** (**2**), 177–186.

Strait, S. and Smith, N. (2006) PaleoView3D: an interactive database of mammals from the Paleocene/Eocene boundary. *Journal of vertebrate paleontology*. Society for Vertebrate Paleontology. 129A–129A.

Strait, S., Smith, N. and Penkrott, T. (2007) The promise of low cost 3D laser scanners. *Journal of Vertebrate Paleontology*. **27**.

Stylianidis, E., Georgopoulos, A. and Remondino, F. (2016) Basics of image-based modelling techniques in cultural heritage 3D recording. In Stylianidis, E. and Remondino, F. (editors). *3D recording, documentation*

and management of cultural heritage. Dunbeath: Whittles Publishing. 253–304.

Sutcliffe, A. J. (1990) Rates of decay of mammalian remains in the permafrost environment of the Canadian High Arctic. *Canada's missing dimension: science and history in the Canadian Arctic Islands*. **1**, 161–186.

Su, X., Sun, K., Cui, F. Z. and Landis, W. J. (2003) Organization of apatite crystals in human woven bone. *Bone*. **32** (**2**), 150–162.

Swindle, M. M., Makin, A., Herron, A. J., Clubb, F. J. and Frazier, K. S. (2012) Swine as models in biomedical research and toxicology testing. *Veterinary pathology online*. **49** (**2**), 344–356.

Swindle, M. M. and Smith, A. C. (1998) Comparative anatomy and physiology of the pig. *Scandinavian journal of laboratory animal science*. **25**, 11–22.

Tanner, P. (2013) *Newport medieval ship project - digital reconstruction and analysis of the Newport ship*. Newport Museum.

Tappen, M. (1994) Bone weathering in the tropical rain forest. *Journal of archaeological science*. **21** (**5**), 667–673.

Tappen, N. C. and Peske, G. R. (1970) Weathering cracks and split-line patterns in archaeological bone. *American antiquity*. **35** (**3**), 383–386.

Taylor, J., Blais, F., Beraldin, J.-A., Godin, G., Borgeat, L., El-Hakim, S. F., Paquet, E., Cournoyer, L., Picard, M., Rioux, M., Lahanier, C. and Aitken, G. (2005) NRC's 3D technology for museum and heritage applications. In Salimbeni, R. and Pezzati, L. (editors). *Optical methods for art and archaeology. Proceedings of SPIE.* Bellingham, WA: SPIE. 585708–1–585708–11.

Texas State University. (2013) *Forensic Anthropology Research Facility*. Texas State University San Marcos. http://www.txstate.edu/anthropology/facts/labs/farf.html Accessed February 17, 2015.

Texier, J. P., Bertran, P., Coutard, J. P., Francou, B., Gabert, P., Guadelli, J. L., Ozouf, J. C., Plisson, H., Raynal, J. P. and Vivent, D. (1998) TRANSIT, an experimental archaeological program in periglacial environment: problem, methodology, first results. *Geoarchaeology*. **13** (**5**), 433–473.

Thieme, H. (1997) Lower Palaeolithic hunting spears from Germany. *Nature*. **385** (**6619**), 807–810.

Thieme, H. (1999) Altpaläolithische Holzgeräte aus Schöningen, Lkr. Helmstedt: Bedeutsame Funde zur Kulturentwicklung des frühen Menschen. *Germania*. **77** (**2**), 451–487.

Thompson, D. D., Simmons, H. A., Pirie, C. M. and Ke, H. Z. (1995) FDA guidelines and animal models for osteoporosis. *Bone*. **17** (**4 Suppl**), S125–S133.

Thompson, T. (2002) The assessment of sex in cremated individuals: some cautionary notes. *Canadian Society of Forensic Science journal*. **35** (**2**), 49–56.

Thurner, P. J., Chen, C. G., Ionova-Martin, S., Sun, L., Harman, A., Porter, A., Ager, J. W., 3rd, Ritchie, R. O. and Alliston, T. (2010) Osteopontin deficiency increases bone fragility but preserves bone mass. *Bone*. **46** (**6**), 1564–1573.

Todisco, D. and Monchot, H. (2008) Bone weathering in a periglacial environment: the Tayara site (KbFk-7), Qikirtaq Island, Nunavik (Canada). *Arctic*. **61** (**1**), 87–101.

Toneva, D., Nikolova, S. and Georgiev, I. (2016) Reliability and accuracy of angular measurements on laser scanning created 3D models of dry skulls. *Journal of Anthropology*. **2016**.

Tremayne, A. (2010) An analysis of Denbigh flint complex burin technology from Matcharak Lake, Alaska. *Alaska Journal of Anthropology*. **8** (**1**), 73–86.

Trueman, C. N. G., Behrensmeyer, A. K., Tuross, N. and Weiner, S. (2004) Mineralogical and compositional changes in bones exposed on soil surfaces in Amboseli National Park, Kenya: diagenetic mechanisms and

the role of sediment pore fluids. *Journal of archaeological science*. **31** (**6**), 721–739.

Trueman, C. N. and Martill, D. M. (2002) The long–term survival of bone: the role of bioerosion. *Archaeometry*. **44** (**3**), 371–382.

Tuniz, C. and Zanini, F. (2014) Microcomputerized Tomography (MicroCT) in archaeology. *Encyclopedia of global archaeology*.

Turner-Walker, G. (2007) Degradation pathways & conservation strategies for ancient bone from wet anoxic sites. *The 10th triennial meeting of the ICOM-CC working group for wet organic archaeological materials*.

Turner-Walker, G. (2008) The chemical and microbial degradation of bones and teeth. In Pinhasi, R. and Mays, S. (editors). *Advances in human palaeopathology*. Chichester: John Wiley & Sons, Ltd. 3–29.

Turner-Walker, G., Nielsen-Marsh, C. M., Syversen, U., Kars, H. and Collins, M. J. (2002) Sub-micron spongiform porosity is the major ultra-structural alteration occurring in archaeological bone. *International journal of osteoarchaeology*. **12** (**6**), 407–414.

Turner-Walker, G. and Parry, T. V. (1995) The tensile strength of archaeological bone. *Journal of archaeological science*. **22** (**2**), 185–191.

Turner-Walker, G. and Peacock, E. E. (2008) Preliminary results of bone diagenesis in Scandinavian bogs. *Palaeogeography, palaeoclimatology, palaeoecology*. **266** (**3–4**), 151–159.

van Turnhout, A. G., Kleerebezem, R. and Heimovaara, T. J. (2016) A toolbox to find the best mechanistic model to predict the behavior of environmental systems. *Environmental modelling & software*. **83**, 344–355.

Ueland, M., Breton, H. A. and Forbes, S. L. (2014) Bacterial populations associated with early-stage adipocere formation in lacustrine waters. *International journal of legal medicine*. **128** (**2**), 379–387.

Ural, A., Zioupos, P., Buchanan, D. and Vashishth, D. (2011) The effect of strain rate on fracture toughness of human cortical bone: a finite element

study. *Journal of the mechanical behavior of biomedical materials*. **4** (**7**), 1021–1032.

Urban, B. and Sierralta, M. (2012) New palynological evidence and correlation of Early Palaeolithic sites Schöningen 12 B and 13 II, Schöningen open lignite mine. In Behre, K.-E. (editor). *Die pleistozänen Fundstellen in Schöningen - eine Einführung*. Mainz: Römisch-Germanischen Zentralmuseums. 77–96.

Vallverdú, J., Allué, E., Bischoff, J. L., Cáceres, I., Carbonell, E., Cebrià, A., García-Antón, D., Huguet, R., Ibáñez, N., Martínez, K., Pastó, I., Rosell, J., Saladié, P. and Vaquero, M. (2005) Short human occupations in the Middle Palaeolithic level I of the Abric Romaní rock-shelter (Capellades, Barcelona, Spain). *Journal of human evolution*. **48** (**2**), 157–174.

Valverde, B. N. (2009) Small parts: Crisóstomo Martínez (1638–1694), bone histology, and the visual making of body wholeness. *Isis*. **100** (**3**), 505–536.

Van der Jeught, S. and Dirckx, J. J. J. (2016) Real-time structured light profilometry: a review. *Optics and lasers in engineering*. **87**, 18–31.

Van Gestel, N., Cuypers, S., Bleys, P. and J-P. (2009) A performance evaluation test for laser line scanners on CMMs. *Optics and lasers in engineering*. **47** (**3–4**), 336–342.

Van Kolfschoten, T., Buhrs, E. and Verheijen, I. (2015) The larger mammal fauna from the Lower Paleolithic Schöningen Spear site and its contribution to hominin subsistence. *Journal of human evolution*. **89**, 138–153.

Vannier, M. W., Pilgram, T., Bhatia, G., Brunsden, B. and Commean, P. (1991) Facial surface scanner. *IEEE computer graphics and applications*. **11** (**6**), 72–80.

Vass, A. A. (2001) Beyond the grave - understanding human decomposition. *Microbiology today*. **28**, 109–192.

Villaluenga, A., Hutson, J. M., García-Moreno, A., Turner, E., Gaudzinski-Windheuser, S. and Alt, K. (2015), July 1 *A landscape perspective of hominin behaviour at Schöningen 13II-4 "Spear Horizon."*

Villa, P. and Mahieu, E. (1991) Breakage patterns of human long bones. *Journal of human evolution*. **21** (**1**), 27–48.

Viola, P. and Wells, W. M., III. (1997) Alignment by maximization of mutual information. *International journal of computer vision*. **24** (**2**), 137–154.

Voegtle, T., Schwab, I. and Landes, T. (2008) Influences of different materials on the measurements of a terrestrial laser scanner (TLS). *The international archives of the photogrammetry, remote sensing and spatial information sciences.* **37** (**B5**), 1061–1066.

Voide, R., van Lenthe, G. H. and Müller, R. (2008) Bone morphometry strongly predicts cortical bone stiffness and strength, but not toughness, in inbred mouse models of high and low bone mass. *Journal of bone and mineral research*. **23** (**8**), 1194–1203.

Voormolen, B. (2008)(a) *Ancient hunters, modern butchers: Schöningen 13II – 4, a kill–butchery site dating from the North West European Lower Paleolithic*. PhD thesis, Faculty of Archaeology.

Voormolen, B. (2008)(b) Ancient hunters, modern butchers. Schöningen 13II–4, a kill–butchery site dating from the Northwest European Lower Palaeolithic. *Journal of taphonomy*. **6** (**2**), 71–247.

Vukašinović, N., Bračun, D., Možina, J. and Duhovnik, J. (2010) The influence of incident angle, object colour and distance on CNC laser scanning. *International journal of advanced manufacturing technology*. **50** (**1-4**), 265–274.

Vukašinović, N., Nikola, V., Janez, M. and Jože, D. (2012) Correlation between incident angle, measurement distance, object colour and the number of acquired points at CNC laser scanning. *Journal of mechanical engineering*. **58** (**1**), 23–28.

Wang, X. D., Masilamani, N. S., Mabrey, J. D., Alder, M. E. and Agrawal, C. M. (1998)(a) Changes in the fracture toughness of bone may not be reflected in its mineral density, porosity, and tensile properties. *Bone*. **23** (**1**), 67–72.

Wang, X., Mabrey, J. D. and Agrawal, C. M. (1998)(b) An interspecies comparison of bone fracture properties. *Bio-medical materials and engineering*. **8** (**1**), 1–9.

Wang, Y., Von Euw, S., Fernandes, F. M., Cassaignon, S., Selmane, M., Laurent, G., Pehau-Arnaudet, G., Coelho, C., Bonhomme-Coury, L., Giraud-Guille, M.-M., Babonneau, F., Azaïs, T. and Nassif, N. (2013) Water-mediated structuring of bone apatite. *Nature materials*. **12** (**12**), 1144–1153.

Weber, G. W. and Bookstein, F. L. (2011) *Virtual anthropology: a guide to a new interdisciplinary field*. Wien, Austria: Springer.

Weber, G. W., Bookstein, F. L. and Strait, D. S. (2011) Virtual anthropology meets biomechanics. *Journal of biomechanics*. **44** (**8**), 1429–1432.

Weckenmann, A., Estler, T., Peggs, G. and McMurtry, D. (2004) Probing systems in dimensional metrology. *CIRP annals - manufacturing technology*. **53** (**2**), 657–684.

Wedel, V. L. and Galloway, A., editors. (2013) *Broken bones: anthropological analysis of blunt force trauma*. 2nd edition. Springfield: Charles C. Thomas.

Weigelt, J. (1927) Über Biostratonomie. *Der geologe*. **42**, 1069–1076.

Weiner, S., Goldberg, P. and Bar-Yosef, O. (1993) Bone preservation in Kebara Cave, Israel using on-site Fourier transform infrared spectrometry. *Journal of archaeological science*. **20**, 613–627.

Weiner, S., Schiegl, S., Goldberg, P. and Bar-Yosef, O. (1995) Mineral assemblages in Kebara and Hayonim Caves, Israel: excavation strategies, bone preservation, and wood ash remnants. *Israel journal of chemistry*. **35** (**2**), 143–154.

Weiner, S. and Traub, W. (1992) Bone structure: from angstroms to microns. *FASEB journal*. **6**.

Wenzel, K., Abdel-Wahab, M., Cefalu, A. and Fritsch, D. (2012) High-resolution surface reconstruction from imagery for close range cultural heritage applications. *International archives of the photogrammetry, remote sensing and spatial information sciences*. **34**, 133–138.

Wergedal, J. E., Sheng, M. H.-C., Ackert-Bicknell, C. L., Beamer, W. G. and Baylink, D. J. (2005) Genetic variation in femur extrinsic strength in 29 different inbred strains of mice is dependent on variations in femur cross-sectional geometry and bone density. *Bone*. **36** (**1**), 111–122.

Western Carolina University. (2015) *Western Carolina Human Identification Laboratory*. http://www.wcu.edu/academics/departments-schools-colleges/cas/casdepts/anthsoc/academic-programs/foranth/western-carolina-human-identification-laboratory.asp Accessed February 17, 2015.

White, L. and Booth, T. J. (2014) The origin of bacteria responsible for bioerosion to the internal bone microstructure: results from experimentally-deposited pig carcasses. *Forensic science international*. **239**, 92–102.

White, T. D. and Folkens, P. A. (2005) *The human bone manual*. Oxford: Academic Press.

White, T. D. and Suwa, G. (1987) Hominid footprints at Laetoli: facts and interpretations. *American journal of physical anthropology*. **72** (**4**), 485–514.

Widya, M., Moffatt, C. and Simmons, T. (2012) The formation of early stage adipocere in submerged remains: a preliminary experimental study. *Journal of forensic sciences*. **57** (**2**), 328–333.

Wieberg, D. A. M. and Wescott, D. J. (2008) Estimating the timing of long bone fractures: correlation between the postmortem interval, bone moisture content, and blunt force trauma fracture characteristics. *Journal of forensic sciences*. **53** (**5**), 1028–1034.

Williams, R. A. D. and Elliott, J. C. (1990) *Basic and applied dental biochemistry*. 2nd Edition. London: Churchill Livingstone.

Wilson, A. S., Holland, A. D. and Sparrow, T. (2017) Laser scanning of skeletal pathological conditions. In Thompson, T. and Errickson, D. (editors). *Human remains: another dimension: the application of imaging to the study of human remains*. London: Academic Press. 123–134.

Wilson, A. S., Janaway, R. C., Holland, A. D., Dodson, H. I., Baran, E., Pollard, A. M. and Tobin, D. J. (2007) Modelling the buried human body environment in upland climes using three contrasting field sites. *Forensic science international*. **169** (**1**), 6–18.

Wilson, L. (2004) *Geochemical approaches to understanding in situ archaeological diagenesis: application of soil solution chemistry and geochemical modelling to investigate diagenetic pathways in inorganic and bioinorganic archaeological materials*. PhD Thesis, University of Bradford.

Wilson, M. V. H. (1988) Taphonomic processes: information loss and information gain. *Geoscience Canada*. **15** (**2**), 131–148.

Wilson-Taylor, R. J. and Dautartas, A. M. (2012) Time since death estimation and bone weathering. In Tersigni-Tarrant, M. A. and Shirley, N. R. (editors). *Forensic anthropology: an introduction*. Boca Raton: CRC Press. 273–309.

Wittur, J. (2013) *Computer-generated 3D-visualisations in archaeology: between added value and deception*. British Archaeological Reports.

Wolniewicz, P. (2009) Easily-accessible digital palaeontological databases - a new perspective for the storage of palaeontological information. *Geologos*. **15** (**3-4**), 181–188.

Wood, B., Aiello, L., Wood, C. and Key, C. (1998) A technique for establishing the identity of “isolated” fossil hominin limb bones. *Journal of anatomy*. **193** (**01**), 61–72.

Wood, B. and Leakey, M. (2011) The Omo-Turkana Basin fossil hominins and their contribution to our understanding of human evolution in Africa. *Evolutionary anthropology*. **20** (**6**), 264–292.

Xie, Z., Wang, X. and Chi, S. (2014) Simultaneous calibration of the intrinsic and extrinsic parameters of structured-light sensors. *Optics and lasers in engineering*. **58**, 9–18.

Yin, Z., Wei, L., Li, X. and Manhein, M. (2011) An automatic assembly and completion framework for fragmented skulls. In Lin, S.,Schiele, B.,Soatto, S. and Sturm, P. (editors). *2011 IEEE International conference on computer vision (ICCV), Barcelona, Spain, 6 – 13 November 2011*. New York: IEEE. 2532–2539.

Zayat, M., Garcia-Parejo, P. and Levy, D. (2007) Preventing UV-light damage of light sensitive materials using a highly protective UV-absorbing coating. *Chemical Society reviews*. **36** (**8**), 1270–1281.

Zerlaut, G. A. (1994) Solar ultraviolet radiation: Aspects of importance to the weathering of materials. In Grossman, D. and Ketola, W. D. (editors). *Accelerated and outdoor durability testing of organic materials*. West Conshohocken, PA: ASTM International. 3–24.

Zhang, C. and Chen, T. (2001) Efficient feature extraction for 2D/3D objects in mesh representation. *Proceedings 2001 international conference on image processing*. 935–938 vol.3.

Zhang, S. (2010) Recent progress on real-time 3D shape measurement using digital fringe projection techniques. *Optics and lasers in engineering*. **48** (**2**), 149–158.

Zhang, S. and Yau, S.-T. (2008) Three-dimensional shape measurement using a structured light system with dual cameras. *Optical engineering*. **47** (**1**), 013604–1–013604–12.

Zylberberg, L. and Laurin, M. (2011) Analysis of fossil bone organic matrix by transmission electron microscopy. *Comptes rendus. Palevol*. **10** (**5–6**), 357–366.

Appendix A: Weather Data for Field Weathering Exposure Site

The weather data for the field weathering exposure site is included on the SD card attached to the back cover of the thesis.

Appendix B: Digitised Samples from Turkana Basin Kenya

K0001

Fragments: K0001_F01 & K0001_F02

Location information: East Lake Turkana, Koobi Fora Formation Area 6

Location Notes: Found at two positions approximately 7.8m apart within a water erosion gulley cut into the Upper Burgi Member. One fragment (K0001_F01) was further up slope and closer to the point of erosion.

Description: Two refitting pieces of fossilised cortical bone of a large mammal. Both had Upper Burgi Member deposits adhering to their surfaces.

K0002

Fragments: K0002 – single piece

Location information: East Lake Turkana, Koobi Fora Formation Area 6

Location Notes: Found within a water erosion gulley cut into the Upper Burgi Member in close proximity to K0001_F01 and K0001_F02.

Description: A fossilised cortical bone fragment of a large mammal. The sample had Upper Burgi Member deposits adhering to its surfaces. Digitised as a non-refitting example (Control).

K0003

Fragments: K0003_F01 to K0003_F012

Location Information: East Lake Turkana, Koobi Fora Formation Area 6

Location Notes: Associated with Fossil Finder Image number 912183

Description: Fossilised long bone

K0004

Fragments: K0004_F01 & K004_F02

Location Information: East Lake Turkana, Area 10 (Upper Burgi member), Shelf A1a

Description: Hippopotamus rib, Species aff. *Hippopotamus karumensis*

KNM-ER62818 ; Field Number: f6116a-09

K0005

Fragments: K0005_F01, K0005_F02 & K0005_F03

Location Information: East Lake Turkana, Area 105, Shelf A1a

Description: Hippopotamus rib pieces (4 fragments) and a right incisor. Species aff. *Hippopotamus karumensis*

KNM-ER62866 ; Field Number f19294

K0006

Fragments: K0006_F01 to K0006_F015

Location Information: East Lake Turkana, Koobi Fora Formation Area 6

Location Notes: Associated with Fossil Finder 940440 (from FH source image 09570)

Description: Fossilised long bone, Sample labels: (GT1)

K0007

Fragments: K0007_F01 & K0007_F02

Location Information: East Lake Turkana, Koobi Fora Formation Area 6

Location Notes: Found 26/02/2016; Lat 4.276388 E Long 36.257026 N

Description: Fossilised long bone

K0008

Fragments: K0008_F01, K0008_F02 and K0008_F03

Location Information: East Lake Turkana, Koobi Fora Formation Area 6

Location Notes: Found 26/02/2016; Lat 4.276388 E Long 36.257026 N

Description: Fossilised long bone

Appendix C: Digitised Samples from Schöningen 13, Germany

Sample	Site No.	Local Find No.	Description
SCH_7574	13II-4	698/13-8	Equine femur fragment
SCH_7707	13II-4	699/13-4	Equine femur fragment
SCH_7094	13II-4	696/12-13	Equine femur shaft fragment
SCH_5167	13II-4	691/17-5	Equine distal femur
SCH_6056	13II-4	693/15-26	Equine right radius shaft fragment
SCH_6540	13II-4	694/16-29	Equine right radius shaft fragment
SCH_6726	13II-4	694/20-24	Equine right radius mid-shaft fragment
SCH_12487	13II-4	695/20-4	Equine right radius distal end
SCH_2926	13II-4	687/21-1	Equine right radius shaft fragment
SCH_3058	13II-4	687/24-15	Equine right radius shaft fragment
SCH_2499	13II-4	686/25-5	Equine right radius shaft fragment
SCH_3134	13II-4	687/27-8	Equine right radius shaft fragment
SCH_2525	13II-4	686/26-28	Equine left radius shaft fragment
SCH_1158	13II-4	683/28-19	Equine left radius shaft fragment
SCH_5140	13II-4	691/16-6	Equine left radius shaft fragment
SCH_4283	13II-4	689/19-75	Equine left radius shaft fragment
SCH_6835	13II-4	695/11-17	Equine left radius distal end
SCH_4772	13II-4	690/18-52	Equine left radius distal end
SCH_6880	13II-4	695/13-20	Equine left ulna (olecranon process)
SCH_6599	13II-4	694/17-3	Equine left ulna (prox artic surfaces)
SCH_6599_b	13II-4	694/17-3	Equine left ulna
SCH_17702	13II-4	689/22-15	Equine left radius shaft fragment
SCH_3702	13II-4	688/21-16	Equine left radius shaft fragment

Appendix D: Colour Technique Standards Data

Laser scan data for colour patches

Sample	Colour Patch	Mean point cloud to plane distance	Point cloud to plane distance standard deviation	Classes
S0010	Black	-0.662	18.065	986
S0010	Three Colour	-0.56	15.925	995
S0010	Blue	-0.425	18.594	998
S0010	Cyan	-0.426	14.261	994
S0010	Green	-0.555	10.226	995
S0010	Magenta	-0.541	13.884	999
S0010	Red	-0.226	14.769	997
S0010	Yellow	0.118	11.268	995
S0010	Grey	-1.515	13.647	984
S0010	Light 3 Colour	-0.561	11.79	998
S0010	Light Blue	-0.308	17.888	999
S0010	Light Cyan	-0.535	13.506	999
S0010	Light Green	-0.52	10.643	1000
S0010	Light Magenta	-0.545	11.346	999
S0010	Light Red	0.469	15.621	993
S0010	Light Yellow	0.324	18.018	991
S0010	White	1.023	20.516	984

Structured light data for colour patches

Sample	Colour Patch	Mean point cloud to plane distance	Point cloud to plane distance standard deviation	Classes
S0010	Black	No Response		
S0010	Three Colour	-0.396	27.946	986
S0010	Blue	0.192	22.451	994
S0010	Cyan	0.158	12.331	998
S0010	Green	-0.026	10.853	994
S0010	Magenta	0.033	12.668	994
S0010	Red	0.129	10.798	989
S0010	Yellow	0.094	9.884	994
S0010	Grey	-0.014	8.682	992
S0010	Light 3 Colour	-0.033	9.685	989
S0010	Light Blue	-0.144	12.958	988
S0010	Light Cyan	-0.007	9.662	990
S0010	Light Green	-0.269	10.396	994
S0010	Light Magenta	-0.059	6.269	994
S0010	Light Red	-0.157	7.968	994
S0010	Light Yellow	-0.246	8.833	994
S0010	White	-0.205	12.274	994

Macro structured light data for colour patches

Sample	Colour Patch	Mean point cloud to plane distance	Point cloud to plane distance standard deviation	Classes
S0010	Black	No Response		
S0010	Three Colour	-1.106	19.586	900
S0010	Blue	-2.776	22.37	901
S0010	Cyan	-0.192	13.105	892
S0010	Green	-0.765	9.151	897
S0010	Magenta	-0.507	11.441	899
S0010	Red	0.132	16.373	901
S0010	Yellow	-1.027	10.357	900
S0010	Grey	0.118	17.712	910
S0010	Light 3 Colour	0.057	16.809	905
S0010	Light Blue	-1.106	19.586	903
S0010	Light Cyan	-0.044	21.681	905
S0010	Light Green	-0.766	14.329	902
S0010	Light Magenta	-0.525	21.092	915
S0010	Light Red	0.029	15.488	902
S0010	Light Yellow	-0.654	19.212	939
S0010	White	1.125	24.932	941

Inverse gamma corrected RGB and weighted Euclidean distance values for colour patches

Colour	Gamma^{-1} red value	Gamma^{-1} green value	Gamma^{-1} blue component	Weighted Euclidean distance from black
Blue	0.03	0.03	0.25	0.08
Cyan	0.00	0.33	0.99	0.33
Green	0.01	0.28	0.07	0.13
Yellow	1.00	1.00	0.00	0.60
Red	1.00	0.04	0.05	0.43
Black	0.03	0.04	0.04	0.02
Three Colour	0.04	0.04	0.07	0.05
Magenta	1.00	0.04	0.26	0.51
Light Blue	0.81	0.73	0.57	0.83
Light Cyan	0.81	0.97	1.00	0.91
Light Green	0.83	0.95	0.86	0.87
Light Yellow	1.00	1.00	0.87	0.95
Light Red	1.00	0.85	0.76	0.87
Grey	0.77	0.78	0.80	0.79
Light 3 Colour	0.82	0.72	0.71	0.75
Light Magenta	1.00	0.86	0.98	0.97
White	1.00	1.00	1.00	1.00

Colour patch corresponding wavelengths

Colour	Wavelength (nm)
Blue	475
Cyan	492
Green	510
Yellow	570
Red	650

Appendix E: Opacity Technique Standards Data

Opacity standards: roughness data

Sample	Phase	Experiment type	Opacity	Mean C2Plane	SD C2Plane	Classes
S0011	LaS	Opacity	91.65%	0.019	0.116	420
S0012	LaS	Opacity	94.45%	-0.001	0.035	422
S0013	LaS	Opacity	96.13%	0.001	0.023	424
S0014	LaS	Opacity	97.31%	0.006	0.013	431
S0015	LaS	Opacity	98.70%	0.000	0.014	418
S0016	LaS	Opacity	99.04%	0.000	0.010	425
S0017	LaS	Opacity	99.73%	0.000	0.018	419
S0011	MSL	Opacity	91.65%	0.000	0.018	429
S0012	MSL	Opacity	94.45%	0.000	0.015	429
S0013	MSL	Opacity	96.13%	0.002	0.022	431
S0014	MSL	Opacity	97.31%	0.000	0.019	428
S0015	MSL	Opacity	98.70%	0.000	0.010	423
S0016	MSL	Opacity	99.04%	0.000	0.008	428
S0017	MSL	Opacity	99.73%	0.000	0.014	423
S0011	StL	Opacity	91.65%	0.000	0.016	387
S0012	StL	Opacity	94.45%	0.000	0.011	400
S0013	StL	Opacity	96.13%	0.000	0.011	406
S0014	StL	Opacity	97.31%	0.000	0.016	403
S0015	StL	Opacity	98.70%	0.000	0.007	397
S0016	StL	Opacity	99.04%	0.000	0.005	402
S0017	StL	Opacity	99.73%	0.000	0.011	401

Opacity standards: horizontal measures (true values)

Sample	Opacity	AB	CD	EH	FG
S0011	91.65%	23.960	23.930	24.580	24.680
S0012	94.45%	23.700	23.630	24.100	24.150
S0013	96.13%	23.690	23.840	23.560	23.720
S0014	97.31%	23.840	23.740	23.530	23.450
S0015	98.70%	24.680	24.750	24.250	24.210
S0016	99.04%	24.160	24.180	23.670	23.700

Opacity standards: vertical measures (true values)

Sample	Opacity	J	K	L	M
S0011	91.65%	49.930	49.650	49.460	49.640
S0012	94.45%	49.360	49.270	49.200	49.370
S0013	96.13%	50.100	50.060	49.790	49.800
S0014	97.31%	49.590	49.930	49.630	49.260
S0015	98.70%	49.080	49.110	48.870	48.730
S0016	99.04%	49.810	49.400	49.260	49.540

Sample	Tech-nique	Opacity	3D model AB	Difference at AB	3D model CD	Difference at CD	3D model EH	Difference at EH	3D model FG	Difference at FG
S0011	LaS	91.65%	22.932	-1.028	22.987	-0.943	24.441	-0.139	23.509	-1.171
S0012	LaS	94.45%	23.156	-0.544	23.497	-0.133	23.519	-0.581	23.199	-0.951
S0013	LaS	96.13%	23.370	-0.320	23.084	-0.756	22.814	-0.746	23.269	-0.451
S0014	LaS	97.31%	23.080	-0.761	23.155	-0.585	23.374	-0.156	22.979	-0.471
S0015	LaS	98.70%	24.417	-0.263	24.089	-0.661	24.107	-0.143	23.627	-0.583
S0016	LaS	99.04%	23.746	-0.414	23.949	-0.231	23.337	-0.333	23.318	-0.382
S0017	LaS	99.73%	24.324	-0.236	24.586	-0.054	23.592	-0.368	23.601	-0.399
S0011	MSL	91.65%	23.736	-0.224	23.698	-0.232	24.198	-0.382	24.322	-0.358
S0012	MSL	94.45%	23.280	-0.561	23.019	-0.721	23.219	-0.312	22.873	-0.578
S0013	MSL	96.13%	22.875	-0.815	22.935	-0.905	23.090	-0.470	23.353	-0.368
S0014	MSL	97.31%	23.162	-0.538	23.350	-0.280	23.734	-0.367	23.712	-0.438
S0015	MSL	98.70%	24.000	-0.560	24.070	-0.570	23.571	-0.389	23.624	-0.376
S0016	MSL	99.04%	23.618	-0.542	23.626	-0.554	23.536	-0.134	23.467	-0.233
S0017	MSL	99.73%	24.484	-0.196	24.331	-0.419	23.939	-0.311	23.625	-0.585
S0011	StL	91.65%	23.892	-0.068	23.916	-0.014	24.444	-0.136	24.573	-0.107
S0012	StL	94.45%	23.699	-0.142	23.529	-0.211	23.471	-0.059	23.266	-0.184
S0013	StL	96.13%	23.495	-0.195	23.652	-0.188	23.446	-0.114	23.679	-0.041
S0014	StL	97.31%	23.433	-0.267	23.453	-0.177	24.076	-0.024	24.004	-0.146
S0015	StL	98.70%	24.296	-0.264	24.413	-0.227	23.657	-0.303	23.823	-0.177
S0016	StL	99.04%	23.910	-0.250	23.839	-0.341	23.482	-0.188	23.553	-0.147
S0017	StL	99.73%	24.443	-0.237	24.447	-0.303	24.265	0.015	23.998	-0.212

Sample	Tech-nique	Opacity	3D model height at J	Difference at J	3D model height at K	Difference at K	3D model height at L	Difference at L	3D model height at M	Difference at M
S0011	LaS	91.65%	49.277	-0.653	50.046	0.396	49.424	-0.036	49.109	-0.531
S0012	LaS	94.45%	49.111	-0.249	48.876	-0.394	48.877	-0.323	49.439	0.069
S0013	LaS	96.13%	49.946	-0.154	49.880	-0.181	49.393	-0.397	49.845	0.045
S0014	LaS	97.31%	49.247	-0.343	49.714	-0.216	49.503	-0.127	49.141	-0.119
S0015	LaS	98.70%	48.895	-0.185	48.933	-0.177	48.863	-0.007	48.506	-0.224
S0016	LaS	99.04%	49.797	-0.013	49.014	-0.386	49.044	-0.216	49.520	-0.020
S0017	LaS	99.73%	49.543	0.053	49.298	-0.432	49.504	-0.256	49.486	-0.084
S0011	MSL	91.65%	49.862	-0.068	49.396	-0.254	49.286	-0.174	49.732	0.092
S0012	MSL	94.45%	49.750	0.160	50.129	0.199	49.900	0.270	49.436	0.176
S0013	MSL	96.13%	50.145	0.045	50.040	-0.020	49.539	-0.251	49.694	-0.106
S0014	MSL	97.31%	49.354	-0.006	49.087	-0.183	49.124	-0.076	49.391	0.021
S0015	MSL	98.70%	49.518	0.028	49.685	-0.045	49.827	0.067	49.542	-0.028
S0016	MSL	99.04%	49.835	0.025	49.347	-0.053	49.121	-0.139	49.557	0.017
S0017	MSL	99.73%	49.113	0.033	49.120	0.010	48.819	-0.051	48.716	-0.014
S0011	StL	91.65%	49.872	-0.058	49.479	-0.171	49.263	-0.197	49.663	0.023
S0012	StL	94.45%	49.443	-0.147	49.834	-0.096	49.526	-0.104	49.018	-0.242
S0013	StL	96.13%	50.067	-0.033	49.973	-0.087	49.461	-0.329	49.563	-0.237
S0014	StL	97.31%	49.172	-0.188	48.988	-0.282	48.927	-0.273	49.238	-0.132
S0015	StL	98.70%	49.382	-0.108	49.558	-0.172	49.668	-0.092	49.273	-0.297
S0016	StL	99.04%	49.753	-0.057	49.146	-0.254	48.988	-0.272	49.522	-0.018
S0017	StL	99.73%	48.954	-0.127	49.017	-0.093	48.756	-0.114	48.553	-0.177

Sample	Tech-nique	Opacity	Mean difference (horizontal measurements)	Standard deviation (horizontal measurements)	Mean difference (vertical measurements)	Standard deviation (vertical measurements)	Mean difference (all measurements)	Standard deviation (all measurements)
S0011	LaS	0.917	-0.820	0.464	-0.206	0.482	-0.513	0.547
S0012	LaS	0.945	-0.552	0.335	-0.224	0.205	-0.388	0.311
S0013	LaS	0.961	-0.568	0.218	-0.172	0.181	-0.370	0.282
S0014	LaS	0.973	-0.493	0.254	-0.201	0.104	-0.347	0.238
S0015	LaS	0.987	-0.412	0.249	-0.148	0.096	-0.280	0.225
S0016	LaS	0.990	-0.340	0.080	-0.159	0.178	-0.249	0.160
S0017	LaS	0.997	-0.264	0.157	-0.180	0.210	-0.222	0.178
S0011	MSL	0.917	-0.299	0.082	-0.101	0.150	-0.200	0.154
S0012	MSL	0.945	-0.543	0.170	0.201	0.049	-0.171	0.414
S0013	MSL	0.961	-0.639	0.261	-0.083	0.128	-0.361	0.353
S0014	MSL	0.973	-0.406	0.109	-0.061	0.091	-0.233	0.206
S0015	MSL	0.987	-0.474	0.106	0.005	0.051	-0.234	0.268
S0016	MSL	0.990	-0.366	0.214	-0.038	0.076	-0.202	0.230
S0017	MSL	0.997	-0.377	0.165	-0.006	0.036	-0.191	0.228
S0011	StL	0.917	-0.081	0.053	-0.101	0.102	-0.091	0.076
S0012	StL	0.945	-0.149	0.066	-0.147	0.067	-0.148	0.062
S0013	StL	0.961	-0.134	0.072	-0.172	0.136	-0.153	0.103
S0014	StL	0.973	-0.153	0.100	-0.219	0.072	-0.186	0.088
S0015	StL	0.987	-0.243	0.054	-0.167	0.093	-0.205	0.081
S0016	StL	0.990	-0.232	0.084	-0.150	0.132	-0.191	0.111
S0017	StL	0.997	-0.184	0.138	-0.128	0.036	-0.156	0.098

Appendix F: Surface Roughness Technique Standards Data

Laser scan data for surface roughness patches

Sample	Mean point cloud to plane distance	Point cloud to plane distance standard deviation	Classes
S0001	0.0000	0.0320	930
S0002	0.0000	0.0259	936
S0003	0.0000	0.0216	982
S0004	-0.0171	0.0158	970
S0005	-0.0166	0.0168	716
S0006	0.0000	0.0166	989
S0007	0.0000	0.0211	988
S0008	0.0000	0.0238	997
S0009	0.0000	0.0222	997

Structured light data for surface roughness patches

Sample	Mean point cloud to plane distance	Point cloud to plane distance standard deviation	Classes
S0001	0.0000	0.0326	977
S0002	0.0001	0.0284	973
S0003	-0.0136	0.0210	795
S0004	-0.0265	0.0180	607
S0005	-0.0273	0.0194	667
S0006	-0.0004	0.0202	977
S0007	0.0000	0.0252	973
S0008	0.0000	0.0257	973
S0009	0.0000	0.0249	976

Macro structured light data for surface roughness patches

Sample	Mean point cloud to plane distance	Point cloud to plane distance standard deviation	Classes
S0001	-0.0004	0.0244	995
S0002	0.0061	0.0215	915
S0003	0.0073	0.0120	935
S0004	0.0000	0.0132	998
S0005	-0.0046	0.0118	866
S0006	-0.0088	0.0117	805
S0007	-0.0070	0.0088	828
S0008	-0.0157	0.0124	779
S0009	-0.0113	0.0091	766

Measured average surface roughness for patches

Sample	Average surface roughness (microns)	Manufacturer stated grade (particles/area)
S0001	118.04	1500
S0002	100.6	1800
S0003	53.94	2400
S0004	43.67	3200
S0005	36.16	3600
S0006	27.64	4000
S0007	16.65	6000
S0008	7.076	8000
S0009	4.32	12000

Appendix G: Volume, Area and Noise Data from Experimental Samples

Field Weathering: Area, Volume and Noise Data: Whole Bone

Sample	Phase	Days	Technique	Volume (mm^3)	Area (mm^2)	Verts (Raw)	Faces (Raw)	Verts (Clean)	Faces (Clean)	Vertices Noise %	Faces Noise %
A0001	1	1	LaS	105645	19425	194450	369422	194105	366959	0.177	0.667
A0001	2	448	LaS	95107	18128	152306	299430	151952	296664	0.232	0.924
A0002	1	1	LaS	136090	22896	317856	631228	317797	630025	0.019	0.191
A0002	2	448	LaS	138390	22685	246754	488361	246583	486831	0.069	0.313
A0003	1	1	LaS	141332	24619	281698	553588	281490	551728	0.074	0.336
A0003	2	448	LaS	141164	23938	236995	471474	236927	470451	0.029	0.217
A0003	3	630	LaS	141385	23875	299577	595397	299522	594513	0.018	0.148
A0004	1	1	LaS	136146	24099	185960	358923	185370	353608	0.317	1.481
A0004	2	448	LaS	139395	23584	394821	782619	394617	780712	0.052	0.244
A0004	3	630	LaS	138945	23506	327579	650899	327489	649691	0.027	0.186
A0005	1	1	LaS	99183	19971	131442	247159	130477	236560	0.734	4.288
A0005	2	448	LaS	99770	19178	151664	297682	151260	294545	0.266	1.054
A0005	3	630	LaS	98388	19235	115947	223547	115075	217023	0.752	2.918
A0006	1	1	LaS	145560	24153	178425	344206	177835	337450	0.331	1.963
A0006	2	448	LaS	145303	23824	243027	480807	242854	478828	0.071	0.412
A0006	3	630	LaS	146240	24109	219996	431010	219398	425617	0.272	1.251
A0001	1	1	StL	92490	18059	1046090	2091779	1046090	2088221	0.000	0.170
A0001	2	448	StL	95194	17873	551930	1102916	551908	1102870	0.004	0.004
A0002	1	1	StL	137709	22903	1184046	2368087	1184046	2368080	0.000	0.000
A0002	2	448	StL	130309	22642	992290	1983401	992248	1983307	0.004	0.005
A0003	1	1	StL	139861	24119	1258002	2516001	1258002	2512024	0.000	0.158

Sample	Phase	Days	Technique	Volume (mm^3)	Area (mm^2)	Verts (Raw)	Faces (Raw)	Verts (Clean)	Faces (Clean)	Vertices Noise %	Faces Noise %
A0003	2	448	StL	139689	23810	1101417	2202705	1101417	2201209	0.000	0.068
A0003	3	630	StL	137793	24030	1088990	2177758	1088989	2176237	0.000	0.070
A0004	1	1	StL	137878	23825	1265644	2531258	1265644	2527666	0.000	0.142
A0004	2	448	StL	142979	23284	1066303	2132045	1066301	2130716	0.000	0.062
A0004	3	630	StL	141495	23529	1073712	2146769	1073710	2145117	0.000	0.077
A0005	1	1	StL	96742	19105	944200	1887861	944200	1884116	0.000	0.198
A0005	2	448	StL	96778	18884	884342	1767211	884317	1767153	0.003	0.003
A0005	3	630	StL	90859	18939	862614	1724929	862614	1723548	0.000	0.080
A0006	1	1	StL	140516	23775	1292262	2584061	1292262	2580146	0.000	0.152
A0006	2	448	StL	144072	23676	1127721	2255024	1127721	2253267	0.000	0.078
A0006	3	630	StL	143048	23910	1096124	2192240	1096123	2190535	0.000	0.078
A0005	3	630	PtG	98503	20810	295056	590080	295049	585052	0.002	0.852
A0006	3	630	PtG	141199	23514	419187	838370	419180	831883	0.002	0.774

High pH: Area, Volume and Noise Data: Whole Bone

Sample	Phase	Days	Technique	Volume (mm^3)	Area (mm^2)	Verts (Raw)	Faces (Raw)	Verts (Clean)	Faces (Clean)	Vertices Noise %	Faces Noise %
A0011	1	1	LaS	180107	27399	345845	689203	345812	688340	0.010	0.125
A0011	2	28	LaS	176082	27006	243481	483675	243346	482294	0.055	0.286
A0012	1	1	LaS	194929	28647	232409	458062	232110	454926	0.129	0.685
A0012	2	28	LaS	195505	28568	259258	511406	258914	508664	0.133	0.536
A0013	1	1	LaS	118431	20991	159561	311525	159362	308788	0.125	0.879
A0013	2	28	LaS	118279	20980	194727	386941	194612	385629	0.059	0.339
A0013	3	56	LaS	119420	21348	105885	192521	103605	178119	2.153	7.481
A0014	1	1	LaS	130826	22763	193597	383271	193496	381833	0.052	0.375
A0014	2	28	LaS	128467	22495	162289	318972	161845	316071	0.274	0.909
A0014	3	56	LaS	133956	23109	111805	205719	110095	195288	1.529	5.071
A0015	1	1	LaS	136633	22393	190141	370893	189768	366783	0.196	1.108
A0015	2	28	LaS	137695	22471	173451	344094	173254	342638	0.114	0.423
A0015	3	56	LaS	135159	22652	126869	231685	124512	216035	1.858	6.755
A0015	4	84	LaS	123863	20796	180901	356138	180444	332815	0.253	6.549
A0016	1	1	LaS	116892	20983	171939	335735	171642	331789	0.173	1.175
A0016	2	28	LaS	120638	21299	194569	386647	194395	385307	0.089	0.347
A0016	3	56	LaS	119682	21570	138558	261781	137095	251227	1.056	4.032
A0016	4	84	LaS	111944	20343	177000	348605	175883	331755	0.631	4.834
A0011	1	1	StL	180219	27543	1184502	2368027	1184501	2366290	0.000	0.073
A0011	2	28	StL	175535	27155	1779216	3557902	1779213	3555041	0.000	0.080
A0012	1	1	StL	197406	28666	1276986	2553234	1276986	2551593	0.000	0.064
A0012	2	28	StL	188499	28858	1958080	3914748	1958078	3911808	0.000	0.075
A0013	1	1	StL	118111	21180	800646	1600867	800645	1599587	0.000	0.080
A0013	2	28	StL	118148	20995	1359277	2718112	1359277	2715991	0.000	0.078

Sample	Phase	Days	Technique	Volume (mm^3)	Area (mm^2)	Verts (Raw)	Faces (Raw)	Verts (Clean)	Faces (Clean)	Vertices Noise %	Faces Noise %
A0013	3	56	StL	118104	21734	1198683	2395899	1198675	2393587	0.001	0.096
A0014	1	1	StL	133622	22822	888520	1776164	888520	1774984	0.000	0.066
A0014	2	28	StL	132374	22786	1515555	3029637	1515555	3026850	0.000	0.092
A0014	3	56	StL	134378	23689	1301345	2601720	1301343	2599258	0.000	0.095
A0015	1	1	StL	138750	22730	952537	1904556	952535	1903136	0.000	0.075
A0015	2	28	StL	135824	22506	1468521	2936641	1468521	2934264	0.000	0.081
A0015	3	56	StL	134303	22966	1261268	2521234	1261262	2518636	0.000	0.103
A0015	4	84	StL	125341	21094	1159174	2317572	1159170	2315435	0.000	0.092
A0016	1	1	StL	123709	21376	935099	1868203	935089	1866735	0.001	0.079
A0016	2	28	StL	119078	21359	1377187	2753586	1377185	2751411	0.000	0.079
A0016	3	56	StL	118111	21940	1196191	2391408	1196187	2389116	0.000	0.096
A0016	4	84	StL	109216	20739	1148288	2296255	1148287	2294292	0.000	0.085
A0011	2	28	PtG	174495	27098	349042	698080	349042	697180	0.000	0.129
A0012	2	28	PtG	194391	28739	306433	612858	306433	610742	0.000	0.345
A0013	2	28	PtG	117134	21218	309665	619282	309665	617429	0.000	0.299
A0013	3	56	PtG	119452	21239	428918	857844	428917	855339	0.000	0.292
A0014	2	28	PtG	129344	22424	263544	527084	263544	527077	0.000	0.001
A0014	3	56	PtG	136473	23994	393826	787612	393815	781273	0.003	0.805
A0015	2	28	PtG	134693	23046	252365	504746	252365	503598	0.000	0.227
A0015	3	56	PtG	139850	23404	438652	877260	438634	870451	0.004	0.776
A0015	4	84	PtG	121882	20594	509189	1018366	509177	1010573	0.002	0.765
A0016	2	28	PtG	120383	21295	255150	510296	255150	510118	0.000	0.035
A0016	3	56	PtG	126993	24214	401592	802960	401585	796282	0.002	0.832
A0016	4	84	PtG	109537	20004	356321	712638	356321	712463	0.000	0.025

Low pH: Area, Volume and Noise Data: Whole Bone

Sample	Phase	Days	Technique	Volume (mm^3)	Area (mm^2)	Verts (Raw)	Faces (Raw)	Verts (Clean)	Faces (Clean)	Vertices Noise %	Faces Noise %
A0017	1	1	LaS	146398	24428	192085	378266	191884	375735	0.105	0.669
A0017	2	28	LaS	103914	20579	136386	256952	134141	240323	1.646	6.472
A0018	1	1	LaS	153390	24908	206323	405510	206159	402911	0.079	0.641
A0018	2	28	LaS	131733	23316	97906	178419	95828	163891	2.122	8.143
A0019	1	1	LaS	151744	24952	238967	473145	238829	471341	0.058	0.381
A0019	2	28	LaS	126196	23241	117185	212788	114544	194362	2.254	8.659
A0019	3	56	LaS	101025	22382	155947	257706	147523	209259	5.402	18.799
A0020	1	1	LaS	173305	26728	229877	454403	229774	452713	0.045	0.372
A0020	2	28	LaS	143699	24254	112747	218490	112151	212834	0.529	2.589
A0020	3	56	LaS	143495	24450	130342	237813	127912	218352	1.864	8.183
A0021	1	1	LaS	174717	26302	222868	441578	222723	439836	0.065	0.394
A0021	2	28	LaS	146722	24096	112283	212371	110971	201779	1.168	4.987
A0021	3	56	LaS	144302	24098	107765	198616	105702	183110	1.914	7.807
A0021	4	84	LaS	145970	24303	97413	174077	94756	155122	2.728	10.889
A0022	1	1	LaS	123015	21318	198608	393746	198533	392720	0.038	0.261
A0022	2	28	LaS	90355	18118	92751	175788	91574	167365	1.269	4.792
A0022	3	56	LaS	88867	18120	104457	190288	102485	174483	1.888	8.306
A0022	4	84	LaS	78345	17024	86533	153803	84047	137642	2.873	10.508
A0017	1	1	StL	151271	24463	956083	1911348	956078	1909721	0.001	0.085
A0017	2	28	StL	95787	19814	1392636	2781122	1392625	2778165	0.001	0.106
A0018	1	1	StL	155720	25178	1048681	2096093	1048679	2094152	0.000	0.093
A0018	2	28	StL	119587	22141	1612661	3225321	1612659	3221900	0.000	0.106
A0019	1	1	StL	146641	24824	1400529	2800885	1400529	2798260	0.000	0.094
A0019	2	28	StL	113541	21734	1599073	3197856	1599066	3194305	0.000	0.111

Sample	Phase	Days	Technique	Volume (mm^3)	Area (mm^2)	Verts (Raw)	Faces (Raw)	Verts (Clean)	Faces (Clean)	Vertices Noise %	Faces Noise %
A0019	3	56	StL	114693	21916	1382926	2765830	1382926	2763088	0.000	0.099
A0020	1	1	StL	167582	26818	1495867	2991307	1495865	2988811	0.000	0.083
A0020	2	28	StL	135010	23675	1754352	3508695	1754350	3504824	0.000	0.110
A0020	3	56	StL	134269	23631	1483130	2966211	1483128	2963506	0.000	0.091
A0021	1	1	StL	163259	26190	1419877	2839213	1419877	2837179	0.000	0.072
A0021	2	28	StL	139093	23513	1603210	3206408	1603210	3203641	0.000	0.086
A0021	3	56	StL	140162	23718	1444540	2889078	1444540	2886358	0.000	0.094
A0021	4	84	StL	131446	23128	1442830	2885242	1442826	2882355	0.000	0.100
A0022	1	1	StL	114707	21306	1149720	2299017	1149720	2297191	0.000	0.079
A0022	2	28	StL	84160	17473	1219580	2438902	1219579	2436395	0.000	0.103
A0022	3	56	StL	84813	17557	1119752	2239492	1119751	2237066	0.000	0.108
A0022	4	84	StL	71649	16624	1008897	2017525	1008894	2015558	0.000	0.097
A0017	2	28	PtG	99476	19536	237214	474424	237214	474011	0.000	0.087
A0018	2	28	PtG	119347	22018	337363	674714	337363	674426	0.000	0.043
A0019	2	28	PtG	113363	21547	258507	517010	258507	515836	0.000	0.227
A0019	3	56	PtG	119964	24432	402446	804624	402442	799576	0.001	0.627
A0020	2	28	PtG	137528	23745	283224	566436	283224	565751	0.000	0.121
A0020	3	56	PtG	138700	26520	470906	941328	470889	933421	0.004	0.840
A0021	2	28	PtG	138032	23109	279601	559198	279601	559061	0.000	0.024
A0021	3	56	PtG	149414	27053	492497	984546	492483	976781	0.003	0.789
A0021	4	84	PtG	135705	23649	575848	1151156	575835	1143320	0.002	0.681
A0022	2	28	PtG	86290	17545	244647	489290	244646	488773	0.000	0.106
A0022	3	56	PtG	83062	18710	330912	661445	330903	655792	0.003	0.855
A0022	4	84	PtG	73771	16009	383460	766892	383451	760302	0.002	0.859

High UV: Area, Volume and Noise Data: Whole Bone

Sample	Phase	Days	Technique	Volume (mm^3)	Area (mm^2)	Verts (Raw)	Faces (Raw)	Verts (Clean)	Faces (Clean)	Vertices Noise %	Faces Noise %
A0023	1	1	LaS	133124	22375	236277	456509	235578	449354	0.296	1.567
A0023	2	28	LaS	131504	22580	126268	241319	125222	232284	0.828	3.744
A0024	1	1	LaS	143220	23439	182237	356759	182024	354032	0.117	0.764
A0025	1	1	LaS	209681	30560	156494	293418	154254	276327	1.431	5.825
A0026	1	1	LaS	153622	24856	123170	228413	120739	209431	1.974	8.310
A0026	2	28	LaS	152313	25304	121965	215701	117947	202208	3.294	6.255
A0026	3	56	LaS	151958	24097	143167	270439	142034	260773	0.791	3.574
A0027	1	1	LaS	176120	27196	125468	237405	124001	226022	1.169	4.795
A0027	2	28	LaS	176797	27009	156394	300227	155045	289241	0.863	3.659
A0027	3	56	LaS	170568	26394	162354	306909	160971	294795	0.852	3.947
A0028	1	1	LaS	136920	23351	111517	209958	109926	197402	1.427	5.980
A0023	1	1	StL	129787	22373	1309317	2617917	1309317	2615585	0.000	0.089
A0023	2	28	StL	114666	22154	1143602	2286670	1143602	2284775	0.000	0.083
A0024	1	1	StL	141381	23517	1268330	2536340	1268328	2534159	0.000	0.086
A0024	2	28	StL	134583	23317	1146669	2292545	1146669	2290519	0.000	0.088
A0025	1	1	StL	198323	30061	1631911	3262997	1631910	3260181	0.000	0.086
A0026	1	1	StL	145244	24049	1764084	3528149	1764081	3525044	0.000	0.088
A0026	2	28	StL	137184	23699	1203925	2407356	1203917	2405321	0.001	0.085
A0026	3	56	StL	139957	23781	1387500	2773645	1387499	2771497	0.000	0.077
A0027	1	1	StL	170129	26753	1602151	3204290	1602148	3201260	0.000	0.095
A0027	2	28	StL	161238	26409	1377405	2754417	1377404	2752273	0.000	0.078
A0027	3	56	StL	160747	26517	1617262	3233666	1617258	3230917	0.000	0.085
A0028	1	1	StL	132176	22914	1272939	2545870	1272938	2543796	0.000	0.081

Sample	Phase	Days	Technique	Volume (mm^3)	Area (mm^2)	Verts (Raw)	Faces (Raw)	Verts (Clean)	Faces (Clean)	Vertices Noise %	Faces Noise %
A0023	1	1	PtG	129697	22384	312159	624314	312159	624145	0.000	0.027
A0023	2	28	PtG	128724	22044	277846	555688	277837	551211	0.003	0.806
A0024	1	1	PtG	140894	23633	372562	745112	372562	744812	0.000	0.040
A0025	1	1	PtG	210691	30262	479277	958554	479268	950676	0.002	0.822
A0026	1	1	PtG	181355	28061	494983	989272	494982	988956	0.000	0.032
A0026	2	28	PtG	149036	23975	354477	708950	354469	703156	0.002	0.817
A0026	3	56	PtG	146241	23655	430047	860090	430047	859497	0.000	0.069
A0027	1	1	PtG	173763	26785	420146	840266	420145	835807	0.000	0.531
A0027	2	28	PtG	198893	30842	478944	957508	478932	950157	0.003	0.768
A0027	3	56	PtG	168338	26167	489506	979008	489506	978152	0.000	0.087
A0028	1	1	PtG	142239	25693	379554	758980	379539	752259	0.004	0.886

Field Weathering: Noise Data: Refit Samples

Sample	Fragment	Phase	Days	Technique	Verts (Raw)	Faces (Raw)	Verts (Clean)	Faces (Clean)	Vertices Noise %	Faces Noise %
A0002	F01	2	448	LaS	179310	350657	179123	347940	0.104	0.775
A0002	F02	2	448	LaS	239474	472586	239298	469637	0.073	0.624
A0005	F01	3	630	LaS	54464	104161	54212	103718	0.463	0.425
A0005	F02	3	630	LaS	77381	147828	76960	146581	0.544	0.844
A0002	F01	2	448	PtG	267576	534908	267575	530932	0.000	0.743
A0002	F02	2	448	PtG	330493	660841	330479	655660	0.004	0.784
A0005	F01	3	630	PtG	223304	446480	223300	442985	0.002	0.783
A0005	F02	3	630	PtG	316271	632530	316266	627507	0.002	0.794
A0002	F01	2	448	StL	651512	1300258	651509	1299073	0.000	0.091
A0002	F02	2	448	StL	850579	1698989	850579	1697459	0.000	0.090
A0005	F01	3	630	StL	500142	999179	500142	998416	0.000	0.076
A0005	F02	3	630	StL	595239	1188748	595238	1187639	0.000	0.093

High pH: Noise Data: Refit Samples

Sample	Fragment	Phase	Days	Technique	Verts (Raw)	Faces (Raw)	Verts (Clean)	Faces (Clean)	Vertices Noise %	Faces Noise %
A0011	F01	2	28	LaS	194613	384218	194465	382783	0.076	0.373
A0011	F02	2	28	LaS	211068	414752	210952	413374	0.055	0.332
A0011	F01	3	56	LaS	164651	321391	164466	319363	0.112	0.631
A0011	F02	3	56	LaS	193757	374455	193352	370894	0.209	0.951
A0013	F01	3	56	LaS	88302	170059	87962	167738	0.385	1.365
A0013	F02	3	56	LaS	117079	226404	116422	223533	0.561	1.268
A0013	F01	4	84	LaS	103959	200771	103637	198351	0.310	1.205
A0013	F02	4	84	LaS	116775	223661	115885	221195	0.762	1.103
A0011	F01	2	28	MStL	1465870	2927309	1465786	2927118	0.006	0.007
A0011	F02	2	28	MStL	11708852	23346937	11708601	23339745	0.002	0.031
A0011	F01	3	56	MStL	1465870	2927309	1465786	2927118	0.006	0.007
A0011	F02	3	56	MStL	11708852	23346937	11708601	23339745	0.002	0.031
A0013	F01	4	84	MStL	8274960	16501709	8274690	16492106	0.003	0.058
A0013	F02	4	84	MStL	8019768	16008352	8019643	16004054	0.002	0.027
A0011	F01	2	28	PtG	390728	781034	390723	774991	0.001	0.774
A0011	F02	2	28	PtG	417395	834478	417386	828114	0.002	0.763
A0011	F01	3	56	PtG	252802	505439	252795	501067	0.003	0.865
A0011	F02	3	56	PtG	230600	461011	230593	457086	0.003	0.851
A0013	F01	3	56	PtG	431260	862094	431260	861869	0.000	0.026
A0013	F02	3	56	PtG	542462	1084687	542462	1084322	0.000	0.034
A0011	F01	2	28	StL	903058	1804378	903058	1803031	0.000	0.075
A0011	F02	2	28	StL	772045	1539912	772023	1538412	0.003	0.097
A0011	F01	3	56	StL	813477	1624790	813477	1623597	0.000	0.073
A0011	F02	3	56	StL	843581	1682991	843579	1681463	0.000	0.091
A0013	F01	3	56	StL	408599	814285	408598	813459	0.000	0.101

Sample	Fragment	Phase	Days	Technique	Verts (Raw)	Faces (Raw)	Verts (Clean)	Faces (Clean)	Vertices Noise %	Faces Noise %
A0013	F02	3	56	StL	690101	1377993	690100	1376731	0.000	0.092

Low pH: Noise Data: Refit Samples

Sample	Fragment	Phase	Days	Technique	Verts (Raw)	Faces (Raw)	Verts (Clean)	Faces (Clean)	Vertices Noise %	Faces Noise %
A0018	F01	2	28	LaS	67368	107125	63226	85202	6.148	20.465
A0018	F02	2	28	LaS	97479	154177	91642	122454	5.988	20.576
A0020	F01	3	56	LaS	73533	125631	71047	110634	3.381	11.937
A0020	F02	3	56	LaS	98245	156576	93149	126838	5.187	18.993
A0020	F01	4	84	LaS	83210	148760	81080	136274	2.560	8.393
A0020	F02	4	84	LaS	95089	157775	91188	125733	4.102	20.309
A0018	F01	2	28	PtG	316155	632160	316151	627015	0.001	0.814
A0018	F02	2	28	PtG	319202	638174	319193	632424	0.003	0.901
A0020	F01	3	56	PtG	338412	676497	338405	670686	0.002	0.859
A0020	F02	3	56	PtG	471490	942670	471477	934727	0.003	0.843
A0020	F01	4	84	PtG	352053	703934	352043	699511	0.003	0.628
A0020	F02	4	84	PtG	267074	533983	267071	529459	0.001	0.847
A0018	F01	2	28	StL	703603	1404554	703602	1403359	0.000	0.085
A0018	F02	2	28	StL	696518	1390983	696507	1390064	0.002	0.066
A0020	F01	3	56	StL	648779	1294437	648775	1293007	0.001	0.110
A0020	F02	3	56	StL	616485	1229550	616483	1228387	0.000	0.095
A0020	F01	4	84	StL	760215	1515834	760196	1513912	0.002	0.127
A0020	F02	4	84	StL	687503	1371423	687497	1370015	0.001	0.103

High UV: Noise Data: Refit Samples

Sample number	Fragment	Phase	Days	Technique	Verts (Raw)	Faces (Raw)	Verts (Clean)	Faces (Clean)	Vertices Noise %	Faces Noise %
A0025	F04	2	28	LaS	143150	227981	135516	211068	5.333	7.419
A0025	F05	2	28	LaS	94345	165270	91893	154355	2.599	6.604
A0025	F04	3	56	LaS	121871	222272	120409	210543	1.200	5.277
A0025	F05	3	56	LaS	110135	198453	108354	185118	1.617	6.719
A0029	F01	1	1	LaS	70032	133682	69669	131088	0.518	1.940
A0029	F02	1	1	LaS	67006	125669	66510	121694	0.740	3.163
A0025	F04	3	56	MStL	729080	1454121	729061	1454079	0.003	0.003
A0025	F05	3	56	MStL	516577	1031574	516559	1031538	0.003	0.003
A0029	F01	1	1	MStL	2254375	4477589	2254285	4475030	0.004	0.057
A0029	F02	1	1	MStL	2210938	4380267	2210787	4375263	0.007	0.114
A0025	F04	2	28	PtG	390771	781213	390757	774792	0.004	0.822
A0025	F05	2	28	PtG	421700	843392	421695	836546	0.001	0.812
A0025	F04	3	56	PtG	554815	1109297	554798	1100543	0.003	0.789
A0025	F05	3	56	PtG	226006	452004	226001	448408	0.002	0.796
A0029	F01	1	1	PtG	228277	456413	228272	452964	0.002	0.756
A0029	F02	1	1	PtG	284754	569347	284744	564703	0.004	0.816
A0025	F04	2	28	StL	942604	1881900	942598	1880067	0.001	0.097
A0025	F05	2	28	StL	508680	1003882	508672	1002378	0.002	0.150
A0025	F04	3	56	StL	1054243	2105250	1054241	2103283	0.000	0.093
A0025	F05	3	56	StL	597758	1180032	597722	1177750	0.006	0.193
A0029	F01	1	1	StL	589267	1177481	589267	1176620	0.000	0.073
A0029	F02	1	1	StL	688225	1375123	688225	1374222	0.000	0.066

Appendix H: Colour Data from Experimental Samples

Sample	Phase	Days	Exp	F stop	Exp	Pixels	Mean	Std Dev (2σ)	Median
A0001	1	1	Field Exposure	13	1/2	182448	0.46	0.30	123
A0002	1	1		13	1/2	146143	0.38	0.26	100
A0003	1	1		13	1/2	118709	0.51	0.31	134
A0004	1	1		13	1/2	148786	0.39	0.30	104
A0005	1	1		13	1/2	163247	0.41	0.32	110
A0006	1	1		13	1/2	93223	0.45	0.26	119
A0001	2	448		20	1/3	125131	0.50	0.42	134
A0002	3	630		8	1/25	106067	0.56	0.24	146
A0003	2	630		13	1/2	179621	0.42	0.28	112
A0004	2	630		13	1/2	93032	0.39	0.23	104
A0005	2	630		13	1/2	134603	0.49	0.15	136
A0006	2	630		13	1/2	143527	0.47	0.19	117
A0004	2	448		20	1/3	122391	0.50	0.46	129
A0005	2	448		8	1/25	90400	0.51	0.43	143
A0006	2	448		8	1/25	111223	0.47	0.37	121
A0017	1	1	High pH	13	1/2	52690	0.39	0.32	104
A0017	1	1		13	1/2	183231	0.50	0.32	132
A0018	1	1		13	1/2	173300	0.40	0.27	104
A0019	1	1		13	1/2	193438	0.45	0.26	117
A0020	1	1		13	1/2	175807	0.36	0.26	96
A0022	1	1		13	1/2	58780	0.43	0.29	111
A0017	2	28		13	1/15	50435	0.32	0.18	89
A0018	2	28		13	1/15	157699	0.44	0.17	117
A0019	2	28		13	1/15	127325	0.55	0.18	147
A0020	2	28		13	1/15	124866	0.60	0.23	165
A0021	2	28		13	1/15	121086	0.38	0.18	104
A0022	2	28		13	1/15	118031	0.41	0.19	112
A0017	3	56		20	¼	128000	0.48	0.13	127
A0018	3	56		20	1/4	87977	0.54	0.17	143
A0019	3	56		13	1/2	186479	0.75	0.26	200
A0020	3	56		13	1/2	126777	0.71	0.25	187
A0021	3	56		13	1/2	187518	0.77	0.29	207
A0022	3	56		13	1/2	155986	0.72	0.22	192
A0019	4	84		20	1/4	152968	0.40	0.18	107
A0020	4	84		20	1/3	48171	0.53	0.17	140
A0021	4	84		20	1/3	52045	0.57	0.14	150
A0022	4	84		20	1/3	161942	0.54	0.18	142

Sample	Phase	Days	Exp	F stop	Exp	Pixels	Mean	Std Dev (2σ)	Median
A0023	1	1	High UV	13	1/2	175807	0.36	0.23	96
A0024	1	1		13	1/2	183231	0.50	0.33	132
A0025	1	1		13	1/2	58780	0.43	0.31	111
A0026	1	1		13	1/2	193438	0.45	0.27	117
A0027	1	1		13	1/2	52690	0.39	0.32	104
A0028	1	1		13	1/2	173300	0.40	0.27	104
A0023	2	28		13	1/2	37253	0.37	0.32	99
A0024	2	28		13	1/2	50051	0.43	0.33	121
A0025	2	28		13	1/2	78991	0.52	0.33	134
A0026	2	28		13	1/2	162805	0.43	0.40	113
A0027	2	28		13	1/2	52302	0.37	0.37	103
A0028	2	28		13	1/2	132551	0.40	0.30	105
A0023	3	56		20	1/3	78990	0.28	0.27	71
A0024	3	56		20	1/3	47546	0.37	0.30	99
A0025	3	56		20	1/3	104561	0.41	0.37	113
A0026	3	56		20	1/3	63208	0.40	0.36	100
A0027	3	56		20	1/3	69066	0.26	0.29	64
A0028	3	56		20	1/3	90955	0.38	0.29	90
A0011	1	1	Low pH	13	1/2	175807	0.36	0.26	96
A0012	1	1		13	1/2	173300	0.40	0.27	104
A0013	1	1		13	1/2	52690	0.39	0.32	104
A0014	1	1		13	1/2	183231	0.50	0.32	132
A0015	1	1		13	1/2	193438	0.45	0.26	117
A0016	1	1		13	1/2	58780	0.43	0.29	111
A0011	2	28		13	1/40	109753	0.21	0.24	56
A0012	2	28		13	1/40	33501	0.23	0.28	61
A0013	2	28		13	1/40	31900	0.23	0.31	58
A0014	2	28		13	1/40	34271	0.18	0.24	43
A0015	2	28		13	1/40	133784	0.16	0.22	37
A0016	2	28		13	1/40	97572	0.18	0.26	44
A0011	3	56		20	1/8	62348	0.11	0.16	29
A0012	3	56		20	1/5	69280	0.16	0.25	40
A0013	3	56		13	1/2	40352	0.24	0.27	68
A0014	3	56		13	1/2	169744	0.19	0.24	51
A0015	3	56		13	1/2	198852	0.25	0.25	71
A0016	3	56		13	1/2	145028	0.22	0.28	64
A0013	4	84		20	1/5	65383	0.11	0.20	24
A0014	4	84		20	1/5	76920	0.13	0.22	28
A0015	4	84		20	1/5	60511	0.11	0.19	25
A0016	4	84		20	1/5	168476	0.12	0.21	28

Appendix I: Opacity Data from Experimental Samples

Sample	Exp	Phase	Days	T (full)	T (IR)	O (full)	O (IR)	Std Dev (full)	Std Dev (IR)
A0028	Field Exposure	1	1	3.73%	4.16%	96.27%	95.84%	0.051%	0.123%
A0029		1	1	3.92%	4.32%	96.08%	95.68%	0.023%	0.087%
A0030		1	1	3.86%	4.26%	96.14%	95.74%	0.005%	0.018%
A0001		2	448	0.93%	1.18%	99.07%	98.82%	0.033%	0.140%
A0002		2	448	0.83%	1.23%	99.17%	98.77%	0.005%	0.018%
A0003a		3	630	1.14%	2.23%	98.86%	97.77%	0.012%	0.432%
A0003b		3	630	0.55%	1.26%	99.45%	98.74%	0.008%	0.032%
A0005		3	630	0.64%	1.30%	99.36%	98.70%	0.009%	0.039%
A0028	High pH	1	1	3.73%	4.16%	96.27%	95.84%	0.051%	0.123%
A0029		1	1	3.92%	4.32%	96.08%	95.68%	0.023%	0.087%
A0030		1	1	3.86%	4.26%	96.14%	95.74%	0.005%	0.018%
A0011		2	28	1.17%	1.29%	98.83%	98.71%	0.011%	0.040%
A0012		2	28	1.02%	1.14%	98.98%	98.86%	0.013%	0.036%
A0011		3	56	0.18%	0.92%	99.82%	99.08%	0.009%	0.042%
A0012		3	56	0.44%	0.66%	99.56%	99.34%	0.016%	0.077%
A0013		3	56	0.51%	0.53%	99.49%	99.47%	0.012%	0.047%
A0013		4	84	0.06%	0.14%	99.94%	99.86%	0.010%	0.034%
A0014		4	84	0.07%	0.18%	99.93%	99.82%	0.019%	0.082%
A0028	Low pH	1	1	3.73%	4.16%	96.27%	95.84%	0.051%	0.123%
A0029		1	1	3.92%	4.32%	96.08%	95.68%	0.023%	0.087%
A0030		1	1	3.86%	4.26%	96.14%	95.74%	0.005%	0.018%
A0017		2	28	4.87%	4.73%	95.13%	95.27%	0.020%	0.156%
A0018		2	28	4.39%	4.52%	95.61%	95.48%	0.087%	0.114%
A0017		3	56	6.19%	3.02%	93.81%	96.98%	0.232%	0.193%
A0018		3	56	6.41%	3.27%	93.59%	96.73%	0.035%	0.291%
A0019		3	56	6.25%	3.09%	93.75%	96.91%	0.128%	0.104%
A0018		4	84	8.84%	1.89%	91.16%	98.11%	0.061%	0.367%
A0019		4	84	7.94%	2.03%	92.06%	97.97%	0.142%	0.105%
A0020		4	84	9.08%	1.57%	90.92%	98.43%	0.156%	0.089%
A0028	High UV	1	1	3.73%	4.16%	96.27%	95.84%	0.051%	0.123%
A0029		1	1	3.92%	4.32%	96.08%	95.68%	0.023%	0.087%
A0030		1	1	3.86%	4.26%	96.14%	95.74%	0.005%	0.018%
A0024		2	28	3.16%	3.30%	96.84%	96.70%	0.027%	0.083%
A0025		2	28	3.34%	3.62%	96.66%	96.38%	0.016%	0.068%
A0028		2	28	3.18%	3.34%	96.82%	96.66%	0.024%	0.097%
A0023		3	56	1.16%	1.91%	98.84%	98.09%	0.017%	0.055%
A0024		3	56	1.25%	1.54%	98.75%	98.46%	0.016%	0.060%
A0025		3	56	1.15%	1.40%	98.85%	98.60%	0.016%	0.054%
A0028		3	56	1.54%	2.00%	98.46%	98.00%	0.013%	0.050%

Appendix J: Refit Data from Experimental Samples

Experiment	Phase	Days	Scanner type	Reference model	Compared Model	Point Pair Alignment RMS	Segmented Fine Alignment RMS	C2M signed Distance Mean	C2M Signed Distance Std Dev (2σ)	Fitting surface (+/- 0.1 mm) area	% of fracture surface within +- 0.1mm
Field	1	1	Laser scanning	A0029_F01_LaS01	A0029_F02_LaS01	0.2075	0.0598	0.0932	0.4074	92.84	50.11%
Field	1	1	Photogrammetry	A0029_F01_PtG01	A0029_F02_PtG01	0.2306	0.0552	0.0618	0.3617	107.31	51.86%
Field	1	1	Structured light	A0029_F01_StL01	A0029_F02_StL01	0.6246	0.0491	0.0728	0.3462	126.84	55.49%
Field	2	448	Laser scanning	A0002_F01_LaS02	A0002_F02_LaS02	0.0653	0.0829	0.0341	0.3796	306.79	52.29%
Field	2	448	Photogrammetry	A0002_F01_PtG02	A0002_F02_PtG02	0.3203	0.0750	0.0394	0.3449	293.82	57.43%
Field	2	448	Structured light	A0002_F01_StL02	A0002_F02_StL02	0.2032	0.0646	0.0283	0.2820	352.55	64.60%
Field	3	630	Laser scanning	A0005_F01_LaS03	A0005_F02_LaS03	0.3213	0.0776	0.0242	0.3797	99.97	59.18%
Field	3	630	Photogrammetry	A0005_F01_PtG03	A0005_F02_PtG03	0.1444	0.0752	0.0151	0.3528	100.19	62.23%
Field	3	630	Structured light	A0005_F01_StL03	A0005_F02_StL03	0.2020	0.0498	0.0266	0.3199	115.93	70.52%
Low pH	1	1	Laser scanning	A0029_F01_LaS01	A0029_F02_LaS01	0.2075	0.0598	0.0932	0.4074	92.84	50.11%
Low pH	1	1	Photogrammetry	A0029_F01_PtG01	A0029_F02_PtG01	0.2306	0.0552	0.0618	0.3617	107.31	51.86%
Low pH	1	1	Structured light	A0029_F01_StL01	A0029_F02_StL01	0.6246	0.0491	0.0728	0.3462	126.84	55.49%
Low pH	2	28	Laser scanning	A0018_F01_LaS02	A0018_F02_LaS02	0.3827	0.3222	0.4551	3.2334	30.48	16.24%
Low pH	2	28	Photogrammetry	A0018_F01_PtG02	A0018_F02_PtG02	0.5774	0.3346	0.4037	2.8015	32.42	18.21%
Low pH	2	28	Structured light	A0018_F01_StL02	A0018_F02_StL02	0.4185	0.3331	0.2027	1.1396	28.74	16.21%
Low pH	3	56	Laser scanning	A0020_F01_LaS03	A0020_F02_LaS03	0.9608	0.2342	0.4670	2.6352	41.39	16.14%
Low pH	3	56	Photogrammetry	A0020_F01_PtG03	A0020_F02_PtG03	1.3106	0.2864	0.2079	3.0971	22.05	15.71%
Low pH	3	56	Structured light	A0020_F01_StL03	A0020_F02_StL03	1.2345	0.3081	0.6187	0.7107	17.23	16.47%
Low pH	4	84	Laser scanning	A0020_F01_LaS04	A0020_F02_LaS04	1.4018	0.9662	0.1347	2.1477	11.86	5.08%
Low pH	4	84	Photogrammetry	A0020_F01_PtG04	A0020_F02_PtG04	1.0644	1.1328	0.3711	2.2051	6.70	5.48%

Experiment	Phase	Days	Scanner type	Reference model	Compared Model	Point Pair Alignment RMS	Segmented Fine Alignment RMS	C2M signed Distance Mean	C2M Signed Distance Std Dev (2σ)	Fitting surface (+/- 0.1 mm) area	% of fracture surface within +- 0.1mm
Low pH	4	84	Structured light	A0020_F01_StL04	A0020_F02_StL04	1.4927	0.8021	0.5214	1.2452	6.04	7.55%
High pH	3	56	Laser scanning	A0013_F01_LaS03	A0013_F02_LaS03	0.3737	0.0677	0.0577	0.4625	84.67	38.95%
High pH	3	56	Structured light	A0013_F01_StL03	A0013_F02_StL03	0.4434	0.0776	0.0430	0.5792	118.55	55.82%
High pH	4	84	Laser scanning	A0013_F01_LaS04	A0013_F02_LaS04	0.1470	0.0547	0.0516	0.3914	133.45	55.58%
High pH	4	84	Macro structured light	A0013_F01_MSL04	A0013_F02_MSL04	0.3553	0.0618	0.0414	0.3395	155.71	59.99%
High pH	4	84	Photogrammetry	A0013_F01_PtG04	A0013_F02_PtG04	0.2536	0.1103	0.1680	0.7597	70.05	35.31%
High pH	4	84	Structured light	A0013_F01_StL04	A0013_F02_StL04	0.4084	0.0552	0.0437	0.3767	130.18	60.25%
High UV	1	1	Macro structured light	A0025_F04_MSL01	A0025_F05_MSL01	0.2107	0.0479	0.0530	0.3179	182.49	58.73%
High UV	1	1	Laser scanning	A0029_F01_LaS01	A0029_F02_LaS01	0.2075	0.0598	0.0932	0.4074	92.84	50.11%
High UV	1	1	Macro structured light	A0029_F01_MSL01	A0029_F02_MSL01	0.6612	0.0483	0.0526	0.3130	137.44	62.11%
High UV	1	1	Photogrammetry	A0029_F01_PtG01	A0029_F02_PtG01	0.2306	0.0552	0.0618	0.3617	107.31	51.86%
High UV	1	1	Structured light	A0029_F01_StL01	A0029_F02_StL01	0.6246	0.0491	0.0728	0.3462	126.84	55.49%
High UV	2	28	Laser scanning	A0025_F04_LaS02	A0025_F05_LaS02	0.9783	0.0811	0.0541	0.4497	106.83	32.11%
High UV	2	28	Macro structured light	A0025_F04_MSL02	A0025_F05_MSL02	0.4962	0.0899	0.0473	0.3867	155.94	45.99%
High UV	2	28	Photogrammetry	A0025_F04_PtG02	A0025_F05_PtG02	0.1168	0.2465	0.0423	0.7009	33.39	11.71%
High UV	2	28	Structured light	A0025_F04_StL02	A0025_F05_StL02	0.2336	0.0810	0.0560	0.4084	129.36	43.48%
High UV	3	56	Laser scanning	A0025_F04_LaS03	A0025_F05_LaS03	0.3786	0.2181	0.0271	0.4738	108.12	30.21%
High UV	3	56	Macro structured light	A0025_F04_MSL03	A0025_F05_MSL03	0.4316	0.0733	0.0305	0.4239	143.00	39.50%
High UV	3	56	Photogrammetry	A0025_F04_PtG03	A0025_F05_PtG03	0.2188	0.0998	0.0437	0.6112	86.66	31.41%

Experiment	Phase	Days	Scanner type	Reference model	Compared Model	Point Pair Alignment RMS	Segmented Fine Alignment RMS	C2M signed Distance Mean	C2M Signed Distance Std Dev (2σ)	Fitting surface (+/- 0.1 mm) area	% of fracture surface within +- 0.1mm
High UV	3	56	Structured light	A0025_F04_StL03	A0025_F05_StL03	0.2710	0.0666	0.0260	0.4406	120.95	36.97%

Appendix K: 3D Digital Models

The 3D digital models produced for all samples digitised for this thesis are included on the SD card attached to the back cover of the thesis.